Science sets the bar for women in combat *p. 468*

Freshwater governance: Local or global? *pp. 478 & 479*

Legacies of drought in forest ecosystems *p. 528*

Science

$10
31 JULY 2015
sciencemag.org

AAAS

Philae's first look

Reporting back from the surface of comet 67P *pp. 459 & 493*

CONTENTS

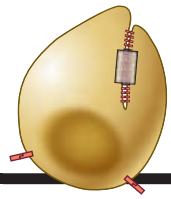

476 & 499
p53 and autoimmunity

31 JULY 2015 • VOLUME 349 • ISSUE 6247

NEWS

IN BRIEF

456 Roundup of the week's news

IN DEPTH

459 **COMET LANDER'S SCIENTIFIC HARVEST MAY BE ITS LAST**
Philae has fallen silent after fragmentary messages *By E. Hand*
▸ PHILAE'S FIRST LOOK SECTION P. 493

460 **TINY BUILT-IN LASERS LIGHT UP LIVING CELLS**
Technique could revolutionize tracking of individual cells *By A. Cho*

461 **RISK OF 'LEAKY' VACCINES DEBATED**
Controversial finding suggests they can speed the spread of deadly pathogens *By K. Kupferschmidt*

462 **FORENSIC LABS EXPLORE BLIND TESTING TO PREVENT ERRORS**
Evidence examiners get practical about fighting cognitive bias *By K. Servick*

463 **FORMER HEAD OF CHINA'S LEADING GENOME INSTITUTE STARTS NEW CHAPTER**
Jun Wang will concentrate on a new artificial intelligence initiative
By D. Normile

464 **ALZHEIMER'S AMYLOID THEORY GETS MODEST BOOST**
Trials of antibody drugs spawn hopes, doubts—and plans for more tests
By E. Underwood

FEATURES

465 **COSMIC CONVERGENCE**
Neutrinos from beyond our galaxy could be close kin to other mysterious visitors from space *By A. Cho*

468 **SETTING THE BAR**
As the U.S. military opens ground combat roles to women, it's looking to scientists to help define the standards
By K. Servick

INSIGHTS

PERSPECTIVES

472 **TWO LEAPS FORWARD FOR ROBOT LOCOMOTION**
Biomimetic robots can jump on land and on water *By D. Vella*
▸ REPORT P. 517

473 **A LEAP AHEAD FOR ACTIVATING C-H BONDS**
Boron-based catalysts add functional groups to normally unreactive carbon-hydrogen bonds
By S. K. Bose and T. B. Marder
▸ REPORT P. 513

475 **ANCIENT PLANETARY DYNAMOS, TAKE TWO**
Magnetic studies of Earth and Mercury constrain their ancient core dynamics
By J. Aubert
▸ REPORT P. 521

476 **A p53-REGULATED IMMUNE CHECKPOINT RELEVANT TO CANCER**
The tumor suppressor p53 may influence the ability of cancer cells to escape immune detection *By L. Zitvogel and G. Kroemer*
▸ RESEARCH ARTICLE P. 499

WATER

478 **Fresh water goes global**
By C. J. Vörösmarty et al.

479 **Local perspectives on water**
By J. G. Hering et al.

481 **AVERTING A NORTH AMERICAN BIODIVERSITY CRISIS**
A newly described pathogen poses a major threat to salamanders via trade
By T. A. Yap et al.

BOOKS *ET AL.*

483 **POSTGENOMICS**
S. S. Richardson and H. Stevens, Eds., reviewed by P. W. Hughes

484 **APPLIED MINDS**
By G. Madhavan, reviewed by S. Derrible

LETTERS

486 **SCIENCE IN CONGRESS: GOOD-FAITH DEBATE**
By J. W. Conrad Jr.

486 **SCIENCE IN CONGRESS: UNNECESSARY CONFLICT**
By R. O. McClellan

487 **SCIENCE IN CONGRESS: DECEPTIVE STATISTICS**
By G. K. Evans

487 **RESPONSE**
By A. A. Rosenberg et al.

487 **TECHNICAL COMMENT ABSTRACTS**

RESEARCH

IN BRIEF

490 From *Science* and other journals

REVIEW

498 **CRYSTAL GROWTH**
Crystallization by particle attachment in synthetic, biogenic, and geologic environments *J. J. De Yoreo* et al.
REVIEW SUMMARY; FOR FULL TEXT: dx.doi.org/10.1126/science.aaa6760

Published by AAAS

472 & 517

Walking on water

459 & 493

Feedback from Philae

SPECIAL SECTION

Philae's first look

INTRODUCTION

493 Philae's first days on the comet *J.-P. Bibring* et al.

RESEARCH ARTICLE ABSTRACTS

The landing(s) of Philae and inferences about comet surface mechanical properties *J. Biele* et al.

Properties of the 67P/Churyumov-Gerasimenko interior revealed by CONSERT radar *W. Kofman* et al.

REPORT ABSTRACTS

The nonmagnetic nucleus of comet 67P/Churyumov-Gerasimenko *H.-U. Auster* et al.

Thermal and mechanical properties of the near-surface layers of comet 67P/Churyumov-Gerasimenko *T. Spohn* et al.

The structure of the regolith on 67P/Churyumov-Gerasimenko from ROLIS descent imaging *S. Mottola* et al.

67P/Churyumov-Gerasimenko surface properties as derived from CIVA panoramic images *J.-P. Bibring* et al.

CHO-bearing organic compounds at the surface of 67P/Churyumov-Gerasimenko revealed by Ptolemy *I. P. Wright* et al.

Organic compounds on comet 67P/Churyumov-Gerasimenko revealed by COSAC mass spectrometry *F. Goesmann* et al.

SEE ALSO

▸ NEWS STORY P. 459

▸ PODCAST

▸ news.sciencemag.org/tags/rosetta

RESEARCH ARTICLES

499 **CELL DEATH**

Control of signaling-mediated clearance of apoptotic cells by the tumor suppressor p53 *K. W. Yoon* et al.

RESEARCH ARTICLE SUMMARY; FOR FULL TEXT: dx.doi.org/10.1126/science.1261669

▸ PERSPECTIVE P. 476

500 **METABOLISM**

S-Nitrosylation links obesity-associated inflammation to endoplasmic reticulum dysfunction *L. Yang* et al.

REPORTS

506 **HEAVY FERMIONS**

Strange metal without magnetic criticality *T. Tomita* et al.

510 **REACTION DYNAMICS**

Spectroscopic observation of resonances in the F + H_2 reaction *J. B. Kim* et al.

513 **BORON CATALYSIS**

Metal-free catalytic C-H bond activation and borylation of heteroarenes *M.-A. Légaré* et al.

▸ PERSPECTIVE P. 473

517 **BIOMECHANICS**

Jumping on water: Surface tension–dominated jumping of water striders and robotic insects *J.-S. Koh* et al.

▸ PERSPECTIVE P. 472

521 **PALEOMAGNETISM**

A Hadean to Paleoarchean geodynamo recorded by single zircon crystals *J. A. Tarduno* et al.

▸ PERSPECTIVE P. 475

524 **NANOELECTRONICS**

Epitaxial growth of a monolayer WSe_2-MoS_2 lateral p-n junction with an atomically sharp interface *M.-Y. Li* et al.

528 **FOREST ECOLOGY**

Pervasive drought legacies in forest ecosystems and their implications for carbon cycle models *W. R. L. Anderegg* et al.

532 **GLOBAL WARMING**

Recent hiatus caused by decadal shift in Indo-Pacific heating *V. Nieves* et al.

535 **ACTIN-DIRECTED TOXIN**

ACD toxin–produced actin oligomers poison formin-controlled actin polymerization *D. B. Heisler* et al.

540 **PLANT EVOLUTION**

Convergent evolution of strigolactone perception enabled host detection in parasitic plants *C. E. Conn* et al.

DEPARTMENTS

455 **EDITORIAL**

A tale of two states *By Mandë Holford and Rodney Nichols*

554 **WORKING LIFE**

Why not have a life? *By Gary McDowell*

ON THE COVER

Artistic rendering of the Philae lander on the surface of comet 67P/Churyumov-Gerasimenko. On 12 November 2014, after descending from the Rosetta orbiter (background), Philae bounced upon touchdown, eventually coming to rest at the site known as Abydos. A set of eight papers describes the initial scientific results from Philae's approach and first days on the comet. See pages 459 and 493 and news.sciencemag.org/tags/rosetta. *Image: © A. Torres (CNES)/J.-P. Bibring (IAS) /Lander CAD: Philae-DLR/Ill. D. Ducros*

Science Staff 454

AAAS News & Notes 488

New Products 547

Science Careers 548

SCIENCE (ISSN 0036-8075) is published weekly on Friday, except the last week in December, by the American Association for the Advancement of Science, 1200 New York Avenue, NW, Washington, DC 20005. Periodicals mail postage (publication No. 484460) paid at Washington, DC, and additional mailing offices.

Copyright © 2015 by the American Association for the Advancement of Science. The title SCIENCE is a registered trademark of the AAAS.

Domestic individual membership and subscription (51 issues): $153 ($74 allocated to subscription). Domestic institutional subscription (51 issues): $1282; Foreign postage extra: Mexico, Caribbean (surface mail) $55; other countries (air assist delivery) $85. First class, airmail, student, and emeritus rates on request. Canadian rates with GST available upon request, GST #1254 88122. Publications Mail Agreement Number 1069624. **Printed in the U.S.A.**

Change of address: Allow 4 weeks, giving old and new addresses and 8-digit account number. **Postmaster:** Send change of address to AAAS, P.O. Box 96178, Washington, DC 20090–6178. **Single-copy sales:** $10.00 current issue, $15.00 back issue prepaid includes surface postage; bulk rates on request.

Authorization to photocopy material for internal or personal use under circumstances not falling within the fair use provisions of the Copyright Act is granted by AAAS to libraries and other users registered with the Copyright Clearance Center (CCC) Transactional Reporting Service, provided that $30.00 per article is paid directly to CCC, 222 Rosewood Drive, Danvers, MA 01923. The identification code for *Science* is 0036-8075. *Science* is indexed in the *Reader's Guide to Periodical Literature* and in several specialized indexes.

Published by AAAS

Science
AAAS
1200 New York Avenue, NW, Washington, DC 20005
Bateman House, 82-88 Hills Road, Cambridge, UK CB2 1LQ

Editor-in-Chief Marcia McNutt
Executive Editor Monica M. Bradford **News Editor** Tim Appenzeller
Managing Editor, Research Journals Katrina L. Kelner
Deputy Editors Barbara R. Jasny, Andrew M. Sugden(UK), Valda J. Vinson, Jake S. Yeston

Research and Insights

SR. EDITORS Caroline Ash(UK), Gilbert J. Chin, Lisa D. Chong, Julia Fahrenkamp-Uppenbrink(UK), Pamela J. Hines, Stella M. Hurtley(UK), Paula A. Kiberstis, Marc S. Lavine(Canada), Kristen L. Mueller, Ian S. Osborne(UK), Beverly A. Purnell, L. Bryan Ray, Guy Riddihough, H. Jesse Smith, Jelena Stajic, Peter Stern(UK), Phillip D. Szuromi, Brad Wible, Nicholas S. Wigginton, Laura M. Zahn **ASSOCIATE EDITORS** Brent Grocholski, Keith T. Smith, Sacha Vignieri **ASSOCIATE BOOK REVIEW EDITOR** Valerie B. Thompson **ASSOCIATE LETTERS EDITOR** Jennifer Sills **CHIEF CONTENT PRODUCTION EDITOR** Cara Tate **SR. CONTENT PRODUCTION EDITORS** Harry Jach **CONTENT PRODUCTION EDITORS** Jeffrey E. Cook, Chris Filiatreau, Cynthia Howe, Lauren Kmec, Barbara P. Ordway, Catherine Wolner **SR. EDITORIAL COORDINATORS** Carolyn Kyle, Beverly Shields **EDITORIAL COORDINATORS** Ramatoulaye Diop, Joi S. Granger, Lisa Johnson, Anita Wynn **PUBLICATIONS ASSISTANTS** Aneera Dobbins, Jeffrey Hearn, Dona Mathieu, Le-Toya Mayne Flood, Shannon McMahon, Scott Miller, Jerry Richardson, Rachel Roberts(UK), Alice Whaley(UK), Brian White **EXECUTIVE ASSISTANT** Anna Bashkirova **ADMINISTRATIVE SUPPORT** Janet Clements(UK), Lizanne Newton(UK), Maryrose Madrid, Laura-Nadine Schuhmacher (UK, Intern), Alix Welch (Intern), John Wood(UK)

News

NEWS MANAGING EDITOR John Travis **INTERNATIONAL EDITOR** Richard Stone **DEPUTY NEWS EDITORS** Daniel Clery(UK), Robert Coontz, Elizabeth Culotta, David Grimm, David Malakoff, Leslie Roberts **CONTRIBUING EDITOR** Martin Enserink(Europe) **SR. CORRESPONDENTS** Jeffrey Mervis, Elizabeth Pennisi **NEWS WRITERS** Adrian Cho, Jon Cohen, Jennifer Couzin-Frankel, Carolyn Gramling, Eric Hand, Jocelyn Kaiser, Catherine Matacic, Kelly Servick, Robert F. Service, Erik Stokstad(Cambridge, UK), Emily Underwood **INTERNS** Hanae Armitage, Emily DeMarco, Annick Laurent, Laura Olivieri, Juan David Romero **CONTRIBUTING CORRESPONDENTS** Michael Balter(Paris), John Bohannon, Ann Gibbons, Mara Hvistendahl, Sam Kean, Richard A. Kerr, Eli Kintisch, Kai Kupferschmidt(Berlin), Andrew Lawler, Christina Larson(Beijing), Mitch Leslie, Charles C. Mann, Eliot Marshall, Virginia Morell, Dennis Normile(Tokyo), Heather Pringle, Tania Rabesandratana(London), Gretchen Vogel(Berlin), Lizzie Wade(Mexico City) **CAREERS** Donisha Adams, Rachel Bernstein **COPY EDITORS** Julia Cole, Jennifer Levin (Chief) **ADMINISTRATIVE SUPPORT** Jessica Williams

Executive Publisher Rush D. Holt
Publisher Kent R. Anderson **Chief Digital Media Officer** Rob Covey

BUSINESS OPERATIONS AND PORTFOLIO MANAGEMENT DIRECTOR Sarah Whalen **BUSINESS SYSTEMS AND FINANCIAL ANALYSIS DIRECTOR** Randy Yi **MANAGER OF FULFILLMENT SYSTEMS** Neal Hawkins **SYSTEMS ANALYST** Nicole Mehmedovich **ASSISTANT DIRECTOR, BUSINESS OPERATIONS** Eric Knott **MANAGER, BUSINESS OPERATIONS** Jessica Tierney **BUSINESS ANALYSTS** Cory Lipman, Cooper Tilton, Celeste Troxler **FINANCIAL ANALYST** Robert Clark **RIGHTS AND PERMISSIONS ASSISTANT DIRECTOR** Emilie David **PERMISSIONS ASSOCIATE** Elizabeth Sandler **RIGHTS, CONTRACTS, AND LICENSING ASSOCIATE** Lili Kiser

MARKETING DIRECTOR Ian King **MARKETING MANAGER** Julianne Wielga **MARKETING ASSOCIATE** Elizabeth Sattler **SR. MARKETING EXECUTIVE** Jennifer Reeves **SR. ART ASSOCIATE, PROJECT MANAGER** Tzeitel Sorrosa **ART ASSOCIATE** Seil Lee **JR. ART ASSOCIATE** Kim Huynh **ASSISTANT COMMERCIAL EDITOR** Selby Frame **MARKETING PROJECT MANAGER** Angelissa McArthur **PROGRAM DIRECTOR, AAAS MEMBER CENTRAL** Peggy Mihelich **FULFILLMENT SYSTEMS AND OPERATIONS** membership@aaas.org **MANAGER, MEMBER SERVICES** Pat Butler **SPECIALISTS** LaToya Casteel, Terrance Morrison, Latasha Russell **MANAGER, DATA ENTRY** Mickie Napoleoni **DATA ENTRY SPECIALISTS** JJ Regan, Brenden Aquilino, Fiona Giblin

DIRECTOR, SITE LICENSING Tom Ryan **DIRECTOR, CORPORATE RELATIONS** Eileen Bernadette Moran **SR. PUBLISHER RELATIONS SPECIALIST** Kiki Forsythe **PUBLISHER RELATIONS MANAGER** Catherine Holland **PUBLISHER RELATIONS, EASTERN REGION** Keith Layson **PUBLISHER RELATIONS, WESTERN REGION** Ryan Rexroth **SALES RESEARCH COORDINATOR** Aiesha Marshall **MANAGER, SITE LICENSE OPERATIONS** Iquo Edim **SENIOR PRODUCTION SPECIALIST** Robert Koepke **SENIOR OPERATIONS ANALYST** Lana Guz **FULFILLMENT ANALYST** Judy Lillibridge **ASSOCIATE DIRECTOR, MARKETING** Christina Schlecht **MARKETING ASSOCIATES** Thomas Landreth, Isa Sesay-Bah

DIRECTOR OF WEB TECHNOLOGIES Ahmed Khadr **SR. DEVELOPER** Chris Coleman **DEVELOPERS** Dan Berger, Jimmy Marks **SR. PROJECT MANAGER** Trista Smith **SYSTEMS ENGINEER** Luke Johnson

CREATIVE DIRECTOR, MULTIMEDIA Martyn Green **DIRECTOR OF ANALYTICS** Enrique Gonzales **SR. WEB PRODUCER** Sarah Crespi **WEB PRODUCER** Alison Crawford **VIDEO PRODUCER** Nguyen Nguyen **SOCIAL MEDIA PRODUCER** Meghna Sachdev

DIRECTOR OF OPERATIONS PRINT AND ONLINE Lizabeth Harman **DIGITAL/PRINT STRATEGY MANAGER** Jason Hillman **QUALITY TECHNICAL MANAGER** Marcus Spiegler **DIGITAL PRODUCTION MANAGER** Lisa Stanford **ASSISTANT MANAGER DIGITAL/PRINT** Rebecca Doshi **DIGITAL MEDIA SPECIALIST** Tara Kelly **SENIOR CONTENT SPECIALISTS** Steve Forrester, Antoinette Hodal, Lori Murphy, Anthony Rosen **CONTENT SPECIALISTS** Jacob Hedrick, Kimberley Oster

DESIGN DIRECTOR Beth Rakouskas **DESIGN EDITOR** Marcy Atarod **SENIOR SCIENTIFIC ILLUSTRATORS** Chris Bickel, Katharine Sutliff **SCIENTIFIC ILLUSTRATOR** Valerie Altounian **SENIOR ART ASSOCIATES** Holly Bishop, Preston Huey **SENIOR DESIGNER** Garvin Grullón **DESIGNER** Chrystal Smith **SENIOR PHOTO EDITOR** William Douthitt **PHOTO EDITORS** Leslie Blizard, Christy Steele

DIRECTOR, GLOBAL COLLABORATION, CUSTOM PUBLICATIONS, ADVERTISING Bill Moran **EDITOR, CUSTOM PUBLISHING** Sean Sanders: 202-326-6430 **ASSISTANT EDITOR, CUSTOM PUBLISHING** Tianna Hicklin: 202-326-6463 **ADVERTISING MARKETING MANAGER** Justin Sawyers: 202-326-7061 science_advertising@aaas.org **ADVERTISING MARKETING ASSOCIATE** Javia Flemmings **ADVERTISING SUPPORT MANAGER** Karen Foote: 202-326-6740 **ADVERTISING PRODUCTION OPERATIONS MANAGER** Deborah Tompkins **SR. PRODUCTION SPECIALIST/GRAPHIC DESIGNER** Amy Hardcastle **PRODUCTION SPECIALIST** Yuse Lajiminmuhip **SR. TRAFFIC ASSOCIATE** Christine Hall **SALES COORDINATOR** Shirley Young **ASSOCIATE DIRECTOR, COLLABORATION, CUSTOM PUBLICATIONS/CHINA/TAIWAN/KOREA/SINGAPORE** Ruolei Wu: +86-186 0822 9345, rwu@aaas.org **COLLABORATION/ CUSTOM PUBLICATIONS/JAPAN** Adarsh Sandhu + 81532-81-5142 asandhu@aaas.org **EAST COAST/E. CANADA** Laurie Faraday: 508-747-9395, FAX 617-507-8189 **WEST COAST/W. CANADA** Lynne Stickrod: 415-931-9782, FAX 415-520-6940 **MIDWEST** Jeffrey Dembski: 847-498-4520 x3005, Steven Loerch: 847-498-4520 x3006 **UK EUROPE/ASIA** Roger Goncalves: TEL/FAX +41 43 243 1358 **JAPAN** Katsuyoshi Fukamizu(Tokyo): +81-3-3219-5777 kfukamizu@aaas.org **CHINA/TAIWAN** Ruolei Wu: +86-186 0822 9345, rwu@aaas.org

WORLDWIDE ASSOCIATE DIRECTOR OF SCIENCE CAREERS Tracy Holmes: +44 (0) 1223 326525, FAX +44 (0) 1223 326532 tholmes@science-int.co.uk **CLASSIFIED** advertise@sciencecareers.org **U.S. SALES** Tina Burks: 202-326-6577, Nancy Toema: 202-326-6578 **SALES ADMINISTRATOR** Marci Gallun **EUROPE/ROW SALES** Axel Gesatzki, Sarah Lelarge **SALES ASSISTANT** Kelly Grace **JAPAN** Hiroyuki Mashiki(Kyoto): +81-75-823-1109 hmashiki@aaas.org **CHINA/TAIWAN** Ruolei Wu: +86-186 0082 9345 rwu@aaas.org **MARKETING MANAGER** Allison Pritchard **MARKETING ASSOCIATE** Aimee Aponte

AAAS BOARD OF DIRECTORS RETIRING PRESIDENT, CHAIR Gerald R. Fink **PRESIDENT** Geraldine (Geri) Richmond **PRESIDENT-ELECT** Barbara A. Schaal **TREASURER** David Evans Shaw **CHIEF EXECUTIVE OFFICER** Rush D. Holt **BOARD** Bonnie L. Bassler, May R. Berenbaum, Carlos J. Bustamante, Stephen P.A. Fodor, Claire M. Fraser, Michael S. Gazzaniga, Laura H. Greene, Elizabeth Loftus, Mercedes Pascual

SUBSCRIPTION SERVICES For change of address, missing issues, new orders and renewals, and payment questions: 866-434-AAAS (2227) or 202-326-6417, FAX 202-842-1065. Mailing addresses: AAAS, P.O. Box 96178, Washington, DC 20090-6178 or AAAS Member Services, 1200 New York Avenue, NW, Washington, DC 20005

INSTITUTIONAL SITE LICENSES 202-326-6755 **REPRINTS:** Author Inquiries 800-635-7181 **COMMERCIAL INQUIRIES** 803-359-4578 **PERMISSIONS** 202-326-6765, permissions@aaas.org **AAAS Member Services** 202-326-6417 or http://membercentral.aaas.org/discounts

Science serves as a forum for discussion of important issues related to the advancement of science by publishing material on which a consensus has been reached as well as including the presentation of minority of conflicting points of view. Accordingly, all articles published in *Science*—including editorials, news and comment, and books reviews—are signed and reflect the individual views of the authors and not official points of view adopted by AAAS or the institutions with which the authors are affiliated.

INFORMATION FOR AUTHORS See pages 678 and 679 of the 6 February 2015 issue or access www.sciencemag.org/about/authors

SENIOR EDITORIAL BOARD

Robert H. Grubbs, *California Institute of Technology,* **Gary King,** *Harvard University*
Susan M. Rosenberg, *Baylor College of Medicine,* **Ali Shilatifard,** *Northwestern University*
Feinberg School of Medicine, **Michael S. Turner**, *U. of Chicago*

BOARD OF REVIEWING EDITORS (Statistics board members indicated with **(S)**)

Adriano Aguzzi, *U. Hospital Zürich*
Takuzo Aida, *U. of Tokyo*
Leslie Aiello, *Wenner-Gren Foundation*
Judith Allen, *U. of Edinburgh*
Sonia Altizer, *U. of Georgia*
Sebastian Amigorena, *Institut Curie*
Kathryn Anderson, *Memorial Sloan-Kettering Cancer Center*
Meinrat O. Andreae, *Max-Planck Inst. Mainz*
Paola Arlotta, *Harvard U.*
Johan Auwerx, *EPFL*
David Awschalom, *U. of Chicago*
Jordi Bascompte, *Estación Biológica de Doñana CSIC*
Facundo Batista, *London Research Inst.*
Ray H. Baughman, *U. of Texas, Dallas*
David Baum, *U. of Wisconsin*
Carlo Beenakker, *Leiden U.*
Kamran Behnia, *ESPCI-ParisTech*
Yasmine Belkaid, *NIAID, NIH*
Philip Benfey, *Duke U.*
Stephen J. Benkovic, *Penn State U.*
May Berenbaum, *U. of Illinois*
Gabriele Bergers, *U. of California, San Francisco*
Bradley Bernstein, *Massachusettes General Hospital*
Peer Bork, *EMBL*
Bernard Bourdon, *Ecole Normale Supérieure de Lyon*
Chris Bowler, *École Normale Supérieure*
Ian Boyd, *U. of St. Andrews*
Emily Brodsky, *U. of California, Santa Cruz*
Ron Brookmeyer, *U. of California Los Angeles* **(S)**
Christian Büchel, *U. Hamburg-Eppendorf*
Joseph A. Burns, *Cornell U.*
Gyorgy Buzsaki, *New York U. School of Medicine*
Blanche Capel, *Duke U.*
Mats Carlsson, *U. of Oslo*
David Clapham, *Children's Hospital Boston*
David Clary, *U. of Oxford*
Joel Cohen, *Rockefeller U., Columbia U.*
James Collins, *Boston U.*
Robert Cook-Deegan, *Duke U.*
Alan Cowman, *Walter & Eliza Hall Inst.*
Robert H. Crabtree, *Yale U.*
Roberta Croce, *Vrije Universiteit*
Janet Currie, *Princeton U.*
Jeff L. Dangl, *U. of North Carolina*
Tom Daniel, *U. of Washington*
Frans de Waal, *Emory U.*
Stanislas Dehaene, *Collège de France*
Robert Desimone, *MIT*
Claude Desplan, *New York U.*
Ap Dijksterhuis, *Radboud U. of Nijmegen*
Dennis Discher, *U. of Pennsylvania*
Gerald W. Dorn II, *Washington U. School of Medicine*
Jennifer A. Doudna, *U. of California, Berkeley*
Bruce Dunn, *U. of California, Los Angeles*
Christopher Dye, *WHO*
Todd Ehlers, *U. of Tuebingen*
David Ehrhardt, *Carnegie Inst. of Washington*
Tim Elston, *U. of North Carolina at Chapel Hill*
Gerhard Ertl, *Fritz-Haber-Institut, Berlin*
Barry Everitt, *U. of Cambridge*
Ernst Fehr, *U. of Zurich*
Anne C. Ferguson-Smith, *U. of Cambridge*
Michael Feuer, *The George Washington U.*
Toren Finkel, *NHLBI, NIH*
Kate Fitzgerald, *U. of Massachusetts*
Peter Fratzl, *Max-Planck Inst.*
Elaine Fuchs, *Rockefeller U.*
Daniel Geschwind, *UCLA*
Andrew Gewirth, *U. of Illinois*
Karl-Heinz Glassmeier, *TU Braunschweig*
Ramon Gonzalez, *Rice U.*
Julia R. Greer, *Caltech*
Elizabeth Grove, *U. of Chicago*
Nicolas Gruber, *ETH Zurich*
Kip Guy, *St. Jude's Children's Research Hospital*
Taekjip Ha, *U. of Illinois at Urbana-Champaign*
Christian Haass, *Ludwig Maximilians U.*
Steven Hahn, *Fred Hutchinson Cancer Research Center*
Michael Hasselmo, *Boston U.*
Martin Heimann, *Max-Planck Inst. Jena*
Yka Helariutta, *U. of Cambridge*
James A. Hendler, *Rensselaer Polytechnic Inst.*
Janet G. Hering, *Swiss Fed. Inst. of Aquatic Science & Technology*
Kai-Uwe Hinrichs, *U. of Bremen*
Kei Hirose, *Tokyo Inst. of Technology*
David Hodell, *U. of Cambridge*
David Holden, *Imperial College*
Lora Hooper, *UT Southwestern Medical Ctr. at Dallas*
Raymond Huey, *U. of Washington*
Steven Jacobsen, *U. of California, Los Angeles*
Kai Johnsson, *EPFL Lausanne*
Peter Jonas, *Inst. of Science & Technology (IST) Austria*
Matt Kaeberlein, *U. of Washington*
William Kaelin Jr., *Dana-Farber Cancer Inst.*
Daniel Kahne, *Harvard U.*
Daniel Kammen, *U. of California, Berkeley*
Masashi Kawasaki, *U. of Tokyo*
V. Narry Kim, *Seoul National U.*
Joel Kingsolver, *U. of North Carolina at Chapel Hill*
Robert Kingston, *Harvard Medical School*
Etienne Koechlin, *Ecole Normale Supérieure*
Alexander Kolodkin, *Johns Hopkins U.*
Alberto R. Kornblihtt, *U. of Buenos Aires*
Leonid Kruglyak, *UCLA*
Thomas Langer, *U. of Cologne*
Mitchell A. Lazar, *U. of Pennsylvania*
David Lazer, *Harvard U.*
Thomas Lecuit, *IBDM*
Virginia Lee, *U. of Pennsylvania*
Stanley Lemon, *U. of North Carolina at Chapel Hill*
Ottoline Leyser, *Cambridge U.*
Marcia C. Linn, *U. of California, Berkeley*
Jianguo Liu, *Michigan State U.*
Luis Liz-Marzan, *CIC biomaGUNE*
Jonathan Losos, *Harvard U.*
Ke Lu, *Chinese Acad. of Sciences*
Christian Lüscher, *U. of Geneva*
Laura Machesky, *CRUK Beatson Inst. for Cancer Research*
Anne Magurran, *U. of St. Andrews*
Oscar Marin, *CSIC & U. Miguel Hernández*
Charles Marshall, *U. of California, Berkeley*
C. Robertson McClung, *Dartmouth College*
Graham Medley, *U. of Warwick*
Tom Misteli, *NCI*
Yasushi Miyashita, *U. of Tokyo*
Mary Ann Moran, *U. of Georgia*
Richard Morris, *U. of Edinburgh*
Alison Motsinger-Reif, *NC State U.* **(S)**
Sean Munro, *MRC Lab. of Molecular Biology*
Thomas Murray, *The Hastings Center*
James Nelson, *Stanford U. School of Med.*
Daniel Neumark, *U. of California, Berkeley*
Kitty Nijmeijer, *U. of Twente*
Pär Nordlund, *Karolinska Inst.*
Helga Nowotny, *European Research Advisory Board*
Ben Olken, *MIT*
Joe Orenstein, *U. of California Berkeley & Lawrence Berkeley National Lab*
Harry Orr, *U. of Minnesota*
Andrew Oswald, *U. of Warwick*
Steve Palumbi, *Stanford U.*
Jane Parker, *Max-Planck Inst. of Plant Breeding Research*
Giovanni Parmigiani, *Dana-Farber Cancer Inst.* **(S)**
Donald R. Paul, *U. of Texas, Austin*
John H. J. Petrini, *Memorial Sloan-Kettering Cancer Center*
Joshua Plotkin, *U. of Pennsylvania*
Albert Polman, *FOM Institute AMOLF*
Philippe Poulin, *CNRS*
Jonathan Pritchard, *Stanford U.*
David Randall, *Colorado State U.*
Colin Renfrew, *U. of Cambridge*
Felix Rey, *Institut Pasteur*
Trevor Robbins, *U. of Cambridge*
Jim Roberts, *Fred Hutchinson Cancer Research Ctr.*
Barbara A. Romanowicz, *U. of California,Berkeley*
Jens Rostrup-Nielsen, *Haldor Topsoe*
Mike Ryan, *U. of Texas, Austin*
Mitinori Saitou, *Kyoto U.*
Shimon Sakaguchi, *Kyoto U.*
Miquel Salmeron, *Lawrence Berkeley National Lab*
Jürgen Sandkühler, *Medical U. of Vienna*
Alexander Schier, *Harvard U.*
Randy Seeley, *U. of Cincinnati*
Vladimir Shalaev, *Purdue U.*
Robert Siliciano, *Johns Hopkins School of Medicine*
Denis Simon, *Arizona State U.*
Alison Smith, *John Innes Centre*
Richard Smith, *U. of North Carolina* **(S)**
John Speakman, *U. of Aberdeen*
Allan C. Spradling, *Carnegie Institution of Washington*
Jonathan Sprent, *Garvan Inst. of Medical Research*
Eric Steig, *U. of Washington*
Paula Stephan, *Georgia State U. and National Bureau of Economic Research*
Molly Stevens, *Imperial College London*
V. S. Subrahmanian, *U. of Maryland*
Ira Tabas, *Columbia U.*
Sarah Teichmann, *Cambridge U.*
John Thomas, *North Carolina State U.*
Shubha Tole, *Tata Institute of Fundamental Research*
Christopher Tyler-Smith, *The Wellcome Trust Sanger Inst.*
Herbert Virgin, *Washington U.*
Bert Vogelstein, *Johns Hopkins U.*
Cynthia Volkert, *U. of Göttingen*
Douglas Wallace, *Dalhousie U.*
David Wallach, *Weizmann Inst. of Science*
Ian Walmsley, *U. of Oxford*
Jane-Ling Wang, *U. of California, Davis*
David A. Wardle, *Swedish U. of Agric. Sciences*
David Waxman, *Fudan U.*
Jonathan Weissman, *U. of California, San Francisco*
Chris Wikle, *U. of Missouri* **(S)**
Ian A. Wilson, *The Scripps Res. Inst.* **(S)**
Timothy D. Wilson, *U. of Virginia*
Rosemary Wyse, *Johns Hopkins U.*
Jan Zaanen, *Leiden U.*
Kenneth Zaret, *U. of Pennsylvania School of Medicine*
Jonathan Zehr, *U. of California, Santa Cruz*
Len Zon, *Children's Hospital Boston*
Maria Zuber, *MIT*

BOOK REVIEW BOARD

David Bloom, *Harvard U.,* **Samuel Bowring,** *MIT,* **Angela Creager,** *Princeton U.,*
Richard Shweder, *U. of Chicago,* **Ed Wasserman,** *DuPont*

Published by AAAS

EDITORIAL

A tale of two states

On 20 July 2015, the United States reopened its embassy in Havana, Cuba, after more than 50 years, creating a spirit of engagement between the two Cold War adversaries. This is a welcome addition to the 285 U.S. embassies and consulates in 190 other countries and should encourage Cuban and American scientists to practice "science diplomacy." Sadly, however, U.S. diplomacy has rarely paid enough attention to science. Given that science and technology (S&T) capabilities affect diplomatic agendas on a global scale, the powerful S&T base of the United States must be better linked to its foreign policy goals.

The 2015 U.S. National Research Council (NRC) report *Diplomacy for the 21st Century* makes a convincing case to "embed a culture of science and technology throughout the U.S. Department of State." The report underscores many obstacles to achieving an S&T culture. One glaring problem is the thin S&T workforce at the State Department. Although it employs a small core of S&T professionals in Washington, DC (at the Bureau of Oceans and International Environmental and Scientific Affairs and in the Office of the Science and Technology Adviser), there are too few scientists among the rest of the diplomatic staff, and those few are overburdened. Of the roughly 14,000 Foreign Service Officers worldwide, only about 100 are full-time Science Counselors posted abroad. This increase from a mere 57 in 1999 is hardly sufficient. The NRC committee wisely characterized the situation as a "tale of two States": S&T is alive in Washington, but starving in U.S. foreign missions.

Why should this be a concern to the United States as well as to other countries? Consider health. Long before the Ebola virus hit the front pages, Nobel Laureate Joshua Lederberg said, "The microbe that felled one child in a distant continent yesterday can reach yours today and seed a global pandemic tomorrow." America's S&T strengths span academic research supported by the National Institutes of Health and the National Science Foundation, the pharmaceutical industry, the Centers for Disease Control and Prevention, many universities, and a powerful global network of health care workers and nonprofit organizations. But these assets can only be orchestrated to address global health crises if diplomats understand these resources fully and help to deploy them appropriately.

The broader case for building competency in science diplomacy rests on a fundamental principle: Diplomats and the S&T community are partners. Scientists and engineers aid diplomats in negotiating international agreements, as in the recent negotiations with Iran over limits to its nuclear program, in which the U.S. Secretary of Energy, physicist Ernest Moniz, has had a central role. Diplomats, in turn, assist scientists in implementing S&T projects, from "big science" endeavors such as the International Space Station to smaller-scale projects, such as biological and seismological surveys. And when nations are in conflict, cooperation among S&T specialists from those nations often opens channels to improve understanding.

"Diplomacy is like a 10-speed bicycle—most gears never get used."

Enhancing science diplomacy requires closing the gap between the S&T and foreign policy communities. The NRC report suggests creating a new Science and Technology Advisory Board in the State Department to advise the Secretary and increasing the number of S&T Policy Fellows supported by the American Association for the Advancement of Science (AAAS, the publisher of *Science*) who work in the State Department. Courses in science diplomacy, such as those offered at The Rockefeller University and sponsored by AAAS and The World Academy of Sciences, serve as good models to educate scientists and engineers about foreign affairs and increase the S&T literacy of diplomats.

Diplomacy is like a 10-speed bicycle—most gears never get used. The scientific and diplomatic communities should shift science diplomacy into a higher gear so that nations can confront the many daunting challenges ahead.

–Mandë Holford and Rodney Nichols

Mandë Holford is an associate professor in the Department of Chemistry and Biochemistry at Hunter College and a research associate at the American Museum of Natural History, New York, NY. E-mail: mholford@hunter.cuny.edu

Rodney Nichols is vice chair of the board at CRDF Global, Arlington, VA, and executive vice president emeritus at The Rockefeller University, New York, NY. E-mail: Rodney.nichols12@gmail.com

PHOTOS: (TOP RIGHT) DENIS FINNIN; (BOTTOM RIGHT) NEW YORK ACADEMY OF SCIENCES; (INSET) QUERBEET/ISTOCKPHOTO.COM

10.1126/science.aaa9595

Published by AAAS

105

Average number of years between floods in New York City due to combined storm surge and heavy rainfall—such as during Superstorm Sandy in 2012. Separately, storm surge and precipitation cause floods once in 245 years (*Nature Climate Change*).

IN BRIEF

A hazy ring around Pluto

Since the New Horizons spacecraft began taking close-up pictures of Pluto more than 2 weeks ago, the mission team has rolled out image after fascinating image, offering new insights into the once-mysterious dwarf planet. One image, revealed last week, was taken by the spacecraft when it passed behind Pluto, which blocked the sun. The image showed a ring of haze, created in the thin atmosphere as ultraviolet light strikes molecules of methane and nitrogen and turns them into small smoglike particles (shown). The haze particles were found as much as 130 kilometers above Pluto's surface. New images also reveal that Pluto's bright, icy "heart" isn't a static feature; nitrogen ice is flowing out from the edge of the heart, appearing to curl around obstacles and fill up old craters. "We interpret them to be just like glacial flows on Earth," says William McKinnon, a mission co-investigator from Washington University in St. Louis, Missouri. The flows occurred recently, geologically speaking, within the past few tens of millions of years—further fueling discussion over whether residual heat in the planet's interior is driving surface activity.

AROUND THE WORLD

Malaria vaccine clears hurdle

LONDON | The first-ever vaccine against malaria, which claims about 600,000 lives a year, has gotten a key endorsement on the complicated path to approval. The vaccine, known as RTS,S and made by GlaxoSmithKline (GSK), provides only modest protection. But last week, the European Medicines Agency (EMA) concluded that the vaccine's benefits outweigh its risks; in a large trial among young children in Africa, the vaccine reduced malaria cases by about one-third. Individual countries must still decide whether to approve the drug, but EMA's "scientific opinion" paves the way for a World Health Organization (WHO) recommendation on whether and how to use it. If WHO gives it the green light, poor countries would then face a tough financial decision; bed nets and antimalarial drugs already provide substantial protection. Still, with any other vaccine 5 to 10 years away, says co-developer Moncef Slaoui of GSK, even an imperfect vaccine could "transform" child health in Africa.

Senate boosts DOE research

WASHINGTON, D.C. | A bipartisan energy bill scheduled for markup in the U.S. Senate this week would authorize a strong 4% boost to the budget of the Department of Energy's (DOE's) Office of Science. Sponsored by Lisa Murkowski (R–AK) and Maria Cantwell (D–WA), the bill avoids many areas of controversy, including any mention of offshore drilling for oil and gas; its authors hope that this will speed its passage through the Senate. The bill would also authorize a 4% increase for the Advanced Research Projects Agency-Energy and establish an energy-water "nexus" between DOE and the Department of the Interior to coordinate related activities. Other provisions include creating a DOE research program that includes industry and academia partnerships to develop at least two approaches to exascale computing systems. The bill also pushes

PHOTO: NASA/JHUAPL/SWRI

Published by AAAS

for alternative energy research, including large-scale geothermal energy technologies and ocean wave, tidal, and other marine hydrokinetic technologies.

Cholesterol drugs to market

SILVER SPRING, MARYLAND | A much-heralded new class of cholesterol-lowering agents won their first approvals in the United States and the European Union last week. The injectable treatments, called PCSK9 inhibitors, silence a protein that normally prevents the liver from eliminating low-density lipoprotein (LDL) cholesterol in blood. On 24 July, the U.S. Food and Drug Administration (FDA) approved alirocumab (Praluent), developed by Regeneron and Sanofi, for patients with cardiovascular disease or a genetic condition called familial hypercholesterolemia, and who are unable to reduce their cholesterol with statin drugs. Meanwhile, Amgen won approval for its rival drug, evolocumab (Repatha), in Europe and expects an FDA decision in late August. In clinical trials, both drugs dramatically reduced LDL levels in those at high risk for heart attack or stroke, but have yet to demonstrate a long-term reduction in risk. The cost of the new drugs—Praluent is listed at about $14,600 per year—has raised concerns about the burden on insurers if they are prescribed broadly.

Most Earth-like planet yet

MOUNTAIN VIEW, CALIFORNIA | The prolific exoplanets-hunting satellite Kepler has found its strongest candidate yet for an Earth-like planet in a life-friendly orbit around a sunlike star, scientists announced last week at NASA's Ames Research Center. Known as Kepler 452b, the world is estimated to be a bit on the hefty side, at five times the mass of Earth and 1.6 times its diameter. Its star is a G-type like our sun, but it is 1.5 billion years older, providing the planet with just 10% more heat and light than we receive. "It would feel a lot like home in terms of the sunshine you would experience," says Jon Jenkins, who leads Kepler data analysis. "This is the closest we have ... to another place someone might call home." NASA also announced the latest edition of Kepler's catalog of exoplanet candidates, adding 500 new possible planets for a total of 4175. http://scim.ag/_Kepler452b

Earth 2.0? An artist's conception of exoplanet Kepler-452b, which may—like Earth—be a rocky world.

PHOTO: (TOP TO BOTTOM) JAKE ESTES, NOI; SETI INSTITUTE/DANIELLE FUTSELAAR

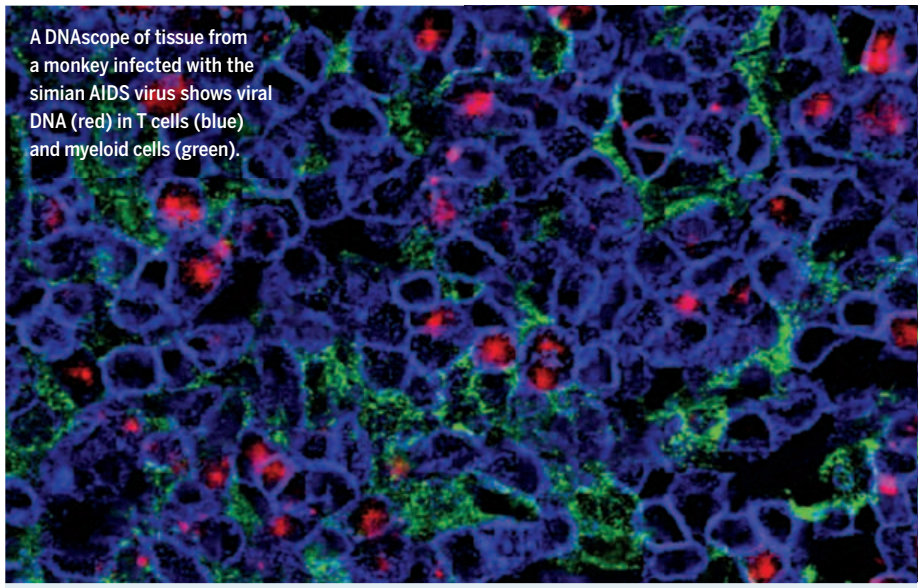

A DNAscope of tissue from a monkey infected with the simian AIDS virus shows viral DNA (red) in T cells (blue) and myeloid cells (green).

New probe finds hidden HIV

Researchers have developed a sophisticated new probe, called a "DNAscope," that detects HIV's hiding places inside and outside of cells. To date, assessments of HIV in tissue have been hampered by one major difficulty. Traditional methods for mapping HIV genetic material use long strings of DNA or RNA nucleotides, called oligomers, to find and bind to complementary strands of DNA or RNA in sample tissues. These oligomers are labeled with a marker; they send a signal when they hit their target so researchers can track them. But the large, clumsy oligomers sometimes bind to cellular components other than the target sequence, creating background noise that throws off the analysis. The new technique, revealed at an international AIDS conference this month, avoids this error by chopping an oligomer in two and sending both halves out to find the target sequence; the probability is extremely low that the two probes would land next to each other on anything other than HIV.

Faulty anthrax tests

WASHINGTON, D.C. | A Department of Defense (DOD) report released last week has unraveled the events that led to a U.S. Army biodefense lab's inadvertent shipping of live anthrax spores to other labs for a decade. The DOD review, triggered by the discovery in May that Dugway Proving Ground in Utah had recently shipped live anthrax to a company, identified faulty procedures or killing and testing samples. Further investigation revealed that the lab had unintentionally sent live samples to at least 86 government, academic, and private labs over the years. The DOD report finds that workers were only checking 5% of an irradiated batch of anthrax, not enough to ensure that all spores are dead. The revelations follow several mishaps last year with risky pathogens at federal labs.

House bill blocks GM food labels

WASHINGTON, D.C. | The U.S. House of Representatives last week approved a bill that would block states and localities from requiring mandatory labeling of food made from genetically modified organisms (GMOs). It would also set up a voluntary federal program for manufacturers to certify foods that don't contain GMOs. The bill's supporters—Republicans, some Democrats, and the food industry—call the bill a science-based effort to balance

Published by AAAS

consumer right-to-know concerns with the need for a uniform national policy. Opponents of the bill, including environmental and food activists and liberal Democrats, argue that it would deny people the right to know what is in their food. The bill's future in the Senate is unclear and the White House has yet to weigh in. http://scim.ag/GMlabeling

South Korea declares MERS over

SEOUL | Noting that the country had gone 23 days without a new case of Middle East respiratory virus (MERS), South Korean Prime Minister Hwang Kyo-ahn on 28 July declared a "de facto end" to the outbreak. (The World Health Organization called the pronouncement premature, as 28 days had not passed since the last case appeared.) The outbreak was sparked by a traveler returning from the Middle East who passed the infection to hospital workers and patients who then went "doctor shopping," carrying the virus to yet other hospitals. The outbreak, the largest outside the Middle East, sickened 186, claimed 36 lives, and required quarantining more than 16,000 contacts.

Weinberg's musical robots play with human musicians.

Three Q's

Gil Weinberg, founding director of the Georgia Tech Center for Music Technology, has pioneered artificially intelligent (AI) robots that can detect musical rhythms, tempos, and genres—and even play music. In 2013, he used a National Science Foundation (NSF) grant to create a robotic drumming prosthesis for Jason Barnes (pictured below), an aspiring drummer who lost his arm. Last week, Barnes performed with Weinberg's band Musicians and Musical Cyborgs at the John F. Kennedy Center for the Performing Arts in Washington, D.C., to celebrate the 25th anniversary of the Americans with Disabilities Act.

Q: Why robots and music?
A: The idea was to develop robots that listen like humans but play music like machines and use algorithms only machines can use to create music humans will never be able to create. ... It might lead to aesthetic results that are interesting.

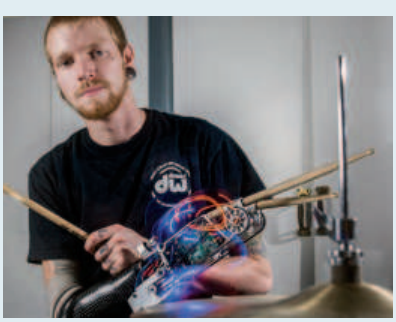

Q: How can AI technology help people with disabilities?
A: I try to blur the lines between creating technology specifically for people with disabilities versus technology for anyone else. I want to see people with disabilities using technology not only to partly bring them back to how they were before, but also to enhance and extend their abilities beyond and above what humans can.

Q: What are your plans for the future?
A: I want to explore how people respond to a body they are not controlling, so I'm creating a third arm for able-bodied people. I'm also trying to get funding from NSF to continue to work with Jason for a robotic prosthetic arm that not only gets signals from the muscles, but also the brain.

NEWSMAKERS

Math star demoted

Manuel de León, one of Spain's star mathematicians, was removed from the head of a national research institute over accusations that the center had mismanaged public funds. De León remains a professor of the Spanish National Research Council (CSIC), but has lost the directorship of the Institute of Mathematical Sciences, a research center run jointly by CSIC and three universities in Madrid. Although he says the institute had spent funds "in a way that the administration may dislike," de León says these practices remained within the law and that no public money was ever stolen. He says he was a "scapegoat," and that the internal audit that caused his demise was prompted by envious rivals from the Institute of Theoretical Physics, which shares a building with the math center. http://scim.ag/deLeonICMAT

FINDINGS

Study questions deworming

An unusual reexamination of an influential study from more than a decade ago has challenged some of the benefits of massive campaigns to give inexpensive deworming medication to children. Researchers from the London School of Hygiene & Tropical Medicine reanalyzed trial data from a study carried out in Kenya from 1998 to 1999; the study had reported that deworming improved attendance in the treated children's schools as well as in other schools because of an apparent decrease in transmission. Granted access to the original trial's data and computer programs used to analyze them, the team identified missing data, mistakes in the statistical analyses, and other problems that led them to conclude that although the antiparasite pills did provide health benefits, they did not improve overall education attainment among the treated children, they reported in the *International Journal of Epidemiology*.

PHOTOS: (TOP TO BOTTOM) SCOTT SUCHMAN; GEORGIA INSTITUTE OF TECHNOLOGY

Published by AAAS

PLANETARY SCIENCE

Comet lander's scientific harvest may be its last

Philae has fallen silent after fragmentary messages

By **Eric Hand**

About 6 weeks ago, an 85-second message from the Philae lander put its project manager, Stephan Ulamec, in a justifiably exultant mood. After 7 months of silence, the lander was alive and well on the surface of comet 67P/Churyumov-Gerasimenko. But Ulamec's mood has darkened since then, as radio links with the lander have become short and spotty, then faded out. The team has not heard from Philae since 9 July. "It's a bit frustrating to have an apparently working lander on a comet surface and not being able to communicate with it," says Ulamec, of the German Aerospace Center in Cologne.

But even if little Philae's working life is over, its short career yielded solid returns. On 12 November 2014, the orbiting mother ship Rosetta dropped Philae to the surface. The harpoons and retrorockets meant to hold it there did not work, but the lander did not fly off into space. Instead, it bounced and came to an awkward stop on its side in the shadow of a cliff. It had less than 3 days to perform science before its batteries were exhausted and it went into hibernation. This week in *Science*, the lander's science team publishes the fruit of those 3 days: a suite of seven papers that describe the mechanical, compositional, and textural properties of the comet surface and its interior.

Philae's investigators had hoped to build on those findings. After Philae woke up on 13 June, it was in contact with Rosetta six more times over 10 days. It sent encouraging "housekeeping" data: The lander was warm and its solar panels were receiving sunlight, which will increase up until 13 August, when 67P reaches its closest point to the sun. Engineers lowered the altitude of Rosetta's orbits in hopes of improving the radio link.

But since 24 June, the team has heard from the lander just once—on 9 July. Ulamec says one of Philae's two receivers is dead, and one of its two transmitters may also be on the fritz. Flight engineers are reluctant to send Rosetta too close to the comet, which is belching an expansive halo of dust as the sun warms ices in its interior, causing them to sublimate into jets of gas. Too much bright, reflective dust can mimic the stars that Rosetta relies on for navigation, overwhelming the spacecraft's star trackers and causing it to reboot—a process that wastes days of valuable scientific time and risks leaving Rosetta stranded in an orientation in which it cannot receive commands from Earth.

Stars shine behind the rugged cliff that shades Philae's landing site on comet 67P.

On 11 July, 2 days after the last contact, the craft had star tracker problems at about 165 kilometers above the comet. Engineers have since pulled back to safer orbits 190 to 210 kilometers above the surface. Moreover, during August, the orbiter will spend more time exploring the comet's southern terrains, which are now illuminated—but that will mean fewer passes over Philae, which sits in the north.

The lander team can console itself with what it did find. Two mass spectrometer experiments designed to ingest and analyze samples never received material drilled from the subsurface, as planned. But scientists working on the experiments think they did capture material that accidentally fell in after the lander's first bounce kicked up dust. The instruments detected organic compounds similar to those that astronomers have spotted in the dust and gas of other comets' comas. But they found no sulfur-bearing compounds—a surprise given that the Rosetta orbiter has remotely detected such compounds just above the surface. And one of the two experiments found four compounds never before detected on comets.

An experiment that analyzed radio waves traveling through the body of the comet when the orbiter and lander were on opposite sides of it found that 75% to 85% of 67P's interior is nothing but void space. If comets are icy dirtballs instead of the dirty snowballs scientists once pictured, those dirtballs must be loosely packed. Valerie Ciarletti, a member of the radio experiment team, says the interior was also strikingly uniform. That's odd, she says, because the orbiter has detected strong variations in both the abundance and composition of ices outgassing from the surface. Some areas are rich in carbon monoxide, for instance, whereas others are enriched in water.

The uniformity also raises doubts about theories that comets accreted layer by layer in the early solar system, says Jessica Sunshine, a comet researcher at the University of Maryland, College Park, who is not on the mission. However, the radio experiment fell short in one of its key tasks: explaining whether the two lobes of 67P began as separate cometesimals that stuck together, or whether they formed from a uniform body that eroded away preferentially around its neck. The experiment had time only for the lobe where Philae came to rest—the "head" of the duck-shaped comet. "It's really a pity that we were not able to sound both of them," says Ciarletti, a planetary scientist at LATMOS-IPSL, a research institute near Paris.

PHOTO: BIBRING *ET AL.*/*SCIENCE*

Published

Philae even sent pictures from its 360° camera, CIVA. Jean-Pierre Bibring, who led the camera team and is one of Philae's two lead scientists, says he was surprised to see very little ice. Instead, he found grains of dust that were far bigger than expected, stuck together to form meter-sized blocks resembling conglomerate rocks on Earth. "The cement of a comet is probably not ice," says Bibring, a planetary scientist at the Institute of Space Astrophysics in Orsay, France. Instead, it may be the stickiness of the dust grains themselves—complex organic material from the presolar nebula in which the comet formed more than 4.5 billion years ago.

Sunshine isn't convinced yet. She says the surface materials may not be pristine—they may have been altered by ultraviolet light. "We're still dealing with the skin-deep problem," she says. For her, one of the surprising results came from an analysis of the lander's initial bounce. Sunshine says most scientists expected comets to be "fluffy," but Philae's trajectory showed that, underneath about 20 centimeters of soft dust, the comet has a thin, relatively strong layer, perhaps formed as ice sublimed and left behind dust that "sintered" together. The soft outer layer may consist of dust that blew off and settled back to the surface. Computer simulations work showed that larger infalling objects can splash dust across the surface, covering its features like drifting snow—but with no need to invoke any cometary "wind." "Material is moving around this thing," Sunshine says. "That's sedimentary geology."

Layers of settling dust could eventually become a problem for Philae's solar panels. For now, light levels look good, and Ulamec says that, since the 13 June contact, they have increased beyond what would be expected with the change in seasons—an indication the lander has shifted to a more favorable angle (although the tilt may have also made its radio connections worse). He is looking to September and October as the last chance to get the lander doing science again before the comet leaves the inner solar system and sunlight dims too much. "We of course keep trying," he says. "The lander surprises us again and again." ■

Gathering dust

As comet 67P/Churyumov-Gerasimenko approaches the sun, increasing dust in the coma has hindered Rosetta's ability to fly close and communicate with the Philae lander.

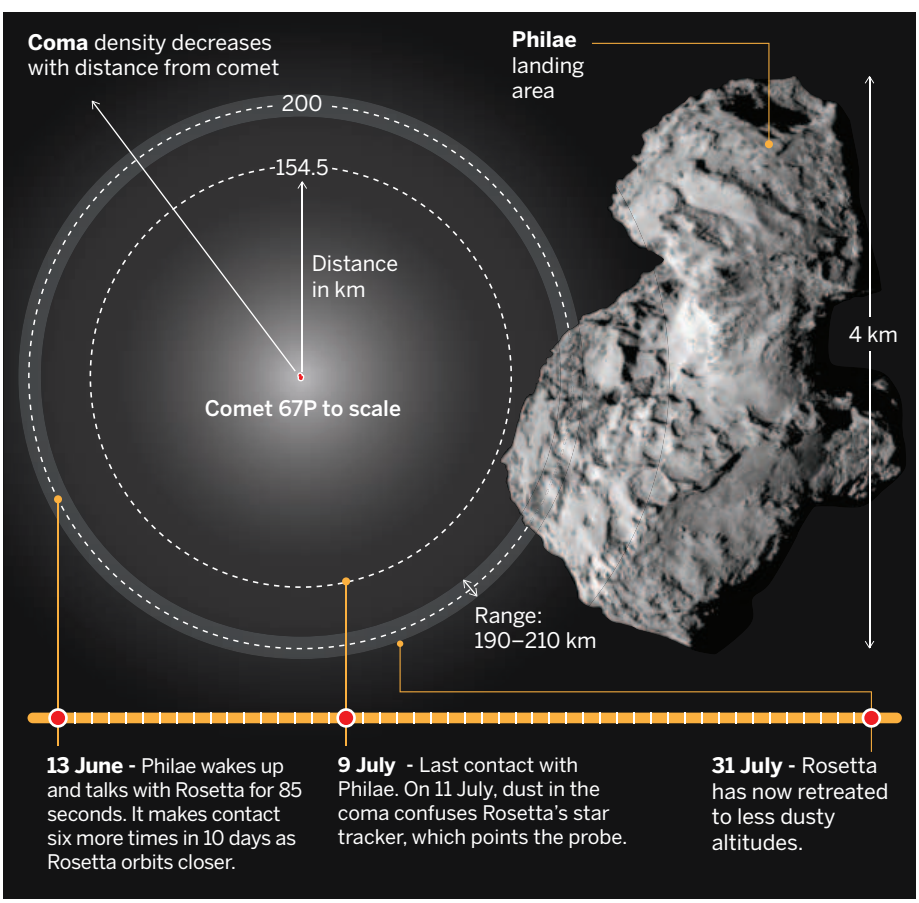

BIOPHYSICS

Tiny built-in lasers light up living cells

Technique could revolutionize tracking of individual cells

By **Adrian Cho**

Two groups of researchers have independently fashioned tiny lasers within living cells. They may sound like weapons for Ant-Man's next nemesis, but the microscopic lasers could greatly improve biologists' ability to track the movement of individual cells—a possible boon to fields ranging from developmental biology to cancer research.

"It has potential to do things you can't do with other techniques," says David McGloin, a biophysicist at the University of Dundee in the United Kingdom. For example, the lasers could potentially track more cells than fluorescent tagging can and could be easier to use than budding techniques such as radio-frequency ID. Kristian Franze, a neurobiologist at the University of Cambridge in the United Kingdom, agrees. "If they can develop this so that it's applicable in living tissue, that would be very, very interesting to many people," he says.

To make a laser, you need two things: a material or "medium" that can be excited to produce light, and a "resonant cavity" that will ring with light of specific wavelengths, just as an organ pipe rings with sound waves of specific frequencies. The medium fills the cavity with light, and when the light crosses a certain intensity threshold it stimulates the medium to radiate far more strongly. The result is a feedback loop that greatly amplifies the light, which gushes out at wavelengths set by the cavity.

Scientists have toyed with making cell-based lasers before. For example, in 2011, Seok Hyun Yun, a biomedical scientist at Harvard Medical School (HMS) in Boston, and Malte Gather, a physicist now at the University of St. Andrews in the United Kingdom, made a laser using a single cell engineered to contain a green fluorescent protein as the light-emitting medium, placing it within a resonant cavity. But no one had created a laser within a single cell. Gather and Yun have now done that inde-

CREDITS: (DIAGRAM) A. CUADRA/*SCIENCE*; (IMAGE) NASA

Published by AAAS

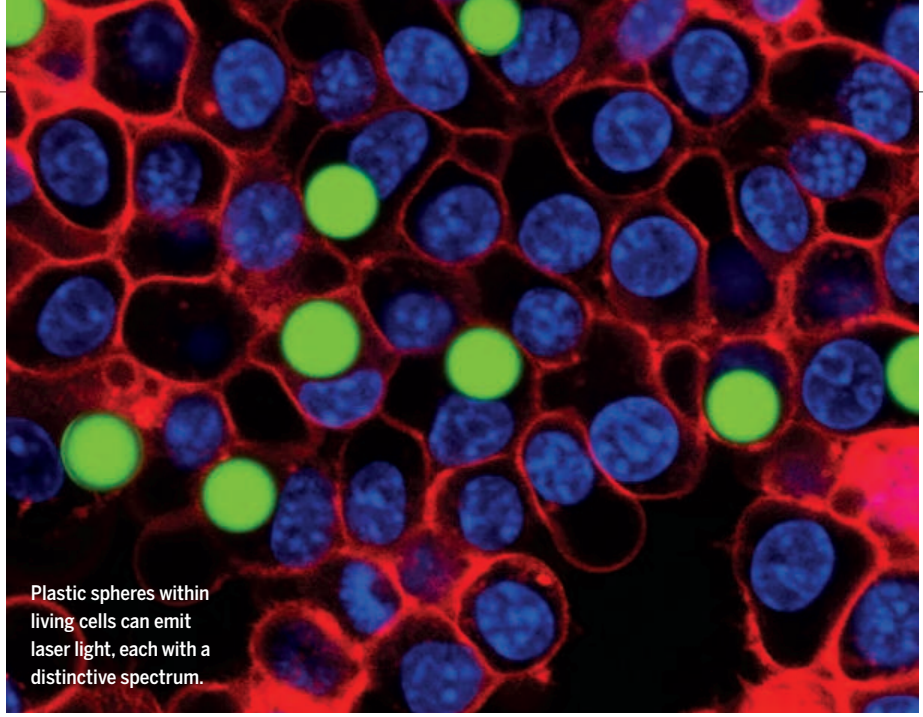

Plastic spheres within living cells can emit laser light, each with a distinctive spectrum.

IMAGE: M. SCHUBERT ET AL., *NANOLETT* (2015); ACS

pendently, using much the same technique.

The hard part is putting a cavity in a cell. Gather and colleagues got cells to do that for themselves. In culture, they mixed cells with tiny plastic spheres 5 to 10 micrometers in diameter that had been "doped" with a fluorescent dye. The beads served as the cavities, the dye as the medium. The cells absorbed the spheres through endocytosis, the same process by which immune cells gobble up pathogens, the team reported online on 17 July in *Nano Letters*. The trick worked with four types of cells, including human macrophages, a type of white blood cell.

The researchers then applied a 5-nanosecond pulse of light to excite the dye. It emitted light that raced around the sphere's equator, held in by a process called total internal reflection. Specific wavelengths—those for which a whole number of light waves wrapped exactly around a bead's circumference—resonated and grew more intense, until the bead "lased" at a couple of those wavelengths.

Yun and his HMS colleague Matjaž Humar also managed to get cells to take up plastic beads, and they created two other kinds of resonating spheres as well, they reported online on 27 July in *Nature Photonics*. They injected cells with droplets of dyed oil and also showed that the natural lipid globules in fat cells could be made to serve as resonating spheres.

The most obvious application of the lasers would be to track the movements of individual cells, Yun and Gather say. Each plastic bead has a slightly different diameter and optical properties, so it shines at distinctive wavelengths, which serve as a barcode to identify a cell. Gather and colleagues tracked a handful of macrophages in culture for 19 hours, and Yun and Humar did a similar demonstration.

The lasers' ability to shine at narrowly defined wavelengths should give them an edge over rival cell-tracking techniques such as fluorescent tags. Because a fluorescent molecule gives off a spectrum of wavelengths, researchers cannot tag many cells before the tags' spectra overlap. But the lasers' spike-like spectra should make it possible to track thousands of the tiny beacons simultaneously. Researchers might even be able to expand the number to millions or billions by loading each cell with multiple spheres. Every cell would then lase at a distinctive combination of wavelengths.

But that prospect is a way off. First, the teams need to show that various types of cells will take up the spheres, especially in living tissue. Gather predicts that won't be a problem. "I'm confident that this [technique] is generalizable," he says. Developers must also reduce the size of the plastic beads. Now, the beads stuff the cells full, Yun acknowledges. "You feel a bit of pity for them," he says. However, both he and Gather have shown that they can use smaller glass beads instead of the plastic ones.

The tiny lasers might be put to use in research right away to track cultured immune cells as they migrate in response to chemical stimuli, Franze says. A bigger payoff would come if they can be used in vivo, he says, for example, to track cells in developing embryos, the immune system, or cancerous tumors. To do that, researchers would need to get light into and out of living tissue. Zebrafish, which can be made transparent, would be an ideal organism to start experimenting with, Franze says.

Ultimately, laser cells might find uses nobody has imagined. "Regardless of anything else," McGloin says, "it's very cool." ■

INFECTIOUS DISEASES

Risk of 'leaky' vaccines debated

Controversial finding suggests they can speed the spread of deadly pathogens

By **Kai Kupferschmidt**

When people talk about the impact of vaccines, they usually mean the millions of humans saved from disease and death. But Andrew Read, an evolutionary biologist at Pennsylvania State University, University Park, likes to think about what vaccination does to pathogens. In 2001, he published a theory in *Nature* suggesting that some vaccines may cause viruses and bacteria to become more deadly.

Now, Read has some evidence to back that up—at least in animals. A paper published in *PLOS Biology* this week suggests that widespread vaccination against Marek's disease, a viral infection in chickens, explains why it has evolved to become more lethal the past few decades. Something similar might happen with certain human vaccines, Read cautions.

But other researchers say the study has little relevance for public health. Read "should stop scaremongering," says vaccine researcher Adrian Hill of the University of Oxford in the United Kingdom. He and others worry that the paper—and news stories like this one—will only play into the hands of the antivaccine movement.

Read's ideas are built on the widely accepted idea that pathogens often evolve to become less lethal over time. After all, killing their host quickly reduces their chances of being passed on, whereas causing mild symptoms, or none at all, should aid their spread. So-called leaky or imperfect vaccines, which don't prevent infection but merely reduce symptoms, upend that notion, Read argues. They allow the spread of deadlier pathogens that would normally burn out quickly.

Leaky vaccines are common for animal infections, including Marek's disease. Most human vaccines, on the other hand, actually prevent infection, but that may soon change. With diseases like malaria or HIV, for which protection is very hard

Published by AAAS

to achieve, researchers may settle for vaccines that save lives by preventing severe disease, but not infection.

In the study, Read and his co-workers, working at the Pirbright Institute in Compton, U.K., showed that unvaccinated birds infected with highly virulent strains of Marek's disease didn't shed much virus; they also died too fast to pass the disease on to healthy, unvaccinated birds. But just as Read predicted, the opposite occurred in vaccinated birds: They shed more virus when infected with a virulent strain, readily infecting and killing unvaccinated cagemates. To Read, the result suggests that vaccines can favor strains that would otherwise be too lethal to spread.

It's a convincing study, says Michael Lässig, who studies influenza evolution at the University of Cologne in Germany, "But it's a very special set of circumstances ... I would be careful about drawing general conclusions." Hill also thinks that Marek's disease may be a special case; nothing suggests that human vaccines have ever made a disease more virulent, he says. What's more, natural immunity is "leaky," too, Hill argues, allowing infected people to survive and transmit a disease that is deadly to others. "For malaria, whatever today's vaccine does is a drop in the ocean of all the immunity that is happening in Africa from all the infections," he says.

> ***"It's a very special set of circumstances ... I would be careful about drawing general conclusions."***
> **Michael Lässig**, University of Cologne

Read suspects the phenomenon is more widespread. Feline calicivirus, which causes a respiratory infection in cats, also appears to have increased in virulence as a result of vaccination, Read says, and he is worried about the same thing happening with avian influenza, which some countries keep at bay with poultry vaccines. "You could have the emergence of superhot strains," he says.

As for human disease, the study offers no support whatsoever for those who oppose vaccination, Read stresses. And if leaky vaccines are proven safe and effective, they should be used, he adds, but perhaps with closer monitoring and additional measures to reduce transmission, such as bed nets for malaria. "We need to have a responsible discussion about this." ■

PHOTO: (LEFT) BGI; (TOP) © CULTURA/CORBIS

SCIENCE AND THE LAW

Forensic labs explore blind testing to prevent errors

Evidence examiners get practical about fighting cognitive bias

By **Kelly Servick**

Shaken by revelations of unreliable results in crime labs, some forensic scientists are urging their colleagues to adopt a basic research practice: the blind experiment. Last week, at the first International Symposium on Forensic Science Error Management in Arlington, Virginia, nearly 500 scientists, lab managers, and other practitioners confronted the factors that lead them to make mistakes. A key problem, many said, is that people who evaluate evidence from crime scenes have access to information about a case that could bias their analysis.

This subconscious influence can take many forms, explained Itiel Dror, a cognitive neuroscientist at University College London. It can arise from irrelevant contextual information, such as the nature of the crime, the race of a suspect or a victim, and police investigators' beliefs about a suspect's guilt. It can also arise from the physical evidence itself. For example, seeing a suspect's fingerprint before analyzing one from a crime scene might change how an examiner interprets ambiguous features. "That's backward reasoning," Dror told the audience. "You go to such trouble not to contaminate the evidence physically, so take account of cognitive contamination."

Dror has been a longtime critic of the lack of blinding procedures in forensic science. His presence at the meeting, organized by the National Institute of Standards and Technology (NIST), was one sign of the field's eagerness for reform after a decade of humbling revelations. A 2009 report from the National Research Council concluded that many forensic disciplines lacked a firm foundation in science and produced inconsistent, unreliable results. In response, NIST and the Department of Justice assembled both a national commission on forensic science to suggest policies that will strengthen the field and 24 discipline-specific expert committees to make practical recommendations to more than 400 U.S. labs.

Meanwhile, a handful of studies—many led by Dror—have revealed how cognitive bias might contribute to forensic errors. DNA examiners who did not know that an assailant in a gang rape case had implicated another suspect, for example, were more likely to conclude that this suspect's DNA was absent from a vaginal swab of the victim. Another study revealed that, at least in untrained volunteers, exposure to emotional background stories and crime scene photos made people more likely to declare a match between fingerprints whose similarities were ambiguous.

Last week's meeting explored practical steps to combat such bias. Dror, whose consulting company has given workshops to various labs, including ones run by the FBI

Published by AAAS

Fingerprint examiners annotate subtle features known as minutiae to compare known prints to evidence.

and the Los Angeles Police Department, recommended a strategy he calls linear sequential unmasking. The approach was published online last month in the *Journal of Forensic Sciences*, co-authored by Dror and six forensic scientists—"a whole bunch of people that you like very much," he assured the attendees. It recommends that examiners be shielded from all information not relevant to a given stage of analysis and prevented from backtracking once new information is revealed. For example, a fingerprint examiner must mark up the important features of a crime scene print before viewing a suspect's print and can't change key features of that markup after seeing the second print.

Some labs already incorporate elements of that approach. FBI fingerprint examiners view the crime scene print before the reference, for example. But applying a blinding strategy like Dror's across different disciplines and crime labs won't be straightforward. In some cases, contextual information, such as the surface from which a print was collected, can help an examiner better interpret the evidence.

"There's a yin and a yang to this," says Elissa Mayo, an assistant bureau chief in the California Department of Justice's Bureau of Forensic Services in Sacramento. "There's no hard and fast rule about what is contextual."

One solution might be to designate a rotating case manager who decides what information to feed to an examiner. However, thorough blinding likely won't be feasible at small crime labs, where the same employee may collect evidence from the scene and later examine it at the bench.

Experts in a panel discussion encouraged lab managers to take modest steps: eliminating unnecessary fields on evidence submission forms, such as the race of the person whose sample is being analyzed or their alleged role in a crime; and calling in a second, blinded examiner to verify tough calls. "Stop looking at Mount Everest, and kind of take one pebble at a time," said Henry Swofford, a fingerprint examiner at the U.S. Army Criminal Investigation Laboratory in Forest Park, Georgia.

Despite the practical hurdles, many labs are eager to set up new safeguards for their employees. Mayo, who oversees operations for several state labs, hopes to make cognitive bias training standard for both managers and incoming analysts. "We're going to try to move forward and make things better," she says. "Forensic scientists want to be scientists." ■

PHOTO: BGI

Q&A

Former head of China's genome powerhouse starts new chapter

Jun Wang will concentrate on applying artificial intelligence to making sense of genome data

By **Dennis Normile**, *in Shanghai, China*

Surprising many in the worldwide genomics community, the head of the Shenzhen-based sequencing powerhouse BGI stepped down earlier this month to concentrate on research into artificial intelligence (AI). Jun Wang, 39, has been with BGI from its 1999 inception as the Beijing Genomics Institute. While still a Ph.D. candidate at Peking University, he led a BGI bioinformatics team that completed China's contribution to the Human Genome Project and then sequenced the rice genome. Wang took on additional responsibilities as BGI launched more ambitious projects, including sequencing the giant panda and silk worms. He became executive director in 2008 and is known for his quick decision-making and a willingness to take on ambitious projects, such as an ongoing effort to sequence the genomes of all 10,500 or so bird species (*Science*, 12 December 2014, p. 1275).

With BGI now firmly established as a global operation, with more than 5000 employees, Wang told *Science* that "I don't see myself continuing doing the same thing." Instead, he will lead a new BGI initiative focusing on applying AI to the challenge of analyzing and managing increasingly huge life science data sets. Wang recently discussed his plans with *Science*. His comments have been edited for clarity and brevity.

Wang oversaw BGI's rise to one of the world's premier sequencing centers.

Q: What led to this decision?
A: To me, both life science and genomics have now run into a bottleneck in handling data from tens of thousands of samples, yet that is still not enough to understand the genetics of disease. These huge data sets need new tools for analysis. Artificial intelligence and machine learning could do something with big data and for peoples' health.

Q: How will work on AI fit into BGI's overall strategy?
A: Artificial intelligence is only one way to analyze data. BGI will be involved, but I'll be looking for strategic partners, large information technology companies and small data companies. The strategy will evolve. The goal is a system to serve ordinary people by making data accessible throughout [a health care] system. This will need both science and service. It may eventually have some business model. Like the old BGI, there will be research but also a commercial product.

Q: What aspect of AI will you focus on?
A: Artificial intelligence is a sexy word people use. The first goal is digitize the "omics" data for 1 million individuals—DNA, RNA, proteins, the metabolomics—and follow up with clinical and even behavioral data. This needs new networks and the use of machine learning, things I started to play with 20 years ago.

Q: When you started at BGI, did you ever envision it becoming what it is today?
A: I can't say we designed BGI to become what it is. But we followed strategic thinking at certain time points and it evolved. I'm a risk-taker. I'm always aiming for something bigger, more challenging, for something to change the world. With BGI where it is, it's a good time for me to move on. ■

Published by AAAS

NEUROSCIENCE

Alzheimer's amyloid theory gets modest boost

Trials of antibody drugs spawn hopes, doubts—and plans for more tests

By **Emily Underwood**

Neuroscientist Colin Masters has attended countless conferences devoted to Alzheimer's disease over the course of his decades-long career, and they usually aren't uplifting. The failure, year after year, of clinical trials of drugs aimed at slowing or stopping the disease has caused many in the field to grow "despondent," says Masters, of the University of Melbourne in Australia.

At the Alzheimer's Association International Conference in Washington, D.C., last week, however, he and others expressed cautious optimism that the field is gaining momentum. The primary reason: tantalizing hints from two high-profile, phase II trials of antibodies that latch onto β amyloid, a protein that forms sticky masses in the brains of people with Alzheimer's. The pharmaceutical company Eli Lilly reported that its antibody solanezumab slowed cognitive decline in people with mild Alzheimer's by 34%, at least by one measure. Another company, Biogen, found that its antibody aducanumab not only slowed cognitive decline at some doses but also lowered brain levels of amyloid.

To some, the small number of people studied and the modest results were far from persuasive. But for Masters, one of the scientists who in 1985 initially purified amyloid from brains of deceased Alzheimer's patients, the findings provide some of the first "encouraging" evidence that β amyloid is a target for treatment. One next step, he and others say, is to try to stimulate the body's own immune defenses with an antiamyloid vaccine—an approach that failed in the past but is now getting a second look.

Biogen's antibody, aducanumab, set the Alzheimer's community abuzz this spring, when the company reported that 27 people with mild Alzheimer's who took a 10-mg dose of the drug showed significant cognitive benefits over controls, as well as reduced levels of β amyloid in PET brain scans. But that dose caused brain swelling and microscopic hemorrhages in some cases. And much smaller doses had statistically insignificant benefits, so the company decided to try an intermediate dose of 6 mg. As it reported last week, that dose reduced levels of amyloid in the brain but failed to significantly slow the mental decline in 30 people. Despite the setback, the company will soon launch an 18-month phase III trial of the 6-mg dose with 2700 participants.

The Lilly study has its own caveats. It didn't actually measure amyloid decline, says Dennis Selkoe, a neuroscientist at Harvard University and, like Masters, a major proponent of the hypothesis that amyloid buildup is the central cause of Alzheimer's. "It might go down, but we don't know that." And the cognitive benefit in participants was seen in only one of three tests. In hopes of seeing clearer benefits, the company is currently running a phase III trial slated to end in October 2016.

In the past, several antiamyloid drugs failed in large clinical trials. That has upped the stakes in the follow-up trials of the antibodies, says neurologist Rakez Kayed of the University of Texas Medical Branch in Galveston. "If they fail later and we get another black eye, that will be tough."

The amyloid hypothesis will soon get several other tests. Several companies are once again pursuing an Alzheimer's vaccine after dangerous brain inflammation stymied initial efforts a decade ago. Ricardo Dolmetsch, the director of neuroscience research at Novartis in Cambridge, Massachusetts, says the company, in collaboration with the Banner Institute in Phoenix, will this year launch the first phase III trial of a vaccine called CAD106. Composed of a small bit of β amyloid linked to a virus-like particle, the vaccine aims to rev up the immune response to β amyloid without recruiting the inflammatory T cells that previous vaccines did.

Another key change: Rather than testing the vaccine in people who have already developed Alzheimer's, the trial will focus on more than 1300 cognitively normal people with two copies of a gene variant, *APOE4*, that leads to excess amyloid production and significantly increases the risk of developing Alzheimer's. In that same presymptomatic population, Novartis is also testing a BACE inhibitor, which targets an enzyme involved in amyloid production. Other companies also have BACE inhibitors in clinical trials of people with Alzheimer's, but by treating *APOE4* carriers early in their life, Novartis hopes to stop the disease before it starts, Dolmetsch says.

If the *APOE4* trials succeed, "that would be cause for elation," Masters says. Still, he says the field has a "fundamental problem": Researchers don't yet know if β amyloid directly causes cognitive decline, or does so by triggering other Alzheimer's pathologies, such as the abnormal brain deposition of a different protein, tau.

Indeed, new brain imaging data presented at the meeting added to earlier evidence that increased levels of tau are more strongly linked to memory loss than β amyloid deposits, says William Jagust, a neuroscientist at the University of California, Berkeley. That could mean that amyloid-targeting treatments would work best in presymptomatic people, but tackling tau would be necessary later in Alzheimer's disease. "If we go all in on β amyloid and ignore other therapeutic approaches, that will be devastating," Kayed cautions. ■

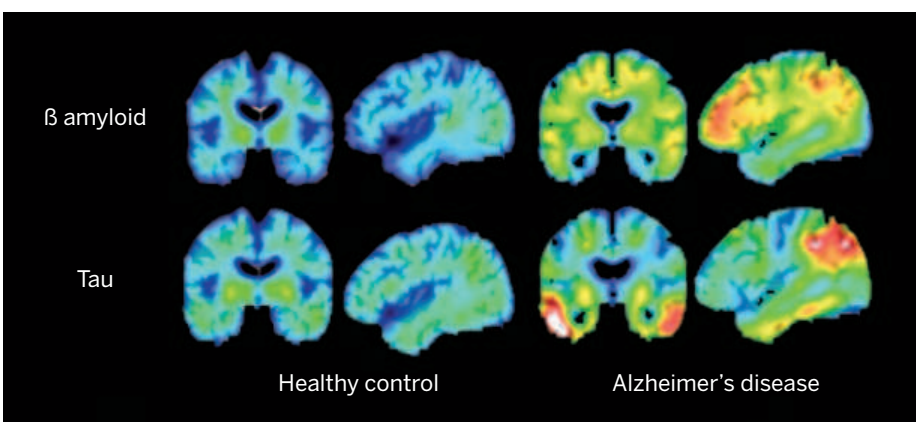

As Alzheimer's disease develops, β amyloid and tau build up in the brain and become visible in PET scans (red and yellow). But scientists are only beginning to understand how the proteins relate memory loss and dementia.

IMAGES: WILLIAM JAGUST, UC BERKELEY

Published by AAAS

COSMIC CONVERGENCE

Neutrinos from beyond our galaxy could be close kin to other mysterious visitors from space

By **Adrian Cho**

This lab at the South Pole gathers signals from the massive IceCube detector 1.5 kilometers below.

PHOTO: FELIPE PEDREROS, ICECUBE/NSF

A year and half ago, physicists working with one of the world's odder scientific instruments scored a bittersweet breakthrough. The massive IceCube particle detector—a 3D array of 5160 light sensors buried kilometers deep in ice at the South Pole—spotted ghostly subatomic particles called neutrinos from beyond our galaxy (*Science*, 22 November 2013, p. 920). Researchers had previously detected lower energy neutrinos gushing from the sun and raining down from particle interactions in the atmosphere. But—except for a burp from a nearby supernova explosion in 1987—neutrinos from the far reaches of the cosmos had eluded capture.

The discovery is Nobel-caliber stuff, some physicists say, but it also sounded a cautionary note. IceCube saw only about a dozen cosmic neutrinos per year. At that meager rate, the $279 million detector might never spot enough of them to work as advertised: as a neutrino telescope that could open up a whole new view of the heavens.

But as the data continue to come in, researchers are optimistic. After all, the fact that cosmic neutrinos have been spotted means that a big enough detector should be able to harvest enough of them to study the sky, says Francis Halzen, a theoretical physicist at the University of Wisconsin, Madison, and the driving force behind IceCube. "We see the flux, and now we have to figure out what it takes to do astronomy with it," he says. Halzen and his team are pushing to expand IceCube, which already fills a volume of a cubic kilometer. Meanwhile, other researchers have developed approaches that they say could be cheaper and more efficient.

More important, cosmic neutrinos are already telling a story, especially when combined with other particles from space: highly energetic photons called gamma rays, and ultrahigh-energy cosmic rays—protons and heavier atomic nuclei that reach energies a million times higher than humans have achieved with particle accelerators. Physicists have long wondered where in the universe the most energetic neutrinos, gamma rays, and cosmic rays are born. Now, in a tantalizing convergence, all three questions appear to share the same answer, says Olga Botner, a physicist and IceCube team member from Uppsala University in Sweden. "We believe that the engines that generate the cosmic rays also generate the gamma rays and neutrinos," she says.

If so, physicists have only one mystery to solve. The convergence also suggests the solution won't require exotic new particle physics: The conventional astrophysics of stars and galaxies should suffice.

AS TRACERS of the heavens, neutrinos offer many advantages over other particles from space. Electrically charged cosmic rays swirl in galactic magnetic fields; gamma rays tangle with radiation lingering from the big

Published by AAAS

bang—the cosmic microwave background (CMB). Uncharged neutrinos, by contrast, zoom straight from their sources through almost everything the universe throws at them. "Neutrinos are the ultimate high-energy messenger," says Abigail Vieregg, a physicist at the University of Chicago in Illinois. "They're perfect—if you can see them."

That's the hard part. Neutrinos interact with other matter so feebly that trillions of them pierce each of us every second, unnoticed. To spot even a few interactions, a detector must be huge. So IceCube contains a gigatonne of ice.

That ice is IceCube's neutrino trap. On the rare occasions when a neutrino strikes an atomic nucleus in the ice, one of two things happens. The neutrino can create a "cascade" of light and other particles that generate more light as they zing through the ice. IceCube's sensors detect that light, and from the readings physicists deduce the energy and direction of the original neutrino. Alternatively, a muon neutrino—one of the three neutrino "flavors"—can ping off a nucleus to create a lone bulletlike particle called a muon, which also radiates light and leaves a long "track" in the detector that traces the direction of the neutrino.

Unfortunately for cosmic neutrino hunters, lots of other particles make similar signals in the detector. Cosmic rays crashing into the atmosphere also produce copious neutrinos and muons. These atmospheric neutrinos outnumber cosmic ones by 1000 to 1. To weed them out, researchers exploit the fact that they peter out above an energy of roughly 100 teraelectron volts (TeV). Atmospheric muons are even more numerous, outnumbering muons from cosmic neutrinos by a factor of 1 billion. To toss out the spurious tracks they make, physicists use an array of detectors on the ice surface above, called IceTop, to spot the muons as they enter the ice. They also ignore any track that appears to start outside IceCube, ensuring that they see the actual conversion from neutrino to muon.

After ruthless culling, IceCube physicists initially spotted 28 neutrinos with energies above 30 TeV, of which no more than 11 were likely to be atmospheric, they reported in 2013 in *Science*. Now the harvest is 54, Uppsala's Botner reported at a meeting on cosmic neutrinos at the University of Wisconsin, Madison, in May. Three of them boast energies above 1000 TeV—150 times higher than any particle accelerator has reached. Those are surely cosmic neutrinos, says Pierre Sokolsky, a cosmic ray physicist at the University of Utah in Salt Lake City.

However, if neutrinos have opened a new window on the universe, it's still a murky one. Most of IceCube's events are cascades, which trace a neutrino's direction only to within 10° or 15°. "Astronomers are adamant about what astronomy means, and it's measuring things to less than a tenth of a degree," Sokolsky quips. All IceCube physicists can say so far is that cosmic neutrinos appear to arrive in equal numbers from all over the sky. That suggests they originate beyond our Milky Way galaxy, which forms a band in the sky.

As for finding the neutrinos' sources directly, so far IceCube has ruled out one likely candidate. Stellar explosions called gamma-ray bursts can briefly outshine the rest of the universe. Physicists thought they might also pump out high-energy neutrinos. But IceCube physicists see no correlation between the arrival times of cosmic neutrinos and the gamma-ray bursts recorded by other instruments. At most 1% of cosmic neutrinos come from the bursts, Botner says.

BUT EVEN IF ICECUBE hasn't spotted the sources of cosmic neutrinos, its data already reveal information about thm. In particular, the results may tie cosmic neutrinos to perhaps the most mysterious particles in the cosmos: the highest energy cosmic rays.

Ultrahigh-energy cosmic rays pack energies as high as 100 million TeV, as much energy as a golf ball striking the green. They pelt Earth at a rate of one per square kilometer per century. To spot them, physicists deploy vast arrays of detectors, such as the Pierre Auger Observatory in Argentina and the Telescope Array in the desert of eastern Utah. The arrays pick up the showers of particles the cosmic rays unleash when they slam into the atmosphere. No one knows where ultrahigh-energy cosmic rays come from or how they reach such energies. Some theorists have suggested that they come from the decays of massive particles lingering since the big bang. Or they could come from more conventional astrophysical accelerators such as the remnants of supernovae or the hearts of certain galaxies.

So far, IceCube's data support the astrophysical scenario. That's because they jibe with a calculation made in 1998 by Eli Waxman, now at the Weizmann Institute of Science in Rehovot, Israel, and the late John Bahcall of the Institute for Advanced Study in Princeton, New Jersey. Waxman and Bahcall assumed that cosmic neutrinos

The big chill

IceCube's 2500-meter-long detector strings watch for light triggered when a neutrino strikes a nucleus in the ice, kicking out other particles such as muons. Researchers want to increase its volume 10-fold by adding strings.

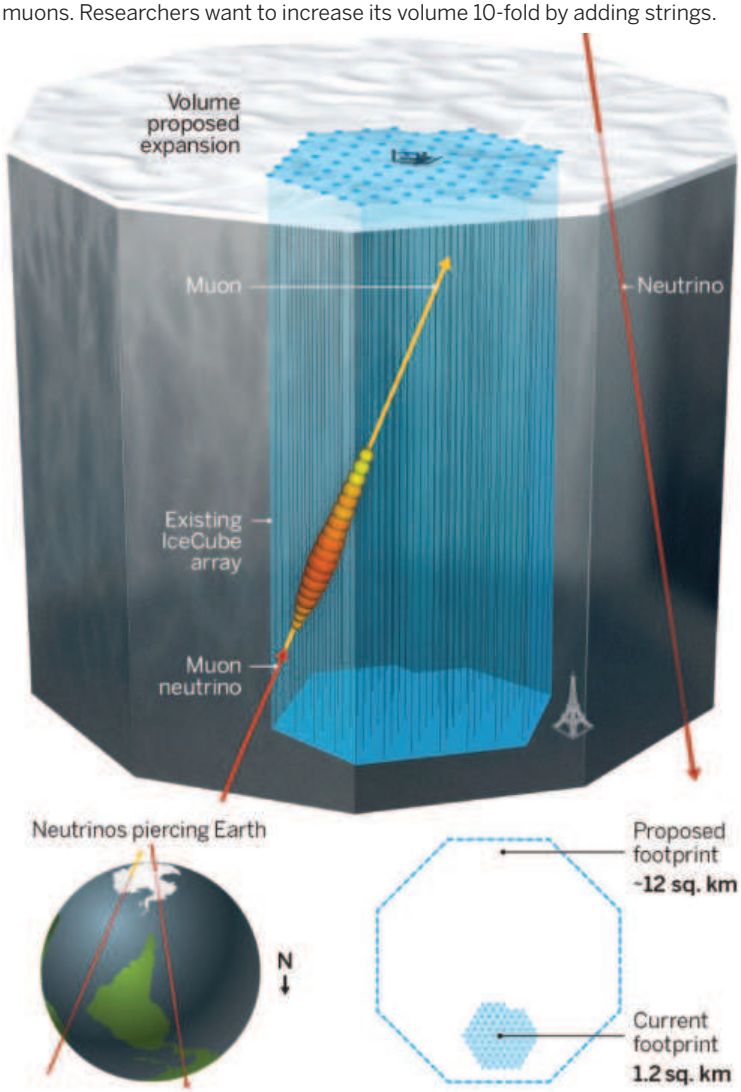

ILLUSTRATION: JAMES PROVOST

Published by AAAS

emerge from a chain of standard particle interactions that begins when an ultrahigh-energy proton in space collides with a photon. The collision spits out a particle called a charged pion, which decays into a muon and three neutrinos. In that picture, Waxman and Bahcall concluded, the number of cosmic neutrinos reaching Earth would be tied to the number of protons arriving as ultrahigh-energy cosmic rays. Thus, they calculated a limit on the number of cosmic neutrinos.

In fact, IceCube's measurements neatly match the Waxman-Bahcall bound, says Uppsala's Botner. The agreement suggests that the same astrophysical sources that kick out ultrahigh-energy cosmic rays also produce cosmic neutrinos. If, instead, the cosmic rays and neutrinos came from different sources or from the decays of supermassive particles, there would be no reason for measurements to match in that way.

A third kind of cosmic messenger also supports that conclusion, Halzen says. In Waxman and Bahcall's scenario, the proton-photon collisions that create charged pions also produce uncharged versions of the same particles, which decay into pairs of gamma rays. Those gamma rays can't be counted directly, as they interact with microwaves from the CMB to produce lower energy particles. But those interactions still produce a diffuse haze of lower energy gamma rays, and the total energy in that haze, as measured by scientists with NASA's orbiting Fermi Gamma-ray Space Telescope, equals the prediction of the Waxman-Bahcall scenario. "That's a huge breakthrough," Halzen says.

Waxman's model doesn't predict precisely what the ultimate sources of the ultrahigh-energy cosmic rays, neutrinos, and diffuse gamma rays are. But Waxman says he knows where they must reside. It has to be a place where magnetic fields are strong enough to enable protons to circulate and rev up to the energies seen in the highest energy cosmic rays, he says. The only parts of the universe that qualify are gas-dense star-forming regions of galaxies.

Others agree that Waxman's unified picture fits the data so far. "I'm a bit cautious because I have a prejudice against monotheism," says Utah's Sokolsky, who works on Telescope Array. Still, he says, "Waxman's model is about the only reasonable one."

TO TEST THAT MODEL, physicists need to see many more neutrinos and find at least a few sources. IceCube researchers have a straightforward plan to do that: expand the detector sideways to 10 times its current volume. Doing that would require only doubling the number of light sensors, Halzen says. The South Pole ice is clearer than expected, he says, so the new sensors could be farther apart than the current ones are.

IceCube researchers plan to submit a proposal for the $300 million upgrade to the National Science Foundation (NSF) this summer, and they hope to have it completed by the middle of the next decade. That schedule isn't as leisurely as it sounds. Researchers can work at the South Pole only during the summer, and the specialized water drill they use takes days to bore each of the holes for the detector strings. "If you start counting backward from 2026, it's not so much time left," Botner says. Indeed, it took 7 years to install IceCube's current detectors.

But it might be possible to up IceCube's rate by simply adding more detectors on the surface above it. Currently, 81 surface detectors neatly fill IceCube's 1.2-square-kilometer footprint. Expanding that array to 150 square kilometers would greatly enhance physicists' ability to sift tracks triggered by cosmic neutrinos from those generated by muons from the atmosphere, Jan Auffenberg, a physicist at RWTH Aachen University in Germany, told the meeting.

Now, IceCube researchers ignore all tracks that begin outside the detector and slant through its sides, as such tracks could be caused by muons raining down from the atmosphere. Stretching the surface array would enable physicists to pick out slanting tracks produced by neutrinos, even if they don't begin within IceCube, Auffenberg says. That would increase the data rate by a factor of 10 at only one-tenth the cost of expanding IceCube as a whole, he says.

Other approaches are also in the works. European physicists plan to build a network of three detectors, each with a volume of a cubic kilometer, by stringing light sensors in the Mediterranean Sea—a project called KM3NeT. And some physicists hope to snare cosmic neutrinos by another technology altogether: detecting the radio waves generated when a neutrino strikes the ice and triggers a cascade of particles. Radio waves travel much farther through ice than light does, so widely spaced antennas could observe a far bigger volume. Two groups plan to test the technology, in Antarctica and Greenland.

Which approach is better remains to be seen. But some physicists say the choice is obvious. "Putting more strings in IceCube is guaranteed to work," says John Learned of the University of Hawaii, Manoa. "So far, [the radio antennas] haven't had a sniff."

Ultimately, spotting the sources of cosmic neutrinos may take a combination of different measurements, Waxman says. "You need to see the neutrinos and gamma rays together," he says. If he's right that cosmic neutrinos are born in star-forming regions of galaxies, pinpointing the sources could prove difficult because galaxies like that are plastered all over the sky. So picking a neutrino's source galaxy out of the crowd will require seeing it together with an easy-to-pinpoint optical signal, Waxman says—although that's the kind of link IceCube has failed to make with gamma-ray bursts.

If scientists can expand IceCube, then at least a few sources should emerge, Waxman predicts. Such observations should put the emerging all-in-one model to the test. "The real story is that this tentative picture is greatly strengthened by what we see," he says, "and that people are confident about what we need to do in the next step." The realm of neutrino astronomy isn't yet here, but it may finally be within reach. ■

Scattershot data

The 54 likely cosmic neutrinos that IceCube has seen come from all over the sky and show no obvious sources or correlation with the galactic plane (horizontal line).

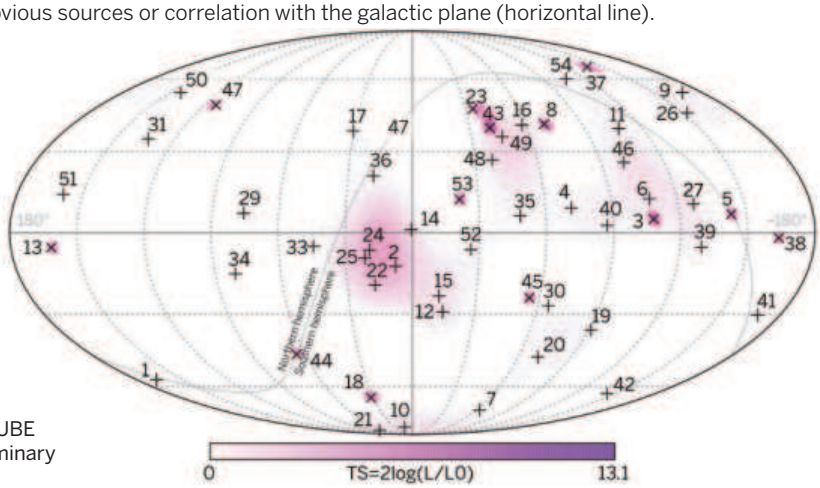

DATA: ICECUBE COLLABORATION

Published by AAAS

SETTING THE BAR

As the U.S. military opens ground combat roles to women, it's looking to scientists to help define the standards

By **Kelly Servick**, *at Lackland Air Force Base, San Antonio, Texas*

On a sunny June afternoon, a U.S. Air Force airman is staring up at a 2.5-meter wall. The young woman has just lugged more than half her weight in gear down 5 kilometers of a dirt jogging path and dragged a 98-kilogram dummy across a long stretch of grass. She's already failed at one attempt to clear the wall. Now the clock is ticking: She has 2 minutes to make it or move on to the next task.

"Why am I so dizzy?" asks the airman, who cannot be identified by *Science* under the study's privacy rules. She's determined to get over. This obstacle course, designed to mimic the physical demands of military combat, is her last challenge in a 2-week Air Force study. So far, she hasn't had to leave anything unfinished.

She has volunteered for the grueling exercise along with nearly 200 other airmen (the term used for both men and women) in order to help answer a thorny question: How should the U.S. military decide who is physically qualified to be a combat soldier? That question is getting urgent attention since the Department of Defense moved in 2013 to integrate women into ground combat roles—the last military occupations to remain male-only.

By January 2016, each branch of the military—the Army, Air Force, Navy, and Marines—must open up its combat specialties to females or ask the Secretary of Defense to keep the gender restriction on certain jobs. The deadline has prompted a slew of new research projects, including studies of physical standards, gender differences in injury rates, and service members' attitudes towards integration. But the surge of new science has also prompted suspicions that the services will arbitrarily lower standards in order to meet political demands for equality.

"For a lot of people, this isn't a scientific issue. It's a very emotional issue," says Jennifer Hunt, an Army Reserve staff sergeant and Iraq veteran in Gaithersburg, Maryland, who

PHOTO: U.S. AIR FORCE PHOTO/1ST LT. JOSE R. DAVIS

Downloaded from www.sciencemag.org on July 30, 2015

Published by AAAS

An Air Force volunteer performs a rescue simulation as part of a study of combat's physical demands.

is one plaintiff in an ongoing lawsuit against the Pentagon aimed at lifting the ban on women in combat. "There's a big sociological aspect to it—of how we conceptualize a woman's role." The lawsuit is on hold as the military decides whether to keep any positions closed.

The legal and political backdrop can make for a highly charged research environment, in which a wall standing on a Texas air base is more than just a wall. The airman, who in her spare time is a competitive weightlifter, has her eye on one of the soon-to-open combat specialties, such as pararescue. "I work behind a computer and there's no windows, all damn day," she explains at one point. "I absolutely hate it." That may be why, on her second try, she approaches the barrier with a certain ferocity.

THE QUESTION OF whether to open ground combat positions to women has sparked decades of controversy, but attitudes—and government policies—are evolving. In the past 3 decades, Canada, Australia, and many nations in Western Europe have moved to do away with combat restrictions, and the United Kingdom is currently reconsidering its policy. In part, the changes reflect the fact that women have already served and died alongside men in combat, despite their formal exclusion. In conflicts without clear front lines—in Afghanistan and Iraq, for example—female medics, pilots, engineers, and intelligence analysts have all been exposed to enemy fire.

Women in the U.S. military have been selected for increasingly risky jobs. In 2010, for instance, the military created all-female "cultural support teams" that served as liaisons between U.S. forces and Afghani women, collecting information and sometimes joining Army Rangers on dangerous raids. Former Secretary of Defense Leon Panetta emphasized women's combat experience when he announced, in January 2013, that the military would lift a categorical ban on women in units whose mission is to "engage in direct combat on the ground." At the time, the policy applied to more than 250,000 positions. "The fact is that [women] have become an integral part of our ability to perform our mission," Panetta said.

Still, questions persist about the physical abilities of female service members. On average, women have smaller hearts, slighter skeletons, less muscle mass, and more fat than males, noted a report on woman in combat published last December by the U.K. Ministry of Defence. Analysts worry those attributes could make it difficult for women to perform certain critical combat tasks, such as loading heavy artillery, conducting rescues, or bearing heavy combat loads, which can exceed 45 kilograms of weapons and gear. The U.K. report concluded that "the relative strength of females, compared to the combat load carried, is likely to result in a distinct cohort with lower survivability in combat."

THE YOUNG AIRMAN eyeing the wall is intent on proving to military leaders that such statistics about "average" females aren't meaningful—that some women can meet the physical demands of combat. In the Air Force, those demands might include scouting for days behind enemy lines to coordinate an air attack, or parachuting into a battle zone to evacuate the wounded. "We are going up against a pretty big cultural block," the airman says. "Women in these career fields are generally seen as a hindrance, a burden: 'Oh, she's not going to be able to keep up. I'm going to have to drag her equipment.'"

So for the last 2 weeks, she has been sweating in the Texas sun and feeding data to Neal Baumgartner, a longtime exercise physiologist for the Air Force who designed and is running the study. Baumgartner, 55, is a retired major who has been "bleeding blue for the Air Force since I was 17." And he has been waiting for more than a decade to do this research.

Baumgartner has long argued that the physical standards that combat airmen must meet to advance through training (which can last 6 to 24 months) should be based directly on the demands of real-world fighting—not, as is currently the case, on the physical fitness traits of previous candidates who have successfully completed the training. But in 1998, when Baumgartner first proposed running a study to reexamine the standards, the Air Force said funding wasn't available. He kept chipping away at the project, and in 2011 worked with the RAND Corporation to design the study.

When Baumgartner first conceived the research, he didn't anticipate that some of his subjects would be women. But the funding only began to flow after the Pentagon lifted its ground combat exclusion. Military leaders developed a policy, known as the Women in Service Review (WISR), which required the Air Force and other services to demonstrate that the occupational standards for combat jobs were scientifically defensible and gender neutral. Air Force officials asked: "Is anybody doing this work?" Baumgartner recalls. "Boom. We already had it in place." His study finally had official backing—and a hard deadline.

Fit for combat?

Current standards most battlefield Airmen must meet to maintain their status as "operators":

6 pull-ups

50 sit-ups

35 push-ups

3 mile run in 24 minutes

1500 meter fin swim in 34 minutes

DATA: U.S. AIR FORCE

Published by AAAS

To simulate combat, subjects in an Air Force study crawled across a simulated battlefield while wearing 43 kilograms of gear (left) and carried a nearly 50 kilogram barbell—about one half the weight of a casualty on a stretcher.

By this week, he will submit his recommended standards to the secretary of the Air Force.

Baumgartner moved quickly to recruit subjects—63 female airmen and 109 male airmen, about half of them current combat soldiers. During their first week in the study, subjects took 39 physical fitness tests: They squat-lifted dumbbells of increasing weights to find their limits, did crunches to the beep of a metronome until exhaustion, and tested their upper body strength on a pull-up bar.

Week 2 brought 15 combat and rescue simulations, all based on "mission profiles" that current battlefield airmen carry out to prepare for deployment. The test subjects evacuated a dummy named Rescue Gumby from a vehicle and towed another, Rescue Randy, back and forth across a swimming pool. They scaled a 6-meter rope ladder with 30 kilograms of gear. The weight makes most climbers tilt backward towards the horizontal, Baumgartner notes. "You end up like a turtle."

After collecting data, he began comparing the results of the 39 fitness tests and 15 simulations. He's looking for correlations. For example, does the ability to do crunches predict how fast an airman can climb a rope ladder, or do push-ups correlate better? He will also define what constitutes "success" on a simulation by surveying experienced combat airmen who have performed the tasks and consulting a panel of military experts. For instance, how long should it take a rescuer to drag an injured comrade from a damaged vehicle, or hoist a rucksack over the slippery side of an inflatable Zodiac boat? Finally, he is developing practical standards that the Air Force can use to judge whether an airman is physically fit for combat: a minimum number of crunches, for example, or swimming a certain distance within a time limit.

Setting those magic numbers is a balancing act. Ideally, any cutoff should minimize the number of people who might meet the fitness standard but then fail the simulations. But it will also need to avoid axing less fit recruits who might succeed on actual combat tasks.

Although Baumgartner is often careful to explain the study's nuances to his subjects, misconceptions abound. The young female airman shooting for a perfect completion record, for instance, can't shake the notion that her data will count for more if her performance is exceptional. "We are here to set the standards as high as humanly possible so that when women behind us actually start moving into the community, they are absolutely equals [to men]," she says. "I have this phrase in the back of my head: 'I will not be the reason they lower that standard.'"

In reality, the study is gender-neutral; Baumgartner is trying to develop measures that can predict whether any recruit, male or female, can handle the physical demands of certain combat tasks. A strong performance won't necessarily bump the standard higher. It just adds another point to Baumgartner's scatterplot—designed to detect good correlations and compensate for outliers.

Still, some fear that the Air Force will lower the bar so that more women will clear it. One experienced battlefield airman in the study admits that he came in skeptical. "If you're going to open up career fields to females and make it gender-neutral, just have them run in, and shoot for the [existing] standard," he says. "We have guys that have been doing it for years, and the standard has been the standard."

Ultimately, any final decisions about which positions to integrate and where to set the standards will be made behind closed doors at the highest levels of the Pentagon and White House. For now, however, the Air Force doesn't anticipate keeping any of its combat positions closed to women.

OTHER BRANCHES of the U.S. military are also scrambling for new data. The Army, for example, plans to create a screening test for new recruits. The goal is to disqualify some recruits—male or female—from pursuing combat training if the results suggest they are unlikely to complete the training or likely to get injured attempting it. Using actual combat tasks for such screening often isn't practical, notes Jack Myers,

PHOTOS: U.S. AIR FORCE PHOTO/1ST LT. JOSE R. DAVIS

Published by AAAS

a senior planner with the Army's Training and Doctrine Command and a lead on the integration initiative. "Imagine a high school senior showing up at a recruiting station and we're like, 'Okay, I need you to load this howitzer.'"

Instead, physiologists at the U.S. Army Institute of Environmental Medicine in Natick, Massachusetts, are designing a predictive model. It reduces previously male-only jobs to their five to seven most physically demanding tasks, which are further simplified into exercises like a long jump or a grip test that could be performed at a recruiting station.

The Marine Corps is trying to evaluate another issue: how females might affect a team's performance in a combat mission. The Corps' 350-person study group, known as the Ground Combat Element Integrated Task Force, includes about 65 women who have already completed the occupational specialty schools that feed into combat jobs. Some are trained as machine gunners, for example, and others learned to operate antitank missiles. This past spring, at a base in Twentynine Palms, California, the volunteers were tested in 12-member teams, some all-male, some including either one woman or two. The teams carried out test missions, sometimes with live ammunition, while GPS sensors and heart monitors tracked each volunteer's accuracy, speed, and exertion.

The data will allow researchers to compare the performance of male-only teams with integrated ones—how accurately the team explodes its target, for example, or how quickly it traverses difficult terrain. Researchers can also compare how much females must exert themselves on a given mission relative to their male teammates, and whether they sustain more injuries.

"That's a really important landmark study," says Daniel Billing, a human performance scientist with the Australian Defence Force, which in 2011 announced it would open 24 combat roles to women. The government's Defence Science and Technology Organisation in Melbourne has been evaluating its own occupational standards, and is watching the U.S. research with interest. "I'm hoping that with the facts on the table, it will allow people to move from identifying reasons why women should not serve in these roles, to start getting really productive and looking at the strategies that might best accommodate and support females," Billing says.

Injury experts are already thinking about how to provide such support to women. Musculoskeletal injuries—damage to joints, muscles, tendons, ligaments, and cartilage, often from overuse during training—have long taken a major toll on service members. An estimated 24% of evacuations from recent U.S. operations, for example, were the result of musculoskeletal injuries, not combat injuries. And military women appear to be at greater risk: In the Army, which has the highest rate of training-related injuries, studies have found that about twice as many women as men sustain a musculoskeletal injury during basic training.

Whether the women in the newly opened positions will also face a heightened injury risk is "the big open question," says Bruce Jones, a physician and epidemiologist who manages the injury prevention program at the U.S. Army Public Health Command in Aberdeen, Maryland. He has been analyzing injury data since the early 1980s, when a commander asked him to figure out whether his trainees would be better off running in running shoes or combat boots. ("We were never allowed to do the study," Jones says, because "the issue was resolved" when the chief of staff simply decreed that trainees would wear running shoes.)

Jones and his colleagues have found that fitness, not gender, may underlie the injury risks. In a 2000 study of basic training recruits, they showed that differences in aerobic fitness, as measured by run times, accounted for most of the twofold difference in injury rates between men and women. That suggests "men and women of the same fitness level have similar risk," Jones says, adding that it's not yet clear whether that pattern will hold among combat soldiers.

In a bid to prevent injuries, a new working group within the Army Medical Command is developing recommendations for safer training regimens. There is already some evidence that high-intensity, low-volume training—substituting short sprints for long hikes and jogs, for example—can reduce overuse injuries and improve performance in both men and women. And as women join the combat ranks, the working group hopes to use records of medical visits and time lost to injuries to identify any female-specific risks and suggest prevention measures. But it will be up to unit commanders to decide whether and how to implement any injury-prevention recommendations.

WITH OTHER SUBJECTS threatening to overtake her, the airman takes another shot at the wall. She flings herself up, grips the top, and wriggles like a worm. When she manages to get a foot over the wall, other subjects, who Baumgartner has discouraged from watching or cheering, watch and cheer.

Half an hour later, she hauls a 48-kilogram barbell up an incline that replicates the ramp of a C-17 cargo plane and hoists one end of a weighted stretcher above her shoulders. The task simulates loading a casualty—and it's the last one of the day. "Everything is a pass, right?" she asks. "Somebody look me straight in the eyes and tell me I passed everything."

She doesn't get a response. But as she gets ready to return to her desk job, the airman says she's proud she was able to "get some data in the system" to support women entering the new positions. She knows that even this study can't accurately gauge how women will perform in combat—in part because those in the study haven't trained for it. But she's confident that she and many of the female volunteers could make the cut. "Give us the proper time and training to build those muscles, and we'll keep up with the boys, no problem," she predicts. "We absolutely could have smoked this stuff."

A final decision on whether she will get that chance is expected early next year. ■

Barred from the ranks

In 2013, when the U.S. defense department lifted its categorical ban on women in combat, more than 250,000 direct ground combat positions were male-only.

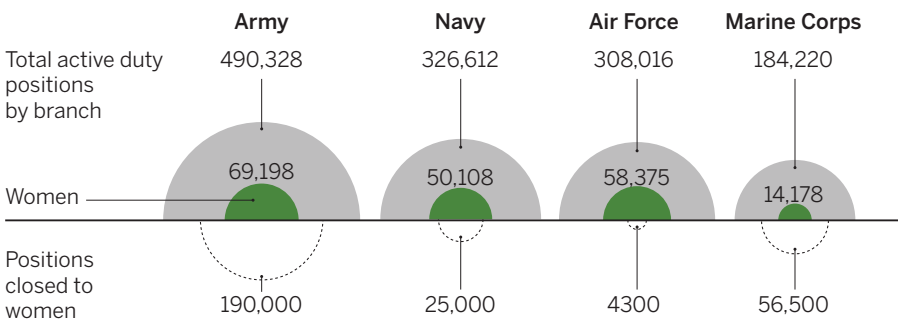

GRAPHIC: A. CUADRA/*SCIENCE*; DATA: U.S DEPARTMENT OF DEFENSE

Published by AAAS

Tale of two planets p. 475 ▸

Global versus local water p. 478

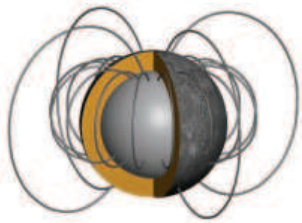

PERSPECTIVES

ROBOTICS

Two leaps forward for robot locomotion

Biomimetic robots can jump on land and on water

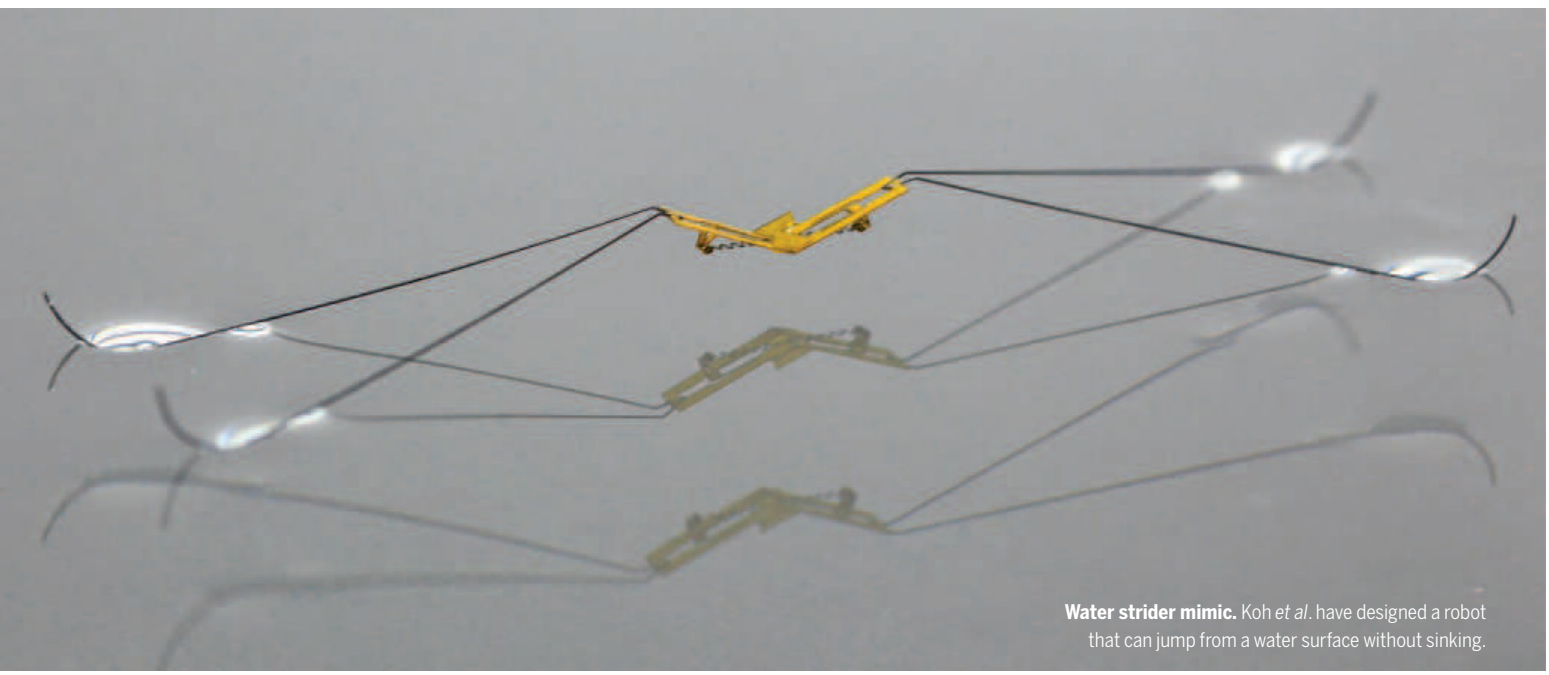

Water strider mimic. Koh *et al*. have designed a robot that can jump from a water surface without sinking.

By **Dominic Vella**

The designers of mobile robots often take their inspiration from animals. In recent years, examples have included SmartBird, a flying robot that is modeled on a herring gull; BigDog, a rough-terrain robot that can walk, run, climb, and carry heavy loads; and the humanoid Asimo. With the exception of SmartBird, however, these robots can only move horizontally and over land. Being able to cope with different terrains remains a key challenge for robotics. Perhaps no two terrains are more different than land and water, and yet several animals can move equally well on either (*1*). On page 517 of this issue, Koh *et al*. describe a robot that is so at home on the water surface that it can leap to heights of 14 cm without piercing the surface (*2*).

Walking and jumping on water poses a number of challenges for robots that motion on land does not. Most obviously, the robot must stay afloat, which in general means that it must be sufficiently small—dense objects smaller than a few centimeters can float thanks to the surface tension of water (*3*). However, producing small, water-walking robots requires ingenious engineering. The first water-walking robot, RoboStrider (*4*), was intended as a proof-of-principle for the "rowing" mechanism employed by water striders. Its design was extremely simple, with a twisted rubber band storing the energy to drive its legs. Subsequent refinements of RoboStrider (*5*) and other water-walking robots (*6*) have used more sophisticated actuation mechanisms, but the motion has remained almost exclusively horizontal.

However, the most remarkable feature of water-walking insects is their agility and, in particular, their ability to jump clear of the water surface. Replicating these jumps has proved to be a severe technical challenge: Jumping requires the robot to push down on the water surface, potentially endangering its precarious state at the surface and ultimately causing it to sink.

To design a robot capable of jumping from water, Koh *et al*. first studied carefully how real water striders jump. This revealed that rather than pushing purely downwards, they rotate their legs, accelerating the motion rap-

Mathematical Institute, Andrew Wiles Building, Woodstock Road, Oxford OX2 6GG, UK.
E-mail: dominic.vella@maths.ox.ac.uk

PHOTO: BIOROBOTICS LAB/SEOUL NATIONAL UNIVERSITY

Published by AAAS

idly and allowing the insects to attain high vertical accelerations without piercing the water surface. It also allows the insects to jump as high on water as they can on land, distinguishing this mechanism from that used by other semi-aquatic insects that can jump much more effectively on dry land (*7*).

Revealing the mechanics of water strider jumping was only the first step; Koh *et al.* took further inspiration from flea jumps and used "pop-up" manufacturing to create a simple, light mechanism that can generate the rapid sweeping motion needed. The result is strikingly similar to the jumping of the real water strider. What is more, the robot jumps on water equally well as, and sometimes better than, on land.

To generate the rapid sweeping motion of the legs, Koh *et al.* use the snap-through of a hinge. However, this motion is triggered by an external heat source, rather than by the robot itself. A completely different solution to this rapid actuation problem has been suggested recently (albeit on dry land). Bartlett *et al.* (*8*) reported a soft robot that uses the controlled explosion of an oxygen-butane mixture to generate the large accelerations needed to jump. The high energy density of the oxygen-butane mixture makes this a promising way to generate up to 30 jumps without refueling. However, the extreme forces involved mean that thought needs to be given to the materials used in construction: Soft parts are important to allow jumping, but a partly rigid top focuses the acceleration downward and enhances the jumping efficiency. Using computer simulations and experiments, Bartlett *et al.* showed that the ideal combination is to grade the material from soft to hard. This grading also makes the robot more robust and can now be achieved relatively easily with multimaterial three-dimensional printing.

For many soft robots, the necessity of making a rapid leap will be a relatively rare occurrence, rather than the primary mode of locomotion. If so, instabilities of soft, elastic materials offer the ability to produce rapid motions and can be primed over much longer time scales. Examples of this abound in the plant kingdom, where several species use variants of the snap-through instability that is also seen in the popular hopper popper children's toy (*9*). For example, the Venus flytrap (*10*) and fern sporangium (*11*) both store elastic energy gradually but release it rapidly to generate extremely rapid motions. Taking inspiration from plants (rather than animals) to facilitate robot locomotion sounds counterintuitive, but it seems a possibility that has thus far been underexploited. ■

High jump expert. Koh *et al.* based their design on a detailed study of water strider motion. For movies of robot and water strider motion, see the supplementary materials in (*2*).

PHOTO: DENNIS DRENNER/VISUALS UNLIMITED/CORBIS

REFERENCES

1. J. W. M. Bush, D. L. Hu, *Annu. Rev. Fluid Mech.* **38**, 339 (2006).
2. J.-S. Koh *et al.*, *Science* **349**, 517 (2015).
3. D. Vella, *Annu. Rev. Fluid Mech.* **47**, 115 (2015).
4. D. L. Hu, B. Chan, J. W. M. Bush, *Nature* **424**, 663 (2003).
5. D. L. Hu, M. Prakash, B. Chan, J. W. M. Bush, *Exp. Fluids* **43**, 769 (2007).
6. O. Ozcan, H. Wang, J. D. Taylor, M. Sitti, *Int. J. Adv. Robot. Syst.* **11**, 85 (2014).
7. M. Burrows, G. P. Sutton, *Curr. Biol.* **22**, R990 (2012).
8. N. W. Bartlett *et al.*, *Science* **349**, 161 (2015).
9. A. Pandey, D. E. Moulton, D. Vella, D. P. Holmes, *Europhys. Lett.* **105**, 24001 (2014).
10. Y. Forterre, J. M. Skotheim, J. Dumais, L. Mahadevan, *Nature* **433**, 421 (2005).
11. X. Noblin *et al.*, *Science* **335**, 1322 (2012).

10.1126/science.aac7882

ORGANIC CATALYSIS

A leap ahead for activating C-H bonds

Boron-based catalysts add functional groups to normally unreactive carbon-hydrogen bonds

By **Shubhankar Kumar Bose** *and* **Todd B. Marder**

Although great strides have been taken in recent decades, the catalytic and selective functionalization of normally unreactive carbon-hydrogen bonds (*1*) as a route to high value-added compounds remains one of the major challenges in catalysis, and in chemistry in general. On page 513 of this issue, Légaré *et al.* (*2*) describe a metal-free process for the catalytic borylation of carbon-hydrogen bonds in heteroarenes. Their catalyst incorporates a "frustrated" pair comprising a Lewis acid and base, and this approach to the problem may have wider applications in other carbon-hydrogen bond functionalization reactions.

As synthetic intermediates, organoboronate esters and boronic acids (*3*) feature in the synthesis of pharmaceuticals, agrochemicals, liquid crystals, and organic light-emitting diodes. Their importance is, in part, the result of the Suzuki-Miyaura cross-coupling reaction (*4*) but also because of their applications in other carbon-carbon, carbon-oxygen, carbon-nitrogen, and carbon-halogen bond-forming processes and the ease with which the boronate moiety can be replaced by a wide variety of functional groups. Boronates are not only among the most useful intermediates in contemporary organic synthesis but also appear directly in new boron-containing drugs—for example, the anticancer agent bortezomib (Velcade) and antifungal agent tavaborole (Kerydin). Boronates are being explored as biologically relevant sensors for sugars and hydrogen peroxide, as building blocks for novel covalent organic framework materials for gas storage, and in hydrogels, among other applications.

Thus, it is not surprising that interest in new methods for their synthesis has increased enormously. Boronates are often air- and water-stable reagents, tolerant to many

Published by AAAS

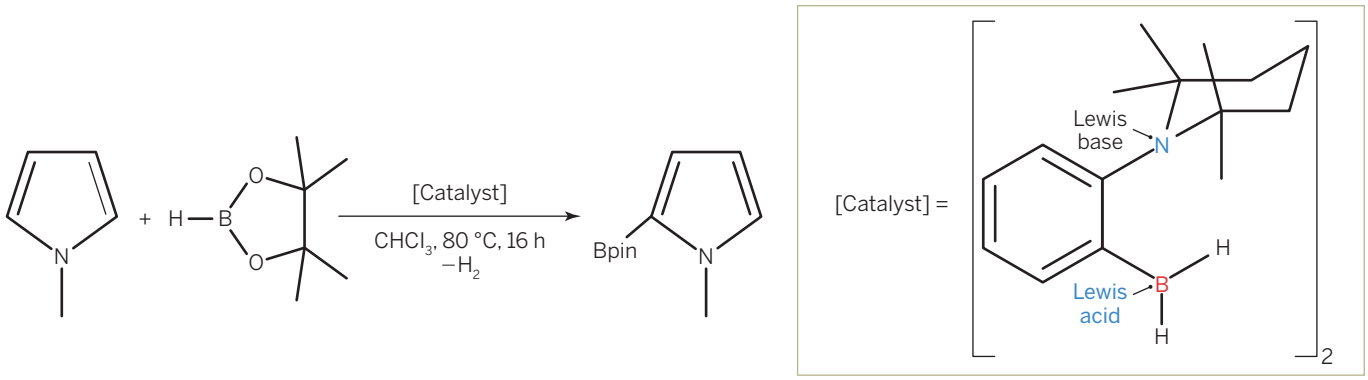

Metal-free catalysis. The carbon-hydrogen borylation process developed by Légaré *et al*. generates heteroarylboronates using frustrated Lewis pair catalysts; Bpin is $B(OCMe_2CMe_2O)$, where Me is methyl. In the catalyst, the boron is a Lewis acid and the nitrogen is a Lewis base that cannot satisfy one another, hence the term "frustrated." The specific example shown is for 1-methylpyrrole, but the substrate scope includes other aromatic rings containing nitrogen, oxygen or sulfur. The catalyst binds the substrate, then releases H_2, and finally reacts with HBpin to release the product and regenerate the catalyst.

key functional groups, which can nonetheless function as carbon nucleophiles, especially in metal-catalyzed transformations. They provide a replacement for conventional carbanion nucleophiles, such as Grignard reagents, that are such highly reactive species that they have limited utility in the last stages of multistep synthetic processes. For example, in the preparation of complex drug molecules, the use of very reactive nucleophiles requires the protection of sensitive functional groups.

However, traditional syntheses of aryl and heteroarylboronates typically involved just these highly reactive carbanion reagents until Miyaura first reported the metal-catalyzed coupling of arylhalides with diboron reagents in 1995 (*5*). More recently, methods for the direct borylation of aromatic and heteroaromatic carbon-hydrogen bonds have been developed, notably the iridium catalyzed reactions (*6*) of Smith and co-workers (*7*) and of Ishiyama, Miyaura, Hartwig, and co-workers (*8*) that are based on carbon-hydrogen activation at an Ir(III)-tris-boryl center (*9*). The selectivity of the now widely used iridium-catalyzed borylation reaction is largely dominated by steric effects (*6*), often in complete contrast with conventional electrophilic aromatic substitution processes. However, underlying electronic effects (*10*, *11*) correlate well with proton nuclear magnetic resonance chemical shifts. Acidic carbon-hydrogen bonds with more deshielded proton resonances are most likely to be substituted, which is clearly evident for heteroarenes.

Organic synthesis requires a toolbox of procedures, because no single process will be optimized for all cases. Alternative selectivities to those obtained via iridium- or rhodium-catalyzed carbon-hydrogen borylation reactions are thus welcome, as are processes that do not require expensive and toxic metal catalysts. The use of borenium cations for arene and heteroarene borylation gives regioselectivity typical of an electrophilic substitution process (*12*, *13*), but these reactions are not catalytic.

The alternative, metal-free borylation of carbon-hydrogen bonds of heteroarenes, developed by Légaré *et al*., uses an intramolecular FLP (frustrated Lewis pair) as the catalyst (see the figure) at which the carbon-hydrogen bond activation takes place. The close proximity of donor and acceptor sites in frustrated Lewis pairs makes them of considerable interest for the heterolytic cleavage of H_2, as well as the capture, activation, or both of gases such as carbon dioxide, nitrous oxide, sulfur dioxide, and carbon monoxide (*14*, *15*). Other applications include metal-free catalytic hydrogenation of unsaturated bonds in alkenes, alkynes, arenes, and imines.

"The selectivity, activity, and development of a metal-free catalytic process are all attractive features of this catalyst system based on frustrated Lewis pairs."

The aminoarylborane (ortho-TMP-C_6H_4-BH_2, where TMP is 2,2,6,6-tetramethylpiperid-1-yl)—a frustrated Lewis pair in which the BH_2 group is the Lewis acid and the bulky TMP is the base—has now been shown to activate carbon-hydrogen bonds of heteroarenes. The nucleophilic carbon of the heteroarene approaches the smaller Lewis acidic BH_2 site, whereas the larger amine group favors the abstraction of the proton. The resulting intermediate, possessing an acidic hydrogen on the N atom and an hydridic hydrogen on the B atom, undergoes H_2 elimination and then exchanges with pinacolborane (HBpin) to give the heteroaryl-Bpin product while it regenerates the catalyst.

Although some of the selectivities coincide with those of the iridium-catalyzed reactions, others are complementary and are reminiscent of an electrophilic borylation process. The selectivity, activity, and development of a metal-free catalytic process are all attractive features of this catalyst system based on frustrated Lewis pairs. Modifications of the catalyst have the potential to result in even higher activity for borylation and, possibly, other carbon-hydrogen bond functionalization processes. ■

The authors are at the Institute of Inorganic Chemistry, Universität Würzburg, 97074 Würzburg, Germany. E-mail: todd.marder@uni-wuerzburg.de

REFERENCES AND NOTES

1. X. Ribas, Ed., *C-H and C-X Bond Functionalization: Transition Metal Mediation* (Royal Society of Chemistry, Cambridge, UK, 2013).
2. M.-A. Légaré, M.-A. Courtemanche, É. Rochette, F.-G. Fontaine, *Science* **349**, 513 (2015).
3. D. G. Hall, Ed., *Boronic Acids: Preparation and Applications in Organic Synthesis, Medicine and Materials* (Wiley-VCH, Weinheim, Germany, ed. 2, 2011).
4. N. Miyaura, A. Suzuki, *Chem. Rev.* **95**, 2457 (1995).
5. W. K. Chow *et al*., *RSC Adv.* **3**, 12518 (2013).
6. I. A. I. Mkhalid, J. H. Barnard, T. B. Marder, J. M. Murphy, J. F. Hartwig, *Chem. Rev.* **110**, 890 (2010).
7. J.-Y. Cho, M. K. Tse, D. Holmes, R. E. Maleczka Jr., M. R. Smith 3rd, *Science* **295**, 305 (2002).
8. T. Ishiyama *et al*., *J. Am. Chem. Soc.* **124**, 390 (2002).
9. P. Nguyen *et al*., *J. Am. Chem. Soc.* **115**, 9329 (1993).
10. H. Tajuddin *et al*., *Chem. Sci.* **3**, 3505 (2012).
11. B. A. Vanchura 2nd *et al*., *Chem. Commun.* **46**, 7724 (2010).
12. V. Bagutski *et al*., *J. Am. Chem. Soc.* **135**, 474 (2013).
13. A. Prokofjevs *et al*., *Angew. Chem. Int. Ed.* **50**, 2098 (2011).
14. G. C. Welch *et al*., *Science* **314**, 1124 (2006).
15. D. W. Stephan, G. Erker, *Angew. Chem. Int. Ed.* **54**, 6400 (2015).

ACKNOWLEDGMENTS

We gratefully acknowledge the support of the Deutsche Forschungsgemeinschaft.

10.1126/science.aac9244

Published by AAAS

PLANETARY SCIENCE

Ancient planetary dynamos, take two

Magnetic studies of Earth and Mercury constrain their ancient core dynamics

By **Julien Aubert**

Within our solar system, the Earth and Mercury are in a class of their own, being the only rocky planets presently possessing global magnetic fields of internal origin. Given how different these fields are (see the figure), how these two planets got into this situation is a complicated story. With the recent discovery by Johnson *et al.* (*1*) of ancient remanent magnetism trapped in crustal rocks dating as far back as 3.9 billion years ago on Mercury, and, on page 521 of this issue, by Tarduno *et al.* (*2*) of a remanent magnetism for Earth dating back 4.2 billion years ago, the plot may thicken even more. Or could a tape rewind provide us with the clues we may have missed so far to explain the observations?

Many rocks include iron-bearing minerals that act as tiny permanent magnets that can record the ambient magnetic field in which they were originally immersed as they were cooled below their Curie point temperature (the temperature below which magnetic order sets in). For rocks to preserve their ancient magnetization, no appreciable event of dramatic heating or high-pressure metamorphosis should have occurred at a later time. Whenever rocks are available for a detailed laboratory analysis, controlled demagnetization experiments enable a reconstruction of the history leading to these remanent fields.

The scientific and technical challenges underlying the discoveries of Johnson *et al.* and Tarduno *et al.* are huge in both cases, but of a different nature. Johnson *et al.* have carefully analyzed the magnetic recordings provided by the MESSENGER mission launched in 2004, which ended its life on 30 April 2015 with a controlled crash on Mercury after 4 years and more than 4000 orbits of the planet. The final orbits were performed at spacecraft altitudes below 100 km, which allowed a closer study of the surface magnetism. After filtering out all other known field contributions, temporally coherent signals emerge, which are attached to certain regions of limited extent at the surface. Their properties are highly suggestive of magnetic sources being confined in the planetary crust at a depth of a few tens of kilometers. The largest signals are observed over smooth plains corresponding to the youngest major volcanic deposits, providing a lower bound for the age of this magnetization.

Mercury ceasing its surface activity early in its history is the key to the hypothesis that the remanent magnetization is so ancient. This last point is precisely what makes ancient paleomagnetic measurements so difficult on our ever-dynamic Earth. There are only a handful of locations on the surface where quasi-pristine rocks can be found that have survived the complex tectonic history of our planet. At these locations, the chances of success can be increased by

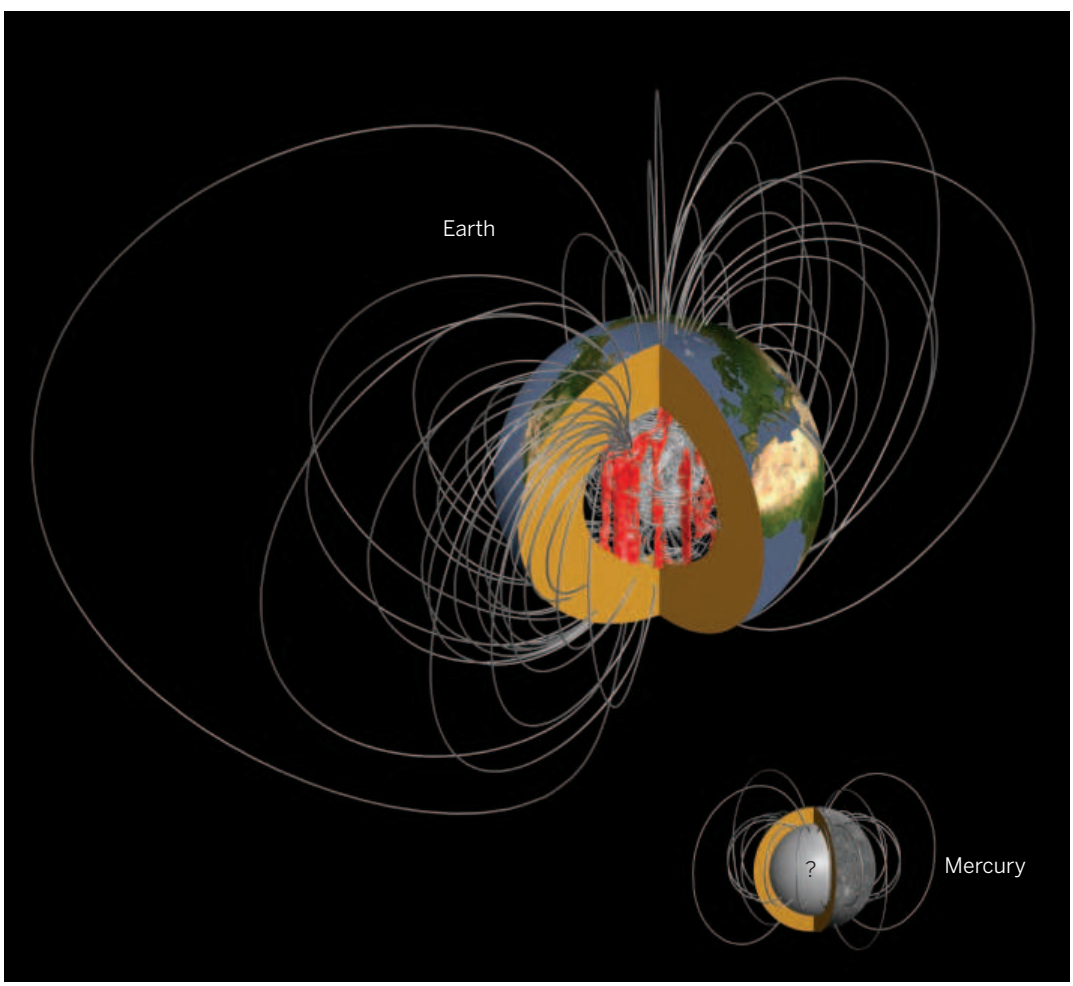

Similarities and differences. Mercury is about one-third the size of Earth and has a solid silicate mantle (orange) much thinner than that of the Earth, surrounding a partially molten core (*8*). Mercury and Earth both have an internal magnetic field similar to that of a giant magnet. Earth's equivalent magnetic field is roughly geocentric, whereas that of Mercury is slightly offset to the north and has an intensity one-hundredth that of Earth's (*9*). Both fields are thought to be generated by core dynamos, where the electrically conducting, liquid iron is stirred by convective motion (depicted in red in Earth), sustaining the magnetic lines of force (gray).

ILLUSTRATION: JULIEN AUBERT, IPGP/CNRS. WITH MERCURY SURFACE TEXTURE MAP NASA/JOHNS HOPKINS UNIVERSITY APPLIED PHYSICS LABORATORY/CARNEGIE INSTITUTION OF WASHINGTON

Institut de Physique du Globe de Paris, Sorbonne Paris Cité, Université Paris-Diderot, CNRS, 1 rue Jussieu, F-75005 Paris, France. E-mail: aubert@ipgp.fr

Published by AAAS

studying single-crystal magnetic inclusions within rocks. Subtle remanent magnetic fields are revealed by the extremely sensitive magnetometry used by Tarduno *et al.* on geochronologically dated zircon inclusions from the Jack Hills conglomerate in Australia.

A self-sustained dynamo operating in the partially molten, electrically conducting iron cores of Earth and Mercury is the most robust hypothesis for the generation of such long-lasting internal fields (see the figure). For this mechanism to operate, the liquid part of the core has to be vigorously stirred so that magnetic field lines (lines of magnetic force acting on the fluid in a way remotely similar to elastic ropes) are stretched, twisted, and folded in such a way that converts some of the energy driving the stirring into electromagnetic energy. The primary energy source is the planet's cooling, which leads to thermal core convection, accompanied by solutal convection in the event that the core has cooled down enough to start freezing. Other mechanical sources such as planetary precession or giant impacts can also play a role, but their sustainability and efficiency need to be assessed. The magnetic signal is thus an excellent probe of the planets' past and present internal activity.

"A self-sustained dynamo operating in the partially molten, electrically conducting iron cores of Earth and Mercury is the most robust hypothesis for the generation of such long-lasting internal fields."

Numerical simulations of Earth's convective dynamo have revealed that the magnetic field intensity is related to the strength of convection (*3*). Tarduno *et al.* report on ancient Earth field intensities ranging between 0.12 and 1 times that of the present value, while models provided by Johnson *et al.* lead to ancient fields 1 to 100 times the present value on Mercury. Although the ranges are extensive for both planets, this suggests an ancient core convection possibly as strong as at present.

Maintaining such an efficient core stirring over long time scales represents one of the tightest constraints on the thermal history of the two planets. Four billion years ago, the cores of Earth and Mercury were presumably fully molten, such that convection was solely of thermal origin. The existence of thermal core convection implies a fast core cooling, faster than the rate at which simple conduction in liquid iron can remove the heat without generating motion. Pushing the age of their dynamos backward in time then implies that Mercury and Earth should have had a hotter start than previously thought (*4*, *5*), all the more so considering that in the first few hundred million years the core was thermally blanketed by early radioactive decay in the mantle. That start cannot be impossibly hot, though, as the crust should have been solid and cold enough by the time when the remanent magnetizations were acquired.

Another riddle related to thermal history concerns Mars and the Moon, which also have remanent magnetism of a similar age. Why did the dynamos die there but survive on Earth and Mercury? Cessation of mantle convection and plate tectonics can be invoked, resulting in a cooling slowdown, but Mercury's case largely defeats the generality of this explanation.

Comparative planetary dynamo theory involves factors other than thermal history, such as core composition, timing and localization of core freezing, and the geometry of the resulting fluid motions (*6*). Evolutionary approaches have emerged that couple thermodynamic, structural, and geodynamic models in one single framework accounting for variations on geological time scales (*7*). Data points provided by ancient dynamos will be extremely useful to such models, with the ultimate goal of testing whether the mechanisms proposed to explain the presently observed diversity of planetary magnetic fields can stand the test of a backward run in time. The results of Johnson *et al.* and Tarduno *et al.* provide milestones toward the fascinating perspective of a unified theory. ■

REFERENCES

1. C. L. Johnson *et al.*, *Science* **348**, 892 (2015).
2. J. A. Tarduno, R. D. Cottrell, W. J. Davis, F. Nimmo, R. K. Bono, *Science* **349**, 521 (2015).
3. U. R. Christensen, J. Aubert, *Geophys. J. Int.* **166**, 97 (2006).
4. S. Labrosse, *Phys. Earth Planet. Int.* 10.1016/j.pepi.2015.02.002 (2015).
5. N. Tosi, M. Grott, A. C. Plesa, D. Breuer, *J. Geophys. Res.* **118**, 2474 (2013).
6. J. Wicht, D. Heyner, in *Planetary Geodesy and Remote Sensing*, S. Jin, Ed. (CRC Press, Boca Raton, FL, 2014), chap. 10, pp. 223–262.
7. P. Olson, R. Deguen, L. A. Hinnov, S. Zhong, *Phys. Earth Planet. Inter.* **214**, 87 (2013).
8. J. L. Margot, S. J. Peale, R. F. Jurgens, M. A. Slade, I. V. Holin, *Science* **316**, 710 (2007).
9. B. J. Anderson *et al.*, *Science* **333**, 1859 (2011).

10.1126/science.aac6224

CANCER

A p53-regulated immune checkpoint relevant to cancer

The tumor suppressor p53 may influence the ability of cancer cells to escape immune detection

By **Laurence Zitvogel**[1,2,3,4] *and* **Guido Kroemer**[5,6,7,8,9]

A major challenge in biomedical research is elucidating connections between stress responses within the cell and the extracellular microenvironment. This dialogue can transcend cellular life, and as such, premortem stress responses condition the mechanism through which corpses are cleared postmortem (*1*, *2*). This implies that the reason why, and the means by which, cells die determine whether their demise ultimately triggers immune responses against dead-cell antigens (*3*). On page 499 of this issue, Yoon *et al.* (*4*) explore the role of p53, a major stress-elicited transcription factor and tumor suppressor protein (*5*, *6*), in the clearance of dying cells by macrophages. The authors determine that p53 operates in a signaling pathway that protects against a systemic, life-threatening autoimmune disease encompassing ulcerative dermatitis, seizures, otitis, eye lesions, and glomerulonephritis (*4*, *7*).

Yoon *et al.* reveal that Death Domain 1α (DD1α), a member of the immunoglobulin superfamily, is expressed by three immunologically relevant cell types—dying cells, macrophages, and T cells (see the figure). Its expression can be induced by p53 in human cancer cells, as well as in normal mouse cells, and DD1α is constitutively expressed by macrophages and mature T cells. When DD1α is present on the surface of dying cells, as well as on that of macrophages, it can engage in homophilic interactions. This facilitates the recognition, engulfment

Published by AAAS

(phagocytosis), and clearance of dying and dead cells by macrophages. Importantly, the presence of DD1α on the surface of live cells does not trigger their phagocytotic removal. Rather, a combination of DD1α expression and programmed cell death (apoptosis) is required for cell corpse elimination. Given that multiple other dead cell recognition signals have been described, the specificity of DD1α to this particular removal process is intriguing (*1*, *2*). Interestingly, Yoon *et al.* noted that DD1α can also engage in homotypic interactions on the surface of the same cell (cis association). This may induce a "rounding up" of apoptotic cells, and the resulting smaller size could facilitate their uptake by macrophages or other phagocytes.

Yoon *et al.* also observed that the presence of DD1α on the surface of T cells renders them susceptible to immunosuppression. Thus, homophilic cis interaction of DD1α reduces T cell receptor–stimulated proliferation of both $CD4^+$ and $CD8^+$ T cells. It may be possible that p53-induced expression of DD1α on stressed normal cells or cancer cells contributes to the inactivation of those T cells that recognize self antigens or tumor-associated antigens.

Although mice engineered to lack DD1α manifest a severe systemic autoimmune disease (*4*, *7*), it is not clear whether this pathology results from failed clearance of dead cells, defective inhibition of T cell responses, or both. The absence of p53 predisposes mice to autoimmune disease (*8*–*10*). However, it may be an oversimplification to directly connect deficient p53 to deficient DD1α expression and autoimmunity. Indeed, p53 may transactivate a number of immunosuppressive genes including programmed death–ligand 1 (PD-L1), which stimulates the immunosuppressive receptor programmed death–1 (PD-1) on T cells, thus activating one of the major immunological checkpoints (*4*, *11*). p53 also transactivates the expression of forkhead box P3 (FOXP3), a transcription factor that is essential for the generation and function of regulatory T cells, a subpopulation that maintains tolerance to self antigens (*12*). Macrophages lacking p53 produce increased amounts of proinflammatory cytokines in response to bacterial lipopolysaccharide and interferon-γ (*9*), and conditional ablation of *p53* in T cells only is sufficient to reduce the frequency of regulatory T cells and to stimulate the production of autoantibodies in mice (*12*), as it may facilitate the expansion of $CD4^+$ T cells in response to antigens (*13*). Moreover, p53-independent signaling pathways control DD1α expression as well (*4*), calling for a systematic search of stress response pathways that might affect the DD1α-mediated regulation of immune responses.

Although p53 has multiple functions in the adaptation of normal cells to environmental stress (*14*), it is best known for its role as a tumor suppressor (*5*, *6*). More than half of human cancers develop in a context in which the p53 pathway is inactivated (*5*). It will be important to study whether p53 mutations or other pathways leading to p53 inactivation result in changes in the density, localization, composition, and function of intratumoral immune cells (either before or after radiation or chemical therapy) that induce at least a partially p53-dependent DNA damage response. Such changes in the immune contexture might affect the capacity of p53 to control cross talk between cancer cell–autonomous premortem stress pathways and postmortem immune responses. The absence of DD1α in stressed or dying p53-deficient tumor cells might ultimately stimulate local anticancer immune responses for numerous reasons—the uncontrolled release of antigenic debris into the interstitial space that connects to lymphoid vessels (and hence the draining lymph node), the preferential uptake of tumor cell antigens by immunostimulatory dendritic cells (rather than their scavenging by macrophages), or exacerbated local T cell responses.

Yoon *et al.* show that the homotypic interaction of DD1α can be competitively inhibited by a soluble fusion protein containing the protein's extracellular domain. As well, antibodies specific for DD1α can stimulate anticancer immunosurveillance in mouse models (*15*), suggesting that they may be used as checkpoint blockers for the immunotherapy of malignant disease (*11*). If so, they could be efficient against tumors that possess a conserved p53 pathway. Nevertheless, as for other clinically used checkpoint blockers (*11*), autoimmune side effects may constitute a major obstacle for the clinical use of DD1α inhibitors in cancer treatment. Preclinical investigations should assess the opportunity of confining DD1α blockade in cancerous lesions either physically (by intratumoral injections) or pharmacologically (with reagents that direct DD1α blockers to antigens that are solely expressed by neoplastic cells).

DD1α constitutes a fascinating link between p53-mediated tumor suppression and anticancer immunosurveillance. This connection warrants further preclinical characterization as a potential therapeutic target. ■

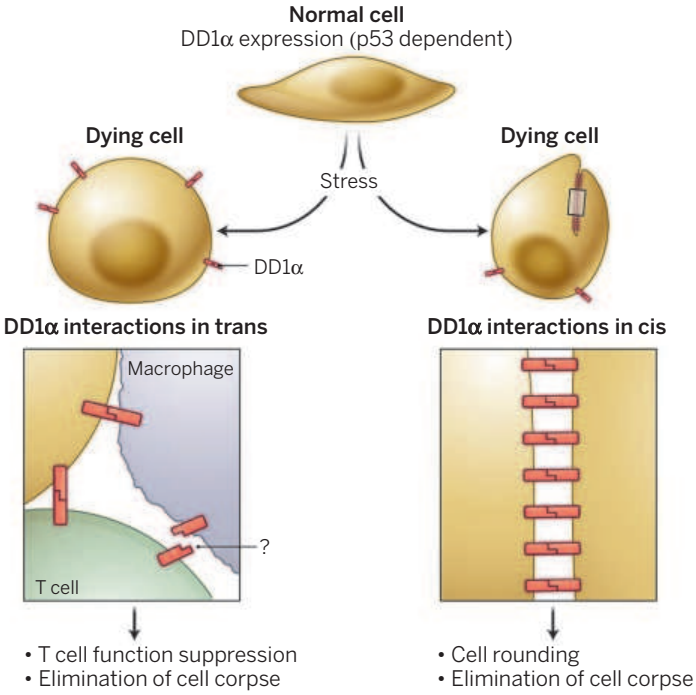

Palatable to phagocytes. DD1α is expressed by stressed and dying cells, facilitating interaction between macrophages and T cells. DD1α interactions on the same cell may cause the rounding up of dying cells, enhancing their engulfment by macrophages and other phagocytes.

[1]*Gustave Roussy Cancer Campus, F-94805 Villejuif, France.* [2]*INSERM U1015, F-94805 Villejuif, France.* [3]*Université Paris Sud-XI, Faculté de Médecine, Le Kremlin Bicêtre, France.* [4]*Center of Clinical Investigations in Biotherapies of Cancer (CICBT) 507, F-94805 Villejuif, France.* [5]*Equipe 11 labellisée par la Ligue Nationale contre le Cancer, Centre de Recherche des Cordeliers, INSERM U1138, F-75006 Paris, France.* [6]*Université Paris Descartes, Sorbonne Paris Cité, F-75006 Paris, France.* [7]*Université Pierre et Marie Curie, F-75006 Paris, France.* [8]*Pôle de Biologie, Hôpital Européen Georges Pompidou, AP-HP, F-75015 Paris.* [9]*Metabolomics and Cell Biology Platforms, Institut Gustave Roussy, F-94805 Villejuif, France.*
E-mail: kroemer@orange.fr

ILLUSTRATION: V. ALTOUNIAN/*SCIENCE*

REFERENCES

1. L. Zitvogel, O. Kepp, G. Kroemer, *Cell* **140**, 798 (2010).
2. I. K. Poon *et al.*, *Nat. Rev. Immunol.* **14**, 166 (2014).
3. D. R. Green *et al.*, *Nat. Rev. Immunol.* **9**, 353 (2009).
4. K. W. Yoon *et al.*, *Science* **349**, 1261669 (2015).
5. K. H. Vousden, D. P. Lane, *Nat. Rev. Mol. Cell Biol.* **8**, 275 (2007).
6. D. R. Green, G. Kroemer, *Nature* **458**, 1127 (2009).
7. L. Wang *et al.*, *Proc. Natl. Acad. Sci. U.S.A.* **111**, 14846 (2014).
8. Y. Okuda *et al.*, *J. Neuroimmunol.* **135**, 29 (2003).
9. S. J. Zheng *et al.*, *Diabetes* **54**, 1423 (2005).
10. J. S. Park *et al.*, *Arthritis Rheum.* **65**, 949 (2013).
11. P. Sharma, J. P. Allison, *Science* **348**, 56 (2015).
12. H. Kawashima *et al.*, *J. Immunol.* **191**, 3614 (2013).
13. M. Watanabe *et al.*, *Immunity* **40**, 681 (2014).
14. C. R. Berkers *et al.*, *Cell Metab.* **18**, 617 (2013).
15. I. Le Mercier *et al.*, *Cancer Res.* **74**, 1933 (2014).

10.1126/science.aac8475

Published by AAAS

WATER

What scale for water governance?

Water management is a central responsibility of civil society. Major questions persist regarding practice, policy, and the underlying evidence and methods to inform both. Over the next 3 weeks, *Science* presents essays invited to debate key issues in freshwater research and management. This week: local versus global. When, and to what extent, should a global viewpoint replace, or work in tandem with, enduring localized perspectives?

Fresh water goes global

By **C. J. Vörösmarty,[1]* A. Y. Hoekstra,[2] S. E. Bunn,[3] D. Conway,[4] J. Gupta[5,6]**

Although water problems have been traditionally perceived, understood, and acted on locally, recent progress in Earth-system simulation, remote sensing, and analysis of water governance is producing new perspectives on fresh water. The advances reveal previously unrecognized global forces at work driving local-scale problems. The stage is reset for water research and policy-making.

POLICY

LOCAL ACTION, GLOBAL CONCERN. Although water problems come best into focus locally, countless local stressors and impacts have accumulated to global significance (*1*). Local misuse provokes regional water crises that could easily spill into the global domain should transboundary cooperation collapse for rivers (*2*) or should source waters fail in the Himalayan "Third Pole," which would affect one billion people (*3*). Local water management even transcends fresh water itself, as when a large reservoir traps river-borne sediment destined for the ocean and reduces the capacity of the shoreline to withstand coastal erosion (*4*).

Fresh water is essential to human development. It is no surprise then that Amazonia, the Congo, and Borneo are targeted for massive water engineering projects (*5*), yet protecting biodiversity in these ecosystems generates little conservation investment, even if its loss would have global effects (*6*). Despite the importance of water to community prosperity, social fabric, and environment, the World Economic Forum declared proliferation of water crises to be the greatest collective risk to the global economy (*7*).

GLOBAL ACTION, LOCAL CONCERN. The sources of local water problems may not be as local as they seem. They are influenced by global mechanisms, primarily climate (water availability) and the world economy (patterns of water use). These define the spatial and temporal character of water scarcity. These patterns show current usage already reaching maximum renewable global supplies (*8*, *9*).

ILLUSTRATION: DAVIDE BONAZZI

Published by AAAS

Much of the world's water use and pollution arises from production for global trade, which embodies impressive flows of virtual water. Such trade exacerbates local overexploitation and creates potential conflicts over water. It outsources environmental problems to countries with lax regulation that host highly polluting manufacturing or agriculture (*8*). Decisions on water infrastructure are made far from its ultimate point of installation or impact, and externalities largely remain unregulated.

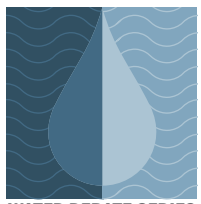

WATER DEBATE SERIES

GLOBAL GOVERNANCE FOR LOCAL STEWARDSHIP? Persistent water syndromes show local water governance unable to prevent global damage (*1*). At the same time, many global actors (United Nations, banks, multinationals) and rules are already in play, like the UN Watercourses and Ramsar conventions.

Yet, global water governance has not found its place among other scales of authority. Existing regimes are legally fragmented and dominated by local and mesoscale solutions (10). Large-scale governance focuses mainly on transboundary surface waters (versus groundwater), pays scant attention to pollution, fails to reconcile mismatches between river basins (and aquifers) and administrative jurisdictions, and has few incentives for sustainable water use in a globalized economy. It is difficult to harmonize ownership, rights and access to water, and cultural norms across the international playing field. Absent a global perspective, nexus issues on food, energy, and climate will be hard to address because linkages will remain essentially invisible, as with virtual water trade, which is regulated by trade agreements for commodities and not water.

With clear guidelines and legal responsibilities, consumers, governments, and investors could reverse the proliferation of free riding, commodification of public goods, secret international contracts and arbitration, and environmental neglect. Without such, widespread damage and nonsustainable water use will remain the norm.

A GLOBAL TEST CASE. An example of comprehensive water planning is unfolding in the intergovernmental arena with the post-2015 Sustainable Development Goals (SDGs) (*11*), which build on the earlier Millennium Development Goals (MDGs). Although MDG outcomes have been mixed [the drinking water target for the poor attained ahead of schedule, but delayed for sanitation (*12*)], they served as an important motivator for member states to prioritize water development efforts. SDGs expand the MDG agenda to include developing and developed world alike. Current SDG water proposals seek ecosystem protection, limits to pollution, and early responses to water-related hazards.

SDGs should lead to converging national policies, but much of the planning still focuses on local-scale solutions that fail to recognize broader-scale realities, like the connectivity of water systems. Thus, whereas sewering a developing world city improves the lot of urban dwellers, failure to install wastewater treatment destroys aquatic biodiversity and elevates health risks and water treatment costs downstream. Because 80% of today's sewage is discharged untreated (*11*), the issue is far from theoretical. Water systems will require substantial rehabilitation, nearly always much more costly than problem prevention, and will miss opportunities to apply new ecosystem-based approaches (*1*).

Despite their importance, the water-related SDGs alone will not effect a transition to global governance. International trade agreements need to be supplemented with context-specific but universally agreed-upon rules and standards on sustainable water use, water quality, and environmental flows. Principles like polluter/user pays and equitable water sharing are key to avoiding perverse incentives that have historically externalized impacts.

The global perspective is essential—but not a panacea. It may be counterproductive should it obscure, devalue, or fail to reflect the unique character of local or national settings. Experience shows that implementation of global measures is contingent upon political will, robust design, and institutional capacity at subsidiary scales (*7*).

In conclusion, acknowledging that local actions on water continue to trigger global-scale syndromes is a necessary first step toward effective governance. A global perspective is essential for providing context to local conditions, recognizing commonalities in both problems and solutions, identifying where prevention or remediation is needed most, and tracking progress or backsliding. Global thinking will help craft international agreements on water stewardship that ensure social equity and sustainability. Persistent focus on the local scale will miss such opportunities, which could otherwise make meaningful progress in solving 21st-century water problems that are, in fact, global. ■

REFERENCES AND NOTES

1. C. J. Vörösmarty *et al.*, *Nature* **467**, 555 (2010).
2. A. Subramanian, B. Brown, A. T. Wolf, *Water Policy* **16**, 824 (2014).
3. National Research Council, *Himalayan Glaciers: Climate Change, Water Resources, and Water Security* (National Academy Press, Washington, DC, 2012).
4. J. P. M. Syvitski *et al.*, *Nat. Geosci.* **2**, 681 (2009).
5. C. Zarfl, A. E. Lumsdon, J. Berlekamp, L. Tydecks, K. Tockner, *Aquat. Sci.* **77**, 161 (2015).
6. D. Dudgeon *et al.*, *Biol. Rev. Camb. Philos. Soc.* **81**, 163 (2006).
7. World Economic Forum, *Global Risks 2015* (WEF, Geneva, 2015).
8. A. Y. Hoekstra, M. M. Mekonnen, *Proc. Natl. Acad. Sci. U.S.A.* **109**, 3232 (2012).
9. P. H. Gleick, M. Palaniappan, *Proc. Natl. Acad. Sci. U.S.A.* **107**, 11155 (2010).
10. J. Gupta, C. Pahl-Wostl, R. Zondervan, *Curr. Opin. Environ. Sustain.* **5**, 573 (2013).
11. UN-Water, *A Post-2015 Global Goal for Water* (UN-Water, 2014).
12. WHO/UNICEF, *Progress on Drinking Water and Sanitation: 2014 Update* (WHO, Geneva, 2012).

ACKNOWLEDGMENTS

The authors acknowledge support from the NSF (CNH-1115025), Global Environment Facility (TWAP/DHI-11813758), NASA (LCLUC-NNX12AD28G), Global Water System Project, and Grantham Foundation for the Protection of the Environment.

10.1126/science.aac6009

Local perspectives on water

By **J. G. Hering**,[1,2,3]* **D. L. Sedlak**,[4] **C. Tortajada**,[5,6] **A. K. Biswas**,[5,6] **C. Niwagaba**,[7] **T. Breu**[8]

A global perspective on water management predominates in high-level policy discussions. This has the advantage that over-arching issues can be highlighted and international resources mobilized. But water issues arise from local conditions and can only be resolved by people and institutions with local authority and responsibility. High-level policies can only have meaningful impact if they are informed by and responsive to local and regional contexts. In keeping with the principle of subsidiarity, high-level policy-making should support local and regional interests, efforts, and policies.

LOCATION IS IMPORTANT. Renewable freshwater resources derive from precipitation over land, which exhibits substantial spatial and temporal variability. Natural conveyance and storage are also spatially differentiated. The geography of major rivers, deltas, and coastlines has strongly influenced patterns of human settlements, trade, fishing, and agriculture. This is reflected in localized patterns of

[1]*Advanced Science Research Center, City University of New York, New York, USA.* [2]*Twente Water Centre, University of Twente, Enschede, Netherlands.* [3]*Australian Rivers Institute, Griffith University, Brisbane, Australia.* [4]*London School of Economics and Political Science, London, UK.* [5]*Amsterdam Institute for Social Science Research, University of Amsterdam, Amsterdam, Netherlands.* [6]*UNESCO-IHE Institute for Water Education, Delft, Netherlands.*
**E-mail: Charles.Vorosmarty@asrc.cuny.edu*

Published by AAAS

water demand and alteration of water systems, including draining of wetlands, river channelization, and construction of dams and canals. Urban areas have been local sources of pollution to waterways and coastal areas (*1*).

How infrastructure investment decisions are made can have profound impacts on local livelihoods and development. A global perspective is likely to distract attention and resources away from opportunities to adopt proven effective measures and build on past reforms whose success was based on principle and pragmatism (*2*). Installation of drinking water treatment plants in North America in the early 20th century is estimated to have extended life spans by up to 7 years (*3*). Investments in urban drainage reduced losses from flooding, draining of wetlands removed habitat for disease vectors, and construction of sewers and municipal wastewater treatment improved public health and supported recovery of aquatic habitat and fisheries. Dam construction provided water for irrigation, municipal and industrial supply, and electricity generation, as well as flood protection. These gains and associated economic development were accompanied by costs and environmental impacts (*1*), some of which are no longer considered acceptable. This has led to investment in restoration and alternative approaches to water management.

"Local actors are well positioned to deal with management issues subject to specific needs and constraints…"

Developing countries face substantial infrastructure deficits. An estimated 2.5 billion people, mainly in low- and middle-income countries, still lack access to improved sanitation; uncontrolled release of human waste and inadequate sewage treatment pose severe health risks (*4*). Water quality in rapidly industrializing countries is degraded by discharge of inadequately treated domestic and industrial effluents (*1*). Waste management that is appropriate for local conditions is needed to recover water, energy, and nutrients.

DOES A GLOBAL PERSPECTIVE HELP? Global policy-making, specifically adoption of the Millennium Development Goals (MDGs), has directed attention to lack of access to safe drinking water and sanitation. Yet the sanitation goal remains unmet (*4*), and pressing issues that go beyond access (e.g., fecal sludge management) have not been adequately addressed (*5*). The drinking water goal is compromised because access to improved water sources does not guarantee adequate water quality (*4*). The post-MDG Sustainable Development Goals will require integrated approaches for water management tailored to local conditions, as well as water-quality standards that can be monitored and related to health outcomes.

Institutions with a global reach (*6*) have an important role to play in sharing information on effective agricultural practices. Irrigated agriculture contributes to increased food security but also can negatively affect biodiversity and groundwater reserves. Increasing water productivity of crop yield in rain-fed areas will require improved water- and land-management practices that are adapted to local conditions and practices. Crop rotation, mulching, and minimizing tillage could increase water-use efficiency. Floodwater harvesting and rainwater runoff trapping are underexploited opportunities for increasing water storage in soil (*7*). Management of soil water, evaporation, and noncrop evapotranspiration is needed.

Agricultural demand for water is linked globally through trade in agricultural commodities, which results in a modest increase in the efficiency of water use (*8*). Virtual water transfer is an observable phenomenon, but it does not constitute a viable policy instrument. It fails to account for local damage resulting from poor water management practices in agriculture. For example, export–oriented agricultural production may increase the competition for water at the expense of local land-use systems, especially in arid and semiarid areas. Agricultural production in areas with high water productivity can be constrained by other factors, including energy demand, labor costs, or higher-value uses of land.

Calls for a global perspective on water governance have accompanied shifts in power from local authorities to a broader coalition of officials, bureaucrats, and interest groups. It is at the local level that interactions, tradeoffs, and choices matter most. Local actors are well positioned to deal with management issues subject to specific needs and constraints and reflecting relevant perceptions, aspirations, interests, and agendas (*2*, *9*). Local-level capacity development for water management may improve governance more generally.

International water management is needed where rivers or lakes cross or define national boundaries. There are often no agreements on how to structure development to the benefit of the countries involved. Past agreements focusing mainly on water allocation were negotiated on a "zero-sum" basis. Many institutions for transboundary water management have limited enforcement authority and effectiveness. Static agreements and institutions are not responsive to changing conditions. A more positive direction in transboundary water management incorporates potential benefits to multiple development sectors (*10*). This can only be effective if assessment of potential benefits reflects local conditions, constraints, and opportunities.

Water resources should be assessed and managed at the scale that is most effective. Concepts promoted from a global perspective may be insufficiently transferable to local contexts and/or may fail to reflect changing circumstances. A focus on the river-basin scale may be counterproductive if the size and complexity of the system overwhelm capacity for joint decision-making and management by the riparian states. A nested, tiered framework for analysis (*11*) may help identify the most effective scale for water management; a single scale may not be most effective in all cases or for all aspects of a single case. ■

[1]*Eawag, Swiss Federal Institute of Aquatic Science and Technology, Dübendorf, Switzerland.* [2]*Institute of Biogeochemistry and Pollutant Dynamics (IBP), Swiss Federal Institute of Technology (ETH), Zürich, Switzerland.* [3]*School of Architecture, Civil and Environmental Engineering (ENAC), Swiss Federal Institute of Technology (EPFL), Lausanne, Switzerland.* [4]*University of California, Berkeley, ReNUWIt Engineering Research Center, Berkeley, USA.* [5]*Cofounder, Third World Centre for Water Management, Atizapán, Mexico.* [6]*Lee Kuan Yew School of Public Policy, National University of Singapore, Singapore.* [7]*Department of Civil and Environmental Engineering, College of Engineering, Design, Art, and Technology (CEDAT), Makerere University, Kampala, Uganda.* [8]*Centre for Development and Environment (CDE), University of Bern, Bern, Switzerland.*
**E-mail: janet.hering@eawag.ch*

REFERENCES AND NOTES

1. United Nations Environment Programme, "Environment for the future we want" (UNEP, Malta, 2012), www.unep.org/geo/geo5.asp.
2. J. Briscoe, paper presented at the OECD Global Forum on Environment: Making Water Reform Happen, Paris, 25 to 26 October 2011; www.oecd.org/env/resources/48925318.pdf.
3. D. Sedlak, *Water 4.0: The Past, Present, and Future of the World's Most Vital Resource* (Yale Univ. Press New Haven, CT, 2014).
4. United Nations, "The Millennium Development Goals report 2014" (UN, New York, 2014); www.un.org/millenniumgoals/reports.shtml.
5. L. Strande, M. Ronteltap, D. Brdjanovic, Eds., *Faecal Sludge Management: Systems Approach for Implementation and Operation* (IWA publishing, London, 2014).
6. Institutions such as the International Water Management Institute (www.iwmi.cgiar.org/) and the UN Convention to Combat Desertification (www.unccd.int/en/Pages/default.aspx) serve as clearinghouses for information.
7. R. Mekdaschi-Studer, H. Liniger, "Water harvesting: Guidelines to good practice" (Centre for Development and Environment, University of Bern, Bern, 2013); http://bit.ly/WaterHarvest-pdf.
8. M. M. Mekonnen, A. Y. Hoekstra, . *Hydrol. Earth Syst. Sci.* **15**, 1577–1600 (2011).
9. A. K. Biswas, C. Tortajada, . *Int. J. Water Resour. Dev.* **26**, 129–139 (2010).
10. O. Varis, C. Tortajada, A. K. Biswas, Eds., *Management of Transboundary Rivers and Lakes* (Springer, Berlin, 2008).
11. E. Ostrom, *Proc. Natl. Acad. Sci. U.S.A.* **104**, 15181–15187 (2007).

10.1126/science.aac5902

Published by AAAS

BIODIVERSITY

Averting a North American biodiversity crisis

A newly described pathogen poses a major threat to salamanders via trade

By **Tiffany A. Yap[1,2,3], Michelle S. Koo[2], Richard F. Ambrose[1,4], David B. Wake[2,5], Vance T. Vredenburg[2,3]***

In the midst of an ongoing sixth mass extinction (*1*), more than 40% of all amphibians are threatened (*2*). Chytridiomycosis, an emerging infectious disease (EID) caused by the fungal pathogen *Batrachochytrium dendrobatidis* (*Bd*), has been more devastating than any infectious wildlife disease recorded, with >200 amphibian species collapsing to or near extinction (*3*). Recently, a new infectious chytrid fungal pathogen from Asia and specific to salamanders (*4*), *Batrachochytrium salamandrivorans* (*Bsal*), has been described (*5*). With no effective means to control spread of *Bsal* once it is established in wild host populations, *Bsal* invasion of North America could lead to rapid epizootic (wildlife epidemic) declines and extinctions in the world's richest and most diverse salamander fauna. We demonstrate the likelihood of *Bsal* introduction to North America via international trade, the likelihood of species being exposed to *Bsal*, and the potential impact of species exposure to *Bsal*. This presents a unique opportunity for wildlife management officials and the international amphibian trade community to prevent the spread of this deadly pathogen and to develop and implement rapid risk assessments and international responses to EIDs in wildlife.

POLICY

This highly virulent *Bsal* pathogen was discovered in the Netherlands during a mass die-off in European fire salamanders (*4*, *5*). Martel *et al.* (*4*) proposed that *Bsal* originated in Asia and spread to wild European salamanders via the international salamander pet trade. They warned that *Bsal* represents a substantial threat to salamanders in other regions (e.g., North America) that may also be naïve to the pathogen. Furthermore, they identified three actively traded Asian salamander species as reservoirs for *Bsal*: *Cynops cyanurus*, *Cynops pyrrhogaster*, and *Paramesotriton deloustali*.

Bsal has already spread from the Netherlands to Belgium (*4*), and there is evidence of its spread in international trade (*6*). The introduction of *Bsal* to naïve areas could lead to major salamander declines, which would have severe ecosystem impacts. In woodland communities, salamanders represent a substantial portion of vertebrate biomass and play key roles in trophic dynamics and the carbon cycle (*7*).

NORTH AMERICAN THREAT. North America is the world's salamander biodiversity hotspot with 48% of 676 recognized salamander species representing 9 of the 10 known families within the order Caudata (190 species in the United States, 137 in Mexico, and 21 in Canada) (*8*). *Bsal* has not been reported in North America, although few studies have been published in the short time since *Bsal* was described (*9*, *10*).

We combined projections from a *Bsal* habitat suitability model (HSM) (see the map, top left) (Fig. 1A) with a host species-richness map (see the map, top right) (Fig. 1B) to create a predictive model of host vulnerability (see the map, bottom) (Fig. 1C). We assumed host risk to be higher in areas of greater salamander species richness. Because the true niche of *Bsal* is unknown, we estimated occur-

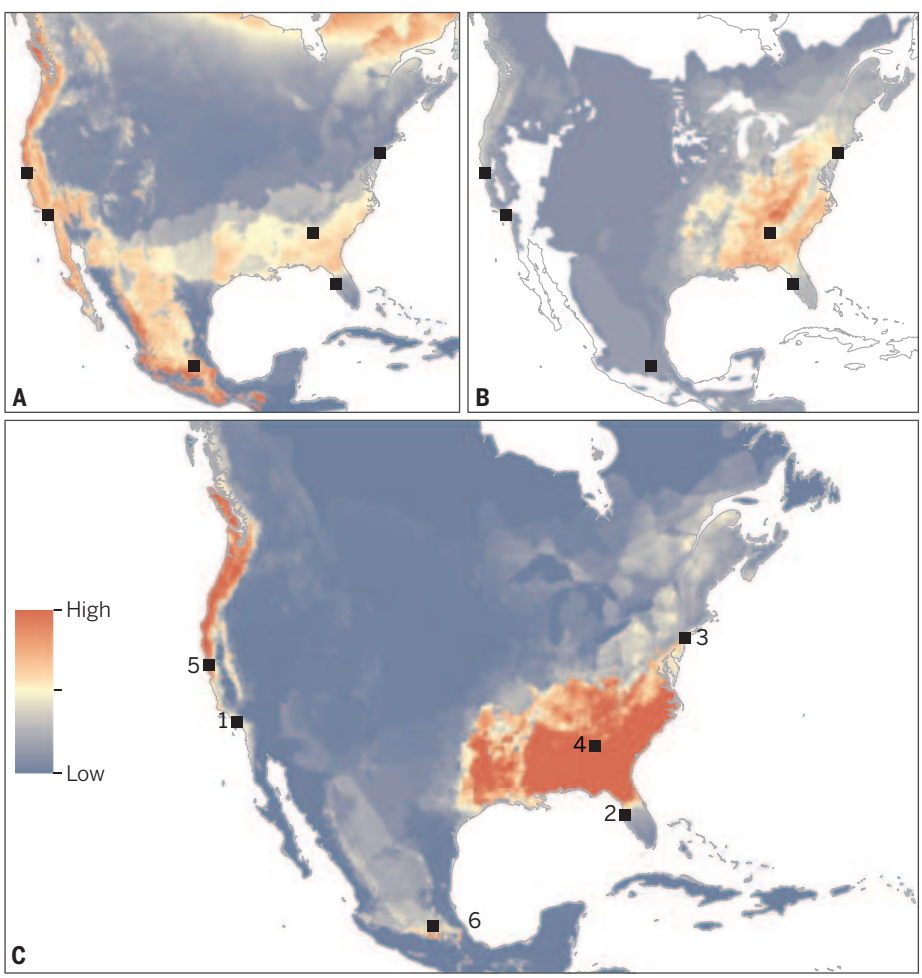

Mapping the threat of *Bsal* to North American salamanders. (**A**) *Bsal* habitat suitability model based on 133 carrier occurrences and six bioclimatic variables. (**B**) Salamander species-richness map. (**C**) Salamander *Bsal* vulnerability model. Major ports (black squares) for salamander imports follow the table (*22*). Port 6 represents Mexico City.

[1]Institute of the Environment and Sustainability, University of California, Los Angeles, CA, USA. [2]Museum of Vertebrate Zoology, University of California, Berkeley, CA, USA. [3]Department of Biology, San Francisco State University, San Francisco, CA, USA. [4]Department of Environmental Health Sciences, University of California, Los Angeles, CA, USA. [5]Department of Integrative Biology, University of California, Berkeley, CA, USA. *E-mail: vancev@sfsu.edu

Published by AAAS

rences on the basis of native ranges of the three putative *Bsal* reservoir species in Asia (fig. S1). We identified three zones of high risk in North America (see the map, bottom): southeastern United States (the southern extent of the Appalachian Mountains and neighboring southeast region), western United States (the Pacific Northwest and the Sierra Nevada), and the highlands of central Mexico (portions of the Sierra Madre Oriental and the Trans-Mexican volcanic belt).

Major U.S. ports for salamander imports

PORT	*Bsal* THREAT	NON-*Bsal* THREAT	ALL SHIPMENTS
1 Los Angeles, CA	418,692	1,198	419,890
2 Tampa, FL	272,338	1,140	273,478
3 New York, NY	55,441	70	55,511
4 Atlanta, GA	13,272	40	13,312
5 San Francisco, CA	3,164	6,459	9,623
Total (top 5 U.S. ports)	762,907	8,907	771,814
All U.S. ports combined	768,572	10,430	779,002

Imported salamanders were considered a *Bsal* threat if they have native ranges in Asia or were in shipments that passed through Asian ports before entering the United States. Those not considered a *Bsal* threat are not native to Asia and never passed through an Asian port before entering the United States. All values are number of salamanders (*22*).

The U.S. vulnerability zones contain numerous species from the two most *Bsal*-susceptible families, Plethodontidae and Salamandridae (*4*). North American newts (Family Salamandridae), which exhibited high levels of infection and 100% mortality (*5*), have large, vagile populations important in both terrestrial and freshwater ecosystems, and they may act as superspreaders of infectious disease by greatly increasing *Bsal* transmission in these regions (*11*). The Mexican vulnerability zone, located in an area of high beta diversity and endemism, has already been experiencing severe salamander declines (*12*, *13*).

RISK IN TRADE. Risk of *Bsal* invasion is compounded by the magnitude of international salamander trade. We examined the most recent 5 years (2010–2014) of live salamander trade entering the United States and identified the most active ports of entry using total gross imports (779,002 salamanders). About 99% originated from Asia, and 98% were species native to Asia (see the table). The major sources were Hong Kong, mainland China, Singapore, and Japan. Alarmingly, species in the genera *Cynops* and *Paramesotriton*, which included all three putative *Bsal* reservoirs (*4*), made up 91% of all salamander imports.

The five most-active U.S. ports were located within or near the predicted salamander vulnerability zones (see the map, bottom) and accounted for more than 98% of all U.S. salamander imports. Trade data from Canada and Mexico were not analyzed; however, Mexico City is a likely port of entry and is located within a predicted salamander high-vulnerability area.

Bsal is highly transmissible by direct contact (*4*); therefore, shipments containing cohoused animals and shared water increase the potential for pathogen spread. Given the magnitude of international salamander trade originating from Asia and containing potential *Bsal* reservoirs, the risk of *Bsal* introduction to North America is high.

MITIGATION AND RESPONSE. Species declines and extinctions due to wildlife EIDs and the lack of rapid responses (*14*, *15*) warrant immediate action to mitigate the spread of *Bsal*. Preventive action is far more cost-effective than emergency responses to disease outbreaks due to pathogen spread (*16*), and potentially irreversible environmental consequences could be avoided (*17*). The U.S. Fish and Wildlife Service can play a pivotal role in mitigating the threat of *Bsal* spread by placing an immediate ban on live salamander imports until effective EID prevention and management protocols are in place.

Immediate action in the United States, although critically important, is not sufficient. Because of globalization and human-mediated movements, an international infrastructure that facilitates rapid responses—similar to that of the World Health Organization (WHO) for human disease—is required to mitigate the spread of EIDs in wildlife (*14*).

Although the World Organization for Animal Health (OIE) and the Convention on International Trade in Endangered Species of Wild Fauna and Flora (CITES) provide guidelines for animal disease and the trade of endangered species, respectively, membership is voluntary, systematic record-keeping is limited, and wildlife EIDs are not prioritized. These institutions should work with government agencies and experts in disease ecology and animal trade to implement an international effort for surveillance, research, and management actions in an adaptive management framework for effective wildlife EID intervention (*16*). To enhance global biosecurity and to help prevent the spread of *Bsal* and other wildlife EIDs, a mandatory international system that will track all traded species, identify potential wildlife EID threats, and develop and facilitate emergency protocols is needed (*18*).

Immediate efforts are required to monitor zones of salamander *Bsal* high vulnerability (see the map, bottom). New studies on the basic biology of *Bsal* and on host-pathogen dynamics should also be a priority. Future studies should incorporate new data on transmission, susceptibility, and other potentially influential variables (e.g., species life-history traits, host microbiome, or co-occurring pathogens) to better understand the complex disease system. In the interim, the trade industry should take preventive measures from protocols that have been developed for the detection of *Bsal* (*19*) and the treatment of infected individuals (*20*, *21*). ■

REFERENCES AND NOTES

1. D. B. Wake, V. T. Vredenburg, *Proc. Natl. Acad. Sci. U.S.A.* **105** (suppl. 1), 11466 (2008).
2. S. N. Stuart *et al.*, *Science* **306**, 1783 (2004).
3. L. F. Skerratt *et al.*, *EcoHealth* **4**, 125 (2007).
4. A. Martel *et al.*, *Science* **346**, 630 (2014).
5. A. Martel *et al.*, *Proc. Natl. Acad. Sci. U.S.A.* **110**, 15325 (2013).
6. A. A. Cunningham *et al.*, *Vet. Rec.* **176**, 468 (2015).
7. M. L. Best, H. H. Welsh Jr., *Ecosphere* **5**, art16 (2014).
8. AmphibiaWeb, Information on amphibian biology and conservation (2015); http://amphibiaweb.org/.
9. C. Muletz, N. M. Caruso, R. C. Fleischer, R. W. McDiarmid, K. R. Lips, *PLOS ONE* **9**, e103728 (2014).
10. E. K. Bales *et al.*, *PLOS ONE* **10**, e0116405 (2015).
11. J. O. Lloyd-Smith, S. J. Schreiber, P. E. Kopp, W. M. Getz, *Nature* **438**, 355 (2005).
12. K. R. Lips *et al.*, *Proc. Natl. Acad. Sci. U.S.A.* **103**, 3165 (2006).
13. T. L. Cheng, S. M. Rovito, D. B. Wake, V. T. Vredenburg, *Proc. Natl. Acad. Sci. U.S.A.* **108**, 9502 (2011).
14. J. Voyles *et al.*, *EcoHealth* **11**, 2008 (2014).
15. D. M. Tompkins, S. Carver, M. E. Jones, M. Krkošek, L. F. Skerratt, *Trends Parasitol.* **31**, 149 (2015).
16. K. E. Langwig *et al.*, *Front. Ecol. Environ* **13**, 195 (2015).
17. K. A. Oye *et al.*, *Science* **345**, 6 (2014).
18. H.-K. Chan, H. Zhang, F. Yang, G. Fischer, *Science* **348**, 291 (2015).
19. M. Blooi *et al.*, *J. Clin. Microbiol.* **51**, 4173 (2013).
20. M. Blooi *et al.*, *Sci. Rep* **5**, 1 (2015).
21. M. Blooi *et al.*, *Sci. Rep.* **5**, 11788 (2015).
22. Materials and methods are available as supplementary materials on *Science* Online.

ACKNOWLEDGMENTS

This work was supported by UCLA–Charles F. Scott Fellowship (T.A.Y.) and NSF IOS-1258133 (V.T.V.). We thank S. M. Rovito for Mexican species occurrence data and the Museum of Vertebrate Zoology at University of California, Berkeley, for technical support. Original data are archived at AmphibiaWeb, VertNet, the International Union for Conservation of Nature, WorldClim, and the U.S. Fish and Wildlife Service, and we thank these organizations and collections for sharing their data. We also thank the anonymous reviewers.

SUPPLEMENTARY MATERIALS

www.sciencemag.org/content/349/6247/481/suppl/DC1

10.1126/science.aab1052

Published by AAAS

BOOKS *et al.*

GENOMICS

After the genome rush

How the life sciences changed in the wake of the genomics revolution

By **P. William Hughes**

In *Postgenomics*, philosophers and social scientists place genomic data into historical, social, and political context.

Postgenomics
Perspectives on Biology After the Genome
Sarah S. Richardson and Hallam Stevens, Eds.
Duke University Press, 2015. 304 pp.

The Human Genome Project (1998–2003) has been described as the frontier after which biology irrevocably changed. *Postgenomics: Perspectives on Biology After the Genome* contains 12 essays from philosophers and social scientists that reflect on the diverse consequences of this "genomics revolution." Topics range from the history of network theory and its effect on the development of bioinformatic modeling to broader ethical and philosophical considerations, such as data donation and curation, and the role that genomic data should play in eliminating health disparities.

The primary theme of this volume is that postgenomics research is characterized by a fundamental shift in how problems are identified, hypotheses are proposed, and data are treated, rather than by improvements in DNA sequencing technology. In chapter 7, Rachel Ankeny and Sabina Leonelli define postgenomics as "a historical marker for an era where the results of genomics … are being brought together with other types of biological traditions and outputs." In some cases, this synthesis challenges researchers' abilities to provide explanations for biological phenomena. For example, the effort to reconcile genomic data with insights from other biological sciences can call into question the reductionistic goal of articulating a simple relationship between genotype and phenotype.

An important secondary theme of the book is that while postgenomics presents new technical and theoretical challenges for scientists, it also allows science studies scholars to observe firsthand how scientists react to new discoveries. In chapter 3, anthropologist Mike Fortun highlights the importance of affect—specifically, emotional reactions such as surprise—as a driver of scientific discovery and change. Fortun argues that in repetitive, data-driven sciences such as genomics, where the formulation of hypotheses may follow rather than precede data collection, scientists' affective reactions to unexpected phenomena will become increasingly common as a defensible justification for research.

In chapter 4, John Dupré elegantly argues that the notion that individuals have a unique, fixed genome is untenable in light of contemporary scientific knowledge. He maintains that genomes are both dynamic—because epigenetic regulation is variable and reversible—and cooperative, because genetic chimeras and obligate symbiotes use proteins transcribed from multiple genomes. (He claims that humans fall under the category of obligate symbiotes because we have both a symbiotic relationship with our own gut flora and mitochondrial endosymbiotes.) Dupré concludes that it is no simple matter to speak of "the genome" of any individual organism, given that many dynamic genomes act in concert to facilitate individual survival and reproduction.

As in many edited volumes, there are notable tensions between the perspectives of the authors of these essays. The most important is a fundamental disagreement over the mutability of the postgenomic genome, a debate that is derived from the question of whether or not postgenomics is a methodologically distinct research program from genomics or classical genetics. Some authors maintain that postgenomics is more or less continuous with classical genetics, arguing that the ultimate goal is to find relationships between phenotypes and genomic causes. These authors treat genomes as invariant and believe that the distinction between pre- and postgenomic biology is that postgenomicists reveal insights by analyzing whole genomes instead of individual genes. Other authors argue that postgenomics is more or less distinct from genetics and is characterized by an antireductionistic (i.e., holist or emergentist) understanding of genetic material that attempts to describe syndromes of correlated phenotypes by means of developmental and probabilistic models. I believe that these unresolved tensions faithfully reflect those in the field and are a strength of the volume, which represents an honest and timely discussion of important issues in contemporary bioscience.

> ***"The volume … represents an honest and timely discussion of important issues in contemporary bioscience."***

I recommend this book to all biologists and philosophers interested in an accessible overview of the effect of the genomic revolution on the biosciences. It capably discusses both the new discoveries and the technical improvements that have been made since the advent of genomics, as well as the attendant philosophical and sociological implications. ■

The reviewer is at the Max Planck Institute for Plant Breeding Research, Köln 50829, Germany. E-mail: whughes@mpipz.mpg.de

10.1126/science.aac6181

PHOTO: ASKPANG/FLICKR

Published by AAAS

ENGINEERING

Inside the mind of an engineer

Engaging anecdotes offer readers a glimpse into the problem-solving processes employed by engineers

By **Sybil Derrible**

Applied Minds
How Engineers Think
Guru Madhavan
Norton, 2015.
267 pp.

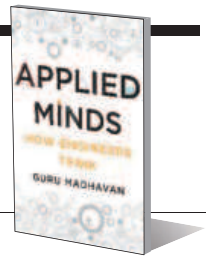

From fairly technical objects like cell phones and refrigerators to simpler ones like furniture, or even books, nearly everything that surrounds us has been affected in one way or another by engineers. In *Applied Minds*, Guru Madhavan takes us from the French wars of the 18th century to our digital era, discussing various challenges that engineers have tackled throughout history. The focus of the book is on the mindset of the engineer as opposed to feats of engineering, exploring the individual thought process rather than the development or construction of large engineering systems such as the Panama Canal or the Burj Khalifa.

Madhavan, who is himself a biomedical engineer as well as a policy adviser, argues that engineers possess three traits that enable them to tackle complex challenges. First, they can visualize the structure of a problem by breaking it down into elements linked by logic, time, sequence, and function. Second, they know how to design under constraints. Third, they are able to make trade-offs to ensure a reasonable solution to a problem despite the constraints. "Engineering is at the center of producing utility under constraints," Madhavan says, and for this, engineers need to be creative. Madhavan argues that these three traits enable engineers to adopt "modular systems thinking," a method that allows them to divide complex problems into manageable pieces. Engineers also tend to favor a trial-and-error approach. For example, "instead of debating at length about the best way to do something," Google engineers "prefer to get going immediately and then iterate and refine the approach" (*1*).

Throughout the book, Madhavan uses stories to convey his message, in a style reminiscent of Malcolm Gladwell. Beginning as early as the 18th century, with the story of de Vallière and Gribeauval, who designed cannons for Louis XV's army, Madhavan proceeds to tell us how Clarence Saunders revolutionized the design of the supermarket in the early 1900s, how Margaret Hutchinson Rousseau developed a way to mass produce penicillin during World War II, how Steve Sasson pioneered the digital camera industry in the 1970s, and how modern-day engineers G. D. Agarwal and Veer Bhadra Mishra have been working to develop solutions to clean the Ganges River in India. At a more systemic level, Madhavan explains how engineers use standardization to improve a system's efficiency, discussing the development of the standard time zone system, the ZIP code, and the bar code.

Chemical engineer Margaret Hutchinson Rousseau developed the process of deep-tank fermentation that enabled large-scale production of penicillin.

Madhavan also discusses the influence that several engineers have had in nonengineering fields. He tells the story of former New York assemblyman David Koon, who had previously worked as an industrial engineer at Bausch & Lomb. During his time in office, Koon successfully pushed to incorporate location-tracking technology into the 911 emergency system. Alfred Hitchcock also greatly benefited from his engineering training, applying it in both the technical aspect of filming and in the methodical preparation of story lines and scripts.

Although insightful, the ensemble of stories leaves the reader with a desire to know more substantive information about how engineers solve problems. Indeed, the book does not explain why or whether "applied minds" are inherently different and whether it is possible to train oneself to think like an engineer, although perhaps it is just my own engineering mind-set that makes me want to see more data and technical details.

As a result, despite the fact that the book was clearly written for a broad audience, it is difficult to identify the type of people who will most benefit from it. Teenagers and young adults may find it useful for determining whether engineering is a career path for them. Practicing engineers and history buffs will likely enjoy these engaging vignettes as well.

More fundamentally, the book is missing a section on the changing role of the engineer in society. Engineers once played a major role in society's decision-making processes; however, this has gradually shifted to more of a technical advisory role. Undoubtedly, many of the problems humanity is now facing will require that we adopt the structure–constraints–trade-offs approach well explained in this book. Madhavan himself is part of this change, as a senior policy adviser at the National Academy of Sciences. His expertise in this arena could have offered an inspirational road map for how to ensure that engineers become more active in the decision-making process in the future. ■

The reviewer is in the Complex and Sustainable Urban Networks (CSUN) Laboratory, University of Illinois at Chicago, Chicago, IL 60607, USA. E-mail: derrible@uic.edu

REFERENCES

1. A. Dragomir *et al.*, *Computer* **43**, 6 (2010).

10.1126/science.aac7726

PHOTO: REUTHER LIBRARY

Published by AAAS

LETTERS

Edited by **Jennifer Sills**

Science in Congress: Good-faith debate

A. A. ROSENBERG *et al.*'s Policy Forum "Congress's attacks on science-based rules" (29 May, p. 964) unfortunately adopts a common political gambit: Endorse desirable policy goals, but denounce efforts to advance them without offering better alternatives.

Rosenberg *et al.* target five bills that they claim would "weaken the ability of science to inform federal rule-making." The authors declare that "public trust in science increases when we all have access to the same base of evidence," but they assail bills that would require agencies to disclose the data, models, and methods on which their proposed rules rely. They laud the concept of "using credible scientific knowledge in U.S. government regulation," but criticize legislation that would require agencies to give greatest weight to experimental, empirical, quantifiable, and reproducible data. They say "we must strengthen peer review," but oppose bills that would largely codify the Environmental Protection Agency's leading practices for scientific advisory panels. They call increasing accountability "of course… a worthwhile goal," but decry efforts to do so.

In a good-faith political debate, the constructive response to bills that promote good ideas in a flawed way is to suggest ways to correct the flaws. While the Secret Science Reform Act does not clearly prohibit agencies from issuing rules based on data that are legally confidential, it is ambiguous about whether agencies can proceed in that case. So let's clarify it. Does a requirement to "give greatest weight" to empirical data mean that "modeling studies [must] be excluded?" Presumably, it means that model results should receive less weight, but that could be made explicit.

Rosenberg *et al.* clearly prefer regulatory decisions to be made by "career employees in federal agencies working with experts," among whom they no doubt count themselves. But efforts to make that process more transparent, participatory, or accountable should not "raise alarm among all scientists." Such efforts would promote democracy, not "put [it] at risk."

James W. Conrad Jr.

Conrad Law and Policy Counsel, Washington, DC 20005-2725, USA. E-mail: jamie@conradcounsel.com

Science in Congress: Unnecessary conflict

IN THEIR POLICY Forum "Congress's attacks on science-based rules" (29 May, p. 964), A. A. Rosenberg *et al.* charge that there is an assault on using credible scientific knowledge to inform U.S. government regulations. To make this claim, they use false premises to attack constructive criticisms of how the U.S. Environmental Protection Agency (EPA) obtains and uses scientific advice. Although Rosenberg *et al.* are loath to admit it, that process can be improved, and the proposed legislation could help.

Many highly qualified scientists are employed in academic, government, and private organizations, yet most EPA committees consist almost exclusively of academic scientists. The Policy Forum fosters a "science versus industry" conflict that does not serve the public good. Public corporations have as much interest in regulations being based on credible science as do academic and government institutions. Corporations recognize that the costs of meeting regulations are borne by their customers or shareholders. Scientists from all sectors, including industry, bring unique perspectives to advisory committees that advance the use of credible science to inform regulatory decisions.

Rosenberg *et al.* suggest that the proposed legislation will marginalize independent scientists. To the contrary, the proposed legislation will encourage the kind of independent advice that all committee members should be offering. I agree with the authors that "public trust in science increases when we all have access to the same base of evidence." Thus, I strongly support efforts that will make critical databases that undergird regulatory decisions available to scientists beyond the original investigators for replication and extended analyses. Alternative analyses and interpretations help advance science and increase confidence in the use of all the analyses to inform regulatory policies. Looking to the future, I urge that we move beyond the "science versus industry" attitudes of the past and focus on how best to use science to inform regulatory decisions and advance society.

Roger O. McClellan

Advisor, Toxicology and Risk Analysis, Albuquerque, NM 87111, USA. E-mail: roger.o.mcclellan@att.net

Science in Congress: Deceptive statistics

IN THEIR POLICY Forum "Congress's attacks on science-based rules" (29 May, p. 964), A. A. Rosenberg *et al.* attempt to make a case that only technical experts should be granted the privilege of decision-making on technical issues. They write that decisions on data weighting "should be left to technical experts who understand how to interpret the data."

That is a revealing statement in light of the numerous journal articles just in the past year on the corruption of "p-hacking" (*1*), misinterpretation of data and statistical significance (*2*), retractions of research because of data mismanagement and fraud, and inability to replicate experimental results (*3*). The misuse of statistical significance in null hypothesis significance testing led the journal *Basic and Applied Social Psychology* in February to ban it from all future submissions (*4*).

Rosenberg *et al.* justify their insular call for experts to be in control because "otherwise, decisions might not be based on the best understanding of the scientific evidence." There is a huge assumption hiding

PHOTO: LAWRENCE JACKSON/WHITE HOUSE.GOV

Published by AAAS

in that sentence: that the scientific evidence is accurate. The literature suggests this is often not the case.

Gary K. Evans

Evanetics, Inc. and FitVantage, LLC, Columbia, SC 29212, USA. E-mail: gkevans@evanetics.com

REFERENCES

1. M. L. Head *et al.*, *PLOS Biol.* **13**, e1002106 (2015).
2. R. Nuzzo, *Nature* **506**, 150 (2014).
3. L. Freedman *et al.*, *PLOS Biol.* **13**, e1002165 (2015).
4. D. Trafimow, M. Marks, *Basic Appl. Soc. Psych.* **37**, 1 (2015).

Response

CONRAD MISSES THE key point of our argument: The bills we highlight are fundamentally flawed because they are based on a series of false premises about how agencies use science to make policy.

Taken together, these bills pervert the idea of a more "transparent, participatory, or accountable" regulatory process by sidelining independent science and scientists and creating redundant bureaucratic hoops that hamstring the ability of agencies to protect the public. Simply tweaking their language cannot achieve the goal of improving the process.

Conrad also misrepresents the true intent of these bills: to shut down or block regulations that sponsors, and those who support their campaigns, don't like. Collectively, the bills shift analysis and decision-making authority from subject-matter experts to politically motivated generalists.

McClellan, who has worked closely with the chemical industry throughout his career, notes that there are highly qualified scientists in industry, government, and academia that can usefully contribute to the policy process. We agree. But we disagree that these bills take the right approach or can be made to do so with some minor modifications to the language.

Evans calls attention to incidents of bias and misuse of statistics, which can occur in any study that requires technical analyses. He actually helps to make our point: The process of assessing science for the purpose of developing the best policies needs to be in the hands of independent scientists. Attempts to distort this process by including analysts who have an agenda are dangerous for society.

Can the process be improved? Absolutely. But only by encouraging the full participation of the science community rather than solely through industry lobbying efforts. We must begin from a rational starting point by recognizing that while enormous public health, safety, and environmental benefits have come from regulatory processes, a better connection between truly independent science and the policy-making process will result in still greater benefits for the public and for industry. We and our colleagues in science organizations, academia, and civil society are ready to fully engage in making those improvements. Are elected officials willing to work with us?

Andrew A. Rosenberg,[1]* L. M. Branscomb,[2] V. Eady,[3] P. C. Frumhoff,[4] G. T. Goldman,[1] M. Halpern,[1] K. Kimmell,[4] Y. Kothari,[1] L. D. Kramer,[5] N.F. Lane,[6] J.J. McCarthy,[7] P. Phartiyal,[1] K. Rest,[4] R. Sims,[8] C. Wexler[1]

[1]Center for Science and Democracy, Union of Concerned Scientists, Cambridge, MA 02138, USA. [2]University of California, San Diego, La Jolla, CA 92093, USA. [3]Conservation Law Foundation, Boston, MA 02110, USA. [4]Union of Concerned Scientists, Cambridge, MA 02138, USA. [5]William and Flora Hewlett Foundation, Menlo Park, CA 94025, USA. [6]Baker Institute of Public Policy, Rice University, Houston, TX 77005, USA. [7]Harvard University, Cambridge, MA 02138, USA. [8]Seattle, WA 98101, USA.

*Corresponding author. E-mail: arosenberg@ucsusa.org

TECHNICAL COMMENT ABSTRACTS

Comment on "Phylogenomics resolves the timing and pattern of insect evolution"

K. Jun Tong, Sebastián Duchêne, Simon Y. W. Ho, Nathan Lo

Misof *et al.* (Reports, 7 November 2014, p. 763) used a genome-scale data set to estimate the relationships among insect orders and the time scale of their evolution. Here, we reanalyze their data and show that their method has led to systematic underestimation of the evolutionary time scale. We find that key insect groups evolved up to 100 million years earlier than inferred in their study.

Full text at http://dx.doi.org/10.1126/science.aaa5460

Response to Comment on "Phylogenomics resolves the timing and pattern of insect evolution"

K. M. Kjer, J. L. Ware, J. Rust, T. Wappler, R. Lanfear, L. S. Jermiin, X. Zhou, H. Aspöck, U. Aspöck, R. G. Beutel, A. Blanke, A. Donath, T. Flouri, P. B. Frandsen, P. Kapli, A. Y. Kawahara, H. Letsch, C. Mayer, D. D. McKenna, K. Meusemann, O. Niehuis, R. S. Peters, B. M. Wiegmann, D. K. Yeates, B. M. von Reumont, A. Stamatakis, B. Misof

Tong *et al.* comment on the accuracy of the dating analysis presented in our work on the phylogeny of insects and provide a reanalysis of our data. They replace log-normal priors with uniform priors and add a "roachoid" fossil as a calibration point. Although the reanalysis provides an interesting alternative viewpoint, we maintain that our choices were appropriate.

Full text at http://dx.doi.org/10.1126/science.aaa7136

Published by AAAS

TECHNICAL COMMENT

INSECT PHYLOGENOMICS

Comment on "Phylogenomics resolves the timing and pattern of insect evolution"

K. Jun Tong, Sebastián Duchêne, Simon Y. W. Ho, Nathan Lo*

Misof *et al*. (Reports, 7 November 2014, p. 763) used a genome-scale data set to estimate the relationships among insect orders and the time scale of their evolution. Here, we reanalyze their data and show that their method has led to systematic underestimation of the evolutionary time scale. We find that key insect groups evolved up to 100 million years earlier than inferred in their study.

Insects are the most diverse group of animals on Earth, occupying a broad range of niches across ecosystems. However, many insect groups have a poor fossil record, meaning that the early evolution of hexapod orders remains shrouded in mystery (*1*). For this reason, studies of insect diversification, the timing of evolutionary innovations, and the arthropod phylogeny rely on molecular date estimates. This places considerable importance on the estimate obtained by Misof *et al*. (*2*).

Here, we examine the robustness of the date estimates reported by Misof *et al*. (*2*). The accuracy of evolutionary date estimates relies on several factors, including the estimation of the phylogenetic tree topology, branch lengths, and the calibrating information (*3*). The analysis of genome-scale data means that there is relatively little uncertainty in the estimates of the tree topology and branch lengths (*4*). However, the choice of calibrations will affect the accuracy of molecular date estimates.

The molecular-clock analysis of Misof *et al*. (*2*) was calibrated with a range of fossils throughout the insect phylogeny. These fossils were chosen on the basis of criteria relating to the confidence in their phylogenetic placement and isotopic dating (*5*). However, some key polyneopteran fossils were omitted from the analysis. For example, numerous "roachoid" fossils from the late Carboniferous period [~315 million years ago (Ma)] are widely considered more closely related to Dictyoptera (cockroaches, termites, and mantids) than to insects of any other order (*1*, *6*, *7*). The close relationship between these stem group dictyopteran roachoids and extant Dictyoptera was inferred on the basis of synapomorphies that include pronotum shape, tegminous forewings, and wing venation (*1*). Misof *et al*. estimated an origin of 250 Ma for the clade comprising Dictyoptera, Phasmatodea (stick insects), Embioptera (webspinners), Grylloblattodea (ice crawlers), Mantophasmatodea (gladiators), and Orthoptera (crickets and katydids), corresponding to node 130 in figure 1 in (*2*). The diversification of this clade is thus presumed to have occurred after the Permian mass extinction, but this is inconsistent with the presence of fossil roachoid representatives from the Carboniferous.

We also investigated the dating analysis of Misof *et al*.. Although they followed sound criteria for choosing their fossil calibrations, their approach to implementing these calibrations was less conservative. For 20 nodes in the insect phylogeny, the fossil evidence was summarized in the form of a log-normal prior on the age of the clade to which the fossil was assigned. As with all calibration priors, this is a quantitative statement of the relationship between the age of a clade and the timing of its earliest appearance in the fossil record (*8*). This relationship is typically very difficult to quantify, even for groups

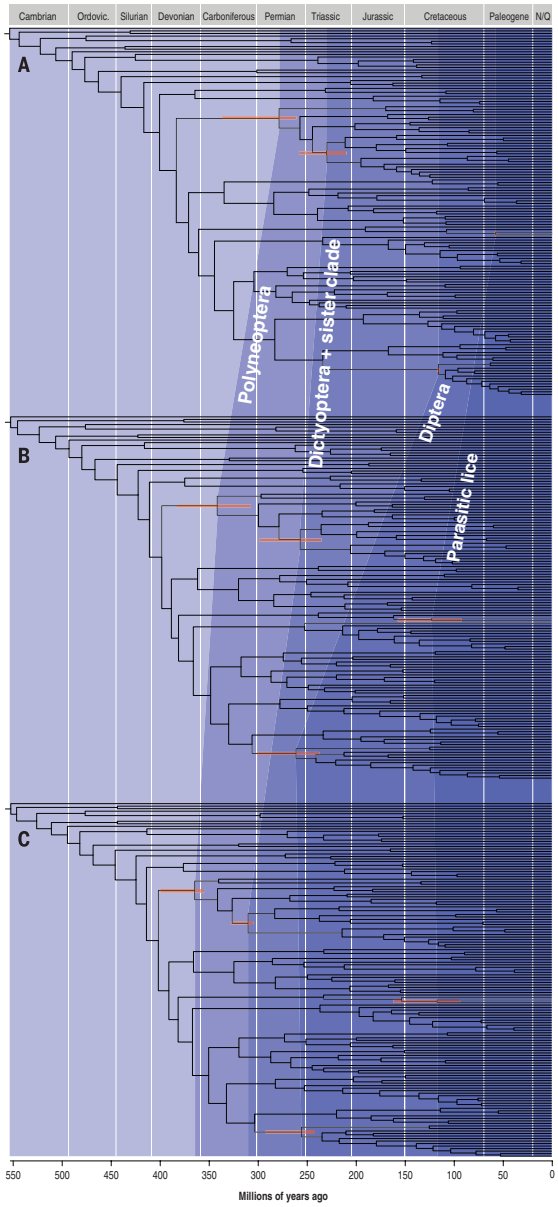

Fig. 1. Bayesian estimates of the insect evolutionary time scale using three different calibration schemes. (**A**) Calibration scheme of Misof *et al*., which comprised 37 age constraints and 20 log-normal priors. In place of the latter, we used uniform priors with soft bounds (*13*) chosen to match the 95% highest prior densities of the log-normal calibrations used by Misof *et al*. (**B**) Conservative calibration scheme. All calibrations were treated as soft minimum-age constraints, with soft maximum-age constraints as shown in table S9 of (*2*). (**C**) Conservative calibration scheme with additional constraint determined on the basis of multiple Carboniferous (~315 My old) roachoid fossils, corresponding to node 125 in figure 1 of (*2*). All node times represent the mean estimates from 105 data metapartitions identified by Misof *et al*. Shading indicates the variation in date estimates for corresponding nodes in the three trees; the error bars indicate 95% credibility intervals for these nodes. Date estimates were obtained from each data metapartition using Markov chain Monte Carlo (MCMC) sampling. We drew a total of 20,000 samples from the posterior, sampling every 50th step after a discarded burn-in of 100,000 steps. If this did not yield an effective sample size of at least 200 for each parameter, we doubled the number of MCMC steps until we reached sufficient sampling. Two independent replicates of the analysis converged on the same date estimates; we present the results of only one analysis here.

School of Biological Sciences, University of Sydney, Sydney NSW 2006, Australia.
*Corresponding author. E-mail: nathan.lo@sydney.edu.au

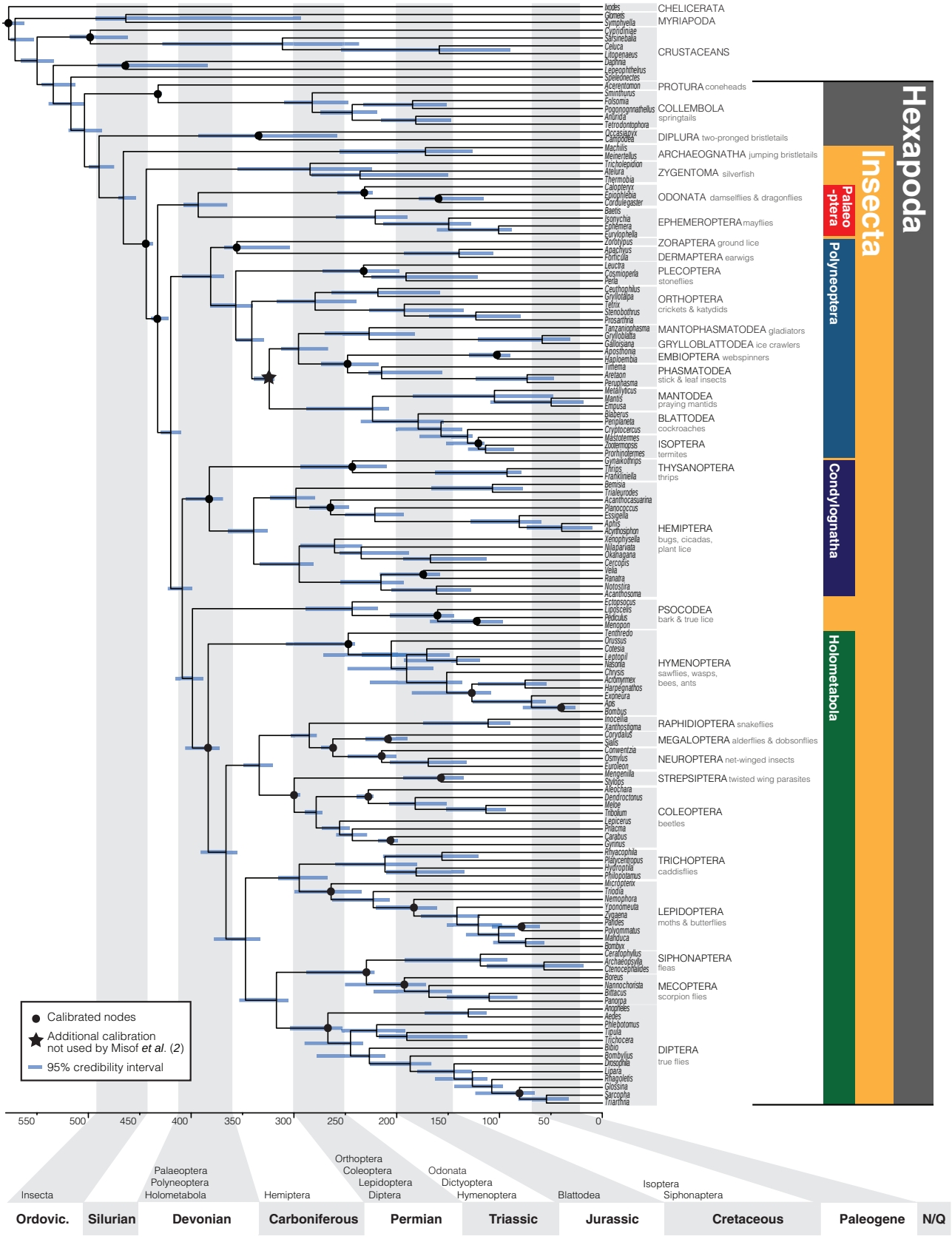

Fig. 2. Bayesian estimate of the insect evolutionary time scale using the 37 fossil minimum-age constraints of Misof *et al*. (black circles) and an additional roachoid fossil–based constraint in the polyneopteran clade (black star). Horizontal blue bars denote 95% credibility intervals of node-time estimates. Major clades are labeled on the right of the tree. First appearances of notable clades are shown below the time scale.

with detailed fossil records. In fact, the parameterization of the log-normal priors by Misof *et al.* embodies an expectation that the age of each calibrated node is only 7.4 million years (My) older than the earliest fossil appearance of any of its descendants. Moreover, the prior density allows only a 2.5% probability of the node being >19.7 My older than the earliest fossil. The potential effect of using log-normal priors for their calibrations is that the ages of nodes are more likely to be underestimated. A more conservative approach, using uniform priors, provides a better reflection of the uncertainty in fossil evidence.

We reanalyzed the genomic data of Misof *et al.* with a Bayesian dating approach in MCMCTREE (*9*), which is able to use an approximate likelihood calculation to reduce computational burden (*10*). This allowed us to investigate the effects of different calibration treatments, which was not possible using the computationally intensive approach employed by Misof *et al.*. First, we emulated their analysis by matching their implementation of 37 fossil-based calibrations, of which 20 were specified as highly restrictive age priors (Fig. 1A). We then reanalyzed the data using less restrictive uniform priors across the 37 nodes. This calibration scheme yielded older estimates of evolutionary divergence times (Fig. 1B). Finally, we added a calibration within the polyneopteran clade [node 125 of figure 1 in (*2*)] on the basis of late Carboniferous roachoid fossils (from ~315 Ma) (*6*, *7*) that had not been included in the original analysis. The inclusion of this calibration led to a further increase in the estimates of node times, whether the calibrations were treated as highly restrictive age priors (results not shown) or as less restrictive uniform priors (Fig. 1C).

Our revised estimate of the insect evolutionary time scale calls for reinterpretation of some of the conclusions drawn by Misof *et al.*. First, the origin of Polyneoptera is estimated at ~380 Ma [95% confidence interval (CI) 367 to 408 Ma], ~80 My earlier than in the original analysis (Fig. 2). Our estimate is more consistent with the widespread increase in fossils allied with Polyneoptera during the Carboniferous (*1*, *7*). Our estimate is consistent with the hypothesized close relationship between several Carboniferous fossils and particular polyneopteran groups, such as oedischoids and Orthoptera (*1*).

We infer that parasitic lice evolved ~120 Ma (95% CI 87 to 166 Ma), compared with the estimate of ~56 Ma by Misof *et al.* Our estimate is congruent with the hypothesis that parasitic lice evolved on feathered theropod dinosaurs (*11*). Finally, we estimate the ages of the megadiverse orders Diptera (flies) and Lepidoptera (butterflies and moths) at ~266 and ~263 Ma, respectively. These are ~100 My earlier than those of Misof *et al.* Our estimates are consistent with the fossil record (*1*, *6*, *12*) and challenge the hypothesis that these two orders diversified contemporaneously with angiosperms.

Our results demonstrate the effect of relaxing some of the assumptions made by Misof *et al.* and provide alternative scenarios for the time scale of insect evolution. We expect that the insect evolutionary time scale will continue to be revised in the light of fossil discoveries, developments in molecular-clock methods, and new data sets of the caliber generated by Misof *et al.* This will lead to ongoing improvement of our understanding of this important group of animals.

REFERENCES AND NOTES

1. D. Grimaldi, M. S. Engel, *Evolution of the Insects* (Cambridge University Press, Cambridge, 2005).
2. B. Misof *et al.*, *Science* **346**, 763–767 (2014).
3. S. Y. W. Ho, *Trends Ecol. Evol.* **29**, 496–503 (2014).
4. M. dos Reis, Z. Yang, *J. Syst. Evol.* **51**, 30–43 (2013).
5. J. F. Parham *et al.*, *Syst. Biol.* **61**, 346–359 (2012).
6. C. C. Labandeira, *Contrib. Biol. Geol.* **88**, 1–71 (1994).
7. R. Garwood, M. Sutton, *Biol. Lett.* **6**, 699–702 (2010).
8. S. Y. W. Ho, M. J. Phillips, *Syst. Biol.* **58**, 367–380 (2009).
9. Z. Yang, *Mol. Biol. Evol.* **24**, 1586–1591 (2007).
10. M. dos Reis, Z. Yang, *Mol. Biol. Evol.* **28**, 2161–2172 (2011).
11. V. S. Smith *et al.*, *Biol. Lett.* **7**, 782–785 (2011).
12. B. M. Wiegmann *et al.*, *Proc. Natl. Acad. Sci. U.S.A.* **108**, 5690–5695 (2011).
13. Z. Yang, B. Rannala, *Mol. Biol. Evol.* **23**, 212–226 (2006).

ACKNOWLEDGMENTS

This work was supported by Australian Research Council Discovery Project Grants DP1097265 to N.L. and DP110100383 to S.Y.W.H.

22 December 2014; accepted 8 June 2015
10.1126/science.aaa5460

TECHNICAL RESPONSE

INSECT PHYLOGENOMICS

Response to Comment on "Phylogenomics resolves the timing and pattern of insect evolution"

K. M. Kjer,[1] J. L. Ware,[2] J. Rust,[3] T. Wappler,[3] R. Lanfear,[4] L. S. Jermiin,[5] X. Zhou,[6,7] H. Aspöck,[8] U. Aspöck,[8,9] R. G. Beutel,[10] A. Blanke,[11] A. Donath,[3,12] T. Flouri,[13] P. B. Frandsen,[2,14] P. Kapli,[13] A. Y. Kawahara,[15] H. Letsch,[8] C. Mayer,[3,12] D. D. McKenna,[16] K. Meusemann,[5,12] O. Niehuis,[12,17] R. S. Peters,[3,12] B. M. Wiegmann,[18] D. K. Yeates,[5] B. M. von Reumont,[12,19] A. Stamatakis,[13] B. Misof[12]*

Tong *et al*. comment on the accuracy of the dating analysis presented in our work on the phylogeny of insects and provide a reanalysis of our data. They replace log-normal priors with uniform priors and add a "roachoid" fossil as a calibration point. Although the reanalysis provides an interesting alternative viewpoint, we maintain that our choices were appropriate.

We welcome reanalyses of our data (*1*), yet we disagree with several key points raised by Tong *et al.* (*2*). Regarding priors, they state that "uniform priors...better [reflect]... the uncertainty in fossil evidence." Although priors can greatly influence node-age estimates, uniform priors are not necessarily "conservative" either; more testing is needed for large data sets. Perhaps our priors were restrictive (as priors may be). Our log-normal priors affected our posterior estimates. For example, the internode leading to Polyneoptera in our figure 1 (*1*) appears longer than the corresponding internode in our maximum-likelihood trees, and this was likely influenced by our priors.

An informative discussion of the influence of priors on node ages is welcome, as are comments on our presentation. It is not a matter of controversy that priors can influence posterior estimates, but what needs to be demonstrated here is that the priors suggested by Tong *et al.* yield more reliable results. Indeed the source(s) of differences between their results and those in our paper remain unclear. To permit a more direct comparison, multiple analyses are necessary, using the same software and with the additional calibration point suggested by Tong *et al.*, first using our priors and then using their uniform priors.

Tong *et al.* used MCMCTREE, which tends to estimate older ages with broader confidence intervals than BEAST (used in our paper), especially at the root (*3*). The error bars in Tong *et al.* are very narrow, which illustrates a difference that we find puzzling. Additionally, MCMCTREE requires a user-specified soft maximum constraint at the root of the tree. Tong *et al.* do not indicate whether this was the same as ours. It is also unclear how thoroughly they evaluated convergence among the runs of their analyses. Two, and preferably more, chains should have been used to evaluate convergence. These data [i.e., analyses with several priors, detailed confidence intervals (CIs) for each node, and convergence values] are vital in an evaluation of the accuracy of node ages.

According to our estimates, stem dictyopterans extend back to only 287 million years ago (Ma). Tong *et al.* are particularly critical of this conclusion, noting that the "diversification of this clade...after the Permian...is inconsistent with the presence of fossil roachoid representatives from the Carboniferous." Indeed, if Carboniferous "roachoids" are shown to be dictyopterans, then our dates are underestimates. Any ambiguity is in classifying these fossils. The origin of Polyneoptera may extend back to 335 Ma, considering our CIs. Therefore, if "roachoid" fossils are not stem dictyopterans, but rather, generalized polyneopterans, then our estimates fit the fossil record (our age estimates range from 307 to 195 Ma).

Adding different fossils to an analysis may change the results. The synapomorphies for Bashkirian "roachoids" mentioned by Tong *et al.* have been interpreted in contradictory ways by different (and even the same) authors. They have not been evaluated in a formal phylogenetic analysis, so their placement is unclear. Following strict criteria (*4*), all of our calibration points were selected in light of modern phylogenetic analyses. We excluded fossils whose phylogenetic placement is highly speculative or founded only on older catalogs or compendia. Much of the disagreement between Tong *et al.* and our work stems from whether a particular "roachoid" fossil is, or is not, a stem dictyopteran. If we reject the use of tenuously identified fossils as calibration points, perhaps we can use our data to shed some light on the identity of these fossils. Our dating analysis suggests that these fossils are not stem dictyopterans.

Tong *et al.* are also critical of our findings on the timing of the origin of lice. Of the five papers reporting the discovery of a "fossil louse," only one (*5*) describes an unambiguously placed Cenozoic phthirapteran. We calculate the origin of extant Phthiraptera to have coincided with the radiations of modern bird and mammal orders—the contemporary hosts of parasitic lice. Tong *et al.* do not differentiate between the origin of parasitic lice with their extant diversification. We agree that our conclusion that parasitic lice did not evolve on feathered nonavian dinosaurs (theropods) might have been premature. It is difficult to tell the difference between feathered nonavian dinosaurs and early birds (which are also theropod dinosaurs). Feathered nonavian dinosaurs could have existed until the end of the Cretaceous. Therefore, our estimated split between book lice and stem lineage representatives of parasitic lice between 102 and 116 Ma is compatible with the hypothesis that the earliest parasitic lice fed on feathered nonavian dinosaurs. Regardless, our work finds that modern lice diversified after the Cretaceous. What the stem lineage fed upon is currently only speculation.

Tong *et al.* state that Lepidoptera and Diptera appeared 100 million years earlier than we estimate. Their comparison refers to the crown group, but our figure 2 (nodes 86 and 100) shows that the timing of the origin of the stem lineage of both orders encompasses their estimates (*1*). Indeed, analyses of Triassic dipteran fossils from Virginia (*6*) indicate that crown-group Diptera is older than our estimates. Clearly, the origin of Diptera is in need of further analyses. One strength of our analysis is that many of our node-age estimates are within the range of known fossils. Detailed phylogenetic analyses of known fossil groups can now potentially be used to falsify our results and/or further focus paleontological and molecular research.

In conclusion, we disagree with Tong *et al.*'s premise that they used fewer assumptions. They implemented strong assumptions about the identity of fossils and the understudied influence of node-age priors. The effect of priors was not thoroughly tested and should be more thoroughly

[1]University of California, Davis, CA, USA. [2]Rutgers University, New Brunswick, NJ, USA. [3]Universität Bonn, Germany. [4]Macquarie University, Sydney, Australia. [5]Commonwealth Scientific and Industrial Research Organization, Canberra, ACT, Australia. [6]China National GeneBank, BGI–Shenzhen, China. [7]BGI-Shenzhen, China. [8]Universität Wien, Vienna, Austria. [9]Naturhistorisches Museum Wien, Vienna, Austria. [10]Phyletischem Museum Jena, Friedrich-Schiller-Universität Jena, Germany. [11]University of Tsukuba, Japan. [12]Zoologisches Forschungsmuseum Alexander Koenig (ZFMK), Bonn, Germany. [13]Heidelberg Institute for Theoretical Studies (HITS), Heidelberg, Germany. [14]Smithsonian Institution, Washington, DC, USA. [15]University of Florida, Gainesville, FL, USA. [16]University of Memphis, Memphis, TN, USA. [17]Arizona State University, Tempe, AZ, USA. [18]North Carolina State University, Raleigh, NC, USA. [19]Natural History Museum London, London, UK.
*Corresponding author. E-mail: bmisof@uni-bonn.de

evaluated. Most of Tong *et al.*'s results confirm our results, and differences can be explained by opposing opinions or analytical choices that are not directly comparable. We described clear and consistent, repeatable justifications for our choices. What would be required for an improved critique would be a thorough analysis regarding the use of priors and a consistent usage of criteria justifying placement of fossils that we excluded.

REFERENCES AND NOTES

1. B. Misof *et al*., *Science* **346**, 763–767 (2014).
2. K. J. Tong, S. Duchêne, S. Y. W. Ho, N. Lo, *Science* **349**, 487 (2015).
3. R. C. Warnock, J. F. Parham, W. G. Joyce, T. R. Lyson, P. C. Donoghue, *Proc. Biol. Sci.* **282**, 20141013 (2014).
4. J. F. Parham *et al*., *Syst. Biol.* **61**, 346–359 (2012).
5. T. Wappler, V. S. Smith, R. C. Dalgleish, *Proc. Biol. Sci.* **271** (suppl. 5), S255–258 (2004).
6. V. Blagoderov, D. A. Grimaldi, N. C. Fraser, *Am. Mus. Novit.* **3572**, 1–39 (2007).

ACKNOWLEDGMENTS

The first seven authors and the corresponding author wrote this Comment. Those following, listed alphabetically, approved and commented. Full institutional affiliations are listed in our original paper. We thank D. Grimaldi for comments and K. J. Tong, S. Duchene, S. Ho, and N. Lo for their helpful responses to our questions.

2 February 2015; accepted 8 June 2015
10.1126/science.aaa7136

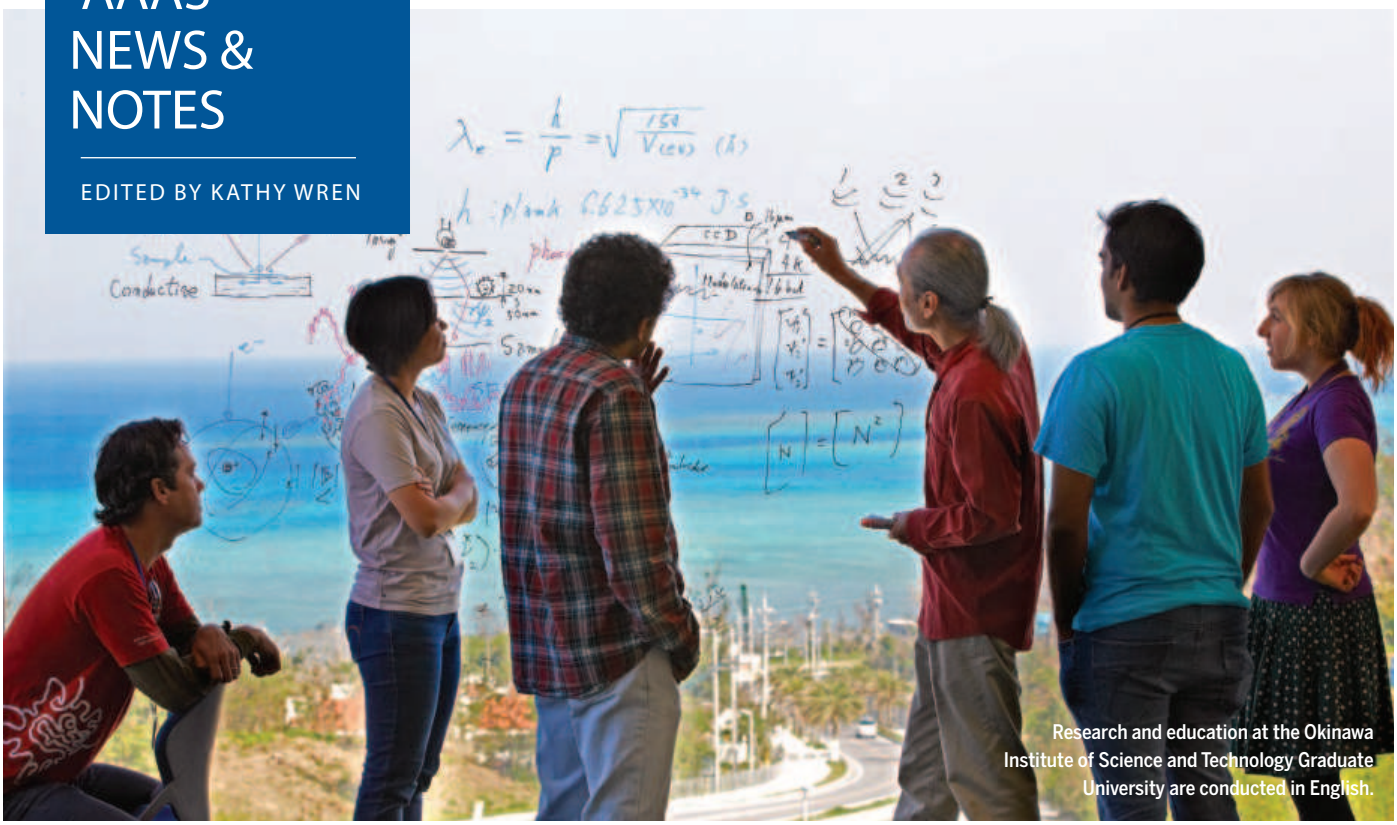

Research and education at the Okinawa Institute of Science and Technology Graduate University are conducted in English.

PHOTO: OIST/GINTER

Japan's universities open up to the world

A quest to globalize and engage with a wary public has sparked enthusiasm for science communication at Japanese universities

By **Brian Lin**, *in Tokyo*

A devastating natural disaster, a dire need to internationalize its universities, and lucrative funding programs have ushered in a renaissance of science communication in a country better known for its corporate R&D.

Leading the pack is a small, young university on a resort island 400 miles south of Japan's mainland, the Okinawa Institute of Science and Technology (OIST) Graduate University.

Capitalizing on its strengths—English is OIST's official language, and half of its 400 researchers are overseas recruits—OIST has set out to communicate its achievements globally. An international internship program brings science and communications grads on campus to interview researchers and write about their work. And the use of its fully bilingual website, social media, and news distribution services like the AAAS-operated EurekAlert! has helped OIST punch above its weight in garnering foreign media attention.

That's good news for OIST, as the Japanese government is increasingly telling universities to step up internationalization and science communication—and rewarding them handsomely for doing so.

Compared to other world-class universities, Japanese institutions can be cloistered places, where Japanese is the dominant language, even in funding applications and conference proceedings. This isolation has taken its toll: Only two of Japan's 781 universities made it within the top 100 in the 2015 *Times Higher Education* World University Rankings.

Japan's Top Global University Project, launched last year by the Ministry of Education, Culture, Sports, Science and Technology (MEXT), aims to boost the global standing of 37 institutions by offering a total of 7.7 billion yen over 10 years to increase international exchange and the number of foreign faculty and students. A year earlier, MEXT committed up to 400 million yen per year over 10 years to 22 institutions. The funds are earmarked for the hiring of University Research Administrators (URAs), who perform myriad roles within the research enterprise, from strategic planning, to partnership development, to communications.

For the sizable number of URAs newly assigned to improve communication, on-the-job training has become a top priority. Through the Research University Network of Japan, URAs and press officers from 25 universities have banded together to share expertise and find solutions. More than 30 communicators traveled to the 2015 AAAS Annual Meeting in San Jose, CA, and more than 60 attended a 29 May workshop in Tokyo, which included case studies of how universities have used EurekAlert!'s redesigned Japanese news portal to disseminate their bilingual press releases to the site's global audience that includes some 11,000 science journalists.

"There is some anxiety but even greater enthusiasm to learn," said Amane Koizumi, a professor at the National Institutes of Natural Sciences, who organized both gatherings. "But we're taking our first baby steps towards greater internationalization."

The push for more and better science communication had been iterated in the government-endorsed 4th Science and Technology

Published by AAAS

Basic Plan, with an aim to secure public support for S&T innovation. The emphasis took on even greater urgency after the 2011 Tohoku earthquake and the subsequent Fukushima nuclear accidents.

In a study conducted a year after the earthquake, published in the *Journal of Science Communication,* more than 70% of nearly 2000 Japanese parents said that they felt anxious about the risks of low-dose radiation. Respondents rated academic institutions and publications as the second-most trustworthy source of information (behind credible media outlets such as public broadcaster NHK), but often described them as inaccessible. This and other studies have also shown that public trust in scientists declined sharply after the disaster.

Hiroshima University, a recipient of both MEXT funding programs, wants to change that. It has assigned five URAs to support science communication and is also recruiting an international intern. Senior URA Norifumi Miyokawa said that while faculty have been positive about doing media outreach—some have been contacted by industries, other researchers, and Japanese media as a result—"the role of the public information officer is still not well understood, and we need more staff specialized in public relations."

One challenge, said Motoko Kakubayashi, a press officer at University of Tokyo's Kavli Institute for the Physics and Mathematics of the Universe, is that science communication is still a new concept in Japan, and while resources have been promised, there are "very few or no permanent positions for science communicators."

But there is no shortage of scientists willing to communicate. A 2013 survey of 9000 scientists, conducted by Koizumi for the Japan Science and Technology Agency's Center for Science Communication, showed that 71% of respondents agreed with the government's plan to improve communication with the public, and nearly 65% said that they were already doing it. More than 80% cited a sense of responsibility as their main reason for public outreach.

"[For faculty], there are no advantages to doing communication," Kakubayashi said. "The ones who do it, do it voluntarily because they're passionate about their research and want to raise awareness of their field."

Hiromi Yokoyama, an associate professor at the University of Tokyo's School of Science and author of the *Journal of Science Communication* study, added: "There is no doubt that interactive science communication activities between scientists and the public have contributed to advancing the public democratic debate." ■

Invention ambassadors challenge others to follow innovation path

By **Sarah Zielinski**

Successful inventors need more than a fabulous idea. They also need inspiration, great collaborators, and a lot of persistence, said seven new AAAS-Lemelson Invention Ambassadors introduced 14 July at the "Celebrate Invention" event at AAAS.

The ambassadors program, entering its second year, is a joint effort of AAAS and The Lemelson Foundation. "We began this partnership with AAAS, as we had a mutual belief in the power of invention to improve lives and create a better tomorrow, what we like to think of as 'impact inventing,'" said Carol Dahl, executive director of The Lemelson Foundation. Dahl hopes the program will foster a strong ecosystem for inventors as well as inspire a new generation of them.

"All of us have an inventor inside of us," said Lisa Seacat DeLuca, the most prolific female inventor in IBM history. But the inventing path is often full of hurdles. Juan Gilbert of the University of Florida has been developing a universally accessible voting system. Over and over, he was told, "it can't be done," Gilbert said. But he and his team persisted, and in September their Prime III voting system will be released as an open-source platform.

Sometimes, inventions can be the work of a single person, but more often, collaboration is involved, noted Suzie Pun of the University of Washington: "You should realize that in most of these cases, it's not just one person, but it's a whole team of collaborators making these technologies available."

Inventing can have many rewards, not just financial, speakers noted. Rebecca Richards-Kortum of Rice University described her lab's efforts to develop a cheaper bubble CPAP, a device used to help premature babies breathe. Her group's machine is now used in health facilities in Malawi and other developing countries. "I'll never forget the first time I saw a baby who went on treatment with a device that had been developed by our team," she said. "It was really an amazing moment to see how much that baby just relaxed…but even better was to see the relief on his mother's face."

Inspiration for these inventions came from sources as varied as hanging chads and sick infants. But getting from idea to invention can be a challenge. "If you see things that other people don't, they generally think you're crazy," said Andrew Hessel of Autodesk, Inc. and the Pink Army Cooperative. But, if you also see a path to achieving it, "you're not crazy. You could be a futurist, or really just be an inventor." ■

A machine that helps babies born with underdeveloped lungs is prohibitively expensive in developing countries, so a team led by AAAS-Lemelson Ambassador Rebecca Richards-Kortum developed a cheaper alternative.

PHOTO: MICHAEL COLELLA/COLELLADIGITAL.COM

Published by AAAS

RESEARCH

Mistletoe and other parasitic plants hijack host hormones

Conn et al., *p. 540*

IN *SCIENCE* JOURNALS

Edited by **Stella Hurtley**

Forest trees "remember" droughts for several years

FOREST ECOLOGY

Drought effects on carbon cycling

The response of forest ecosystems to drought is increasingly important in the context of a warming climate. Anderegg *et al*. studied a tree-ring database of 1338 forest sites from around the globe. They found that forests exhibit a drought "legacy effect" with 3 to 4 years' reduced growth following drought. During this postdrought delay, forests will be less able to act as a sink for carbon. Incorporating forest legacy effects into Earth system models will provide more accurate predictions of the effects of drought on the global carbon cycle. — AMS

Science, this issue p. 528

BORON CATALYSIS

A metal-free catalyst born of frustration

Boron (a Lewis acid) and nitrogen or phosphorus fragments (both Lewis bases) tend to pair up. Keeping them separated on opposite ends of the same molecule creates a "frustrated" Lewis pair. Such molecules can manifest powerful reactivity, such as scission of the hydrogen-hydrogen bond in H_2. Légaré *et al*. now extend this reactivity to the cleavage of carbon-hydrogen bonds in heteroaromatic compounds such as furans and pyrroles (see the Perspective by Bose and Marder). Their frustrated Lewis pair complex catalyzed borylation of these compounds. The selectivity pattern of the reaction complemented that seen with the metal catalysts conventionally used. — JSY

Science, this issue p. 513; see also p. 473

BIOMECHANICS

How to walk and jump on water

Jumping on land requires the coordinated motion of a number of muscles and joints in order to overcome gravity. Walking on water requires specialized legs that are designed to avoid breaking the surface tension during motion. But how do insects, such as water striders and fishing spiders, manage to jump on water, where extra force is needed to generate lift? Koh *et al*. studied water striders to determine the structure of the legs needed to make jumping possible, as well as the limits on the range of motion that avoids breaking the surface tension (see the Perspective by Vella). They then built water-jumping robots to verify the key parameters of leg design and motion. — MSL

Science, this issue p. 517; see also p. 472

GLOBAL WARMING

Looking for the missing heat

Global warming apparently slowed, or even stopped, during the first decade of the 21st century. This pause is commonly called the "hiatus." We know, however, that Earth's climate system is accumulating excess solar energy owing to the build-up of greenhouse gases in the atmosphere. Where, then, has this energy gone if not into the air? Nieves *et al*. find that over this period, the surface Pacific Ocean has cooled but the upper Indian and Southern Oceans have warmed. Thus, the decade-long hiatus that began in 2003 would appear to be the result of a redistribution of heat within the ocean, rather than a change in the whole-Earth warming rate. — HJS

Science, this issue p. 532

ACTIN-DIRECTED TOXIN

A little toxin can do a lot

The actin cross-linking domain (ACD) is an actin-specific toxin produced by several bacterial pathogens. Heisler *et al*. discovered that ACD's pathogenic mechanism involves a highly unusual toxicity amplification cascade. Rather than directly inactivating the actin cytoskeleton, ACD blocks the activity of formins, actin regulatory

PHOTOS: (FROM TOP) TED KINSMAN/SCIENCE SOURCE; © ASHLEY COOPER PICS/ALAMY

Published by AAAS

proteins that play crucial roles in numerous cellular activities. ACD is exceptionally potent, even though its substrate is the most abundant protein of a eukaryotic cell: actin. — SMH

Science, this issue p. 535

CALCIUM CHANNELS

One gene for three calcium currents

Mammals produce alternative forms of the Orai1 protein, which forms the pore of various calcium channels. This involves using two different translation initiation start sites in the encoding transcripts. Desai *et al*. showed that these long and short forms produce calcium channels with distinct properties. Both forms can participate in two kinds of channels that respond to the depletion of calcium from internal stores. However, only the long form contributes to a channel that is activated by arachidonic acid and leukotriene C_4, lipids that promote inflammation. Thus, alternative translation initiation of the *Orai1* message produces at least three types of calcium channels with distinct signaling and regulatory properties. — NRG

Sci. Signal. **8**, ra74 (2015).

METABOLISM

S-nitrosylation links obesity and cell stress

Obesity and other diseases are somehow linked to malfunction of the protein-protecting functions of the endoplasmic reticulum (ER). Yang *et al*. propose a mechanism by which obesity and associated chronic inflammation may be linked to the accumulation of unfolded proteins in the ER. Such stress would normally trigger the process known as the unfolded protein response (UPR). However, obese mice had increased S-nitrosylation of inositol-requiring protein-1 (IRE1α), a ribonuclease that regulates the UPR. The modified IRE1α had decreased RNAse activity. The authors expressed an IRE1α mutant protein that could not be nitrosylated in the liver of obese mice. This approach improved the UPR and helped restore glucose homeostasis. — LBR

Science, this issue p. 500

HIV

How antibodies mature

Antibodies are stalwart protectors against infection, but even they need a little help from their friends. Through a process called affinity maturation, T follicular helper (T_{FH}) cells guide B cells to produce antibodies with improved specificity to a particular pathogen. Now Yamamoto *et al*. report that in nonhuman primates, the frequency and quality of T_{FH} cells were associated with the development of broadly neutralizing antibodies that might be protective against simian HIV. These findings suggest that HIV vaccines that incorporate T_{FH} cell stimulation could boost broadly neutralizing antibody production. — ACC

Sci. Transl. Med. 7, 298ra120 (2015).

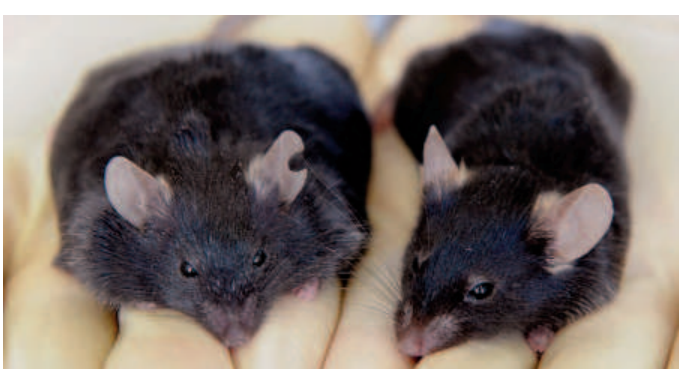

PHOTOS: (LEFT TO RIGHT) © DPA PICTURE ALLIANCE ARCHIVE/ALAMY; DR. KARI LOUNATMAA/SCIENCE SOURCE

Obese mice exhibit more cellular stress

IN OTHER JOURNALS

Edited by **Sacha Vignieri** *and* **Jesse Smith**

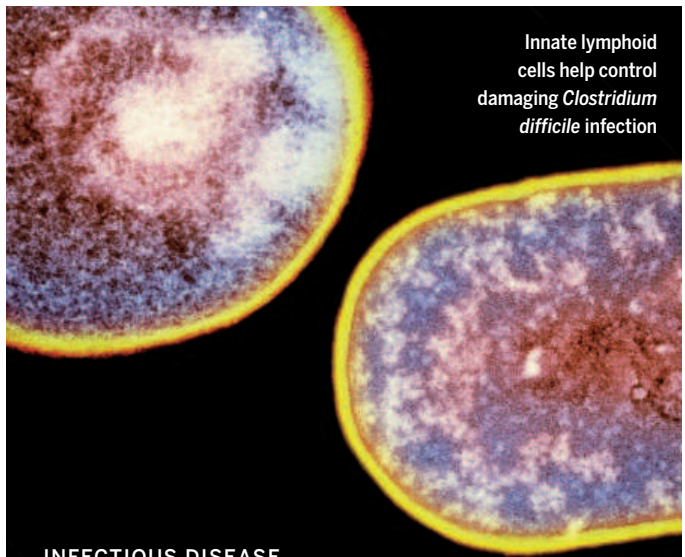

Innate lymphoid cells help control damaging *Clostridium difficile* infection

INFECTIOUS DISEASE

Innate lymphoid cells to the rescue

Most people enter the hospital with the hope of getting better, but recent increases in hospital-acquired infections have made hospitals deadly in their own right. For instance, deaths caused by the enteric bacterium *Clostridium difficile* increased by 400% in the last decade. *C. difficile* is an opportunistic pathogen that takes advantage of disruptions in the microbiota caused by antibiotic treatment. Abt *et al*. provide new insight into how the host defends itself against this unwelcome intruder. Studying *C. difficile*–infected mice, the authors found that the mice required innate lymphoid cells (ILCs) to survive the infection. ILCs did not substantially contribute to reducing pathogen burden but instead appeared to limit pathology and systemic dissemination. – KLM

Cell Host Microbe **18**, 27 (2015).

SIGNAL TRANSDUCTION

Signaling probed by single-molecule tracking

Developmental signaling through the so-called Hedgehog pathway is transduced through the receptor-like protein Smoothened. Hedgehog signaling requires highly specific localization of Smoothened in target cells at the primary cilium, a structure that functions somewhat like an antenna to receive and transmit signals. Milenkovic *et al*. tracked movement of single molecules of Smoothened in the cilia of cultured mouse embryo fibroblasts. Movement of Smoothened was restricted by binding events at the base of the cilium. Activation of Hedgehog signaling decreased the affinity of such binding. Such regulated binding of Smoothened to its yet-to-be-defined partner(s) within the cilium is likely an important step in the Hedgehog signaling mechanism. – LBR

Proc. Natl. Acad. Sci. U.S.A. 10.1073/pnas.1510094112 (2015).

NEUROSCIENCE

At the center of our own spatial social network

Neurons in the hippocampus

Published by AAAS

Relict microatoll on southeastern island of Simeulue, Sumatra

GEOPHYSICS

Allowing faults out of lock-up

The crust around a locked, earthquake-prone fault responds to the two sides pulling in opposite directions by bowing and bulging over time. Meltzner *et al.* and Wesson *et al.* challenge a common assumption that this deformation progresses mostly in a uniform, linear way. Deformation shows up in seafloor bathymetry, which changes abruptly for both Sumatra and Isla Santa Maria, Chile, over a seismic cycle. Periods during which the fault is weakly locked explains the non-uniform behavior. Quantifying the effect clarifies subduction zone mechanics, which may require updating estimates of earthquake hazard. — BG

Quat. Sci. Rev. 10.1016/j.quascirev.2015.06.003 (2015); *Nat. Geosci.* 10.1038/ngeo2468 (2015).

create a maplike representation of the environment, forming what is called spatial memory. Tavares *et al.* suggest that humans also create a 3D map of social space with themselves at the center. They measured the representation of a map of social interactions based on a role-playing game where participants could interact with fictional characters along power (dominance, hierarchy, etc.) and affiliation (intimacy, trustworthiness, etc.) gradients, while placed in an fMRI scanner. Left hippocampal activity correlated with the angle of a vector created by these two measures, but not by either of them alone, while the strength of correlation also depended on the social skills and personality traits like neuroticism and conscientiousness of the individual. – LNS

Neuron **87,** 231 10.1016/j.neuron.2015.06.011 (2015).

OBESITY MANAGEMENT

New drug—and new hope—for a losing game

Many people would gladly trade a dip in the fountain of youth for a safe drug that makes them thinner. Despite years of effort, the pharmaceutical industry has yet to deliver such a drug. New hope is offered by Pi-Sunyer *et al.*, who report the results of a 56-week, double-blind clinical trial examining the metabolic effects of a drug called liraglutide, which mimics a hormone produced in the gastrointestinal tract (glucacon-like peptide 1) that increases satiety. People taking liraglutide, in conjunction with dieting and exercise, lost a mean of 8.4 kilograms as compared with 2.8 kilograms in those taking a placebo. Drawbacks include the delivery method (injection) and hints that cessation of the drug results in regain of weight. – PAK

New Engl. J. Med. **373**, 11 (2015).

Injectable weight loss: In the long run, is it too good to be true?

NUCLEAR CHEMISTRY

Subsurface corrosion of uranium

Uranium dioxide, the most common form of nuclear fuel, becomes mobile as it oxidizes. Although oxidative corrosion is inherently a surface-mediated process, interstitial oxygen atoms can induce oxidation many atomic layers deeper. By detailing the surface structure and composition of UO_2 after exposure to oxygen in air and water, Stubbs *et al.* show that oxidation does not follow a classical diffusion pattern. Instead, interstitial oxygens preferentially occupy every third atomic layer below the terminal (111) surface. This pattern is a product of the delocalized electronic structure of nonsurface U atoms, which also allows for the coexistence of three U oxidation states. — NW

Phys. Rev. Lett. **114**, 246103 (2015).

APPLIED OPTICS

Dealing with big data

Data generation often occurs at such a high rate that it cannot be analyzed on the fly but must be stored and archived for access later on. While banks of magnetic hard drives are the storage medium of choice at present, the total capacity, recording times, and required energy burden are not expected to keep pace with the data generation rate. Li *et al.* look to optical recording as a possible solution. Combining superresolution nanoscopy to record tiny binary bits in a photosensitive medium with multifocusing array techniques to access multiple layers within the medium, it should be possible to achieve storage capacities of about 30 terabits per disk and data recording rates exceeding gigabits per second. — ISO

Optica **2**, 567 (2015).

PHOTOS: (TOP TO BOTTOM) ARON J. MELTZNER/EARTH OBSERVATORY OF SINGAPORE; DR. P. MARAZZI/SCIENCE SOURCE

Published by AAAS

ALSO IN *SCIENCE* JOURNALS

Edited by **Stella Hurtley**

CRYSTAL GROWTH

Growing crystals by attaching particles

Crystals grow in a number a ways, including pathways involving the assembly of other particles and multi-ion complexes. De Yoreo *et al*. review the mounting evidence for these nonclassical pathways from new observational and computational techniques, and the thermodynamic basis for these growth mechanisms. Developing predictive models for these crystal growth and nucleation pathways will improve materials synthesis strategies. These approaches will also improve fundamental understanding of natural processes such as biomineralization and trace element cycling in aquatic ecosystems. — NW

Science, this issue p. 498

NANOELECTRONICS

Electronic junctions on edge

Two-dimensional materials such as graphene are attractive materials for making smaller transistors because they are inherently nanoscale and can carry high currents. However, graphene has no band gap and the transistors are "leaky"; that is, they are hard to turn off. Related transition metal dichalcogenides (TMDCs) such as molybdenum sulfide have band gaps. Transistors based on these materials can have high ratios of "on" to "off" currents. However, it is often difficult to make a good voltage-biased (p-n) junction between different TMDC materials. Li *et al*. succeeded in making p-n heterojunctions between two of these materials, molybdenum sulfide and tungsten selenide. They did this not by stacking the layers, which make a weak junction, but by growing molybdenum sulfide on the edge of a triangle of tungsten selenide with an atomically sharp boundary — PDS

Science, this issue p. 524

PLANT EVOLUTION

How plant parasites evolved to find hosts

The seeds of parasitic plants need to be able to sense their host's presence to germinate at the correct time and in the correct place. This is done through the detection of plant hormones, strigolactones. However, the origin of this sensory system is unknown. Conn *et al*. investigated the diversity of strigolactone receptors in multiple lineages of parasitic plants and their close relatives. They found a greater copy number and accelerated evolution in parasitic plants as compared with nonparasitic relatives. Functional analyses of parasitic plant strigolactone receptors in transgenic *Arabidopsis* suggested that convergent evolution has occurred to allow the parasitic plants to detect their hosts. — LMZ

Science, this issue p. 540

PALEOMAGNETISM

Unlocking Earth's ancient magnetic past

The magnetic field protects Earth's surface from deadly cosmic radiation and provides clues about the planet's interior. Tarduno *et al*. found that some of the oldest minerals on Earth, Jack Hills zircons, preserved a record of a magnetic field over 4 billion years ago (see the Perspective by Aubert). Earth's magnetic field appears to have been fully operational a mere few hundred million years after the planet formed. This suggests an early start for plate tectonics and an ancient cosmic radiation shield that was important for habitability — BG

Science, this issue p. 521; see also p. 475

REACTION DYNAMICS

Glimpsing resonances as F and H_2 react

The reaction of fluorine atoms with hydrogen molecules has long provided a window into the subtle effects of quantum mechanics on chemical dynamics. Kim *et al*. now show that the system still has some secrets left to reveal. The authors applied photodetachment to FH_2^- anions and their deuterated analogs. This allowed them to intercept the reaction trajectory in the middle and thereby uncover unanticipated weakly bound resonances. Theoretical calculations explain these observations and predict additional similar features that have yet to be seen. — JSY

Science, this issue p. 510

CELL DEATH

Tumor suppressor p53 linked to immune function

We thought we knew all we needed to about the tumor suppressor p53. However, Yoon *et al*. now describe a previously unrecognized function of p53 (see the Perspective by Zitvogel and Kroemer). p53 induces expression of the gene encoding DD1α, a receptor-like transmembrane protein of the immunoglobulin superfamily. In conditions of stress, p53 activation can lead to cell death. p53-induced expression of DD1α also promotes the clearance of dead cells by promoting engulfment by macrophages. Furthermore, expression of DD1α on T cells inhibits T cell function. Thus, p53 offers protection from inflammatory disease caused by the accumulation of apoptotic cells, and its suppression of T cells might help cancer cells to escape immune detection. — LBR

Science, this issue p. 499; see also p. 476

HEAVY FERMIONS

A mysteriously misbehaving phase

Two electrons in a vacuum repel each other because they carry like charges. But in a metal, with a bunch of other electrons, in some ways they behave as if they didn't interact. This phenomenon, known as the Fermi liquid (FL) behavior, comes with a typical quadratic dependence of the solid's electrical resistance on temperature. Cases where the resistance deviates from the FL dependence are commonly associated with magnetic quantum criticality. Tomita *et al*. measured the resistivity of the heavy-fermion compound β-$YbAlB_4$ over a range of pressures and temperatures to identify a non-FL phase removed from a magnetic phase by an intervening FL. Explaining the non-FL behavior in the absence of magnetism presents a challenge to theorists. — JS

Science, this issue p. 506

Published by AAAS

PHILAE'S
FIRST DAYS ON THE COMET

by **J.-P. Bibring,[1] M. G. G. T. Taylor,[2] C. Alexander,[3] U. Auster,[4] J. Biele,[5] A. Ercoli Finzi,[6] F. Goesmann,[7] G. Klingelhoefer,[8] W. Kofman,[9] S. Mottola,[10] K. J. Seidensticker,[10] T. Spohn,[10] I. Wright[11]**

On 12 November 2014, Philae landed on the surface of comet 67P/Churyumov-Gerasimenko (67P), making an almost 30-year dream a reality. The pioneering flybys of 1P/Halley in 1986 revealed that despite being made primarily of ice, it was covered in highly absorbing carbon-rich molecules. What is their composition? When did they form, and through which chemical routes? Might they have constituted prebiotic molecules necessary for life? At a larger scale, what can one learn from comets that has relevance to the evolution of the solar system and planets?

To address such questions, the Rosetta mission sought to perform a broad range of in-depth structural, physical, and chemical measurements from remote, in situ, and landed vantages. The candidate payload opened for a competitive selection included an instrumented Surface Science Platform (SSP). The initial two that were selected later merged into what is known as Philae, instrumented by 10 principal investigators selected by the SSP providers. The Philae platform and payloads were developed and operated by a highly integrated consortium of institutes, agencies, and industries.

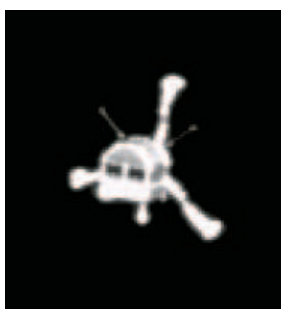

12 NOVEMBER 2014: PHILAE LANDED ON THE NUCLEUS OF COMET 67P

Philae's scientific objectives were to provide ground-truth information and complement remote measurements performed from the Rosetta orbiter (*Science* **347**, 23 January 2015) and to offer a self-standing suite of in situ measurements never before performed on a comet. This issue presents a first set of results acquired aboard Philae in the first 63 hours after it separated from Rosetta, descended, initially touched down on the comet at the site known as Agilkia, and finally came to rest at the site known as Abydos.

The release and descent happened as planned, precisely documented by imaging (Mottola *et al.*), ranging (Kofman *et al.*), thermal mapping (Spohn *et al.*), and the evolution of the magnetic properties (Auster *et al.*). The prospect of landing on such an alien body, at 515 million km from Earth and 3 astronomical units (AU) from the Sun, was far more challenging than imagined. The unexpected bounce at touchdown required a major reshuffling and adaptation of the first sequence of science operations. It also provided the opportunity for additional measurements, whereas the bouncing and traversing constrained the mechanical (Biele *et al.*) and magnetic properties of the surface.

ROLIS imagery at its highest resolution (1 cm per pixel) showed the surface of the comet near Agilkia to be dominated by the presence of granular material free of any dust deposits (Mottola *et al.*). Regolith mobilization processes appear to be involved with the formation of these features. Once Philae came to rest at Abydos, the revised first science sequence began. CIVA panoramic images characterized the surrounding cometary material down to the millimeter scale and the attitude of Philae at rest (Bibring *et al.*). The MUPUS package measured and constrained the thermal and mechanical properties of the near-surface material of the comet surface at Abydos (Spohn *et al.*), indicating that the near-surface layers consist of a hard dust-rich sintered ice, possibly covered by a thin dust layer. The CONSERT bistatic radar provided an opportunity to investigate the comet's internal structure (Kofman *et al.*). The upper "head" of 67P is fairly homogeneous on a spatial scale of tens of meters. The average permittivity provides ranges of the volumetric dust/ice ratio and the internal porosity. The dust component may be comparable, from the dielectric properties, to that of carbonaceous chondritic meteorites. COSAC and Ptolemy independently measured the composition of the volatile constituents of the grains lifted at touchdown and of the species outgassed at the final landing site (Goesmann *et al.* and Wright *et al.*). The grains are primarily made of carbon-rich species in a complex suite of molecules, including precursors to some biomolecules and other compounds never before identified in comets.

Taken together, these first measurements performed at the surface of 67P profoundly modify our view of comets. 67P is nonmagnetized on a scale of less than a meter, with its surface layers composed of both sintered ices, which are hard in nature, and fluffy grains and pebbles of organic materials, possible remnants from the era of comet formation itself. Although it remains to be seen whether these observations hold true for all comets, the discoveries made by Philae—including these initial results—will continue to shape our view of the history of the solar system.

10.1126/science.aac5116

[1]*Institut d'Astrophysique Spatiale, Orsay, France.* [2]*European Space Research and Technology Centre, Noordwijk, Netherlands.* [3]*Jet Propulsion Laboratory, California Institute of Technology, Pasadena, CA, USA, deceased.* [4]*Institute for Geophysics and Extraterrestrial Physics, TU-Braunschweig, Germany.* [5]*DLR RB-MUSC, Cologne, Germany.* [6]*Politecnico di Milano, Milan, Italy.* [7]*Max Planck Institute for Solar System Research, Göttingen, Germany.* [8]*University of Mainz, Mainz, Germany.* [9]*Institut de Planétologie et d'Astrophysique de Grenoble, Grenoble, France.* [10]*DLR, Institute of Planetary Research, Berlin, Germany.* [11]*Open University, Milton Keynes, UK.* *The authors express their recognition and immense gratitude to Dr. Helmut Rosenbauer, for his outstanding vision and skills, which drove most of the design and hence capabilities of Philae.*

CREDIT: ESA/ROSETTA/MPS FOR OSIRIS TEAM MPS/UPD/LAM/IAA/SSO/INTA/UPM/DASP/IDA

Published by AAAS

COMETARY SCIENCE

The landing(s) of Philae and inferences about comet surface mechanical properties

Jens Biele,[1]* Stephan Ulamec,[1] Michael Maibaum,[1] Reinhard Roll,[3] Lars Witte,[2] Eric Jurado,[9] Pablo Muñoz,[5,12] Walter Arnold,[10] Hans-Ulrich Auster,[6] Carlos Casas,[5,12] Claudia Faber,[4] Cinzia Fantinati,[1] Felix Finke,[1] Hans-Herbert Fischer,[1] Koen Geurts,[1] Carsten Güttler,[3] Philip Heinisch,[6] Alain Herique,[8] Stubbe Hviid,[4] Günter Kargl,[7] Martin Knapmeyer,[4] Jörg Knollenberg,[4] Wlodek Kofman,[8] Norbert Kömle,[7] Ekkehard Kührt,[4] Valentina Lommatsch,[1] Stefano Mottola,[4] Ramon Pardo de Santayana,[5,12] Emile Remetean,[9] Frank Scholten,[4] Klaus J. Seidensticker,[4] Holger Sierks,[3] Tilman Spohn[4]

The Philae lander, part of the Rosetta mission to investigate comet 67P/Churyumov-Gerasimenko, was delivered to the cometary surface in November 2014. Here we report the precise circumstances of the multiple landings of Philae, including the bouncing trajectory and rebound parameters, based on engineering data in conjunction with operational instrument data. These data also provide information on the mechanical properties (strength and layering) of the comet surface. The first touchdown site, Agilkia, appears to have a granular soft surface (with a compressive strength of 1 kilopascal) at least ~20 cm thick, possibly on top of a more rigid layer. The final landing site, Abydos, has a hard surface.

To land on comet 67P/ Churyumov-Gerasimenko (67P), Philae was ejected from the Rosetta main spacecraft with a predefined velocity, stabilized by a flywheel, and descended ballistically to the cometary surface. At touchdown it was planned to activate a cold gas system, pushing the lander to the surface, as well as firing two anchoring harpoons to fix Philae to the ground. Unfortunately, both subsystems did not work, leading to a bouncing of the lander. An analysis of the exact bouncing dynamics, however, fortuitously allowed determinations of the comet surface properties at the ~10-cm–to–meter scale.

The mechanical strength of cometary surface material cannot be measured remotely, yet it is an important parameter for understanding the evolution and activity of cometary nuclei. Furthermore, mechanical strength is linked to porosity and grain properties (*1*), thus providing insight into the structural features of cometary matter (*2*) and informing future comet missions. Indirect observations (*3*–*6*) and models (*2*, *3*) have resulted in wide ranges of material strength. The Deep Impact experiment on comet Tempel-1 yielded initially an extremely low ("effective") strength (<65 Pa) (*7*), raising questions as to whether a comet lander could land on such weak material. Experimental work on the aerodynamic (i.e., tensile?) strength of meteoroids (*5*), as well as particles collected by Stardust in the coma of comet 81P/Wild 2 (*6*), also indicated a strength range of 3 to 80 kPa on the submillimeter-to-centimeter scale. The landings of Philae, despite not proceeding as planned, provide direct observations of the surface mechanical properties and thus a baseline for comparison with these previous studies.

[1]Deutsches Zentrum für Luft- und Raumfahrt (DLR)/ Raumflugbetrieb und Astronautentraining, Microgravity User Support Center (MUSC), Linder Höhe 1, 51147 Cologne, Germany. [2]DLR/Institut für Raumfahrtsysteme, Robert Hooke-Straße 7, 28359 Bremen, Germany. [3]Max-Planck-Institut für Sonnensystemforschung (MPS), Justus-von-Liebig-Weg 3, 37077 Göttingen, Germany. [4]DLR/Institut für Planetenforschung Rutherfordstraße 2, 12489 Berlin, Germany. [5]European Space Agency/European Space Operations Centre (ESA/ESOC), Robert-Bosch-Straße 5, 64293 Darmstadt, Germany. [6]Institut für Geophysik und Extraterrestrische Physik, Technische Universität Braunschweig Mendelssohnstrasse 3, 38106 Braunschweig, Germany. [7]Institut für Weltraumforschung (IWF) Graz, Austria Austrian Academy of Sciences, Space Research Institute, Schmiedlstraße 6, 8042 Graz, Austria. [8]Université Grenoble Alpes and CNRS, Institut de Planétologie et d'Astrophysique de Grenoble, F-38000 Grenoble, France. [9]Centre National d'Études Spatiales, 18 Avenue Édouard Belin, 31400 Toulouse, France. [10]1. Physikalisches Institut, Georg August Universität, 37077 Göttingen, Germany; permanent address: Department of Materials Science, Saarland University, 66123 Saarbrücken, Germany. [11]Magellium, 24 Rue Hermès, Boîte Postale 12113, 31521 Ramonville Saint-Agne Cedex, France. [12]Grupo Mecánica de Vuelo at ESA/ESOC - GMV Robert-Bosch-Straße 5, 64293 Darmstadt, Germany.
***Corresponding author. E-mail: jens.biele@dlr.de**

Circumstances of Philae landings and bounces

On 12 November 2014, at 06:01 (all times are in UTC), a pre-delivery spacecraft maneuver put Rosetta in a hyperbolic trajectory with a 5-km miss distance to the comet nucleus, almost on a collision course with the comet. The distance from the Sun was 2.99 astronomical units (AU). At 07:20, Rosetta slewed to separation attitude. The (formal reconstructed 1σ) uncertainties in attitude, position, and velocity of the spacecraft with respect to the comet at separation were 0.015°, 10 m, and 2 mm/s, respectively. Separation occurred with a relative velocity (Δv) of 0.1876 m/s by the motor-driven mechanical separation device from the Rosetta orbiter at an altitude of about 20.5 km (radius vector = 22.7 km) and as planned on 12 November 2014, 08:35:00.

After 6:59:04 hours of ballistic descent, of which the first 90% were tracked by the CONSERT (Comet Nucleus Sounding Experiment by Radiowave Transmission) instrument (*8*, *9*), Philae landed at 15:34:03.98 ± 0.10 s, in Agilkia (formerly called "area J") on 67P. This instant (TD1, the first touchdown site) refers to the time of the trigger signal at the vertical axis of the +Y foot SESAME-CASSE (Surface Electrical Sounding and Acoustic Monitoring Experiments/Cometary Acoustic Sounding Surface Experiment) accelerometer (Fig. 1).

The design of the descent trajectory was such that the incoming velocity, in the comet-fixed frame, was at touchdown parallel to the normal of the target landing site. The descent reconstruction shows that the angle between the incoming velocity vector and the normal to the target landing site was 0.9°. The reconstructed landing site's local normal was 12° (slope) away from the target normal, and the incoming velocity was 11.5° away from the local normal at touchdown. The comet-fixed coordinates of the TD1 point are 112 m and only 51 s away from the targeted landing site and time (Table 1). A priori landing uncertainties were stated as ±500 m in position and ±40 min in time. The touchdown speed relative to the comet surface was about 1.0 m/s.

At touchdown, as foreseen, the central damping tube of Philae's landing gear was pushed in. The landing gear was designed such as to dissipate a large fraction of the lander impact kinetic energy by a damping motor within this mechanism. The damping coefficient was 567 Ns/m (*10*). The motion of the damping tube also generated the touchdown signal, which actually occurred at 15:34:06.471 ± 1 s. The stroke length of the damper was 42.6 ± 0.1 mm out of a full length of ~170 mm. During TD1, the lander tilt changed by –1.375° and +0.575° in two perpendicular axes and +0.335° in rotation around the z axis. The landing gear damper did not move after TD1; i.e., the component of force in the lander z direction during the further touchdowns must have been <30 N, due to static friction in the mechanism.

The signals recorded by the CASSE accelerometer mounted on the +Y foot, together with the translational motion of the damper, are shown in Fig. 1. Vibrations due to the flywheel as well as the noise of the recording system are below the least significant bit of the recording. There is an interval of 266 ms from the first samples that are different from zero until the beginning of the strong signal. The damper then takes another 170 ms until it clearly moves and another 250 ms until damping sets in. The damper motion in the following 156 ms was only recorded by the platform (end position), because the TD signal had been generated by then. Ultimately, the damping tube position moved from 199.6 to 156.9 mm.

Because the anchor harpoons did not fire upon touchdown and the hold-down thrust of the cold gas system did not work, the lander bounced several times until it came to rest after about

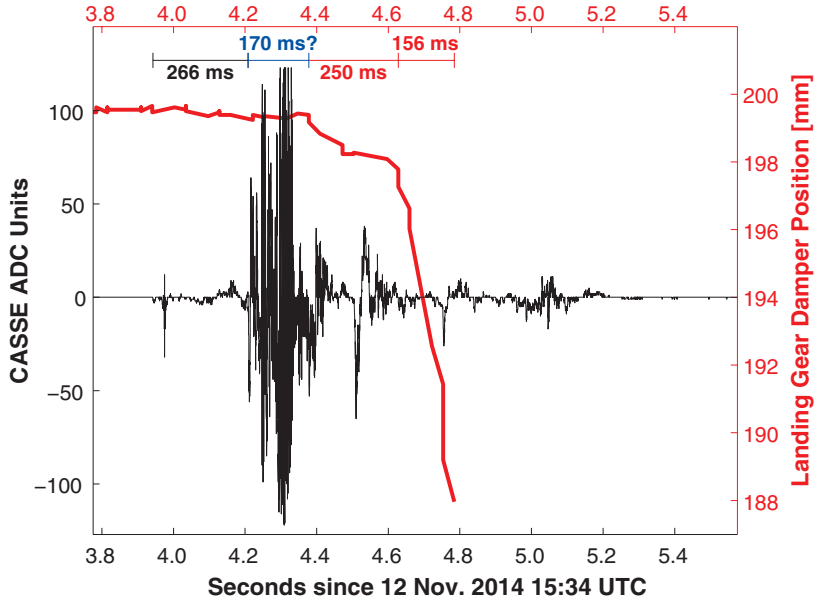

Fig. 1. Touchdown signals at Agilkia. Black: Vertical acceleration of the +Y foot as recorded by CASSE (sampling frequency of 5 kHz, 8-bit amplitude resolution; electronics include a high-pass filter, cutting off DC and frequencies below ~1 Hz). Peak accelerations were clipped. Red: Position of the damper as recorded by a potentiometer at intervals between 10 and 100 ms, terminating when position 188 mm was reached. The durations of the time intervals discussed in the text are indicated (black, based on CASSE data alone; red, based on landing gear data alone; blue, combined data with a higher systematic uncertainty).

Table 1. Main events of Philae's landings. ROMAP times (*17*) and MUPUS events and times (*12*). RMOC is ESA's Rosetta Mission Operation Centre at ESOC Darmstadt. Coordinates are comet-fixed and in the ESA-RMOC reference frame (version 00085).

Event	Onboard time 2014-11-12	Main source	Comments; coordinates where applicable ([*x*,*y*,*z*], unit km)
Separation from Rosetta	08:35:00 ± 1s	ESA flight dynamics	[−17.1652762547, 10.1582193407, 10.6887254384], 22.38 km radius
TD1 (Agilkia)	15:34:03.98 ± 0.10s	SESAME; Damper event time: 15:34:06.471	[2.123468, −0.959272, 0.497006] or 335.689° longitude, 12.041° latitude, 2.3825 km radius; see also table S2
COL (collision with crater rim)	16:20:00 ± 2s	Solar generator, MUPUS, ROMAP	For coordinates, see table S3
TD2	17:25:26 ± 1s	ROMAP, MUPUS	For coordinates, see table S3
TD3 (final rest, Abydos)	17:31:17 ± 1s	ROMAP	Most likely position: longitude 358.2°, latitude −8.2° (RMOC 00085 frame)
LOS (loss of signal)	17:59:44 ± 1 s	ESA flight dynamics	Final lander attitude determined by ROMAP, ffl15° uncertainties in all axes (*12*)

2 hours of ballistic flight. The S-band communications link was functional until 17:59:44 (an expected loss of signal due to orbiter-lander geometry), although numerous very short link breaks occurred roughly every 0.5 to 3.5 min, causing, however, almost no data loss. Unfortunately, the initial anchoring was not successful. This affected lander operations, in particular drilling, but in addition, the accelerometers connected with the harpoons could not carry out the various planned measurements as a function of depth (*11*).

After the TD1, the lander bounced. This soon became clear at the Lander Control Center (LCC, Cologne) when data from the solar generator was interpreted, indicating that the lander was rotating. Communications telemetry and the MUPUS TM (Multipurpose Sensors for Surface and Sub-Surface Science Thermal Mapper) and ROMAP (Rosetta Magnetometer and Plasma Monitor) instruments also indicated movement. Only after about 1:57 hours, at 17:31:17 (Table 1), Philae came to rest after having reached its final landing site.

About 27 min after the final landing, the communications link with the orbiter was interrupted for geometrical reasons. It was reestablished four more times, until the batteries ran out of power, early on 15 November. Visibility periods followed more or less the expected sequence; however, they were shorter than predicted for site Agilkia, and numerous brief link breaks were observed. The unexpected situation after landing (no anchoring and short illumination periods) led to the adaptation of the originally planned first scientific sequence (FSS), but eventually, all scientific instruments were activated. Because the exact location of Philae was unclear, three additional campaigns were executed, using CONSERT for ranging. Consequently, Philae's location was narrowed down to an area of 150 × 15 m^2, not taking into account the shape model uncertainties. New communication with Philae starting in June 2015, as well as very close approaches of Rosetta in the extended mission phase, will hopefully help refine the attitude and location estimates.

On 15 November 2014 00:07, the lander bus voltage dropped below 21 V, the threshold for lander platform operations, and the link between orbiter and lander broke. The battery lifetime was as expected. Philae entered "hibernation" (*12*). Table 1 gives an overview of the main events during Philae's landings.

We refer to the event at ~16:20 as a collision, not a touchdown, because no vertical deceleration of the ROMAP boom was detected. After this encounter, Philae started to tumble. The collision at about 16:20 must have been a very slight grazing contact, because it only changed the rotational characteristics measured clearly by ROMAP and MUPUS. It induced a stronger nutation and deflected the flight trajectory, but it did not lead to a crash or complete destabilization of the lander attitude.

Lander trajectory reconstruction

The bouncing trajectory could be constrained by optical images of the lander in flight, its shadow, and its end point by CONSERT ranging data, together with solar generator housekeeping (SG HK) values [mainly day length; see definition in (*12*)]. The times of touchdowns and collisions were derived from the analysis of SG HK, ROMAP, MUPUS, and SESAME data.

Two teams independently reconstructed the descent and bouncing trajectory of Philae: RMOC (Rosetta Mission Operations Centre, Flight Dynamics) and SONC (the Lander Science Operations and Navigations Centre) (*12*) (Figs. 2 and 3). The two reconstructions are based on similar sets of data but used slightly different comet models and constraints. They are very similar from the separation to the "collision," then diverge somewhat, but end in the same region. The differences after the collision are mainly due to the different sets of data used: The ESOC (European Space Operations Centre) reconstruction used observations of the lander in the OSIRIS (Optical, Spectroscopic, and Infrared Remote Imaging System) wide-angle camera (WAC) images at 16:45 and 17:20, with the end point of the trajectory as a free

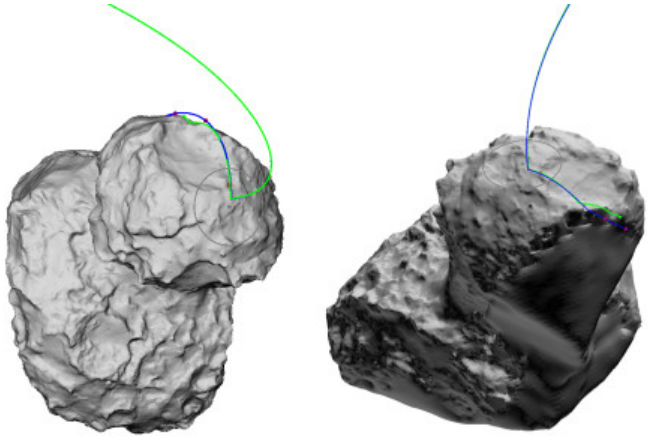

Fig. 2. SONC (green) and ESOC (blue) reconstructed trajectories in the comet-fixed frame from two observation angles (left and right panels). Plotting a three-dimensional trajectory in the rotating frame may give the impression that the collision at 16:20 has deflected the trajectory considerably, whereas in reality, the comet has rotated (29°/hour) as well. If the WAC observations (red dots) were indeed the lander, then the trajectory would be clearly higher, as indicated by ESOC reconstruction. Before the collision, the two reconstructions are very close. The SONC trajectory includes a third touchdown, which, however, is unconstrained except for its time. The shape model used for this figure was RMOC version 5.

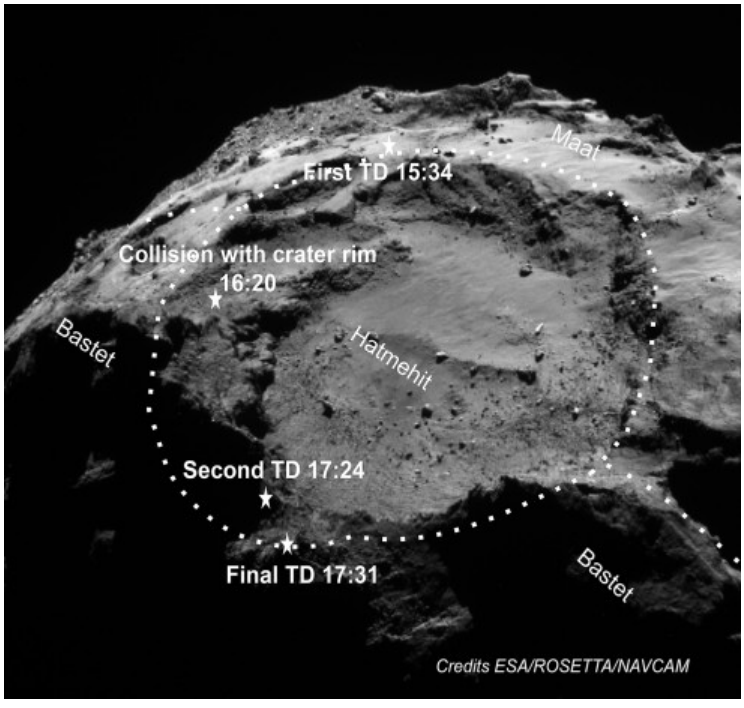

Fig. 3. Landing points (SONC) on a NAVCAM image. A second TD2, here taken at 17:24 (observed time: 17:25:26), is not modeled by RMOC and here only an example is given, because it is not well constrained. We expect that the last bounce was only a few meters.

parameter, whereas SONC reconstruction did not use these observations but constrained the end point of the trajectory to match the best estimate of the final landing site coordinates based on CONSERT measurements. Given the uncertainties of the near-surface gravity field (*12*) and the few observations in the last part of the trajectory, the agreement between these preliminary trajectories is quite satisfactory.

The reconstructed comet-fixed incoming velocity at TD1/rebound is, in the horizontal frame local to the landing point [east, north, up] (*12*) [2.0, −20.7, −99.0] cm/s, 101.2 cm/s in magnitude, 20.8 cm/s of lateral velocity; whereas outgoing conditions were [21.3, −23.5, 7.2] cm/s, 32.5 cm/s in magnitude, 31.7 cm/s of lateral velocity.

The pre-touchdown velocity component perpendicular to the surface was strongly reduced, whereas the north-south component was hardly affected. Most of the remaining kinetic energy went into a strong east-west lateral component, leading to a bouncing angle of 86.3 ± 0.5°. The escape velocity at Agilkia is ~0.9 m/s, slightly below the pre-touchdown velocity.

OSIRIS NAC (Narrow Angle Camera) images were used together with ROLIS (Rosetta Lander Imaging System) descent images for determining the actual landing coordinates and attitude at Philae's first landing site, Agilkia (Fig. 4 and Table 1). Altitude, attitude with respect to the surface, and the rotational state were derived independently from this analysis.

Philae has not yet been found unambiguously in optical images, so its final landing site Abydos is the area constrained by the CONSERT ranging data (*8*, *12*–*14*). It is consistent with the measured solar generator HK values (day length, sunrise, and sunset by solar cell output from the scattered light of the surroundings) and the new communications pattern starting on 13 June 2015 and telemetry received since then. Fortunately, this area in the Bastet (*15*) region is still near the equator and was imaged by the orbiter's cameras. A global and local digital terrain model with an effective resolution on the order of 5 to 10 m exists (*16*).

Description of the rebounds

After TD1, the lander retained its inertial z-axis attitude, but rotated much faster. ROMAP data (*17*) show to ~1-s accuracy when the lander touched the comet surface, revealing a triple bounce, touching the surface at the rim of the Hatmehit depression about 46 min after TD1. Eight seconds after TD1, the CASSE sensors were again in "listening mode" until 16:02:16 but registered no signal above the trigger limit of about 20 m/s^2.

OSIRIS and NAVCAM images have been used for reconstructing the trajectory. One of the images even shows the "footprints" at TD1, and another image shows the dust cloud produced by the impact (fig. S17). The rotation and attitude of Philae could be inferred from a number of observations, including ROMAP magnetometer data (*17*), solar generator HK values, MUPUS-TM sensor and thermal reference sensor data (*12*), and system temperature sensors. During descent, the rotation and attitude were also measured by CONSERT signal amplitude periodicities, by direct imaging by OSIRIS, and by analysis of ROLIS descent images. Directly after separation, the rotation period was 5.1 min (*17*). After the successful deployment of the landing gear, Philae's spin period changed to 8 to 10 min (~0.002 Hz), all counterclockwise (as seen from the top) around the lander z axis. This rotation was expected and is due to residual imperfections of the MSS and the change in the moments of inertia. The flywheel, which stabilized the lander in the z direction during descent, was switched off at TD1 and then ran down in ~32 min, transferring its angular momentum of 5.17 N·m/s by friction to the lander body. The attitude stability of Philae, a prerequisite also for the rather stable RF link, is also due to that angular momentum. After TD1, just before the collision, Philae rotated with about 0.075 Hz (period 13 s), after the collision with ~0.04 Hz.

Analysis of the lander footprints

We analyzed the footprint surface features seen at the TD1 site by OSIRIS NAC and NAVCAM

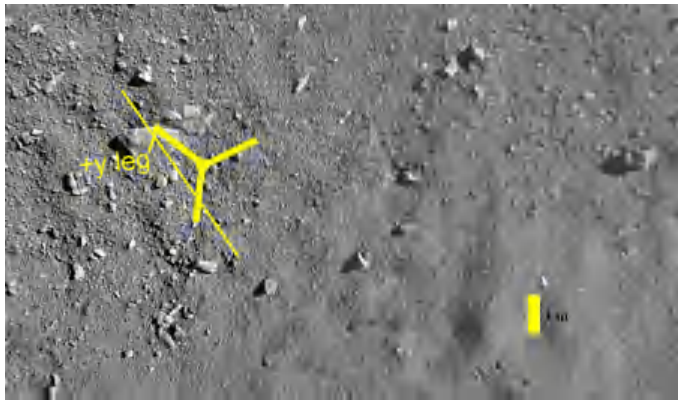

Fig. 4. Extrapolated lander position and orientation at TD1, site Agilkia. The lander legs are to scale and superimposed on merged and rectified ROLIS images. North is up. The thin yellow line indicates the –X ("balcony") side. Positional accuracy ±20 cm, yaw rotation accuracy ±1°. Philae is arriving mainly vertical, but with a lateral velocity component to the south; Philae rotates by ~0.67°/s counterclockwise (top view) about its *z* axis, ~12 ± 1° inclined to the local surface normal.

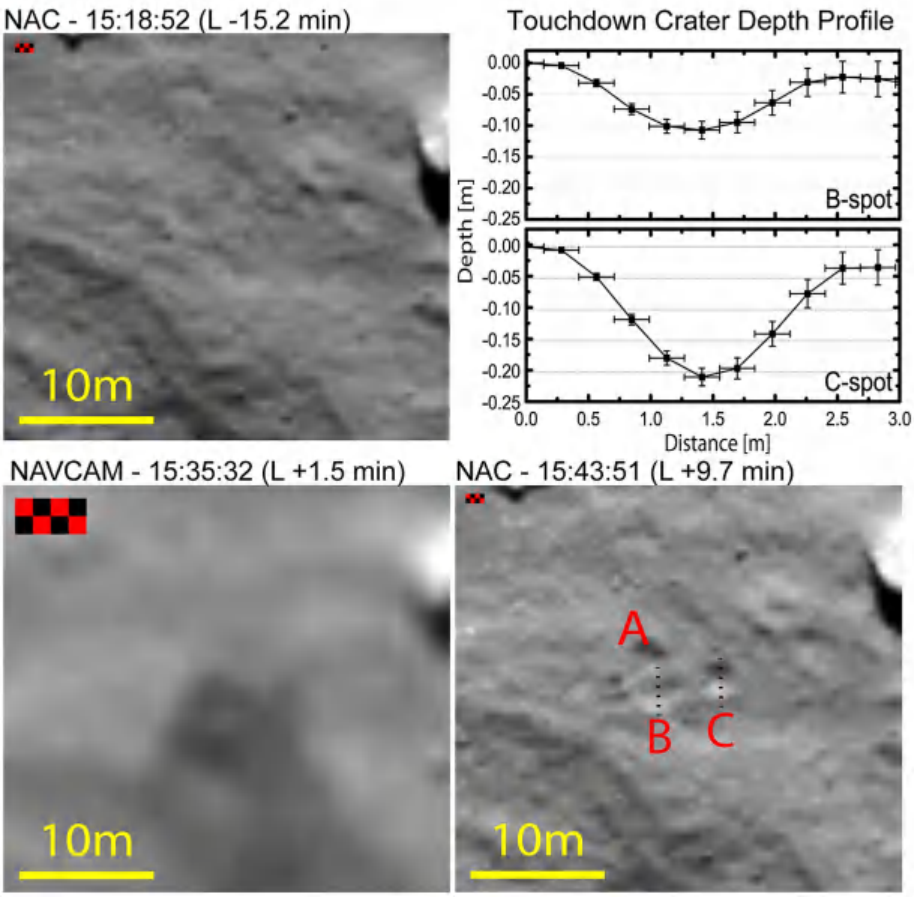

Fig. 5. Surface morphology changes at TD1 and associated depth profiles. Rosetta orbiter imaging of the Philae landing site: (top left) OSIRIS NAC image from landing (L) –15.2 min (0.29 m/pixel); (bottom left) NAVCAM image from L + 1.5 min (1.30 m/pixel); (bottom right) OSIRIS NAC image from L + 9.7 min (0.28 m/pixel). The top right shows the depth profile through the B spot and C spot, respectively. The images were acquired from a distance of ~15.2 km (*12*). The black and red checkerboard bars indicate the pixel size.

images (Fig. 5 and figs. S12 to S15). It is not fully understood yet which feature was caused by which structural part of the lander and in which sequence; however, it appears almost certain that two of the new features are depressions, some 0.1 and 0.2 m deep and 2 m in diameter (Fig. 5, features B and C). Feature A, apparently, is not a depression, because there is no change in reflectance as we see it in the two other features: A is probably the projection of the dust cloud (and/or its shadow) stirred up by the impact. Alternatively, A could also be "fallback" material: The NAC image was taken at TD1 + 10 min, at which time one would expect most of the material in the dust cloud to have moved away.

We used an unconstrained "shape from shading" with a generic comet surface photometric parameter set (*18*). The sensitivity of slopes and thus depth is low to Hapke parameter changes, because the angles are far away from the opposition peak of the photometric function (a full stereo photoclinometry would use multiple illumination conditions to constrain this function). We estimate the relative height uncertainties to be 10 to 20%. The horizontal accuracy is given by the image resolution (28 cm/pixel), resulting in a tentative 3σ error estimate of ~56 cm on the diameters (two pixels).

Assuming the known nucleus bulk density of 440 kg/m^3 (*19*), we roughly estimated the excavated volumes and masses of depressions B and C as V_B = 0.13 m^3, M_B ~60 kg, and V_C ~0.27 m^3, M_C ~120 kg. The total mass excavated is M = 180 kg.

Analysis of lander mechanics and inference of surface mechanical properties

We performed a preliminary energy balance analysis to determine the amount of mechanical energy dissipated in the soil for the TD1 event. From the impact kinetic energy of 49.5 J, a fraction of 5.0 J remained with the lander after TD1, where the velocity was reduced from 1 to 0.32 m/s. Friction and damping inside the lander were estimated to be 5 to 21 J during TD1. An amount of 23 to 39 J of the impact energy was transferred to the ground (*12*). Thus, the comet surface is strongly damping: 50 to 80% of the lander's kinetic energy before TD1 was dissipated in the comet soil, 10 to 40% in the damping element; and 10% was not dissipated but went into kinetic and some rotational energy after TD1.

In relation to the excavated masses (a total of depressions B and C), the energy dissipated at TD1 can theoretically accelerate all the particles up to 50 to 66 cm/s or lift them vertically up to 800 to 1400 m (gravity = 0.16 mm/s^2). These are upper limits with the assumption that no kinetic energy is transformed into heat and that there is no work against cohesion. This shows that in principle, high ejecta plumes can be formed or regolith can easily be displaced over long distances.

During Philae's FSS, several mechanical actuations were executed. A sampling by the Sampling, Drilling and Distribution Subsystem (SD2) instrument was attempted, the MUPUS-PEN (Penetrator) was deployed (*20*), and in the last moment, a translation rotation of the landing gear [a lifting by 46.3 mm and a rotation of the main body with the SG of 22.7° ± 2.5° (clockwise in top view, compare fig. S20)] was executed. In the first two cases, no major change in attitude was registered after the actuations.

The penetration of the MUPUS-PEN probe into the Abydos surface did not succeed, despite

3 hours of hammering at increasing energy levels. From this observation, the MUPUS team concludes that the crushing strength of the surface material is higher than 4 MPa (*20*).

The lander's feet carry so-called ice screws, passive elements that move out, relative to the feet soles, if a sufficient force acts on either one or both soles and the surface roughness or surface material strength permits. They can be extruded up to 70 mm if both soles are pressed up (by 70 mm) and up to 22 mm if only one sole moves (by 44 mm). At Abydos, only one ice screw (that of the +X foot) can be confirmed (*21*) to have moved (the right sole seen from the center ~50 mm up); on the +Y foot, possibly the left sole has moved ≤10 mm up. The –Y foot cannot be analyzed because of lack of illumination. We do not know at which surface contact this ice screw was activated, but suspect TD1. Because the ice screws have an internal reverse lock, they remain extended after first activation. The lander's feet and ice screws hardly, if at all, penetrated the surface at Abydos. This can be seen in CIVA (Comet Infrared and Visible Analyser) panoramic images showing the feet (*21*), supporting the idea that the surface at Abydos is much harder than at Agilkia.

Discussion

Because the mechanical response of Philae (damping element, structural elasticity, rotation, and flywheel) is complicated and superimposed on the surface strength decelerations upon touchdown, we combined a soil mechanics force model (*3*, *11*) with a numerical multibody simulation of Philae (*10*) that was calibrated and verified with test data from a Philae mockup (*10*, *22*). The goal is to determine the soil properties, including strength, elastic constants, dissipation, excavation mechanics, possible layering, and horizontal inhomogeneity (e.g., boulder versus finer regolith).

We performed a first parameter study using the above multibody lander model and assumed a simple soil model: homogeneous regolith characterized only by its uniaxial compressive strength C set equal to the constant penetration resistance; i.e., the material can be displaced to the sides. The results obtained by varying only C indicate that foot-sole penetrations were in the range of a few centimeters for C ~ 10 kPa and below. Compressive strength values much exceeding 10 kPa reduce the footpad penetration to millimeters. The rebound velocity is reproduced to ±20% in magnitude but not yet its direction. All these values are to be taken with caution, because they are sensitive to the transversal velocity component, due to less-effective damping, additional sliding friction, the induced angular momentum, and the inhomogeneity of the soil.

From Fig. 4, it is intriguing to imagine that for the first contact, the +Y foot just hit an approximately 1-m sized "boulder." However, there is still a ~0.2-m uncertainty in the foot position at first contact relative to the terrain, so the +Y foot might just have missed the edge of that boulder. Also, the horizontal component of the impact velocity could have led to a sliding motion on the boulder, or the impact on a boulder is mechanically not very different from that on finer regolith. We do not exclude the possibility that the SESAME-CASSE data can be explained by either scenario.

We discuss an alternative interpretation of SESAME-CASSE data at TD1. Here, it is assumed that the first signal seen on the +Y foot (at 15:34:03.98) corresponds to the first contact with a soft layer, and the beginning of the strong signal ~0.27 s later to impact on a stiff and hard surface. With the initial normal velocity of the foot (1 m/s), the soft layer then has a maximum thickness of 0.25 m and less if the foot was noticeably decelerated by this layer (which is not supported by the CASSE accelerometer data). This would be consistent with the depth profile of the lander footprint features. For the estimated thickness of the upper soft layer of 0.1 to 0.2 m, a conservative upper limit for the compressive strength C_{max} of that layer, if assumed homogeneous, can be estimated: Neglecting the (slower) damping mechanism, penetrating a homogenous layer with compressive strength C, by a mass M, initial velocity v_0, frontal area A gives a maximum depth $y_e = Mv_0^2/(2CA)$. With the reduced mass (*12*) M = 17.4 kg, v_0 = 1.01 m/s, $A = 0.017n$ m^2 (n = 2: the number of feet penetrating almost simultaneously), C_{max} = 1 to 3 kPa. The postulated competent layer below has an unknown thickness, with an unknown compressive strength. Only its elastic parameters can be estimated from the CASSE signals using Hertz's contact theory and the sole's resonances (*22*). Yet this layer appears to be strong and/or thick enough to withstand the dynamical loads exerted by Philae's feet, because breakage of that layer and transition to the presumably soft granular material beneath is not seen in the data. The minimum thickness of the assumed hard layer to withstand landing without failure can be estimated to be on the order of 0.3 to 3 cm, using realistic parameters (*12*).

The tentative mechanical model of the upper surface layers is as follows: At Agilkia, there is a granular soft surface consisting of regolith with a depth of at least ~20 cm and typical ≤1-cm particle sizes with a compressive strength on the order of 1 kPa, and at Abydos (and probably also at the COL (collision with crater rim) and TD2 sites, there is a hard and stiff surface with a (crushing) strength of at least 2 MPa. This layer may be similar to the possible subsurface "competent" layer at Agilkia. The unexpectedly high strength of the hard material is similar to that of the "sintered layer" found in the Kometensimulation (KOSI) laboratory experiments on insolated cometary analog materials in vacuum (*1*), suggesting that the cometary matter near the surface may be processed and thus not representative of the pristine state after formation.

The two sites Agilkia and Abydos are situated in two different morphological regions: very likely in Ma'at and Bastet. Whereas the Ma'at region appears to be covered by a smooth "dust" layer (*15*, *23*) with a brittle underlayer, Bastet is described as an exposed consolidated surface with minimal bouldering, possibly part of the basal unit. The size distribution of the regolith at Ma'at is now constrained by ROLIS data as still granular at 0.9 cm/pixel and is interpreted as "airfall" (*15*). Both morphological descriptions are consistent with our observations.

The tensile strength of some overhangs on 67P has been previously estimated at between 10 and 200 Pa (*15*). We believe that this represents a lower bound, because the overhangs still exist (although debris is seen at the lower edges). The breaking stresses at the rim of the overhang are caused by gravity. If there are any cavities or crack-like features in the overhangs, they act as a stress concentrator, and that would explain the variability. These low values for the (minimum) tensile strength on large scales do not contradict the findings as reported here; they are not even comparable: We measure compressive strength here on 0.1–to–1-m scales, whereas the estimate in (*15*) refers to tensile (or shear) strength on >10-m scales. Compressive strength can be orders of magnitude higher than tensile strength in a granular material (*3*, *24*).

Although previous ex situ determinations of the strength of cometary matter (*5*, *6*) are consistent with our conclusions, it is important to note that the values of strength on scales on the order of ~10 cm (the diameter of the lander feet) or meters (the lander body) on the surface of an active comet follow different physical processes, including the interaction of individual grains, sintering processes, the presence of cracks and pores, or the formation of a crust layer. In particular, the formation of a crust layer, at places overlaid with airfall regolith, also explains differences in strength of a cometary surface as compared to the bulk regolith properties [e.g., as modeled in (*2*)].

REFERENCES AND NOTES

1. H. Thomas, L. Ratke, H. Kochan, Crushing strength of porous ice-mineral bodies-relevance for comets. *Adv. Space Res.* **14**, 207–216 (1994). doi: 10.1016/0273-1177(94)90271-2; pmid: 11539952
2. J. Blum, B. Gundlach, S. Mühle, J. M. Trigo-Rodriguez, Comets formed in solar-nebula instabilities! - An experimental and modeling attempt to relate the activity of comets to their formation process. *Icarus* **235**, 156–169 (2014); correction: *Icarus* **248**, 135–136 (2015). doi: 10.1016/j.icarus.2014.03.016
3. J. Biele *et al*., The putative mechanical strength of comet surface material applied to landing on a comet. *Acta Astronaut.* **65**, 1168–1178 (2009). doi: 10.1016/j.actaastro.2009.03.041
4. K. A. Holsapple, K. R. Housen, in *Proceedings of the 37th LPSC, XXXVII*, League City, TX, 13 to 17 March 2006, no. 1068.
5. J. M. Trigo-Rodríguez, J. Llorca, The strength of cometary meteoroids: Clues to the structure and evolution of comets. *Mon. Not. R. Astron. Soc.* **372**, 655–660 (2006); erratum: *Mon. Not. R. Astron. Soc.* **375**, 415–415 (2007). doi: 10.1126/science.1135840; pmid: 17170289
6. D. Brownlee *et al*., Comet 81P/Wild 2 under a microscope. *Science* **314**, 1711–1716 (2006). doi: 10.1126/science.1135840; pmid: 17170289
7. M. F. A'Hearn *et al*., Deep Impact: Excavating comet Tempel 1. *Science* **310**, 258–264 (2005). doi: 10.1126/science.1118923; pmid: 16150978
8. W. Kofman *et al*., Properties of the 67P/Churyumov-Gerasimenko interior revealed by CONSERT radar. *Science* **349**, aab0639 (2015).
9. S. Hegler *et al*., Operation of CONSERT aboard Rosetta during the descent of Philae. *Planet. Space Sci.* **89**, 151–158 (2013). doi: 10.1016/j.pss.2013.09.015
10. L. Witte *et al*., Experimental investigations of the comet Lander Philae touchdown dynamics. *J. Spacecr. Rockets* **51**, 1885–1894 (2014). doi: 10.2514/1.A32906

11. N. Kömle *et al.*, Impact penetrometry on a comet nucleus-interpretation of laboratory data using penetration models. *Planet. Space Sci.* **49**, 575–598 (2001). doi: 10.1016/S0032-0633(00)00169-0
12. Complete materials and methods are available as supplementary materials on *Science* Online.
13. E. Heggy *et al.*, Radar properties of comets: Parametric dielectric modeling of Comet 67P/Churyumov-Gerasimenko. *Icarus* **221**, 925–939 (2012).
14. P. Kamoun, P. L. Lamy, I. Toth, A. Herique, Constraints on the subsurface structure and density of the nucleus of Comet 67P/Churyumov–Gerasimenko from ARECIBO radar observations. *Astron. Astrophys.* **568**, A21 (2014). doi: 10.1051/0004-6361/201423544
15. N. Thomas *et al.*, The morphological diversity of comet 67P/Churyumov-Gerasimenko. *Science* **347**, aaa0440 (2015). pmid: 25613893
16. ESA's Planetary Science Archive, www.rssd.esa.int/index.php?project=PSA&page=rosetta.
17. H.-U. Auster *et al.*, The nonmagnetic nucleus of comet 67P/Churyumov-Gerasimenko. *Science* **349**, aaa5102 (2015).
18. S. Fornasier *et al.*, Spectro-photometric properties of the 67P/Churyumov-Gerasimenko's nucleus from the OSIRIS instrument onboard the ROSETTA spacecraft. *Astron. Astrophys.* 10.1051/0004-6361/201525901 (2015).
19. H. Sierks *et al.*, On the nucleus structure and activity of comet 67P/Churyumov-Gerasimenko. *Science* **347**, aaa1044 (2015). doi: 10.1126/science.aaa1044; pmid: 25613897
20. T. Spohn *et al.*, Thermal and mechanical properties of the near-surface layers of comet 67P/Churyumov-Gerasimenko. *Science* **349**, aab0464 (2015).
21. J.-P. Bibring *et al.*, 67P/Churyumov-Gerasimenko surface properties as derived from CIVA panoramic images. *Science* **349**, aab0671 (2015).
22. C. Faber *et al.*, A method for inverting the touchdown shock of the Philae Lander on Comet 67P/Churyumov-Gerasimenko. *Planet. Space Sci.* **106**, 46–55 (2015). doi: 10.1016/j.pss.2014.11.023
23. S. Mottola *et al.*, The structure of the regolith on 67P/Churyumov-Gerasimenko from ROLIS descent imaging. *Science* **349**, aab0232 (2015).
24. J. Tomas, Fundamentals of cohesive powder consolidation and flow. *Granul. Matter* **6**, 75–86 (2004). doi: 10.1007/s10035-004-0167-9

ACKNOWLEDGMENTS

Rosetta is an ESA mission with contributions from its member states and NASA. Rosetta's Philae lander is provided by a consortium led by DLR, MPS, CNES, and Agenzia Spaziale Italiana (ASI). Further important contributions came from the Magyar Tudományos Akadémia Wigner Fizikai Kutatóközpont, Max-Planck-Institut für Extraterrestrische Physik (MPE), the Finnish Meteorological Institute (FMI), the UK Space Agency, Space Technology Ireland Ltd. (STIL), and IWF. The contribution of the ROMAP and RPC-MAG [Rosetta Plasma Consortium (RPC) Fluxgate Magnetometer] team was financially supported by the German Ministerium für Wirtschaft und Energie and the Deutsches Zentrum für Luft- und Raumfahrt under contract 50QP1401. The contribution of the CONSERT team was supported by CNES, CNRS, and Université Joseph Fourier, Grenoble. The images and data used in this study are archived in (*16*). The authors thank the teams of Rosetta and Philae, including those for the scientific instruments, for making this endeavor possible. Special thanks go to the ESA flight dynamics team for its strong support to prepare and realize the landing of Philae. This mission would not have been possible without the outstanding contributions of the orbiter instrument teams needed for landing site selection and lander operations, in particular the OSIRIS, MIRO (Microwave Instrument for the Rosetta Orbiter), VIRTIS (Visible, Infrared, and Thermal Imaging Spectrometer); ALICE (An ultraviolet imaging spectrometer for the Rosetta orbiter), and ROSINA (Rosetta Orbiter Spectrometer for Ion and Neutral Analysis) teams. Special thanks go to M. Hilchenbach for stimulating discussions and M. Hofmann, P. Gutiérrez-Marqués, and C. Tubiana for the processing of OSIRIS images for this paper. The authors also express their appreciation to H. Rosenbauer, whose effort and inspiration were essential ALICE (An ultraviolet imaging spectrometer for the Rosetta orbiter)for the realization of Philae.

SUPPLEMENTARY MATERIALS

www.sciencemag.org/content/349/6247/aaa9816/suppl/DC1
Materials and Methods
Supplementary Text
Figs. S1 to S20
Tables S1 to S6
Movie S1

23 February 2015; accepted 26 June 2015
10.1126/science.aaa9816

COMETARY SCIENCE

Properties of the 67P/Churyumov-Gerasimenko interior revealed by CONSERT radar

Wlodek Kofman,[1] Alain Herique,[1] Yves Barbin,[2] Jean-Pierre Barriot,[3] Valérie Ciarletti,[4] Stephen Clifford,[5] Peter Edenhofer,[6] Charles Elachi,[7] Christelle Eyraud,[15] Jean-Pierre Goutail,[4] Essam Heggy,[7,17] Laurent Jorda,[12] Jérémie Lasue,[14] Anny-Chantal Levasseur-Regourd,[13] Erling Nielsen,[8] Pierre Pasquero,[1] Frank Preusker,[16] Pascal Puget,[1] Dirk Plettemeier,[9] Yves Rogez,[1] Holger Sierks,[8] Christoph Statz,[9] Hakan Svedhem,[10] Iwan Williams,[11] Sonia Zine,[1] Jakob Van Zyl[7]

The Philae lander provides a unique opportunity to investigate the internal structure of a comet nucleus, providing information about its formation and evolution in the early solar system. We present Comet Nucleus Sounding Experiment by Radiowave Transmission (CONSERT) measurements of the interior of Comet 67P/Churyumov-Gerasimenko. From the propagation time and form of the signals, the upper part of the "head" of 67P is fairly homogeneous on a spatial scale of tens of meters. CONSERT also reduced the size of the uncertainty of Philae's final landing site down to approximately 21 by 34 square meters. The average permittivity is about 1.27, suggesting that this region has a volumetric dust/ice ratio of 0.4 to 2.6 and a porosity of 75 to 85%. The dust component may be comparable to that of carbonaceous chondrites.

Long-wavelength radars are currently extensively used to study the subsurface of planetary bodies down to a few kilometers in depth, examples being the Mars Advanced Radar for Subsurface and Ionospheric Sounding on the Mars Express European Space Agency (ESA) mission (*1*, *2*), Shallow Radar on the Mars Reconnaissance Orbiter NASA mission (*3*), and Lunar Radar Sounder on the Kaguya Japan Aerospace Exploration Agency mission (*4*). Because comet nuclei are on the order of a few kilometers in size and made of highly porous material, we modified the above technique to study the nucleus of a comet. The Comet Nucleus Sounding Experiment by Radiowave Transmission (CONSERT) was first proposed in 1994 and selected by ESA in 1996 as one of the experiments on the Rosetta mission. It was initially intended to explore comet 46P/Wirtanen, but, due to delay in the launch date, the target had to be changed to comet 67P/Churyumov-Gerasimenko (67P), which has a larger nucleus.

CONSERT (*5*), a bistatic radar instrument, propagates long-wavelength electromagnetic signals between the orbiting Rosetta spacecraft and the lander, Philae. In general, part of the signal path travels through the nucleus [see the supplementary materials (SM)]. The measured quantities are the signal travel time and the amplitude of the received signals. The travel time depends on the real part of the permittivity (dielectric constant), whereas the imaginary part of the permittivity (linked to the electrical conductivity) has an effect on the signal's amplitude. Thus, the CONSERT measurements give direct information about the permittivity of the comet nucleus and its spatial structure. The permittivity is a function of several properties of the nucleus: porosity, composition of the material, temperature, internal structure, and/or scale of potential heterogeneities. Theoretical models of the internal structure of the comet have been produced encompassing a range of values for the above parameters to obtain a match to the observed time delay and amplitude of the signals, thus allowing conclusions to be drawn regarding the interior of the comet nucleus.

Measurements during the First Science Sequence

Philae separated from the Rosetta orbiter at 08:35 UTC on 12 November 2014. CONSERT operated throughout the descent of Philae until 14:51 UTC, 40 min before the scheduled touchdown on the surface of comet 67P. Unfortunately, Philae bounced a couple of times before finally coming to rest in an unknown location and an unknown orientation at 17:31 UTC. CONSERT restarted operating at 18:56 UTC and continued until 04:06 UTC on 13 November 2014. The whole series of observations carried out by Philae after landing is named the First Science Sequence (FSS).

The observations to be made by CONSERT were predetermined long before the landing. It was intended that Philae and Rosetta be initially visible to each other so that, for calibration purposes, the signal would travel only through vacuum. As Rosetta moved about its orbit and the comet nucleus rotated, the geometry would evolve so that an occultation would occur (that is, the nucleus would be between Philae and Rosetta), so that the radio waves would travel through the nucleus. Because Philae was not at the intended landing point, normal communication between Philae and Rosetta was impossible at that time, implying that there was no direct visibility between the communication antennas. Then, Philae and Rosetta were already in occultation when the measurements started. Hence, there was no direct visibility for CONSERT either, making calibration difficult.

Because Rosetta moves along its orbit, while at the same time the nucleus rotates, the relative positions of Rosetta and Philae were continually changing during the FSS (Fig. 1). Both the path length and its trajectory were changing. A strong signal was detected for about 30 min (18:56 to 19:22 UTC) at the beginning of the FSS and for about 80 min at the end of the FSS (02:47 to 04:06 UTC) (Fig. 2). During these two periods, the signals at both Philae and Rosetta were strong and CONSERT worked as intended (SM). The results presented in the paper are mainly based on the data acquired during these two periods.

Outside these two periods, the observed signal-to-noise ratio (SNR) was much lower. This can be explained by some of following factors: (i) the FSS orbit was not well adapted to the CONSERT bistatic measurements; (ii) the lander antennas were not well positioned with respect to the local environment at the surface (resulting in a gain loss and a polarization mismatch between the lander and orbiter); (iii) the noise level at the receiver on Philae during the FSS measurements was much larger (about 12 dB) than

[1]Université Grenoble Alpes, IPAG, F-38000 Grenoble, France (2) Centre National de la Recherche Scientifique (CNRS), Institut de Planétologie et d'Astrophysique de Grenoble (IPAG), F-38000 Grenoble, France. [2]MIO, UM 110, CNRS-Institut National des Sciences de l'Univers (INSU), Université de Toulon, Aix-Marseille Université, IRD 83957 La Garde, France. [3]Geodesy Observatory of Tahiti BP6570, 98702 Faa'a, Tahiti. [4]Université de Versailles Saint-Quentin-en-Yvelines (UVSQ) (UPSay); Université Pierre et Marie Curie (UPMC) (Sorbonne Univ.); CNRS/INSU; Laboratoire Atmosphéres, Milieux, Observations Spatiales (LATMOS)-Institut Pierre-Simon Laplace (IPSL), 11 Boulevard d'Alembert, 78280 Guyancourt, France. [5]Lunar and Planetary Institute, 3600 Bay Area Boulevard, Houston, TX 77058, USA. [6]Ruhr-University of Bochum, Faculty of Electrical Engineering and Information Technology, 44780 Bochum, Germany. [7]Jet Propulsion Laboratory, 4800 Oak Grove Drive, MS 300-243E, Pasadena, CA 91109, USA. [8]Max-Planck-Institüt fur Sonnensystemforschung (MPS), Justus-von-Liebig-Weg 3, 37077 Göttingen, Germany. [9]Technische Universitaet Dresden Helmholtzstraße 10 D-01069 Dresden, Germany. [10]European Space Agency (ESA)/European Space Research and Technology Centre (ESTEC) Noordwijk, Netherlands. [11]Queen Mary University of London, Mile End Road, London E1 4NS, UK. [12]Laboratoire d'Astrophysique de Marseille Pôle de l'Étoile Site de Château-Gombert 38, Rue Frédéric Joliot-Curie 13388 Marseille, France. [13]UPMC (Sorbonne Univ.); UVSQ (UPSay); CNRS/INSU; LATMOS-IPSL, BC 102, 4 place Jussieu, 75005 Paris, France. [14]Université de Toulouse; UPS-OMP; IRAP; (2) CNRS; IRAP; 9 Avenue Colonel Roche, BP 44 346, F-31028 Toulouse Cedex 4, Toulouse, France. [15]Aix-Marseille Université, CNRS, Centrale Marseille, Institut Fresnel UMR 7249, 13013 Marseille, France. [16]German Aerospace Center (DLR) Rutherfordstraße 2 12489 Berlin, Germany. [17]University of Southern California, Ming Hsieh Department of Electrical Engineering, Viterbi School of Engineering, Los Angeles, CA 90089, USA.
***Corresponding author. E-mail: wlodek.kofman@obs.ujf-grenoble.fr**

the one measured during the cruise phase; and (iv) the absorption inside the comet, linked to the length of propagation path and electrical properties of the nucleus, could also contribute to decrease the signal power. Fortunately enough, since the noise level at the receiver on Rosetta was much lower than the one experienced at the receiver on Philae, signals could still be clearly measured on Rosetta during some additional

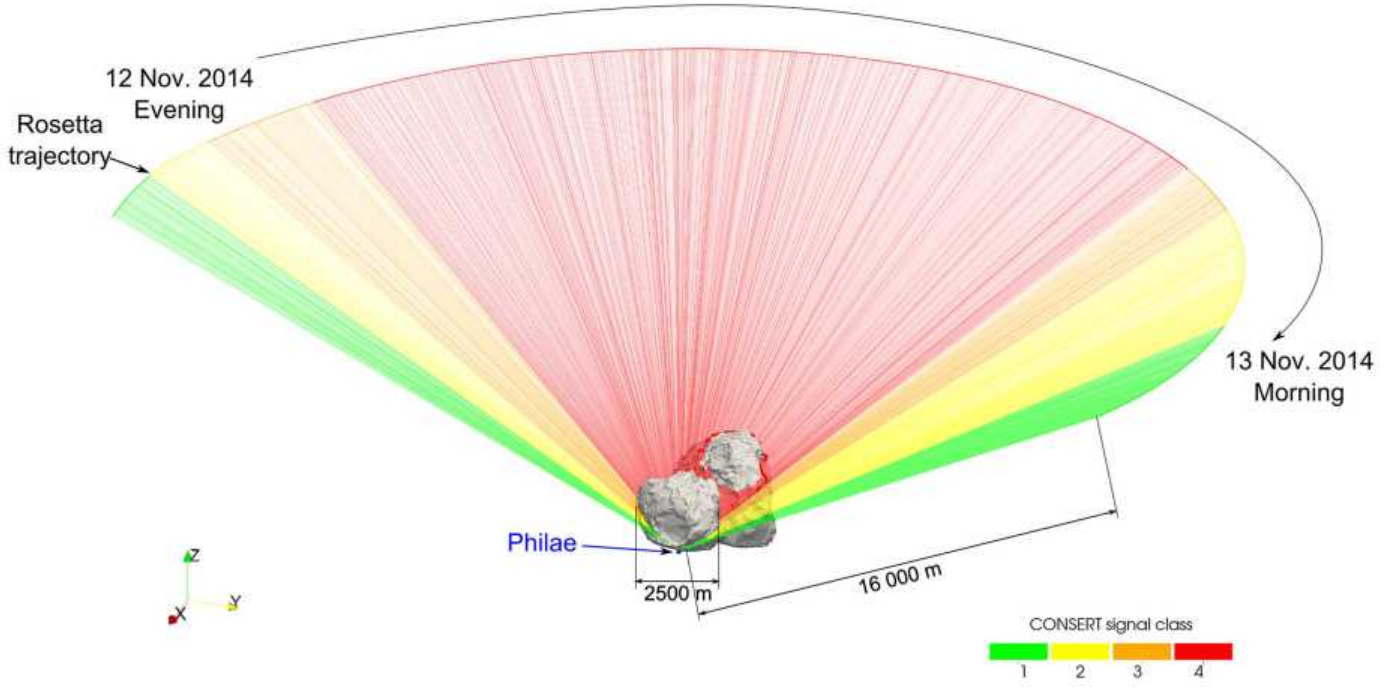

Fig. 1. Propagation of signals from Philae on the nucleus to Rosetta on its orbit. The orbit of Rosetta and the location of Philae inside the strip determined by CONSERT are shown. The rotation of the nucleus dominates the relative motion of Rosetta versus Philae. Different colors for the propagation lines correspond to different qualities of CONSERT data. The class of the signal is color-coded in (1) green for strong SNR and good synchronization, (2) yellow for acceptable SNR without synchronization, (3) orange for low SNR, and (4) red for absence of signal. In the figure, we indicated on the comet nucleus model the lines (ground track) where the signals from Philae that go to Rosetta cross the surface of the comet. The width of the antenna beam is about 78°, and its footprint covers the whole comet. Figures S1 and S2 show closer views of the ground tracks. The green lines show the locations of Rosetta during the period when the measurements we discuss in this paper were obtained.

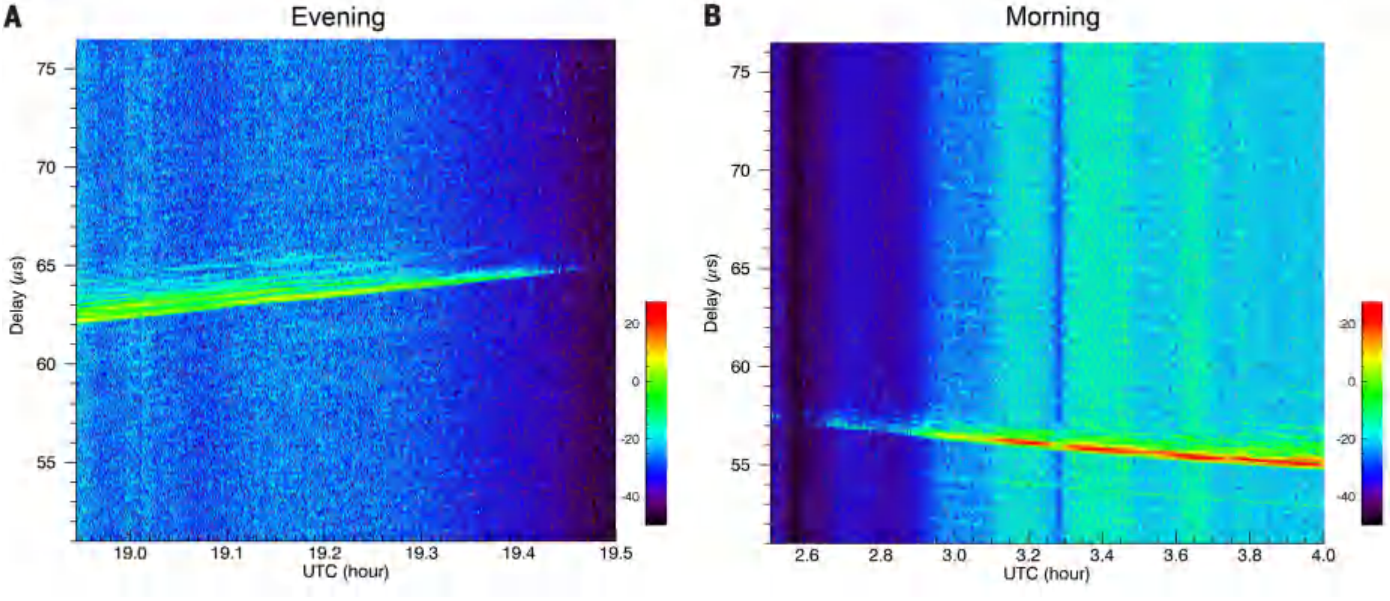

Fig. 2. The signal power in dB or in logarithmic scale on 12 to 13 November 2014. Times on (**A**) 12 November (evening) and (**B**) 13 November (morning) are in universal time coordinated (UTC); for the same diagram expressed in a linear power scale, see the SM. The figure shows the signal received as a function of propagation time between Philae and Rosetta in μs (vertical axis) and time of measurements UTC (every 2.5 s) (horizontal axis). The color code indicates the power of the signal (red being the strongest).

periods despite a partial loss of synchronization, so that useful results could be obtained. Another measurement period corresponds to a situation in which the statistics of the signal at Rosetta show the presence of a signal that propagated through the comet but where a clear detection is not possible because the signal is less powerful than the noise.

CONSERT is able to measure the distance between Philae and Rosetta when they are visible to each other simply by multiplying the signal travel time by the speed of the radio wave in vacuum. Because Philae's location was unknown, CONSERT carried out three additional measurements while Rosetta and Philae were visible to each other, in an attempt to locate the position of Philae on the surface by triangulation. The triangulation was made during three additional measurements of about 15 min each, on 13 November at 22:00 UTC and on 14 November at 10:30 and 23:45 UTC. The location of Philae was pinned down to a strip measuring approximately 150 by 15 m^2, with accuracies on the order of 10 to 20 m (*6*).

Signals that were received by CONSERT on Rosetta during the two nominal periods of measurements propagated through parts of the nucleus and are as narrow as the calibration signal (Fig. 3). Thus, we conclude that there is not, at least down to the level of 20 dB below the maximum of the peak, any signature of volume or surface scattering effects in the signal form. If scattering were present, a long tail of decay in the signal should be visible (*7*). The absence of this scattering indicates that the medium explored by the waves is rather homogeneous and/or that the dielectric contrast (difference) between potential inclusions inside the nucleus is low, at least at the scale of a few wavelengths of CONSERT. This conclusion is important for our approach to the data interpretation.

This result does not, however, exclude a slow variability in the dielectric properties or the existence of blocks much larger than the wavelength inside the nucleus. Two or three well-defined propagation paths could indeed be potentially due to the presence of a large structure inside the nucleus or to surface features on a large scale (Fig. 3 and fig. S3).

We processed and analyzed the data to determine the propagation time between Philae and Rosetta (Fig. 4). Had the operations been normal, a propagation time in free space would have been calculated, and the difference with the measured time combined with the knowledge of the nucleus shape model would have led to the determination of average dielectric properties of the materials. In reality, because the position of Philae was only known to be within a strip measuring approximately 150 by 15 m^2, the exact propagation time in free space cannot be calculated, and this straightforward approach to data analysis could not be used.

Instead, we had to assume a series of potential lander locations within the strip (Fig. 5), larger than mentioned above, in order to take into account the possible inaccuracies, and a range of realistic permittivity values for the nucleus. For every combination, we calculate the propagation time and compare it with the values obtained by CONSERT so that the best matches can be identified.

To analyze the dielectric properties of 67P, a considerable amount of data, both from ground-based observations and other instruments on Rosetta, is already available. This allows restrictions to be placed on the values of the parameters that had to be considered. The measured low average density of the nucleus indicates that the porosity is very high (70 to 80%) (*8*). Nuclei are composed of ices, mainly H_2O, CO, and CO_2 (*9*), and of refractory dust particles, mostly silicate material and nonvolatile macromolecular material (*8*, *10*), already detected by Rosetta (*11*, *12*). From these facts and values for the real part of the permittivity of ices and the expected dust-to-ices ratio, using a mixing law (*13*), we deduce that the permittivity of the cometary interior should be low, much less than 2, with a low imaginary part. The Wentzel, Kramers, and Brillouin (WKB) (*14*, *15*) approximation is valid for a wave propagation model inside the nucleus when the spatial variations of the permittivity are smooth. This requires a scale length L, to be much larger than the wavelength (*16*), and a relative variability $\Delta\varepsilon/\varepsilon$ less than 10% where ε is the permittivity. The scale length is defined by $L = \varepsilon / |\nabla\varepsilon|$. Using the Born (*14*) approximation to estimate the propagation of waves, it is reasonable to assume that the permittivity, with a potential addition of a small perturbation, is constant inside the part of the nucleus explored by CONSERT. This implies that the deviation from a straight line of the propagation path inside the comet is low (*16*). For a zero-order data analysis, we assumed that the path is a straight line. However, account has to be taken of refraction at the surface due to the difference between the dielectric properties of the nucleus and free space. We ran simulations (SM) of the signal propagation between Philae and Rosetta, taking into account the three-dimensional (3D) shape model provided by the Optical, Spectroscopic, and Infrared Remote Imaging System (OSIRIS) team (shape 4S v0.2 model) (*8*).

For each of the Rosetta positions on its orbit and for each set of hypothetical Philae position and range of parameters, these 3D simulations produced a set of predicted signals that would be observed, together with their propagation time and propagation paths both inside and outside the comet. These simulations were carried out for 243 hypothetical landing sites along the strip defined for Philae potential position, assuming a constant average permittivity inside the comet. Values of the permittivity ranging from 1.025 to 1.45 have been considered for the simulations due to the low 67P density (*8*) (SM).

For each simulation, we compare the predicted fastest ray-propagation times with the measured one. The accuracy in time in any one measurement is better than 0.1 μs, so any hypothetical configuration for which the difference between measured and calculated time is larger than ±0.2 μs is rejected. This corresponds to a 60-m difference in the optical propagation path between Rosetta and Philae. Comparisons between the simulated and measured data have been made separately for each of the two nominal periods of the FSS corresponding to the evening and the morning (figs. S1 and S2). This was done so that any difference in the results could be investigated.

For each Rosetta position on the orbit and for each potential Philae location, the permittivity value that leads to the best match with the experimental data [i.e., minimizes the root mean square (RMS) difference between experimental and simulated delays] can be determined (SM) (figs. S4 and S5). The data taken in the evening show a higher sensitivity to the permittivity, which is consistent with a larger length of the propagation path inside the comet. Eventually, to constrain as much as possible both the location of Philae and the mean permittivity value, we assumed that the mean permittivity value should be the same inside the volume investigated during the morning and evening period. In the evening sector, the length of the propagation path inside the comet is between 560 and 760 m for all measurements, and in the morning, the variability of length is bigger, 190 to 710 m, most measurements being for smaller lengths. The inferred permittivity range is 1.27 ± 0.05 for the evening measurements and 1.27 ± 0.1 for the morning ones. The permittivy is normalized with respect to the value for free space. The error was determined assuming that the root mean square deviation on the delays, varies around the minimum by two times the average accuracy of time measurements (20 ns). The results also lead to the area of the possible locations for the lander of ~21 by 34 m^2 (Fig. 5).

Interpretation of the permittivity measurements

To deduce the bulk nucleus permittivity from the CONSERT results, the effective permittivity of various ices and dust mixtures with different porosities were calculated using mixing formulas and making assumptions regarding the dust and ice ratio (tables S3 to S5). This gives a range of ice/dust volume fraction compatible with the CONSERT values deduced for the mean permittivity.

The permittivity of hexagonal water ice at low temperature is 3.1 at 90 MHz (*17*, *18*). The permittivity of amorphous ice, the presence of which in the comets was postulated (*9*, *19*), is 3.1 to 3.4 for frequencies of 100 kHz (*20*). As water ice, whether in its crystalline or amorphous phases, it is nondispersive for frequencies from kHz to GHz; similar values can be expected at 90 MHz. In this analysis, we use a value of 3.1 to estimate the effect of the lower limit of amorphous ice. In the literature, the permittivity of CO_2 is given as 2.1 at 200 K in the 1-MHz frequency range (*21*). We are unaware of any published measurements for CO. In this analysis, we considered two boundary conditions on the permittivity for the ice fraction component. The first is a permittivity of 3.1 corresponding to the case of pure water ice [upper limit (SM)], and the second is a permittivity of

2.83 corresponding to a mixture of 75% H_2O amorphous ice (or crystalline ice) and 25% CO_2 ice volume ratio corresponding to ~80%/20% molecular abundances in comets and interstellar material (*22*). These limits are estimated using the Hashin-Shtrikman bounds (*13*).

The non-icy fraction of the material plays an important role in modifying the dielectric properties. Ground-based observations suggest that most cometary dust is an unequilibrated, heterogeneous mixture of crystalline and glassy silicate minerals, organic refractory material, and other constituents such as iron sulfides and FeNi metal (*23*).

The mean elemental composition of comet Wild 2 samples (collected by Stardust) suggests a CI (i.e., similar to carbonaceous chondrite meteorites such as Ivuna meteorite)–like composition

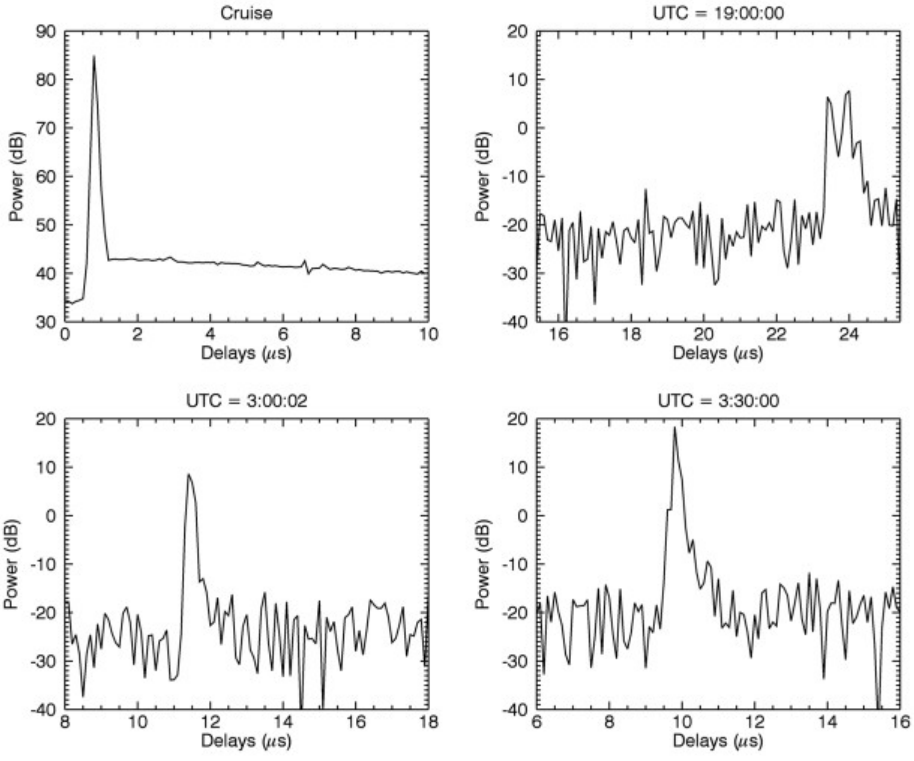

Fig. 3. CONSERT signals as a function of time delay. Signals that have propagated through the nucleus, as measured at the output of the matched filter, are presented for different measurement times and compared to the calibration signal during the cruise phase.

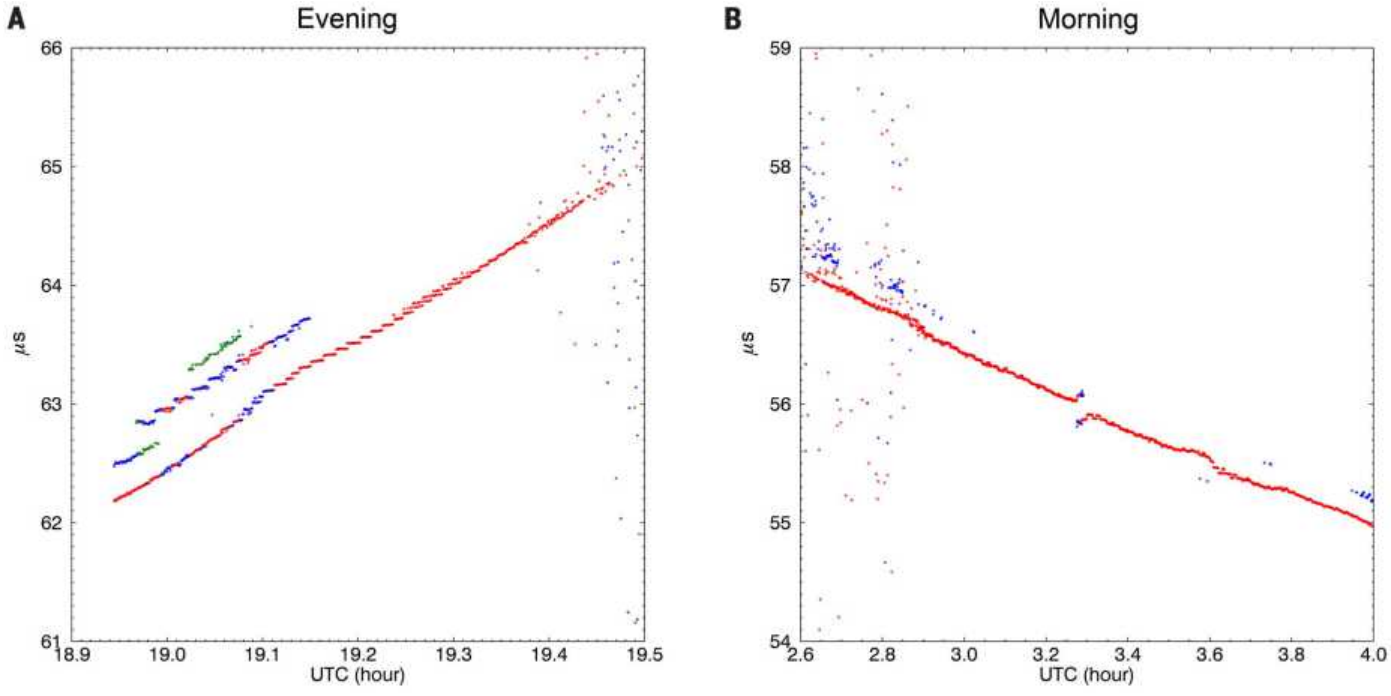

Fig. 4. Measured propagation time between Philae and Rosetta as a function of observation time. Evening (**A**) and morning (**B**) measurements. Red corresponds to the strongest signal, blue to the second strongest, and green to the third strongest. Second and third are in the interval of 6 dB below the red one. The dispersed dots correspond to delays not correctly detected due to the noise.

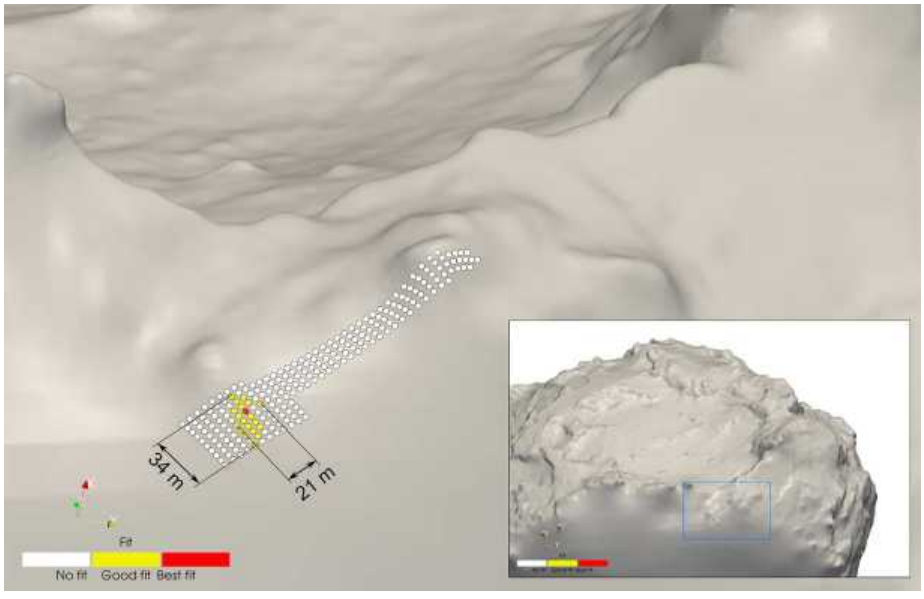

Fig. 5. Expected landing site(s) within the strip defined by CONSERT. On the shape model of the upper lobe region corresponding to the final landing region, the hypothetical landing sites are marked by dots. Possible landing sites (low RMS of the arriving time difference between observations and simulations) are marked in yellow, with the best fit in red. Unlikely landing sites [RMS too large and impossible location for two periods (SM)] are marked in white.

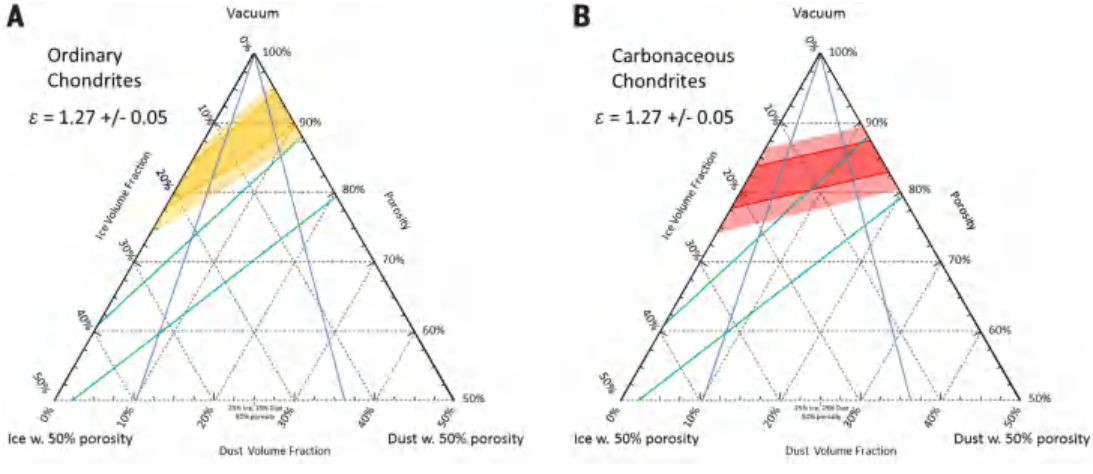

Fig. 6. Ternary diagram dust/ice/porosity volumetric fractions for cometary material. The three axes correspond to the fraction by volume of dust, ice, and vacuum (*28*). The vacuum volume fraction is so that the total porosity is equal to the sum of micro- and macroporosities, whereas refractory dust material is assumed to have no porosity. Constraints imposed by estimates of the comet density and dust/ice ratio coming from other instruments or observations are also indicated. The continuous lines delimit regions of (**A**) and (**B**) (yellow and red, respectively), where the calculated permittivity is equal to 1.27, as derived from the CONSERT observations, using a dust permittivity of ordinary chondrites (yellow region) and carbonaceus chondrites (red region). The lines (delimitating each region with darker color) correspond to limits obtained by Hashin-Shtrikman bounds. The region with lighter color indicates the influence of the error in the measurement on the permittivity of ± 0.05. The green lines delimit regions for the possible density, and the blue lines delimit regions for the possible dust/ice ratio (SM).

consistent with a bulk solar system composition for primitive material (*24*–*26*). They appear to be primarily composed of ferromagnesian silicates, Fe-Ni sulfides, and Fe-Ni metal. Abundant amorphous silicates were also detected in addition to the crystalline ones, consistent with mixing between processed solar system matter and interstellar matter. The accreted material could include Al-rich and Si-rich chondrule fragments together with some CAI (i.e., similar to calcium-aluminium-rich-inclusions)–like fragments. These materials, combined with fine-grained components in the tracks, are analogous to components in unequilibrated chondritic meteorites and cluster interplanetary dust particles, as collected in the stratosphere of the Earth (*27*). Therefore, potential analog meteoritic materials for comparison with cometary dust include the ordinary and the carbonaceous chondrite groups.

To calculate the effective permittivity for the nuclei, we consider the measured permittivity on two types of chondritic meteorites. The first type consists of two ordinary chondrites (OC), and the second one consists of two carbonaceous chondrites (CC). The laboratory-measured permittivity of the samples is then used to calculate the dust/ice volume ratio using the Hashin-Shtrikman bounds for the maximum and minimum of the effective permittivity (*13*). Hence, we assume that in the head of comet 67P, the mixture consists of the two most common materials in comets' chondritic dust (with permittivity of 2.6 to 2.9 for CC and of 4.7 to 5.6 for OC) and porous ice (with permittivity of 2.8 to 3.1) [table S3 (SM)].

The permittivity derived from CONSERT data provides additional constraints to those arising from the density and ice/dust ratio, as derived from other data. Altogether, they are used to build ternary diagrams (Fig. 6 and figs. S7 to S9). Our value of the permittivity (about 1.27) excludes, as expected for primitive small bodies, the presence of ordinary chondrites in the refractory component. From laboratory measurements on material with a porosity of 30%, the permittivity has to be lower than 2.9. This corresponds, using the Maxwell Garnett (*13*) formula for inversion, to a typical permittivity lower than 4 for a material without any porosity.

The range of dust/ice volume ratio is about 0.4 to 2.6, and the porosity range is 75 to 85%. These values correspond to the head of the comet. Deeper analysis of CONSERT based on more precise location information may reveal some variability of permittivity between different parts of the cometary head. However, it is unlikely that the values will change much from the low and narrow range of permittivity deduced here.

REFERENCES AND NOTES

1. G. Picardi *et al*., Radar soundings of the subsurface of Mars. *Science* **310**, 1925–1928 (2005). doi: 10.1126/science.1122165; pmid: 16319122
2. J. J. Plaut *et al*., Subsurface radar sounding of the south polar layered deposits of Mars. *Science* **316**, 92–95 (2007). doi: 10.1126/science.1139672; pmid: 17363628
3. R. J. Phillips *et al*., Massive CO_2 ice deposits sequestered in the south polar layered deposits of Mars. *Science* **332**, 838–841 (2011). doi: 10.1126/science.1203091; pmid: 21512003
4. T. Ono *et al*., Instrumentation and observation target of the Lunar Radar Sounder (LRS) experiment on-board the SELENE spacecraft. *Earth Planet. Sci.* **60**, 321–332 (2008). doi: 10.1186/BF03352797
5. W. Kofman *et al*., Comet Nucleus Sounding Experiment by Radiowave Transmission. *Adv. Space Res.* **21**, 1589–1598 (1998). doi: 10.1016/S0273-1177(97)00952-6
6. J. Biele *et al*., The landing(s) of Philae and inferences on comet surface mechanical properties. *Science* **349**, aaa9816 (2015).
7. J. Boisson *et al*., Radar sounding of temperate permafrost in Alaska: Analogy to the Martian midlatitude to high-latitude ice-rich terrains. *J. Geophys. Res.* **116**, E11003 (2011). doi: 10.1029/2010JE003768
8. H. Sierks *et al*., On the nucleus structure and activity of comet 67P/Churyumov-Gerasimenko. *Science* **347**, aaa1044 (2015). doi: 10.1126/science.aaa1044; pmid: 25613897
9. M. C. Festou, H. U. Keller, H. A. Weaver, Eds., *Comets II* (University of Arizona Press, Tucson, AZ, 2004).
10. E. Hadamcik, A. K. Sen, A. C. Levasseur-Regourd, R. Gupta, J. Lasue, Polarimetric observations of comet 67P/Churyumov-Gerasimenko during its 2008–2009 apparition. *Astron. Astrophys.* **517**, A86 (2010). doi: 10.1051/0004-6361/201014167
11. F. Capaccioni *et al*., The organic-rich surface of comet 67P/Churyumov-Gerasimenko as seen by VIRTIS/Rosetta. *Science* **347**, aaa0628 (2015). doi: 10.1126/science.aaa0628; pmid: 25613895
12. R. Schulz *et al*., Comet 67P/Churyumov-Gerasimenko sheds dust coat accumulated over the past four years. *Nature* **518**, 216–218 (2015). doi: 10.1038/nature14159; pmid: 25624103
13. A. Sihvola, *Electromagnetic Mixing Formulas and Applications* (The Institution of Electrical Engineers, London, 2004).
14. M. Born, E. Wolf, *Principles of Optics* (Pergamon Press, New York, 1970).
15. M. Benna, J.-P. Barriot, W. Kofman, Y. Barbin, Generation of 3-D synthetic data for the modeling of the CONSERT experiment (the radiotomography of comet 7P/Churyumov Gerasimenko). *IEEE Trans. Antenn. Propag.* **52**, 709–716 (2004). doi: 10.1109/TAP.2004.825564
16. A. Herique, W. Kofman, T. Hagfors, G. Caudal, J.-P. Ayanides, A characterization of a comet nucleus interior: Inversion of simulated radio frequency data. *Planet. Space Sci.* **47**, 885–904 (1999). doi: 10.1016/S0032-0633(98)00144-5
17. S. R. Gough, A low temperature dielectric cell and the permittivity of hexagonal ice to 2 K. *Can. J. Chem.* **50**, 3046–3051 (1972). doi: 10.1139/v72-483
18. E. Heggy *et al*., Radar properties of comets: Parametric dielectric modeling of Comet 67P/Churyumov-Gerasimenko. *Icarus* **221**, 925–939 (2012). doi: 10.1016/j.icarus.2012.09.023
19. J. Klinger, A.-C. Levasseur-Regourd, N. Bouziani, A. Enzian, Towards a model of cometary nuclei for engineering studies for future space missions to comets. *Planet. Space Sci.* **44**, 637–653 (1996). doi: 10.1016/0032-0633(96)00067-0
20. O. Andersson, Dielectric relaxation of the amorphous ices. *J. Phys. Condens. Matter* **20**, 244115 (2008). doi: 10.1088/0953-8984/20/24/244115
21. E. Pettinelli *et al*., Frequency and time domain permittivity measurements on solid CO_2 and solid CO_2-soil mixtures as Martian soil simulants. *J. Geophys. Res.* **108** (E4), 8029 (2003). doi: 10.1029/2002JE001869
22. P. Ehrenfreund, S. B. Charnley, Organic molecules in the interstellar medium, comets, and meteorites: A voyage from dark clouds to the early Earth. *Annu. Rev. Astron. Astrophys.* **38**, 427–483 (2000). doi: 10.1146/annurev.astro.38.1.427
23. M. S. Hanner, M. S., J.P. Bradley, in *Comets II*, M. C. Festou, H. U. Keller, H. A. Weaver, Eds. (University of Arizona Press, Tucson, AZ, 2004), pp. 555–564.
24. G. J. Flynn *et al*., Elemental compositions of comet 81P/Wild 2 samples collected by Stardust. *Science* **314**, 1731–1735 (2006). pmid: 17170294
25. T. Stephan, Assessing the elemental composition of comet 81P/Wild 2 by analyzing dust collected by Stardust. *Space Sci. Rev.* **138**, 247–258 (2008). doi: 10.1007/s11214-007-9291-2
26. D. Brownlee, D. Joswiak, G. Matrajt, Overview of the rocky component of Wild 2 comet samples: Insight into the early solar system, relationship with meteoritic materials and the differences between comets and asteroids. *Meteorit. Planet. Sci.* **47**, 453–470 (2012). doi: 10.1111/j.1945-5100.2012.01339.x
27. D. J. Joswiak *et al*., Comprehensive examination of large mineral and rock fragments in Stardust tracks: Mineralogy, analogous extraterrestrial materials, and source regions. *Meteorit. Planet. Sci.* **47**, 471–524 (2012). doi: 10.1111/j.1945-5100.2012.01337.x
28. P. Kamoun, P. L. Lamy, I. Toth, A. Herique, Constraints on the subsurface structure and density of the nucleus of Comet 67P/Churyumov–Gerasimenko from Arecibo radar observations. *Astron. Astrophys.* **568**, A21 (2014). doi: 10.1051/0004-6361/201423544

ACKNOWLEDGMENTS

Rosetta is an European Space Agency (ESA) mission with contributions from its member states and National Aeronautics and Space Administration (NASA). Rosetta's Philae lander is provided by a consortium led by Deutsches Zentrum für Luft- und Raumfahrt (DLR), Max Planck Institut fur Sonnesystemforschung (MPS), Centre National d'Etudes Spatiales (CNES), and Agenzia Spaziale Italiana (ASI). The CONSERT instrument was designed, built, and operated by IPAG, LATMOS, and MPS and was financially supported by CNES, CNRS, Université Joseph Fourier (UJF), DLR, and MPS. The authors thank the teams of Rosetta [Rosetta Mission Operation Center (RMOC) and Rosetta Science Ground Segment (RSGS)] and Philae (Rosetta Lander Control Center (LCC) and Rosetta Lander Science Operation & Navigation Center (SONC)) for making possible the CONSERT operations. Most of the computations presented in this paper were performed using the Calcul Intensif, Modélisation, Expérimentation Numérique (CIMENT) infrastructure (https://ciment.ujf-grenoble.fr), including the Froggy platform, which is supported by the Rhône-Alpes region (GRANT CPER07_13 CIRA), the OSUG@2020 labex (reference ANR10 LABX56), the Equip@Meso project (reference ANR-10-EQPX-29-01) of the program Investissements d'Avenir supervised by the Agence Nationale pour la Recherche and France-Grille (www.france-grilles.fr). Part of this research was carried out at the Jet Propulsion Laboratory, California Institute of Technology, under a contract with the National Aeronautics and Space Administration. All CONSERT data are released through the PSA archive of ESA (www.rssd.esa.int/index.php?project=PSA&page=rosetta).

SUPPLEMENTARY MATERIALS

www.sciencemag.org/content/349/6247/aab0639/suppl/DC1
Materials and Methods
Figs. S1 to S9
Tables S1 to S5
References (*29*–*42*)

5 March 2015; accepted 30 June 2015
10.1126/science.aab0639

COMETARY SCIENCE

The nonmagnetic nucleus of comet 67P/Churyumov-Gerasimenko

Hans-Ulrich Auster,[1]* Istvan Apathy,[2] Gerhard Berghofer,[3] Karl-Heinz Fornacon,[1] Anatoli Remizov,[1,4] Chris Carr,[5] Carsten Güttler,[6] Gerhard Haerendel,[7] Philip Heinisch,[1] David Hercik,[1] Martin Hilchenbach,[6] Ekkehard Kührt,[8] Werner Magnes,[3] Uwe Motschmann,[8,9] Ingo Richter,[1] Christopher T. Russell,[10] Anita Przyklenk,[1] Konrad Schwingenschuh,[3] Holger Sierks,[7] Karl-Heinz Glassmeier[1,7]

Knowledge of the magnetization of planetary bodies constrains their origin and evolution, as well as the conditions in the solar nebular at that time. On the basis of magnetic field measurements during the descent and subsequent multiple touchdown of the Rosetta lander Philae on the comet 67P/Churyumov-Gerasimenko (67P), we show that no global magnetic field was detected within the limitations of analysis. The Rosetta Magnetometer and Plasma Monitor (ROMAP) suite of sensors measured an upper magnetic field magnitude of less than 2 nanotesla at the cometary surface at multiple locations, with the upper specific magnetic moment being $<3.1 \times 10^{-5}$ ampere–square meters per kilogram for meter-size homogeneous magnetized boulders. The maximum dipole moment of 67P is 1.6×10^{8} ampere–square meters. We conclude that on the meter scale, magnetic alignment in the preplanetary nebula is of minor importance.

Comets are believed to have been formed in the outer solar nebula beyond the snow line, where icy aggregates can grow in size to form larger bodies (*1*–*3*). Both the Kuiper belts as well as the Oort cloud are possible reservoirs of comets, with different processes leading to their formation (*3*). The dust-to-ice ratio of comets is on the order of 1 (*4*, *5*). Thus, a large fraction of cometary material is refractory material. Analysis of NASA Stardust mission (Comet Sample Return Mission) samples indicates a high contribution of Fe to this refractory material (*6*, *7*). Up to 1% of the Fe content can be present as magnetite. Processes such as accretional remanent magnetization (*8*) or detrital remanent magnetization (*9*) are possible candidates to form larger-scale magnetic dust grains and cometesimals. These in turn allow the possibility for a comet to possess a larger-scale remanent magnetic field.

Detection of any cometary magnetization is difficult because a dipole field decreases with the cube of the distance from the object. Global magnetization of small solar system bodies can be detected either with spacecraft flybys or direct measurements on the surface. Whereas the flybys of the Galileo and Deep Space spacecraft at asteroids 951 Gaspra and 9969 Braille suggested the possibility of notable magnetization of these bodies (*10*–*12*), the distant flybys of the Rosetta spacecraft (*13*) at asteroids 2867 Steins and 21 Lutetia provided an upper limit on the specific magnetic moment of 10^{-6} A-m^2/kg (*14*, *15*).

Magnetic field measurements obtained during the flyby of the Giotto spacecraft at comet 1P/Halley offered an opportunity to estimate cometary magnetization because they revealed an almost magnetic field–free (<50 pT) region around the nucleus (*16*, *17*). Taking into account the closest approach distance of 596 km to Halley's nucleus, this corresponds to a formal dipole magnetic moment of $<5 \times 10^{13}$ A-m^2 or an upper specific magnetic moment of <0.25 A-m^2/kg, a physically unrealistic value indicating the limitations of the observation. Other spacecraft encounters with comets did not allow any reliable estimate of an intrinsic cometary magnetic moment owing to the perturbed magnetic field induced by the comet–solar wind interaction (*18*–*20*).

These inferences, however, are based on measurements acquired on distant flybys and have necessarily relied on modeling the modification of the solar wind magnetic field at rather large distances from the asteroids. To determine whether planetary bodies are magnetized requires measurements of magnetic fields on and near surfaces. Pioneering such an observational situation was the Near Earth Asteroid Rendezvous (NEAR)–Shoemaker's spacecraft fluxgate magnetometer (*21*). Near-surface measurements at asteroid 433 Eros provide an upper limit of the global remanent magnetic dipole moment of 1.3×10^{10} A-m^2 and a maximum specific magnetic moment for Eros of 1.9×10^{-6} A-m^2/kg. Eros is therefore a remarkably nonmagnetic object (*21*).

We present combined space and near-surface measurements from Rosetta and the subsequent multiple touches of its lander Philae on the surface of comet 67P/Churyumov-Gerasimenko (67P). Both Rosetta and Philae are equipped with fluxgate magnetometer instruments. The fluxgate magnetometer of the Rosetta Plasma Consortium, RPC-MAG (*22*, *23*), serves as a solar wind monitor for the Rosetta Magnetometer and Plasma Monitor (ROMAP) measurements taken during descent, hopping, and landing on the nucleus. The ROMAP instrument (*24*) is a highly integrated plasma and magnetic field sensor assembly. Both fluxgate magnetometers allow measuring the magnetic field at a resolution of ~30 pT at a cadence of up to 32 Hz during the Philae phase of the Rosetta mission. The combined measurements onboard the two spacecraft allow separation of the field of local sources from external field variations. The ROMAP measurements we present from Philae were not taken in a stationary phase.

Philae was released from Rosetta on 12 November 2014 at 08:35 UTC. Both magnetometers were powered on a few hours before and thus were able to monitor the release and successful deployment of the ROMAP boom at 08:43 UTC. RPC-MAG measured a maximum change of the magnetic field magnitude by ~20 nT, indicating the successful release of the probe. During release, Philae was put into a rotational state around its z axis by its Mechanical Support System (MSS), the rotation frequency (period) being 3.3 mHz (300 s). After the deployment of the landing gear, Philae's rotation frequency changed to 2 mHz (500 s). Rotation at these frequencies was clearly identifiable in the ROMAP magnetic field measurements.

During the ROMAP boom deployment, the field magnitude decreased from 2022 to 155 nT, indicating a substantial Philae-generated bias magnetic field present in predeployment measurements. The first touchdown was recorded by the magnetometer at 15:34:04 UTC. Because of its inertia, the boom was partly folded back into its stored position at touchdown and tilted up again. Touchdown was detected by a clear change of the field magnitude due to Philae's spacecraft bias field. Initiated by the touchdown sensors, the control electronics of Philae's fly wheel was turned off, and during the following 2400 s, the flywheel transferred its angular momentum to the lander as Philae was lifted off the cometary surface. As a result, the rotation rate changed to 76.9 mHz (13 s), again monitored by the magnetometer.

Philae's rotation and nutation induced by descent and touchdown was advantageous; the rotations permitted precise in-flight calibration for all three magnetic field components. Further lander-biased field changes (δB_X = +3 nT, δB_Y = +9 nT, and δB_Z = −7nT) occur mainly during the first 3 hours after separation as a result of temperature variations. At the time of all four surface contacts, temperatures were almost constant, and the magnetometer offsets changed by only ~1 nT.

At 16:20 UTC, ROMAP measurements provide clear evidence that Philae touched a cliff structure.

[1]Institut für Geophysik und extraterrestrische Physik, Technische Universität Braunschweig, Mendelssohnstrasse 3, D-38106 Braunschweig, Germany. [2]Centre for Energy Research, Hungarian Academy of Sciences, H-1121 Konkoly Thege Street 29-33, Budapest, Hungary. [3]Space Research Institute, Austrian Academy of Sciences, Schmiedlstrasse 6, A-8042 Graz, Austria. [4]Space Research Institute, Russian Academy of Sciences, Moscow, Profsoyuznaja Street 84/32, 117810 Moscow, Russia. [5]Imperial College London, Exhibition Road, London SW7 2AZ, UK. [6]Max-Planck-Institut für Sonnensystemforschung, Justus-von-Liebig-Weg 3, D-37077 Göttingen. [7]Max-Planck-Institute für Extraterrestrische Physik, Giessenbachstrasse, D-85741 Garching bei München. [8]German Aerospace Center (DLR), Institute of Planetary Research, D-12489 Berlin, Rutherfordstrasse 2, Germany. [9]Institut für Theoretische Physik, Technische Universität Braunschweig, Mendelssohnstrasse 3, D-38106 Braunschweig, Germany. [10]Institute of Geophysics and Planetary Physics, University of California, Los Angeles, Los Angeles, CA 90095-1567, USA.
*Corresponding author. E-mail: uli.auster@tu-bs.de

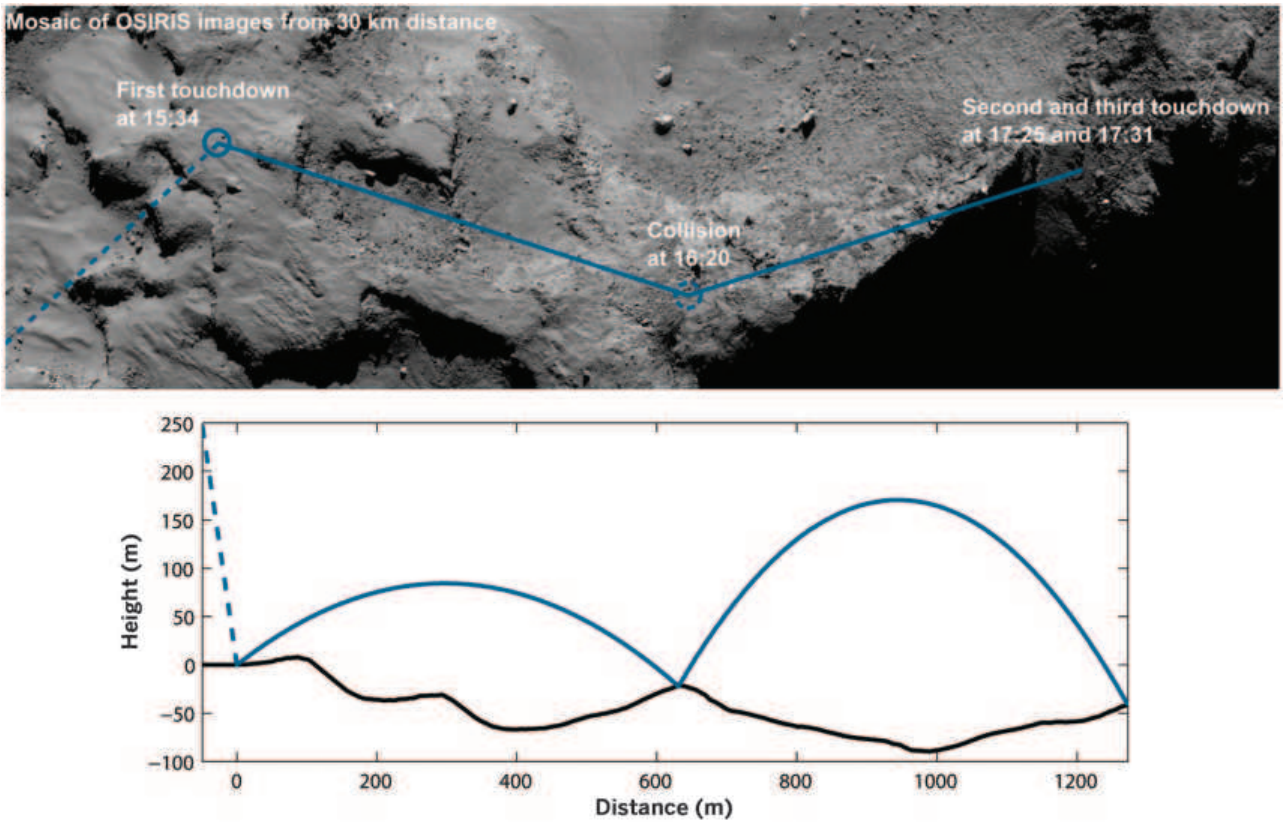

Fig. 1. Philae's preliminary trajectory. (**Top**) The mosaic from OSIRIS images displays the horizontal path of Philae on the surface of 67P. (**Bottom**) The ballistic trajectory (dark blue) as well as the surface profile (black) relative to reference sphere indicates the shallow flight of Philae above the surface.

This was not an actual landing because no vertical deceleration of the boom was detected. After this encounter with an as-yet unknown surface structure, Philae started to tumble, no longer rotating about the z axis. This complex dynamical motion—rotation and nutation dominated—caused a more complex magnetic field variation. The main rotation frequency changed to 41.7 mHz (24 s). At 17:25:26 UTC, a second touchdown was recorded by ROMAP, and at 17:31:17 UTC, probably only a few meters away, the final landing position was reached.

Because the actual surface of the nucleus is highly structured, we use a spherical surface as a reference for any further height information as well as to display the locations where Philae had ground contact and finally landed (Fig. 1). The center of this sphere is the center of mass of the comet that is the origin of the Cheops system (*25*). The positive z axis of the Cheops system is pointing along the cometary rotation axis, and the x axis is in the equatorial plane, parallel to the longest axis of the nucleus, in the direction of the small lobe of the nucleus. The y axis completes the right-handed system; the x axis prime meridian is through the Cheops boulder (*26*). The radius of the reference sphere is determined as R_{sphere} = 2393 m, the radial distance of the first touchdown point in the Cheops system.

On the basis of the position of the first touchdown as determined by the Rosetta Mission Operation Center (RMOC) and considering the

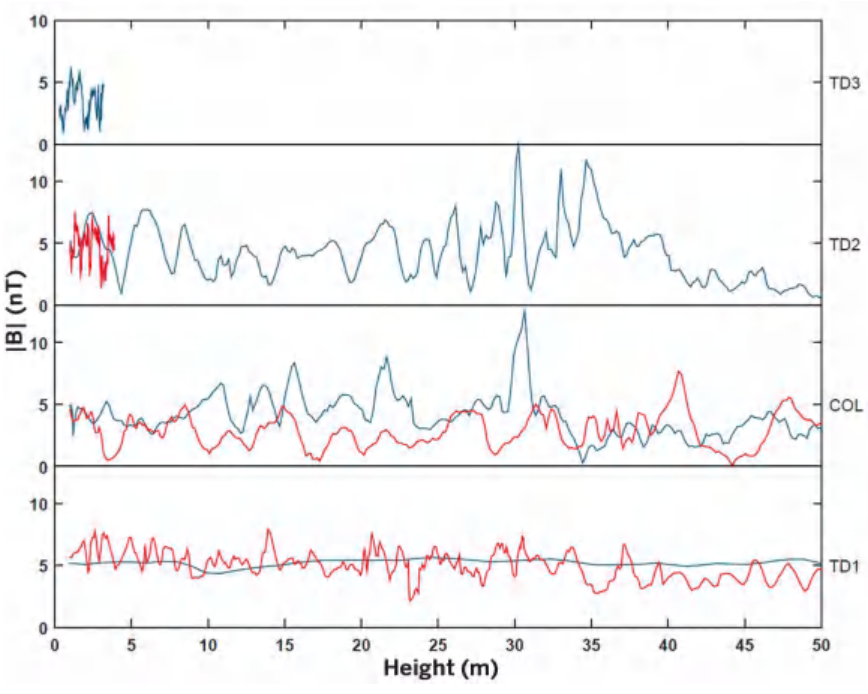

Fig. 2. Magnetic field observations. The blue curve gives the magnitude during each descent, the red during ascent. TD1 displays measurements taken during descent toward TD_1 and ascent to the first apex, COL shows data taken from the first apex down to the cliff collision point and the second apex, TD2 gives the observations from the second apex to the second touchdown point and the third apex, and TD3 displays measurements taken along the short trajectory to the final landing site.

direction of flight after the first touchdown as indicated from the Optical, Spectroscopic, and Infrared Remote Imaging System (OSIRIS) camera (*27*) observations, preliminary coordinates of the touchdown points are TD_1 = (2.133, −0.963, 0.500) km and $TD_{2,3}$ = (2.482, −0.063, −0.185) km in Cheops coordinates. The distance between the second and third touchdown point is only a few meters.

The point of contact with the cliff structure is estimated at C = (2.361, −0.668, −0.009) km. This position has been determined from the collision time as seen in the ROMAP measurements, in the OSIRIS determined flight direction and speed, as well as by searching for a surface structure in OSIRIS pictures suitable for a collision. The collision time determined for this structure by using the OSIRIS-determined Philae speed agrees very well with the ROMAP-determined collision time. With respect to the reference sphere, the heights of the four points are h_1 = 0 m, $h_{2,3}$ = 97 m, and h_C = 61 m.

To reconstruct the lander trajectory between the points of ground contact, ballistic trajectories are assumed. With a preliminary nucleus mass value of 10^{13} kg (*25*), the local gravity was estimated as $g = 10^{-4}$ m/s^2. The distance between the first touchdown and the cliff contact points is ~631 m, the maximum height reached by Philae being 123 m. The distance to the second touchdown point is 641 m, with a maximum flight height of 240 m. The final landing point is probably very close to the second touchdown point. From the ballistic trajectory determination, we infer for the collision point descent and ascent velocities of 0.26 and 0.25 m/s, respectively. This is in agreement with Philae flying uphill toward $TD_{2,3}$.

From this preliminary flight trajectory determination, we infer that ROMAP is able to provide very precise magnetic field measurements not only at the two touchdown points, the contact point, and the final landing site, but also at a range of heights above the nucleus surface (Fig. 2). Furthermore, measurements during both descent and ascent are available, which is different from measurements at 433 Eros, where only descent observations were possible (*21*).

Because of the dynamics of the landing process, the precise height of the ROMAP instrument above the surface is not known. In its deployed state, the boom-mounted sensor has a nominal height above the plane (defined by the three landing gear feet) of 1.2 m. At the final landing site, we estimate the distance of the sensor to the closest cometary surface structure to be less than 0.4 m, as derived from Comet Infrared and Visible Analyser (CIVA) pictures.

Moving toward and away from the first touchdown point, TD_1, clearly demonstrates no large spatial variation in the observed field. The field measured at and close to the surface is dominated by the solar wind magnetic field transported to the surface by the solar wind flow. Observed variations of up to 10 nT in magnitude, over a frequency range of 100 to 1 mHz, are inherent to the interaction-modified interplanetary magnetic field (*28*). The average field magnitude is 4 nT for both descent and ascent.

No noticeable spatial variation in field magnitude is observed along the path from the first touchdown to the cliff contact point COL, either. The field measured in the vicinity of the surface is identified as the solar wind magnetic field, with no clear indication of a field attributed to the nucleus.

The segment COL-TD_2 exhibits a pronounced set of field variations close to the surface at a height below ~20 m, between 17:21 and 17:23 UTC during descent. Because no ascent measurements are available, we used RPC-MAG data to rule out any radial magnetic field variation caused by a putative local magnetic anomaly. During the Philae landing, Rosetta was positioned above the landing area at a distance of ~17 km. Magnetic field measurements taken with RPC-MAG exhibit field variations similar to those detected with ROMAP (Fig. 3). These are due to ultralow-frequency waves seen in the inner coma (*28*). For the time interval 17:21 to 17:23 UTC, the correlation coefficient between both time series is r = 0.78, with a lag of −2 s. Observations provided with RPC-MAG thus support our conclusion that the field variations recorded with ROMAP are due to variations of the interplanetary magnetic field and not caused by spatial variations related to a magnetized cometary crust.

No spatial variation of the magnetic field strength during descent and ascent to the surface is observed in any of the magnetic field components (supplementary materials). The mean value between 10 m and touchdown of the averaged absolute values for descent and ascent is used as an error estimate. It varies between 0.6 and 1.9 nT. Therefore, we used the value 2 nT as a conservative estimate for the magnetic field caused by local surface magnetization. For a nucleus dipole-generated field <2 nT, measured at a distance of 2.5 km, which is the distance of the observation sites from the center of gravity of the nucleus, we determined a magnetic dipole strength of $<1.6 \times 10^8$ A-m^2.

A lower bound for the magnetization required to cause an observed field value can be estimated by using Parker's optimal magnetization criteria (*29*). However, an upper bound for the magnetization requires a different treatment. A worst-case scenario is a randomly oriented distribution of magnetic dipoles of uniform strength M. In such a frustrated dipole situation, field compensation of neighboring dipoles requires a larger magnetization to generate a given surface magnetic field. Furthermore, our measurements were not made directly at the surface. This limits the horizontal spatial resolution to ~1 m. Also, descent and ascent trajectories were not along the local surface normal. To account for all of these effects, model calculations have been performed (supplementary materials) assuming a set of rectangular cubes with uniform magnetization magnitude, but random orientation. With these model calculations, we reason a magnetic dipole $\vec{M}$ in the second Gaussian position to provide a suitable estimate for the magnetic field

$$\vec{B}(\vec{r}) = \frac{\mu_0}{4\pi}\frac{\vec{M}}{r^3}$$

where μ_0 denotes the vacuum permeability, and r is the distance of the measurement to the dipole center. With $|\vec{M}| = m \cdot D^3$, where m is the magnetization and D is the scale of the cube, we set an upper bound

$$m \le m_{\mathrm{Upper}} = \frac{4\pi}{\mu_0} \cdot \left(\frac{h}{D} + \frac{1}{2}\right)^3 \cdot B$$

For D, the granularity of the magnetization distribution, we chose D = 1 m, the spatial resolution of our measurements. With B = 2 nT and h = 0.4 m, we estimate m_{Upper} = 0.0146 A/m, or using the cometary density of 470 kg/m^3 (*25*), an upper value for the specific magnetic moment of 3.1×10^{-5} A-m^2/kg. For larger homogeneously magnetized grains ($D >> h$), the upper value for the specific magnetic moment decreases to 5.4×10^{-6} A-m^2/kg. We cannot rule out the possibility that boulders with a stronger magnetic moment are present at larger distances from the observational points.

As a comparison, lunar material is characterized by a specific magnetic moment in the range of 2.5×10^{-5} to 10^{-3} A-m^2/kg (*30*). The natural

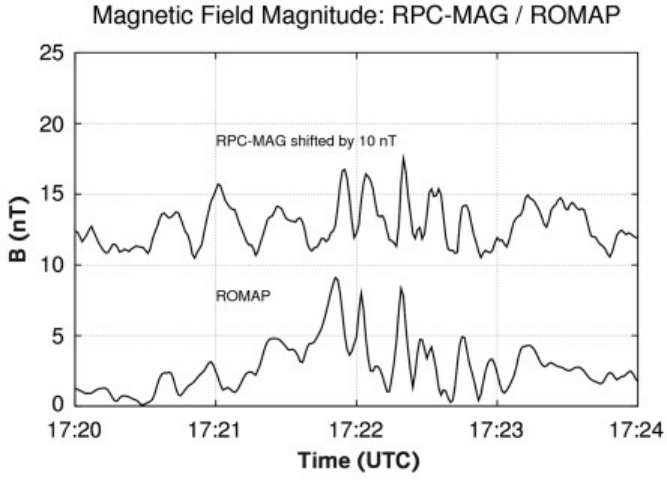

Fig. 3. RPC-MAG and ROMAP comparison. Magnetic field magnitude (band passed 1 to 100 mHz) determined from measurements from ROMAP measurements onboard the lander Philae (bottom line) and RPC-MAG of the Rosetta orbiter (top line) for the time interval just before the second touchdown. For reason of enhanced visibility, the RPC-MAG data are shifted by 10 nT.

remanent specific magnetic moment of meteorites collected in the Atacama Desert ranges between 10^{-4} and 7×10^{-3} A-m^2/kg (*31*). The weakest magnetization of achondrites and shergottite, nakhlite, and chassigny (SNC) meteorites is reported as 5×10^{-4} and 2×10^{-5} A-m^2/kg (*32*). The specific magnetic moment we report here for cometary material, depending on granularity $<3.1 \times 10^{-5}$ to $<5.64 \times 10^{-6}$ A-m^2/kg, is smaller than that of lunar and meteoritic planetary material. Therefore, much like Eros, we consider 67P a nonmagnetic object.

The magnetization found at 67P is much too low to enforce alignment of 10^{-1} m and larger cometesimals in a preplanetary nebular. The orientation of such grains and bodies may be determined mainly by gas drag. If comet 67P is representative of cometary nuclei, magnetic forces are unlikely to play a role in the accumulation of planetary building blocks on scales of >1 m—that is, in the critical diameter range of 10^{-1} to 10^2 m (*33*).

REFERENCES AND NOTES

1. S. J. Weidenschilling, The origin of comets in the solar nebula: A unified model. *Icarus* **127**, 290–306 (1997). doi: 10.1006/icar.1997.5712
2. A. Kataoka, H. Tanaka, S. Okuzumi, K. Wada, Fluffy dust forms icy planetesimals by static compression. *Astron. Astrophys.* **557**, L4 (2013). doi: 10.1051/0004-6361/201322151
3. J. Blum, B. Gundlach, S. Mühle, J. M. Trigo-Rodriguez, Comets formed in solar-nebula instabilities!—An experimental and modeling attempt to relate the activity of comets to their formation process. *Icarus* **235**, 156–169 (2014). doi: 10.1016/j.icarus.2014.03.016
4. P. D. Singh, A. A. de Almeida, W. F. Huebner, Dust release rates and dust-to-gas mass ratios of eight comets. *Astron. J.* **104**, 848–858 (1992). doi: 10.1086/116279
5. M. Küppers *et al*., A large dust/ice ratio in the nucleus of comet 9P/Tempel 1. *Nature* **437**, 987–990 (2005). doi: 10.1038/nature04236; pmid: 16229066
6. R. C. Ogliore *et al*., Comparison of the oxidation state of Fe in comet 81P/Wild 2 and chondritic-porous interplanetary dust particles. *Earth Planet. Sci. Lett.* **296**, 278–286 (2010). doi: 10.1016/j.epsl.2010.05.011
7. E. L. Berger, T. J. Zega, L. P. Keller, D. S. Lauretta, Evidence for aqueous activity on comet 81P/Wild 2 from sulfide mineral assemblages in Stardust samples and CI chondrites. *Geochim. Cosmochim. Acta* **75**, 3501–3513 (2011). doi: 10.1016/j.gca.2011.03.026
8. H. Nübold, K. H. Glassmeier, Accretional remanence of magnetized dust in the solar nebula. *Icarus* **144**, 149–159 (2000). doi: 10.1006/icar.1999.6273
9. R. R. Fu, B. P. Weiss, *J. Geophys. Res.* **117**, E02003 (2012). doi: 10.1029/2011JE003925
10. M. G. Kivelson *et al*.., Magnetic field signatures near Galileo's closest approach to Gaspra. *Science* **261**, 331–334 (1993). doi: 10.1126/science.261.5119.331; pmid: 17836843
11. X. Blanco-Cano, N. Omidi, C. T. Russell, Hybrid simulations of solar wind interaction with magnetized asteroids: Comparison with Galileo observations near Gaspra and Ida. *J. Geophys. Res.* **108** (A5), 1216 (2003). doi: 10.1029/2002JA009618
12. I. Richter *et al*., First direct magnetic field measurements of an asteroidal magnetic field: DS1 at Braille. *Geophys. Res. Lett.* **28**, 1913–1916 (2001). doi: 10.1029/2000GL012679
13. K. H. Glassmeier, H. Boehnhardt, D. Koschny, E. Kührt, I. Richter, The Rosetta Mission: Flying towards the origin of the solar system. *Space Sci. Rev.* **128**, 1–21 (2007). doi: 10.1007/s11214-006-9140-8
14. H. U. Auster *et al*., Magnetic field investigations during Rosetta's 2867 Steins flyby. *Planet. Space Sci.* **58**, 1124–1128 (2010). doi: 10.1016/j.pss.2010.01.006
15. I. Richter *et al*., Magnetic field measurements during the ROSETTA flyby at asteroid (21)Lutetia. *Planet. Space Sci.* **66**, 155–164 (2012). doi: 10.1016/j.pss.2011.08.009
16. F. M. Neubauer *et al*., First results from the Giotto magnetometer experiment at comet Halley. *Nature* **321** (6067s), 352–355 (1986). doi: 10.1038/321352a0
17. F. M. Neubauer, The ionopause transition and boundary layers at comet Halley from Giotto magnetic field observations. *J. Geophys. Res.* **93** (A7), 7272–7281 (1988). doi: 10.1029/JA093iA07p07272
18. E. J. Smith *et al*., International cometary explorer encounter with giacobini-zinner: Magnetic field observations. *Science* **232**, 382–385 (1986). doi: 10.1126/science.232.4748.382; pmid: 17792150
19. F. M. Neubauer *et al*., *Astron. Astrophys.* **268**, L5–L8 (1993).
20. I. Richter, C. Koenders, K. H. Glassmeier, B. T. Tsurutani, R. Goldstein, Deep Space 1 at comet 19P/Borrelly: Magnetic field and plasma observations. *Planet. Space Sci.* **59**, 691–698 (2011). doi: 10.1016/j.pss.2011.02.001
21. M. H. Acuña *et al*., NEAR magnetic field observations at 433 Eros: First measurements from the surface of an asteroid. *Icarus* **155**, 220–228 (2002). doi: 10.1006/icar.2001.6772
22. K. H. Glassmeier *et al*., RPC-MAG The fluxgate magnetometer in the ROSETTA Plasma Consortium. *Space Sci. Rev.* **128**, 649–670 (2007). doi: 10.1007/s11214-006-9114-x
23. C. M. Carr *et al*., RPC: The Rosetta Plasma Consortium. *Space Sci. Rev.* **128**, 629–647 (2007). doi: 10.1007/s11214-006-9136-4
24. H. U. Auster *et al*., ROMAP: Rosetta Magnetometer and Plasma Monitor. *Space Sci. Rev.* **128**, 221–240 (2007). doi: 10.1007/s11214-006-9033-x
25. H. Sierks *et al*., On the nucleus structure and activity of comet 67P/Churyumov-Gerasimenko. *Science* **347**, aaa1044 (2015). doi: 10.1126/science.aaa1044; pmid: 25613897
26. H. Sierks *et al*., Boulder Close-Up (European Space Agency, Noordwijk, 2014); available at http://blogs.esa.int/rosetta/2014/10/09/boulder-close-up.
27. H. U. Keller *et al*., OSIRIS—The Scientific Camera System Onboard Rosetta. *Space Sci. Rev.* **128**, 433–506 (2007). doi: 10.1007/s11214-006-9128-4
28. K. H. Glassmeier, The Singing Comet (ESA, Noordwijk, 2014); published at http://blogs.esa.int/rosetta/2014/11/11/the-singing-comet.
29. R. L. Parker, Ideal bodies for Mars magnetics. *J. Geophys. Res.* **108** (E1), 5006 (2003). doi: 10.1029/2001JE001760
30. P. Rochette, J. Gattacceca, A. V. Ivanov, M. A. Nazarov, N. S. Bezaeva, Magnetic properties of lunar materials: Meteorites, Luna and Apollo returned samples. *Earth Planet. Sci. Lett.* **292**, 383–391 (2010). doi: 10.1016/j.epsl.2010.02.007
31. M. Uehara, J. Gattacceca, P. Rochette, F. Demory, E. M. Valenzuela, Magnetic study of meteorites recovered in the Atacama desert (Chile): Implications for meteorite paleomagnetism and the stability of hot desert surfaces. *Phys. Earth Planet. Inter.* **200-201**, 113–123 (2012). doi: 10.1016/j.pepi.2012.04.007
32. M. Terho, L. J. Pesonen, I. T. Kukkonen, Magnetic properties of asteroids from meteorite data? Implications for magnetic anomaly detections. *Earth Moon Planets* **72**, 225–231 (1996). doi: 10.1007/BF00117522
33. C. Güttler, J. Blum, A. Zsom, C. W. Ormel, C. P. Dullemond, The outcome of protoplanetary dust growth: Pebbles, boulders, or planetesimals? *Astron. Astrophys.* **513**, A56 (2010). doi: 10.1051/0004-6361/200912852

ACKNOWLEDGMENTS

Rosetta is a European Space Agency (ESA) mission with contributions from its member states and NASA. The contribution of the ROMAP and RPC-MAG team was financially supported by the German Ministerium für Wirtschaft und Energie and the Deutsches Zentrum für Luft- und Raumfahrt under contract 50QP1401. We are indebted to the whole Rosetta Mission Team, the Lander Control Centre (LCC) in Cologne, the Scientific Operation and Navigation Centre (SONC) in Toulouse, the Science Ground System (SGS) at the European Space Astronomy Centre (ESAC), as well as RMOC in Darmstadt for their outstanding efforts making this mission possible. The ROMAP and RPC-MAG data will be made available through ESA's Planetary Science Archive (PSA) Web site (www.rssd.esa.int/index.php?project=PSA&page=index).

SUPPLEMENTARY MATERIALS

www.sciencemag.org/content/349/6247/aaa5102/suppl/DC1
SupplementaryText
Figs. S1 to S6
Table S1

16 December 2014; accepted 1 April 2015
Published online 14 April 2015;
10.1126/science.aaa5102

COMETARY SCIENCE

Thermal and mechanical properties of the near-surface layers of comet 67P/Churyumov-Gerasimenko

T. Spohn,[1]* J. Knollenberg,[1] A. J. Ball,[2] M. Banaszkiewicz,[3] J. Benkhoff,[2] M. Grott,[1] J. Grygorczuk,[3] C. Hüttig,[1] A. Hagermann,[4] G. Kargl,[5] E. Kaufmann,[4] N. Kömle,[5] E. Kührt,[1] K. J. Kossacki,[6] W. Marczewski,[3] I. Pelivan,[1] R. Schrödter,[1] K. Seiferlin[7]

Thermal and mechanical material properties determine comet evolution and even solar system formation because comets are considered remnant volatile-rich planetesimals. Using data from the Multipurpose Sensors for Surface and Sub-Surface Science (MUPUS) instrument package gathered at the Philae landing site Abydos on comet 67P/Churyumov-Gerasimenko, we found the diurnal temperature to vary between 90 and 130 K. The surface emissivity was 0.97, and the local thermal inertia was 85 ± 35 J m^{-2} K^{-1}s$^{-1/2}$. The MUPUS thermal probe did not fully penetrate the near-surface layers, suggesting a local resistance of the ground to penetration of >4 megapascals, equivalent to >2 megapascal uniaxial compressive strength. A sintered near-surface microporous dust-ice layer with a porosity of 30 to 65% is consistent with the data.

The Multipurpose Sensors for Surface and Sub-Surface Science (MUPUS) package (*1*, *2*) operated on the approach to and on the surface of 67P/Churyumov-Gerasimenko (67P) between 12 and 14 November 2014. MUPUS (Fig. 1) is composed of three separate instruments: (i) a thermal probe, MUPUS-PEN, which is equipped with 16 resistance temperature detector–type titanium temperature sensors to be inserted into the cometary surface by a hammer mechanism; (ii) an infrared radiometer, MUPUS-TM; and (iii) a thermal sensor and an accelerometer in each of the two harpoon anchors of the lander. MUPUS-PEN was stowed on Philae during flight, and landing and was nominally deployed. MUPUS-TM is mounted to the lander in a fixed position, with the line of sight having an angle of 45° relative to the lander vertical axis and an opening angle of ±30° around the line of sight. The total field of view (FOV) of ~1 m^2 and the full-width-half-maximum FOV of 0.3 m^2 include the MUPUS-PEN deployment location.

MUPUS was designed to measure thermal and mechanical properties of the surface and the near-surface layers and to monitor the subsurface temperature. Because the harpoon anchors failed to fire (for reasons still being investigated by the lander engineers) and because MUPUS-PEN could not be fully inserted, subsurface thermal and mechanical properties could not be measured, unfortunately. Instead, a lower bound on the strength of the subsurface material was derived from the observed failure to penetrate of MUPUS-PEN. MUPUS-TM data were inverted in order to calculate the local daily temperature variation, the thermal emissivity, and the thermal inertia.

MUPUS-TM was switched on 1 hour before the release of Philae from Rosetta and recorded during the descent of the lander and its involuntary flight across the surface until final touchdown. These data include coverage of the surface along the flight path, which need to be evaluated separately. The MUPUS-TM data have been used to help reconstruct the flight path of the lander (*3*). After the lander had settled at its final landing site, Abydos, MUPUS-TM recorded for another 41 hours.

The diurnal temperature variation (Fig. 2) was synthesized from 3 days of radiometer data and from MUPUS-PEN temperature recordings (figs. S2 to S4). The emissivity ε was determined by means of least-square analysis of the TM data and was found to be ~0.97. The temperature varies between 90 and 130 K. This is an equivalent gray-body temperature. It should be representative of the average temperature in the FOV of MUPUS-TM. Also shown is our estimate of the 2σ uncertainty range. A characteristic peak in temperature of ~36 min duration is shown in Fig. 2. The complete temperature history recordings at Abydos (figs. S2 and S4), derived from the flux measured with MUPUS-TM and from MUPUS-PEN temperature recordings, show three peaks separated by 12.4 hours, which is the rotation period of the nucleus (*4*). We interpret these peaks as infrared radiation from the directly insolated surface, whereas the more gentle variation of the temperature outside a peak is interpreted as being due to indirect lighting.

Thermal models have been calculated to fit the data (Fig. 2). The calculation is described in more detail in the supplementary materials. We show three curves for thermal inertia $I = \sqrt{k\rho c}$, where k is the thermal conductivity, ρ is the density, and c is the specific heat, varying between 50 and 120 J m^{-2} K^{-1}s$^{-1/2}$, with 85 J m^{-2} K^{-1}s$^{-1/2}$ providing the best fit. A thermal inertia of 10 to

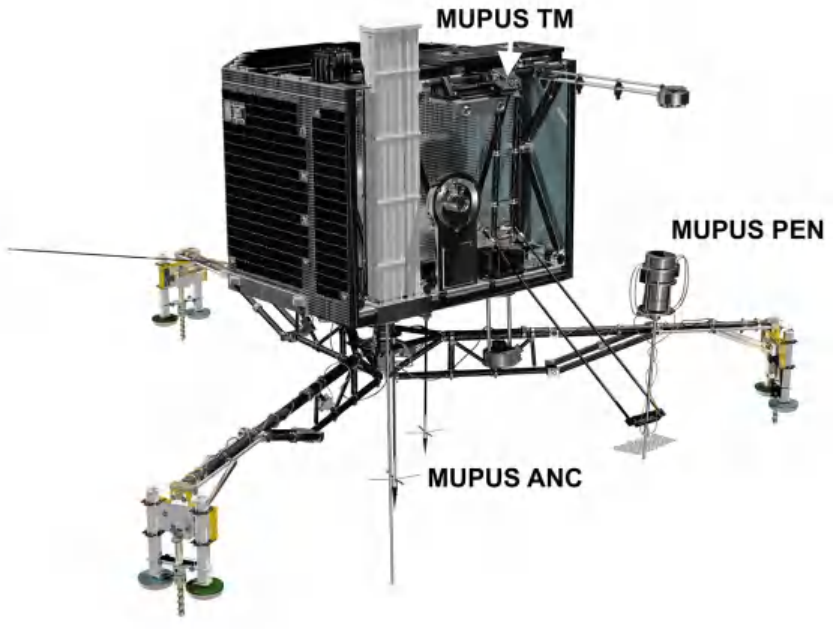

Fig. 1. Elements of the MUPUS package on the Rosetta lander Philae. Shown is Philae with the instrument bench (also termed the balcony). The thermal mapper MUPUS-TM is shown along with the deployed thermal probe MUPUS-PEN and the two anchors, each of which houses an accelerometer, MUPUS ANC-M, and a temperature sensor, ANC-T. MUPUS-PEN is shown connected to its deployment device extending from the balcony. This double strut device was retracted 300 min after MUPUS switched on so as to allow a later rotation of the lander body. [Image courtesy ESA/ATG media lab]

[1]Institute of Planetary Research, Deutsches Zentrum für Luft- und Raumfahrt (DLR), Berlin, Germany. [2]European Space Research and Technology Centre (ESTEC), European Space Agency (ESA), Noordwijk, Netherlands. [3]Space Research Center, Warsaw, Poland. [4]Department of Physical Sciences, The Open University, Milton Keynes, UK. [5]Space Research Institute, Austrian Academy of Sciences Graz, Austria. [6]Faculty of Physics, University of Warsaw, Warsaw, Poland. [7]Physics Institute, University of Berne, Berne, Switzerland.
*Corresponding author. E-mail: tilman.spohn@dlr.de

50 J m^{-2} $K^{-1}s^{-1/2}$ has been inferred from the measurements reported by the Microwave Instrument for the Rosetta Orbiter (MIRO) as a representative value of the overall surface of 67P (*5*). Our value is clearly larger, although considering the variability of the parameters determining the thermal inertia, not dramatically so. Abydos may simply have a thinner spread of low-conductivity and -density dust than on average, underlain by a sintered but still porous dust-ice layer. Other differences may be in the dust-to-ice ratio, dust composition, and local versus global average temperature and subsurface temperature gradients. MIRO as a millimeter and submillimeter instrument samples a thicker layer than does MUPUS-TM. From unresolved Spitzer observations of 67P, an upper limit of 15 J m^{-2} $K^{-1}s^{-1/2}$ was proposed (*6*). Other estimates of the thermal inertia of cometary nuclei are <45 and 200 J m^{-2} $K^{-1}s^{-1/2}$ (*7*, *8*) for comet 9P/Tempel 1—both studies using the same Deep Impact data—and <250 J m^{-2} $K^{-1}s^{-1/2}$ (*7*) for comet Hartley 2. Our value is smaller than that of kilometer-sized near-Earth asteroids (*9*) and suggests a near-surface porous layer. Differences in thermal inertia may further indicate differences in degrees of compaction and sintering and concentrations of organics in near-surface layers (*10*).

Unfortunately, the local values of k, ρ, and c have not been individually measured (*11*). Using the overall density of the comet of 470 ± 45 kg m^{-3} (*4*) and a specific heat of 300 to 600 J kg^{-1} K^{-1} as appropriate for a mixture of silicate dust (*12*) and water ice (*13*), with a dust-to-ice ratio of 2 to 6 (*14*) at temperatures of 90 to 130 K, a thermal conductivity of 0.02 to 0.06 W m^{-1} K^{-1} is implied for I = 85 J m^{-2} $K^{-1}s^{-1/2}$ (8×10^{-3} to 0.11 W m^{-1} K^{-1} if the full uncertainty of the thermal inertia is considered). These values compare with values of 2×10^{-3} to 0.02 W m^{-1} K^{-1} reported for silicate dust in vacuum (*15*), albeit at ambient temperatures, and with values of 0.02 to 0.03 W m^{-1} K^{-1} for nonsintered porous ice at 100 K (*16*). Our values are consistent with porosities between 40 and 55% (30 to 65% for the full range of uncertainty), using the data from (*15*). The thermal conductivity of highly porous media depends more on the porosity and on the contact area between the grains than on the bulk thermal conductivity of the matrix material (*15*, *16*).

The MUPUS-PEN probe was nominally commanded to start the hammering sequence 40 min after it had been deployed. The depth-of-penetration sensor, DS, measured the progress of the hammering. The hammering was also recorded by the three accelerometers of the Surface Electrical, Seismic and Acoustic Monitoring Experiment (SESAME) installed in the feet of the lander (*17*). The DS recorded an initial progress of ~27 mm, and then its readings oscillated for 3.5 hours by a total of 10 to 15 mm, indicating no net progress on penetration (Fig. 3). The rapid initial penetration could have been through a thin layer of dust, but this is speculative in the absence of precise knowledge of the initial height of the PEN tip above the ground and other independent evidence for a dust layer at Abydos. Hammering started with the lowest energy setting (Table 1 and supplementary materials). Because progress measured by the DS was smaller than a threshold value of 1.7 mm, the energy level was increased by one level after the other and had been increased after a total of 56 strokes to its maximum, where it remained for 3.1 hours. The evidence for failure to penetrate comes foremost from the recording of the DS but is supported by the temperatures measured along the PEN (fig. S4). These temperatures follow the temperature changes recorded by the thermal mapper, in particular, when the environment is warmed by indirect light.

The lack of progress into the subsurface can be interpreted as being caused by a near-surface layer of a strength the PEN was not capable of penetrating. Alternative interpretations invoke malfunctioning of MUPUS-PEN but are not independently confirmed. These are discussed in the supplementary materials. It is very probable that the mechanism worked nominally at least for three of the four levels. For level 4, housekeeping data suggest that hammering occurred only once per four-stroke sequence, thus at a rate of only a quarter of what was designed. This indicates a lack of full synchronization between charging of the capacitor and release of the hammer, and it is possible that the hammer mechanism could not use the full energy of level 4. A very conservative estimate would then assume that the PEN hammer worked only at level 3. From a comparison with calibration data collected in Table 1, we conclude that the material must have provided a resistance to penetration by the PEN of more than 4 MPa, which is equivalent to a uniaxial compressive strength of the material of about 2 MPa.

An independent estimate of the strength can be made by using the efficiency χ of the hammer mechanism of 10% and taking the downward movements of the hammer tip δ of ~3 mm recorded by the DS as deformation of the surface (the stronger upward movements interpreted as recoil). With energy E stored in the capacitor

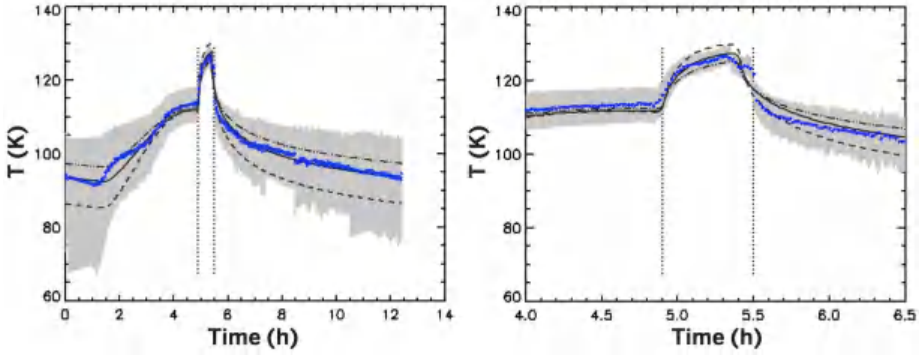

Fig. 2. Variation of temperature during a comet day at Abydos. The temperature record (blue) was synthesized from 3 days of radiometer data. (**Left**) The diurnal variation. (**Right**) The temperature during a 40-min direct illumination of part of the FOV of the thermal mapper. The gray area indicates the 2σ uncertainty estimate. The model calculations are for a thermal inertia of 85 J m^{-2} $K^{-1}s^{-1/2}$ (solid line), a ratio between stray light and direct illumination of β_0 = 0.32, and 69% of the FOV illuminated. The dashed line is for 50 J m^{-2} $K^{-1}s^{-1/2}$, β_0 = 0.27, and 46% of the FOV illuminated, and the dash-dotted line is for 120 J m^{-2} $K^{-1}s^{-1/2}$, β_0 = 0.35, and 80% of the FOV illuminated. Details of the calculation are provided in the supplementary materials.

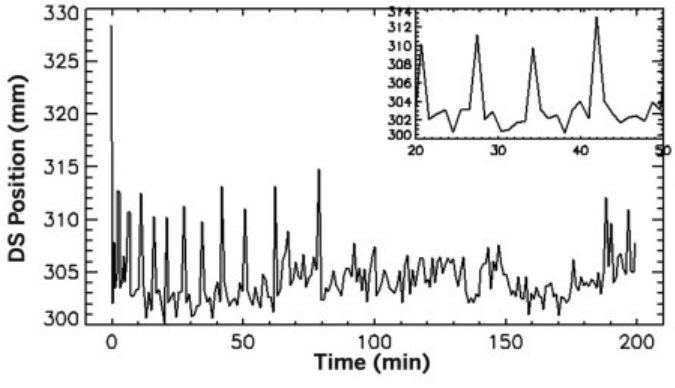

Fig. 3. Displacement of the MUPUS-PEN depth sensor (DS). The sensor records the progress of penetration with MUPUS-PEN. There is a clear downward motion of 27 mm at the beginning, followed by oscillatory displacements by 10 to 15 mm, followed by smaller displacements. The reason for the reduction in amplitude after time (t) = 80 min is not understood. One possibility is that the barbs at the tip of the PEN locked to the ground. Overall, it appears as though the PEN was hammering more or less on the spot (but not necessarily at exactly the same spot), with indentations of a few millimeters and recoils of up to 10 mm.

Table 1. PEN hammer calibration data. The table collects PEN hammer calibration results in three foam glasses of differing strength. Foam glasses T4 and F are commercially available. Foam glass SRC was produced at Space Research Centre (SRC) Warsaw for the prelaunch calibration measurements. The samples were kept for reference at SRC Warsaw. Listed are the uniaxial compressive strengths as given by the manufacturers for foam glasses T4 and F, and the results of control measurements done at Technische Universität (TU) Graz in 2015 for foam glasses F and SRC along with a value calculated for T4 (*22*) using data of a shear deformation measurement. Also given is the static penetration resistance measured at SRC Warsaw (supplementary materials). The static penetration resistance per unit area is the strength of a material into which a pile is driven. The compressive strength is measured by placing a sample cylinder between two plates of the same radius. For a homogenous, isotropic medium and a thin pile, the static penetration resistance per unit area should be twice the uniaxial compressive strength for geometrical reasons of stress propagation. The table further gives the rate of penetration progress in millimeters per four hammer strokes at the four energy levels of the hammer mechanism. The energy stored in the capacitor of the mechanism is listed per level. The efficiency of the PEN mechanism, defined as the ratio of deformational energy to the energy stored, was found to be ~10%.

	Foam glass T4	Foam glass F	Foam glass SRC
Compressive strength (MPa) (nominal by manufacturer)	0.85	1.70	—
Uniaxial compressive strength (MPa)	0.23*	0.52†	2.11†
Static penetration resistance per unit area of pile (MPa) (SRC, 2015)‡	0.52 ± 0.09	1.24 ± 0.32	4.19 ± 1.05
PEN hammer calibration results			
Progress per four hammer strokes (mm)			
Level 1, 0.49 J	2.1		
Level 2, 1.59 J	4.8	2.6	
Level 3, 2.17 J	8.3	4.4	0.3
Level 4, 4.23 J			2.0

*From Kömle *et al*. (*22*). †TU Graz, 2015. ‡Average values from four measurements are described in more detail in the supplementary materials, each with the same sample; error estimates are 2σ.

(Table 1) and an opening angle of the PEN tip α of 28.5°, the force per unit area of tip surface to overcome the strength is $\sigma = \chi E \cos^2\alpha/\delta^2 \sin\alpha$. Considering only energy level 3, we find a value of 7 MPa. Given the uncertainty of the exercise—in particular, in the deformation δ—we take this value as a confirmation of the above lower bound of the resistance to penetration of 4 MPa.

Deep Impact crater observation for comet Tempel-1 resulted in a tensile strength estimate of <12 kPa (*18*). Observation of cometary meteoroids suggest tensile strengths of ~10 kPa for particles that originated from pristine comets and up to 80 kPa for those from evolved comets (such as taurids from 2P/Encke) (*19*). Tensile strengths are typically at least one order of magnitude smaller than compressive strengths (*20*).

Laboratory data on the strength of ice and ice dust mixtures are rare at relevant temperatures as measured at Abydos. Granular ice of 1 mm grain size has a compressive strength of 60 to 70 MPa at 100 to 150 K (*21*), which is an order of magnitude larger than our lower bound. The static penetration resistance of sintered porous ice with an initial porosity of 73% is 10 MPa at 220 K, whereas the static penetration resistance of sintered CO_2 ice with an initial porosity of 48% is 6.5 MPa at 193 K (*22*). Moreover, sintering of highly porous ice during the Comet Simulation (KOSI) experiments (*23*–*25*) resulted in a penetration resistance of 5 MPa (*24*). These values compare quite well with our estimates and with our independent estimate of the porosity from the MUPUS-TM data. According to a comet thermal evolution model, sintering can result in a strong near-surface layer of a comet nucleus (*26*) but requires the grains to be tens of micrometers in radius, or smaller. Thus, high strength suggests that the material is at least locally fine-grained.

Both the thermal inertia and the strength on the surface of 67P are larger than commonly thought. In particular, our lower bound on the strength of the subsurface material is larger than previous estimates from the stability of large-scale features both on 67P (*27*) and on other comets. The reason may lie with layering or with large-scale cracks in the nucleus that may render parts of it unstable. From our data, we envisage the nucleus as a low–thermal conductivity, highly porous body with a near-surface layer consisting of sintered ice-dust with substantial local strength. The layer could be covered by a thin layer of dust of low strength. The estimated porosity is consistent with earlier models of comet nucleus formation (*28*, *29*).

REFERENCES AND NOTES

1. T. Spohn *et al*., MUPUS—A thermal and mechanical properties probe for the Rosetta lander Philae. *Space Sci. Rev.* **128**, 339–362 (2007). doi: 10.1007/s11214-006-9081-2
2. MUPUS was originally developed at the Institute of Planetology of the University of Münster together with the Space Research Center in Warsaw, the DLR Institute of Planetary Research, the Space Research Institute Graz, the University of Kent, and the Open University, and other international partners. It is now maintained and operated by an international team led by the DLR Institute of Planetary Research in Berlin.
3. J. Biele *et al*., The landing(s) of Philae and inferences about comet surface mechanical properties. *Science* **349**, aaa9816 (2015).
4. H. Sierks *et al*., On the nucleus structure and activity of comet 67P/Churyumov-Gerasimenko. *Science* **347**, aaa1044 (2015). doi: 10.1126/science.aaa1044; pmid: 25613897
5. S. Gulkis *et al*., Subsurface properties and early activity of comet 67P/Churyumov-Gerasimenko. *Science* **347**, aaa0709 (2015). doi: 10.1126/science.aaa0709; pmid: 25613896
6. S. Lowry *et al*., The nucleus of Comet 67P/Churyumov-Gerasimenko - A new shape model and thermophysical analysis. *Astron. Astrophys.* **548**, A12 (2012).
7. O. Groussin *et al*., The temperature, thermal inertia, roughness and color of the nuclei of Comets 103P/Hartley 2 and 9P/Tempel 1. *Icarus* **222**, 580–594 (2013). doi: 10.1016/j.icarus.2012.10.003
8. B. J. R. Davidsson, P. J. Gutiérrez, H. Rickmann, Physical properties of morphological units on comet 9P/Tempel 1 derived from near-IR Deep Impact spectra. *Icarus* **201**, 335–357 (2009). doi: 10.1016/j.icarus.2008.12.039
9. M. Delbo, A. dell'Oro, A. W. Harris, S. Mottola, M. Mueller, Thermal inertia of near-Earth asteroids and implications for the magnitude of the Yarkovsky effect. *Icarus* **190**, 236–249 (2007). doi: 10.1016/j.icarus.2007.03.007
10. B. J. R. Davidsson *et al*., Thermal inertia and surface roughness of Comet 9P/Tempel 1. *Icarus* **224**, 154–171 (2013). doi: 10.1016/j.icarus.2013.02.008
11. A densitometer originally planned to be included with MUPUS had to be descoped for lack of funding. The direct measurement of the thermal conductivity with the PEN was not performed because the PEN had not been inserted and time was lacking.
12. D. F. Winter, J. M. Saari, A particulate thermophysical model of the lunar soil. *Astrophys. J.* **156**, 1135–1151 (1969). doi: 10.1086/150041
13. G. Herman, P. R. Weissman, Numerical simulation of cometary nuclei: III. Internal temperatures of cometary nuclei. *Icarus* **69**, 314–328 (1987). doi: 10.1016/0019-1035(87)90108-4
14. A. Rotundi *et al*., Dust measurements in the coma of comet 67P/Churyumov-Gerasimenko inbound to the Sun. *Science* **347**, aaa3905 (2015). doi: 10.1126/science.aaa3905; pmid: 25613898
15. M. Krause, J. Blum, Yu. V. Skorov, M. Trieloff, Thermal conductivity measurements of porous dust aggregates: I. Technique, model and first results. *Icarus* **214**, 286–296 (2011). doi: 10.1016/j.icarus.2011.04.024
16. K. Seiferlin, N. Kömle, G. Kargl, T. Spohn, Line heat-source measurements of the thermal conductivity of porous H_2O ice, CO_2 ice and mineral powders under space conditions. *Planet. Space Sci.* **44**, 691–704 (1996). doi: 10.1016/0032-0633(96)00068-2
17. K. J. Seidensticker *et al*., SESAME—An experiment of the Rosetta lander Philae: Objectives and general design. *Space Sci. Rev.* **128**, 301–337 (2007).
18. K. A. Holsapple, K. R. Housen, A crater and its ejecta: An interpretation of Deep Impact. *Icarus* **187**, 345–356 (2007). doi: 10.1016/j.icarus.2006.08.029
19. J. M. Trigo-Rodriguez, J. Blum, Tensile strength as an indicator of the degree of primitiveness of undifferentiated bodies. *Planet. Space Sci.* **57**, 243–249 (2009). doi: 10.1016/j.pss.2008.02.011
20. J. Biele *et al*., The putative mechanical strength of comet surface material applied to landing on a comet. *Acta Astronaut.* **65**, 1168–1178 (2009). doi: 10.1016/j.actaastro.2009.03.041
21. R. M. Schulson, P. Duval, *Creep and Fracture of Ice* (Cambridge Univ. Press, Cambridge, 2009).

22. N. Kömle *et al*., Impact penetrometry on a comet nucleus—Interpretation of laboratory data using penetration models. *Planet. Space Sci.* **49**, 575–598 (2001). doi: 10.1016/S0032-0633(00)00169-0
23. KOSI experiments were performed between 1987 and 1993 in the space simulator at DLR in Cologne/Germany and are described in (*24*, *25*). The experiments placed a sample of granular ice at liquid nitrogen temperatures in a vacuum chamber. The samples were insolated mostly with one solar constant, but the insolation was varied between experiments. The thermal histories and the modifications of the ice—in particular, sublimation and sintering—were observed and documented.
24. E. Grün, H. Kochan, K. J. Seidensticker, Laboratory simulation, a tool for comet research. *Geophys. Res. Lett.* **18**, 245–248 (1991). doi: 10.1029/90GL02522
25. H. W. Kochan, W. F. Huebner, D. W. G. Sears, Simulation experiments with cometary analogous material. *Lab. Astrophys. Space Res.* **236**, 623–665 (1999). doi: 10.1007/978-94-011-4728-6_25
26. K. J. Kossacki, Comet 9P/Tempel 1: Evolution of the surface. *Icarus* **245**, 348–354 (2015). doi: 10.1016/j.icarus.2014.09.044
27. N. Thomas *et al*., The morphological diversity of comet 67P/Churyumov-Gerasimenko. *Science* **347**, aaa0440 (2015). doi: 10.1126/science.aaa0440; pmid: 25613893
28. J. Blum, R. Schräpler, B. J. R. Davidsson, J. M. Trigo-Rodriguez, The physics of protoplanetesimal dust agglomerates. I. Mechanical properties and relations to primitive bodies in the solar system. *Astrophys. J.* **652**, 1768–1781 (2006). doi: 10.1086/508017
29. J. Blum, B. Gundlach, S. Mühle, J. M. Trigo-Rodriguez, Comets formed in solar-nebula instabilities!—An experimental and modeling attempt to relate the activity of comets to their formation process. *Icarus* **235**, 156–169 (2014). doi: 10.1016/j.icarus.2014.03.016

ACKNOWLEDGMENTS

The authors are indebted to DLR, the Helmholtz Association (grant PD-106 to I.P.), the Polish Academy of Sciences, the Austrian Academy of Sciences, and the UK Science and Technology Facilities Council (grant ST/L000776-1 to A.H.) for funding and to ESA for providing the opportunity to be on this exciting mission. The data used in this letter are available through the ESA Planetary Science Archive www.rssd.esa.int/psa.

SUPPLEMENTARY MATERIALS

www.sciencemag.org/content/349/6247/aab0464/suppl/DC1
Materials and Methods
Figs. S1 to S6
Table S1
References (*30*–*32*)

3 March 2015; accepted 23 June 2015
10.1126/science.aab0464

COMETARY SCIENCE

The structure of the regolith on 67P/Churyumov-Gerasimenko from ROLIS descent imaging

S. Mottola,[1]* G. Arnold,[1] H.-G. Grothues,[2] R. Jaumann,[1,3] H. Michaelis,[1] G. Neukum,[3]† J.-P. Bibring,[4] S. E. Schröder,[1] M. Hamm,[1,5] K. A. Otto,[1] I. Pelivan,[1] G. Proffe,[1] F. Scholten,[1] D. Tirsch,[1] M. Kreslavsky,[6] E. Remetean,[7] F. Souvannavong,[8] B. Dolives[8]

The structure of the upper layer of a comet is a product of its surface activity. The Rosetta Lander Imaging System (ROLIS) on board Philae acquired close-range images of the Agilkia site during its descent onto comet 67P/Churyumov-Gerasimenko. These images reveal a photometrically uniform surface covered by regolith composed of debris and blocks ranging in size from centimeters to 5 meters. At the highest resolution of 1 centimeter per pixel, the surface appears granular, with no apparent deposits of unresolved sand-sized particles. The thickness of the regolith varies across the imaged field from 0 to 1 to 2 meters. The presence of aeolian-like features resembling wind tails hints at regolith mobilization and erosion processes. Modeling suggests that abrasion driven by airfall-induced particle "splashing" is responsible for the observed formations.

On 12 November 2014, the Rosetta Lander Imaging System (ROLIS) (*1*) recorded the descent of the Philae lander from its vantage point on the lander's instrument deck. During this phase, ROLIS acquired high-resolution imagery of Agilkia, the first touchdown site (TD1). The main goal was to characterize the morphology and texture of the surface of comet 67P/Churyumov-Gerasimenko (67P) with a resolution up to 1 cm, more than one order of magnitude higher than achievable from orbit. In addition to providing a glimpse of the finer structure of the cometary surface, fundamental for understanding cometary activity, ROLIS imaging provides a context for the interpretation of the measurements of the lander's in situ analyzers.

The descent activity consisted of two series of panchromatic images: the far-field sequence (FFS) and the near-field sequence (NFS). During the FFS, two images were acquired at a range of about 3100 m from the surface, which resulted in a pixel scale of about 3.3 m per pixel. These images, which captured the region of the landing site in the context of the whole body, were compressed and relayed to the orbiter during descent (fig. S1). The NFS was initiated immediately after, with the camera operating in the so-called ring-buffer mode. With this setting, the images were acquired at a cadence of 10 s and stored in real time in a memory buffer with a capacity of seven images, with the newest image overwriting the oldest. The images were shuttered at 76.8 ms and 38.4 ms, for the FFS and the NFS, respectively. These exposure times were chosen as the best trade-off between signal to noise and image smearing due to the lander terminal speed (about 1 m/s) and rotation around its axis (about 0.6°/s). The frames were acquired under nearly ideal imaging conditions, with a solar elevation around 40°, nearly vertical descent, and nadir pointing. The sequence was stopped upon touchdown by a signal dispatched by the lander, and the contents of the buffer—the last seven images—were compressed and uplinked to the orbiter. This acquisition scheme allowed us to retain the descent images with the highest resolution without the need for accurately knowing the exact time of touchdown. Because the devices responsible for anchoring the lander to the ground after touchdown did not function properly (*2*), the lander rebounded multiple times before settling 2 hours later in a location about 1 km away from TD1. Fortunately the lander continued to function during the rebound and retained its attitude so that the established radio link was maintained for the time needed for all ROLIS images to be uplinked to the orbiter. Only a few short and sporadic signal dropouts occurred, which caused the loss of nine ROLIS data packets, which are recognizable as missing "tiles" in a few of the images. Two of the ROLIS images acquired during the NFS are shown in Figs. 1 and 2. Slight changes in the observation geometry during descent have allowed us to reconstruct a digital terrain model (DTM) of TD1 by means of stereophotogrammetric techniques (*3*), as shown in Fig. 1.

The images reveal a topographically smooth terrain, characterized by gentle undulations over typical scale lengths on the order of tens of meters. The whole area has gravitational slopes smaller than 15°, averaged over scales of a few tens of meters. The surface at TD1 mainly consists of blocks (1 to 2 m), coarse regolith (10 to 50 cm) and gravel-size particles (<10 cm). The largest boulder present in the ROLIS field is roughly the shape of a triangular prism, with ~5 m in height and length (Figs. 1 and 4). The boulder appears to be partly embedded in the ground, although it cannot be excluded that it expresses an outcrop from underlying bedrock. The boulder shows a complex morphology, with a peculiar bumpy structure of decimeter-scale rounded knobs. No planar facets are seen. Features resembling fracture lines run across the boulder surface, which are particularly evident in the anaglyph shown in Fig. 4. The bumpy structure could hint at the body being a conglomeration of smaller, harder units embedded in a matrix, possibly a remnant of the comet's formation mechanism. This structure could be the result of erosional evolution, which tends to smoothen the harder material into knobs and excavate fractures by eroding the softer matrix material.

Smaller blocks show diverse morphologies (Fig. 2): Some are smooth and rounded, whereas others are angular with large, flat, polygonal faces. The rounder blocks could be the result of disaggregation of a boulder following the complete erosion of the matrix material. The blocks with flat faces, on the other hand, could result from the fragmentation of the harder units, possibly upon impact with the surface. Furthermore, a few block clusters are observed, suggesting the occurrence of recent fragmentation. Some blocks are partly embedded in the regolith layer, whereas others are overlying, suggesting the presence of processes that bury or exhume blocks.

The texture of the fine-grained regolith appears unresolved in all but the last image (Fig. 2). In particular, at the highest resolution (about 1 cm/pixel at closest range), the surface appears granular, with a mixture of grain sizes. Sand- and dust-sized particles on the surface, if present, are not organized in well-sorted deposits and do not dominate the upper regolith layer. From the extent of their shadows, some granules appear to be on top of an underlying layer, whereas others appear to be partly embedded in the soil. It is likely that the overlying particles are unconsolidated material, whereas the underlying layer may either be unconsolidated or an indurated substrate. All the blocks and granules have a competent appearance, which does not, however, exclude the possibility that particles in the centimeter-size range could be weakly bonded dust aggregates. The ratio of interparticle cohesion to gravity forces under the microgravity conditions present on the comet is estimated to be in the range of 10 to 100 for cm-sized particles, a regime for which self-organization in particle aggregates is thought to occur (*4*).

After correction for the effects of changing phase angle over the observed field of view (*5*), the average brightness of the surface is notably constant. Blocks with planar faces oriented toward the general direction of the sun do show a much higher reflectance than average. This effect is particularly evident for the largest boulder but is also recognizable for smaller blocks. However,

[1]German Aerospace Center (DLR), Institute of Planetary Research, Berlin, Germany. [2]DLR, Space Management, Space Science. Bonn, Germany. [3]Freie Universität Berlin, Institute of Geological Sciences, Berlin, Germany. [4]Institute of Space Astrophysics, Orsay, France. [5]Humboldt University Berlin, Germany. [6]Earth and Planetary Sciences, University of California, Santa Cruz, CA, USA. [7]Centre National d'Études Spatiales, Toulouse, France. [8]Magellium, Ramonville Saint-Agne, France.
*Corresponding author. E-mail: stefano.mottola@dlr.de
†Deceased.

when the brightness is integrated over a patch including the blocks and their shadows, the reflectance drops to the level of the unresolved background.

This high level of photometric uniformity is in stark contrast with what is observed on other planetary bodies. For example, boulders on asteroids are generally darker than the surrounding soil. The reflectivity of a particulate medium generally increases with decreasing particle size, due to the increasing transparency of the individual grains (*6*). The fact that the surface of 67P appears photometrically uniform suggests that the regolith particles are opaque, most likely due to the regolith being coarse and/or the soil material having a high absorption coefficient. Alternatively, the surface might be blanketed by an opaque coating.

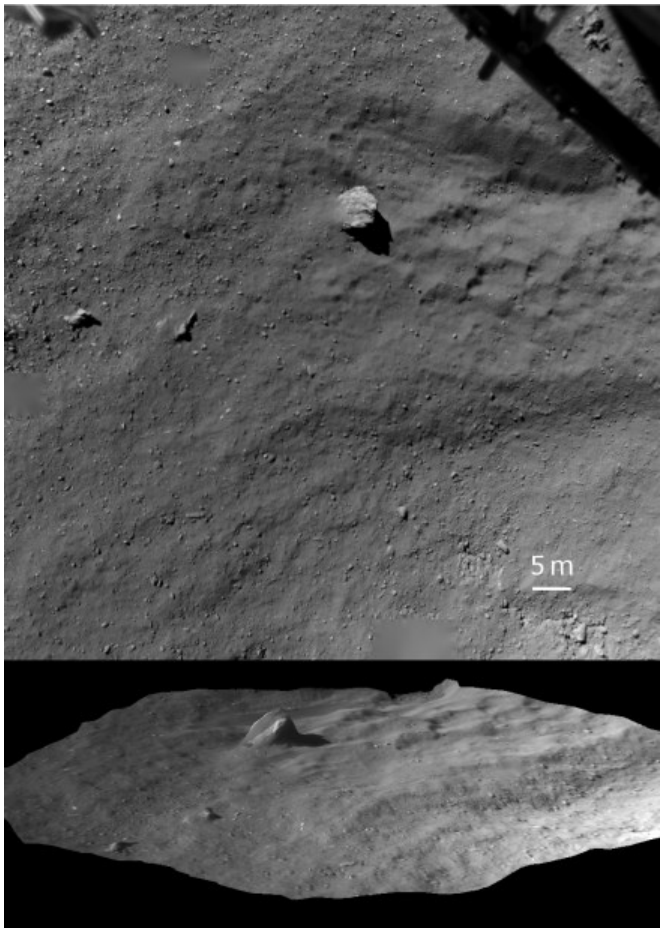

Fig. 1. First image of the NFS acquired from an altitude of 67.4 m. (**Top**) TD1 is located approximately at the center of the image. The structure on the top right is part of the Philae landing gear. (**Bottom**) Perspective view of the DTM reconstructed from NFS images.

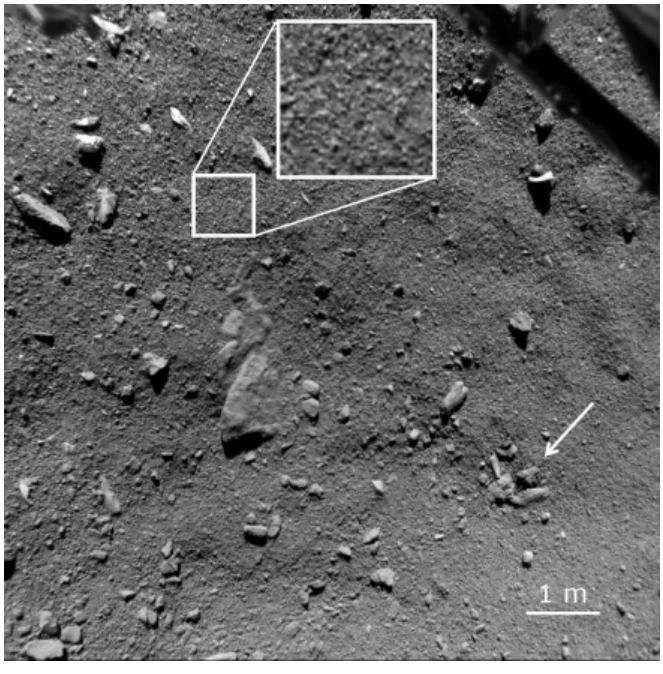

Fig. 2. Last image of the NFS acquired a few seconds before touchdown from an altitude of 9 m. The inset represents an enlarged view of the surface, illustrating the granular nature of the surface at the maximum resolution of 0.95 cm/pixel. The arrow shows a cluster of blocks.

Two qualitatively different types of terrains are readily recognizable in the ROLIS fields (Fig. 1 and fig. S2). The first one appears rougher, being characterized by a coarse regolith layer. The second terrain appears smoother on the scales imaged by ROLIS and shows a smaller frequency of decimeter-sized blocks. We have determined the frequency-size distributions of the blocks and particles for the smooth and rough regions and presented them in Fig. 3 in an incremental representation (*7*) and in fig. S3 in a cumulative representation. Although we could detect individual grains down to a (circle-equivalent) diameter of 1 cm (due to the combined effect of shape and shadow), we included in the analysis only particles larger than 4 cm, for which we could confidently achieve counting completeness. The distribution of the blocks in the smooth region (Fig. 3) follows quite closely an incremental power-law distribution with an exponent of -2.8 ± 0.2. An extrapolation of this trend to smaller sizes would imply saturation with a dense packing of particles at a size of 0.4 mm. In the rough terrain, on the other hand, two regimes are present: Sizes larger than approximately 40 cm have a steeper distribution slope, with an index of -3.5 ± 0.3, whereas particles smaller than 40 cm have a shallower slope of -2.2 ± 0.1. Furthermore, the absolute density of blocks for the rough region in the approximate size range from 6 to 60 cm is about 4 times as large as in the smooth region. This confirms the visual impression of the rough region showing an excess of blocks in the intermediate size range. The presence of domains with different size distributions suggests the existence of mechanisms for particle size evolution, sorting, and/or transport.

A few locations in the coarse terrain show outcrops from what appears to be an underlying layer (Fig. 1 and fig. S2). Assuming that this layer extends throughout the imaged field, based on the DTM we infer a regolith thickness ranging from 0 to 50 cm for the coarse terrain and from 1 to 2 m for the smooth terrain.

The smooth region is part of one of a few formations visible on orbital imagery (fig. S4) by the Optical, Spectroscopic, and Infrared Remote Imaging System (OSIRIS) camera (*8*) which are interpreted by Thomas *et al.* (*9*) to be mantling deposits due to particles falling back on the comet surface on ballistic trajectories. This phenomenon is referred to as "airfall" by the authors. Thomas *et al.* propose the Hapi region located in the comet's "neck" as a possible source for the mantling deposits, although other sources are possible. It is interesting to note that Rosetta's

OSIRIS camera has detected single grains with a size up to 17 mm on outbound trajectories (*10*) on images taken when the comet was at a heliocentric distance of 3.6 astronomical units. It is therefore conceivable that part of the outbound particle flux, on the low end of the velocity distribution, could contribute to particle airfall. Rotundi *et al.* (*10*) have also determined an approximate differential size distribution slope of –4 (corresponding to an incremental slope of –3) for the largest particles. This result is in agreement with our determination for the smooth terrains and may hint at a common origin of the observed particles.

The observed deposits are morphologically similar to aeolian bedforms on Mars (*11*) and are characterized by ridges roughly aligned along the south-north direction (fig. S4). Furthermore, spatially organized pitlike depressions with typical diameters on the order of a few meters are associated with the bedform-like structures (Fig. 1 and figs. S2 and S4), especially in the locations where the deposits appear thicker. The pits have circular or semiconical shapes and present a preferential orientation. The nature of the pits is not clear. They could be the expression of collapsed subsurface volatile-rich pockets due to sublimation. Alternatively, the pitlike depressions could arise as a consequence of regolith mobilization processes.

The largest boulder present in the ROLIS field is located in the smooth terrain (fig. S2). Associated with the boulder is a triangular-shaped apron of fine debris with a tapered morphology (Fig. 4). Opposite the debris apron is a depression that partly surrounds the boulder. These features are reminiscent of the wind tails and associated moats observed on Earth and on Mars (*12*), which are the result of functional interaction of aeolian erosion and deposition (*13*). We have identified more wind tail–like structures in the vicinities of the landing site on the OSIRIS context image (fig. S4), for a total of 17, extending over a region approximately 300 m in diameter. The wind tails show lengths ranging from 5 to 30 m and have maximum heights of approximately one-third of the height of the boulder associated with them. Also the wind tails, as the ridges, are oriented along the same general south-north direction.

OSIRIS images also indicate the presence of aeolian-like features on 67P (*9*). In conjunction with airfall deposits, these formations strongly suggest that transport and erosional processes are at work. On other planetary objects, such phenomena are associated with aeolian activity, with the wind drag providing the necessary lift to excite particle saltation. Cheng *et al.* (*14*) have shown that aeolian erosion is possible also under cometary conditions. Within their framework, gas outflow from reservoirs of subsurface sublimating ice is capable of mobilizing particles along channels connecting the reservoir to the surface. During this process, the gas flow erodes the sides of the channel. If the channel vents at the surface in the vicinity of a vertical wall, then the wall also is possibly eroded, causing wall recession. Cheng *et al.* further predicted that ventifacts such as pinnacles could be produced on comets as a consequence of aeolian erosion. The authors, however, stress that such aeolian features are to be expected at small spatial scales in the immediate vicinities of the gas outlet. As the gas expands, the pressure profile rapidly decreases, preventing erosion from occurring at large distances from the jet. It therefore appears unlikely that erosion from "cometary wind" alone could explain the presence of aeolian features that, as observed in Agilkia, have constant orientation over scale lengths of a few hundred meters (fig. S4). We therefore suggest the alternative possibility for the formation of wind tails, that particle mobilization is not initiated by a gas stream, but by "splashing"—i.e., ejection of one or more soil particles by the impact of an incoming projectile (*15*). A concomitant gas stream, although not required for the process to work, could help sustain transport, even at gas speeds much lower than the threshold friction speed (*16*). A likely source of splashing

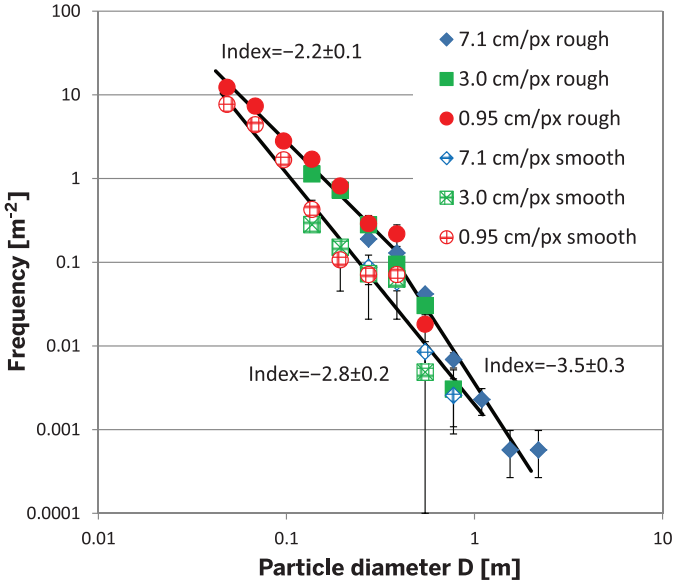

Fig. 3. Particle size distribution in the TD1 region. The graph shows the incremental size distribution of particles for the smooth and rough regions separately, derived from images 1, 5, and 7. The data are binned with a constant bin size in logarithmic scale, such that the bin limits are $D_{i+1} = D_i\sqrt{2}$. With this representation, the incremental power-law slopes have the same index as a cumulative power law (*7*).

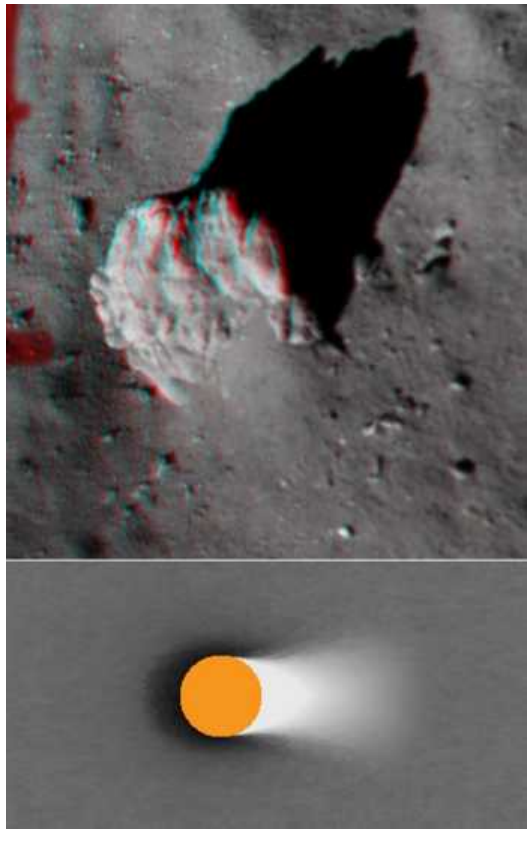

Fig. 4. Largest boulder present in the ROLIS field. (**Top**) Stereo anaglyph. Red, left eye; cyan, right eye. The orientation of the image has been rotated with respect to that in Fig. 1 for optimum stereoscopic effect. The tapered wind tail, the moat, and the "bumpy" structure of the boulder are well visible, as well as the fractures between the "knobs." (**Bottom**) Results from numerical modeling (see the supplementary materials) showing that abrasion from particles impinging from the left side of the image can produce the observed moat and wind tail–like features around an obstacle. The modeled boulder is shown in orange. Shades of gray denote the elevation; brighter shades mean higher elevation.

particles is airfall, the putative source of the mantling deposits on 67P (*9*).

In this scenario, aeolian-like features such as wind tails result from abrasion of the surface by impinging particles, except for regions that are shielded by obstacles. To test this hypothesis, we developed a simple, idealized three-dimensional cellular automaton model that, through the definition of simple rules, approximates the effects of splashing as a consequence of the impact of particles on a sandbox in the presence of an obstacle (see details in the supplementary text). The results (Fig. 4 and fig. S5) show that such a simple model can reproduce the basic morphology of the observed wind tails and moats and suggest that such structures, as observed on 67P, are of erosional nature, rather than depositional. The rough terrain observed in the ROLIS images would therefore represent a lag deposit.

REFERENCES AND NOTES

1. S. Mottola *et al*., The ROLIS experiment on the Rosetta lander. *Space Sci. Rev.* **128**, 241–255 (2007). doi: 10.1007/s11214-006-9004-2
2. J. Biele *et al*., The landing(s) of Philae and inferences about comet surface mechanical properties. *Science* **349**, aaa9816 (2015).
3. S. K. Ghosh, *Fundamentals of Computational Photogrammetry* (Concept Publishing Company, New Delhi, 2005.
4. D. J. Scheeres, C. M. Hartzell, P. Sánchez, M. Swift, Scaling forces to asteroid surfaces: The role of cohesion. *Icarus* **210**, 968–984 (2010). doi: 10.1016/j.icarus.2010.07.009
5. The solar phase angle shows a corner-to-corner variation of about 60° over the NFS fields imaged by ROLIS.
6. J. B. Adams, A. L. Filice, Spectral reflectance 0.4 to 2.0 microns of silicate rock powders. *J. Geophys. Res.* **72**, 5705–5715 (1967). doi: 10.1029/JZ072i022p05705
7. W. K. Hartmann, Terrestrial, lunar, and interplanetary rock fragmentation. *Icarus* **10**, 201–213 (1969). doi: 10.1016/0019-1035(69)90022-0
8. H. U. Keller *et al*., OSIRIS: The scientific camera system onboard Rosetta. *Space Sci. Rev.* **128**, 433–506 (2007). doi: 10.1007/s11214-006-9128-4
9. N. Thomas *et al*., The morphological diversity of comet 67P/Churyumov-Gerasimenko. *Science* **347**, aaa0440 (2015). doi: 10.1126/science.aaa0440; pmid: 25613893
10. A. Rotundi *et al*., Dust measurements in the coma of comet 67P/Churyumov-Gerasimenko inbound to the Sun. *Science* **347**, aaa3905 (2015). doi: 10.1126/science.aaa3905; pmid: 25613898
11. R. Greeley *et al*., Gusev crater: Wind-related features and processes observed by the Mars Exploration Rover Spirit. *J. Geophys. Res.* **111**, E02S09 (2006). doi: 10.1029/2005JE002491
12. R. Greeley, N. T. Bridges, R. O. Kuzmin, J. E. Laity, Terrestrial analogs to wind-related features at the Viking and Pathfinder landing sites on Mars. *J. Geophys. Res.* **107** (E1), E001481 (2002). doi: 10.1029/2000JE001481
13. R. Greeley *et al*., Columbia Hills, Mars: Aeolian features seen from the ground and orbit. *J. Geophys. Res.* **113**, E06S06 (2008). doi: 10.1029/2007JE002971
14. A. F. Cheng, C. M. Lisse, M. A'Hearn, Surface geomorphology of Jupiter Family Comets: A geologic process perspective. *Icarus* **222**, 808–817 (2013). doi: 10.1016/j.icarus.2012.10.004
15. J. F. Kok, E. J. R. Parteli, T. I. Michaels, D. B. Karam, The physics of wind-blown sand and dust. *Rep. Prog. Phys.* **75**, 106901 (2012). doi: 10.1088/0034-4885/75/10/106901; pmid: 22982806
16. J. F. Kok, Difference in the wind speeds required for initiation versus continuation of sand transport on mars: Implications for dunes and dust storms. *Phys. Rev. Lett.* **104**, 074502 (2010). doi: 10.1103/PhysRevLett.104.074502; pmid: 20366891

ACKNOWLEDGMENTS

ROLIS was funded, built, and managed by the DLR, German Aerospace Center, which we gratefully acknowledge. The ROLIS Team is indebted to the Lander Control Center (LCC, Cologne), CNES's Science, Operation, and Navigation Center (SONC) and the European Space Agency (ESA) for their support during the operations. The authors thank W. Bresch for his continued support during the development and operations of the experiment. The ROLIS calibrated data will be available through the ESA's Planetary Science Archive website (www.rssd.esa.int/index.php?project=PSA&page=index). This paper is dedicated to the memory of Gerhard Neukum.

SUPPLEMENTARY MATERIALS

www.sciencemag.org/content/349/6247/aab0232/suppl/DC1
Supplementary Text
Figs. S1 to S5
Table S1

2 March 2015; accepted 17 June 2015
10.1126/science.aab0232

COMETARY SCIENCE

67P/Churyumov-Gerasimenko surface properties as derived from CIVA panoramic images

J.-P. Bibring,[1]* Y. Langevin,[1] J. Carter,[1] P. Eng,[1] B. Gondet,[1] L. Jorda,[2] S. Le Mouélic,[3] S. Mottola,[4] C. Pilorget,[1] F. Poulet,[1] M. Vincendon[1]

The structure and composition of cometary constituents, down to their microscopic scale, are critical witnesses of the processes and ingredients that drove the formation and evolution of planetary bodies toward their present diversity. On board Rosetta's lander Philae, the Comet Infrared and Visible Analyser (CIVA) experiment took a series of images to characterize the surface materials surrounding the lander on comet 67P/Churyumov-Gerasimenko. Images were collected twice: just after touchdown, and after Philae finally came to rest, where it acquired a full panorama. These images reveal a fractured surface with complex structure and a variety of grain scales and albedos, possibly constituting pristine cometary material.

Cometary nuclei preserve the initial conditions of the evolution of the solar system and of its resulting planets, satellites, and small bodies. Although their distribution has been modified by gravitational effects over solar system history, comets have likely never undergone global thermal resets, thus maintaining their original volatiles and icy contents up to now.

Part of these initial conditions is recorded in the microscopic and macroscopic properties of the surface of the nucleus: size and shape of individual grains and matrix components, from micrometer- to meter-sized crustal features and boulders, and molecular and mineralogical composition of their constituent materials. The combination of OSIRIS (Optical, Spectroscopic, and Infrared Remote Imaging System) remote imaging and in situ imaging performed by CIVA (Comet Infrared and Visible Analyser) and ROLIS (Rosetta Lander Imaging System) (*1*) on board Philae offers an unprecedented potential for deciphering these properties on comet 67P/Churyumov-Gerasimenko (67P).

Here, we focus on the set of CIVA-P (CIVA-Panorama) images acquired in situ. CIVA-P is a set of seven identical miniaturized microcameras (*2*), implemented as five single cameras and one stereoscopic pair of two coaligned cameras with their optical axes separated by 10 cm; CIVA-P acquires a ~360° panoramic field of view (FOV) by six adjacent FOVs of 60° each (figs. S1 and S2). The angular sampling of CIVA-P is ~1.02 mrad, which corresponds to ~1 mm at 1 m, the distance of the landing feet, and up to a few centimeters at the local horizon. The spectral response of each broadband camera, integrating the properties of both the detector and the optics, extends from 400 to 1100 nm. CIVA shares a common Imaging Main Electronics (IME) with ROLIS.

The sequence of operations was loaded in the Philae on-board Command and Data Management System to be run automatedly during descent, landing, and just after touchdown. It included a CIVA-P panorama to be performed ~5 min after touchdown. The first image, received from camera 6 (fig. S3), indicated unambiguously that Philae was not at rest when it was acquired, at 15:38:52 UT on 12 November, less than 5 min after the nominal touchdown (15.34.06 UT on-board time). Coupled to other measurements [from MUPUS (Multipurpose Sensors for Surface and Sub-Surface Science), ROMAP (Rosetta Magnetometer and Plasma Monitor), and the solar panels], it confirmed that Philae had bounced; the lander eventually came to rest ~2 hours later.

A new set of commands was then uploaded so as to obtain a subsequent CIVA-P panorama, to be run during the next visibility window between the Orbiter and the Lander. The goal was to confirm that Philae had indeed landed and to characterize its environment and attitude, in order to enable reshuffling and adapting, accordingly, the First Science Sequence (FSS), for which the available energy was expected to support up to another ~50 hours of scientific operations. The upload was successful, and this second CIVA-P panorama was performed on 13 November, at 06:13:46 UT on-board time.

All seven images were nominally acquired, compressed on board as planned (at a rate of 1.5 bits/pixel), transmitted, and received, with no error. After decompression, they were processed by the CIVA team and at CNES's Science, Operation, and Navigation Center (SONC): Images were bias-subtracted, corrected for optical distortion, linearity, readout smear, and flat-fielded.

The image acquired by camera 1 (fig. S4) exhibits the +Y Philae foot (see fig. S2), largely sunlit, with the brightest parts near saturation [820 analog-to-digital units (ADU)]. No illuminated cometary surface is seen in contact, indicating that Philae is likely not resting on this foot, as would be the nominal configuration. Essentially no features can be identified at first sight in the background. However, thanks to the very high dynamic range of CIVA-P microcameras, combined with the very low electronic noise (0.4 ADU), it was possible to substantially stretch the signal, which covers the dynamical range 0 to 8 ADU (Fig. 1). A large fractured

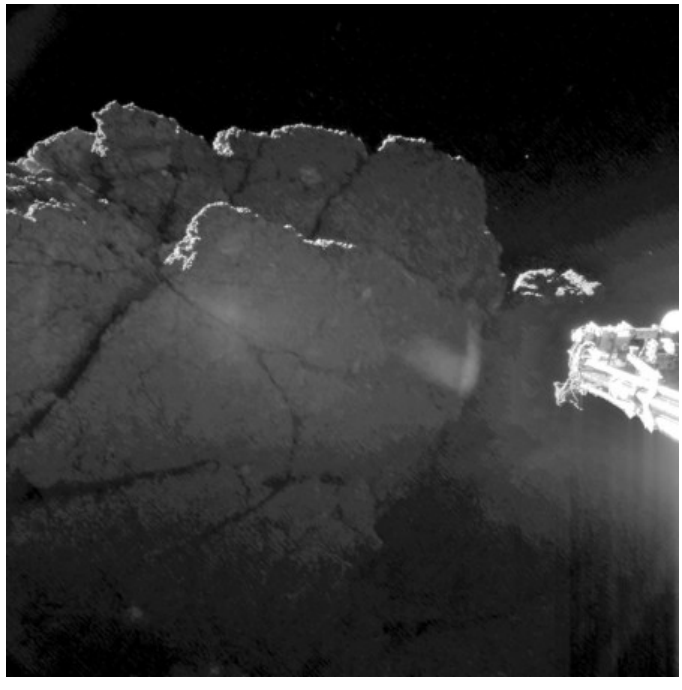

Fig. 1. Image acquired by camera 1. The dynamics have been highly stretched and custom flat-fielding has been applied, so as to exhibit the backlit fractured cliff, shadowing part of the lander. The image is further processed to mitigate detector electronic noise and low dynamics quantification error. The +Y foot is well illuminated and partly reflects on the shadowed surface facing Philae (see also fig. S5).

[1]Institut d'Astrophysique Spatiale (IAS), CNRS/Université Paris Sud, Orsay, France. [2]Laboratoire d'Astrophysique de Marseille (LAM), UMR7326,CNRS/INSU/Université Aix-Marseille, France. [3]Laboratoire Planétologie et Géodynamique, CNRS UMR6112 and Université de Nantes, Nantes, France. [4]Deutschen Zentrum für Luft und Raumfahrt (DLR), Institute of Planetary Research, Berlin, Germany.
*Corresponding author. E-mail: bibring@ias.u-psud.fr

boulder can then be observed, backlit: The shadowed part of the boulder is weakly illuminated by sunlight likely reflected by the lander itself (fig. S5).

The image acquired by camera 2 (fig. S6) indicates that this camera is exposed to open sky, with direct sunlight illumination of the front lens (glare). The only structure visible on this image is one of the two CONSERT (Comet Nucleus Sounding Experiment by Radiowave Transmission) antennas, which seems nominally deployed. The image acquired by camera 3 (fig. S7) displays a scene that would be expected for a landing in nominal configuration, with one Philae foot (later identified as the +X foot; see fig. S2) most likely in contact with the nucleus surface (red circle).

The image acquired by camera 4 (fig. S8) also exhibits a scene that would be expected for a successful landing on the nucleus, with good sunlight illumination conditions. The other CONSERT antenna is visible (red circle), in contact with the surface. The images acquired by cameras 3 and 4 have been mosaicked (fig. S9) to show the sunlit part of the nucleus surrounding Philae at the time the images were acquired. The dimensions of the CONSERT antenna (5 mm in diameter, 693 mm long), apparently in contact with the nucleus, enable us to estimate the distance of this cometary material, and the scale of the structures that we identify.

In contrast with the images acquired by cameras 3 and 4, the image acquired by the camera 5 (fig. S10) covers a part of the surface that is entirely in shadow, with a dynamic range limited to 7 ADU only. The –Y foot (fig. S2) is identified on the lower right of the image. The stereo cameras 6 and 7 also face an entirely shadowed part of the local cometary environment (fig. S11), with a dynamic limited to 5 ADU.

The attitude of Philae at the landing site can be in part reconstructed from the CIVA-P images, given the location and geometry of the relevant cameras. Indeed, Philae legs and feet, as well as the CONSERT antennas, can be identified on specific images, the close-ups of which exhibit, through shadows, the direction of illumination. Philae was far from the near-"horizontal" three-legs-resting that was targeted and assumed for the sequence of scientific operations. Philae seems to rest in a hole about its own size, partially shadowed by nearby boulders or cliffs, with the –Y foot pointing downward (most likely stuck in a local cavity), the +X foot resting on the Sun-lighted surface and the +Y foot pointing upward. The landing site is dominated by meter-scale blocks, with a large elongated cliff, starting ~1 m away. These large structures are responsible for Philae being partially shadowed at the time of the FSS, drastically limiting its energy intake for both warming up the internal compartment and supplying the solar panels.

Despite the very low signal level, the three-dimensional (3D) reconstruction of the pair of stereo images illustrates the nucleus topography facing the Philae balcony (figs. S12 to S15). A large fraction of the FOV is at distances close to 1 m (Fig. 2, zone 1). However, distant regions, as far as ~7 m, are observed in other parts of the images (Fig. 2, zone 3). They likely correspond to the continuation of the backlit cliff observed with camera 1 (Fig. 1). The pebbles, blocks, and cliffs observed by CIVA-P at centimeter-to-meter scale can be linked to the rugged terrain and boulders observed by OSIRIS (*3*) at a 20-cm to 20-m scale in the rougher regions of the nucleus.

The surface material imaged by CIVA-P in the immediate vicinity of Philae exhibits a diversity of structures and brightnesses, with two end-members (Fig. 3A). The first are agglomerates of dark granular material, with grain size in the millimeter-to-centimeter range, as evaluated with reference to the diameter (5 mm) of the CONSERT antenna, imaged by camera 4. Several pebble-like grains seem loosely attached to the surface, possibly resulting from a redeposition process. This material, by its texture, looks similar to the "regolith-type" material identified by the ROLIS descent images of the nominal landing site where touchdown took place (*1*); however, this rough morphology could correspond to consolidated terrains rather than dust-covered smooth terrains as revealed by OSIRIS (*4*). Representing the

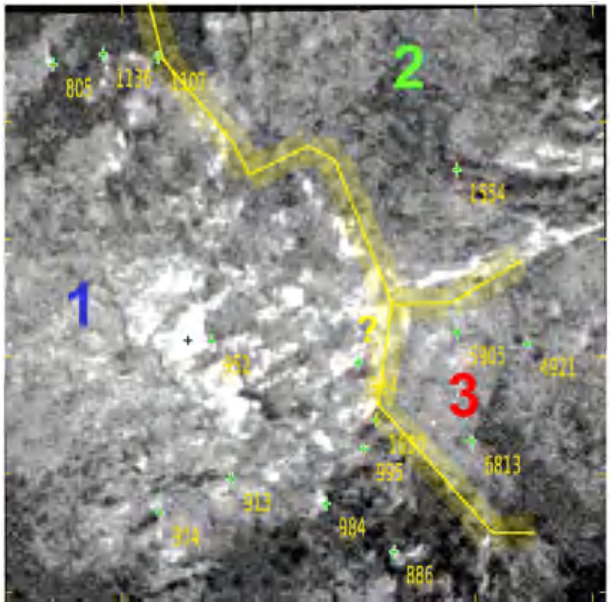

Fig. 2. Three-dimensional reconstruction of the stereo pair. The numbers (yellow) indicate the distance (in millimeters) of the points marked by green crosses. With Philae on its side, the right side of the image (where the most distant regions are observed) is facing up.

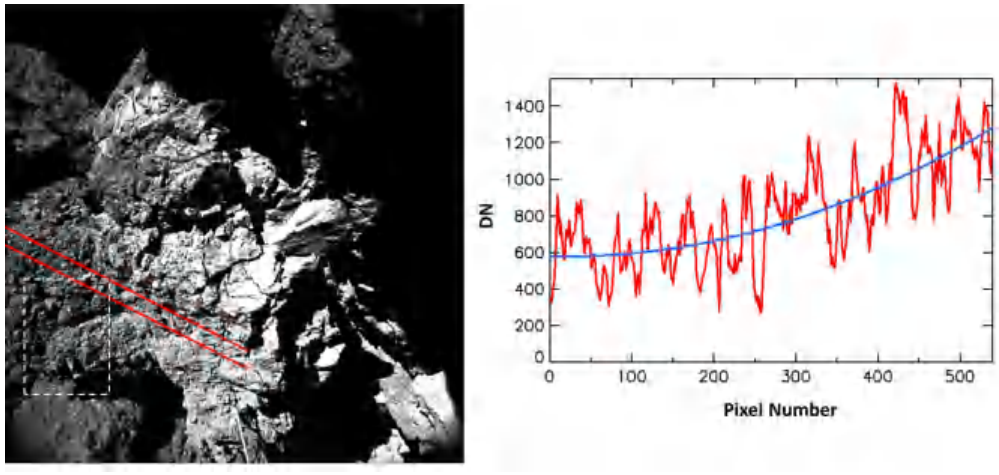

Fig. 3. Surface reflectance. Left: profile (red) along which the signal intensity has been measured on the image corrected for flat-field. Right: signal intensity (in ADU) along the profile and polynomial adjustment (blue). The CONSERT antenna reflectance is ~1200.

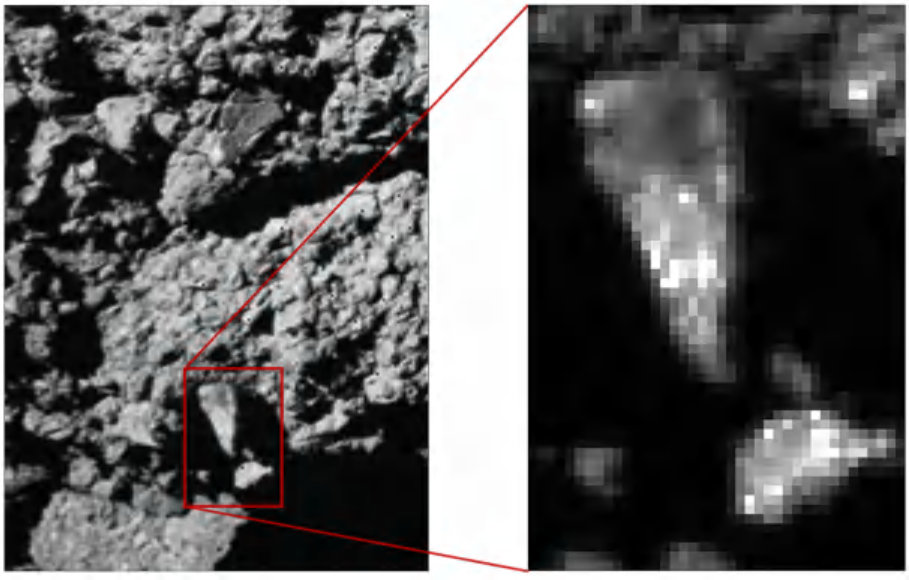

Fig. 4. Enlargement of the white rectangular zone in Fig. 3 (left). The image exhibits reflectance variations at centimeter down to millimeter scale.

second end-member are brighter grains and decametric-scale areas with smoother texture, imaged as saturated pixels on CIVA-P charge-coupled devices.

To obtain a quantitative evaluation of the reflectance of this surface material (Figs. 3 and 4), we used the CONSERT antenna, imaged by camera 4 as a reference, after having performed laboratory imaging of a spare model of the flight antenna using an identical microcamera, from the spare CIVA set. The antenna reflectance varies from 4.5 to 5.9%, for phase angles varying from 50° to 20° (fig. S9). Using the reference to the CONSERT antenna, the absolute reflectance of the nucleus material along the profile varies typically from 3 to 5%. It is in agreement with the OSIRIS and VIRTIS measurements (*3*, *5*), with the illumination geometry accounting for at least part of the variation. The similarity of the reflectance of this material, and of that of the soil mobilized by the touchdown and analyzed by PTOLEMY (*6*) and COSAC (*7*) while bouncing, would indicate its being dominated by carbon-rich species, agglomerated into grains, possibly constituting pristine accreted material.

In contrast to the low-albedo materials that dominate the granular agglomerates, a few brighter spots, as well as larger blocks (mid to bottom right of Fig. 3, left), appear saturated, corresponding to a reflectance of 10% or higher. They could either be mineral grains, with intrinsic reflectance >10%, facets observed with a geometry favoring specular reflection, or icy-rich phases; indeed, fractures, mostly linear, observed both in Fig. 3 (left) and on the cliff (Fig. 1 and fig. S5), are interpreted as resulting from thermal stress driven by the comet trajectory around the Sun. Fractures and cracks are ubiquitous at both grain scale and block scale; they are likely responsible for the fragmentation and the erosion of the nucleus surface.

CIVA-P extends, at a subcentimeter scale, structures observed in the 10-cm to 10-m scale both from the Orbiter (OSIRIS) and the ROLIS descent camera (*3*). CIVA-P indicates that, when observing the nucleus material at a subcentimeter scale, large heterogeneities also appear in texture and/or albedo. Although it is not possible, at this point, to correlate these inhomogeneities with compositional variations, Philae's landing site exhibits a variety of materials translating the cometary diversity and likely preserving their pristine properties.

REFERENCES AND NOTES

1. S. Mottola *et al*., The structure of the regolith on 67P/Churyumov-Gerasimenko from ROLIS descent imaging. *Science* **349**, aab0232 (2015).
2. J.-P. Bibring *et al*., CIVA. *Space Sci. Rev.* **128**, 397–412 (2007). doi: 10.1007/s11214-006-9135-5
3. H. Sierks *et al*., On the nucleus structure and activity of comet 67P/Churyumov-Gerasimenko. *Science* **347**, aaa1044 (2015). doi: 10.1126/science.aaa1044; pmid: 25613897
4. N. Thomas *et al*., The morphological diversity of comet 67P/Churyumov-Gerasimenko. *Science* **347**, aaa0440 (2015). doi: 10.1126/science.aaa0440
5. F. Capaccioni *et al*., The organic-rich surface of comet 67P/Churyumov-Gerasimenko as seen by VIRTIS/Rosetta. *Science* **347**, aaa0628 (2015). doi: 10.1126/science.aaa0628
6. I. P. Wright *et al*., CHO-bearing organic compounds at the surface of 67P/Churyumov-Gerasimenko revealed by Ptolemy. *Science* **349**, aab0673 (2015).
7. F. Goesmann *et al*., Organic compounds on comet 67P/Churyumov-Gerasimenko revealed by COSAC mass spectrometry. *Science* **349**, aab0689 (2015).

ACKNOWLEDGMENTS

The CIVA team extends their deepest thanks to all those at the European Space Agency (ESA), Max Planck Gesellschaft, Centre National d'Etudes Spatiales (CNES), DLR, Agenzia Spatiale Italiana, and Központi Fizikai Kutatólntézet, who made this Philae venture possible. The CIVA set of instruments has been developed, and the acquired data have been processed, with full CNES support, gratefully acknowledged here. CIVA was developed at IAS, Orsay, in close cooperation with the LAM at Marseille and the ROLIS team in Berlin, first under the direction of A. Soufflot, then of M. Berthé. We wish to convey our deep recognition to their outstanding achievement. We thank N. Aragó Higueras, T. Germa, and E. Rémétéan for the 3D reconstruction in Fig. 2 and P. Puget for providing the antenna spare used in fig. S9. All CIVA-P data are available on the ESA's Planetary Science Archive website (www.rssd.esa.int/index.php?project=PSA&page=index).

SUPPLEMENTARY MATERIALS

www.sciencemag.org/content/349/6247/aab0671/suppl/DC1
Figs. S1 to S15

6 March 2015; accepted 22 June 2015
10.1126/science.aab0671

COMETARY SCIENCE

CHO-bearing organic compounds at the surface of 67P/Churyumov-Gerasimenko revealed by Ptolemy

I. P. Wright,[1]* S. Sheridan,[1] S. J. Barber,[1] G. H. Morgan,[1] D. J. Andrews,[1] A. D. Morse[1]

The surface and subsurface of comets preserve material from the formation of the solar system. The properties of cometary material thus provide insight into the physical and chemical conditions during their formation. We present mass spectra taken by the Ptolemy instrument 20 minutes after the initial touchdown of the Philae lander on the surface of comet 67P/Churyumov-Gerasimenko. Regular mass distributions indicate the presence of a sequence of compounds with additional -CH_2- and -O- groups (mass/charge ratios 14 and 16, respectively). Similarities with the detected coma species of comet Halley suggest the presence of a radiation-induced polymer at the surface. Ptolemy measurements also indicate an apparent absence of aromatic compounds such as benzene, a lack of sulfur-bearing species, and very low concentrations of nitrogenous material.

The Philae lander contacted the surface of comet 67P/Churyumov-Gerasimenko (67P) at 15:34:04 UTC, but it failed to anchor itself to the surface as planned (*1*) and instead "bounced," eventually coming to land at the site now known as Abydos. This bouncing may have occurred because of the presence of a surface layer of loosely consolidated "dust" overlying a relatively hard interior composed of sintered ice (*2*). Philae is equipped with a drilling system (*3*) capable of procuring samples from the surface and to depths of at least 20 cm. The Ptolemy instrument (*4*) is designed to accept these solid samples and measure stable isotope ratios of elements such as hydrogen, carbon, nitrogen, and oxygen. Additionally, the instrument can operate in a compositional analytical mode and can use its mass spectrometer to measure volatiles. As part of the First Science Sequence of Philae, the instrument was preprogrammed to perform analyses in "sniff mode" ~20 min after touchdown.

The Ptolemy instrument is located inside Philae and connected to space via a vent pipe, the exhaust for which is located on the top of the lander. Ptolemy was switched on 9 min after the touchdown signal, and (after executing sequences for initialization and confirmation that the oven tapping station was undocked) it began collecting mass spectra in sniff mode some 11 min later. The ion trap mass spectrometer (supplementary materials) collected a total of six mass spectra at 14-s intervals, each with an ionization time of 0.2 s. Two types of spectra, similar to those used for the Lutetia flyby (*5*) and for operations while in orbit, were acquired alternately. The first had a mass range of mass/charge ratio (*m/z*) 13 to 89; the second had a mass range of *m/z* 25 to 136. Based on a number of similar sniff-mode measurements taken during post-hibernation commissioning and at various distances from the comet, the mass spectra collected after the initial touchdown on 67P (Fig. 1) appear to be of cometary origin. Background observations, made in orbit at distances farther than 30 km from the comet while still attached to the spacecraft, typically had ion counts of 30, 2, and 4 for H_2O, CO, and CO_2, respectively. These ion counts are significantly lower than the measurements made at Agilkia and are similar to background measurements made during the Lutetia flyby (*5*). Instrumental biases can affect the relative sensitivities of different species and masses, but they do not affect the overall pattern of the mass spectra.

In our data, we expected to see the main components of the coma, namely, H_2O, CO, and CO_2 (*m/z* 18, 28, and 44, respectively). The most abundant peak arose from H_2O, which occurred at *m/z* 19 because of protonation (i.e., H_3O^+; see the supplementary materials), with an accompanying cracking pattern at *m/z* 18, 17, and 16 from H_2O^+, OH^+, and O^+, respectively. The ions ascribed to H_2O only constitute about 30% of the total number of ions in the mass spectra. The signal at *m/z* 45 represents a combination of protonated CO_2 and organics. Based on sniff-mode measurements made after the lander came to rest and on data from ROSINA (the Rosetta Orbiter Spectrometer for Ion and Neutral Analysis) (*6*), the estimated H_2O/CO_2 ratio of about 5:1 indicates that 60% of the signal at *m/z* 45 is from CO_2. Finally, the ion count at *m/z* 29 reflects a combination of signals due to the presence of CO and N_2 organics and the cracking of CO_2. The low *m/z* 14 signal indicates that N_2 is not in high abundance, which is in agreement with the average N_2/CO ratio of 5.7×10^{-3} obtained by ROSINA (*7*). Assuming that the CO_2 contribution to *m/z* 29 is 10% of the CO_2 peak at *m/z* 45 (*8*), the remaining spectra reflect the amount of CO and organics present. In this way, we put an upper limit of 2:1 on the CO_2/CO ratio. Taken together, the ratio of $H_2O/CO_2/CO$ is on the order of 10:2:>1.

In these mass spectra, some peaks (compounds) are notable by their absence (i.e., the compounds were below detection limits). For instance, there is no evidence for any sulfur-bearing components (neither H_2S nor SO_2 signals were present). There was no significant signal at *m/z* 78 (benzene, $C_6H_6^+$), suggesting that aromatic compounds are not present in large concentrations. The very small peak at *m/z* 14 constrains the presence of nitrogen-bearing compounds to very low levels. We believe that the peak at *m/z* 15 is from CH_3^+

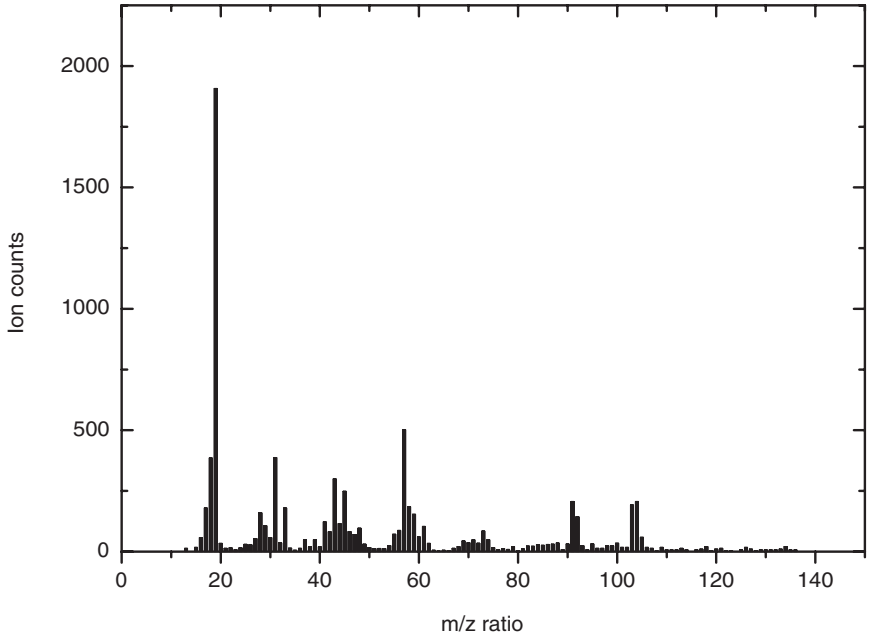

Fig. 1. Mass spectra taken by Ptolemy in sniff mode. The first combined mass spectra taken 20 min after the initial touchdown event.

[1]Department of Physical Sciences, The Open University, Walton Hall, Milton Keynes MK7 6AA, UK.
*Corresponding author. E-mail: ian.wright@open.ac.uk

rather than from NH^+. Unambiguous detection of NH_3 was not possible because of the presence of H_2O and other potential compounds, such as CH_4. Clear detection of NH_3 would require a concentration of >10% relative to that of H_2O.

Almost all of the species present had *m/z* ratios <105 (ions of higher mass were detected, but the signals were very low, making it difficult to be confident of their exact nature) (Fig. 1). Therefore, it appears that relatively low-mass compounds and fragments dominated the sample. Ptolemy only operates over a range of *m/z* 13 to 136, meaning that heavier compounds may have been present. However, were such compounds present, it would have been reasonable to expect some peaks from cracking in the range of *m/z* 105 to 136. An alternative explanation for the absence of peaks in this range is that high-molecular-weight components were present but did not reach the mass spectrometer ionization source. Greater insight into the nature of higher–molecular-weight compounds may come from the Cometary Sampling and Composition experiment (COSAC) if it is able to analyze a drilled sample (*9*). For the COSAC measurements that were made at Agilkia (*10*), the conditions of analysis were similar to those of Ptolemy's sniff mode. There are similarities in the mass spectra of the two instruments but also some intriguing differences (*10*).

In a process guided by the pattern of peaks observed by the PICCA (Positive Ion Cluster Composition Analyzer) instrument (*11*), which identified polyoxymethylene in mass spectral measurements of coma materials from comet Halley during the Giotto mission (*12*), we superimposed mass increments of 14 and 16 (representing additions and losses of $-CH_2-$ and $-O_2-$, respectively) on the mass spectra, with peaks ascribed to H_2O and CO_2 removed (Fig. 2). The data presented here do not reflect a single idealized compound polymer [e.g., $(CH_2O)_n$] with its ends terminated by H atoms. Rather, they indicate a number of different terminations, with the chain running as either $-O-CH_2-$ or $-CH_2-O-$ (i.e., repeating units of 16:14 or 14:16 *m/z*) (Fig. 3). In principle, such terminations result from H-, HCO-, or CH_3CO-, which can be thought of as radicals arising from hydrogen, formaldehyde, and acetaldehyde, respectively (although it depends on exactly where in the chain one considers the termination to occur). The mass spectra are consistent with the presence of formaldehyde (peaks at *m/z* 29 to 31) and acetaldehyde (peaks at *m/z* 29, 43, and 44), although Ptolemy has insufficient mass resolution to identify these individual compounds.

An apparent regularity in the mass spectra does not necessarily confirm the presence of a polymer; rather, the spectra could represent a collection of individual compounds. In principle, a polymer might be expected to produce peaks at higher masses, but we cannot be certain that some aspect of its volatility did not prevent higher-mass fragments from entering the instrument. If the data do reflect the presence of a polymer, that does not necessarily imply the presence of polyoxymethylene (*13*, *14*). Other polymers may be possible, including an "ice tholin" (*15*). Ice tholins can form through the irradiation of mixtures of simple components such as water, methanol, carbon dioxide, and ethane, a combination of molecules similar to those present on 67P. Related experiments (*16*) indicate that acetaldehyde is not produced in ice tholins, yet it appears likely that it is one of the main termination compounds reflected by the Ptolemy data. Glycerol (glycerine, $C_3H_8O_3$) is produced in ice tholins and has a peak at *m/z* 92, which is prominent in our results (and ostensibly is not accounted for by a polyoxymethylene fit). In principle, there is no reason why polyoxymethylene could not be a component of an ice tholin, but it has been suggested (*16*) that the structure of the latter is based on a substituted polyalcohol (i.e., a material that results from direct polymerization of methanol radicals and water, as opposed to formaldehyde, which produces polyoxymethylene).

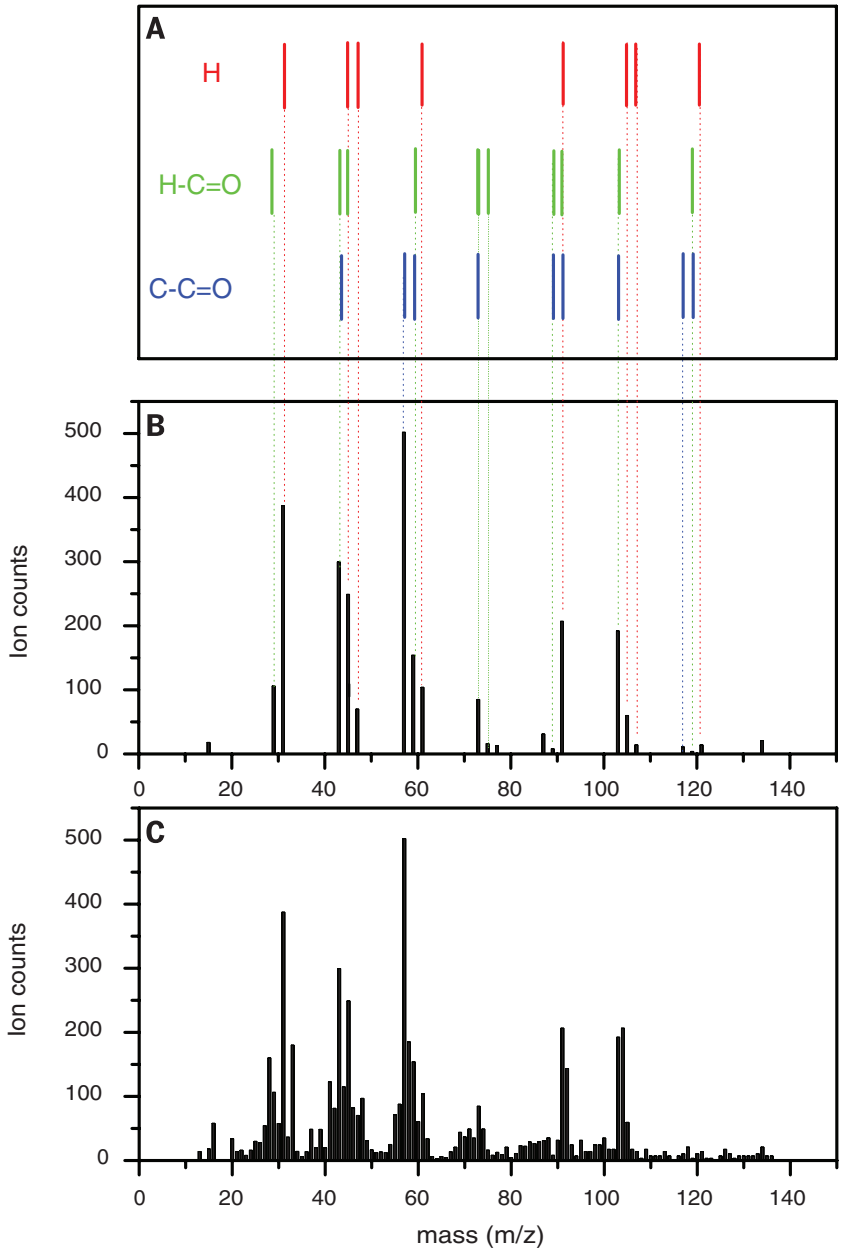

Fig. 2. Proposed polyoxymethylene fit to the Ptolemy spectra. (**A**) Schematic for proposed mass fragments of polyoxymethylene with different terminations. (**B**) Peaks that are considered to be from polyoxymethylene. (**C**) Ptolemy spectra with peaks from H_2O and CO_2 removed.

Three notable peaks in the mass spectra do not fit with an interpretation of the presence of polyoxymethylene. These occur at *m/z* 33, 41, and 37. For the peak at 33, we considered the possibility of hydroxylamine (H_2NOH). Although it has not been detected either in the interstellar medium or in cometary comae, it may be a precursor to amino acids (*17*). A cracking pattern for this molecule could fit within the mass spectra

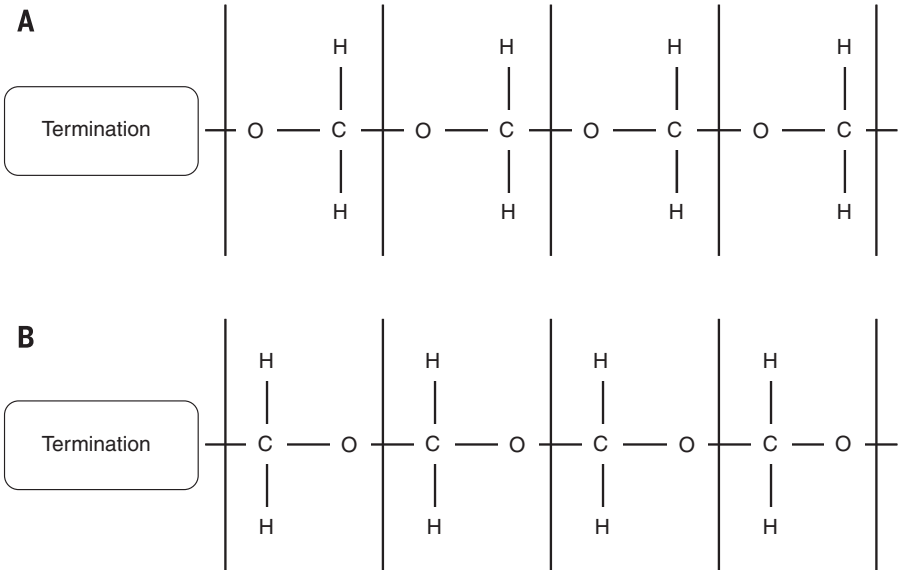

Fig. 3. Idealized polyoxymethylene chains. (**A**) Idealized polyoxymethylene chain with repeating units of 16:14 *m/z* (-O-, -CH_2-). For the mass spectra taken by Ptolemy, we considered three different types of termination: H-, HCO-, and CH_3CO-. The H- termination would produce peaks at 1, 17, 31, 47, 61, 77, 91, 107, and 121 *m/z*. For HCO-, peaks would occur at 29, 45, 59, 75, 89, 105, and 119. For CH_3CO-, peaks would occur at 43, 59, 73, 89, 103, and 119. Here, we consider only those peaks up to a mass of about 120. (**B**) The equivalent chain, but with repeating units in the reverse order [14:16 *m/z* (-CH_2-, -O-)]. In this case, the H- termination would produce peaks at 1, 15, 31, 45, 61, 75, 91, 105, and 121 *m/z*. For HCO-, peaks would occur at 29, 43, 59, 73, 89, 103, and 119. For CH_3CO-, peaks would occur at 43, 57, 73, 87, 103, and 117.

obtained by Ptolemy (the molecule has, for instance, a relatively minor peak at *m/z* 14). However, considering the apparent lack of other N-bearing species, this molecule seems implausible. We propose instead that the peak at *m/z* 33 probably indicates an oxonium ion, namely $CH_3.OH_2^+$ (analogous to the peak at *m/z* 19, which is effectively $H.OH_2^+$). The possibility of protonated methanol ($CH_3OH.H^+$) is discounted because of a lack of fit for the cracking pattern.

It is tempting to ascribe the peak at *m/z* 41 to acetonitrile or methyl isocyanide (CH_3CN), both of which have been detected in cometary comae (*18*). However, we discount this in favor of $C_3H_5^+$; that is, a fragment of a hydrocarbon (assuming that hydrocarbons are present). The peak at *m/z* 37 also has several possible explanations. If it is organic in origin, then the only possibility is C_3H^+, and therefore it could be related to the peak at *m/z* 41. However, it seems unlikely that there would be such a prominent fragment without the larger peaks expected to accompany it. On the other hand, argon readily protonates in the ion trap mass spectrometer, making $^{36}Ar.H^+$ a possibility. This would require that argon be present at an extremely high level of ~2%; we consider this unlikely because a high argon value has not been reported in ROSINA measurements. An alternative possibility is that an ion molecule reaction between neutral H_2O and $H.OH_2^+$ in the ion trap formed an ion cluster of $H_2O.H.OH_2^+$, although this identification remains speculative.

The mass spectra obtained during the first contact with the comet 67P indicate that the surface contains a complicated mixture of organics, as well as H_2O and CO_2. Many of the features of the mass spectra can be explained by the presence of polyoxymethylene, but undoubtedly many other compounds are present at low concentrations. Before the Giotto encounter with Halley, researchers had already conjectured that interstellar grains may contain polyoxymethylene (*19*). The possible presence of similar materials on a comet, as postulated by a consideration of the PICCA results, raised interest in the subject of prebiotic polymers. The most immediate scientific impact of the possible presence of polyoxymethylene was that it provided an explanation for the presence of observable formaldehyde in cometary comae—that is, at distances beyond which the molecular species, if released directly from the nucleus, would be expected to survive (*20*). However, after somewhat straightforward initial interpretations *(21)*, more detailed enquiries have uncovered issues that remain unresolved (*22*–*25*).

REFERENCES AND NOTES

1. J. Biele *et al*., The landing(s) of Philae and inferences about comet surface mechanical properties. *Science* **349**, aaa9816 (2015).
2. T. Spohn *et al*., Thermal and mechanical properties of the near-surface layers of comet 67P/Churyumov-Gerasimenko. *Science* **349**, aab0464 (2015).
3. E. Finzi *et al*., SD2 - How to sample a comet. *Space Sci. Rev.* **128**, 281–299 (2007). doi: 10.1007/s11214-006-9134-6
4. A. D. Morse *et al.*, in *Rosetta: ESA's Mission to the Origin of the Solar System*, R. Schulz, C.A. Alexander, H. Böhnhardt, K. H. Glaßmeier, Eds. (Springer-Verlag, New York, 2009), pp. 669–686.
5. D. J. Andrews *et al*., Ptolemy operations and results during the Lutetia flyby. *Planet. Space Sci.* **66**, 179–186 (2012). doi: 10.1016/j.pss.2011.09.005
6. M. Hässig *et al*., Time variability and heterogeneity in the coma of 67P/Churyumov-Gerasimenko. *Science* **348**, aaa0276 (2015). doi: 10.1126/science.aaa0276; pmid: 25613892
7. M. Rubin *et al*., Molecular nitrogen in comet 67P/Churyumov-Gerasimenko indicates a low formation temperature. *Science* **348**, 232–235 (2015). doi: 10.1126/science.aaa6100; pmid: 25791084
8. National Institute of Standards and Technology (NIST), *NIST Chemistry WebBook* (NIST Standard Reference Database Number 69, NIST, Gaithersburg, MD, 2015); http://webbook.nist.gov/chemistry/.
9. F. Goesmann *et al*., COSAC, the cometary sampling and composition experiment on Philae. *Space Sci. Rev.* **128**, 257–280 (2007). doi: 10.1007/s11214-006-9000-6
10. F. Goesmann *et al*., Organic compounds on comet 67P/Churyumov-Gerasimenko revealed by COSAC mass spectrometry. *Science* **349**, aab0689 (2015).
11. A. Korth *et al*., Mass spectra of heavy ions near comet Halley. *Nature* **321**, 335–336 (1986). doi: 10.1038/321335a0
12. R. Reinhard, The Giotto encounter with comet Halley. *Nature* **321**, 313–318 (1986). doi: 10.1038/321313a0
13. M. H. Moore, T. Tanabé, Mass spectra of sputtered polyoxymethylene: Implications for comets. *Astrophys. J.* **365**, L39–L42 (1990). doi: 10.1086/185883
14. D. L. Mitchell *et al*., Evidence for chain molecules enriched in carbon, hydrogen, and oxygen in comet Halley. *Science* **237**, 626–628 (1987). doi: 10.1126/science.237.4815.626; pmid: 17758562
15. C. Sagan, B. N. Khare, Tholins: Organic chemistry of interstellar grains and gas. *Nature* **277**, 102–107 (1979). doi: 10.1038/277102a0
16. G. D. McDonald *et al*., Production and chemical analysis of cometary ice tholins. *Icarus* **122**, 107–117 (1996). doi: 10.1006/icar.1996.0112
17. J. He, G. Vidali, J.-L. Lemaire, R. T. Garrod, Formation of hydroxylamine on dust grains via ammonia oxidation. *Astrophys. J.* **799**, 49–57 (2015). doi: 10.1088/0004-637X/799/1/49
18. M. J. Mumma, S. J. Charnley, The chemical composition of comets—Emerging taxonomies and natal heritage. *Annu. Rev. Astron. Astrophys.* **49**, 471–524 (2011). doi: 10.1146/annurev-astro-081309-130811
19. N. C. Wickramasinghe, Polyoxymethylene polymers as interstellar grains. *Mon. Not. R. Astr. Soc.* **170**, 11P–16P (1975).
20. H. Cottin, N. Fray, Distributed sources in comets. *Space Sci. Rev.* **138**, 179–197 (2008). doi: 10.1007/s11214-008-9399-z
21. W. F. Huebner, First polymer in space identified in comet Halley. *Science* **237**, 628–630 (1987). doi: 10.1126/science.237.4815.628; pmid: 17758563
22. S. N. Milam *et al*., Formaldehyde in comets C/1995 O1 (Hale-Bopp), C/2002 T7 (LINEAR) and C/2001 Q4 (NEAT): Investigating the cometary origin of H_2CO. *Astrophys. J.* **649**, 1169–1177 (2006). doi: 10.1086/506501
23. D. L. Mitchell *et al*., The origin of complex organic ions in the coma of comet Halley. *Icarus* **98**, 125–133 (1992). doi: 10.1016/0019-1035(92)90213-Q
24. W. A. Schutte, L. J. Allamandola, S. A. Sandford, An experimental study of the organic molecules produced in cometary and interstellar ice analogs by thermal formaldehyde reactions. *Icarus* **104**, 118–137 (1993). doi: 10.1006/icar.1993.1087; pmid: 11540089
25. H. Cottin, M. C. Gazeau, Y. Benilan, F. Raulin, Polyoxymethylene as parent molecule for the formaldehyde extended source in comet Halley. *Astrophys. J.* **556**, 417–420 (2001). doi: 10.1086/321579

ACKNOWLEDGMENTS

The paper is dedicated to the memory of C. Pillinger, who was the original proposer of the Ptolemy instrument. We acknowledge the interest and inputs from our colleagues involved with the Ptolemy science team. Ptolemy was developed in a collaborative venture between The Open University and RAL Space, with funding provided by the Science and Technology Facilities Council and the UK Space Agency. We acknowledge the efforts and patience of our colleagues at the Lander Control Centre and the Science Operation and Navigation Centre, as well as the lander principal scientists J.-P. Bibring and H. Böhnhardt. All Ptolemy data are available from the Planetary Science Archive of the European Space Agency and the Planetary Data System archive of NASA.

SUPPLEMENTARY MATERIALS

www.sciencemag.org/content/349/6247/aab0673/suppl/DC1
Materials and Methods

6 March 2015; accepted 30 June 2015
10.1126/science.aab0673

COMETARY SCIENCE

Organic compounds on comet 67P/Churyumov-Gerasimenko revealed by COSAC mass spectrometry

Fred Goesmann,[1]* Helmut Rosenbauer,[1] Jan Hendrik Bredehöft,[2] Michel Cabane,[3] Pascale Ehrenfreund,[4,5] Thomas Gautier,[6] Chaitanya Giri,[1,7] Harald Krüger,[1] Léna Le Roy,[8] Alexandra J. MacDermott,[9] Susan McKenna-Lawlor,[10] Uwe J. Meierhenrich,[7] Guillermo M. Muñoz Caro,[11] Francois Raulin,[12] Reinhard Roll,[1] Andrew Steele,[13] Harald Steininger,[1] Robert Sternberg,[12] Cyril Szopa,[3] Wolfram Thiemann,[2] Stephan Ulamec[14]

Comets harbor the most pristine material in our solar system in the form of ice, dust, silicates, and refractory organic material with some interstellar heritage. The evolved gas analyzer Cometary Sampling and Composition (COSAC) experiment aboard Rosetta's Philae lander was designed for in situ analysis of organic molecules on comet 67P/Churyumov-Gerasimenko. Twenty-five minutes after Philae's initial comet touchdown, the COSAC mass spectrometer took a spectrum in sniffing mode, which displayed a suite of 16 organic compounds, including many nitrogen-bearing species but no sulfur-bearing species, and four compounds—methyl isocyanate, acetone, propionaldehyde, and acetamide—that had not previously been reported in comets.

The study of the chemical composition of comets provides key information about the raw materials present in the early solar system (*1*, *2*). Ground and space-based observations have identified over 20 organic molecules in comet comae (*3*, *4*), a subset of which are of prebiotic interest (*5*, *6*).

The Cometary Sampling and Composition (COSAC) experiment on Rosetta's lander Philae was designed to detect and identify organic molecules in the material of comet 67P (*7*). It consists of a gas chromatograph (GC) and a time-of-flight mass spectrometer (TOF-MS) to analyze samples delivered by the sample drilling and distribution system (SD2). COSAC can also operate in sniffing mode, in which the MS accumulates data without active sampling by SD2. Molecules that have passively entered the instrument are ionized, accelerated, and finally registered by COSAC. MS sniffings were made several times between launch and arrival at the comet, including during a fly-by of Lutetia (*8*). MS sniffings were made on arrival at 67P from 10 km above the surface, after initial touchdown, and at the final resting site (Fig. 1).

The Philae lander first touched down on 67P on 12 November 2014 at 15:34:04 UTC and then bounced. The impact excavated about 0.4 m^3 of solid material (*9*), some of which would have entered COSAC's two exhaust pipes, which are on the bottom of the lander (*10*), and then stuck to the inside of the 2-cm-wide pipes. The temperature in these pipes was 12° to 15°C (*10*), midway between the cold cometary exterior and the heated interior of the lander, allowing volatile organics to sublime and be detected by the MS in a measurement that began at 16:00:30 UTC and ended at 16:02:50 UTC, when the lander was about 150 m above the surface on its first bounce. We focus here on this spectrum (green in Fig. 1), which differs fundamentally in the number and intensity of its peaks from the undisturbed spectra taken before and after, and represents excavated cometary material (*10*). Our approach was to find the best fit to this spectrum of a superposition of standard National Institute of Standards and Technology (NIST) mass spectra (*11*) of candidate cometary molecules. The spectral deconvolution methodology used is similar to that used in other space missions [such as the Ion and Neutral Mass Spectrometer (INMS) measurements by Cassini and the GCMS on the Huygens probe] (*12*–*14*).

Because COSAC has a mass resolution of only 300, single mass peaks cannot be resolved into different molecular species [e.g., CO, N_2, and C_2H_4, all at a mass/charge ratio (m/z) of 28, are indistinguishable]. Analysis (*10*) was limited to compounds below m/z 62 because signals beyond this value are too faint to be distinguished reliably from noise. The peak at m/z 78, for example, is not real: Several ions coincidentally ended up in a single channel, leaving neighboring ones empty (*10*). All conceivable molecules were first listed and their fragmentation patterns evaluated (table S1). Elimination of molecules with incompatible fragmentation patterns (for reasons described in table S3) led to a short-list of candidate molecules (table S2). We further reduced the short list by making the fit in order of decreasing mass,

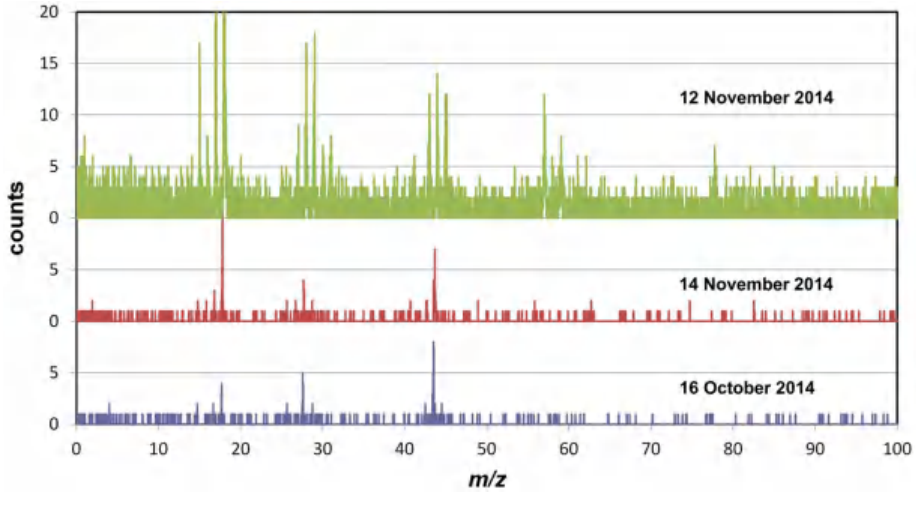

Fig. 1. Mass spectra taken by COSAC in "sniffing mode." Top (green): spectrum taken 25 min after first touchdown; the m/z 18 peak reached a height of 330 counts, but the spectrum is truncated to show smaller peaks more clearly; middle (red): final spectrum, taken 2 days later at the current Philae position; bottom (blue): first spectrum, obtained in orbit 27 days before landing, from a distance of 10 km.

[1]Max Planck Institute for Solar System Research, Justus von Liebig Weg 3, 37077 Göttingen, Germany. [2]University of Bremen, Institute for Applied and Physical Chemistry, Leobener Strasse NW2, 28359 Bremen, Germany. [3]Université Versailles St-Quentin, Sorbonne Universités, Université Pierre et Marie Curie Univ. Paris 06, Centre National de la Recherche Scientifique (CNRS)–Institut National des Sciences de l'Univers, Laboratoire Atmosphéres, Milieux, Observations Spatiales–Institut Pierre Simon Laplace (LATMOS-IPSL), 4 Place Jussieu 75005 Paris. [4]Leiden Observatory, Post Office Box 9513, 2300 RA Leiden, Netherlands. [5]Space Policy Institute, George Washington University, Washington, DC, USA. [6]Goddard Space Flight Center, Greenbelt, MD 20771, USA. [7]University Nice Sophia Antipolis, Institut de Chimie de Nice Unite Mixte de Recherche (UMR) 7272 CNRS, Avenue Valrose, 06108 Nice, France. [8]Center for Space and Habitability, University of Bern, Sidlerstrasse 5, CH-3012 Bern, Switzerland. [9]University of Houston–Clear Lake, 2700 Bay Area Boulevard, Houston, TX 77058, USA. [10]Space Technology Ireland, Ltd., Maynooth, Co. Kildare, Ireland. [11]Centro de Astrobiología, Instituto Nacional de Técnica Aeroespacial–Consejo Superior de Investigaciones Científicas, Ctra. de Ajalvir, km 4, Torrejón de Ardoz, 28850 Madrid, Spain. [12]Laboratoire Interuniversitaire des Systèmes Atmosphériques (LISA), UMR CNRS 7583, Université Paris-Est Créteil and Université Paris-Diderot, 94000 Créteil, France. [13]Geophysical Laboratory, Carnegie Institution of Washington, Washington, DC, USA. [14]German Aerospace Center, Deutsches Zentrum für Luft und Raumfahrt (DLR), 51147 Cologne, Germany.
*Corresponding author. E-mail: goesmann@mps.mpg.de

starting from m/z 59 (*10*), and eliminating unstable and unsaturated species. This yielded a good fit to all peaks (except m/z 15 and a fraction of m/z 29, Fig. 2) with 16 species from several families of molecules—alcohols, carbonyls, amines, nitriles, amides, and isocyanates—in a consistent combination (Table 1). Peaks for $m/z < 10$ were not included in the fit because they are not listed in the standard NIST mass spectra (*11*). The molecular abundances of these compounds relative to that of water (Table 1) were corrected for electron cross section (table S4). The absence of ions at m/z 32 indicates a lack of sulfur-bearing species (Fig. 2 and Table 1). Amino acids were not included in the fit because the molecular ion peaks of glycine (m/z 75) and alanine (m/z 89) are negative after background subtraction, thereby suggesting that they are noise. Although fragment peaks assigned to glycine and alanine in the NIST standard spectra (*11*) are present in the COSAC spectrum (in the m/z 30s to 40s range), any contribution to these fragment peaks from amino acids is difficult to disentangle from the contributions of other species.

The main source of error is the low signal intensity, averaging about 100 counts (table S1). A statistical square-root of n approach yields a standard deviation of 10%. In addition, the NIST standard spectra (*11*) have a 15% error. Considering formal error propagation and the uncertainties in our peak-fitting algorithm, we estimate that the abundances given in Table 1 are accurate to about a factor of 2. The fit of a mass spectrum whose peaks result from the superposition of different molecular species is intrinsically degenerate, with several possible solutions (*10*).

The absence of large quantities of NH_3, HCHO, and CO_2 in our best fit may seem surprising because they were expected to be present as components of cometary ice. NH_3 (m/z 17) was not needed for the fit, but the presence of small quantities seems likely. However, this is hard to quantify because the large H_2O peak at m/z 18 implies a substantial contribution to the m/z 17 peak from the OH fragment peak of H_2O, which is difficult to distinguish from any NH_3 contribution. HCHO (m/z 30) and CO_2 (m/z 44) are not included because m/z 30 is mainly accounted for by fragment peaks of other molecules, rather than by the molecular ion of HCHO, and m/z 44 is mainly accounted for by fragment contributions from acetamide, formamide, and acetaldehyde, rather than by CO_2.

We initially tried a fit that started with the assumption that m/z 44 came from CO_2, but no acceptable fit could be achieved to the remaining peaks. If all of m/z 44 were ascribed to CO_2, our sample would only contain 3% of CO_2 relative to water. Using the procedure described above, we found that a more sensible fit for all mass peaks, especially m/z 57, 58, and 59, could only be achieved by assuming a CO_2 concentration of less than 0.1%. The low abundance of CO_2, NH_3, and HCHO could indicate that the excavated COSAC sample came from an area depleted in volatile ice components. Observations by the Visible, Infrared and Thermal Imaging Spectrometer (VIRTIS) from the Rosetta orbiter (*15*) do suggest a dark surface depleted in volatiles, consisting mainly of refractory organic macromolecular materials, with very little ice on the surface. Studies (*16*) using the Rosetta Orbiter Spectrometer for Ion and Neutral Analysis (ROSINA) indicate that volatile ices sublime diurnally and seasonally, with CO_2 ranging from 3% relative to water in local summer (the present case) to 80% in local winter.

The COSAC findings differ from those of Ptolemy (*17*) because COSAC sampled particles excavated by the impact (*10*) that entered the warm

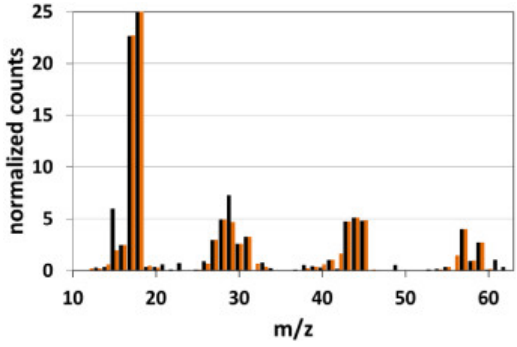

Fig. 2. The fit to the observed spectrum. Comparison of the COSAC original mass spectrum (black bars for each integer mass) and the spectrum reconstructed from the best fit (orange bars to right of original signal). The peak heights are normalized to 100 for the m/z 18 peak (which has been truncated).

Table 1. The 16 molecules used to fit the COSAC mass spectrum.

Name	Formula	Molar mass (u)	MS fraction	Relative to water
Water	**H_2O**	18	80.92	100
Methane	**CH_4**	16	0.70	0.5
Methanenitrile (hydrogen cyanide)	**HCN**	27	1.06	0.9
Carbon monoxide	**CO**	28	1.09	1.2
Methylamine	**CH_3NH_2**	31	1.19	0.6
Ethanenitrile (acetonitrile)	**CH_3CN**	41	0.55	0.3
Isocyanic acid	**HNCO**	43	0.47	0.3
Ethanal (acetaldehyde)	**CH_3CHO**	44	1.01	0.5
Methanamide (formamide)	**$HCONH_2$**	45	3.73	1.8
Ethylamine	**$C_2H_5NH_2$**	45	0.72	0.3
Isocyanomethane (methyl isocyanate)	**CH_3NCO**	57	3.13	1.3
Propanone (acetone)	**CH_3COCH_3**	58	1.02	0.3
Propanal (propionaldehyde)	**C_2H_5CHO**	58	0.44	0.1
Ethanamide (acetamide)	**CH_3CONH_2**	59	2.20	0.7
2-Hydroxyethanal (glycolaldehyde)	**CH_2OHCHO**	60	0.98	0.4
1,2-Ethanediol (ethylene glycol)	**$CH_2(OH)CH_2(OH)$**	62	0.79	0.2

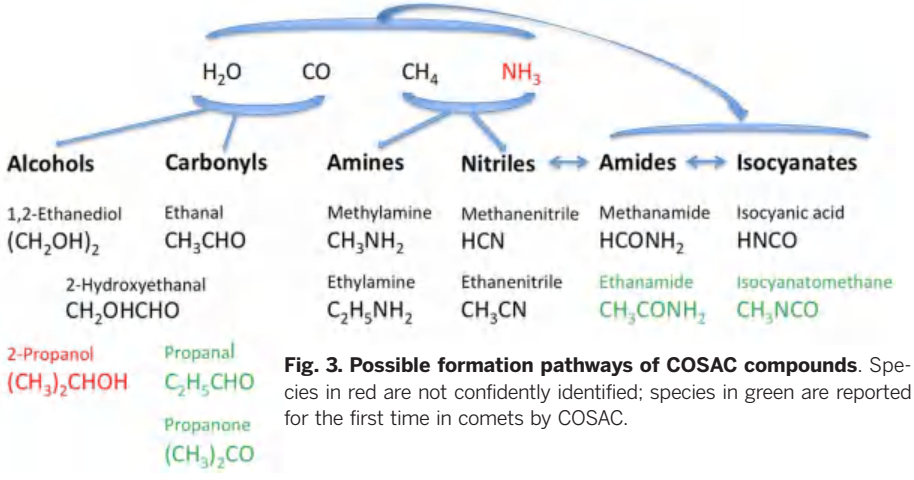

Fig. 3. Possible formation pathways of COSAC compounds. Species in red are not confidently identified; species in green are reported for the first time in comets by COSAC.

exhaust tubes located on the bottom of the lander, where they pointed toward the surface, whereas Ptolemy sampled ambient coma gases entering exhaust tubes located on top of the lander, where they pointed toward the sky (possibly with the addition of some dust that made its way around the lander). That COSAC detected far more nitrogen-bearing compounds than Ptolemy agrees with earlier observations that nitrogen was more abundant in the dust than in the gas of comet Halley (*18*). The Ptolemy team interpret their mass spectrum as fragments of polyoxymethylene polymer, with a strong CO_2 peak of intensity 20% relative to water. COSAC did not detect ambient coma gases (which were dominated in Ptolemy data by CO_2 with a few polymer fragments). The COSAC MS maintains a constant pressure; thus, subliming gases from our ground sample pushed the ambient coma gases outside the COSAC MS. Before sublimation, the total pressure inside the COSAC MS was dominated by CO_2, in line with Ptolemy data and prelanding COSAC spectra. After sublimation, the total pressure inside the COSAC MS was due to the sum of the partial pressures of all the sublimed ground materials. This can explain the missing CO_2 in the post-touchdown spectrum. The displacement of ambient coma gases by subliming ground materials and the temperature of 12° to 15°C in the COSAC exhaust tubes, which is too low to break down any refractory polymers in the ground materials, combine to explain why COSAC did not detect any polymer fragments.

The COSAC molecules form a consistent set related by plausible formation pathways (Fig. 3). A nitrogen source such as NH_3 must originally have been abundant to form the many N-bearing species, but could since have mostly evaporated or been used up in reactions. All the COSAC organics can be formed by UV irradiation and/or radiolysis of ices due to the incidence of galactic and solar cosmic rays: alcohols and carbonyls derived from CO and H_2O ices (*19*), and amines and nitriles from CH_4 and NH_3 ices (*20*). Hydrolysis of nitriles produces amides, which are linked to isocyanates by isomerization.

Several of the COSAC compounds, such as HCN, CH_3CN, and HNCO, are present in the comae of most comets (*1*). Others, such as CH_3CHO, $HCONH_2$, $CH_2(OH)CH_2(OH)$, CH_3NH_2, and $C_2H_5NH_2$, have only been found in a few comets. Four molecules reported by COSAC—CH_3NCO, CH_3COCH_3, C_2H_5CHO, and CH_3CONH_2—have not been previously reported in a cometary environment, and CH_2OHCHO has only been reported as an upper limit. These cometary molecules are all predicted by our generalized formation scheme (Fig. 3). CH_2OHCHO is an efficient initiator in the prebiotic formation of sugars (*21*). HCN is a key molecule in the prebiotic synthesis of amino acids (*21*, *22*) and nucleobases (*21*) and even offers an elegant pathway to sugars (*23*). $HCONH_2$ provides a prebiotic route to nucleobases (*24*). $HCONH_2$ (*24*) and CH_3CONH_2 (*21*) catalyze phosphorylation of nucleosides to nucleotides, in which amines also play a role (*21*). Isocyanates play a major role in the prebiotic synthesis of peptides, through the so-called isocyanate route (*22*). The complexity of cometary nucleus chemistry and the importance of N-containing organics imply that early solar system chemistry fosters the formation of prebiotic material in noticeable concentrations.

REFERENCES AND NOTES

1. M. J. Mumma, S. B. Charnley, The chemical composition of comets—emerging taxonomies and natal heritage. *Annu. Rev. Astron. Astrophys.* **49**, 471–524 (2011). doi: 10.1146/annurev-astro-081309-130811
2. J. Greenberg, *Astron. Astrophys.* **330**, 375–380 (1998).
3. J. Crovisier *et al*., The chemical diversity of comets: Synergies between space exploration and ground-based radio observations. *Earth Moon Planets* **105**, 267–272 (2009). doi: 10.1007/s11038-009-9293-z
4. M. DiSanti, M. Mumma, Reservoirs for comets: Compositional differences based on infrared observations. *Space Sciences Series* **28**, 127–145 (2008). doi: 10.1007/978-0-387-85455-7_8
5. J. Oró, T. Mills, A. Lazcano, Comets and the formation of biochemical compounds on the primitive Earth—a review. *Orig. Life Evol. Biosph.* **21**, 267–277 (1992). doi: 10.1007/BF01808302; pmid: 11537542
6. W. M. Irvine, Extraterrestrial organic matter: A review. *Orig. Life Evol. Biosph.* **28**, 365–383 (1998). doi: 10.1023/A:1006574110907; pmid: 9742722
7. F. Goesmann *et al*., Cosac, The cometary sampling and composition experiment on Philae. *Space Sci. Rev.* **128**, 257–280 (2007). doi: 10.1007/s11214-006-9000-6
8. F. Goesmann *et al*., Interpretation of COSAC mass spectrometer data acquired during Rosetta's Lutetia fly-by 10 July 2010. *Planet. Space Sci.* **66**, 187–191 (2012). doi: 10.1016/j.pss.2012.01.012
9. J. Biele *et al*., The landing(s) of Philae and inferences on comet surface mechanical properties. *Science* **349**, aaa9816 (2015).
10. Full details and methods are in the supplementary materials on *Science* Online.
11. S. E. Stein, in *NIST Chemistry WebBook*, NIST Standard Reference Database Number 69, P. J. Linstrom, W. G. Mallard, Eds. (National Institute of Standards and Technology, Gaithersburg, MD); http://webbook.nist.gov.
12. J. H. Waite Jr. *et al*., Ion neutral mass spectrometer results from the first flyby of Titan. *Science* **308**, 982–986 (2005). doi: 10.1126/science.1110652; pmid: 15890873
13. K. E. Mandt *et al*., Ion densities and composition of Titan's upper atmosphere derived from the Cassini Ion Neutral Mass Spectrometer: Analysis methods and comparison of measured ion densities to photochemical model simulations. *J. Geophys. Res. Solid Earth* **117** (E10), E10006 (2012). doi: 10.1029/2012JE004139
14. J. H. Waite Jr. *et al*., Cassini ion and neutral mass spectrometer: Enceladus plume composition and structure. *Science* **311**, 1419–1422 (2006). doi: 10.1126/science.1121290; pmid: 16527970
15. F. Capaccioni *et al*., Cometary science. The organic-rich surface of comet 67P/Churyumov-Gerasimenko as seen by VIRTIS/Rosetta. *Science* **347**, aaa0628 (2015). pmid: 25613895
16. M. Hässig *et al*., Time variability and heterogeneity in the coma of 67P/Churyumov-Gerasimenko. *Science* **347**, aaa0276 (2015). doi: 10.1126/science.aaa0276; pmid: 25613892
17. I. P. Wright *et al*., CHO-bearing organic compounds at the surface of 67PChuryumov-Gerasimenko revealed by Ptolemy. *Science* **349**, aab0673 (2015).
18. S. Wyckoff, S. C. Tegler, L. Engel, Nitrogen abundance in Comet Halley. *Astrophys. J.* **367**, 641–648 (1991). doi: 10.1086/169659
19. G. M. Muñoz Caro, E. Dartois, Prebiotic chemistry in icy grain mantles in space. An experimental and observational approach. *Chem. Soc. Rev.* **42**, 2173–2185 (2013). doi: 10.1039/c2cs35425j; pmid: 23340705
20. Y. S. Kim, R. I. Kaiser, on the formation of amines (RNH_2) and the cyanide anion (CN^-) in electron-irradiated ammonia-hydrocarbon interstellar model ices. *Astrophys. J.* **729**, 68–75 (2011). doi: 10.1088/0004-637X/729/1/68
21. L. E. Orgel, Prebiotic chemistry and the origin of the RNA world. *Crit. Rev. Biochem. Mol. Biol.* **39**, 99–123 (2004). doi: 10.1080/10409230490460765; pmid: 15217990
22. R. Pascal, L. Boiteau, A. Commeyras, From the prebiotic synthesis of α-amino acids towards a primitive translation apparatus for the synthesis of peptides. *Top. Curr. Chem.* **259**, 69–122 (2005). doi: 10.1007/b136707
23. D. Ritson, J. D. Sutherland, Prebiotic synthesis of simple sugars by photoredox systems chemistry. *Nat. Chem.* **4**, 895–899 (2012). doi: 10.1038/nchem.1467; pmid: 23089863
24. R. Saladino, C. Crestini, F. Ciciriello, G. Costanzo, E. Di Mauro, Formamide chemistry and the origin of informational polymers. *Chem. Biodivers.* **4**, 694–720 (2007). doi: 10.1002/cbdv.200790059; pmid: 17443884

ACKNOWLEDGMENTS

This work was supported by Deutsches Zentrum für Luft- und Raumfahrt (DLR) under contract no. 50 QP 1302, and by Centre National d'Etudes Spatiales (CNES) grants at LATMOS and LISA. U.J. M. was funded by L'Agence Nationale de la Recherche (ANR-12-IS07-0006). Support from the NASA Astrobiology Institute (P.E.), the NASA Postdoctoral Program at Goddard Space Flight Center (T.G.), Programme de Développement d'Expériences scientifiques through Enterprise Ireland (S.McK.L.), and the Welch Foundation (A.J.MacD.) is acknowledged. Rosetta is a European Space Agency (ESA) mission with contributions from member states and NASA. The Philae lander was provided by a consortium led by DLR, Max-Planck-Institut für Sonnensystemforschung, CNES, and Agenzia Spatiale Italiana. The data used in this study are available through ESA's Planetary Science Archive (www.rssd.esa.int/index.php?project=PSA&page=rosetta).

SUPPLEMENTARY MATERIALS

www.sciencemag.org/content/349/6247/aab0689/suppl/DC1
Materials and Methods
Figs. S1 and S2
Tables S1 to S4
References (*25*–*32*)

9 March 2015; accepted 1 July 2015
10.1126/science.aab0689

REVIEW SUMMARY

CRYSTAL GROWTH

Crystallization by particle attachment in synthetic, biogenic, and geologic environments

James J. De Yoreo, Pupa U. P. A. Gilbert, Nico A. J. M. Sommerdijk, R. Lee Penn, Stephen Whitelam, Derk Joester, Hengzhong Zhang, Jeffrey D. Rimer, Alexandra Navrotsky, Jillian F. Banfield, Adam F. Wallace, F. Marc Michel, Fiona C. Meldrum, Helmut Cölfen, Patricia M. Dove*

BACKGROUND: Numerous lines of evidence challenge the traditional interpretations of how crystals nucleate and grow in synthetic and natural systems. In contrast to the monomer-by-monomer addition described in classical models, crystallization by addition of particles, ranging from multi-ion complexes to fully formed nanocrystals, is now recognized as a common phenomenon. This diverse set of pathways results from the complexity of both the free-energy landscapes and the reaction dynamics that govern particle formation and interaction.

Whereas experimental observations clearly demonstrate crystallization by particle attachment (CPA), many fundamental aspects remain unknown—particularly the interplay of solution structure, interfacial forces, and particle motion. Thus, a predictive description that connects molecular details to ensemble behavior is lacking. As that description develops, long-standing interpretations of crystal formation patterns in synthetic systems and natural environments must be revisited.

Here, we describe the current understanding of CPA, examine some of the nonclassical thermodynamic and dynamic mechanisms known to give rise to experimentally observed pathways, and highlight the challenges to our understanding of these mechanisms. We also explore the factors determining when particle-attachment pathways dominate growth and discuss their implications for interpreting natural crystallization and controlling nanomaterials synthesis.

ADVANCES: CPA has been observed or inferred in a wide range of synthetic systems—including oxide, metallic, and semiconductor nanoparticles; and zeolites, organic systems, macromolecules, and common biomineral phases formed biomimetically. CPA in natural environments also occurs in geologic and biological minerals. The species identified as being responsible for growth vary widely and include multi-ion complexes, oligomeric clusters, crystalline or amorphous nanoparticles, and monomer-rich liquid droplets.

Particle-based pathways exceed the scope of classical theories, which assume that a new phase appears via monomer-by-monomer addition to an isolated cluster. Theoretical studies have attempted to identify the forces that drive CPA, as well as the thermodynamic basis for appearance of the constituent particles. However, neither a qualitative consensus nor a comprehensive theory has emerged. Nonetheless, concepts from phase transition theory and colloidal physics provide many of the basic features needed for a qualitative framework. There is a free-energy landscape across which assembly takes place and that determines the thermodynamic preference for particle structure, shape, and size distribution. Dynamic processes, including particle diffusion and relaxation, determine whether the growth process follows this preference or another, kinetically controlled pathway.

OUTLOOK: Although observations of CPA in synthetic systems are reported for diverse mineral compositions, efforts to establish the scope of CPA in natural environments have only recently begun. Particle-based mineral formation may have particular importance for biogeochemical cycling of nutrients and metals in aquatic systems, as well as for environmental remediation. CPA is poised to provide a better understanding of biomineral formation with a physical basis for the origins of some compositions, isotopic signatures, and morphologies. It may also explain enigmatic textures and patterns found in carbonate mineral deposits that record Earth's transition from an inorganic to a biological world.

A predictive understanding of CPA, which is believed to dominate solution-based growth of important semiconductor, oxide, and metallic nanomaterials, promises advances in nanomaterials design and synthesis for diverse applications. With a mechanism-based understanding, CPA processes can be exploited to produce hierarchical structures that retain the size-dependent attributes of their nanoscale building blocks and create materials with enhanced or novel physical and chemical properties. ■

ON OUR WEB SITE

Read the full article at http://dx.doi.org/10.1126/science.aaa6760

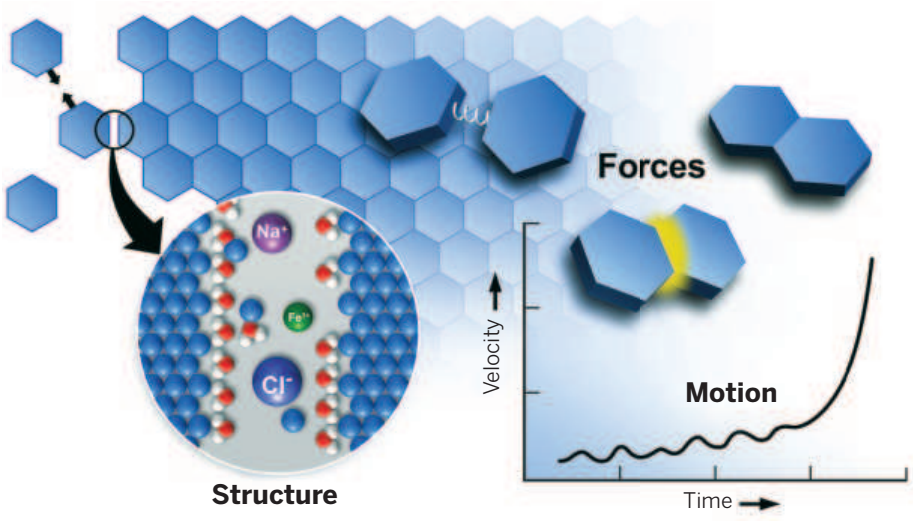

Major gaps in our understanding of CPA. Particle attachment is influenced by the structure of solvent and ions at solid-solution interfaces and in confined regions of solution between solid surfaces. The details of solution and solid structure create the forces that drive particle motion. However, as the particles move, the local structure and corresponding forces change, taking the particles from a regime of long-range to short-range interactions and eventually leading to particle-attachment events.

The list of author affiliations is available in the full article online.
*Corresponding author. E-mail: dove@vt.edu
Cite this article as J. J. De Yoreo *et al.*, *Science* **349**, aaa6760 (2015). DOI: 10.1126/science.aaa6760

REVIEW

CRYSTAL GROWTH

Crystallization by particle attachment in synthetic, biogenic, and geologic environments

James J. De Yoreo,[1,2] Pupa U. P. A. Gilbert,[3,4]* Nico A. J. M. Sommerdijk,[5,6] R. Lee Penn,[7] Stephen Whitelam,[8] Derk Joester,[9] Hengzhong Zhang,[10] Jeffrey D. Rimer,[11] Alexandra Navrotsky,[12] Jillian F. Banfield,[10] Adam F. Wallace,[13] F. Marc Michel,[14] Fiona C. Meldrum,[15] Helmut Cölfen,[16] Patricia M. Dove†[14]

Field and laboratory observations show that crystals commonly form by the addition and attachment of particles that range from multi-ion complexes to fully formed nanoparticles. The particles involved in these nonclassical pathways to crystallization are diverse, in contrast to classical models that consider only the addition of monomeric chemical species. We review progress toward understanding crystal growth by particle-attachment processes and show that multiple pathways result from the interplay of free-energy landscapes and reaction dynamics. Much remains unknown about the fundamental aspects, particularly the relationships between solution structure, interfacial forces, and particle motion. Developing a predictive description that connects molecular details to ensemble behavior will require revisiting long-standing interpretations of crystal formation in synthetic systems, biominerals, and patterns of mineralization in natural environments.

The central roles of crystallization in geochemical, biological, and synthetic materials systems have motivated decades of research into crystal nucleation and growth. Since the mid-1900s, most studies have interpreted the results through the lens of classical nucleation theory (*1*) and the terrace-ledge-kink model of crystal growth (*2*), both of which are based on monomer-by-monomer addition of simple chemical species. Despite the successes of classical nucleation and growth models (*3*, *4*), there are a number of phenomena associated with crystal formation that cannot satisfactorily be explained or predicted either quantitatively or qualitatively. For example, amorphous phases are reported to nucleate at concentrations well below those predicted by classical models (*5*). Equally perplexing are the irregular and branched crystal morphologies observed in synthetic nanocrystals (*6*) and the habits and microstructures of biominerals found in organisms (*7*). Similarly, the geologic record shows extensive mineral deposits with unusual mineralogical and textural patterns (*8*) that are not readily interpreted within the framework of classical mineral formation processes.

These characteristics have been attributed to nonclassical (*9*) crystal growth processes that are distinct from those envisioned by the traditional models. For example, mineralization of sea urchin embryonic spicules proceeds by accumulation of nanoparticles of an amorphous calcium carbonate (ACC) precursor, which subsequently transforms into a crystal of calcite (*10*, *11*). Similar amorphous-to-crystalline pathways occur in diverse biominerals, including sea urchin spines (*12*) and teeth (*13*), mammalian tooth enamel (*14*), vertebrate bones (*15*), crustacean exoskeletons (*16*), annelid calcareous concretions (*17*), and mollusk larval shells (*18*). Likewise, aggregation of poorly ordered precursors precedes formation of biogenic magnetite (*19*) and zeolites (*20*), and biomimetic polymers introduced as proxies for biological macromolecules induce formation of liquid phases that transform into crystalline products through aggregation and dehydration (*21*).

Another nonclassical mechanism of crystal growth, oriented attachment (OA), proceeds by repeated attachment events of crystalline particles on specific crystal faces that are lattice-matched, either with true crystallographic alignment or across a twin boundary or stacking fault (*22*). Similarly, mesocrystals, which are kinetically stabilized superstructures of nanocrystals in crystallographic alignment (*23*, *24*), form as intermediates between dispersed particles and true single crystals. They may fuse and transform into single crystals (*24*) or remain kinetically stabilized by adsorbates—often polymeric—at the particle interfaces (*9*). Structured macromolecules can promote the OA process. For example, mineral precursors of tooth enamel assemble in vitro into chains with co-orientation imparted by structured protein oligomers within which the mineral resides before fusion into single-crystal rods (*25*).

These discoveries show that in many systems, crystallization can occur by attachment of a wide range of species more complex than simple ions (Fig. 1). We refer to these higher-order species as particles, broadly defined to include multi-ion complexes (*5*), oligomers (or clusters) (*26*), and nanoparticles—whether crystalline (*27*), amorphous (*14*), or liquid (*21*). We review the current understanding of crystallization by particle attachment (CPA) and examine thermodynamic and dynamic mechanisms that give rise to CPA. Our analysis also explores the intrinsic and extrinsic factors that determine when particle-based pathways dominate growth. Although many of the principles discussed here are likely to apply to organic and macromolecular crystals, such as the involvement of liquid precursors, this examination of CPA is largely restricted to inorganic systems, both because the study of inorganic crystal growth by CPA is more mature at this time and because the conformational degrees of freedom in macromolecular systems introduce dynamical factors that render them distinct from inorganic systems. Looking ahead, we identify areas where our mechanistic understanding is weak and highlight directions for future research.

Evidence, indicators, and consequences of crystallization by particle attachment

In situ observations of crystal growth from solution at a resolution where the atomic-scale lattice and the addition of growth units are observable are rare and generally limited to liquid-phase scanning probe (*28*) and transmission electron microscope (TEM) (*27*, *29*, *30*) studies. Consequently, there are very few systems in which CPA has been unequivocally demonstrated, and most evidence is based on observations of crystals made after the pathway from solvated state to crystal phase has been traversed. Nonetheless, static images showing apparent assemblies of co-aligned nanocrystals (Fig. 2A) have been frequently accepted as evidence for CPA via OA. Moreover, definitive confirmation of OA through in situ liquid-phase electron microscopy (Fig. 2, B and C) in both oxide and metallic systems (*27*, *29*) forms a basis for inferring its occurrence from features observed ex situ.

[1]Physical Sciences Division, Pacific Northwest National Laboratory, Richland, WA 99352, USA. [2]Department of Materials Science and Engineering, University of Washington, Seattle, WA 98195, USA. [3]Departments of Physics and Chemistry, University of Wisconsin, Madison, WI 53706, USA. [4]Radcliffe Institute for Advanced Study, Harvard University, Cambridge, MA 02138, USA. [5]Laboratory of Materials and Interface Chemistry and Soft Matter CryoTEM Unit, Department of Chemical Engineering and Chemistry, Eindhoven University of Technology, P.O. Box 513, 5600 MB Eindhoven, Netherlands. [6]Institute for Complex Molecular Systems, Eindhoven University of Technology, P.O. Box 513, 5600 MB Eindhoven, Netherlands. [7]Department of Chemistry, University of Minnesota, 207 Pleasant Street, SE, Minneapolis, MN 55455, USA. [8]The Molecular Foundry, Lawrence Berkeley National Laboratory, Berkeley, CA 94720, USA. [9]Department of Materials Science and Engineering, Northwestern University, Evanston, IL 60208, USA. [10]Department of Earth and Planetary Science, University of California Berkeley, Berkeley, CA 94720, USA. [11]Department of Chemical and Biomolecular Engineering, University of Houston, 4800 Calhoun Road, Houston, TX 77204, USA. [12]Peter A. Rock Thermochemistry Laboratory, Department of Chemistry, University of California Davis, 1 Shields Avenue, Davis, CA 95616, USA. [13]Department of Geological Sciences, University of Delaware, Newark, DE 19716, USA. [14]Department of Geosciences, Virginia Polytechnic Institute, Blacksburg, VA 24061, USA. [15]School of Chemistry, University of Leeds, Leeds LS2 9JT, West Yorkshire, England. [16]Physical Chemistry, Department of Chemistry, University of Konstanz, D-78457 Constance, Germany. *Previously publishing as Gelsomina De Stasio. †Corresponding author. E-mail: dove@vt.edu

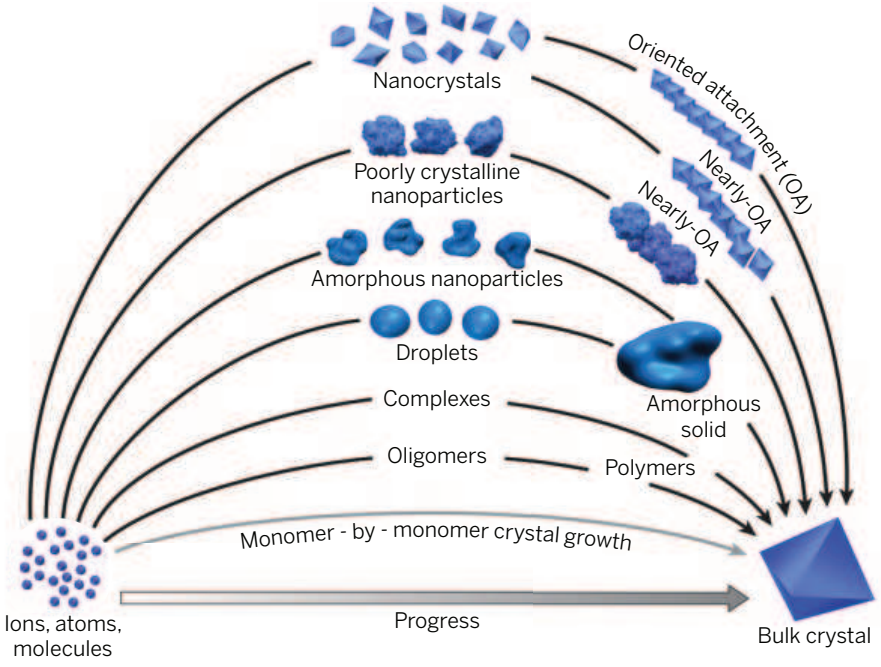

Fig. 1. Pathways to crystallization by particle attachment. In contrast to monomer-by-monomer addition as envisioned in classical models of crystal growth (gray curve), CPA occurs by the addition of higher-order species ranging from multi-ion complexes to fully formed nanocrystals. (The final faceted bulk crystal is a schematic representation of a final single-crystal state. As Figs. 2 and 3 show, the final crystal can have more complex morphologies, including spheroidal.)

Electron microscopy—particularly cryogenic TEM (cryo-TEM)—of synthetic crystals has proven to be highly valuable for characterizing features associated with CPA (Fig. 2). TEM images have revealed primary particles ranging from crystalline (Fig. 2, A to F) to partially ordered (Fig. 2, I and L) to wholly amorphous (Fig. 2K). These images have provided indicators of CPA in both secondary particles and fully formed crystals, including chainlike (Fig. 2A) and branched (Fig. 2G) morphologies that defy expectations based on crystal symmetry (Fig. 2, A, F, G, I, and M). Other indicators provided by TEM are rounded protrusions comparable in size to the primary particles residing in the crystallizing solution (Fig. 2, B, C, and I to L), internal pores (Fig. 2H), the retention of apparent interfaces between primary particles (Fig. 2, D to G), and incorporation of defects at these inferred interfaces. Defects can consist of dislocations (Fig. 2D) that form due to small misalignments during attachment (Fig. 2B) and twin planes or stacking faults that reflect attachment of particles along symmetry-related lattice vectors (Fig. 2F). Defects can also be eliminated through the rearrangement or recrystallization of primary particles after their aggregation (Fig. 2, C, I, J, and L).

The potential role of CPA in biomineral formation has been widely discussed and is often conjectured based on external morphologies and/or internal microstructure. In certain cases, evidence comes from both nanoscale imaging and spectroscopic documentation of phases (*10*–*12*, *14*, *15*) (Fig. 3). As in the case of synthetic crystals, the resulting structures exhibit unexpected morphologies (Fig. 3, A to D) and internal microstructure (Fig. 3, A to D). In all of these cases, the primary particles are amorphous (Fig. 3, A, B, and E).

Although external morphology (e.g., Fig. 2, I and J, and Fig. 3D), microstructure, and texture provide important evidence of attachment-based growth, they alone do not prove formation by a particle-based growth process. In fact, such features can be misleading. For example, irregular or branched morphologies can form through dendritic and spherulitic growth mechanisms from solution at high supersaturation (*31*). Such solids can retain pores, branches, and rounded features formed during growth. Moreover, crystals grown though classical mechanisms within physical templates (*32*) or with the addition of organic polymers (*33*) can exhibit similar morphologies to those seen in natural biominerals and in synthetic crystals attributed to CPA, so interpreting particulate-like morphologies in terms of pathways requires other substantiating evidence. Conversely, even when formation pathways are dominated by particle addition in the early stages, coarsening or recrystallization can subsequently obliterate characteristic signatures (*34*). Thus, the absence of such features is not conclusive evidence of monomer-by-monomer growth. As a result, a holistic suite of characterization techniques is essential to building a strong case for CPA in any given system. Combinations of direct imaging, scattering, and spectroscopy—particularly data collected at different time points throughout crystallization that can detail the kinetics of growth—imply that CPA is a prevalent growth mechanism at the early stages of crystallization (*5*, *11*, *35*–*37*).

Particle-based pathways have important consequences for the structure and properties of materials. They can lead to unique morphologies (Fig. 2, A and G to I, and Fig. 3, A, C, and D), nonequilibrium symmetries (Fig. 2, F to H, and Fig. 3, D and E), distinct internal defect distributions (Fig. 2, C to F, and Fig. 3, A, B, and D), and organic-inorganic hybrid structures in which the coaligned nanoparticles are surrounded by organic matter (*9*, *38*, *39*) (Fig. 2H and Fig. 3, E and F). In addition, crystals formed by CPA can presumably exhibit heterogeneous distributions of elements composing the crystals, either because the primary particles have distinct compositions or because species that formerly resided on primary nanoparticle surfaces are incorporated at the interface generated during attachment events. The stability, mechanical behavior, surface adsorption, transport, catalytic activity, and optical properties of nanomaterials should all depend critically on such characteristics.

Interplay of thermodynamics and kinetics lead to key features of CPA

Despite the structural diversity of the particles involved in CPA, key features of many crystallization pathways can be understood by considering the interplay of free-energy landscapes and reaction dynamics (Fig. 4). The first of these determines the thermodynamic preference for the structure, shape, and size distribution of particles at various stages of assembly. Dynamic processes, in turn, including monomer and particle diffusion and internal particle relaxation, determine whether this set of preferences occurs or whether an alternate, kinetically controlled pathway is traversed.

Monomers dispersed in solution that interact through Brownian motion can aggregate to form larger structures via a wide variety of pathways (Fig. 4, A to E), which can be correlated with distinct points in typical phase diagrams (identified by the labels A to E in Fig. 4F). These pathways may be simple, comprising monomer-by-monomer addition to incipient nuclei that display a single structure (Fig. 4A). However, they may also be complex, involving particles (Fig. 4, B and C) that may be structurally distinct from the final, thermodynamically stable, bulk phase (e.g., Fig. 2, G, K, and L, and Fig. 3, A and B).

The magnitude of the free-energy barrier to nucleation with respect to the thermal energy, k_BT, is a crucial factor in determining the number and nature of particles produced. As the free-energy barrier varies in shape and magnitude, there is a change from monomer-based (Fig. 4A) to particle-based (Fig. 4, B to E) pathways (*40*). At low supersaturation (Fig. 4A), the free-energy barrier is relatively large. The generation of a critical nucleus is then a rare event, and any particles that nucleate are unlikely to see other particles in their immediate vicinity. Thus, one observes a monomer-by-monomer nucleation-and-growth pathway assumed by classical nucleation theories (*1*).

As supersaturation increases (Fig. 4D), the free-energy barrier to phase change diminishes and particles are generated in greater numbers. They can then grow (or shrink) by exchanging monomers

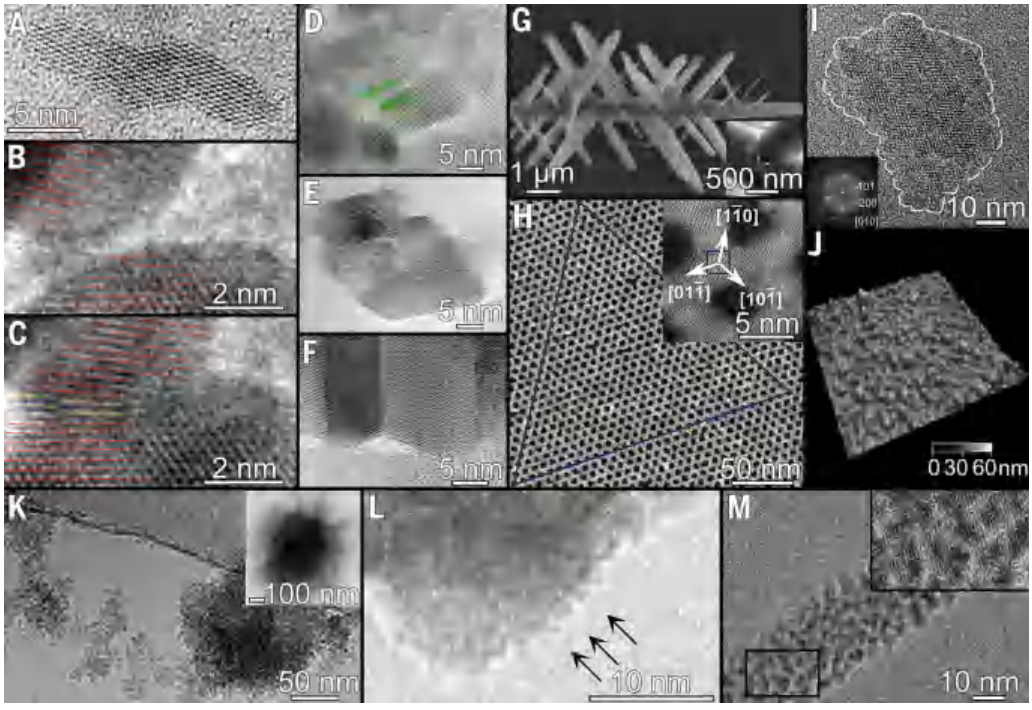

Fig. 2. Examples of inorganic crystals formed by CPA. (**A**) Nanoparticles of anatase (TiO_2) with perfect alignment after apparent attachment event with the *c* axis oriented along the long dimension of the aggregate (*116*). (**B** and **C**) Sequential in situ images showing oriented attachment of ferrihydrite with creation of an edge dislocation (yellow lines) and resulting tilt of lattice planes above and below the edge dislocation (red lines) (*27*, *30*). (**D** to **F**) TiO_2 nanocrystals showing defects incorporated through CPA, including (D) low-angle tilt boundaries, (E) screw dislocations, and (F) twin planes. In (E), the variations in contrast and slight shift in lattice fringe clarity and alignment indicate incorporation of defects. The blue lines highlight the orientation and shift in lattice fringe alignment to either side of the region that contains the dislocations; the bright-dark contrast is consistent with a dislocation having a screw component. (**G**) Branched nanowire of rutile (TiO_2), where each branch occurs on a set of twin boundaries (inset) (*60*). (**H**) Single-crystal honeycomb superlattice formed through oriented attachment of PbSe nanocrystals in an octahedral symmetry. The equilateral triangle shows the long-range ordering of the structure, and the inset shows the relationship of the crystalline axes with the superlattice pattern (*39*) (**I**) Cryo-TEM micrograph of a single zeolite nanoparticle (*117*). (**J**) Atomic force micrograph of a zeolite surface showing that its growth proceeds by attachment of silica nanoparticles (*28*). (**K**) Calcium phosphate prenucleation complexes aggregating to form amorphous calcium phosphate nanoparticles. (Inset) Amorphous calcium phosphate nanoparticle is replaced by outgrowths of calcium-deficient octacalcium phosphate (*5*). (**L**) Magnetite crystal growing through the accretion of disordered ferrihydrite-like nanoparticles (*57*). (**M**) Goethite mesocrystal formed by the assembly of nanocrystals shows lattice fringes that correspond to (021) planes (*62*).

with other particles, as well as through collision and occasional collision and coalescence events (*41*). When supersaturation is increased until the free-energy barrier is comparable with k_BT, the solution undergoes spinodal decomposition (*42*, *43*), at which point the particles are generated in such large numbers that growth by direct collision and coalescence with other particles can dominate (Fig. 4D).

In the cases described above (Fig. 4, A and D), the free-energy landscape displays a barrier (large in the nucleation regime and small or nonexistent in the spinodal regime) but does not exhibit any features that would suggest the existence of multiple particles during nucleation. Thermodynamically speaking, the system should prefer to grow as one large particle. This is because particles have no special thermodynamic status: They are neither stable nor metastable; that is, they do not reside in a global or a local free-energy minimum. Nonetheless, multiple particles (Fig. 4D) appear for dynamic reasons, and this gives rise to particle-based pathways

If the free-energy landscape exhibits local minima (Fig. 4B), the formation of particles of particular sizes or morphologies becomes thermodynamically favored, and one can observe assembly pathways involving thermodynamically metastable particles that need not appear on a bulk phase diagram. Examples of such intermediates include the metastable aggregates of particles that form by the association of calcium phosphate complexes at high supersaturations, before their transformation to amorphous calcium phosphate (*5*, *44*), and possibly the polymeric states predicted for calcium carbonate solutions (*26*).

Another type of complex assembly pathway involves thermodynamically metastable bulk phases that are subsequently replaced by more stable phases (*45*) (Fig. 4C). There are at least two distinct examples of this type of pathway. In the first, a metastable solid phase forms because the barrier to its nucleation is smaller than that opposing nucleation of the stable phase. Nucleation of the stable phase eventually occurs either heterogeneously on (or in) the metastable particles or homogeneously in the surrounding solution, leading to dissolution or recrystallization of the metastable phase, as is often observed, for example, in the calcium carbonate system (*30*, *46*–*48*). This pathway is commonly referred to as the Ostwald-Lussac rule of stages or the Ostwald step rule. In the second example, monomers associate in an unstructured way, resulting in the formation of amorphous particles or, in the case of spinodal decomposition, of monomer-rich liquid droplets that subsequently crystallize. Such two-step pathways are seen during crystallization of proteins (*49*), of some inorganic electrolytes such as $MgSO_4$ (*50*), and in simple computer models of spheres with isotropic attractions (*51*). Two-step pathways via liquid precursors are also proposed for the $CaCO_3$ system based on electron microscopy (*52*), calorimetry and nuclear magnetic resonance (NMR) studies (*53*), and molecular dynamics simulations (*40*).

When the internal relaxation of metastable species is sufficiently slow, the formation of long-lived metastable or nonequilibrium materials such as gels becomes possible for dynamic reasons (Fig. 4E) either before or instead of the formation of a stable crystal (*54*). Moreover, hierarchical pathways that result in growth by OA reflect dynamic factors that bias attachment on specific faces, despite the fact that the global minimum in free energy is independent of such factors.

Thus, well-known physical mechanisms lead generically to a range of hierarchical and multistep assembly pathways, including monomer-by-monomer addition, often occurring simultaneously (*27*, *30*). Nonetheless, interpretations of recent experimental observations and simulations raise new challenges to the classifications described above. For example, proposed pathways involving aggregation of stable "prenucleation cluster" species (*26*, *55*) are inconsistent with the existing understanding of phase change that considers subcritical clusters to be unstable (Fig. 4A) or, perhaps, metastable (Fig. 4B).

The influence of surface energy on pathways

When the free-energy landscape includes multiple minima representing different polymorphs of

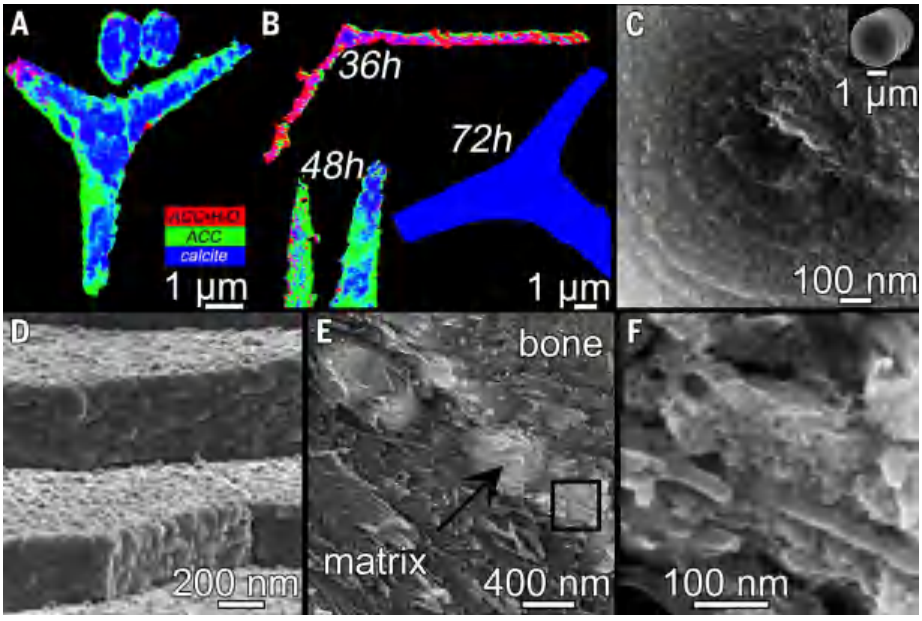

Fig. 3. Examples of biogenic crystals proposed to form by aggregation of nanosized particles. (**A**) Photoelectron emission microscopy component map of the mineral phases in sea urchin embryonic spicules: ACC-H_2O (red), ACC (green), and calcite (blue) (*11*). (**B**) Component maps of sea urchin spicules at three different developmental stages: At 36 hours, the dominant phase is ACC-H_2O; at 48 hours, it is ACC; and at 72 hours, it is calcite. (**C**) Cryo-fractured surface of a sea urchin spicule from *Strongylocentrotus purpuratus*. The inset shows a lower magnification micrograph of the same portion of a spicule. (**D**) Field-emission scanning electron microscope (FE-SEM) micrograph of terraced nacre tablets from the mollusk shell of *Pinctada fucata*, which are made of aragonite nanoscale building blocks (*118*). (**E** and **F**) Cryo-SEM micrographs of the bone growth zone in high-pressure frozen fin tissue of the zebrafish (*Danio rerio*). Newly deposited, nonmineralized bone matrix contains large, mineral-bearing globules, which fuse into the mineralizing bone matrix (black arrow) (*119*). These globules fuse into the mineralizing bone. Spectroscopic measurements show that the edges of the forming bone are amorphous calcium phosphate, whereas the bone region is crystalline hydroxyapatite. (F) Higher magnification of area delineated by the box in (E), showing post-attachment particulate substructure of a globule.

the same crystal (Fig. 4D), the interfacial free energy (or surface energy) can have a large influence on pathways of CPA, because it affects the size of the free-energy barrier. (Here, we use the term polymorph to include hydrated phases of an otherwise identical composition.) If the surface energy of the metastable polymorph is much smaller than that of the stable phase, then Ostwald's step rule is likely to be observed. However, if the differences in thermodynamic stability, and hence surface free energy, of two polymorphs are subtle or the supersaturations with respect to both polymorphs are high, then the free-energy barriers to nucleation of either can be so small that both will form. Particle-particle interaction and aggregation events can then involve particles of distinct phases (*56*, *57*) (e.g., Fig. 2, G and L, and Fig. 3, A, B, and E).

Although the relative stability of the polymorphs depends on bulk properties such as the enthalpy of formation and molar volume, the contribution of surface free energy often results in a dependence of stability on crystal size (*58*, *59*). This dependence can even invert the sequence of polymorph stability relative to that observed for the bulk phases (*58*). Thus, primary particles may be a polymorph that is only stable at a small size, while the secondary particles have the structure of the stable bulk form (*34*, *56*, *57*, *60*). That is, the free-energy barrier to nucleating small particles possessing a form that is metastable in the bulk phase will be lower than the barrier to nucleating particles of the same size possessing the stable bulk form. For CPA to generate single crystals in such systems, the attachment events must accommodate the structural differences between the two phases, either through a structural match at the interface (*60*) or through postattachment phase transformation (*34*, *56*, *57*).

Recent computational work suggests that the solvent plays important roles in mediating particle interactions and attachment events (*61*). Cryo-TEM observations showing coaligned arrays of particles that appear separated by a solvent layer underline the importance of the solvent in mediating attachment (*62*). Because the solvation energy of a surface generally becomes more exothermic with increasing surface energy (*59*), the dynamics of CPA should also be affected by surface energies. In particular, high-energy surfaces with loosely held solvent may be more reactive toward other species in the solution, including other particles. Meanwhile, surfaces to which solvation layers are strongly bound may resist attachment, thus biasing OA to occur on specific faces through the influence of kinetic barriers rather than attractive forces (*35*, *61*). Understanding the role of surface energies in phase selection and structural transformation dynamics and relating surface and solvation energies to nucleation, reactivity, and assembly are major challenges still to be addressed.

Precursor phases

The inherent size dependence of thermodynamic drivers (*59*, *63*) and the kinetic constraints placed on nucleation of polymorphs by the barriers in the energy landscape render precursor phases a ubiquitous feature of crystallizing systems (*58*, *59*). Consequently, pathways to a final stable phase via CPA often involve precursor particles (Figs. 1 and 4). Precursors can include one or more solid amorphous phases (*10*, *12*, *14*, *15*, *18*, *30*, *46*, *64*, *65*), dense liquids or gels (*21*, *49*, *53*), or crystalline nanoparticles (*30*, *57*, *60*, *63*). Each results in a distinct growth history, but whether or not the final outcomes are also distinct should depend on the extent to which monomer-by-monomer addition competes with the particle-attachment pathways and coarsening or recrystallization processes modify the structure and morphology of the growing crystal.

Amorphous phases

Mineral systems may crystallize through an amorphous precursor at sufficiently high supersaturation (*5*, *20*, *46*, *66*–*69*), but the mechanism of the transition is unclear for most systems. For calcium carbonate formed abiotically from aqueous solution, the ACC precursor phase is initially hydrated (*64*, *66*). In the bulk, hydrated ACC is stable in dry conditions but crystallizes in humid conditions or upon heating with the release of water (*46*, *70*). Although the observed coexistence of crystalline and amorphous material within early stage nanoparticles both in solution (*69*) and under Langmuir monolayers (*47*) suggests that solid-state crystallization may occur at the onset of the transition, ACC confined in small volumes remains stable for very long times even in the presence of bulk water, indicating that a heterogeneous nucleator for one of the crystalline polymorphs may be required (*71*, *72*). Transformation then typically occurs through local dissolution and reprecipitation (*73*). Because the crystalline polymorphs have a much lower solubility than ACC, in environments free of bulk water, the release of water upon initiation of crystallization of the hydrated phase might then induce local dissolution and reprecipitation. Thus, water release and crystallization may be connected and could result in the appearance of microfacets during crystallization (*36*, *48*). However, ACC can also dehydrate before the onset of crystallization (*64*), in which case faceting may not occur. The generality of this behavior is unclear because the extent to which amorphous phases of other materials contain solvent as a structural element is unknown. Moreover, when crystallite size becomes sufficiently small, the possibility that some materials may exist in a continuum across structural states from crystalline to amorphous has been suggested (*74*).

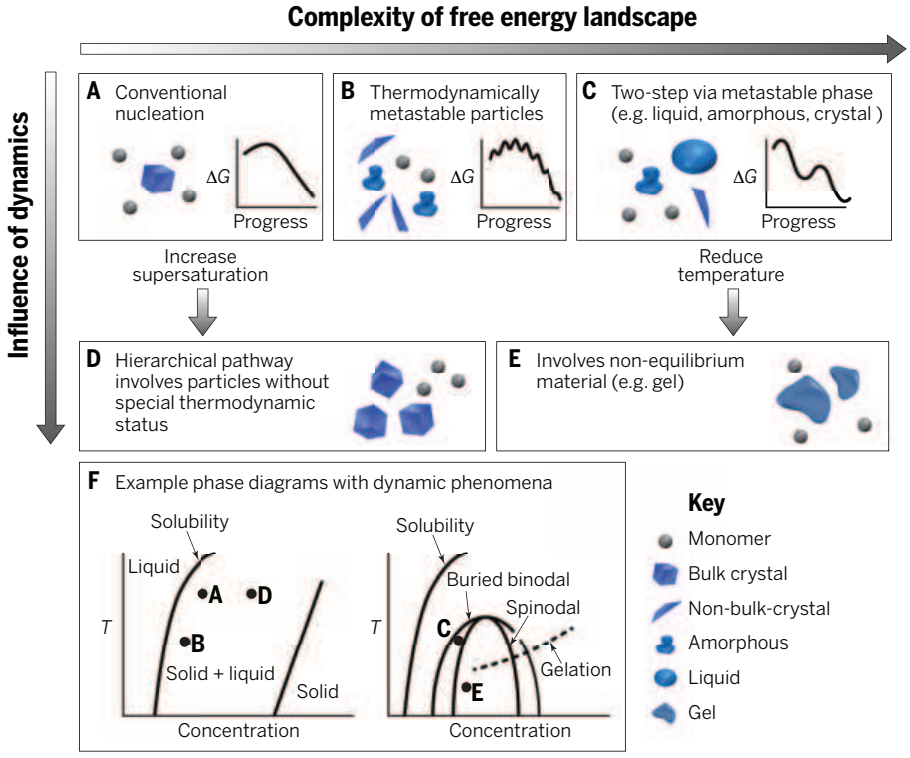

Fig. 4. Crystallization by a wide variety of pathways. The possible pathways by which monomers form a stable bulk crystal, and the physical mechanisms that give rise to them, can have thermodynamic (**A** to **C**) and kinetic (**D** and **E**) origins. Each of the pathways in Fig. 1 can be associated with the mechanisms shown here. (A) Classical monomer-by-monomer addition. (B) Aggregation of metastable particles, such as liquid, amorphous, or poorly crystalline particles, or of oriented (and nearly oriented) attachment of metastable nanocrystals. (C) Crystallization via the formation of a metastable bulk phase, such as a liquid or solid polymorph. (D) Kinetically dominated aggregation of clusters or oligomers. (E) Aggregation of unstable particles whose internal structures are not those of equilibrium phases. The phase diagrams (**F**), with or without a spinodal region, reflect thermodynamic controls on assembly. As indicated, each pathway in (A) through (E) corresponds to a similarly labeled point in these phase diagrams. Modified after (*51*).

In biomineralization, crystallization from transient amorphous precursor particles is believed to be a widespread strategy that enables the efficient transport of mineral constituents with low solubility to the crystallization site (*75*). In cases involving ACC, research indicates that the nanoparticles—which in their initial, hydrated ACC form may be liquid- or gel-like but later dehydrate—likely serve as the initial precursor phase and become a space-filling material (*76*). The full mechanism of the transformation to crystal remains a subject of investigation (*11*, *36*, *77*).

Dense liquid droplets

Protein and polymer solutions often exhibit partial miscibility, with a dense liquid phase (*49*, *78*) that can act as a precursor to crystal formation. The emergence of such a state, however, does not necessarily imply its active participation in crystallization. Aqueous electrolyte solutions may also undergo liquid-liquid phase separation at elevated temperatures (*50*, *79*). In addition, a combination of calorimetry, nanoparticle tracking, NMR experiments (*53*) and in situ liquid phase TEM (*30*), and theoretical investigations (*40*) have provided evidence that a liquid-liquid phase separation occurs near room temperature in the $CaCO_3$ system. Liquid droplets produced by this mechanism should undergo aggregation events due to diffusion and collision (*40*, *78*), but mechanisms by which dense liquid droplets transform to crystalline phases are largely unexplored.

Crystalline nanoparticles

Crystalline particles are distinct from the aforementioned precursor phases due to their ordered structure. Depending on symmetry, a crystal may have heterogeneous surface structure and distribution of surface charge, as well as a net dipole moment. Nanocrystals can possess the expected equilibrium morphologies or have rough surfaces and nonequilibrium shapes. Such morphological characteristics can substantially influence the particle-particle interactions that precede attachment, as well as the structure and microstructure of the resulting single crystals.

Atomic bonding, particle morphology, surface reconstruction, and particle size largely determine the structure of a nanoparticle. However, nanoparticle structure is not static; it changes in response to its environment, as demonstrated by ~3-nm ZnS nanoparticles upon adsorption of water, organic molecules, and inorganic ions (*74*, *80*). Similarly, nanoparticle structure is sensitive to aggregation state, as evidenced by the reversible ordering/disordering structural changes seen upon aggregation and disaggregation of small ZnS nanoparticles (*81*). In some cases, increasing size can result in decreased internal strain and defect content (*82*). Finally, in systems for which there is a switch in phase stability with particle size, as discussed above, nanoparticles of one phase may initially form and transform to the bulk phase as they aggregate and grow in size (*34*, *56*, *57*, *60*). For example ~1-nm ferrihydrite-like primary particles structurally rearrange upon attachment to the surface of magnetite crystals to merge with the magnetite crystal structure (*57*). In such systems, the structural differences may be accommodated if a match between the lattice planes of the two distinct phases can be achieved, as was reported for anatase and rutile TiO_2 (*60*), or may also result in disordered aggregates, as in the case of akaganéite assembly to form single-crystal hematite (*34*). However, after becoming part of the larger mass, the primary particles must transform to the bulk phase. If the interphase boundary is coherent, the transformation can lead to the growth of branched single crystals; this may also result in twin boundaries or stacking faults at the branch sites (e.g., Fig. 2G). Alternatively, if the boundaries are incoherent, a single crystal can only result if recrystallization removes the boundaries, potentially obliterating any structural evidence of CPA (*34*).

Oligomers, polymers, and gels

In some systems, the monomers can form complexes or polymerize or aggregate into clusters before the formation of a new phase (*5*, *28*, *44*, *68*). Consequently, the solution may contain a distribution of monomers, complexes, and clusters, all of which may play an active role in nucleation and growth, complicating identification of one species as the fundamental unit. Alternatively, all but one of the observed species may be spectators, with the active species being consumed as quickly as they are produced. Thus, detectable species may not substantially contribute to nucleation and growth. If, for dynamical reasons, complex species form interconnected networks, they may create a dynamically arrested gel state, which only crystallizes upon heating (Fig. 4E) (*83*).

The dynamics of postnucleation growth by monomers and particles

After the nucleation stage, the newly formed phases grow and coarsen, potentially via many competing processes (Fig. 5). Whether or not CPA dominates over monomer addition depends on numerous factors associated with both the free-energy landscape and the kinetics of the system.

The extent to which monomers participate in the postnucleation stage depends on the relative rates of attachment and detachment. When surfaces are atomically rough, the growth rate is controlled by diffusion. For faceted interfaces, the attachment and detachment rates depend on the kink site density and the energy to create new kinks (*84*). In both limits, the theory of growth is well developed (*84*).

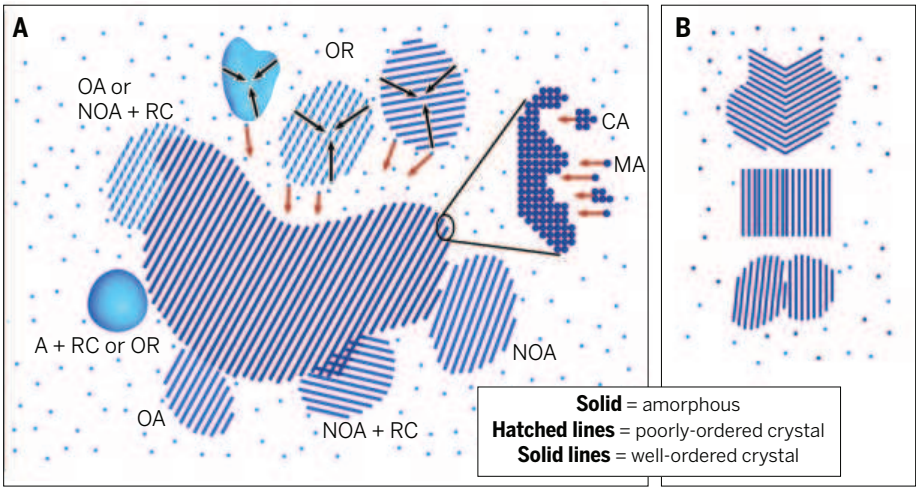

Fig. 5. Multiple growth mechanisms can occur simultaneously within a single crystallizing system, depending on the values of global parameters such as supersaturation, local factors that include interface curvature, and materials parameters such as phase stability versus particle size. (**A**) In this diagram, the arrows indicate the direction of motion of monomers, clusters, or surfaces, and the dashed lines give the crystallographic orientations of nanocrystals. The expanded oval shows molecular-scale processes. OR, Ostwald ripening; MA, molecular attachment; CA, cluster attachment; A, amorphous addition; OA, oriented attachment; NOA, non- or semi-oriented attachment; RC, recrystallization. The phases are denoted by uniform blue for an amorphous crystal, wavy lines for a poorly ordered crystal, and solid lines for a well-ordered crystal. (**B**) Twins, stacking faults, and dislocations can result from the attachment of crystalline particles.

Conventional understanding of particle-particle interactions relies on the theory of Derjaguin, Landau, Verwey, and Overbeek (DLVO) for colloidal particles that are typically much larger than the nanoparticles involved in crystal growth (*85*, *86*). Classical DLVO theory considers the surface charge repulsion and the van der Waals interaction between two particles, with many simplifications in the mathematical derivation. Although successful in interpreting some observations of colloids, DLVO theory is unable to predict the orientation dependence of nanoparticle growth via OA. This is attributed in part to non-DLVO forces, such as solvation, and the omission of Coulombic interactions between interacting particles. For inorganic nanoparticles in close proximity, Coulombic and Lewis acid/base interactions predominate over van der Waals interactions and random Brownian forces, thereby guiding the interacting particles to find energetically favorable crystallographic orientations for attachment (*87*–*89*). Molecular energetic calculations predicted preferred attachment surfaces and crystal growth orientations for more than 30 crystals that largely agree with experimental results (*88*), demonstrating the importance of Coulomb interactions during OA (*29*, *61*).

Because monomer attachment rates scale with solubility, it is arguably the most important parameter determining relative contributions of monomer-by-monomer addition or addition of nanoparticles. For example, as the solubility drops from molar levels to submicromolar levels, at equivalent values of supersaturation the rates of monomer addition drop by a factor of ~10^{10} (*90*). However, the translational and rotational diffusivity of particles is strongly attenuated by particle size, varying as R^{-1} and R^{-3}, respectively. Because critical nucleus size also increases with increasing solubility, these strong dependencies again reduce the likelihood that CPA dominates at high solubility.

Even when CPA dominates, crystallization is unlikely to proceed without the concurrent process of Ostwald ripening (Fig. 5) (*28*). This is because particle solubility increases as the radius decreases via the Gibbs-Thomson relation (*41*). Both attached and dispersed particles with radii of curvature smaller than the ensemble average will tend to dissolve, whereas those with larger radii will grow. Therefore, the competition between monomer-by-monomer growth and growth by attachment of particles of different sizes must be considered. In poorly mixed systems, the local curvature of nearby particles can determine this competition. For example, although small particles near highly curved regions of larger ones may aggregate with little competition from Ostwald ripening, those near flat or negatively curved regions may rapidly dissolve, resulting in net transfer of monomers to the larger mass (*34*).

Because initial nucleation from solution most often produces a polydisperse population of nanoparticles, their assembly typically leads to irregular crystal morphology with protrusions, branches, and pores. The extent and pattern of these structures depends on the degree to which monomer attachment and detachment is rapid enough to smoothen the interface, filling regions of negative curvature formed by attachment events. Therefore, the development of experimental model systems, simulations, and ultimately a theory that predicts growth shape, kinetics, crystallinity, and the resulting defect structure depends on an ability to account for the competing contribution of monomers and particles to postnucleation growth and coarsening.

Effect of extrinsic factors: Surfaces, impurities, and confinement

The presence of a foreign surface in a crystallizing system can dramatically alter the pathway of crystallization for the simple reason that barriers to nucleation can be lowered due to a reduction in the interfacial free energy (*3*, *44*). In the case of calcite, the rate of heterogeneous nucleation on functionalized surfaces has been predicted to be 20 orders of magnitude higher than that of homogeneous nucleation (*3*, *73*). A similar result was found for calcium phosphate nucleation on collagen (*5*). Consequently, although pathways via precursor phases and particle aggregation may dominate in a system free of preexisting interfaces, the presence of an interface can redirect the nucleation pathway toward the classical monomer-by-monomer process at low supersaturation.

A more complex situation exists for monomers confined in restricted volumes—for example, in crevices and small pores (*91*, *92*). Where the pore surface is wetted by the nucleus, nucleation rates should be enhanced over those on flat substrates for pore dimensions on the order of the critical nucleus size, because the curvature of the pore enables a larger fraction of the nucleus to be in contact with the substrate. However, dramatic effects on the stability of metastable phases within confined volumes that are orders of magnitude larger than the length scale expected for the critical nucleus have been reported for solutions confined between crossed cylinders (*71*, *93*) and in liposomes (*72*, *94*). [The latter may be representative of sea urchin embryos (*95*).] Possible factors to which the observed stabilization was attributed include statistical effects associated with small volumes and low probabilities for nucleating the stable phases, exclusion of heterogeneous nucleators, restriction of the mobility and presence of water, lack of contact with the solution phase required for transformation, and/or an inability to aggregate into larger particles for which the bulk phase has greater stability. Moreover, solute and solvent activities, ion mobilities, and ion distributions—and thus interfacial free energy and supersaturation—are all likely to depend on pore size and the nature of the pore surface for sufficiently small pores. Thus, the effect of confinement on nucleation pathways and rates is only beginning to be understood.

Organic molecules in solution can also affect pathways and rates of crystal formation. Additives (e.g., polymers and surfactants) that colloidally stabilize nanoparticles are believed to promote nanoparticle assembly into superlattices and mesocrystals (*6*, *39*, *96*), with stabilizing ligands residing at the nanoparticle interfaces (*37*), although recent investigations highlight the difficulty in determining whether a crystal possesses the attributes of a mesocrystal (*33*). Several mechanisms of nanoparticle alignment by organics have been proposed, including directed nucleation or attachment in a prealigned organic matrix (*9*), such as collagen (*97*) or chitin, or alignment through physical interactions (*9*, *38*).

Organics have also been shown to modulate the kinetics of inorganic nucleation and growth.

In fact, macromolecules, particularly those that are acidic such as polyacrylic acid and aspartic and glutamic acid-rich (poly)peptides and proteins, can dramatically increase induction times (*98*), stabilize amorphous precursors (*97*, *99*), induce formation of dense liquid phases (*21*, *100*), and modify crystal size and shape (*101*) in vitro. Several soluble proteins in biomineral systems are presumed to have similar effects in natural systems, although there are very few biomineral proteins whose function in vivo has been clearly identified, and most proposed functions are primarily based on in vitro observations (*102*–*105*).

Both inorganic and organic additives can play key roles in determining the structural pathways of nucleation and growth in systems where the final crystal structure consists of an open framework (e.g., zeolites). The use of organic or inorganic species as structure-directing agents (SDAs) is a common method to facilitate the formation of microporous materials. In the case of organic SDAs (*106*), their size and structure tend to be commensurate with the pores and/or channels of the structures they direct. The organic is often occluded within the pores of the crystal as it grows, and there is good evidence that the building blocks are complex units consisting of either disordered particles that order upon addition to the framework or preformed oligomeric units of the framework (Fig. 5). Whether these SDAs simply promote the kinetics of certain molecular assembly pathways or create local minima in the free-energy landscape remains unknown.

Challenges and directions for the future

Although geological materials provided early examples of CPA (*107*), efforts to establish the scope of this process in natural environments have barely begun. Particle-based mineral formation may have particular importance for the biogeochemical cycling of nutrients and metals, as well as environmental remediation. The environmental mineral phases involved in elemental uptake and release, such as the iron oxides, are aggregates of primary units whose metal sorption, encapsulation, and release properties are highly size dependent (*58*, *59*). Furthermore, climate reconstructions are based upon the chemical and morphological characteristics of biological and inorganic minerals in the sedimentary record. In addition to a better understanding of the origins and evolution of skeletal structures, particle-based pathways may finally explain the enigmatic textures and compositions of carbonate deposits that formed as Earth transitioned from an inorganic to a biological world (*8*, *108*). Interpreting the patterns in these ancient materials, however, will present multiple challenges because the pathway from precursor particles to final stable phase occurred millions (or even billions) of years in the past.

A predictive understanding of CPA also promises advances in nanomaterials design and synthesis for diverse applications. This mechanism of crystallization is believed to dominate solution-based growth of important semiconductor, oxide, and metallic nanoparticles, such as TiO_2, Fe_2O_3, CeO_2, ZnO, SnO_2, CdSe, PbSe, ZnS, PbS, Cu_7Te_4, Bi_2Te_3, Au, Ag, Pt, and Pt_3Fe (*60*, *88*, *109*), and can be exploited to produce hierarchical structures that retain the size-dependent properties of the nanoscale building blocks (*96*). The branched nanomaterials that can result from CPA (Fig. 2G) are of particular interest because they can have short electron mean free paths (*110*), large photon absorption cross sections (*111*), and complex patterns of optical scattering (*112*), all of which can improve photovoltaic and photocatalytic efficiency.

Similarly, the nanoparticle architecture of mesocrystals and superlattices (Fig. 2H) results in enhanced or novel thermoelectric, photonic, catalytic, and photovoltaic properties (*113*). The intrinsically anisotropic directional properties of the nanoparticle building blocks should promote directional amplification of physical properties and fields. Open framework materials like zeolites (Fig. 2, I and J) and metal organic framework compounds, some of which are known to be formed by CPA (*114*), exhibit pore dimensions and geometries well suited to CO_2 capture, H_2 storage, emissions control, catalysis for biomass conversion, and molecular separation for refrigerant-free dehumidification and biofuel purification (*115*).

For natural and synthetic materials alike, efforts to decipher signals from preexisting particles will require an understanding of mineralization from both forward and reverse perspectives. That is, direct observations and simulations of crystals that are developing by particle-mediated mechanisms will provide mechanistic insights into formation processes, and parallel studies that revisit the structure and composition of preexisting crystals will be needed to critically reevaluate long-standing assumptions about the conditions of their formation.

Despite the numerous implications of CPA in diverse systems, many knowledge gaps remain. We do not understand the structure of solvent and ions at solid-solution interfaces, nor how this structure evolves as a function of interparticle separation (Fig. 6). The fields and forces at these interfaces, their scaling as assembly proceeds, and their translation into particle motions are unknown. The nanoscale physics and chemistry operating within the interfacial region between particles that govern alignment and attachment events are poorly understood, as is the size dependence of surface energy, solvation energy, and phase stability. Moreover, a complete picture of crystallization must include classical monomer-by-monomer dissolution, precipitation, and ripening, which are convolved in space and time with the dynamics of particle motion, collision, and aggregation (Fig. 5). Given the inherent feedback between the dynamics of solvent and ion distributions in the interfacial region and the motion of particles, a predictive description must cross scales to seamlessly connect molecular details with ensemble behavior. Thus, although models of particle interactions and aggregation in simple colloidal systems are mature, they cannot describe CPA due to the complexities of energy landscapes and anisotropies in shape, atomic structure, surface charge, and adsorbate coverage, as well as the dynamic nature of dense liquid, gel, and amorphous particles.

To address these knowledge gaps, in situ measurements will be critical. Powerful new experimental approaches based on x-ray spectroscopy and scattering, electron microscopy, and scanning probe methods hold promise for exploring the dynamics of CPA. When combined with emerging molecular-to-mesoscale modeling techniques, these methods promise to reveal new insights into the nature of the interface, the source of the forces driving aggregation, the role of solvation, and the dynamics of particle movement, alignment,

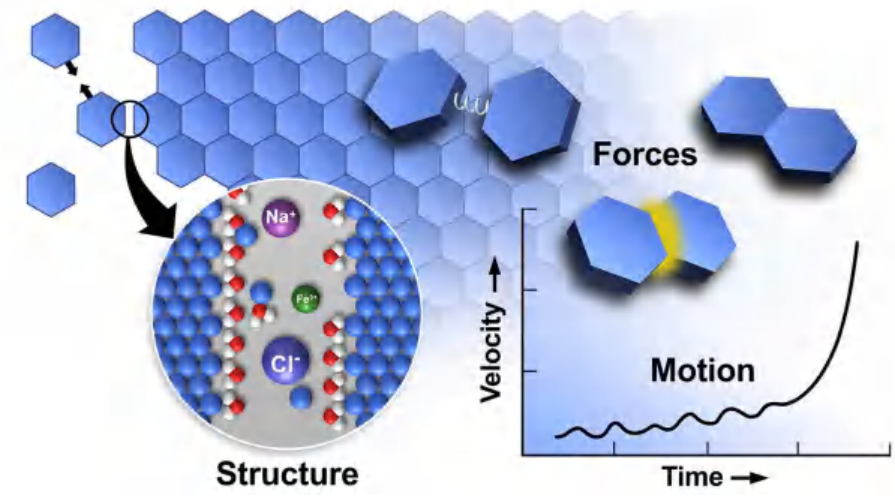

Fig. 6. Major gaps remain in the understanding of CPA. Nanoparticle assembly is influenced by the structure of solvent and ions at solid-solution interfaces and confined regions of solution between solid surfaces. The details of solution and solid structure create the set of forces that drive particle motion. However, as the particles move, the local structure and the corresponding forces change, taking the particles from a regime of long-range to short-range interactions and eventually leading to particle-attachment events.

and attachment. To exploit these new tools, an important challenge is to identify crystal systems that are amenable to a combination of techniques to facilitate comprehensive morphological and structural characterization of crystallization pathways.

Looking ahead, a multidisciplinary effort will be required to decipher the complexity of particle-attachment pathways. Only through integrative approaches will a molecular and quantitative understanding emerge that is comparable to the classical nucleation and growth theories that advanced our understanding over the past 50 years. A complete physical picture of crystallization that encompasses the diversity of potential pathways must now be developed if the many scientific fields in which crystallization is a common phenomenon are to reach their full potential.

Note added in proof: During the development of this article, a review of oriented attachment was published by Ivanov *et al.* (*120*).

REFERENCES AND NOTES

1. D. Kashchiev, Thermodynamically consistent description of the work to form a nucleus of any size. *J. Chem. Phys.* **118**, 1837–1851 (2003). doi: 10.1063/1.1531614
2. W. K. Burton, N. Cabrera, F. C. Frank, The growth of crystals and the equilibrium structure of their surfaces. *Philos. Trans. R. Soc. Lond. A* **243**, 299–358 (1951). doi: 10.1098/rsta.1951.0006
3. A. J. Giuffre, L. M. Hamm, N. Han, J. J. De Yoreo, P. M. Dove, Polysaccharide chemistry regulates kinetics of calcite nucleation through competition of interfacial energies. *Proc. Natl. Acad. Sci. U.S.A.* **110**, 9261–9266 (2013). doi: 10.1073/pnas.1222162110; pmid: 23690577
4. D. N. Petsev, K. Chen, O. Gliko, P. G. Vekilov, Diffusion-limited kinetics of the solution-solid phase transition of molecular substances. *Proc. Natl. Acad. Sci. U.S.A.* **100**, 792–796 (2003). doi: 10.1073/pnas.0333065100; pmid: 12552115
5. W. J. Habraken *et al.*, Ion-association complexes unite classical and non-classical theories for the biomimetic nucleation of calcium phosphate. *Nat. Commun.* **4**, 1507 (2013). doi: 10.1038/ncomms2490; pmid: 23422675
6. K. S. Cho, D. V. Talapin, W. Gaschler, C. B. Murray, Designing PbSe nanowires and nanorings through oriented attachment of nanoparticles. *J. Am. Chem. Soc.* **127**, 7140–7147 (2005). doi: 10.1021/ja050107s; pmid: 15884956
7. H. A. Lowenstam, S. Weiner, *On Biomineralization* (Oxford Univ. Press, New York, 1989).
8. J. P. Grotzinger, N. P. James, in *Carbonate Sedimentation and Diagenesis in the Evolving Precambrian World* (Society for Sedimentary Geology, Tulsa, OK, 2000), vol. 67, pp. 3–20.
9. H. Cölfen, M. Antonietti, *Mesocrystals and Nonclassical Crystallization* (Wiley, Chichester, England; Hoboken, NJ, 2008).
10. E. Beniash, J. Aizenberg, L. Addadi, S. Weiner, Amorphous calcium carbonate transforms into calcite during sea urchin larval spicule growth. *Proc. R. Soc. B-Biol. Sci.* **264**, 461–465 (1997).
11. Y. U. T. Gong *et al.*, Phase transitions in biogenic amorphous calcium carbonate. *Proc. Natl. Acad. Sci. U.S.A.* **109**, 6088–6093 (2012). doi: 10.1073/pnas.1118085109; pmid: 22492931
12. Y. Politi, T. Arad, E. Klein, S. Weiner, L. Addadi, Sea urchin spine calcite forms via a transient amorphous calcium carbonate phase. *Science* **306**, 1161–1164 (2004). doi: 10.1126/science.1102289; pmid: 15539597
13. C. E. Killian *et al.*, Mechanism of calcite co-orientation in the sea urchin tooth. *J. Am. Chem. Soc.* **131**, 18404–18409 (2009). doi: 10.1021/ja907063z; pmid: 19954232
14. E. Beniash, R. A. Metzler, R. S. K. Lam, P. U. P. A. Gilbert, Transient amorphous calcium phosphate in forming enamel. *J. Struct. Biol.* **166**, 133–143 (2009). doi: 10.1016/j.jsb.2009.02.001; pmid: 19217943
15. J. Mahamid, A. Sharir, L. Addadi, S. Weiner, Amorphous calcium phosphate is a major component of the forming fin bones of zebrafish: Indications for an amorphous precursor phase. *Proc. Natl. Acad. Sci. U.S.A.* **105**, 12748–12753 (2008). doi: 10.1073/pnas.0803354105; pmid: 18753619
16. R. Dillaman, S. Hequembourg, M. Gay, Early pattern of calcification in the dorsal carapace of the blue crab, *Callinectes sapidus*. *J. Morphol.* **263**, 356–374 (2005). doi: 10.1002/jmor.10311; pmid: 15688443
17. L. Gago-Duport, M. J. I. Briones, J. B. Rodríguez, B. Covelo, Amorphous calcium carbonate biomineralization in the earthworm's calciferous gland: Pathways to the formation of crystalline phases. *J. Struct. Biol.* **162**, 422–435 (2008). doi: 10.1016/j.jsb.2008.02.007; pmid: 18400515
18. I. M. Weiss, N. Tuross, L. Addadi, S. Weiner, Mollusc larval shell formation: Amorphous calcium carbonate is a precursor phase for aragonite. *J. Exp. Zool.* **293**, 478–491 (2002). doi: 10.1002/jez.90004; pmid: 12486808
19. K. M. Towe, H. A. Lowenstam, Ultrastructure and development of iron mineralization in the radular teeth of *Cryptochiton stelleri* (mollusca). *J. Ultrastruct. Res.* **17**, 1–13 (1967). doi: 10.1016/S0022-5320(67)80015-7; pmid: 6017357
20. S. L. Burkett, M. E. Davis, Mechanism of structure direction in the synthesis of Si-ZSM-5: An investigation by intermolecular ^{1}H-^{29}Si CP MAS NMR. *J. Phys. Chem.* **98**, 4647–4653 (1994). doi: 10.1021/j100068a027
21. L. B. Gower, D. J. Odom, Deposition of calcium carbonate films by a polymer-induced liquid-precursor (PILP) process. *J. Cryst. Growth* **210**, 719–734 (2000). doi: 10.1016/S0022-0248(99)00749-6
22. R. L. Penn, J. F. Banfield, Imperfect oriented attachment: Dislocation generation in defect-free nanocrystals. *Science* **281**, 969–971 (1998). doi: 10.1126/science.281.5379.969; pmid: 9703506
23. M. Li, H. Schnablegger, S. Mann, Coupled synthesis and self-assembly of nanoparticles to give structures with controlled organization. *Nature* **402**, 393–395 (1999). doi: 10.1038/46509
24. D. Schwahn, Y. R. Ma, H. Cölfen, Mesocrystal to single crystal transformation of D,L-alanine evidenced by small angle neutron scattering. *J. Phys. Chem. C* **111**, 3224–3227 (2007). doi: 10.1021/jp068813i
25. P.-A. Fang, J. F. Conway, H. C. Margolis, J. P. Simmer, E. Beniash, Hierarchical self-assembly of amelogenin and the regulation of biomineralization at the nanoscale. *Proc. Natl. Acad. Sci. U.S.A.* **108**, 14097–14102 (2011). doi: 10.1073/pnas.1106228108; pmid: 21825148
26. R. Demichelis, P. Raiteri, J. D. Gale, D. Quigley, D. Gebauer, Stable prenucleation mineral clusters are liquid-like ionic polymers. *Nat. Commun.* **2**, 590 (2011). doi: 10.1038/ncomms1604; pmid: 22186886
27. D. Li *et al.*, Direction-specific interactions control crystal growth by oriented attachment. *Science* **336**, 1014–1018 (2012). doi: 10.1126/science.1219643; pmid: 22628650
28. A. I. Lupulescu, J. D. Rimer, In situ imaging of silicalite-1 surface growth reveals the mechanism of crystallization. *Science* **344**, 729–732 (2014). doi: 10.1126/science.1250984; pmid: 24833388
29. Q. Chen *et al.*, Interaction potentials of anisotropic nanocrystals from the trajectory sampling of particle motion using in situ liquid phase transmission electron microscopy. *ACS Cent. Sci.* **1**, 33–39 (2015). doi: 10.1021/acscentsci.5b00001
30. M. H. Nielsen, S. Aloni, J. J. De Yoreo, In situ TEM imaging of $CaCO_3$ nucleation reveals coexistence of direct and indirect pathways. *Science* **345**, 1158–1162 (2014). pmid: 25190792
31. K. K. Sand, J. D. Rodriguez-Blanco, E. Makovicky, L. G. Benning, S. L. S. Stipp, Crystallization of $CaCO_3$ in water-alcohol mixtures: Spherulitic growth, polymorph stabilization, and morphology change. *Cryst. Growth Des.* **12**, 842–853 (2012). doi: 10.1021/cg2012342
32. F. C. Meldrum, S. Ludwigs, Template-directed control of crystal morphologies. *Macromol. Biosci.* **7**, 152–162 (2007). doi: 10.1002/mabi.200600191; pmid: 17295402
33. Y. Y. Kim *et al.*, A critical analysis of calcium carbonate mesocrystals. *Nat. Commun.* **5**, 4341 (2014). pmid: 25014563
34. M. H. Nielsen *et al.*, Investigating processes of nanocrystal formation and transformation via liquid cell TEM. *Microsc. Microanal.* **20**, 425–436 (2014). doi: 10.1017/S1431927614000294; pmid: 24625923
35. N. D. Burrows, C. R. H. Hale, R. L. Penn, Effect of pH on the kinetics of crystal growth by oriented aggregation. *Cryst. Growth Des.* **13**, 3396–3403 (2013). doi: 10.1021/cg4001939
36. A. Gal *et al.*, Particle accretion mechanism underlies biological crystal growth from an amorphous precursor phase. *Adv. Funct. Mater.* **24**, 5420–5426 (2014). doi: 10.1002/adfm.201400676
37. H. Cölfen, M. Antonietti, Mesocrystals: Inorganic superstructures made by highly parallel crystallization and controlled alignment. *Angew. Chem. Int. Ed.* **44**, 5576–5591 (2005). doi: 10.1002/anie.200500496; pmid: 16035009
38. R. Q. Song, H. Cölfen, Mesocrystals: Ordered nanoparticle superstructures. *Adv. Mater.* **22**, 1301–1330 (2010). doi: 10.1002/adma.200901365; pmid: 20437477
39. M. P. Boneschanscher *et al.*, Long-range orientation and atomic attachment of nanocrystals in 2D honeycomb superlattices. *Science* **344**, 1377–1380 (2014). doi: 10.1126/science.1252642; pmid: 24948734
40. A. F. Wallace *et al.*, Microscopic evidence for liquid-liquid separation in supersaturated $CaCO_3$ solutions. *Science* **341**, 885–889 (2013). doi: 10.1126/science.1230915; pmid: 23970697
41. P. W. Voorhees, The theory of Ostwald ripening. *J. Stat. Phys.* **38**, 231–252 (1985). doi: 10.1007/BF01017860
42. A. J. Bray, Theory of phase-ordering kinetics. *Adv. Phys.* **51**, 481–587 (2002). doi: 10.1080/00018730110117433
43. B. Scheifele, I. Saika-Voivod, R. K. Bowles, P. H. Poole, Heterogeneous nucleation in the low-barrier regime. *Phys. Rev. E Stat. Nonlin. Soft Matter Phys.* **87**, 042407 (2013). doi: 10.1103/PhysRevE.87.042407; pmid: 23679429
44. A. Dey *et al.*, The role of prenucleation clusters in surface-induced calcium phosphate crystallization. *Nat. Mater.* **9**, 1010–1014 (2010). doi: 10.1038/nmat2900; pmid: 21076415
45. P. T. Cardew, R. J. Davey, The kinetics of solvent-mediated phase-transformations. *Proc. R. Soc. London Ser. A-Math. Phys. Eng. Sci.* **398**, 415–428 (1985).
46. T. Y. J. Han, J. Aizenberg, Calcium carbonate storage in amorphous form and its template-induced crystallization. *Chem. Mater.* **20**, 1064–1068 (2008). doi: 10.1021/cm702032v
47. E. M. Pouget *et al.*, The initial stages of template-controlled $CaCO_3$ formation revealed by cryo-TEM. *Science* **323**, 1455–1458 (2009). doi: 10.1126/science.1169434; pmid: 19286549
48. A. Gal *et al.*, Calcite crystal growth by a solid-state transformation of stabilized amorphous calcium carbonate nanospheres in a hydrogel. *Angew. Chem. Int. Ed.* **52**, 4867–4870 (2013). doi: 10.1002/anie.201210329; pmid: 23559356
49. O. Galkin, K. Chen, R. L. Nagel, R. E. Hirsch, P. G. Vekilov, Liquid-liquid separation in solutions of normal and sickle cell hemoglobin. *Proc. Natl. Acad. Sci. U.S.A.* **99**, 8479–8483 (2002). doi: 10.1073/pnas.122055299; pmid: 12070342
50. X. L. Wang, I. M. Chou, W. X. Hu, R. C. Burruss, In situ observations of liquid-liquid phase separation in aqueous $MgSO_4$ solutions: Geological and geochemical implications. *Geochim. Cosmochim. Acta* **103**, 1–10 (2013). doi: 10.1016/j.gca.2012.10.044
51. P. R. ten Wolde, D. Frenkel, Enhancement of protein crystal nucleation by critical density fluctuations. *Science* **277**, 1975–1978 (1997). doi: 10.1126/science.277.5334.1975; pmid: 9302288
52. S. E. Wolf, J. Leiterer, M. Kappl, F. Emmerling, W. Tremel, Early homogenous amorphous precursor stages of calcium carbonate and subsequent crystal growth in levitated droplets. *J. Am. Chem. Soc.* **130**, 12342–12347 (2008). doi: 10.1021/ja800984y; pmid: 18717561
53. M. A. Bewernitz, D. Gebauer, J. Long, H. Cölfen, L. B. Gower, A metastable liquid precursor phase of calcium carbonate and its interactions with polyaspartate. *Faraday Discuss.* **159**, 291–312 (2012). doi: 10.1039/c2fd20080e
54. A. C. Dumetz, A. M. Chockla, E. W. Kaler, A. M. Lenhoff, Protein phase behavior in aqueous solutions: Crystallization, liquid-liquid phase separation, gels, and aggregates. *Biophys. J.* **94**, 570–583 (2008). doi: 10.1529/biophysj.107.116152; pmid: 18160663
55. D. Gebauer, A. Völkel, H. Cölfen, Stable prenucleation calcium carbonate clusters. *Science* **322**, 1819–1822 (2008). pmid: 19095936
56. A. E. S. Van Driessche *et al.*, The role and implications of bassanite as a stable precursor phase to gypsum precipitation. *Science* **336**, 69–72 (2012). doi: 10.1126/science.1215648; pmid: 22491851
57. J. Baumgartner *et al.*, Nucleation and growth of magnetite from solution. *Nat. Mater.* **12**, 310–314 (2013). doi: 10.1038/nmat3558; pmid: 23377292
58. A. Navrotsky, Energetic clues to pathways to biomineralization: Precursors, clusters, and nanoparticles. *Proc. Natl. Acad. Sci. U.S.A.* **101**, 12096–12101 (2004). doi: 10.1073/pnas.0404778101; pmid: 15297621
59. A. Navrotsky, Nanoscale effects on thermodynamics and phase equilibria in oxide systems. *ChemPhysChem* **12**, 2207–2215 (2011). doi: 10.1002/cphc.201100129; pmid: 21744459
60. D. S. Li *et al.*, Growth mechanism of highly branched titanium dioxide nanowires via oriented attachment. *Cryst. Growth Des.* **13**, 422–428 (2013). doi: 10.1021/cg301388e

61. M. Raju, A. C. T. van Duin, K. A. Fichthorn, Mechanisms of oriented attachment of TiO_2 nanocrystals in vacuum and humid environments: Reactive molecular dynamics. *Nano Lett.* **14**, 1836–1842 (2014). doi: 10.1021/nl404533k; pmid: 24601782
62. V. M. Yuwono, N. D. Burrows, J. A. Soltis, R. L. Penn, Oriented aggregation: Formation and transformation of mesocrystal intermediates revealed. *J. Am. Chem. Soc.* **132**, 2163–2165 (2010). doi: 10.1021/ja909769a; pmid: 20112897
63. A. A. Gribb, J. F. Banfield, Particle size effects on transformation kinetics and phase stability in nanocrystalline TiO_2. *Am. Mineral.* **82**, 717–728 (1997).
64. Y. Politi *et al*., Transformation mechanism of amorphous calcium carbonate into calcite in the sea urchin larval spicule. *Proc. Natl. Acad. Sci. U.S.A.* **105**, 17362–17366 (2008). doi: 10.1073/pnas.0806604105; pmid: 18987314
65. A. V. Radha, T. Z. Forbes, C. E. Killian, P. U. P. A. Gilbert, A. Navrotsky, Transformation and crystallization energetics of synthetic and biogenic amorphous calcium carbonate. *Proc. Natl. Acad. Sci. U.S.A.* **107**, 16438–16443 (2010). doi: 10.1073/pnas.1009959107; pmid: 20810918
66. J. Rieger *et al*., Precursor structures in the crystallization/precipitation processes of $CaCO_3$ and control of particle formation by polyelectrolytes. *Faraday Discuss.* **136**, 265–277, discussion 309–328 (2007). doi: 10.1039/b701450c; pmid: 17955814
67. S. Weiner, I. Sagi, L. Addadi, Choosing the crystallization path less traveled. *Science* **309**, 1027–1028 (2005). doi: 10.1126/science.1114920; pmid: 16099970
68. T. M. Davis *et al*., Mechanistic principles of nanoparticle evolution to zeolite crystals. *Nat. Mater.* **5**, 400–408 (2006). doi: 10.1038/nmat1636; pmid: 16617343
69. E. M. Pouget *et al*., The development of morphology and structure in hexagonal vaterite. *J. Am. Chem. Soc.* **132**, 11560–11565 (2010). doi: 10.1021/ja102439r; pmid: 20669942
70. J. Ihli *et al*., Dehydration and crystallization of amorphous calcium carbonate in solution and in air. *Nat. Commun.* **5**, 3169 (2014). doi: 10.1038/ncomms4169; pmid: 24469266
71. C. J. Stephens, S. F. Ladden, F. C. Meldrum, H. K. Christenson, Amorphous calcium carbonate is stabilized in confinement. *Adv. Funct. Mater.* **20**, 2108–2115 (2010). doi: 10.1002/adfm.201000248
72. C. C. Tester *et al*., In vitro synthesis and stabilization of amorphous calcium carbonate (ACC) nanoparticles within liposomes. *CrystEngComm* **13**, 3975–3978 (2011). doi: 10.1039/c1ce05153a
73. Q. Hu *et al*., The thermodynamics of calcite nucleation at organic interfaces: Classical vs. non-classical pathways. *Faraday Discuss.* **159**, 509–523 (2012). doi: 10.1039/c2fd20124k
74. H. Zhang, B. Gilbert, F. Huang, J. F. Banfield, Water-driven structure transformation in nanoparticles at room temperature. *Nature* **424**, 1025–1029 (2003). doi: 10.1038/nature01845; pmid: 12944961
75. L. Addadi, S. Raz, S. Weiner, Taking advantage of disorder: Amorphous calcium carbonate and its roles in biomineralization. *Adv. Mater.* **15**, 959–970 (2003). doi: 10.1002/adma.200300381
76. L. Yang, C. E. Killian, M. Kunz, N. Tamura, P. U. P. A. Gilbert, Biomineral nanoparticles are space-filling. *Nanoscale* **3**, 603–609 (2011). doi: 10.1039/C0NR00697A; pmid: 21082124
77. C. C. Tester *et al*., Time-resolved evolution of short- and long-range order during the transformation of amorphous calcium carbonate to calcite in the sea urchin embryo. *Adv. Funct. Mater.* **23**, 4185–4194 (2013). doi: 10.1002/adfm.201203400
78. J. L. Zryd, W. R. Burghardt, Phase-separation, crystallization, and structure formation in immiscible polymer-solutions. *J. Appl. Polym. Sci.* **57**, 1525–1537 (1995). doi: 10.1002/app.1995.070571212
79. W. L. Marshall, C. E. Hall, R. E. Mesmer, The system dipotassium hydrogen phosphate-water at high temperatures (100–400°C): Liquid-liquid immiscibility and concentrated-solutions. *J. Inorg. Nucl. Chem.* **43**, 449–455 (1981). doi: 10.1016/0022-1902(81)80482-4
80. H. Z. Zhang, B. Chen, Y. Ren, G. A. Waychunas, J. F. Banfield, Response of nanoparticle structure to different types of surface environments: Wide-angle x-ray scattering and molecular dynamics simulations. *Phys. Rev. B* **81**, 125444 (2010). doi: 10.1103/PhysRevB.81.125444
81. F. Huang, B. Gilbert, H. Zhang, J. F. Banfield, Reversible, surface-controlled structure transformation in nanoparticles induced by an aggregation state. *Phys. Rev. Lett.* **92**, 155501 (2004). doi: 10.1103/PhysRevLett.92.155501; pmid: 15169293
82. F. M. Michel *et al*., Ordered ferrimagnetic form of ferrihydrite reveals links among structure, composition, and magnetism. *Proc. Natl. Acad. Sci. U.S.A.* **107**, 2787–2792 (2010). doi: 10.1073/pnas.0910170107; pmid: 20133643
83. T. Gibaud, P. Schurtenberger, A closer look at arrested spinodal decomposition in protein solutions. *J. Phys. Condens. Matter* **21**, 322201 (2009). doi: 10.1088/0953-8984/21/32/322201; pmid: 21693959
84. A. A. Chernov, E. I. Givargizov, *Modern Crystallography III: Crystal Growth*. Springer Series in Solid-State Sciences (Springer, Berlin, 1984), vol. 36.
85. B. Derjaguin, L. Landau, Theory of stability of highly charged liophobic sols and adhesion of highly charged particles in solutions of electrolytes. *Zhurnal Eksperimentalnoi Teor. Fiz.* **15**, 663–682 (1945).
86. E. J. W. Verwey, J. T. G. Overbeek, K. van Nes, *Theory of the Stability of Lyophobic Colloids: The Interaction of Sol Particles Having an Electric Double Layer* (Elsevier, New York, 1948).
87. H. Zhang, J. J. De Yoreo, J. F. Banfield, A unified description of attachment-based crystal growth. *ACS Nano* **8**, 6526–6530 (2014). doi: 10.1021/nn503145w; pmid: 25000275
88. H. Z. Zhang, J. F. Banfield, Energy calculations predict nanoparticle attachment orientations and asymmetric crystal formation. *J. Phys. Chem. Lett.* **3**, 2882–2886 (2012). doi: 10.1021/jz301161j
89. G. V. Gibbs *et al*., Role of long-range intermolecular forces in the formation of inorganic nanoparticle clusters. *J. Phys. Chem. A* **115**, 12933–12940 (2011). doi: 10.1021/jp204044k; pmid: 21939256
90. J. J. De Yoreo, P. G. Vekilov, in *Biomineralization,* P. M. Dove, J. J. DeYoreo, S. Weiner, Eds. (Mineralogical Society of America, Washington, DC, 2003), vol. 54, pp. 57–93.
91. L. O. Hedges, S. Whitelam, Patterning a surface so as to speed nucleation from solution. *Soft Matter* **8**, 8624–8635 (2012). doi: 10.1039/c2sm26038g
92. A. J. Page, R. P. Sear, Heterogeneous nucleation in and out of pores. *Phys. Rev. Lett.* **97**, 065701 (2006). doi: 10.1103/PhysRevLett.97.065701; pmid: 17026175
93. Y. W. Wang, H. K. Christenson, F. C. Meldrum, Confinement leads to control over calcium sulfate polymorph. *Adv. Funct. Mater.* **23**, 5615–5623 (2013). doi: 10.1002/adfm.201300861
94. C. C. Tester, M. L. Whittaker, D. Joester, Controlling nucleation in giant liposomes. *Chem. Commun.* **50**, 5619–5622 (2014). doi: 10.1039/c4cc01457j; pmid: 24728476
95. N. Vidavsky *et al*., Initial stages of calcium uptake and mineral deposition in sea urchin embryos. *Proc. Natl. Acad. Sci. U.S.A.* **111**, 39–44 (2014). doi: 10.1073/pnas.1312833110; pmid: 24344263
96. E. V. Shevchenko, D. V. Talapin, C. B. Murray, S. O'Brien, Structural characterization of self-assembled multifunctional binary nanoparticle superlattices. *J. Am. Chem. Soc.* **128**, 3620–3637 (2006). doi: 10.1021/ja0564261; pmid: 16536535
97. F. Nudelman *et al*., The role of collagen in bone apatite formation in the presence of hydroxyapatite nucleation inhibitors. *Nat. Mater.* **9**, 1004–1009 (2010). doi: 10.1038/nmat2875; pmid: 20972429
98. D. Gebauer, H. Cölfen, A. Verch, M. Antonietti, The multiple roles of additives in $CaCO_3$ crystallization: A quantitative case study. *Adv. Mater.* **21**, 435–439 (2009). doi: 10.1002/adma.200801614
99. T. Kato, Polymer/calcium carbonate layered thin-film composites. *Adv. Mater.* **12**, 1543–1546 (2000). doi: 10.1002/1521-4095(200010)12:20<1543::AID-ADMA1543>3.0.CO;2-P
100. B. Cantaert *et al*., Think positive: Phase separation enables a positively charged additive to induce dramatic changes in calcium carbonate morphology. *Adv. Funct. Mater.* **22**, 907–915 (2012). doi: 10.1002/adfm.201102385
101. J. J. M. Lenders *et al*., A bioinspired coprecipitation method for the controlled synthesis of magnetite nanoparticles. *Cryst. Growth Des.* **14**, 5561–5568 (2014). doi: 10.1021/cg500816z
102. M. Suzuki *et al*., An acidic matrix protein, Pif, is a key macromolecule for nacre formation. *Science* **325**, 1388–1390 (2009). doi: 10.1126/science.1173793; pmid: 19679771
103. I. M. Weiss, S. Kaufmann, K. Mann, M. Fritz, Purification and characterization of perlucin and perlustrin, two new proteins from the shell of the mollusc *Haliotis laevigata*. *Biochem. Biophys. Res. Commun.* **267**, 17–21 (2000). doi: 10.1006/bbrc.1999.1907; pmid: 10623567
104. G. Fu, S. Valiyaveettil, B. Wopenka, D. E. Morse, $CaCO_3$ biomineralization: Acidic 8-kDa proteins isolated from aragonitic abalone shell nacre can specifically modify calcite crystal morphology. *Biomacromolecules* **6**, 1289–1298 (2005). doi: 10.1021/bm049314v; pmid: 15877344
105. R. A. Metzler *et al*., Nacre protein fragment templates lamellar aragonite growth. *J. Am. Chem. Soc.* **132**, 6329–6334 (2010). doi: 10.1021/ja909735y; pmid: 20397648
106. R. F. Lobo, S. I. Zones, M. E. Davis, Structure-direction in zeolite synthesis. *J. Incl. Phenom. Mol. Recogn. Chem.* **21**, 47–78 (1995).
107. J. F. Banfield, S. A. Welch, H. Zhang, T. T. Ebert, R. L. Penn, Aggregation-based crystal growth and microstructure development in natural iron oxyhydroxide biomineralization products. *Science* **289**, 751–754 (2000). doi: 10.1126/science.289.5480.751; pmid: 10926531
108. J. P. Grotzinger, A. H. Knoll, Stromatolites in Precambrian carbonates: Evolutionary mileposts or environmental dipsticks? *Annu. Rev. Earth Planet. Sci.* **27**, 313–358 (1999). doi: 10.1146/annurev.earth.27.1.313; pmid: 11543060
109. M. Kuno, An overview of solution-based semiconductor nanowires: Synthesis and optical studies. *Phys. Chem. Chem. Phys.* **10**, 620–639 (2008). doi: 10.1039/B708296G; pmid: 19791445
110. D. B. Suyatin *et al*., Electrical properties of self-assembled branched InAs nanowire junctions. *Nano Lett.* **8**, 1100–1104 (2008). doi: 10.1021/nl073193y; pmid: 18355057
111. M. J. Bierman, S. Jin, Potential applications of hierarchical branching nanowires in solar energy conversion. *Energy Environ. Sci.* **2**, 1050–1059 (2009). doi: 10.1039/b912095e
112. I. Herman *et al*., Hierarchical weeping willow nano-tree growth and effect of branching on dye-sensitized solar cell efficiency. *Nanotechnology* **23**, 194005 (2012). doi: 10.1088/0957-4484/23/19/194005; pmid: 22538967
113. L. Zhou, P. O'Brien, Mesocrystals: A new class of solid materials. *Small* **4**, 1566–1574 (2008). doi: 10.1002/smll.200800520; pmid: 18844308
114. S. Furukawa, J. Reboul, S. Diring, K. Sumida, S. Kitagawa, Structuring of metal-organic frameworks at the mesoscopic/macroscopic scale. *Chem. Soc. Rev.* **43**, 5700–5734 (2014). doi: 10.1039/C4CS00106K; pmid: 24811425
115. M. E. Davis, Ordered porous materials for emerging applications. *Nature* **417**, 813–821 (2002). doi: 10.1038/nature00785; pmid: 12075343
116. R. L. Penn, J. F. Banfield, Morphology development and crystal growth in nanocrystalline aggregates under hydrothermal conditions: Insights from titania. *Geochim. Cosmochim. Acta* **63**, 1549–1557 (1999). doi: 10.1016/S0016-7037(99)00037-X
117. S. Kumar, Z. Wang, R. L. Penn, M. Tsapatsis, A structural resolution cryo-TEM study of the early stages of MFI growth. *J. Am. Chem. Soc.* **130**, 17284–17286 (2008). doi: 10.1021/ja8063167; pmid: 19049299
118. Y. Oaki, H. Imai, The hierarchical architecture of nacre and its mimetic material. *Angew. Chem. Int. Ed.* **44**, 6571–6575 (2005). doi: 10.1002/anie.200500338; pmid: 16163773
119. J. Mahamid *et al*., Mapping amorphous calcium phosphate transformation into crystalline mineral from the cell to the bone in zebrafish fin rays. *Proc. Natl. Acad. Sci. U.S.A.* **107**, 6316–6321 (2010). doi: 10.1073/pnas.0914218107; pmid: 20308589
120. V. K. Ivanov, P. P Fedorov, A. Y. Baranchikov, V. V. Osiko, Oriented attachment of particles: 100 years of investigations of non-classical crystal growth. *Russ. Chem. Rev.* **83**, 1204–1222 (2014). doi: 10.1070/RCR4453

ACKNOWLEDGMENTS

This article evolved from presentations and discussions at the workshop "Crystallization by Particle Attachment" held in December 2013 in Berkeley, California, sponsored by the Council on Geosciences of the U.S. Department of Energy, Office of Science, Office of Basic Energy Sciences. The authors thank the members of the council for their encouragement and assistance in developing this workshop. We also thank L. Addadi and S. Weiner for valuable comments and advice. In addition, the authors acknowledge the agencies that provided funding for their individual research programs, without which this workshop and article would not have been possible.

10.1126/science.aaa6760

RESEARCH ARTICLE SUMMARY

CELL DEATH

Control of signaling-mediated clearance of apoptotic cells by the tumor suppressor p53

Kyoung Wan Yoon, Sanguine Byun, Eunjeong Kwon, So-Young Hwang, Kiki Chu, Masatsugu Hiraki, Seung-Hee Jo, Astrid Weins, Samy Hakroush, Angelika Cebulla, David B. Sykes, Anna Greka, Peter Mundel, David E. Fisher, Anna Mandinova, Sam W. Lee*

INTRODUCTION: Programmed cell death occurs throughout life in all tissues of the body, and more than a billion cells die every day as part of normal processes. Thus, rapid and efficient clearance of cell corpses is a vital prerequisite for homeostatic maintenance of tissue health. Failure to clear dying cells can lead to the accumulation of autoantigens in tissues that foster diseases, such as chronic inflammation, autoimmunity, and developmental abnormalities. In the normal immune system, phagocytic engulfment of apoptotic cells is accompanied by induction of a certain degree of immune tolerance in order to prevent self-antigen recognition. Over the past few decades, enormous efforts have been made toward understanding various mechanisms of tumor suppressor p53–mediated apoptosis. However, the involvement of p53 in postapoptosis has yet to be addressed.

RATIONALE: One of the most intriguing, yet enigmatic, questions in studying homeostatic control of efficient dead cell clearance and proper immune tolerance is how these two essential activities are interrelated: The complexity of these processes is demonstrated by the many receptors and signaling pathways involved in the engulfment of apoptotic cells and stringent discrimination of self antigens from nonself antigens. Thus, there must be key connection(s) linking the balance between immune homeostasis and inflammation. In addition to the antitumor functions of p53, p53 has been implicated in immune responses and inflammatory diseases, with various roles in the immune system becoming apparent. We identified a postapoptotic target gene of p53, *Death Domain1α* (*DD1α*), that is responsive to genotoxic stresses and expressed in immune cells. DD1α appears to function as an immunoregulator of T cell tolerance. We hypothesized that p53 controls signaling-mediated phagocytosis of apoptotic cells through its target, DD1α. We determined that DD1α functions as an engulfment ligand or receptor that is involved in homophilic intermolecular interaction at intercellular junctions of apoptotic cells and macrophages. We also addressed whether DD1α deficiency caused any defects in dead cell clearance in vivo.

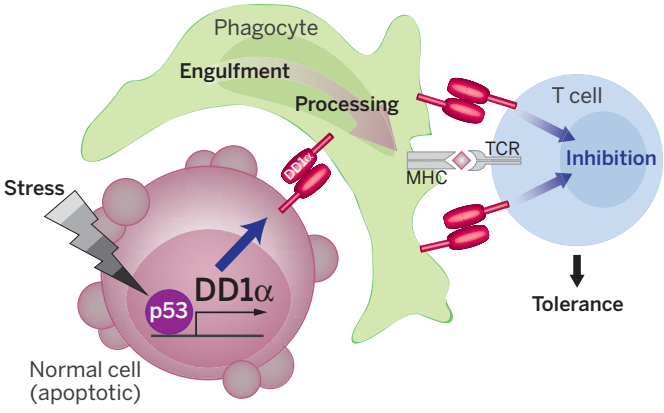

p53-dependent accumulation of DD1α and its involvement in dead cell clearance and immune tolerance. DD1α functions as an engulfment ligand that participates in homophilic intermolecular interaction at intercellular junctions of apoptotic cells and phagocytes. p53 induction of DD1α is a critical step in ensuring proper clearance of cell corpses to warrant the efficient generation of precise immune responses, leading to immune tolerance.

RESULTS: DD1α has similarity with several members of the immunoglobulin superfamily with the extracellular immunoglobulin V (IgV) domain, such as TIM family proteins and an immune checkpoint regulator, PD-L1. We found that the p53 induction and maintenance of DD1α expression in apoptotic cells and its subsequent functional intercellular homophilic interaction between apoptotic cells and macrophages are required for engulfment of apoptotic cells. *DD1α*-deficient mice showed less reduction in organ size and cell number after ionizing radiation (IR), owing to defective dead cell clearance. *DD1α*-null mice are viable and indistinguishable in appearance from wild-type littermates at an early age. However, at a later age, *DD1α* deficiency resulted in the development of autoimmune phenotypes and prominent formation of immune infiltrates in the skin, lung, and kidney, which indicated an immune dysregulation and breakdown of self-tolerance in *DD1α*-null mice. We demonstrated that DD1α also plays an important role as an intercellular homophilic receptor on T cells, which suggests that DD1α is a key-connecting molecule linking postapoptotic processes to immune surveillance. We found that DD1α deficiency in T cells impaired DD1α-mediated inhibitory activity of T cell proliferation. These data indicate that potential homophilic DD1α interactions are important for the DD1α-mediated T cell inhibitory role. Therefore, the results indicate a role for p53 in regulating expression of immune checkpoint regulators, including PD-1, PD-L1, and DD1α.

ON OUR WEB SITE

Read the full article at http://dx.doi.org/10.1126/science.1261669

CONCLUSION: We found that the tumor suppressor p53 controls signaling-mediated phagocytosis of apoptotic cells through its target *DD1α*, which suggests that p53 promotes both the proapoptotic pathway and postapoptotic events. DD1α functions as an engulfment ligand that engages in homophilic intermolecular interaction at intercellular junctions of apoptotic cells and macrophages. *DD1α*-deficient mice showed in vivo defects in clearing dying cells that led to damage to multiple organs indicative of immune dysfunction. p53-induced expression of DD1α is a vital phase for the phagocytic engulfment process of dead cells and then facilitates the stepwise priming of immune surveillance. As a downstream target of the tumor suppressor p53, DD1α activation may extend the repertoire of p53 activities to "guardian of the immune integrity." ■

The list of author affiliations is available in the full article online.
*Corresponding author. E-mail: swlee@mgh.harvard.edu
Cite this paper as K. W. Yoon *et al.*, *Science* **349**, 1261669 (2015). DOI: 10.1126/science.1261669

RESEARCH ARTICLE

CELL DEATH

Control of signaling-mediated clearance of apoptotic cells by the tumor suppressor p53

Kyoung Wan Yoon,[1] Sanguine Byun,[1] Eunjeong Kwon,[1] So-Young Hwang,[1] Kiki Chu,[1] Masatsugu Hiraki,[1] Seung-Hee Jo,[1] Astrid Weins,[2] Samy Hakroush,[3] Angelika Cebulla,[3] David B. Sykes,[4] Anna Greka,[5] Peter Mundel,[3] David E. Fisher,[1] Anna Mandinova,[1,6] Sam W. Lee[1,6]*

The inefficient clearance of dying cells can lead to abnormal immune responses, such as unresolved inflammation and autoimmune conditions. We show that tumor suppressor p53 controls signaling-mediated phagocytosis of apoptotic cells through its target, *Death Domain1α* (*DD1α*), which suggests that p53 promotes both the proapoptotic pathway and postapoptotic events. DD1α appears to function as an engulfment ligand or receptor that engages in homophilic intermolecular interaction at intercellular junctions of apoptotic cells and macrophages, unlike other typical scavenger receptors that recognize phosphatidylserine on the surface of dead cells. *DD1α*-deficient mice showed in vivo defects in clearing dying cells, which led to multiple organ damage indicative of immune dysfunction. p53-induced expression of DD1α thus prevents persistence of cell corpses and ensures efficient generation of precise immune responses.

During development, tissue restoration, and response to injury, numerous cells are damaged and destined to undergo cell death or apoptosis. Thus, rapid and efficient clearance of cell corpses is a vital prerequisite for homeostatic maintenance of tissue health (*1*, *2*). Failure to clear dying cells can lead to the accumulation of autoantigens in tissues that foster diseases, such as chronic inflammatory diseases, autoimmune diseases, and developmental abnormalities (*1*–*4*). Engulfment of apoptotic cells is an active process coordinated by receptors on phagocytes and ligands on apoptotic cells (*5*). The exposure of phosphatidylserine (PtdSer) on the surface of dying cells is a key signal that facilitates recognition and clearance by neighboring phagocytes (*6*). PtdSer on apoptotic cells can be recognized directly by phagocytic receptors—such as T-cell immunoglobulin and mucin domain-1, -3, and -4 (TIM-1, TIM-3, and TIM-4); brain-specific angiogenesis inhibitor 1 (BAI1); and Stabilin-2—or indirectly via soluble bridging proteins [milk fat globule–EGF–factor 8 (MFG-E8) and complement component (C1q)] to engage in engulfment of apoptotic cells (*7*–*13*).

The p53 tumor suppressor is indispensable for maintenance of genomic integrity (*14*–*16*). p53 functions as a transcription factor that is activated by various cellular stresses and governs multiple core programs in cells, including cell cycle arrest and apoptosis (*17*, *18*). p53 has been implicated in immune responses and inflammatory diseases (*19*–*22*). Several interferon (IFN)–inducible genes—such as interferon regulatory factors 5 and 9 (*IRF5* and *IRF9*), interferon-stimulated gene 15 (*ISG15*), and Toll-like receptor 3 (*TLR3*)—are also p53 targets (*20*, *23*–*25*). Among others, it has been reported that the expression of forkhead box P3 (*Foxp3*), a master regulator of regulatory T cells (T_{regs}), is up-regulated by p53, and the number of T_{regs} was significantly reduced in *p53*-deficient mice (*26*, *27*). p53 also stimulates innate immunity by modulating macrophage function to non–cell-autonomously suppress tumorigenesis (*28*). Furthermore, although it remains unknown how p53 suppresses autoimmunity and excessive inflammation, accumulating studies have provided convincing evidence that p53 deficiency is closely associated with the development of autoimmune and inflammatory diseases in mice (*21*, *27*, *29*–*34*).

Results

Identification of a postapoptotic target gene of p53, DD1α, an immunoglobulin superfamily receptor

Through microarray analysis of cDNA expression in EJ-p53 human bladder tumor cells with a tetracycline-regulated wild-type p53 (Wt-p53) overexpression system (*35*), we identified the gene encoding a transmembrane receptor, *Death Domain1α* (*DD1α*), as a downstream target gene of p53. *DD1α* mRNA and protein abundance were increased in response to genotoxic stress in a p53-dependent manner (Fig. 1A and figs. S1 and S2). The characterization of candidate p53 DNA binding consensus sequences by using reporter gene assays, chromatin immunoprecipitation–quantitative real-time polymerase chain reaction (ChIP-qPCR) and electrophoretic mobility-shift assay indicated that *DD1α* was a direct transcriptional target of p53 and that a consensus p53-binding site located at −5401 to −5420 of the *DD1α* promoter conferred p53-dependent DD1α transactivation (Fig. 1B). DD1α is a member of the immunoglobulin superfamily and is also known as Gi24 or VISTA or PD-1H or Dies1 (*36*–*39*). The DD1α protein migrated at ~50 kD on Western blots. Treatment of cells with the glycosylation inhibitor tunicamycin resulted in migration at ~30 kD, its predicted size (fig. S3). Northern blotting of various human tissues demonstrated relatively higher expression of *DD1α* in blood leukocytes, placenta, spleen, and heart and low amounts in lung, kidney, small intestine, and brain (Fig. 1C). Analysis of public database information (http://biogps.org/#goto=genereport&id=64115) (*40*, *41*) also indicated that DD1α is expressed in immune cells, including macrophages, dendritic cells, monocytes, and myeloid and T cells. Although we identified *DD1α* as a bona fide p53 target gene, the depletion of endogenous *DD1α* by short hairpin RNAs (shRNAs) targeting different sequences in *DD1α* mRNA did not affect the DNA damage–induced apoptotic responses (figs. S4, S5C, S6, and S7B) in various cell systems carrying Wt-p53, which suggests that *DD1α* may not function as a typical p53 target gene. DD1α has similarity with several members of the immunoglobulin superfamily with the immunoglobulin variable (IgV) domain (Fig. 1C). We sought to determine whether TIM family proteins, as well as immune checkpoint coinhibitors, programmed cell death 1 (PD-1), and programmed death-ligand 1 (PD-L1), might be regulated by p53 as seen for DD1α. The TIM family proteins, including TIM-1, TIM-2/3, and TIM-4, did not show increased expression in response to p53, but genes encoding PD-L1 and its receptor PD-1 showed increased expression in response to the p53 activator Nutlin-3 small molecule (10 μM) in MCF7 human breast cancer cells (Fig. 1D). Genotoxic stimuli also activated transcription of *PD-L1* and *PD-1* in a p53-dependent manner. We verified p53-mediated activation of PD-L1 or PD-1 expression in several p53 expression systems (Fig. 1D).

p53-induced expression of DD1α is essential for engulfment of apoptotic cells by phagocytes

TIM family molecules have an important role in phagocytosis of apoptotic cells (*8*, *9*, *11*). Because DD1α is structurally similar to TIM family proteins, we investigated whether increased abundance of DD1α induction on apoptotic cells could proceed to phagocytosis of dying cells. We depleted

[1]Cutaneous Biology Research Center, Massachusetts General Hospital and Harvard Medical School, Building 149, 13th Street, Charlestown, MA 02129, USA. [2]Department of Pathology, Brigham and Women's Hospital, and Harvard Medical School, Boston, MA 02115, USA. [3]Division of Nephrology, Department of Medicine, Massachusetts General Hospital, Boston, MA 02114, USA. [4]Center for Regenerative Medicine and Technology, Massachusetts General Hospital and Harvard Medical School, Boston, MA 02114, USA. [5]Department of Medicine, Glom-NExT Center for Glomerular Kidney Disease and Novel Experimental Therapeutics, Brigham and Women's Hospital, and Harvard Medical School, Boston, MA 02115, USA. [6]Broad Institute of Harvard and MIT, 7 Cambridge Center, Cambridge, MA 02142, USA.
*Corresponding author. E-mail: swlee@mgh.harvard.edu

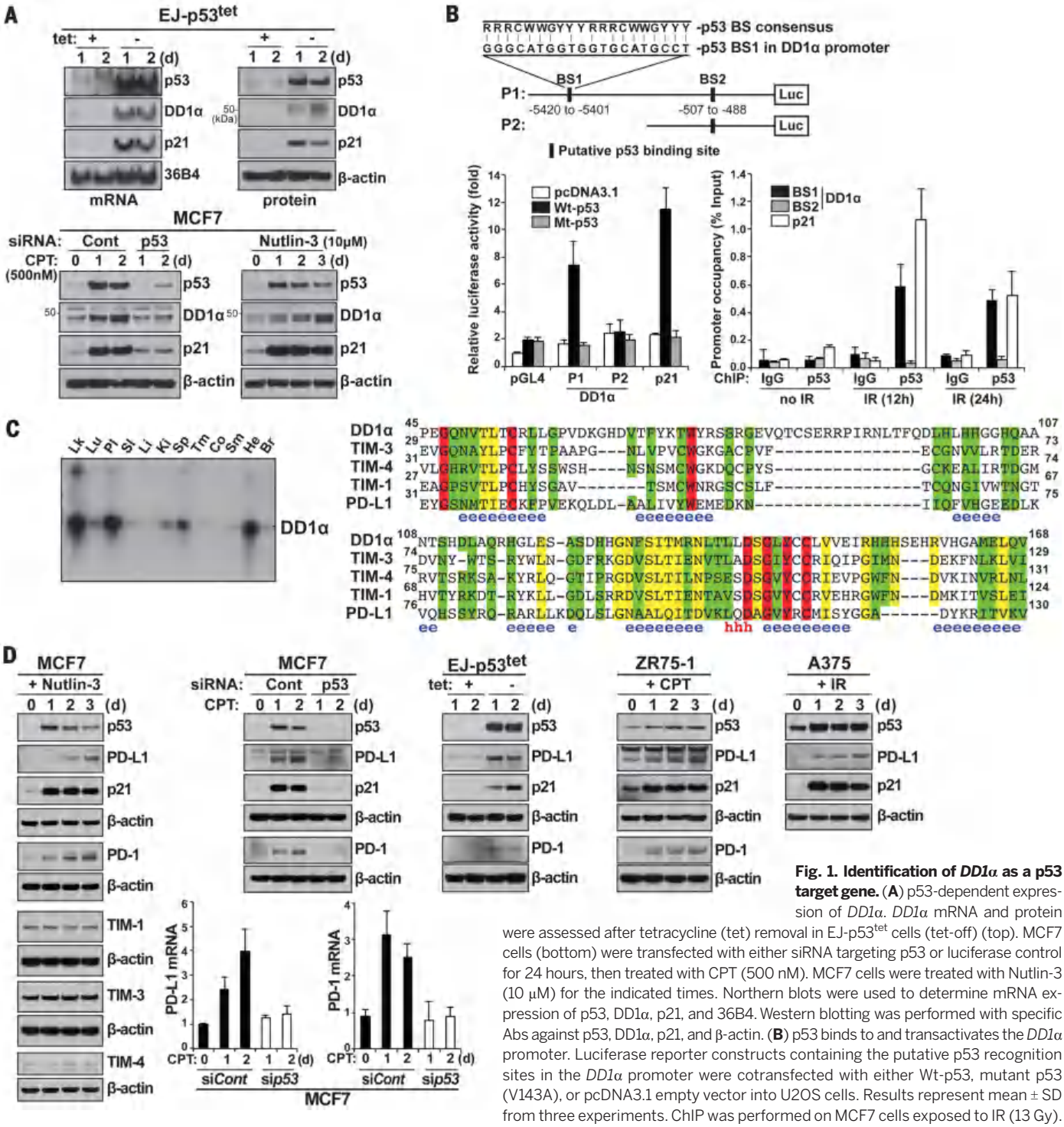

Fig. 1. Identification of *DD1α* as a p53 target gene. (**A**) p53-dependent expression of *DD1α*. *DD1α* mRNA and protein were assessed after tetracycline (tet) removal in EJ-p53^{tet} cells (tet-off) (top). MCF7 cells (bottom) were transfected with either siRNA targeting p53 or luciferase control for 24 hours, then treated with CPT (500 nM). MCF7 cells were treated with Nutlin-3 (10 μM) for the indicated times. Northern blots were used to determine mRNA expression of p53, DD1α, p21, and 36B4. Western blotting was performed with specific Abs against p53, DD1α, p21, and β-actin. (**B**) p53 binds to and transactivates the *DD1α* promoter. Luciferase reporter constructs containing the putative p53 recognition sites in the *DD1α* promoter were cotransfected with either Wt-p53, mutant p53 (V143A), or pcDNA3.1 empty vector into U2OS cells. Results represent mean ± SD from three experiments. ChIP was performed on MCF7 cells exposed to IR (13 Gy). Immunoprecipitation was carried out with Ab against p53 (DO-1) or mouse IgG (negative control). The % input of coprecipitating DNAs was measured by qPCR and presented as mean ± SD (n = 3). (**C**) The expression of human *DD1α* mRNA was analyzed by Northern blotting from various human tissues, including blood leukocyte (Lk), lung (Lu), placenta (Pl), small intestine (Sl), liver (Li), kidney (Ki), spleen (Sp), thymus (Tm), colon (Co), skeletal muscle (Sm), heart (He), and brain (Br). Multiple sequence alignment of the IgV domains of DD1α and its homologous proteins. The predicted secondary structures are shown below the alignment as blue e for β strand and red h for α helix. The identical amino acids are in red box, the conserved amino acids are in yellow box, and the consensus amino acids are in green box. (**D**) p53-dependent expression of immune checkpoint regulators PD-1 and PD-L1. MCF7 cells were treated with 10 μM Nutlin-3 for 1 to 3 days. MCF7 cells were transfected with control siRNA or p53 siRNA for 24 hours and treated with 500 nM CPT or DMSO for 1 or 2 days. The levels of indicated proteins (TIM-1, TIM-3, TIM-4, PD-L1, and PD-1) were analyzed by Western blot analysis. Total RNAs from control siRNA or p53 siRNA transfected MCF7 cells were assessed for mRNA levels of PD-1 or PD-L1 by real-time quantitative PCR. *PD-1* or *PD-L1* mRNA levels were normalized to 36B4 expression and shown as mean ± SD (n = 3). ZR75-1 cells treated with 500 nM CPT or A375 cells exposed to IR (13 Gy) for indicated times.

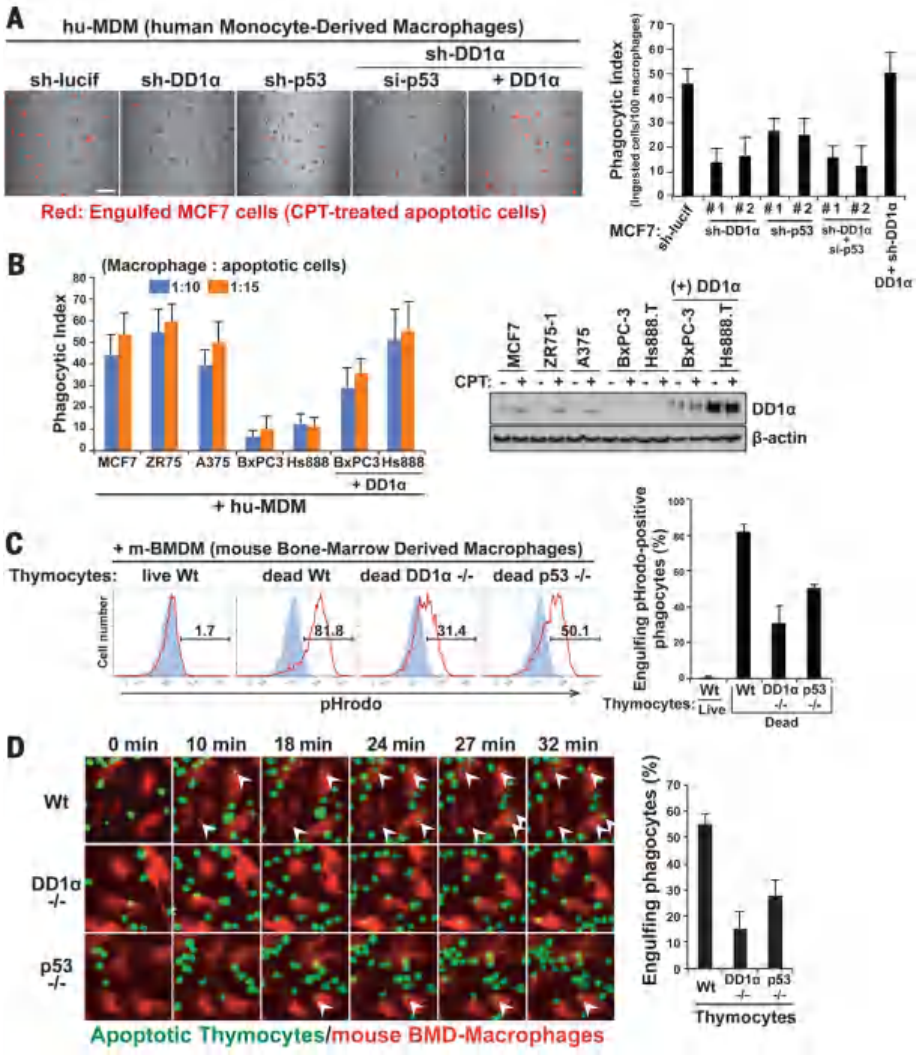

Fig. 2. DD1α plays essential roles in apoptotic cell engulfment. (**A**) DD1α on apoptotic cells contributes to apoptotic cell engulfment. MCF7 cells were transfected with shRNAs including control (luciferase) or DD1α (two different target sequences: #1, #2) or p53 (two different target sequences: #1, #2) and were treated with CPT (10 to 20 μM) for 48 hours to induce apoptosis. Then, apoptotic MCF7 cells were labeled with pHrodo, incubated with hu-MDMs for 2 hours, and examined by immunofluorescence microscopy to detect phagocytosis (red fluorescence: engulfed MCF7 cells). Where indicated, MCF7 cells expressing *DD1α* shRNA (#1) were transfected for 24 hours with siRNA targeting p53 or a vector encoding DD1α before the phagocytosis assay. More than 400 macrophages were counted. Data are mean ± SD from three experiments. The representative images of phagocytosis with control, DD1α, p53, both *DD1α* and p53 knockdowned, and DD1α-reintroduced MCF7 cells plus hu-MDMs are shown. Scale bar, 100 μm. (**B**) Resistance of *DD1α*$^{-/-}$ cancer cells to phagocytosis. Phagocytic indices of DD1α-induced cancer cells (MCF7, ZR75-1, A375), DD1α-nonresponsive cancer cells (BxPC-3, Hs888.T), and DD1α-reintroduced DD1α-absent cancer cells (BxPC-3/DD1α, Hs888.T/DD1α) were determined using hu-MDMs, as shown in Fig. 2A. The levels of DD1α protein were examined by Western blot analysis. (**C**) Engulfment of Wt, *DD1α*$^{-/-}$, and *p53*$^{-/-}$ apoptotic thymocytes by mouse bone marrow–derived macrophages (m-BMDMs) isolated from Wt mice was assessed by flow cytometry analysis. Thymocytes isolated from Wt, *DD1α*$^{-/-}$, or *p53*$^{-/-}$ mice were exposed to IR (2 to 10 Gy) to induce apoptotic populations. The pHrodo-labeled mouse thymocytes (live or apoptotic: live Wt, dead Wt, dead *DD1α*$^{-/-}$, or dead *p53*$^{-/-}$) were incubated with Wt m-BMDMs for 30 min. Phagocytosis was determined by the percentage of macrophages containing positive pHrodo signal. Data are shown as mean ± SD and representative of three independent experiments. (**D**) Engulfment of Wt, *DD1α*$^{-/-}$, and *p53*$^{-/-}$ apoptotic thymocytes by m-BMDMs was assessed by time-lapse imaging analysis. CFSE (green)–labeled apoptotic Wt, *DD1α*$^{-/-}$, or *p53*$^{-/-}$ thymocytes were incubated with PKH26 red-labeled Wt m-BMDMs. The images of phagocytosis were taken every 1 min after incubation. The representative images of engulfments were shown, and arrowheads indicate the engulfed thymocytes. Data represent mean ± SD from three different experiments.

DD1α and p53 expression in MCF7 cells exposed to the apoptotic stimulus camptothecin (CPT) with two different *DD1α* shRNAs or *p53* shRNAs (fig. S4A). About 60% of MCF7 cells expressing sh-luciferase (control), sh-DD1α, sh-p53, or both sh-DD1α and si-p53 were apoptotic after CPT treatment (fig. S4B). We used a pH-sensitive dye (pHrodo), which emits red fluorescence only when located in the phagosome (pH ~5), to distinguish engulfed cells from unengulfed cells, and we calculated the phagocytic index (number of ingested cells per 100 macrophages) (*42*). To examine the functional role of DD1α or p53 in engulfment of dead cells, we used freshly isolated human monocyte–derived macrophages (hu-MDMs) and measured engulfment of CPT-treated apoptotic MCF7 cells. When control apoptotic MCF7 cells were incubated with hu-MDMs, the phagocytic index was ~50 or higher (Fig. 2A), which indicated that macrophages efficiently engulfed most of the apoptotic MCF7 cells present. However, when DD1α- or p53-depleted MCF7 cells, or MCF7 cells depleted of both, were mixed with hu-MDMs, macrophages engulfed a lower number of apoptotic cells (phagocytic index of 10 to 25 for DD1α-depleted, ~30 for p53-depleted, and 10 to 25 for both p53 and DD1α-depleted) (Fig. 2A). Reexpression of DD1α in DD1α-depleted MCF7 cells restored engulfment amounts to similar to those of control cells (Fig. 2A). ZR75-1 human breast cancer cells with Wt-p53 were also used to carry out the phagocytosis assay. Consistent with the behavior of MCF7 cells, when apoptotic ZR75-1 cells were incubated with hu-MDMs, DD1α or p53 depletion also decreased engulfment by macrophages (fig. S5). We also used two human cancer cell lines (BxPC-3, human pancreatic cancer cell line; and Hs888.T, human osteosarcoma cell line) that had very low DD1α expression, and we found that expression of DD1α was not increased by CPT (Fig. 2B, right). Apoptotic cells of both BxPC-3 and Hs888.T were less efficiently engulfed by hu-MDMs than by DD1α-expressing cell lines, such as MCF7, ZR75-1, and A375 (human melanoma cell line) (Fig. 2B, left, and fig. S6). However, ectopic expression of DD1α-HA in BxPC-3 and Hs888.T cells restored engulfment of dead cells by macrophages, which suggested that DD1α expression was sufficient to promote apoptotic cell engulfment by phagocytes (Fig. 2B).

We further examined the effects of p53 or DD1α deficiency on the phagocytosis of apoptotic cells with genetically modified mouse cells. Thymocytes isolated from wild-type (Wt), *DD1α*$^{-/-}$, and *p53*$^{-/-}$ mice were exposed to ionizing radiation (IR) to induce apoptosis and activate DD1α expression. In Wt mouse thymocytes, but not *p53*$^{-/-}$ thymocytes, IR induced accumulation of *DD1α* mRNA expression, which indicated that the regulation of DD1α by p53 is also conserved in mice (fig. S7A). The IR-induced apoptotic responses of Wt and *DD1α*$^{-/-}$ thymocytes were comparable, but *p53*$^{-/-}$ thymocytes showed less apoptosis in response to IR. To use a similar apoptotic population of cells for each phagocytosis assay, we increased the dose of IR to *p53*$^{-/-}$ thymocytes (fig. S7B) in order to increase the proportion of

apoptotic cells. About 60 to 70% of thymocytes from Wt, *DD1α*$^{-/-}$, and *p53*$^{-/-}$ mice underwent apoptosis. Such cells were incubated with bone marrow–derived macrophages (m-BMDMs) from Wt mice, and the phagocytic potential was assessed with two different methods: flow cytometry–based analysis and time-lapse image–based analysis. Measurement of the m-BMDMs with increased red pHrodo signals among total m-BMDMs by flow cytometry revealed that apoptotic *DD1α*$^{-/-}$ or *p53*$^{-/-}$ thymocytes were less efficiently engulfed by macrophages than were Wt thymocytes (Fig. 2C). Time-lapse imaging analyses with carboxyfluorescein succinimidyl ester (CFSE)–labeled (for green fluorescence) Wt, *DD1α*$^{-/-}$ and *p53*$^{-/-}$ thymocytes, and PKH26 red-labeled phagocytic m-BMDMs showed defective phagocytosis of *DD1α*$^{-/-}$ or *p53*$^{-/-}$ thymocytes by macrophages (Fig. 2D and movies S1 to S3). Together, these data demonstrate that the p53-induced accumulation of DD1α is required for engulfment of apoptotic cells by phagocytes.

Impaired clearance of apoptotic cells in the DD1α-deficient mice

We tested whether DD1α deficiency caused defects in dead cell clearance in vivo in *DD1α*-deficient mice. *DD1α*$^{-/-}$ mice were generated using the Flp-Cre system, and DD1α deficiency was confirmed in vivo (fig. S8). In mice with total body exposure to IR, thymocytes undergo apoptosis and are rapidly cleared by phagocytes. Whereas Wt mice showed a decrease in overall thymic size because of dead cell removal after IR exposure, *DD1α*$^{-/-}$ mice showed less of a reduction in thymic size after IR exposure (Fig. 3A, top left). Quantification of cell numbers confirmed that IR-exposed *DD1α*$^{-/-}$ mice retained a larger thymic cell population than did control mice (Fig. 3A, bottom left). We observed similar changes in the spleen, another radiosensitive organ. IR clearly decreased the spleen size and weight of Wt mice, but *DD1α*$^{-/-}$ mice showed significantly less size reduction after IR (Fig. 3B). We also examined the presence of apoptotic cells in whole mounts of thymus at different times after IR exposure, by terminal deoxynucleotidyl transferase–mediated deoxyuridine triphosphate nick end labeling (TUNEL) staining. Quantification of TUNEL-stained cells was calculated as a fraction of DAPI (4′,6-diamidino-2-phenylindole)–positive cells using an imaging analysis program. In Wt and *DD1α*$^{-/-}$ mice, irradiation of thymocytes with IR induced a similar extent of apoptosis at 3 hours (~40%) and 6 hours (more than 80%). After 6 hours, apoptotic cells in Wt thymus were rapidly cleared down to 40% at 12 hours and 20% at 18 hours. However, the clearance of apoptotic cells in DD1α$^{-/-}$ thymus was delayed, with twice as many apoptotic cells remaining in *DD1α*$^{-/-}$ thymus as in Wt thymus (Fig. 3A, right). Thus, DD1α functions in apoptotic corpse clearance in vitro and in vivo. Because apoptotic cells are typically cleared rapidly in vivo, they are rarely detectable histologically. We thus examined whether *DD1α*$^{-/-}$ mice displayed defects in scavenging apoptotic cells by TUNEL staining of tissue sections. In lymph nodes and colons, we observed 7- to 8-fold and ~17-fold increases, respectively, in TUNEL-positive cells in sections from *DD1α*$^{-/-}$ mice as compared with sections from Wt animals (Fig. 3C).

We asked whether DD1α also affected the phagocytic removal of apoptotic cells in a p53-independent manner in vitro and in vivo. Treatment of dexamethasone (Dex) induces prompt and synchronous p53-independent cell death, and the consequent removal of apoptotic cells by phagocytes can provide a quantitative experimental model of apoptotic cell clearance in vitro and in vivo (*43*–*45*). Thymocytes isolated from Wt and *DD1α*$^{-/-}$ mice were exposed to Dex or IR to induce apoptosis. The apoptotic responses by IR and Dex were comparable (fig. S9A). Dex-induced apoptotic thymocytes from Wt and *DD1α*$^{-/-}$ mice were incubated with m-BMDMs isolated from Wt mice, and the phagocytic potential was assessed via flow cytometry–based analysis. Measurement of the m-BMDMs with increased red pHrodo signals among total m-BMDMs by flow cytometry revealed that Dex-treated apoptotic

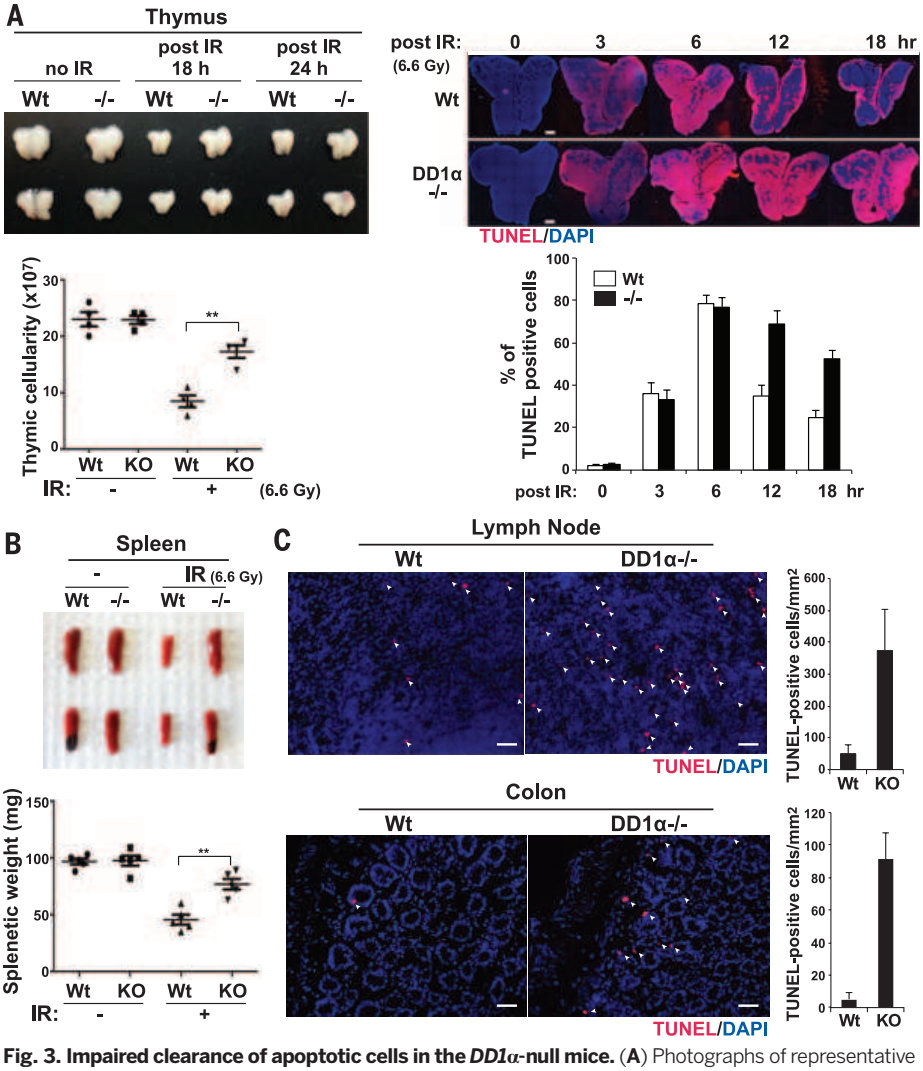

Fig. 3. Impaired clearance of apoptotic cells in the *DD1α*-null mice. (**A**) Photographs of representative thymus from Wt and *DD1α*$^{-/-}$ mice at indicated time points after exposure or nonexposure to IR (6.6 Gy). Total cell numbers per thymus from Wt and *DD1α*$^{-/-}$ mice were determined at 8 hours after ionizing irradiation. Mean ± SD, $n = 4$ per group. $^{**}P < 0.01$ (Tukey's test). The right panels represent whole sections of thymus from Wt and *DD1α*$^{-/-}$ mice exposed to IR that were stained with TUNEL (red) and 4′,6-diamidino-2-phenylindole (DAPI; blue). Scale bar, 1 mm. The percentage of TUNEL-positive cells was determined by percent of the TUNEL-positive cells per DAPI-positive cells using imaging analysis program (CellSens Dimension, Olympus). Data represent mean ± SD, $n = 4$. (**B**) Spleens of Wt and *DD1α*$^{-/-}$ mice exposed to IR. Four- to five-week-old Wt and *DD1α*$^{-/-}$ mice were treated with 6.6 Gy IR. After 6 hours, spleens were isolated from mice and the splenic weight was measured. The photograph of representative spleens of Wt and *DD1α*$^{-/-}$ mice exposed to IR is shown. Each dot represents the value for a single mouse, and mean ± SD ($n = 5$) is shown. $^{**}P<0.01$ (Tukey's test). (**C**) Apoptotic cells in lymph nodes and colon of Wt and *DD1α*$^{-/-}$ mice. The cryosections were stained with TUNEL and DAPI. The apoptotic cells were determined by counting TUNEL-positive cells per mm^2 under a fluorescence microscope. Mean ± SD, $n = 3$. Scale bar, 50 μm.

DD1α$^{-/-}$ thymocytes were less efficiently engulfed by macrophages than were Dex-treated apoptotic Wt thymocytes (fig. S9A, bottom). Wt and *DD1α*$^{-/-}$ mice were also treated with dexamethasone intraperitoneally. Whereas Wt mice showed a decrease in overall thymic size because of dead cell removal 6 hours after Dex injection, *DD1α*$^{-/-}$ mice showed less of a reduction in thymic size after Dex injection (fig. S9B, top left). Quantification of cell numbers confirmed that Dex-treated *DD1α*$^{-/-}$ mice retained a larger thymic cell population than did control mice (fig. S9B, top right). We also examined the presence of apoptotic cells in whole mounts of thymus at different times after Dex injection, by TUNEL staining. In Wt and *DD1α*$^{-/-}$ mice, Dex treatment induced a similar extent of apoptosis at 3 hours (~ 30%) and 6 hours (more than 80%). After 6 hours, apoptotic cells in Wt thymus were cleared down to ~35% at 12 hours and ~20% at 18 hours. However, the clearance of apoptotic cells in *DD1α*$^{-/-}$ thymus was delayed, with twice as many apoptotic cells remaining in *DD1α*$^{-/-}$ thymus as in Wt thymus (fig. S9B, bottom). We observed similar changes in the spleen. A decrease in spleen size and weight was apparent in Dex-treated Wt mice, but *DD1α*$^{-/-}$ mice showed less size reduction after Dex injection (fig. S9C). We also showed that there were no obvious differences in the steady-state levels of DD1α expression in multiple tissues between Wt and *p53*-null mice (fig. S10). Thus, DD1α functions in apoptotic corpse clearance by both p53-dependent and independent ways in vitro and in vivo, and phagocytic engulfment of apoptotic cells is impaired in the absence of DD1α.

DD1α expression in macrophages is required for engulfment of apoptotic cells

DD1α is highly expressed on blood leukocytes (Fig. 1C) and in macrophages (fig. S11) and dendritic cells (*37*, *38*). Because of the expression of DD1α in phagocytes, we investigated whether DD1α expression in macrophages is also necessary for the engulfment of apoptotic cells. We used Wt- or *DD1α*-null thymocytes as prey and incubated them with Wt or *DD1α*$^{-/-}$ m-BMDMs for quantification of phagocytosis analysis using flow cytometry (Fig. 4A). *DD1α*$^{-/-}$ m-BMDMs were deficient in uptake of pHrodo-labeled apoptotic Wt thymocytes, as compared with Wt m-BMDMs, but showed a similarly diminished engulfment rate when DD1α-null apoptotic thymocytes were used as prey. Phagocytosis analysis of Wt- and *DD1α*$^{-/-}$ m-BMDMs with synthetic beads (Fig. 4B) or bacteria (*E. coli*) (Fig. 4C) further revealed that *DD1α*$^{-/-}$ m-BMDMs have no defect in phagocytic ability, which suggests that DD1α-mediated engulfment is dependent upon the presence of DD1α in apoptotic cells but that engulfment of DD1α-independent targets is not. Thus, DD1α participates on both apoptotic cells and macrophages for engulfment of apoptotic cells.

PtdSer-independent engulfment of apoptotic cells by *DD1α*

Dying and/or apoptotic cells expose PtdSer on the outer leaflet of the surface membrane of apoptotic cells, which is considered a primary signal recognized by PtdSer receptor of phagocytes (*1*, *4*). Therefore, we examined whether PtdSer is a ligand of DD1α receptor by protein lipid overlay assay. When membranes, spotted with 15 different lipids, were probed with DD1α recombinant proteins purified from several hosts, such as mammalian cells (293T human embryonic kidney epithelial cells), yeast, or *Escherichia coli*, DD1α did not bind to any lipids including PtdSer (fig. S12). To determine whether the DD1α pathway is functionally sufficient for apoptotic cell engulfment independent from PtdSer signaling, we knocked down DD1α expression in both Raji human lymphoma cells defective for PtdSer exposure (*42*, *46*) and human acute T cell leukemia Jurkat cells defective for PtdSer exposure (*42*, *46*, *47*), and we treated cells with CPT to induce apoptosis and labeled them with pHrodo dye. The apoptotic Jurkat and Raji cells were then incubated with hu-MDM, and phagocytosis was determined as described in Fig. 2. Macrophages efficiently engulfed apoptotic Jurkat cells, but a lower number of apoptotic Raji cells were engulfed, as expected (fig. S13A). When DD1α-depleted Jurkat or Raji cells were mixed with hu-MDMs, engulfment by macrophages was still decreased in DD1α-depleted Raji cells at a similar ratio seen in DD1α-depleted Jurkat cells {phagocytic index of Jurkat cells: ~38 [control knockdown (KD)] to ~16 (DD1α-depleted); phagocytic index of Raji cells: ~15 (control KD) to ~5 (DD1α-depleted)} (fig. S13A). To further confirm the PtdSer signaling–independent role of DD1α in apoptotic cell engulfment, the PtdSer-binding protein, annexin V, was used to inhibit PtdSer exposure, and then we examined phagocytic potentials in DD1α-overexpressing MCF7/DD1α-KD cells. As shown in fig. S13B, the treatment of both annexin V and antibodies (Abs) against DD1α blocking further inhibited phagocytic engulfment as compared with the treatment of annexin V or blocking Abs to DD1a. Thus, DD1α-mediated phagocytosis of apoptotic cells utilizes a different mechanism from the PtdSer pathway–initiated engulfment of apoptotic cells.

Intercellular *DD1α*-*DD1α* interaction between apoptotic cells and phagocytes mediates apoptotic cell engulfment

So far, our data suggest that both DD1α on apoptotic cells and DD1α on phagocytes are required and interdependent for the engulfment of apoptotic cells. To examine the possibility of the DD1α-DD1α homophilic interactions, we studied interactions between beads coated with soluble proteins and cell surface–expressed receptor molecules, using a DD1α-Ig fusion soluble protein (DD1α-Ig) containing the extracellular domain or control Ig proteins [TIM-1–Ig and immunoglobulin (Ig)], in 293T transfected with Wt DD1α or mutant DD1α (IgV domain–deleted). DD1α-Ig proteins (but not control Ig proteins) bound to Wt DD1α proteins expressed on the cell surface, but deletion of the IgV domain abolished this interaction, which suggests the importance of homophilic DD1α binding through the IgV domain (Fig. 5A and fig. S14). To further test whether DD1α could interact with surface DD1α molecules, we used 293T cell transfectants expressing DD1α on the cell surface and several soluble Ig fusion proteins (DD1α-Ig, PD-L1–Ig, and TIM-1–Ig) for cell surface staining. DD1α-Ig, but not PD-L1–Ig or TIM-1–Ig, bound to DD1α transfectants on the cell surface (Fig. 5B). To analyze intercellular DD1α-DD1α binding, we used cell-cell adhesion assays. In addition, U2OS human osteosarcoma cells transfected with full-length DD1α, mutant DD1α with IgV domain deletion, or empty vector were incubated with CFSE-stained MCF7 cells with DD1α overexpression (MCF7-DD1α). After thorough washing to remove unbound green cells, the binding of green-labeled MCF7 cells to U2OS cells was quantified. U2OS cells with full-length DD1α overexpression showed greater binding to green-labeled MCF7-DD1α cells than did control vector or IgV domain–deleted DD1α mutant–transfected U2OS cells, which confirmed the requirement for the IgV domain for potential intercellular DD1α-DD1α interactions (Fig. 5C). Homophilic intermolecular interaction for the DD1α receptor at intercellular junctions was further confirmed by two other experiments. Binding between DD1α-Myc and DD1α-HA was detected in lysates from cultures of 293T cells overexpressing Myc-tagged DD1α and 293T cells overexpressing HA-tagged DD1α by reciprocal coimmunoprecipitation (fig. S15A). We also performed a proximity ligation assay using Duolink in situ fluorescence assay to detect the association of DD1α-DD1α molecules between two different cell types, J774.1 (macrophage) and ZR75-1 (breast carcinoma cell). Colocalization dots (generated by overlapping fluorescence signals) were detected at intercellular junctions (fig. S15B). Further confirming the specificity of intercellular binding, DD1α-transfected Jurkat cells (Jurkat-DD1α) were labeled with either cell tracer CFSE or Far Red, whereas control Jurkat cells were labeled with Far Red. CFSE-labeled Jurkat-DD1α cells were incubated with Far Red–labeled Jurkat-DD1α cells or Far Red–labeled control Jurkat cells. DD1α-DD1α–mediated intercellular bindings were then analyzed by counting the percentage of CFSE- and Far Red–double-positive populations through flow cytometry. Incubation of differently labeled Jurkat-DD1α cell populations increased binding (~26%), but the binding between Jurkat-DD1α and control Jurkat cells was minimal (~3%) (Fig. 5D). To test whether soluble DD1α-Ig proteins compete or cooperate for intercellular DD1α-DD1α binding, we preincubated Jurkat-DD1α cells with soluble DD1α-Ig or Ig proteins. We found that exogenous treatment of DD1α-Ig modestly inhibited DD1α-DD1α–mediated intercellular binding between two differently labeled Jurkat/DD1α cell populations (Fig. 5D).

We mapped the binding region for DD1α-DD1α binding by in vitro binding analysis using glutathione *S*-transferase (GST)– and histidine (His)–fused DD1α variants and observed that the extracellular (amino acids 33–194) DD1α region or the immunoglobulin domain (37–146) bound to the His-fusion protein containing only the extracellular portion of DD1α (33–194) but not

with IgV-deleted DD1α or the cytoplasmic region of DD1α, which indicated that the IgV domain is essential for DD1α-DD1α interactions (Fig. 5E). Cross-linking experiments using GST-fused DD1α variants also revealed self-association of the DD1α extracellular domain in solution (Fig. 5F, left). Cross-linked dimers were observed with the DD1α extracellular domain (33–194) variant in solution but not with the cytoplasmic region of DD1α. Dimerization of DD1α was also examined in intact cells (293T). DD1α-transfected cells were incubated with or without bismaleimidohexane (BMH), another cross-linker for covalent conjugation between sulfhydryl groups. The formation of the DD1α dimer was detected on nonreducing gels after treatment of cells with BMH (Fig. 5F, right).

We tested whether the extracellular IgV region functionally contributes to apoptotic cell engulfment with the IgV domain–deleted DD1α mutant (DD1α-ΔIgV). The full-length DD1α, mutant DD1α-ΔIgV, or empty control vector was transfected into DD1α-depleted MCF7 cells (fig. S16A), followed by induction of apoptosis (fig. S16B). Apoptotic MCF7 cells were incubated with hu-MDMs for phagocytosis analysis. Apoptotic MCF7 cells expressing the full-length DD1α were efficiently engulfed by human macrophages, whereas apoptotic MCF7 cells expressing DD1α-ΔIgV mutant or control vector led to diminished phagocytosis by macrophages (Fig. 5G). To elucidate the possibility of the cis-dimerization for the DD1α-DD1α interaction, we performed a proximity ligation assay using the Duolink technology to detect the association of DD1α-DD1α molecules within the same cell. Colocalization dots were detected only in 293T cells overexpressing both DD1α-HA and DD1α-Myc (fig. S17), which suggests that DD1α interacts with itself in the trans, as well as in the cis, condition. Together, these data from biochemical and cellular assays demonstrate that there is likely a homophilic intermolecular interaction of the DD1α at intercellular junctions, as well as in the cis condition, that contributes to the engulfment of apoptotic cells. Our findings demonstrate an essential role for DD1α in dead cell clearance by phagocytes as the signal on both apoptotic cells and phagocytes.

DD1α-deficient mice develop autoimmune and severe inflammatory disorder

DD1α-null mice are viable, born at the expected Mendelian frequency, and indistinguishable in appearance from Wt littermates at an early age (*48*, *49*). However, at the age of 7 to 10 months, these mice show severe skin inflammation in adult female *DD1α*$^{-/-}$ mice (Fig. 6A). A majority of female *DD1α*$^{-/-}$ mice had ulcerative dermatitis and 35%, 23%, and 12% of female *DD1α*$^{-/-}$ mice showed otitis, eye-related inflammation, and seizures, respectively (Fig. 6A). Impaired clearance of apoptotic cells and accumulated corpses of dead cells can cause susceptibility to autoimmune disease (*1*, *3*, *4*). Because *DD1α*$^{-/-}$ mice showed severe skin inflammation (Fig. 6B), which is one of the clinical manifestations of systemic autoimmune disease, we examined whether *DD1α*$^{-/-}$ mice showed increased autoantibody titers. Starting at 8 to 10 months of age, the abundance of antinuclear antibodies (ANA) was increased in the sera of the phenotypically affected female *DD1α*$^{-/-}$ mice (Fig. 6C and fig. S18). Additionally, Abs to double-stranded DNA (dsDNA) were found in the serum from *DD1α*$^{-/-}$ mice (Fig. 6C). Furthermore, total immunoglobulin G (IgG) in sera from 10-month-old phenotypically affected *DD1α*$^{-/-}$ female mice was increased to ~6-fold in comparison with that of age-matched Wt mice (Fig. 6C). One of the most commonly targeted organs in

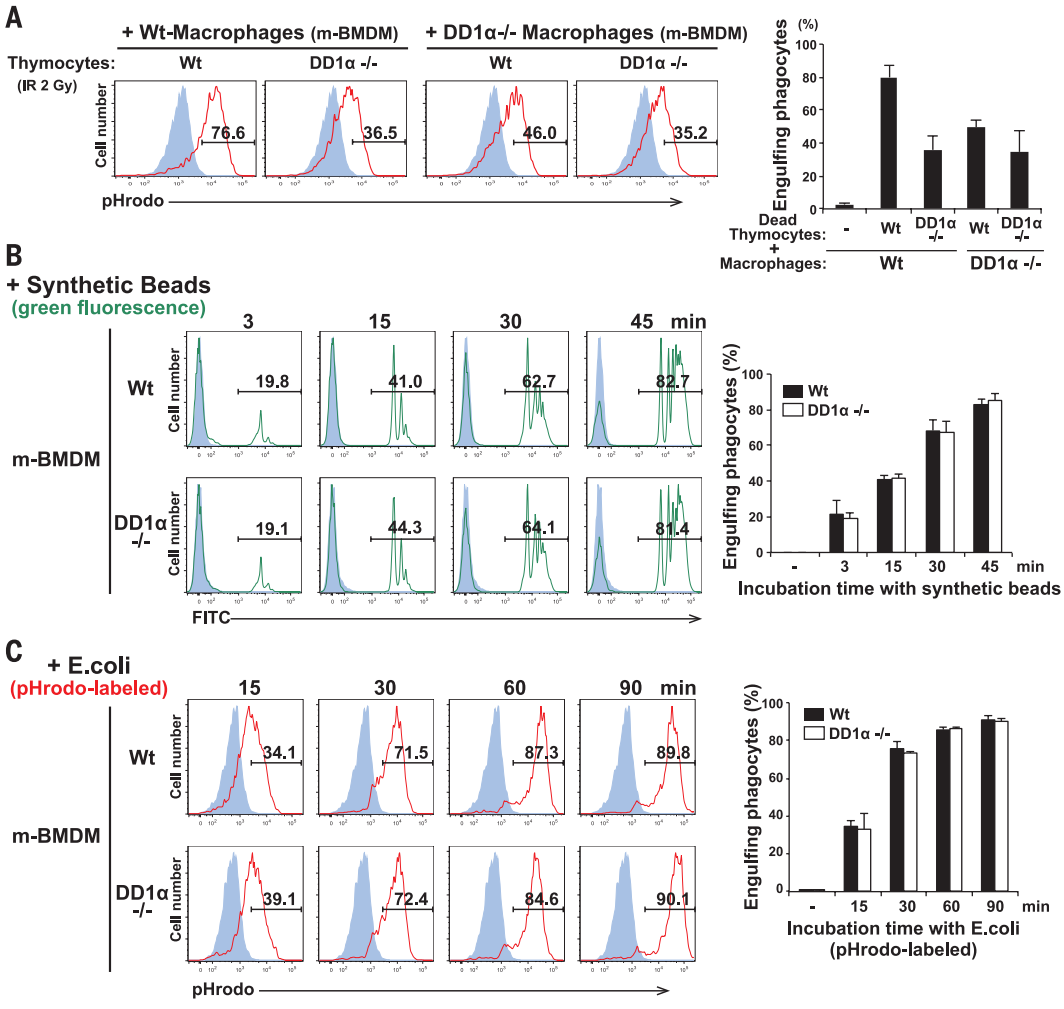

Fig. 4. DD1α expression on macrophages is required for apoptotic cell engulfment. (**A**) Engulfments of apoptotic thymocytes by Wt and *DD1α*$^{-/-}$ m-BMDMs were assessed by flow cytometry. The pHrodo-labeled apoptotic thymocytes were incubated with m-BMDMs for 30 min, and the phagocytosis was determined by measuring the positive pHrodo-containing macrophages. Graph represents mean ± SD from three experiments. (**B**) DD1α deficiency in macrophages does not influence engulfment of synthetic beads. Bone marrow–derived macrophages (m-BMDM) from Wt and *DD1α*$^{-/-}$ mice were incubated with carboxylate-modified green fluorescent beads (synthetic beads) for indicated times. The phagocytosis was determined by the percentage of macrophages containing positive green fluorescence signal. Data are shown as mean ± SD and are representative of three experiments at the same time. (**C**) The phagocytic potential of Wt and *DD1α*$^{-/-}$ m-BMDMs for *E. coli* was assessed using pHrodo-labeled *E. coli*. The phagocytosis was determined by the percentage of macrophages containing positive pHrodo signal. Data represent mean ± SD (n = 3) and are representative of three experiments at the same time.

systemic autoimmune disorders is the kidney (*50*). Consistent with other evidence of autoimmune activity, in the renal glomeruli of *DD1α*$^{-/-}$ mice, we observed immune complex deposition identified by immunofluorescence (Fig. 6D) and diffuse mesangial expansion as shown by periodic acid–Schiff (PAS)–positive material and cellular debris (Fig. 6D). Electron microscope analysis also showed an expanded mesangium with electron-dense deposits and neutrophils within capillary lumens of *DD1α*$^{-/-}$ mice (Fig. 6D). Numerous large electron-dense deposits were also observed in electron micrographs of the glomerular mesangium of *DD1α*$^{-/-}$ glomeruli (Fig. 6D). Consistent with the above kidney phenotypes, *DD1α*$^{-/-}$ mice produced large amounts of protein in their urine (Fig. 6C). Together, the *DD1α*$^{-/-}$ kidney revealed a phenotype of active glomerulonephritis with a

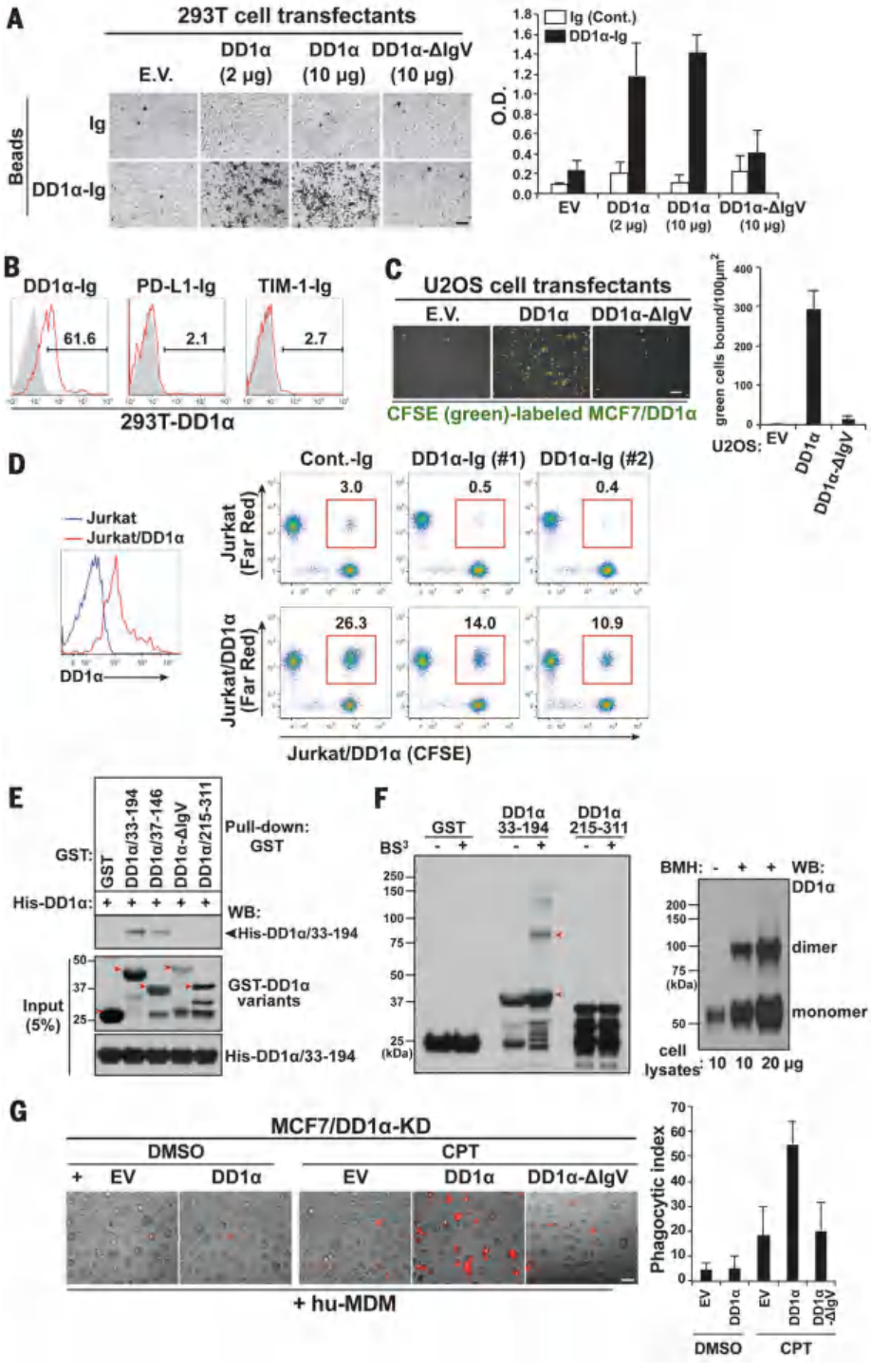

Fig. 5. Intercellular homophilic DD1α interaction between apoptotic cells and phagocytes mediates apoptotic cell engulfment. (**A**) Homophilic DD1α interaction. Binding of blue latex beads coated with DD1α-Ig fusion proteins (the extracellular region of DD1α fused with the immunoglobulin G Fc segment) to 293T cells transfected with empty vector (EV), the Wt DD1α (2 or 10 μg), or a mutant lacking the IgV domain (DD1α-ΔIgV). Ig protein–coated beads were included as control. After 30 min, unbound beads were washed. The binding was examined under an inverted microscope (left) and also determined from the optical density (O.D.) at 492 nm (right). Data are shown as mean ± SD and are representative of three experiments. Scale bar, 50 μm. (**B**) Interaction of DD1α with DD1α on the cell surface. 293T cells stably transfected with DD1α cDNA were stained with DD1α-Ig, PD-L1–Ig, TIM-1–Ig, or control Ig proteins (gray filled). The binding of Ig proteins was detected with Ab against human IgG1-PE. Binding amounts were determined by percentage of fluorescence-positive cells compared with control Ig protein–bound cells. (**C**) Intercellular DD1α interaction. Binding of CFSE-labeled DD1α-overexpressing apoptotic MCF7 cells to U2OS cells expressing empty vector (EV), full-length DD1α, or DD1α-ΔIgV (IgV deletion mutant). Scale bar, 100 μm. Binding was determined by counting the bound cells per 100 μm^2 and normalized by cell number bound to untreated plate. Mean ± SD of three experiments is shown. (**D**) Intercellular DD1α-DD1α interaction and the disruption by recombinant DD1α proteins. The exogenous expression of DD1α in Jurkat cells was validated by flow cytometry analysis (left). CFSE-labeled DD1α-overexpressing Jurkat cells were preincubated with Ig proteins (control Ig: 50 μg/ml; DD1α-Ig: 25 μg/ml for #1, 50 μg/ml for #2) for 30 min and mixed with Far Red–labeled control or DD1α-overexpressing Jurkat cells. After 1-hour incubation, DD1α-DD1α–mediated intercellular bindings were analyzed by counting the percentage of CFSE- and Far Red–positive populations (right). (**E**) Mapping of binding site for homophilic DD1α interaction. His-DD1α (33–194) protein was incubated with GST-DD1α variants (the extracellular region, 33–194; the immunoglobulin domain, 37–146; IgV-deleted mutant, the cytoplasmic region, 215–311) immobilized on glutathione-agarose beads. The bead-bound His-DD1α (33–194) proteins were eluted and detected by immunoblotting using Ab against His. A portion (5%) of the input proteins for the binding reaction was also subjected to immunoblotting. (**F**) Self-association of the extracellular region of DD1α in solution. GST-DD1α (33–194), GST-DD1α (215–311), or control protein GST was untreated or treated with 2.5 mM BS^3 cross-linker for 1 hour at 4°C, and GST proteins were analyzed by Western blotting using Ab against GST (left). Dimerization of DD1α was also examined in intact cells. DD1α-transfected 293T cells were treated or untreated with 1 mM bis(maleinido)hexane (BMH) for 1 hour, and DD1α protein was analyzed by Western blotting under nonreducing condition (right). (**G**) Extracellular IgV domain is required for engulfment. DD1α, DD1α-ΔIgV (IgV-deleted DD1α mutant), and control empty vector were reintroduced into DD1α-depleted MCF7 cells, and the cells were treated with DMSO or CPT (10 μM) for 48 hours. The phagocytosis of MCF7/DD1α knocked-down cells expressing empty vector (EV), DD1α, or DD1α-ΔIgV was determined as in Fig. 2A. Graph represents mean ± SD (n = 3). Scale bar, 50 μm.

mesangioproliferative pattern of injury and immune complex deposition. We observed extensive splenomegaly and lymphadenopathy in DD1α$^{-/-}$ mice by 10 months of age (Fig. 6E). Further histological analysis revealed extensive inflammatory infiltrates in skin and lung, and extramedullary hematopoiesis, including both erythroid and myeloid hyperplasia, was evident, which indicated a major immune dysregulated phenotype of *DD1α*$^{-/-}$ mice (fig. S19).

Inhibitory role of functional DD1α-DD1α interaction in T cell activation

Given the functional and biochemical homophilic DD1α-DD1α interaction between dead cells and macrophages, we next sought to determine whether such an interaction could also occur with naturally expressed DD1α on T cells. Thus, we used flow cytometry to assess binding of DD1α-Ig to surface receptors of CD4$^+$ T cells. DD1α-Ig bound to human CD4$^+$ T cells, but the binding of DD1α-Ig to T cells treated with blocking Abs to DD1α was decreased (fig. S20A). Moreover, this binding of DD1α-Ig to CD4$^+$ T cells purified from *DD1α*$^{-/-}$ mouse was diminished as compared with its binding to Wt-CD4$^+$ T cells (fig. S20B). Expression of DD1α on antigen-presenting cells (APCs) functions as a negative regulator or ligand of T cell response in vitro and its overexpression on tumor cells interferes with protective antitumor immunity in mice (*37*, *51*). DD1α is also expressed on T cells and can function as a coinhibitory receptor of T cell activation (*38*, *49*, *52*). Moreover, preclinical studies with blocking Abs to DD1α enhanced antitumor T cell responses, leading to inhibited tumor growth and better survival (*51*).

Because intercellular DD1α-DD1α interaction is likely required for its scavenger function (Figs. 2 to 5) and DD1α is also expressed on the surface of CD4$^+$ and CD8$^+$ T cells (fig. S21), we further examined whether DD1α on CD4$^+$ T cells functions as a receptor and causes DD1α-mediated inhibition of T cell activation. DD1α-Ig protein strongly inhibited proliferation of CD4$^+$ and CD8$^+$ T cells and cytokine production stimulated by CD3-specific Abs (fig. S22) (*37*). CD4$^+$ and CD8$^+$ T cells from Wt or *DD1α*$^{-/-}$ mice were used for DD1α-Ig–mediated T cell inhibition experiments.

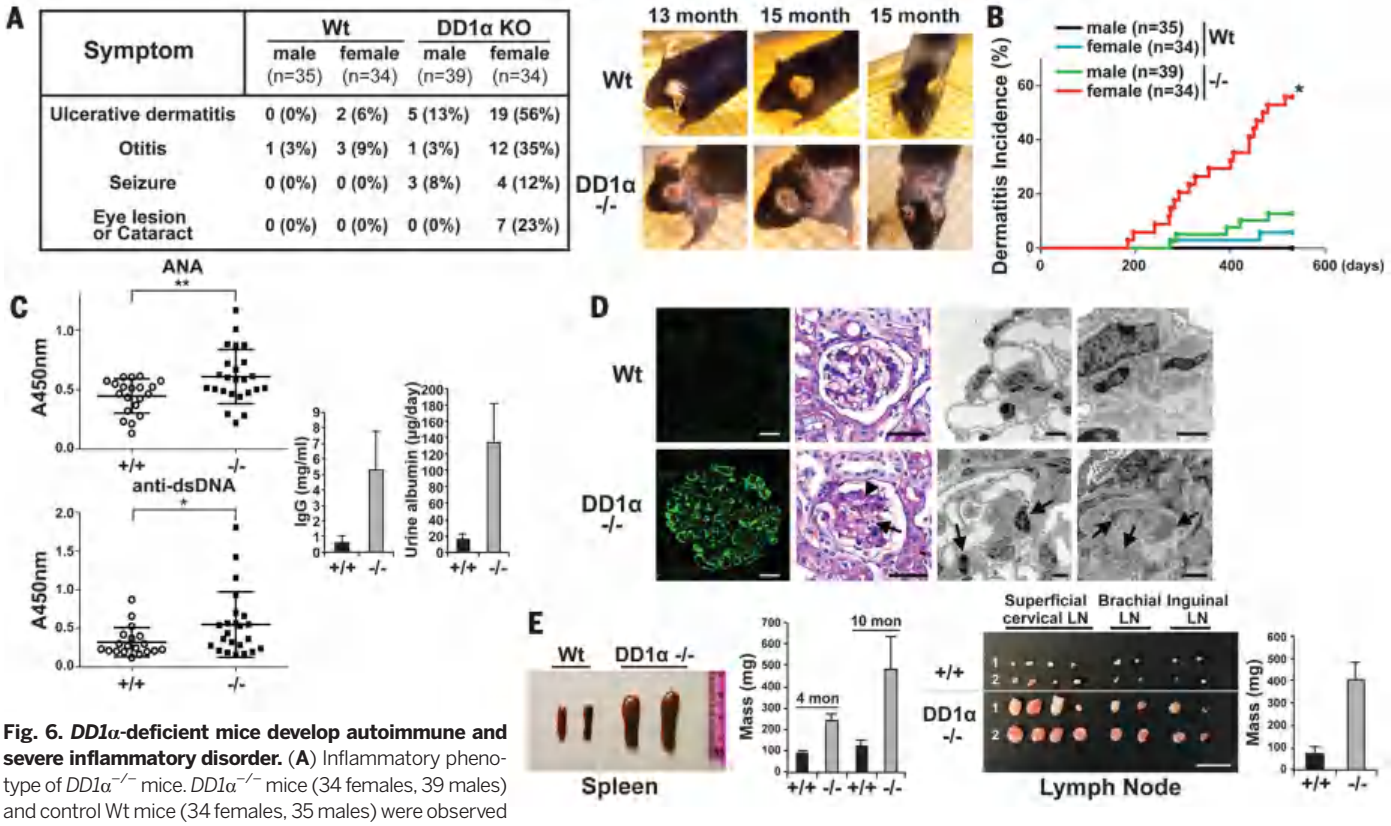

Fig. 6. *DD1α*-deficient mice develop autoimmune and severe inflammatory disorder. (**A**) Inflammatory phenotype of *DD1α*$^{-/-}$ mice. *DD1α*$^{-/-}$ mice (34 females, 39 males) and control Wt mice (34 females, 35 males) were observed over a 19-month period. The left box summarizes the symptoms (ulcerative dermatitis, otitis, seizure, and eye lesion) and incidences of symptoms. Photographs of 13- or 15-month-old female Wt and *DD1α*$^{-/-}$ mice are shown. (**B**) Dermatitis incidence in *DD1α*$^{-/-}$ mice (34 females and 39 males) and control Wt mice (34 females and 35 males). *P < 0.001 (Log-rank test). (**C**) The levels of ANA and Abs against dsDNA in sera of phenotypically affected female Wt and *DD1α*$^{-/-}$ mice were measured by ELISA. (Wt: n = 20, *DD1α*$^{-/-}$: n = 24 for ANA; and Wt: n = 19, *DD1α*$^{-/-}$: n = 23 for Abs against dsDNA). Each dot represents the value for a single mouse. **P < 0.01, *P < 0.05 (Student's t test). Serum IgG levels of phenotypically affected 10-month-old female Wt and *DD1α*$^{-/-}$ mice (n = 7) were assessed by ELISA. The level of albumin in urine collected for 24 hours from affected 10- to 12-month-old female mice (n = 8) was analyzed by SDS–polyacrylamide gel electrophoresis (SDS-PAGE) and imaging analysis. (**D**) Spontaneous glomerulonephritis in *DD1α*$^{-/-}$ mice. Representative images of kidney sections from 10-month-old Wt and *DD1α*$^{-/-}$ mice stained with Ab against mouse IgG show immune complex deposits in glomeruli of *DD1α*$^{-/-}$ mice (the first column of panels). Scale bar, 20 μm. The second column of panels shows kidney sections from Wt and *DD1α*$^{-/-}$ mice stained with PAS. Glomeruli from Wt mice have a regular architecture with delicate mesangium. Glomeruli from *DD1α*$^{-/-}$ mice with dermatitis symptoms show diffuse mesangial expansion by PAS-positive material and cellular debris (arrowhead), as well as occasional neutrophils within capillary lumens (arrow). Scale bar, 50 μm. The third column of panels shows low-magnification electron micrographs of Wt and *DD1α*$^{-/-}$ glomeruli. A normal architecture with delicate mesangium and intact filtration barrier of Wt glomeruli and an expanded mesangium with electron-dense deposits, and neutrophils within capillary lumens (arrows) of *DD1α*$^{-/-}$ glomeruli are shown. Scale bar, 2 μm. The fourth column of panels show high magnification electron micrograph of the glomerular mesangium of Wt and *DD1α*$^{-/-}$ glomeruli. Large electron-dense deposits (arrows), often with tubular substructure in the glomerular mesangium of *DD1α*$^{-/-}$ glomeruli are shown. Scale bars, 2 μm (top) and 500 nm (bottom). (**E**) Splenomegaly and lymphadenopathy observed in *DD1α*$^{-/-}$ mice. Spleens and lymph nodes of 10-month-old female Wt and *DD1α*$^{-/-}$ mice from one littermate were shown. The weight of spleen and lymph nodes was measured as indicated. Data represent mean ± SD. n = 6 to ~11 mice per group.

Engagement of DD1α-Ig inhibited CD3 Ab–induced proliferation of $CD4^+$ or $CD8^+$ T cells (~50% inhibition). However, *DD1α*$^{-/-}$ $CD4^+$ or $CD8^+$ T cells were less sensitive to DD1α-Ig (~30% inhibition) (fig. S22), although DD1α deficiency did not prevent inhibition completely. These data indicate that potential homophilic DD1α interactions are important for the DD1α-mediated T cell inhibitory role and that DD1α functions as a receptor on T cells. These findings indicate a role for tumor suppressor p53 in regulating expression of immune regulators, including PD-1, PD-L1, and DD1α, which suggests a potential role of p53 in immune responses.

Discussion

Our findings reveal that the tumor suppressor p53–induced expression of DD1α regulates efficient clearance of dead cells and proper immune tolerance. Although these two essential activities are seemingly interrelated, the complexity of these processes is demonstrated by the many receptors and signaling pathways involved in the recognition and removal of apoptotic cells by macrophages and stringent discrimination of self antigens from nonself antigens (*1*, *53*, *54*). We found that DD1α is a receptor that engages in homophilic intermolecular interaction or dimerization at intercellular junctions of apoptotic cells and macrophages, which is critical for the engulfment of apoptotic cells. Mice deficient in scavenger receptors develop spontaneous autoimmune disease (*55*–*58*), whereas deficiencies in dead cell clearance do not always elicit autoimmunity because these apoptotic cells in these deficiencies are still able to trigger a downstream immunosuppressive signal to inhibit autoimmunity (*59*, *60*). In a normal immune system, phagocytic engulfment of apoptotic cells is accompanied by induction of a certain degree of immune tolerance in order to prevent self-antigen recognition (*53*, *61*).

At age 10 to 12 months after birth, *DD1α*-deficient mice showed autoimmune phenotypes predominantly in female mice. These results imply that DD1α seems to be critical in dead cell clearance, and its loss directly affects immune tolerance. Previously reported *DD1α* knockout mice were generated by a gene-trapping approach targeting coding exon 1 (*48*). We achieved a Cre-mediated complete deletion of exons 2 and 3 of the *DD1α* gene, which resulted in the development of similar and yet exaggerated phenotypes with moderate to severe increases in size of certain organs and prominent formation of immune infiltrates in the skin, lung, liver, and kidney. Notably the autoimmune defects observed in the aged female *DD1α* mice were apparent even in the absence of other predisposing factors and resulted in an increased late mortality rate in females. Interestingly, the autoimmune phenotype characteristic for late-stage *DD1α* knockout animals is clearly prevalent in female mice. Importantly, similar gender bias has been previously described for various animal models of autoimmune disorders, such as SLE in which female animals are significantly more susceptible to the disease (*55*, *62*). Also, sex hormones have been previously implicated in the development of high-affinity auto-reactive B cells (*63*). Epidemiological studies in humans also show extremely high (9:1) gender bias toward females for systemic autoimmune diseases (*64*).

The process of apoptotic-cell clearance involves extensive numbers of molecules. Based on resulting phenotypes of various knockout mice, it has been suggested that some molecules are critical for proper cell turnover during development (e.g., PSR, Beclin1, Atg5) (*65*–*67*), and other molecules are essential in the adult life, when rates of apoptosis in relevant tissues are physiologically normal during tissue homeostasis or when rates of apoptosis are accelerated under various stress stimuli (e.g., MFG-E8, TIM-4, SCARF1, C1q, CD14, Mer) (*55*–*58*, *68*, *69*). Our data indicate that DD1α primarily responds to apoptotic stress and is more likely to be involved in the regulation of engulfment and phagocytosis of dead cells on the sites of extensive damage because of exogenously induced cellular toxicity. Additionally, public database information [EMAGE gene expression database (http://www.emouseatlas.org/emage/)] shows that DD1α is almost not detectable at the embryonic stage, whereas PSR or Beclin1, which are involved in cell turnover during development, are markedly expressed in the embryo (*70*). Therefore, DD1α deficiency leads to accumulative defects of cellular clearance over prolonged time and results in an age-dependent autoimmune phenotype, which suggests the specific role of DD1α in a stress-responsive environment.

DD1α is expressed in immune cells, including macrophages and T cells, and likely functions as a receptor through DD1α-DD1α binding at intercellular junctions. We further demonstrated that DD1α has an important role as an intercellular homophilic receptor on T cells, which suggests that DD1α is a key-connecting molecule linking postapoptotic processes to immune surveillance. DD1α also appears to inhibit T cell activation. These findings establish a concept for cancer-driven control of immune surveillance: p53-dependent genotoxic stress-mediated expression of DD1α and related immune checkpoint inhibitors, such as PD-1 and PD-L1 molecules on cancer cells, may enable their interactions with T cells in order to impose suppression of the immune response and escape from immune surveillance.

Materials and methods

Plasmids, transfection, and lentiviruses

For mammalian expression vector, full-length human DD1α cDNA was subcloned into pcDNA3.1(-) tagged with HA or Myc at the C terminus using standard procedure. Immunoglobulin V domain (amino acids 45–168)–deleted mutant DD1α-ΔIgV was generated by a PCR-mediated deletion method. For Fc-tagged soluble DD1α proteins (DD1α-Ig), the extracellular region of DD1α was cloned upstream of the mouse IgG-Fc region (DD1α-Ig) in the pCMV6-AC-FC vector (OriGene, Rockville, MD). Plasmid encoding TIM-1–Ig was a gift from Terry B. Strom (Transplant Institute, Beth Israel Deaconess Medical Center and Harvard Medical School, Boston, MA). To tag HA or Flag at the N terminus of DD1α, HA or Flag was inserted between DD1α signal peptide (SP) (1–32) and DD1α peptide (33–311), resulting in the construction of SP (1–32)–HA–DD1α (33–311) and SP (1–32)–Flag–DD1α (33–311). For recombinant DD1α deletion mutants, DD1α (33–194), DD1α (37–146), DD1α-ΔIgV (33–311, ΔIgV), and DD1α (215–311) were generated by PCR and subcloned into pGEX-6P-1 (GE Healthcare Life Sciences, Pittsburgh, PA). DD1α (33–194) was amplified and subcloned into pRSET vector (Invitrogen, Life Technologies, Grand Island, NY). For GST-fused p53 (93–312), p53 (93–312; DNA binding domain) was subcloned into pGEX-6P-1 (GE Healthcare Life Sciences). Transfections were performed using Lipofectamine 2000 (Invitrogen). Plasmids encoding lentivirus expressing DD1α-HA were generated by cloning DD1α-HA into pLenti CMV Neo DEST. Cells were transduced with lentivirus in the presence of polybrene. Infected cells were selected in complete appropriate medium containing 10% fetal bovine serum (FBS) and G418 and were tested 1 week after infection.

Antibodies and additional reagents

The following Abs were used for Western blot analyses or flow cytometry analysis: p53 (DO-1, Santa Cruz), p21 (DSC60, Cell Signaling Technology, Danvers, MA), β-actin (AC-15, Sigma-Aldrich, St. Louis), His (Invitrogen), GST (B-14, Santa Cruz), HA (F-7, Santa Cruz), HA (C29F4, Cell Signaling Technology), Myc (9E10, Santa Cruz), Ab against mouse DD1α (MH5A, BioLegend), Ab against human PD-1 (J116, eBioscience), Ab against human PD-L1 (M1H1, eBioscience), CTLA4 (C-19, Santa Cruz), ICOSL (LifeSpan BioSciences), Ab against human CD14 APC (61D3, eBioscience), Ab against mouse F4/80 APC (BM8, eBioscience), Ab against mouse CD45R/B220 (RA3-6B2, eBioscience), Ab against human CD4-APC (OKT4, eBioscience), Ab against mouse CD4-APC (RM4-5, eBioscience), Ab against human CD8-APC (SK1, eBioscience) and Ab against mouse $CD8a^+$-APC (53-6.7, eBioscience). Rabbit polyclonal and mouse monoclonal Ab against DD1α was raised against human DD1α (amino acids 33–311) as an immunogen. Beads immobilized with Abs against HA (Roche) or Myc (9B11, Cell Signaling) were used for immunoprecipitations. Recombinant human PD-1–Ig, mouse PD-1–Ig, human PD-L1–Ig, mouse PD-L1–Ig, and control Ig proteins were from R&D Systems.

Cells and culture conditions

EJ-p53 and EJ-CAT cells (human bladder cancer cell lines) (*71*) were cultured in the presence or absence of tetracycline (1 μg/ml) in Dulbecco's modified Eagle's medium (DMEM) containing 10% FBS (Gibco), 100 units/ml of penicillin, and 100 μg/ml of streptomycin at 37°C (*72*). Human MCF7 (human breast cancer cell line), ZR75-1 (human breast cancer cell line), Saos-2 (human osteosarcoma cell line), U2OS (human osteosarcoma cell line), A549 (human lung cancer cell line), A375 (human melanoma cell line), HEK293T (human embryonic kidney epithelial cell line), Hs888, and T (human osteosarcoma cell line) cells and J774 (mouse macrophage cell line) cells were maintained in DMEM (Cellgro) supplemented with 10% FBS and antibiotics. LOX-IMVI (human melanoma cell line), BxPC-3 (human pancreatic cancer cell line), Jurkat (human acute T cell leukemia

cell line), and Raji (human Burkitt's lymphoma cell line) cells were grown in Roswell Park Memorial Institute medium (RPMI) (Cellgro) supplemented with 10% FBS and antibiotics. For DD1α-overexpressing Jurkat cells, Jurkat cells infected with lentivirus carrying DD1α-HA were selected with 700 μg/ml geneticin, sorted, and subcloned. The BxPC-3 cells (*73*) were provided by D. Panigrahy (Beth Israel Deaconess Medical Center, Boston, MA). For treatment of DNA damage agents, cells were grown to ~50% confluency prior to exposure to DNA damage agent, CPT (0.5 to 20 μM), etoposide (25 μM), or IR (13 Gy).

shRNA and siRNA experiments

Plasmids (pLKO.1-puro) expressing shRNAs against human DD1α-1 (5′-GCAGAGACAACTTCTAAGAAT-3′; TRCN0000145473, Sigma-Aldrich) and DD1α #2 (5′-GCACGATGTGACCTTCTACAA-3′; TRCN0000140372, Sigma-Aldrich) and pLKO.1-puro Luciferase shRNA Control Plasmid DNA (Sigma-Aldrich) were purchased. p53 siRNA (Validated Stealth RNAi siRNA, oligo ID: VHS40367) and control siRNA (Stealth RNAi Negative Control Low GC) were purchased from Invitrogen. shRNA plasmids and siRNAs were introduced into cells by transfection using Lipofectamine 2000 (Invitrogen) or X-tremeGENE siRNA Transfection Reagent (Roche), respectively. MCF7 or ZR75-1 cells stably expressing shRNAs were generated by selection with puromycin (1.0 μg/ml for MCF7, 1.25 μg/ml for ZR75-1).

RNA analysis

RNA was prepared with TRIzol Reagent (Invitrogen) according to the manufacturer's protocol. Total RNAs of human tissues were purchased from Clontech. The RNAs were analyzed by the Northern blot analysis as described previously (*74*). For real-time qPCR analysis, total RNAs were extracted with the Qiagen RNeasy kit with QIAshredder. cDNA was synthesized using the iScript cDNA Synthesis Kit (Bio-Rad). Primers were as follows: For human: *DD1α*: 5′-GATGTGACCTTCTACAAGACG-3′ and 5′-GTCCTGGAACGTGAGGTTGC-3′; *PD-1*: 5′-CCAGGATGGTTCTTAGACTCCC-3′ and 5′-TTTAGCACGAAGCTCTCCGAT-3′; *PD-L1*: 5′-TGGCATTTGCTGAACGCATTT-3′ and 5′-TGCAGCCAGGTCTAATTGTTTT-3′; *RPLP0*: 5′-CAGATTGGCTACCCAACTGTT-3′ and 5′-GGGAAGGTGTAATCCGTCTCC-3′. For mouse: *DD1α*: 5′-GGAACCCTGCTCCTTGCTATT-3′ and 5′-TTGTAGATGGTCACATCGTGC-3′; *Rplp0*: 5′-TCGGGTCCTAGACCA-3′ and 5′-AGATTCGGGATATGCTGTTGGC-3′. qPCR analysis was performed using an Icycler IQTM5 real-time system (Bio-Rad) with SYBER Green (Roche) for detection. Expression levels of genes analyzed by qPCR were normalized relative to levels of human *RPLP0* or mouse *Rplp0* expression.

Reporter plasmid generation and luciferase assay

A portion (1.7 kb) of the human DD1α promoter region was amplified by PCR and digested with SacI and XhoI and then was subcloned into luciferase expression vector (pGL4.21[luc2P/Puro], Promega). Transcription start site is marked as +1. For 6-kb promoter-report construct, the upstream of *DD1α* promoter from 1.7 kb to 6 kb was amplified by PCR and digested with KpnI and SacI, and then ligated into 1.7-kb *DD1α* promoter-luciferase construct. All constructs are verified by DNA sequencing. For luciferase assay, the luciferase reporter plasmids were transfected into cells. Vector encoding Renilla (pRL-TK) was also cotransfected for normalization of the transfection efficiency. The luciferase activity was determined using the Dual Luciferase Reporter Assay System (Promega).

Chromatin immunoprecipitation (ChIP)

Chromatin immunoprecipitation of IR-exposed MCF7 cells was performed following the manufacturer's protocol (Upstate). Immunoprecipitation was carried out at 4°C overnight with polyclonal Ab against p53 and mouse IgG (Santa Cruz) as a negative control. Immunoprecipitated DNA was analyzed by qPCR with the following primers.

DD1α-BS1: 5′-ATATAGCAAGACCCCACCTCTACA-3′, 5′-CACAGTGCAGCAACAAATAGAAGT-3′

DD1α-BS2: 5′-CCTCAGGCTCTGAATCTACAGTTA-3′, 5′-GGGACAGAGACTTGTACCCTACAT-5′

p21: 5′-CTCACATCCTCCTTCTTCAG-3′, 5′-CACACACAGAATCTGACTCCC-3′

The amount of immunoprecipitated DNA was normalized to inputs.

Electrophoretic mobility-shift assay

After etoposide treatment, nuclear extracts were collected from MCF7 cells using a general nuclear extraction method. Nuclear extracts (5 μg) or purified recombinant p53 was incubated with ^{32}P-labeled oligonucleotides in gel shift binding buffer (5 mM Tris-HCl at pH 7.5, 20 mM NaCl, 0.5 mM $MgCl_2$, 0.25 mM EDTA, 0.2% NP-40, 2.5% glycerol, 1 mM DTT, 20 μg/ml BSA, and 40 μg/ml poly(dI-dC). The DNA-protein complexes were resolved by electrophoresis through 5% polyacrylamide gel containing 0.5% TBE. Gels were dried and exposed to X-ray film. Unlabeled wild-type oligonucleotide or unlabeled mutant oligonucleotide was added in 100-fold excess as specific or nonspecific competitor. Oligonucleotides corresponding to the DNA binding consensus sequence for human p53 (*75*, *76*) were used.

DD1α-BS1: 5′-GCTGGGCATGGTGGTGCATGCCTGTA-3′

DD1α-BS1 Mut: 5′-GCTTTTTGCAGAGGTGTCAAAGGTA-3′

DD1α-BS2: 5′-GTTAAACTGGCTCCAGCTTGCCTAGC-3′

p21-BS: 5′-TGTCCGGGCATGTCCGGGCATGTCCGGG-3′

p21-BS Mut: 5′-TGTCCGGGAATTTCCGGGAATTTCCGGG-3′

Preparation of human and mouse macrophages

For hu-MDM, human peripheral blood mononuclear cells were prepared from normal blood obtained from the Massachusetts General Hospital blood donor center (protocol number 2012P002174). Monocytes were isolated by adhering mononuclear cells to culture plates for one hour at 37°C, after which nonadherent cells were removed by washing. The remaining cells were >95% CD14 positive. Adherent cells were then incubated in DMEM/F12 medium plus 10% FBS, 1% penicillin-streptomycin for 7 days to allow terminal differentiation of monocytes to macrophages (*77*). For mouse bone marrow–derived macrophages (m-BMDM), femurs and tibias were harvested from 5- to 6-week-old mice and the marrow was flushed and placed into a sterile suspension of PBS. The bone marrow suspension was cultured in DMEM/F12 medium plus 10% FBS, 1% penicillin-streptomycin-glutamine with 40 ng/ml recombinant murine macrophage colony-stimulating factor (M-CSF, Peprotech). Six days later, more than 90% of the adherent cells were CD11b positive and 80% of the cells were F4/80 positive.

Generation of apoptotic cells

Apoptosis of human cancer cells was induced by CPT (0.5 to 20 μM). To generate apoptotic thymocytes, thymocytes isolated from mice were exposed to the indicated dose of IR with constant cell concentration of 1.0×10^6 thymocytes/ml. For phagocytosis assays, apoptotic cells were labeled with pHrodo or CFSE (carboxyfluorescein diacetate succinimidyl ester) (Invitrogen). Cells were used when 60 to 70% of cells were apoptotic, as defined by annexin V–positive and propidium iodide-negative staining or TUNEL staining by flow cytometry.

Phagocytosis assay

For flow cytometry analysis of phagocytosis, 2.0×10^5 BMDMs were plated in the 24-well plate 1 day before the phagocytosis assay. Next day, the cells were starved for 30 min with DMEM/F12 containing 2% FBS and incubated with fluorescently labeled targets, such as 4.0×10^6 pHrodo (Invitrogen)-stained apoptotic thymocytes, 1 mg/ml pHrodo Red *E. coli* BioParticles (Invitrogen), or 2-μm carboxylate-modified latex beads (Invitrogen) in 150 μl of the uptake buffer (DMEM/F12 containing 2% FBS, 0.2% penicillin-streptomycin). After incubation for the indicated time, the cells were extensively washed with cold PBS, trypsinized and resuspended in cold medium containing 1% NaN_3, and analyzed by flow cytometry. Forward and side-scatter parameters were used to distinguish unengulfed targets from phagocytes. The data were analyzed using FlowJo software. Fluorescent signal–positive BMDMs were considered to be phagocytes engulfing targets (*78*). For time-lapse image analysis of phagocytosis, CFSE (Invitrogen)–labeled apoptotic thymocytes were added to BMDM with 1:5 ratio (BMDM:thymocyte). The individual BMDMs were monitored by time-lapse confocal microscopy imaging (Nikon Eclipse Ti and Zeiss LSM 510), with images being taken at 1- to 2-min intervals. For image-based analysis of phagocytosis of human cancer cells, human monocyte–derived macrophages (MDMs) were prepared from human peripheral blood and incubated with pHrodo-labeled apoptotic cancer cells with 1:10 to 1:15 ratio (MDM:cancer cell). Two hours after coincubation, wells were washed thoroughly with cold serum-free RPMI five times and examined under a fluorescence microscope (Nikon Eclipse Ti or Zeiss AxioObserver.Z1) using bright field or Texas Red filter set. The phagocytic index was calculated using the following

formula: phagocytic index = number of ingested cells/(number of macrophages/100), as described previously (79). At least 400 macrophages were counted per well.

Generation and genotyping of DD1α knockout mice

A targeting vector for the mouse *DD1α* gene was engineered by InGenious Targeting Laboratory, Inc. (Stony Brook, NY). In brief, a PGK-neomycin cassette flanked by loxP and FRT sites was inserted downstream of exon 3. A third loxP site was inserted upstream of exon 2. The targeted iTL BA1 (C57BL/6 × 129/SvEv) hybrid embryonic stem cells containing the linearized construct were microinjected into C57BL/6 blastocysts. Germline transmission was achieved by backcrossing chimeras to wild-type C57BL/6 mice. To generate the whole-body *DD1α* knockout mice, DD1α^{floxneo} mice were first bred with β-Actin/Flp mice (The Jackson Laboratory; catalog no. 003800) to remove the PGK-neomycin cassette and then bred with EIIa-Cre mice (The Jackson Laboratory; catalog no. 003724). Mice with DD1α heterozygous allele (*DD1α*$^{+/-}$) were backcrossed with C57BL/6J mice for at least seven generations before being intercrossed to generate mice homozygous for the null allele (*DD1α*$^{-/-}$). Routine genotyping was achieved on genomic DNA isolated from tail snips of mice with three primers to identify wild-type and null alleles: P1, 5′-TCCTTGTGCAGGACAGAGTT-3′; P2, 5′-CTAATGGCACAGCAGGGACT-3′; and P3, 5′-CAACAAATCACGGTGGAGTG-3′. All animal experiments were approved by the Subcommittee on Research Animal Care of Massachusetts General Hospital (protocol no. 2005N000022).

Analysis of apoptotic cell clearance in vivo

Four- to 5-week-old Wt and *DD1α*$^{-/-}$ mice were exposed to 6.6 Gy of IR or intraperitoneally injected with 250 μg dexamethasone as described previously (44, 45). At the indicated time points after exposure of IR or injection of dexamethasone, the mice were euthanized and thymuses and spleens were harvested. For quantification of total number of thymocytes in thymus, thymocytes were resuspended with PBS supplemented with 5% FBS. To monitor the TUNEL-positive apoptotic cells in thymus, 6-μm cryosections of whole thymuses were stained using the In Situ Cell Death TMR Red kit and DAPI according to manufacturer's instructions (Roche). Whole-thymus images were obtained using an automated image stitching method under fluorescence microscope (Olympus FSX100). To quantify the clearance of TUNEL-positive cells, the percentage of TUNEL-positive cells was determined by the percentage of TUNEL-positive cells per DAPI-positive cells using an imaging analysis program (CellSens Dimension, Olympus).

Mouse serologic and urine analysis

The levels of total IgG, ANA, and ant-dsDNA in mouse serum were determined by enzyme-linked immunosorbent assay according to the manufacturer's instructions (Bio-Rad) with mouse serum at a dilution of 1:10 to 1:50. For immunofluorescent analysis of ANA, HEp-2 slides were used. The images were analyzed by fluorescence microscope (Olympus FSX100). For mouse urine analysis, 24 hours albuminuria was measured using metabolic cages. Of note, mice were fed a 5% sucrose drinking solution during the 24 hours analysis in the metabolic cages. Urine (10 μl) was analyzed by SDS-PAGE and Coomassie blue staining. Bovine serum albumin (0.25, 0.5, 1.0, 2.5, and 5.0 μg) served as standard. Signals were quantified using ImageJ software (NIH). Resulting values of the 5 multiplication of the "size of the area" and the "mean gray value" of each albumin standards were used for construction of a standard curve and its associated mathematical function. Values were translated into albumin concentrations and extrapolated to 24-hour urine volume.

Histology and transmission electron microscopy

Organs were fixed by retrograde vascular perfusion with 4% paraformaldehyde in PBS, removed, and immersed in the same fixative for a maximum of 2 days until further processing for histology, immunohistochemistry, or transmission electron microscopy (TEM), as previously described (80). For immunocomplex analysis, frozen sections were used. 4 μm paraffin-processed formalin-fixed tissue sections were stained with Periodic Acid Schiff (PAS) or hematoxylin/eosin (H&E). Images were taken with an Olympus BX53 microscope with DP72 camera and processed using Adobe PhotoShop software. Ultra-thin 80-nm sections of resin-embedded kidney tissue were mounted on copper grids, treated with uranyl acetate and lead citrate, and examined by a pathologist (A.W.) in a blinded fashion using a JEOL 1010 transmission electron microscope (Tokyo, Japan).

Homophilic interaction assay

Protein A/G–purified DD1α-Ig proteins or Ig proteins (control) were covalently coupled to 6 μm blue carboxylated microparticles as recommended by the manufacturers (Polyscience, Inc.). 293T cells were transfected with the plasmids expressing full length DD1α, DD1α-ΔIgV, or control empty vector as indicated amount per well of six-well culture plates for 24 hours. The transfected cells were incubated with the Ig protein–coated beads in PBS containing 2% FBS at room temperature. After 30 min, unbound beads were washed with cold PBS and cell monolayers in culture media examined under an inverted microscope, and the binding was determined by measuring the optical density (O.D.) at 492 nm (81).

In situ proximity ligation assay

The assay was performed with the use of a Duolink using PLA Technology (Sigma-Aldrich). J774.1 macrophages and ZR75-1 breast cancer cells were transfected with plasmids encoding DD1α-HA or DD1α-Myc, respectively, for 24 hours. The transfected cells were trypsinized and cocultured on slide glasses in six-well culture plates. After 24 hours, cells were fixed, permeabilized, blocked, and then incubated with rabbit HA–specific Ab and mouse Myc–specific Ab at 4°C overnight. The cells were then subjected to an in situ proximity ligation assay with PLA probes, according to the manufacturer's protocol. All images were taken with a Nikon Eclipse Ti confocal microscope and processed using Adobe Photoshop software with minimal adjustment of brightness or contrast.

In vitro binding assay

His-fused DD1α (33–194) and GST-fused DD1α variants were purified from bacteria using Ni-NTA agarose (Life Technologies) or glutathione-Sepharose beads (GE Healthcare Life Sciences), respectively. For binding of His-DD1α (33–194) to Ig fusion proteins (DD1α-Ig, PD-1–Ig, or Ig), Ig-fused proteins were immobilized on protein A/G agarose. The His-fused DD1α (33–194) protein was incubated at 4°C for 4 hours in a binding buffer containing 20 mM HEPES, pH 7.4, 100 mM NaCl, 5 mM $MgCl_2$, 5 mM $CaCl_2$, 1 mM DTT, 0.1% NP-40, and 100 μg/ml BSA with GST-fused proteins immobilized on glutathione-agarose beads or Ig-fused proteins immobilized on protein A/G. The bound His-fused protein was eluted from the beads and analyzed by SDS-PAGE and Western blot using His-specific Ab.

Protein lipid overlay assay

Membrane lipid strips (Echelon Bioscience) prespotted with 15 different biologically active lipids, at 100 pmol per spot, were purchased. Nonspecific binding of membranes was blocked by incubation for 18 hours with 3% BSA in TBS-T (50 mM Tris at pH 7.4, 0.5 M NaCl, and 0.1% Tween-20). After blocking, membranes were incubated for 2 hours with 2 μg/ml of soluble recombinant proteins, such as DD1α-Ig purified from mammalian cell, DD1α-His purified from yeast, His-DD1α purified from bacteria, and TIM-1–Ig, and then were washed and incubated with indicated Abs, followed by incubation for 1 hour with a horseradish peroxidase–labeled secondary Ab. Binding was detected by chemiluminescent detection.

T cell activation assay

The cell culture plates were coated with CD3-specific Ab (OKT3, eBioscience for human T cells; 145-2C11, eBioscience for mouse T cells) and various concentrations of DD1α-Ig or PD-L1–Ig. The amount of Ig protein was kept constant at 10 μg/ml by the addition of control Ig protein. Mouse $CD4^+$ and $CD8^+$ T cells were purified from splenocytes freshly isolated from mice using $CD4^+$ T Cell Isolation Kit II, mouse or $CD8a^+$ T Cell Isolation Kit II, mouse (Miltenyi Biotec). Purity was confirmed to be over 90% by flow cytometry. The T cells were labeled with 1 μM CFSE, quenched by cold FBS, and incubated in plates coated with CD3-specific Ab and Ig proteins. On day 2 after stimulation, supernatant was collected, and cytokines were assayed by ELISA. On day 3, cells were stained with Ab against CD4-APC (RM4-5, eBioscience for mouse $CD4^+$ T cells) or Ab against CD8-APC (53-6.7, eBioscience for mouse $CD8^+$ T cells) and then analyzed for CFSE dilution by flow cytometry.

Binding assay of Ig fusion proteins to T cells

Purified human $CD4^+$ T cells from freshly isolated PBMCs were stimulated by plate-bound

CD3-specific Ab (5 μg/ml) for 3 days, collected, and then preincubated with 100 μg/ml DD1α-specific or control mouse IgG1 Ab for 30 min. Cells were then washed and incubated with 30 μg/ml DD1α-Ig or control Ig proteins (Fc portion; human IgG1; R&D Systems) for 30 min. After washing once with PBS, cells were incubated with antihuman IgG (5 μg/ml), cross-absorbed against mouse Ig (Southern Biotech), and washed twice with PBS. The bound Ig fusion proteins were analyzed by flow cytometry (*82*, *83*).

Statistical analysis

Statistics were calculated using Prism 6.0 software (GraphPad Software). For analysis of statistical difference between experiments involving two groups, a Student's two-tailed t test was applied. A one-way analysis of variance (ANOVA) was applied for statistical analysis of three or more groups. Significance was defined when P values were <0.05.

REFERENCES AND NOTES

1. S. Nagata, R. Hanayama, K. Kawane, Autoimmunity and the clearance of dead cells. *Cell* **140**, 619–630 (2010). doi: 10.1016/j.cell.2010.02.014; pmid: 20211132
2. M. R. Elliott, K. S. Ravichandran, Clearance of apoptotic cells: Implications in health and disease. *J. Cell Biol.* **189**, 1059–1070 (2010). doi: 10.1083/jcb.201004096; pmid: 20584912
3. L. E. Muñoz, K. Lauber, M. Schiller, A. A. Manfredi, M. Herrmann, The role of defective clearance of apoptotic cells in systemic autoimmunity. *Rheumatology* **6**, 280–289 (2010). doi: 10.1038/nrrheum.2010.46; pmid: 20431553
4. S. Nagata, Apoptosis and autoimmune diseases. *Ann. N. Y. Acad. Sci.* **1209**, 10–16 (2010). doi: 10.1111/j.1749-6632.2010.05749.x; pmid: 20958310
5. I. K. Poon, C. D. Lucas, A. G. Rossi, K. S. Ravichandran, Apoptotic cell clearance: Basic biology and therapeutic potential. *Nat. Rev. Immunol.* **14**, 166–180 (2014). doi: 10.1038/nri3607; pmid: 24481336
6. V. A. Fadok *et al*., Exposure of phosphatidylserine on the surface of apoptotic lymphocytes triggers specific recognition and removal by macrophages. *J. Immunol.* **148**, 2207–2216 (1992). pmid: 1545126
7. D. Park *et al*., BAI1 is an engulfment receptor for apoptotic cells upstream of the ELMO/Dock180/Rac module. *Nature* **450**, 430–434 (2007). doi: 10.1038/nature06329; pmid: 17960134
8. N. Kobayashi *et al*., TIM-1 and TIM-4 glycoproteins bind phosphatidylserine and mediate uptake of apoptotic cells. *Immunity* **27**, 927–940 (2007). doi: 10.1016/j.immuni.2007.11.011; pmid: 18082433
9. M. Miyanishi *et al*., Identification of Tim4 as a phosphatidylserine receptor. *Nature* **450**, 435–439 (2007). doi: 10.1038/nature06307; pmid: 17960135
10. S. Y. Park *et al*., Rapid cell corpse clearance by stabilin-2, a membrane phosphatidylserine receptor. *Cell Death Differ.* **15**, 192–201 (2008). doi: 10.1038/sj.cdd.4402242; pmid: 17962816
11. R. H. DeKruyff *et al*., T cell/transmembrane, Ig, and mucin-3 allelic variants differentially recognize phosphatidylserine and mediate phagocytosis of apoptotic cells. *J. Immunol.* **184**, 1918–1930 (2010). doi: 10.4049/jimmunol.0903059; pmid: 20083673
12. R. Hanayama *et al*., Identification of a factor that links apoptotic cells to phagocytes. *Nature* **417**, 182–187 (2002). doi: 10.1038/417182a; pmid: 12000961
13. H. Païdassi *et al*., C1q binds phosphatidylserine and likely acts as a multiligand-bridging molecule in apoptotic cell recognition. *J. Immunol.* **180**, 2329–2338 (2008). doi: 10.4049/jimmunol.180.4.2329; pmid: 18250442
14. D. P. Lane, p53, guardian of the genome. *Nature* **358**, 15–16 (1992). doi: 10.1038/358015a0; pmid: 1614522
15. B. Vogelstein, D. Lane, A. J. Levine, Surfing the p53 network. *Nature* **408**, 307–310 (2000). doi: 10.1038/35042675; pmid: 11099028
16. B. Zhivotovsky, G. Kroemer, Apoptosis and genomic instability. *Nat. Rev. Mol. Cell Biol.* **5**, 752–762 (2004). doi: 10.1038/nrm1443; pmid: 15340382
17. Y. Aylon, M. Oren, Living with p53, dying of p53. *Cell* **130**, 597–600 (2007). doi: 10.1016/j.cell.2007.08.005; pmid: 17719538
18. J. P. Kruse, W. Gu, Modes of p53 regulation. *Cell* **137**, 609–622 (2009). doi: 10.1016/j.cell.2009.04.050; pmid: 19450511
19. T. Cooks, C. C. Harris, M. Oren, Caught in the cross fire: p53 in inflammation. *Carcinogenesis* **35**, 1680–1690 (2014). doi: 10.1093/carcin/bgu134; pmid: 24942866
20. C. Muñoz-Fontela *et al*., Transcriptional role of p53 in interferon-mediated antiviral immunity. *J. Exp. Med.* **205**, 1929–1938 (2008). doi: 10.1084/jem.20080383; pmid: 18663127
21. S. J. Zheng, S. E. Lamhamedi-Cherradi, P. Wang, L. Xu, Y. H. Chen, Tumor suppressor p53 inhibits autoimmune inflammation and macrophage function. *Diabetes* **54**, 1423–1428 (2005). doi: 10.2337/diabetes.54.5.1423; pmid: 15855329
22. J. S. Park *et al*., p53 controls autoimmune arthritis via STAT-mediated regulation of the Th17 cell/Treg cell balance in mice. *Arthritis Rheum.* **65**, 949–959 (2013). doi: 10.1002/art.37841; pmid: 23280308
23. T. Mori *et al*., Identification of the interferon regulatory factor 5 gene (IRF-5) as a direct target for p53. *Oncogene* **21**, 2914–2918 (2002). doi: 10.1038/sj.onc.1205459; pmid: 11973653
24. B. T. Hummer, X. L. Li, B. A. Hassel, Role for p53 in gene induction by double-stranded RNA. *J. Virol.* **75**, 7774–7777 (2001). doi: 10.1128/JVI.75.16.7774-7777.2001; pmid: 11462054
25. M. Taura *et al*., p53 regulates Toll-like receptor 3 expression and function in human epithelial cell lines. *Mol. Cell. Biol.* **28**, 6557–6567 (2008). doi: 10.1128/MCB.01202-08; pmid: 18779317
26. D. J. Jung *et al*., Foxp3 expression in p53-dependent DNA damage responses. *J. Biol. Chem.* **285**, 7995–8002 (2010). doi: 10.1074/jbc.M109.047985; pmid: 20075077
27. H. Kawashima *et al*., Tumor suppressor p53 inhibits systemic autoimmune diseases by inducing regulatory T cells. *J. Immunol.* **191**, 3614–3623 (2013). doi: 10.4049/jimmunol.1300509; pmid: 24006461
28. A. Lujambio *et al*., Non-cell-autonomous tumor suppression by p53. *Cell* **153**, 449–460 (2013). doi: 10.1016/j.cell.2013.03.020; pmid: 23562644
29. Y. Okuda, M. Okuda, C. C. Bernard, Regulatory role of p53 in experimental autoimmune encephalomyelitis. *J. Neuroimmunol.* **135**, 29–37 (2003). doi: 10.1016/S0165-5728(02)00428-9; pmid: 12576221
30. S. Zhang *et al*., Trp53 negatively regulates autoimmunity via the STAT3-Th17 axis. *FASEB J.* **25**, 2387–2398 (2011). doi: 10.1096/fj.10-175299; pmid: 21471252
31. H. Takatori, H. Kawashima, K. Suzuki, H. Nakajima, Role of p53 in systemic autoimmune diseases. *Crit. Rev. Immunol.* **34**, 509–516 (2014). doi: 10.1615/CritRevImmunol.2014012193; pmid: 25597313
32. M. A. Fray, S. C. Bunnell, p53 keeps bystanders at the gates. *Immunity* **40**, 633–635 (2014). doi: 10.1016/j.immuni.2014.05.001; pmid: 24837097
33. H. G. Campbell *et al*., Does Δ133p53 isoform trigger inflammation and autoimmunity? *Cell Cycle* **11**, 446–450 (2012). doi: 10.4161/cc.11.3.19054; pmid: 22262184
34. M. Watanabe, K. D. Moon, M. S. Vacchio, K. S. Hathcock, R. J. Hodes, Downmodulation of tumor suppressor p53 by T cell receptor signaling is critical for antigen-specific CD4(+) T cell responses. *Immunity* **40**, 681–691 (2014). doi: 10.1016/j.immuni.2014.04.006; pmid: 24792911
35. L. Brown *et al*., CDIP, a novel pro-apoptotic gene, regulates TNFalpha-mediated apoptosis in a p53-dependent manner. *EMBO J.* **26**, 3410–3422 (2007). doi: 10.1038/sj.emboj.7601779; pmid: 17599062
36. M. A. Sakr *et al*., GI24 enhances tumor invasiveness by regulating cell surface membrane-type 1 matrix metalloproteinase. *Cancer Sci.* **101**, 2368–2374 (2010). doi: 10.1111/j.1349-7006.2010.01675.x; pmid: 20666777
37. L. Wang *et al*., VISTA, a novel mouse Ig superfamily ligand that negatively regulates T cell responses. *J. Exp. Med.* **208**, 577–592 (2011). doi: 10.1084/jem.20100619; pmid: 21383057
38. D. B. Flies, S. Wang, H. Xu, L. Chen, Cutting edge: A monoclonal antibody specific for the programmed death-1 homolog prevents graft-versus-host disease in mouse models. *J. Immunol.* **187**, 1537–1541 (2011). doi: 10.4049/jimmunol.1100660; pmid: 21768399
39. L. Aloia, S. Parisi, L. Fusco, L. Pastore, T. Russo, Differentiation of embryonic stem cells 1 (Dies1) is a component of bone morphogenetic protein 4 (BMP4) signaling pathway required for proper differentiation of mouse embryonic stem cells. *J. Biol. Chem.* **285**, 7776–7783 (2010). doi: 10.1074/jbc.M109.077156; pmid: 20042595
40. A. I. Su *et al*., A gene atlas of the mouse and human protein-encoding transcriptomes. *Proc. Natl. Acad. Sci. U.S.A.* **101**, 6062–6067 (2004). doi: 10.1073/pnas.0400782101; pmid: 15075390
41. C. Wu *et al*., BioGPS: An extensible and customizable portal for querying and organizing gene annotation resources. *Genome Biol.* **10**, R130 (2009). doi: 10.1186/gb-2009-10-11-r130; pmid: 19919682
42. J. Suzuki, D. P. Denning, E. Imanishi, H. R. Horvitz, S. Nagata, Xk-related protein 8 and CED-8 promote phosphatidylserine exposure in apoptotic cells. *Science* **341**, 403–406 (2013).doi: 10.1126/science.1236758; pmid: 23845944
43. J. R. Jeffers *et al*., Puma is an essential mediator of p53-dependent and -independent apoptotic pathways. *Cancer Cell* **4**, 321–328 (2003). doi: 10.1016/S1535-6108(03)00244-7; pmid: 14585359
44. M. R. Elliott *et al*., Nucleotides released by apoptotic cells act as a find-me signal to promote phagocytic clearance. *Nature* **461**, 282–286 (2009). doi: 10.1038/nature08296; pmid: 19741708
45. D. Park *et al*., Continued clearance of apoptotic cells critically depends on the phagocyte Ucp2 protein. *Nature* **477**, 220–224 (2011). doi: 10.1038/nature10340; pmid: 21857682
46. B. Fadeel *et al*., Phosphatidylserine exposure during apoptosis is a cell-type-specific event and does not correlate with plasma membrane phospholipid scramblase expression. *Biochem. Biophys. Res. Commun.* **266**, 504–511 (1999). doi: 10.1006/bbrc.1999.1820; pmid: 10600532
47. V. A. Fadok, A. de Cathelineau, D. L. Daleke, P. M. Henson, D. L. Bratton, Loss of phospholipid asymmetry and surface exposure of phosphatidylserine is required for phagocytosis of apoptotic cells by macrophages and fibroblasts. *J. Biol. Chem.* **276**, 1071–1077 (2001). doi: 10.1074/jbc.M003649200; pmid: 10986279
48. L. Wang *et al*., Disruption of the immune-checkpoint VISTA gene imparts a proinflammatory phenotype with predisposition to the development of autoimmunity. *Proc. Natl. Acad. Sci. U.S.A.* **111**, 14846–14851 (2014). doi: 10.1073/pnas.1407447111; pmid: 25267631
49. D. B. Flies *et al*., Coinhibitory receptor PD-1H preferentially suppresses $CD4^+$ T cell-mediated immunity. *J. Clin. Invest.* **124**, 1966–1975 (2014). doi: 10.1172/JCI74589; pmid: 24743150
50. C. A. O'Callaghan, Renal manifestations of systemic autoimmune disease: Diagnosis and therapy. *Best Pract. Res. Clin. Rheumatol.* **18**, 411–427 (2004). doi: 10.1016/j.berh.2004.03.002; pmid: 15158748
51. I. Le Mercier *et al*., VISTA regulates the development of protective antitumor immunity. *Cancer Res.* **74**, 1933–1944 (2014). doi: 10.1158/0008-5472.CAN-13-1506; pmid: 24691994
52. J. L. Lines, L. F. Sempere, T. Broughton, L. Wang, R. Noelle, VISTA is a novel broad-spectrum negative checkpoint regulator for cancer immunotherapy. *Cancer Immunol Res* **2**, 510–517 (2014). doi: 10.1158/2326-6066.CIR-14-0072; pmid: 24894088
53. D. R. Green, H. M. Beere, Apoptosis. Gone but not forgotten. *Nature* **405**, 28–29 (2000). doi: 10.1038/35011175; pmid: 10811203
54. D. R. Green, T. Ferguson, L. Zitvogel, G. Kroemer, Immunogenic and tolerogenic cell death. *Nat. Rev. Immunol.* **9**, 353–363 (2009). doi: 10.1038/nri2545; pmid: 19365408
55. R. Rodriguez-Manzanet *et al*., T and B cell hyperactivity and autoimmunity associated with niche-specific defects in apoptotic body clearance in TIM-4-deficient mice. *Proc. Natl. Acad. Sci. U.S.A.* **107**, 8706–8711 (2010). doi: 10.1073/pnas.0910359107; pmid: 20368430
56. R. Hanayama *et al*., Autoimmune disease and impaired uptake of apoptotic cells in MFG mice. *Science* **304**, 1147–1150 (2004). doi: 10.1126/science.1094359; pmid: 15155946
57. Z. G. Ramirez-Ortiz *et al*., The scavenger receptor SCARF1 mediates the clearance of apoptotic cells and prevents autoimmunity. *Nat. Immunol.* **14**, 917–926 (2013). doi: 10.1038/ni.2670; pmid: 23892722
58. M. Botto *et al*., Homozygous C1q deficiency causes glomerulonephritis associated with multiple apoptotic bodies. *Nat. Genet.* **19**, 56–59 (1998). doi: 10.1038/ng0598-56; pmid: 9590289
59. Y. Hirose *et al*., Inhibition of Stabilin-2 elevates circulating hyaluronic acid levels and prevents tumor metastasis. *Proc. Natl. Acad. Sci. U.S.A.* **109**, 4263–4268 (2012). doi: 10.1073/pnas.1117560109; pmid: 22371575

60. K. Wong *et al*., Phosphatidylserine receptor Tim-4 is essential for the maintenance of the homeostatic state of resident peritoneal macrophages. *Proc. Natl. Acad. Sci. U.S.A.* **107**, 8712–8717 (2010). doi: 10.1073/pnas.0910929107; pmid: 20421466
61. V. A. Fadok *et al*., Macrophages that have ingested apoptotic cells in vitro inhibit proinflammatory cytokine production through autocrine/paracrine mechanisms involving TGF-beta, PGE2, and PAF. *J. Clin. Invest.* **101**, 890–898 (1998). doi: 10.1172/JCI1112; pmid: 9466984
62. A. M. Fairhurst, A. E. Wandstrat, E. K. Wakeland, Systemic lupus erythematosus: Multiple immunological phenotypes in a complex genetic disease. *Adv. Immunol.* **92**, 1–69 (2006). doi: 10.1016/S0065-2776(06)92001-X; pmid: 17145301
63. S. N. Liossis, B. Kovacs, G. Dennis, G. M. Kammer, G. C. Tsokos, B cells from patients with systemic lupus erythematosus display abnormal antigen receptor-mediated early signal transduction events. *J. Clin. Invest.* **98**, 2549–2557 (1996). doi: 10.1172/JCI119073; pmid: 8958217
64. C. H. Feldman *et al*., Epidemiology and sociodemographics of systemic lupus erythematosus and lupus nephritis among US adults with Medicaid coverage, 2000-2004. *Arthritis Rheum.* **65**, 753–763 (2013). doi: 10.1002/art.37795; pmid: 23203603
65. M. O. Li, M. R. Sarkisian, W. Z. Mehal, P. Rakic, R. A. Flavell, Phosphatidylserine receptor is required for clearance of apoptotic cells. *Science* **302**, 1560–1563 (2003). doi: 10.1126/science.1087621; pmid: 14645847
66. J. R. Hong *et al*., Phosphatidylserine receptor is required for the engulfment of dead apoptotic cells and for normal embryonic development in zebrafish. *Development* **131**, 5417–5427 (2004). doi: 10.1242/dev.01409; pmid: 15469976
67. X. Qu *et al*., Autophagy gene-dependent clearance of apoptotic cells during embryonic development. *Cell* **128**, 931–946 (2007). doi: 10.1016/j.cell.2006.12.044; pmid: 17350577
68. A. Devitt *et al*., Persistence of apoptotic cells without autoimmune disease or inflammation in $CD14^{-/-}$ mice. *J. Cell Biol.* **167**, 1161–1170 (2004). doi: 10.1083/jcb.200410057; pmid: 15611337
69. R. S. Scott *et al*., Phagocytosis and clearance of apoptotic cells is mediated by MER. *Nature* **411**, 207–211 (2001). doi: 10.1038/35075603; pmid: 11346799
70. L. Richardson *et al*., EMAGE mouse embryo spatial gene expression database: 2014 update. *Nucleic Acids Res.* **42(D1)**, D835–D844 (2001). doi: 10.1093/nar/gkt1155
71. P. Arizti *et al*., Tumor suppressor p53 is required to modulate BRCA1 expression. *Mol. Cell. Biol.* **20**, 7450–7459 (2000). doi: 10.1128/MCB.20.20.7450-7459.2000; pmid: 11003642
72. L. Fang, G. Li, G. Liu, S. W. Lee, S. A. Aaronson, p53 induction of heparin-binding EGF-like growth factor counteracts p53 growth suppression through activation of MAPK and PI3K/Akt signaling cascades. *EMBO J.* **20**, 1931–1939 (2001). doi: 10.1093/emboj/20.8.1931; pmid: 11296226
73. D. Panigrahy *et al*., PPARalpha agonist fenofibrate suppresses tumor growth through direct and indirect angiogenesis inhibition. *Proc. Natl. Acad. Sci. U.S.A.* **105**, 985–990 (2008). doi: 10.1073/pnas.0711281105; pmid: 18199835
74. P. P. Ongusaha *et al*., RhoE is a pro-survival p53 target gene that inhibits ROCK I-mediated apoptosis in response to genotoxic stress. *Curr. Biol.* **16**, 2466–2472 (2006). doi: 10.1016/j.cub.2006.10.056; pmid: 17174923
75. W. S. El-Deiry *et al*., *WAF1*, a potential mediator of p53 tumor suppression. *Cell* **75**, 817–825 (1993). doi: 10.1016/0092-8674(93)90500-P; pmid: 8242752
76. T. D. Halazonetis, L. J. Davis, A. N. Kandil, Wild-type p53 adopts a 'mutant'-like conformation when bound to DNA. *EMBO J.* **12**, 1021–1028 (1993).pmid: 8458320
77. R. Majeti *et al*., CD47 is an adverse prognostic factor and therapeutic antibody target on human acute myeloid leukemia stem cells. *Cell* **138**, 286–299 (2009). doi: 10.1016/j.cell.2009.05.045
78. K. Segawa *et al*., Caspase-mediated cleavage of phospholipid flippase for apoptotic phosphatidylserine exposure. *Science* **344**, 1164–1168 (2014). doi: 10.1126/science.1252809; pmid: 24904167
79. S. Jaiswal *et al*., CD47 is up regulated on circulating hematopoietic stem cells and leukemia cells to avoid phagocytosis. *Cell* **138**, 271–285 (2009). doi: 10.1016/j.cell.2009.05.046; pmid: 19632178
80. S. Hakroush *et al*., Effects of increased renal tubular vascular endothelial growth factor (VEGF) on fibrosis, cyst formation, and glomerular disease. *Am. J. Pathol.* **175**, 1883–1895 (2009). doi: 10.2353/ajpath.2009.080792; pmid: 19834063
81. C. Santiago *et al*., Structures of T Cell immunoglobulin mucin receptors 1 and 2 reveal mechanisms for regulation of immune responses by the TIM receptor family. *Immunity* **26**, 299–310 (2007). doi: 10.1016/j.immuni.2007.01.014; pmid: 17363299
82. J. H. Meyers *et al*., TIM-4 is the ligand for TIM-1, and the TIM-1-TIM-4 interaction regulates T cell proliferation. *Nat. Immunol.* **6**, 455–464 (2005). doi: 10.1038/ni1185; pmid: 15793576
83. C. J. Chan *et al*., The receptors CD96 and CD226 oppose each other in the regulation of natural killer cell functions. *Nat. Immunol.* **15**, 431–438 (2014). doi: 10.1038/ni.2850; pmid: 24658051

ACKNOWLEDGMENTS

We thank members of the Cutaneous Biology Research Center of MGH, J. H. Lee, J. Park, M. Kashiwagi, J. Seavitt, S. Ezell, A. Gurkar, T. Namba, and M. Choo for helpful suggestions on experiments and C. Ford and T. Woo for technical assistance. We also thank A. Sharpe and G. Freeman for precious advice, guidance during the study, and generous reading of the manuscript. This paper is dedicated to the memory of Victor Fung. We also thank T. Strom for TIM family protein constructs and Z. Wang for the Protein Core from MGH. S.H. was supported by a research stipend from the Deutsche Forschungsgemeinschaft (HA 6334/1-1) and currently is in the Department of Pathology, University Medical Center Göttingen, Göttingen, Germany. A.C. was supported by MD student fellowship stipends from Boehringer Ingelheim Fonds. The work was partially funded by NIH grants CA149477, CA142805, CA80058, S10RR027673, DK57683, DK062472, DK091218, and DK093378.

SUPPLEMENTARY MATERIALS

www.sciencemag.org/content/349/6247/1261669/suppl/DC1
Materials and Methods
Figs. S1 to S12
Tables S1 to S25
Movies S1 to S3

23 September 2014; accepted 17 June 2015
10.1126/science.1261669

RESEARCH ARTICLE

METABOLISM

S-Nitrosylation links obesity-associated inflammation to endoplasmic reticulum dysfunction

Ling Yang,[1]* Ediz S. Calay,[1] Jason Fan,[1]† Alessandro Arduini,[1] Ryan C. Kunz,[2] Steven P. Gygi,[2] Abdullah Yalcin,[1] Suneng Fu,[1]‡ Gökhan S. Hotamisligil[1,3]§

The association between inflammation and endoplasmic reticulum (ER) stress has been observed in many diseases. However, if and how chronic inflammation regulates the unfolded protein response (UPR) and alters ER homeostasis in general, or in the context of chronic disease, remains unknown. Here, we show that, in the setting of obesity, inflammatory input through increased inducible nitric oxide synthase (iNOS) activity causes S-nitrosylation of a key UPR regulator, IRE1α, which leads to a progressive decline in hepatic IRE1α-mediated XBP1 splicing activity in both genetic (*ob/ob*) and dietary (high-fat diet–induced) models of obesity. Finally, in obese mice with liver-specific IRE1α deficiency, reconstitution of IRE1α expression with a nitrosylation-resistant variant restored IRE1α-mediated XBP1 splicing and improved glucose homeostasis in vivo. Taken together, these data describe a mechanism by which inflammatory pathways compromise UPR function through iNOS-mediated S-nitrosylation of IRE1α, which contributes to defective IRE1α activity, impaired ER function, and prolonged ER stress in obesity.

The endoplasmic reticulum (ER) is the major site for the synthesis and folding of proteins, lipid trafficking, and metabolism, as well as an intracellular store of calcium. The ER is equipped with a robust adaptive response system called the unfolded protein response (UPR), which mitigates stress under many challenging conditions that interfere with folding capacity (*1*). This adaptive system is mediated by three canonical signaling pathways, initiated by three lumenal sensors—inositol-requiring protein 1 (IRE1α), protein kinase RNA-like ER kinase (PERK), and activating transcription factor 6 (ATF6)—to control a complex network of adaptive responses to restore normal ER function (*1*, *2*). Obesity is associated with ER stress and chronic metabolic inflammation that collectively disrupt systemic glucose homeostasis (*2*). However, unlike experimental ER stress in which all UPR branches are activated (*3*), obesity features a disproportionate production of key molecules mediating ER defenses, such as a decline in ATF6 in the presence of sustained PERK activation (*4*, *5*). Here, we investigated the differential regulation of the UPR branches in the liver of obese mice and revealed a mechanism that contributes to the impaired resolution of ER stress and consequent metabolic decline in the setting of obesity.

[1]Department of Genetics and Complex Diseases and Sabri Ülker Center, Harvard T.H. Chan School of Public Health, Boston, MA 02115, USA. [2]Department of Cell Biology, Harvard Medical School, Boston, MA 02115, USA. [3]Broad Institute of Harvard and MIT, Cambridge, MA 02142, USA. *Present address: Department of Anatomy and Cell Biology, University of Iowa, Carver College of Medicine, Iowa City, IA 52242, USA. †Present address: Columbia University College of Physicians and Surgeons, New York, NY 10032, USA. ‡Present address: School of Life Sciences, Tsinghua University, Peking-Tsinghua Center for Life Sciences, Beijing, China 100084. §Corresponding author. E-mail: ghotamis@hsph.harvard.edu

Obesity results in impaired IRE1α-mediated XBP1 splicing activity

IRE1α plays an important role in maintaining ER homeostasis through initiating unconventional splicing of the mRNA encoding X-box–binding protein 1 (XBP1) to create a translational frameshift. This produces a potent transcription factor, spliced XBP1 (sXBP1), which regulates expression of genes encoding ER chaperones (*6*), as well as proteins involved in phospholipid synthesis and de novo lipogenesis (*7*). As shown in Fig. 1, A and B, and fig. S1A and reported previously in many independent studies (*4*, *8*–*10*), in the livers of obese mice, we observed sustained activation of the canonical ER stress sensors, indicated by increased PERK and IRE1α phosphorylation, c-Jun N-terminal kinase (JNK) activation, and increased UPR gene expression. However, the level of unspliced XBP1 protein (uXBP1) was increased in obese liver tissue compared with that of lean controls, in the absence of a corresponding increase in sXBP1, which strongly indicated a defect in the processing of uXBP1 to sXBP1 by IRE1α endoribonuclease activity, despite the robust IRE1α phosphorylation and JNK activation (Fig. 1A). In contrast, in lean mice, most of the uXBP1 was converted into the spliced form. In addition, we detected a marked decline in the expression of hepatic sXBP1, as well as its target ER chaperone genes, at later stages of disease in both genetic (*ob/ob*) and high-fat diet (HFD)–induced models of obesity (Fig. 1B and fig. S1A).

To determine whether the progressive decline in XBP1 splicing also affected the direct regulation of potential sXBP1 target gene expression, we performed chromatin immunoprecipitation (ChIP) assays in primary hepatocytes from *ob/ob* mice and matching lean controls. Promoter occupancy of several sXBP1 target genes—including ER chaperones [glucose-regulated protein of 78 kD (Grp78) hypoxia up-regulated 1 (*Hyou1* or *ORP-150*), and protein disulfide isomerase family A member 3 (*Pdia3*)], as well as genes involved in protein degradation, such as ER degradation-enhancing α-mannosidase (*EDEM*), and glycosylation, such as mannosyl (α-1,6-)-glycoprotein β-1,2-*N*-acetylglucosaminyltransferase (*Mgat2*)—was readily detected in the lean samples but markedly diminished in the *ob/ob* hepatocytes (Fig. 1C). These results demonstrated that both the expression and activity of sXBP1 are defective in liver cells from obese mice despite phosphorylation and sustained activation of IRE1α.

Next, we examined sXBP1 expression in the livers of HFD-fed mice, as well as lean controls [regular diet (RD)], upon experimentally induced ER stress. As shown in Fig. 1D, injection of the chemical stress inducer tunicamycin acutely induced the production of sXBP1, but this effect was suppressed in the livers of HFD mice. In a second model, HFD or RD mice were transduced with adenovirus-mediated full-length XBP1. As shown in Fig. 1D, in the setting of obesity, the production of sXBP1 was significantly reduced compared with that of lean controls. Next, we asked whether the decrease in sXBP1 expression in obesity was directly related to impaired ribonuclease activity of IRE1α. In an in vitro splicing assay using endogenous IRE1α protein immunopurified from mouse liver, we observed a significant decline in IRE1α-mediated XBP1 processing in samples from obese mice (both *ob/ob* and HFD) compared with lean controls (Fig. 1E).

Metaflammation is associated with impaired XBP1 splicing

Because IRE1α phosphorylation remained intact in the obese livers but XBP1 splicing activity was markedly diminished, we hypothesized that a phosphorylation-independent, obesity-induced modification of IRE1α might underlie the selective inhibition of its ribonuclease activity. Obesity is characterized by chronic metabolic inflammation, termed metaflammation (*11*–*14*), and numerous inflammatory signaling cascades exhibiting aberrant activity in obesity share a common feature: a marked increase in inducible nitric oxide synthase (iNOS) expression (*15*). Indeed, induction of iNOS and nitric oxide (NO) production is observed in many inflammatory diseases (*16*, *17*). We noted that the decline in the expression of sXBP1 in liver tissue of obese animals coincided with markedly increased iNOS expression in both dietary and genetic obesity models (Fig. 1F), whereas endothelial NOS (eNOS) expression levels were similar between lean and obese tissues,

and neuronal NOS mRNA expression was not detectable. To examine whether the nitrosylation-mediated inhibition of the IRE1α ribonuclease activity was a function of iNOS induction as part of metaflammation, we tested the influence of suppression or overexpression of iNOS on XBP1 splicing in primary hepatocytes. Suppression of iNOS expression resulted in enhanced thapsigargin (Tg)–induced XBP1 splicing in primary hepatocytes isolated from lean mice (Fig. 1G). In contrast, reconstitution of iNOS in primary hepatocytes isolated from iNOS-deficient mice resulted in a significant decrease in Tg-induced sXBP1 generation and Grp78 expression (fig. S1, C and D). To examine whether the IRE1α ribonuclease activity was regulated by iNOS induction, we performed in vitro splicing assays in *ob/ob* liver tissue after in vivo small hairpin RNA (shRNA)–induced suppression of iNOS; expression was reduced more than 75% (fig. S1E). iNOS suppression in vivo led to markedly enhanced IRE1α-mediated XBP1 splicing (Fig. 1H). Consistent with the established role of ER stress in insulin resistance, we observed significantly enhanced hepatic insulin signaling assessed by insulin-induced phosphorylation of insulin receptor and Akt (fig. S1, F and G). There was also a decrease in serum glucose and significantly enhanced systemic glucose tolerance in *ob/ob* mice after the suppression of hepatic iNOS (fig. S1, H and I). Taken together, these results demonstrate that iNOS is a critical mediator of hepatic IRE1α ribonuclease activity, with consequences for systemic glucose homeostasis.

Nitrosative stress results in IRE1α S-nitrosylation

S-Nitrosylation—the covalent attachment of a nitrogen monoxide group to the thiol side chain of

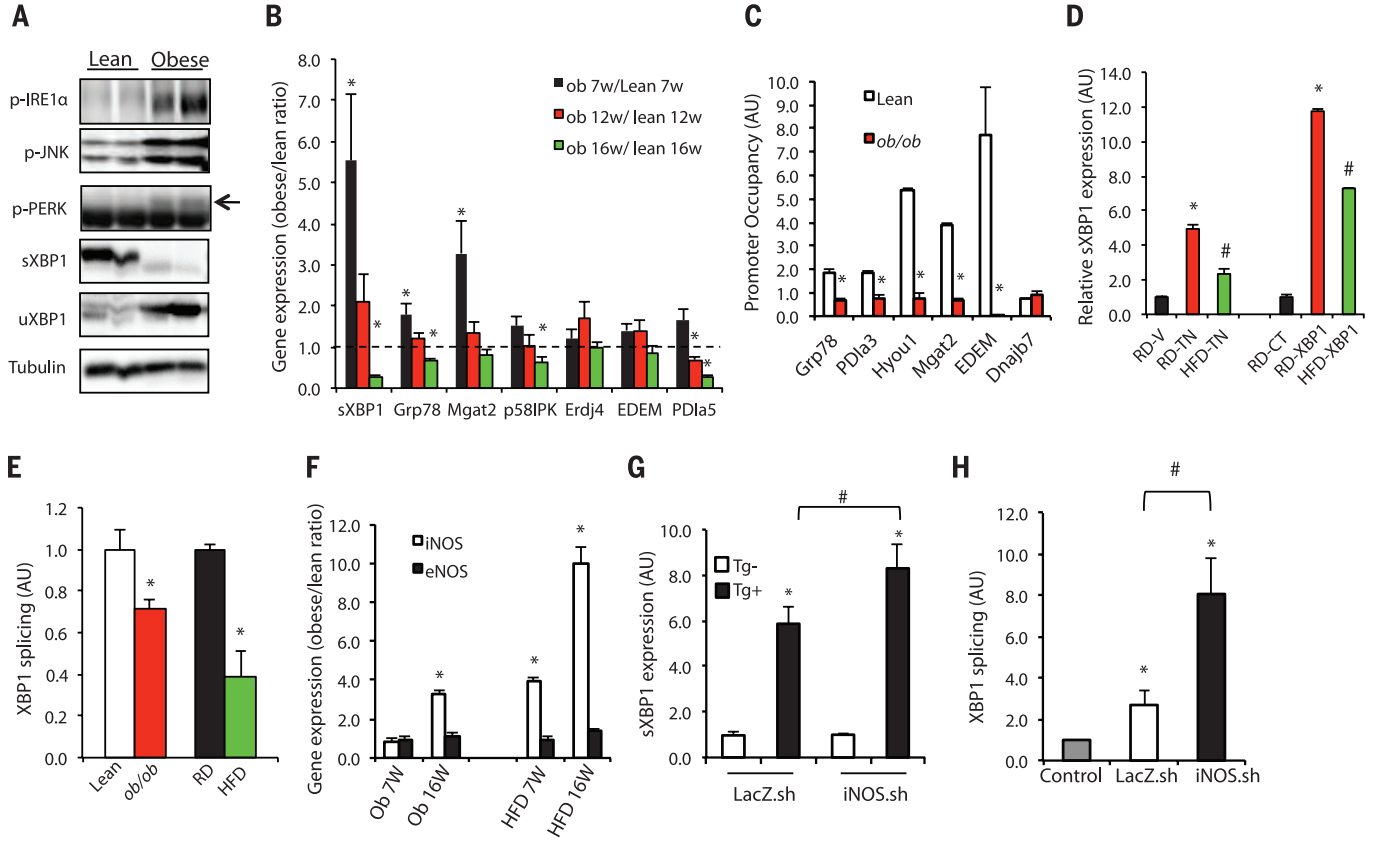

Fig. 1. Inflammation contributes to defective IRE1α-mediated XBP1 splicing in obese liver. (**A**) UPR status was examined in livers of 16-week-old obese (*ob/ob*) and lean mice by using phosphorylation of IRE1α, PERK, and JNK, as well as expression of sXBP1 and uXBP1 as markers. Data are representative of results from two to three independent cohorts of mice. (**B**) Expression of hepatic UPR modulators in 7-, 12- and 16-week-old *ob/ob* mice relative to lean controls (dashed line indicates lean level), $n = 4$. (**C**) ChIP assay examining XBP1 target gene occupancy in primary hepatocytes from 16-week-old *ob/ob* and lean mice. Data were normalized to 2% input, followed by comparison to each immunoglobulin G (IgG) control ($n = 4$). Data are representative of results from two independent sets of mice. Asterisk (*) indicates statistical significance between lean and obese mice in (B) and (C). Statistical analysis was performed by multiple *t* tests and significance was determined by the Holm-Šídák method using Prism (B) and Student's *t* test (C). AU, arbitrary units. (**D**) sXBP1 was examined in the livers from lean (RD) and obese (HFD-fed) mice injected with vehicle (V), or tunicamycin (TN, 6 hours, 0.5 mg/kg per kg body weight). sXBP1 expression was also examined in the livers from control mice fed RD or HFD transduced with full-length XBP1 (RD-XBP1, HFD-XBP1) or lean controls (RD-XBP1). Asterisk (*) indicates statistical significance between treatments within the control group, and # indicates statistical significance between RD and HFD [one-way analysis of variance (ANOVA) followed by post hoc Tukey's test], $n = 6$ to 8 mice. (**E**) In vitro splicing assays measuring the XBP1 splicing efficiency using hepatic IRE1α from mice with dietary (HFD) and genetic (*ob/ob*) obesity and controls. sXBP1 expression was examined by qRT-PCR. Results are normalized to lean samples. Asterisk (*) indicates statistical significance between lean and obese mice (Student's *t* test, $n = 3$). Data are representative of results from two independent sets of mice. (**F**) iNOS and eNOS mRNAs were examined in livers of 7- and 16-week-old *ob/ob* or HFD-fed mice and lean controls by qRT-PCR. Asterisk (*) indicates statistical significance between lean and obese mice (Student's *t* test), $n = 4$ to 6. (**G**) sXBP1 expression was examined by qRT-PCR in primary hepatocytes from lean mice transduced with Ad-shiNOS (iNOS.sh) or control virus (LacZ.sh) followed by treatment with thapsigargin (Tg+) for 2 hours, $n = 4$. (**H**) In vitro XBP1 splicing assay using IRE1α purified from the livers *ob/ob* mice after iNOS suppression (normalized to IgG control). Asterisk (*) indicates statistical significance between treatments and controls, and # indicates statistical significance between iNOS.sh group and LacZ.sh group (one-way ANOVA followed by post hoc Tukey's test). All data are shown as means ± SEM. Data are representative of results from two independent sets of mice. *$P < 0.05$; #$P < 0.05$.

cysteine residues—has emerged as a mechanism for dynamic, posttranslational regulation of proteins, including UPR regulators, such as PDI (*18*). Thus, we next determined whether nitrosylation induced by iNOS-mediated NO production could regulate IRE1α ribonuclease (RNase) activity. For this, we first examined the alterations in general protein S-nitrosylation (SNO) in the livers of lean and obese mice using a biotin switch method (*19*, *20*). There was a significant increase in hepatic protein S-nitrosylation in both dietary and genetic models of obesity (Fig. 2A and fig. S2A). Because protein nitrosylation is highly regulated by glutathione levels (*21*, *22*), we examined the amount of glutathione in its reduced form (GSH) in the livers of *ob/ob* mice and lean controls and observed a significant decrease in GSH in the livers of *ob/ob* mice (fig. S2B), consistent with potentially decreased denitrosylation capacity in the obese condition. To determine whether altered nitrosylation status may affect ER function, S-nitrosylated proteins were isolated from the livers of *ob/ob* mice and lean controls, followed by detection of proteins critical to ER stress and adaptive responses. These experiments demonstrated that several ER chaperones, such as calnexin and protein disulfide isomerase (PDI), exhibited increased nitrosylation (Fig. 2B), as did the insulin receptor (IR), as has been previously reported (*23*). Of note, we detected significantly enhanced S-nitrosylation of IRE1α in the livers of both *ob/ob* mice and HFD-induced obese mice compared with lean controls (Fig. 2B and fig. S2C). These data identified IRE1α as a target for S-nitrosylation and raised the possibility that alterations in IRE1α function in the obese liver may result from its modification by this mechanism.

To examine the direct effect of NO production on IRE1α-mediated XBP1 splicing, *IRE1α*$^{-/-}$ mouse embryonic fibroblasts (MEFs) were reconstituted with FLAG-tagged human IRE1α, followed by treatment with tumor necrosis factor-α (TNFα), a key inflammatory mediator in the induction of NO synthesis. TNFα pretreatment significantly dampened Tg-induced production of sXBP1 (fig. S2D). However, the TNFα-mediated suppression of XBP1 splicing was relieved when the experiment was performed in the presence of an iNOS inhibitor, N^G-monomethyl-L-arginine (NMMA) (fig. S2D). Reciprocally, NO production by the chemical NO donor *S*-nitrosoglutathione (GSNO) resulted in decreased ER stress–induced XBP1 splicing (fig. S2E). To confirm that the NO-mediated decrease in XBP1 splicing under ER stress conditions was caused by impaired IRE1α ribonuclease activity, we performed an XBP1 in vitro splicing assay using IRE1α purified from cells treated with Tg and/or TNFα, and in the absence or presence of an iNOS inhibitor. IRE1α from Tg-treated cells mediated robust XBP1 splicing in vitro, whereas this XBP1 splicing activity was significantly inhibited by TNFα treatment and rescued by inhibition of iNOS (Fig. 2C). We further examined the S-nitrosylation state of IRE1α in the presence of NO. First, *IRE1α*$^{-/-}$ MEFs were reconstituted with FLAG-tagged IRE1α; the cells were then treated with TNFα in the presence or absence of iNOS or iNOS inhibitor, followed by a biotin switch assay. TNFα treatment resulted in S-nitrosylation of IRE1α, which was further enhanced by iNOS overexpression and reduced by iNOS inhibition (Fig. 2D). Furthermore, in vivo, iNOS suppression in liver tissue of *ob/ob* mice led to decreased S-nitrosylated IRE1α, which was associated with enhanced expression of Grp78 and reduced levels of CHOP expression and IRE1α and JNK phosphorylation, which indicated overall improvement in ER function and reduced ER

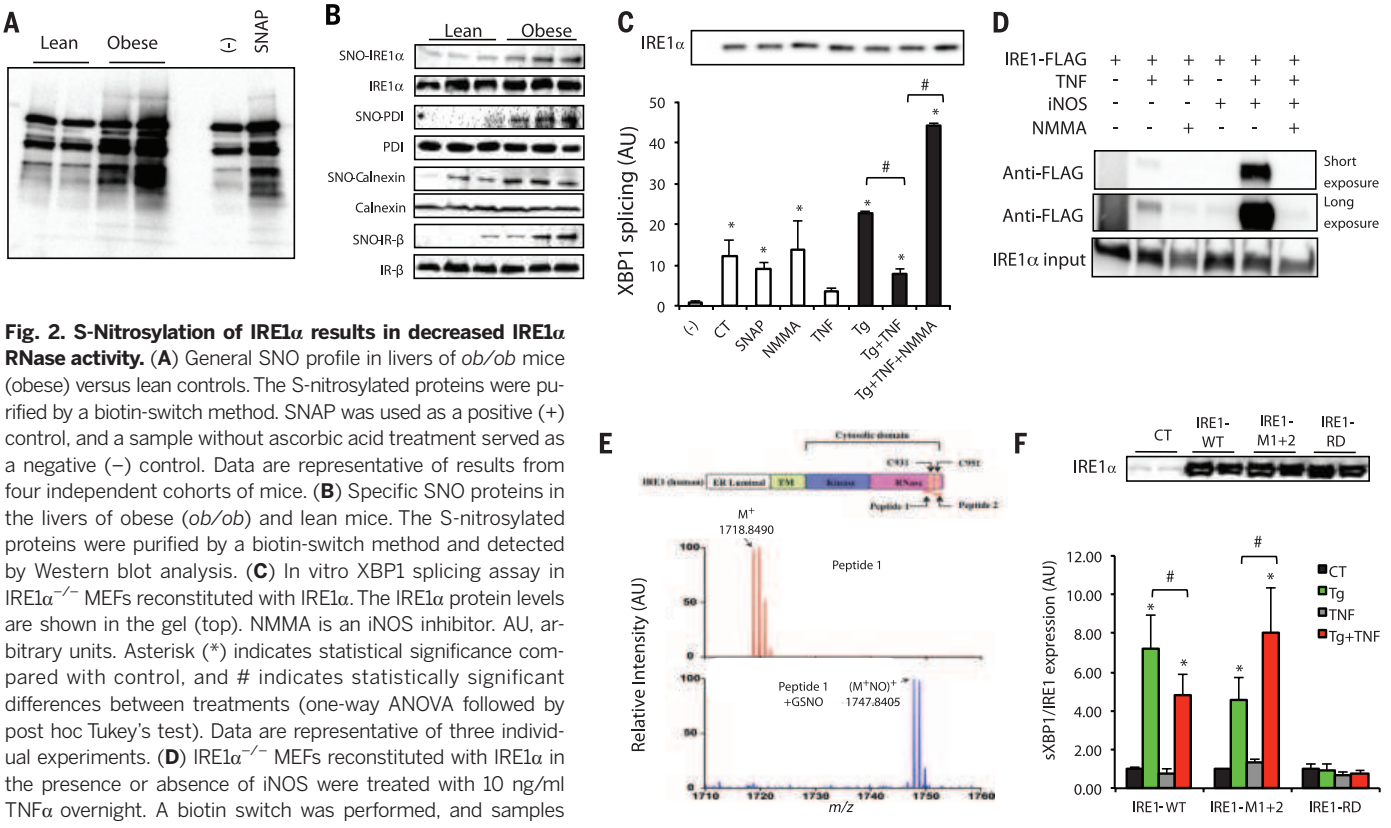

Fig. 2. S-Nitrosylation of IRE1α results in decreased IRE1α RNase activity. (**A**) General SNO profile in livers of *ob/ob* mice (obese) versus lean controls. The S-nitrosylated proteins were purified by a biotin-switch method. SNAP was used as a positive (+) control, and a sample without ascorbic acid treatment served as a negative (–) control. Data are representative of results from four independent cohorts of mice. (**B**) Specific SNO proteins in the livers of obese (*ob/ob*) and lean mice. The S-nitrosylated proteins were purified by a biotin-switch method and detected by Western blot analysis. (**C**) In vitro XBP1 splicing assay in IRE1α$^{-/-}$ MEFs reconstituted with IRE1α. The IRE1α protein levels are shown in the gel (top). NMMA is an iNOS inhibitor. AU, arbitrary units. Asterisk (*) indicates statistical significance compared with control, and # indicates statistically significant differences between treatments (one-way ANOVA followed by post hoc Tukey's test). Data are representative of three individual experiments. (**D**) IRE1α$^{-/-}$ MEFs reconstituted with IRE1α in the presence or absence of iNOS were treated with 10 ng/ml TNFα overnight. A biotin switch was performed, and samples were blotted with the FLAG-specific antibody. Data are representative of two individual experiments. (**E**) MS analysis of S-nitrosylated peptide 1, which includes the C931 in the RNase domain of human IRE1α. Shown is unmodified peptide 1, single-charged M^+ (*m/z* 1718.8490), and the peptide after GSNO modification $(M+NO)^+$ (*m/z* 1747.8405). Nitrosylation of peptide 1 results in a *m/z* change of +28.9915. (Top) A scheme of IRE1α protein structure is shown. (**F**) qRT-PCR for sXBP1 in IRE1α-deficient primary hepatocytes reconstituted with WT IRE1α, or nitrosylation-resistant IRE1α (IRE1-M1+2) with mutations in two SNO sites in the RNase domain, or IRE1α with a mutation in its RNase domain (IRE1-RD). The cells were treated with 10 ng/ml TNFα overnight in the presence or absence of Tg (100 nM, 2 hours). Results are presented as sXBP1/IRE1α expression levels in each group normalized to controls. (Top) The IRE1α protein levels are shown. All data are shown as means ± SEM. Asterisk (*) indicates statistical significance compared with control, and # indicates statistically significant differences between treatments (one-way ANOVA followed by post hoc Tukey's test, $n = 4$). $^*P < 0.05$; $^\#P < 0.05$.

stress (fig. S2, F and G). These data demonstrated that increased iNOS activity in cells results in IRE1α nitrosylation and inhibition of its ribonuclease activity, which may contribute to the decline in ER function in the presence of an inflammatory signal.

We next sought to identify the relevant S-nitrosylated cysteine residues in human IRE1α, focusing on Cys^{931} (C931) and Cys^{951} (C951), the cysteines in the RNase domain. In the presence of a chemical NO donor, GSNO, mass spectrometry (MS) analysis revealed S-nitrosylation of both (C931) and (C951) on human IRE1α peptides (Fig. 2E and fig. S2H). We generated a variant IRE1α with alanine substitutions at these residues to prevent S-nitrosylation (IRE1-M1+2), and introduced this variant into primary hepatocytes isolated from mice with hepatocyte-specific IRE1α deletion (*24*), along with wild-type (WT) IRE1α and an IRE1α with a mutation in its RNase domain (IRE1-RD). Treatment with Tg induced XBP1 splicing in cells reconstituted with the WT IRE1α, but not in cells expressing IRE1-RD (Fig. 2F). Consistent with our previous findings, in cells expressing the WT IRE1α, TNFα treatment resulted in a significant decrease in Tg-induced XBP1 splicing. However, this inhibitory effect of TNFα on ER stress–induced XBP1 splicing was ameliorated in hepatocytes expressing the IRE1-M1+2 variant (Fig. 2F), which likely reflects an improved adaptive capacity in these cells. We also reproduced these results in *IRE1α*$^{-/-}$ MEFs reconstituted with WT IRE1α or IRE1α with single substitutions in the same two nitrosylation sites (fig. S2I). Taken together, these experiments in two cellular systems clearly demonstrate that IRE1α S-nitrosylation results in diminished ribonuclease activity and that this inhibition could be prevented by the mutation of target residues in vitro.

S-Nitrosylation impairs IRE1α oligomerization and RNase activity

To gain insights into how S-nitrosylation affects IRE1α RNase activity, we next modeled the relevant residues on the previously published crystal structure of human IRE1α (PDB 3P23) using the "S-nitrosator" Python script (*25*). As shown in Fig. 3A, C931 and C951 are exposed to a solvent-accessible area of the protein complex, where they are available for S-nitrosylation. Furthermore, because C931 and C951 are equally proximal to the RNA cleavage site and the protein dimerization interface, this modification could potentially prevent binding of another negatively charged molecule (such as XBP1 RNA) or could alter the oligomerization of IRE1α. Either of these outcomes may compromise IRE1α splicing activity (*26*) and provide a mechanistic explanation for the reduction of XBP1 splicing.

We then performed an in vitro cleavage assay to detect the direct effect of S-nitrosylation on IRE1α-mediated XBP1 processing, using a purified cytosolic portion of the human IRE1α (amino acids 465–977, IRE1c) and a fluorescence resonance energy transfer (FRET)–quenched XBP1 RNA minisubstrate (*27*). Chemical NO donor treatment impaired IRE1c-mediated XBP1 cleavage in a dose-dependent manner (Fig. 3B and fig. S3, A and B). In addition to the unique, unconventional splicing of XBP1, IRE1α RNase activity is also directed toward other substrates, including a process known as IRE1-dependent decay of mRNA (RIDD) (*28*). In an in vitro cleavage assay, we found that S-nitrosylation resulted in impaired cleavage of a FRET-RIDD RNA substrate, namely, secreted protein acidic and rich in cysteine (SPARC) (*29*), which suggests that in vitro, nitrosylation may result in a general impairment in IRE1α RNase enzyme activity (fig. S3C).

We next asked whether S-nitrosylation of IRE1α affected XBP1 recognition using an ultraviolet

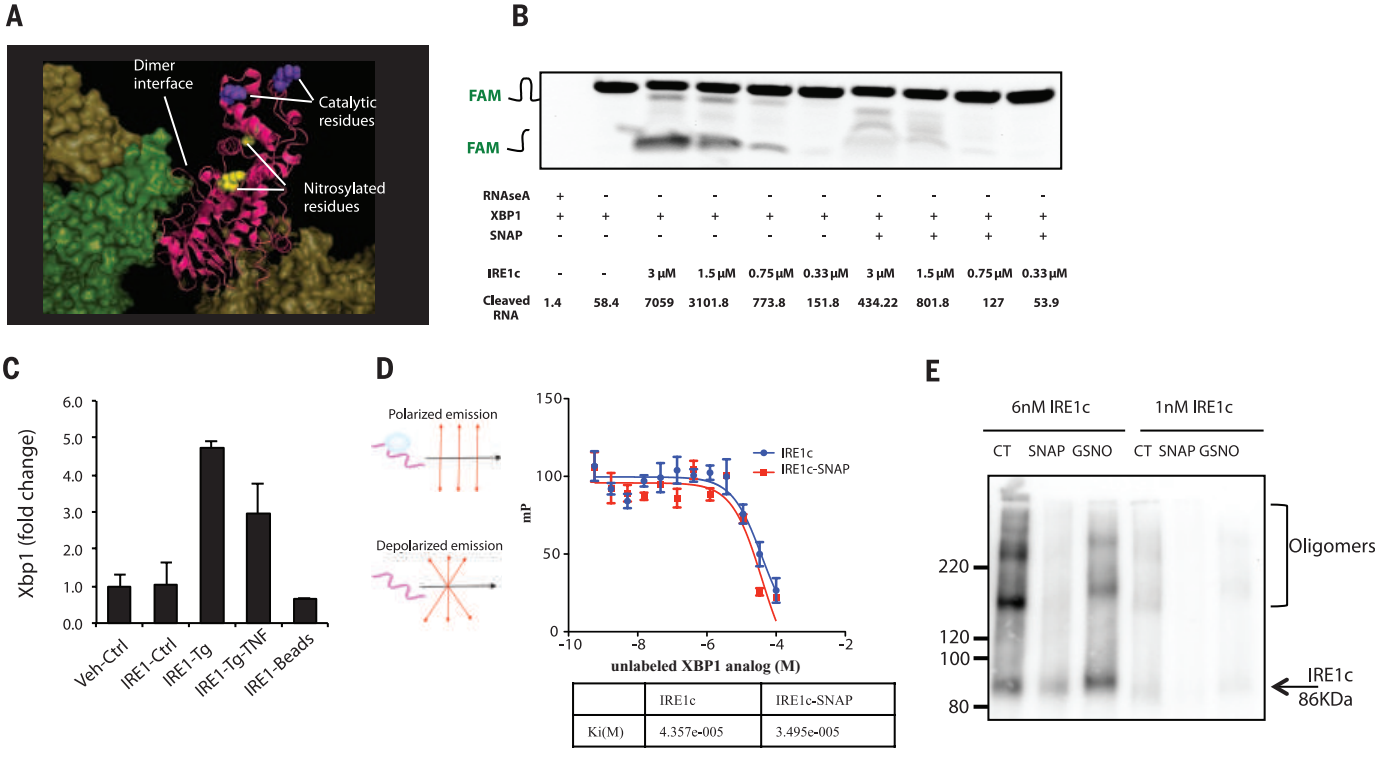

Fig. 3. S-Nitrosylation of IRE1α RNAse domain results in impaired XBP1 processing. (**A**) Nitrosylation on C931 and C951 was modeled onto the crystal structure of human IRE1α (PDB 3P23). (**B**) Urea polyacrylamide gel electrophoresis of sXBP1 substrate (labeled with FAM at the 5′ end) cleaved by different doses of IRE1c in the presence or absence of the chemical NO donor, SNAP (5 mM). RNase A was used as a control. The quantification of cleaved RNA is shown as band intensity (INT mm^2). Data are representative of three individual experiments. (**C**) CLIP assay detecting interaction between IRE1α and unspliced XBP1. IRE1α$^{-/-}$ MEFs were reconstituted with WT IRE1α, followed by treatment with Tg in the absence or presence of TNFα. After UV cross-linking, the IRE1α complexes were immunoprecipitated, and unspliced XBP1 was detected by qRT-PCR. Data are presented as means ± SEM, with $n = 6$. Data are representative of four individual experiments. (**D**) Binding of an RNase-resistant analog of XBP1 RNA, HP21 (FAM-dCdCdGdCdAdG) with IRE1c in the absence or presence of NO donor (*35*) was analyzed by fluorescence polarization assay using a nonfluorescent HP21 as a competitor. The data are presented as units of millipolarization (mP), and the inhibition constant (K_i) is shown (bottom). Data are representative of three individual experiments. (**E**) IRE1c oligomerization in the absence or presence of NO donors, SNAP (5 mM) or GSNO (0.25 mM). Data are representative of three individual experiments. *$P < 0.05$; #$P < 0.05$.

(UV) cross-linking and immunoprecipitation assay (CLIP) (*30*). *IRE1α*$^{-/-}$ MEFs were first reconstituted with WT or S-nitrosylation–resistant IRE1α, followed by treatment with Tg in the absence or presence of TNFα. After UV cross-linking, the IRE1α complexes were immunoprecipitated, followed by RNA isolation, and the unspliced XBP1 abundance was quantified by reverse transcription polymerase chain reaction (qRT-PCR). Tg treatment induced IRE1α interaction with uXBP1, and this was slightly (but not significantly) decreased by TNFα treatment (Fig. 3C and fig. S3D). As a complimentary approach, we used a fluorescence polarization assay (*31*) to address this same question. In this experimental setting, we assessed the physical interaction between IRE1α and an RNase-resistant RNA analog of HP21 RNA (dCdCdGdCdAdG) (*32*). NO donor treatment did not alter the C-terminal fragment of IRE1 (IRE1c) binding to HP21 RNA (Fig. 3D). Similarly, nitrosylation did not alter IRE1c recognition of a 2'-deoxy oligonucleotide bearing the RIDD consensus sequence (A.A.A.A.A.U.dG.dC.A.A.A.A.A) (fig. S3E) (*33*). Taken together, these data did not support the presence of a significant defect in substrate recognition by nitrosylated IRE1α under the experimental conditions tested.

It has been proposed that oligomerization of the ER-lumenal and cytoplasmic domains of IRE1α are important for IRE1α RNase activation (*34*), the IRE1α RNase output, and consequently the determination of cell fate (*35*). There is also evidence showing that the IRE1α RNase output can be directed toward XBP1 splicing or RIDD by IRE1α kinase inhibition (*36*) or alteration of oligomerization (*35*). As described above, the nitrosylation of cysteine residues could modify oligomerization and could lead to reduced general or substrate-specific IRE1α RNase activity. Indeed, in vitro, NO treatment of IRE1c decreased protein oligomerization (Fig. 3E). In this experiment, we also noted altered IRE1c mobility in the presence of GSNO treatment, which we reason might be caused by additional modification, such as *S*-glutathionylation, which can also occur after GSNO treatment (*37*). A similar pattern of reduced higher-molecular-weight oligomers were also observed in obese liver tissue compared with lean controls. Last, it has been suggested that several IRE1α protein partners, such as Bcl2 family proteins and Hsp90 could alter IRE1α-mediated XBP1 splicing (*38*). However, we did not observe significant changes in these interactions in the presence of NO inducers (fig. S3F). In summary,

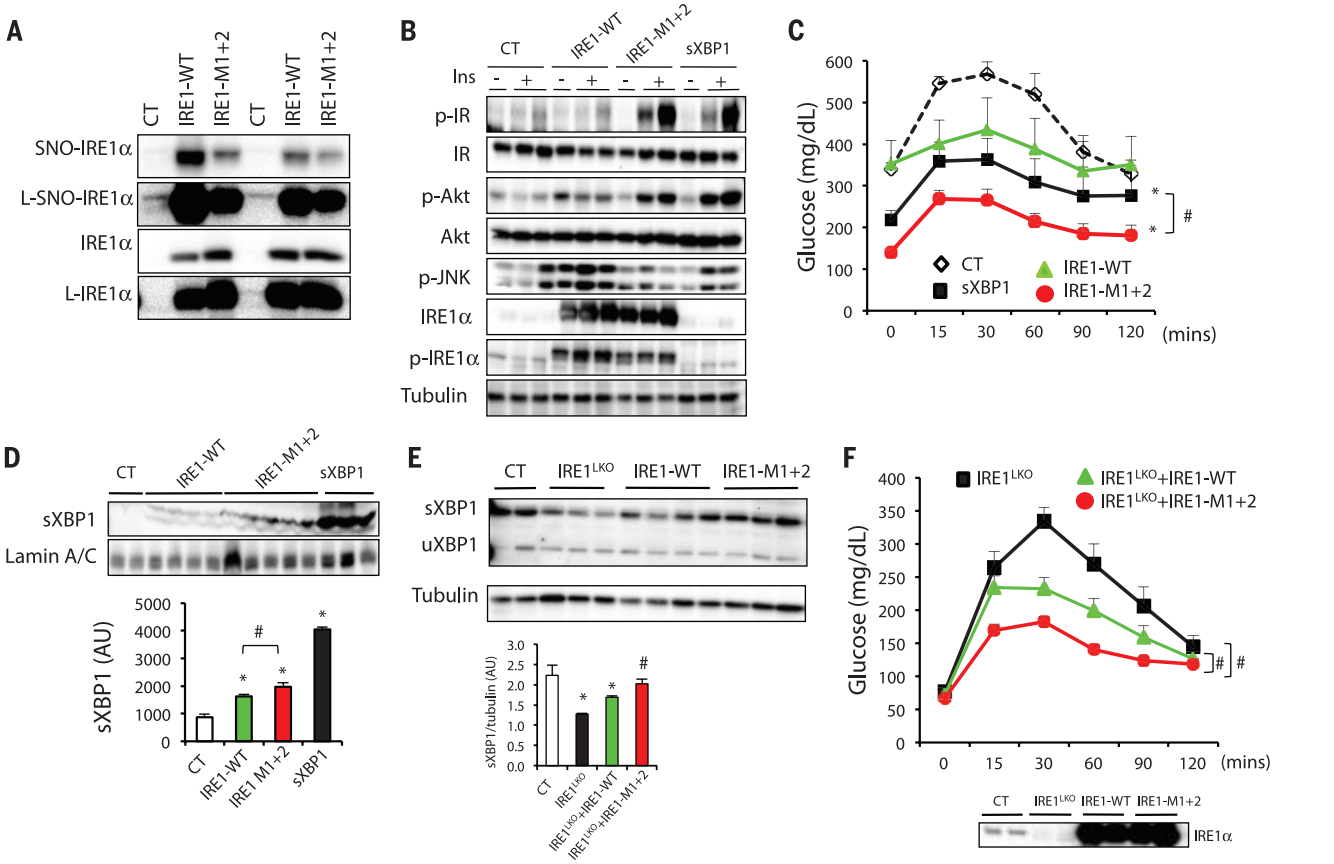

Fig. 4. Effects of IRE1α S-nitrosylation on insulin action and glucose homeostasis. (**A** to **D**) *ob/ob* mice were transduced with adenovirus containing sXBP1, WT IRE1α or nitrosylation-resistant IRE1-M1+2. (A) S-Nitrosylation of IRE1α in primary hepatocytes from these mice. The nitrosylation state of IRE1α was examined by biotin switch assay. L, longer exposure time. Data are representative of two individual mouse cohorts. (B) Hepatic insulin action and UPR status. $N = 6$ to 7, data are representative of two individual cohorts of mice. (C) Glucose tolerance test. All data are presented as means ± SEM, with statistical analysis of the area under the curve (AUC) performed by two-way ANOVA with post hoc Bonferroni test. Asterisk (*) indicates statistical significance compared with control, and # indicates differences between sXBP1 and IRE1-M1+2 expressing mice. Data are representative of two individual cohorts of mice [$n = 8$ (10-week-old mice)]. (D) sXBP1 expression in the nuclear fraction of liver, with densitometric analysis shown at the bottom of panel. Asterisk (*) indicates statistical significance compared with control, and # indicates statistically significant differences between IRE1-WT and IRE1-M1+2 (one-way ANOVA followed by post hoc Tukey's test). Data are representative of two individual mouse cohorts. (**E** and **F**) IRE1α-floxed mice were transduced with Ad-LacZ (Control) or Ad-Cre to delete IRE1α (IRE1^{LKO}), followed by expression of IRE1-WT or the IRE1-M1+2 variant. (E) Hepatic expression of sXBP1 and uXBP1 in the liver of these mice. Quantification of sXBP1/tubulin ratio is shown below. Asterisk (*) indicates statistical significance compared with control, and # indicates statistically significant differences between IRE1-WT and IRE1-M1+2 (one-way ANOVA followed by post hoc Tukey's test). Data are representative of two independent sets of mice. (F) Glucose tolerance test of the mice shown in (E). (Bottom) The IRE1α expression levels are shown [$n = 8$ (9-week old mice)]. Data are presented as means ± SEM, with statistical analysis of AUC performed by two-way ANOVA with post hoc Bonferroni test. Number sign (#) indicates statistically significant differences comparing IRE1^{LKO}+IRE-M1+2 with IRE1^{LKO}+IRE1-WT, as well as IRE1^{LKO}+IRE1-WT with IRE1^{LKO}. Data are representative of two individual cohorts of mice.*$P < 0.05$; #$P < 0.05$.

these data suggest that S-nitrosylation of IRE1α does not impair recognition of substrates or interaction with protein partners, but does alter oligomer formation, ultimately decreasing RNase activity toward XBP1 (fig. S3G).

S-Nitrosylation of IRE1α contributes to the obesity-induced decline in glucose homeostasis

Our experiments demonstrate that inflammation-related nitrosylation impairs IRE1α splicing activity. To more definitively determine whether this mechanism underlies the metabolic decline observed in obesity and whether inhibiting IRE1α nitrosylation could result in metabolic benefit, we exogenously expressed WT IRE1α, as well as the nitrosylation-resistant IRE1-M1+2 variant, in the liver of *ob/ob* mice. We reasoned that in the obese liver, exogenous WT IRE1α would be subject to nitrosylation and would be compromised in its ability to produce sufficient sXBP1, whereas the IRE1α variant would be resistant to modification by NO and therefore would exhibit positive metabolic activity. We first validated the S-nitrosylation status of the exogenously expressed IRE1α in primary hepatocytes from these mice by performing a biotin switch assay. There was a marked reduction in the S-nitrosylation of IRE1α in hepatocytes expressing IRE1-M1+2 variant compared with those expressing the WT form of IRE1α (Fig. 4A). We found that expression of WT IRE1α did not lead to an improvement in hepatic insulin sensitivity, whereas expression of the S-nitrosylation–resistant IRE1α mutant enhanced hepatic insulin action in *ob/ob* mice as measured by insulin receptor and Akt phosphorylation (Fig. 4B and fig. S4A). In addition, expression of the nitrosylation-resistant IRE1α mutant resulted in decreased JNK and IRE1α phosphorylation compared with the WT IRE1α, which indicated an improvement in hepatic ER stress in these animals. In glucose tolerance tests, *ob/ob* mice expressing the S-nitrosylation–resistant form of IRE1α exhibited a marked improvement compared with controls (Fig. 4C). There was also a modest improvement in glucose metabolism in mice expressing the WT IRE1α compared with controls. This effect may reflect residual IRE1α activity resulting from interactions between endogenous and exogenous molecules (*34*), which could partially overcome the S-nitrosylation–mediated suppression of IRE1α. Although we found a similar increase in hepatic insulin action upon expression of sXBP1 (Fig. 4B), we observed that expression of the nitrosylation-resistant form of IRE1α resulted in a greater improvement in glucose tolerance compared with sXBP1 expression. XBP1 is a dynamically regulated transcription factor involved in many aspects of ER function, and thus, this overexpression system may not recapitulate the physiological regulation and feedback patterns. In addition, expression of nitrosylation-resistant IRE1α may result in changes that are independent of XBP1 splicing. Of note, the level of nuclear sXBP1 was significantly increased in the liver of *ob/ob* mice overexpressing the mutant IRE1α compared with those expressing the WT IRE1α (Fig. 4D). These experiments clearly demonstrate that expression of a nitrosylation-resistant IRE1α or replenishment with spliced XBP1 can restore insulin action and glucose tolerance in obese animals.

Finally, considering the possibility that this experimental setting may not rule out the potential influence of endogenous IRE1α expression in obese mice, we tested the function of nitrosylation-resistant IRE1α on XBP1 splicing and glucose metabolism in the absence of endogenous IRE1α in vivo. For this, we first deleted endogenous IRE1α using adenoviral expression of Cre in IRE1α -floxed mice ($IRE1^{LKO}$), followed by restoration of hepatic IRE1α with either WT IRE1α or the IRE1-M1+2 variant. Whereas overexpression of WT IRE1α resulted in a low level of XBP1 splicing, the expression of sXBP1 and its downstream genes was greatly enhanced in mice expressing the nitrosylation-resistant variant (Fig. 4E and fig. S4B). Notably, in this system, residual endogenous IRE1α expression did contribute to a low level of sXBP1 production in $IRE1^{LKO}$ mice. Unlike the in vitro cleavage assay performed on one synthetic target (fig. S3C), among endogenous RIDD target genes we tested, we did not find significant differences in gene expression when WT IRE1α or the nitrosylation-resistant variant was expressed (fig. S4C), which might be due to the complexity of regulation of these genes in vivo. Deletion of IRE1α in liver resulted in a modest impairment of glucose homeostasis compared with control mice with intact endogenous IRE1α or IRE1α-deficient mice restored with WT IRE1α, as determined by glucose tolerance tests (Fig. 4F). Remarkably, expression of the IRE1-M1+2 variant in liver of IRE1α-deficient mice resulted in the greatest improvement in glucose homeostasis compared with all other groups (Fig. 4F). This improvement was accompanied by decreased JNK phosphorylation and increased expression of chaperones Hsp90 and Grp78 (fig. S4, D and E). Last, we observed an increase in IRE1α oligomerization in the livers from $IRE1^{LKO}$ mice with restoration of the IRE1-M1+2 compared with WT IRE1α (fig. S4F). Although we cannot rule out the possibility of additional effects of the cysteine to alanine mutations in IRE1α, taken together these data demonstrate that prevention of S-nitrosylation of IRE1α at the RNase domain improves hepatic IRE1α-mediated XBP1 splicing and glucose homeostasis.

Discussion

In this study, we have defined a mechanism through which obesity-related chronic inflammation cripples the most conserved branch of the UPR and impairs ER function. Increased hepatic iNOS action results in S-nitrosylation of IRE1α, which in turn results in the inhibition of its ribonuclease, but not kinase, activity and prevents the generation of sufficient levels of sXBP1 while promoting high levels of JNK activity. The data presented here indicate that iNOS-mediated nitrosylation of IRE1α is a critical component contributing to impairment of the UPR and prolonged ER stress in the presence of chronic metabolic and inflammatory stress. Consequently, reversal of this sequence of events, at the level of iNOS, sXBP1 production, or IRE1α nitrosylation, all promote ER homeostasis and result in substantial metabolic benefits. It has been reported that obesity results in decreased sXBP1 nuclear translocation or stability (*4*, *39*, *40*); our observations provide a molecular mechanism underlying the defective hepatic XBP1 splicing in obesity, which may be a critical determinant of ER function in metabolic homeostasis.

Previous studies have demonstrated that the N terminus of IRE1α senses stress signals from the ER lumen, which leads to autophosphorylation, which, in turn, activates the C-terminal RNase domain to catalyze site-specific RNA cleavage (*1*). Furthermore, IRE1α RNase activity can be either up- or down-regulated through selective targeting of its kinase domain by chemical inhibition (*1*, *41*, *42*). Ghosh *et al.* showed that the type II IRE1 kinase inhibitor KIRA6 blocks IRE1α RNAse activity through inhibiting oligomerization, which protects against β cell degeneration and ameliorates hyperglycemia in the Akita mouse model (*35*). Our findings suggest that S-nitrosylation of IRE1α uncouples kinase and RNase functions of the protein and that inhibition of S-nitrosylation of IRE1α results in enhanced XBP1 splicing, reduced JNK activity, and improved glucose homeostasis in *ob/ob* mice. Therefore, the regulation of the dual functionalities of IRE1α is complex and multitiered and that the contribution of sXBP1-mediated gene expression, as well as JNK activation, to metabolic homeostasis is fundamentally different between these two mouse models. IRE1α kinase inactivation is predicted to block JNK activation, which may exert a dominant protective effect in the Akita model, which is marked by β cell death (*36*, *43*). On the other hand, preserving the IRE1α-XBP1 axis and, consequently, proper ER homeostasis also leads to suppression of JNK in the liver and recovery of metabolic responses (*8*, *44*).

Finally, our findings indicate that the inflammatory pathways activated in obesity are intimately linked to the UPR and provide strong evidence that inflammatory mechanisms may act upstream of ER dysfunction by compromising the adaptive UPR in conditions of chronic metabolic excess and stress. It will be interesting to examine these interactions in additional tissues that exhibit metaflammation, such as adipocytes in obesity. We suggest that there may be important translational implications of these findings in designing therapeutic interventions against immunometabolic diseases, such as obesity and diabetes, as well as other chronic inflammatory conditions that feature ER dysfunction, to enable the physiological tone of the ER adaptive responses rather than artificially introducing individual components.

REFERENCES AND NOTES

1. D. Ron, P. Walter, *Nat. Rev. Mol. Cell Biol.* **8**, 519–529 (2007).
2. G. S. Hotamisligil, *Cell* **140**, 900–917 (2010).
3. J. H. Lin *et al.*, *Science* **318**, 944–949 (2007).
4. Y. Wang, L. Vera, W. H. Fischer, M. Montminy, *Nature* **460**, 534–537 (2009).
5. F. Engin *et al.*, *Sci. Transl. Med.* **5**, 211ra156 (2013).
6. C. Sidrauski, P. Walter, *Cell* **90**, 1031–1039 (1997).

7. A. H. Lee, N. N. Iwakoshi, L. H. Glimcher, *Mol. Cell. Biol.* **23**, 7448–7459 (2003).
8. U. Ozcan *et al.*, *Science* **306**, 457–461 (2004).
9. N. Sreejayan, F. Dong, M. R. Kandadi, X. Yang, J. Ren, *Obesity (Silver Spring)* **16**, 1331–1337 (2008).
10. T. Mao *et al.*, *Proc. Natl. Acad. Sci. U.S.A.* **108**, 15852–15857 (2011).
11. T. Nakamura *et al.*, *Cell* **140**, 338–348 (2010).
12. X. Zhang *et al.*, *Cell* **135**, 61–73 (2008).
13. C. N. Lumeng, A. R. Saltiel, *J. Clin. Invest.* **121**, 2111–2117 (2011).
14. M. F. Gregor, G. S. Hotamisligil, *Annu. Rev. Immunol.* **29**, 415–445 (2011).
15. M. Kaneki, N. Shimizu, D. Yamada, K. Chang, *Antioxid. Redox Signal.* **9**, 319–329 (2007).
16. B. T. Noronha, J. M. Li, S. B. Wheatcroft, A. M. Shah, M. T. Kearney, *Diabetes* **54**, 1082–1089 (2005).
17. M. Perreault, A. Marette, *Nat. Med.* **7**, 1138–1143 (2001).
18. T. Uehara *et al.*, *Nature* **441**, 513–517 (2006).
19. B. Derakhshan, P. C. Wille, S. S. Gross, *Nat. Protoc.* **2**, 1685–1691 (2007).
20. S. R. Jaffrey, S. H. Snyder, *Sci. STKE* **2001**, pl1 (2001).
21. D. T. Hess, A. Matsumoto, S. O. Kim, H. E. Marshall, J. S. Stamler, *Nat. Rev. Mol. Cell Biol.* **6**, 150–166 (2005).
22. C. I. Murray, H. Uhrigshardt, R. N. O'Meally, R. N. Cole, J. E. Van Eyk, *Mol. Cell. Proteomics* **11**, M111.013441 (2012).
23. M. A. Carvalho-Filho *et al.*, *Diabetes* **54**, 959–967 (2005).
24. T. Iwawaki, R. Akai, K. Kohno, *PLOS ONE* **5**, e13052 (2010).
25. M. R. Talipov, Q. K. Timerghazin, *J. Phys. Chem. B* **117**, 1827–1837 (2013).
26. K. P. Lee *et al.*, *Cell* **132**, 89–100 (2008).
27. R. L. Wiseman *et al.*, *Mol. Cell* **38**, 291–304 (2010).
28. J. Hollien *et al.*, *J. Cell Biol.* **186**, 323–331 (2009).
29. M. Maurel, E. Chevet, J. Tavernier, S. Gerlo, *Trends Biochem. Sci.* **39**, 245–254 (2014).
30. Z. Wang, J. Tollervey, M. Briese, D. Turner, J. Ule, *Methods* **48**, 287–293 (2009).
31. J. M. Pagano, C. C. Clingman, S. P. Ryder, *RNA* **17**, 14–20 (2011).
32. A. V. Korennykh *et al.*, *BMC Biol.* **9**, 47 (2011).
33. Y. Han *et al.*, *Science* **343**, 1244–1248 (2014).
34. A. V. Korennykh *et al.*, *Nature* **457**, 687–693 (2009).
35. R. Ghosh *et al.*, *Cell* **158**, 534–548 (2014).
36. D. Han *et al.*, *Cell* **138**, 562–575 (2009).
37. A. Martínez-Ruiz, S. Lamas, *Cardiovasc. Res.* **75**, 220–228 (2007).
38. C. Hetz, *Nat. Rev. Mol. Cell Biol.* **13**, 89–102 (2012).
39. S. W. Park *et al.*, *Nat. Med.* **16**, 429–437 (2010).
40. J. Winnay *et al.*, *Nat. Med.* **16**, 438–445 (2010).
41. F. Prischi, P. R. Nowak, M. Carrara, M. M. Ali, *Nat. Commun.* **5**, 3554 (2014).
42. L. Wang *et al.*, *Nat. Chem. Biol.* **8**, 982–989 (2012).
43. F. Urano *et al.*, *Science* **287**, 664–666 (2000).
44. J. Hirosumi *et al.*, *Nature* **420**, 333–336 (2002).

ACKNOWLEDGMENTS

We thank the members of the Hotamisligil laboratory for their contributions and discussions. We are especially grateful to K. C. Claiborn, A. Tirosh, G. Tuncman, and S. Widenmaier for their critical reading of the manuscript; T. Nakamura (University of Cincinnati) for providing the IRE1-RD construct; and P. Li (NIH) and Y. Lee for scientific discussions and insights. We thank A. Marette (Laval University, Canada) for providing materials for the preliminary experiments and discussions; T. Iwawaki (Gunma University, Japan) for the generous gift of the conditional IRE1α-deletion mouse model; F. Urano (Washington University in St. Louis) for providing the IRE1α$^{-/-}$ MEFs and constructs; R. Prywes (Columbia University) for providing the FLAG-IRE1α construct; and M. Talipov, M. Ivanov, and Q. Timerghazin (Marquette University) for assistance in computational modeling of nitrosylated IRE1α. L.Y. is supported by American Heart Association Postdoctoral Fellowship. This work is supported in part by a grant from NIH to G.S.H. (DK052539).

SUPPLEMENTARY MATERIALS

www.sciencemag.org/content/349/6247/500/suppl/DC1
Materials and Methods
Figs. S1 to S4
References (*45*–*53*)

7 October 2014; accepted 2 July 2015
10.1126/science.aaa0079

REPORTS

HEAVY FERMIONS

Strange metal without magnetic criticality

Takahiro Tomita,[1,2] Kentaro Kuga,[1] Yoshiya Uwatoko,[1] Piers Coleman,[3,4] Satoru Nakatsuji[1,5]*

A fundamental challenge to our current understanding of metals is the observation of qualitative departures from Fermi liquid behavior. The standard view attributes such non-Fermi liquid phenomena to the scattering of electrons off quantum critical fluctuations of an underlying order parameter. Although the possibility of non-Fermi liquid behavior isolated from the border of magnetism has long been speculated, no experimental confirmation has been made. Here, we report on the observation of a strange metal region away from a magnetic instability in an ultrapure single crystal. In particular, we show that the heavy-fermion superconductor β-YbAlB$_4$ forms a possible phase with strange metallic behavior across an extensive pressure regime, distinctly separated from a high-pressure magnetic quantum phase transition by a Fermi liquid phase.

Qualitative deviations from the standard theory of metals, Landau's Fermi liquid (FL) theory (*1*), develop almost routinely in the vicinity of a magnetic quantum phase transition (*2*, *3*). Conventionally, the origin of such non-Fermi liquid (NFL) behavior is attributed to the strong damping of the quasiparticle's lifetime by quantum critical fluctuations of an underlying order parameter (*4*–*9*).

Physics delineates between the concept of a phase, occupying a finite parameter region of ground state, and quantum critical points, appearing at the transition between phases. Although the possible existence of strange metal phases with NFL behavior, occupying a finite region of the ground-state phase diagram, has long been speculated (*10*–*19*), the close proximity of such phenomena to magnetic instability and a strong sensitivity to impurities has impeded an experimental confirmation of this idea. One of the most challenging questions is whether a fully paramagnetic strange metal phase is possible without magnetic criticality, retaining full symmetry of the underlying crystal structure.

Many prototypical quantum critical (QC) materials have been found within the class of 4*f* heavy-fermion compounds. The highly tunable characterstic energy scales and availability of high-purity crystals make them ideal candidates for the study of quantum criticality (*2*, *3*). In these materials, quantum criticality develops from a competition between local moment magnetism and the conduction electron screening of the local moments (the Kondo effect). Most QC heavy-fermion materials are known to have an almost integral valence that stabilizes the local moments considered essential for the criticality.

An exception to this rule is β-YbAlB$_4$, which exhibits quantum criticality despite strong mixed valency (*20*–*23*). Ultrapure single crystals of this material exhibit intrinsically singular thermodynamic and transport behavior up to an upper limit scale of several K, including a divergent temperature (T) dependence of the magnetic susceptibility ~$T^{-1/2}$ and an anomalous $T^{3/2}$ dependence of the electrical resistivity, both of which are extremely sensitive to a magnetic field B (*20*, *22*, *23*). In particular, T/B scaling of the magnetization has been observed over four decades of T/B, projected to extend down to fields as small as 0.1 mT (*22*). However, the observation of intrinsic quantum criticality as a function of field does not rule out the possibility that this phenomenon is merely a fine-tuned coincidence of lattice structure. Here, we demonstrate that the intrinsic quantum criticality of β-YbAlB$_4$ is not fine-tuned but instead occupies an extended island of pressure in the phase diagram, indicating a formation of a phase without any symmetry breaking external fields for stabilization. Furthermore, we show that the strange metal region is clearly surrounded and separated from a high-pressure magnetic instability by a finite pressure range of Fermi liquid behavior.

Our main experimental observation is that of an extensive region of the strange metal behavior, which evolves to a Fermi liquid phase (Fig. 1). We employed ultrapure crystals of β-YbAlB$_4$ with residual resistivity ratio (RRR) = 300 (with residual resistivity ρ_0 of < 0.5 μΩcm and mean free path of >1000 Å) and performed high-precision resistivity measurements (with noise levels of

[1]Institute for Solid State Physics, University of Tokyo, Kashiwa 277-8581, Japan. [2]College of Humanities and Sciences, Nihon University, Setagaya 156-8550, Japan. [3]Center for Materials Theory, Department of Physics and Astronomy, Rutgers University, Piscataway, N.J. 08854, USA. [4]Department of Physics, Royal Holloway, University of London, Egham, Surrey TW20 0EX, UK. [5]PRESTO, Japan Science and Technology Agency (JST), 4-1-8 Honcho Kawaguchi, Saitama 332-0012, Japan.
***Corresponding author. E-mail: satoru@issp.u-tokyo.ac.jp**

<40 pVHz$^{-1/2}$) using a piston-cylinder pressure cell in a dilution refrigerator (*24*). The pressure was continuously monitored using tin and aluminum superconducting manometers. X-ray diffraction analyses confirm a continuous reduction of the lattice parameters under pressure with a bulk modulus of 189 GPa (fig. S3) (*24*). Strikingly, under pressures up to 0.25 GPa, the resistivity exhibits the same anomalous power law behavior $\rho(T) \sim T^{1.5}$, with the same slope as at ambient pressure (Fig. 1A). In contrast, above $P_c \sim 0.4$ GPa, as we will discuss below, $\rho(T)$ shows a clear deviation from a $T^{1.5}$ dependence at low Ts and transitions to a FL-like T^2 dependence. This can be clearly seen in the T dependence of the power law exponent α (solid circle) in $\rho(T) - \rho_0 \propto T^{\alpha}$ (Fig. 1B). Under $P < P_c \sim 0.4$ GPa, α increases gradually on cooling and becomes constant ~1.5 below 0.3 K down to the superconducting (SC) transition temperature T_c. In contrast, at $P > P_c$ GPa, it saturates to $\alpha = 2.0$, the value characteristic of a FL state.

The superconducting T_c continuously decreases with pressure from $T_c = 80$ mK at ambient pressure and finally vanishes around 0.6 GPa (Fig. 1, A and C). To extend our analysis below T_c, we measured the resistivity by suppressing SC under a weak magnetic field along the *ab* plane, which should be irrelevant to the NFL critical fluctuations, thanks to the Ising character of the 4*f* moments. Figure 1A, inset, plots the resistivity versus $T^{1.5}$ measured at an in-plane field $B_{ab} =$ 0.1 T under various pressures. The corresponding

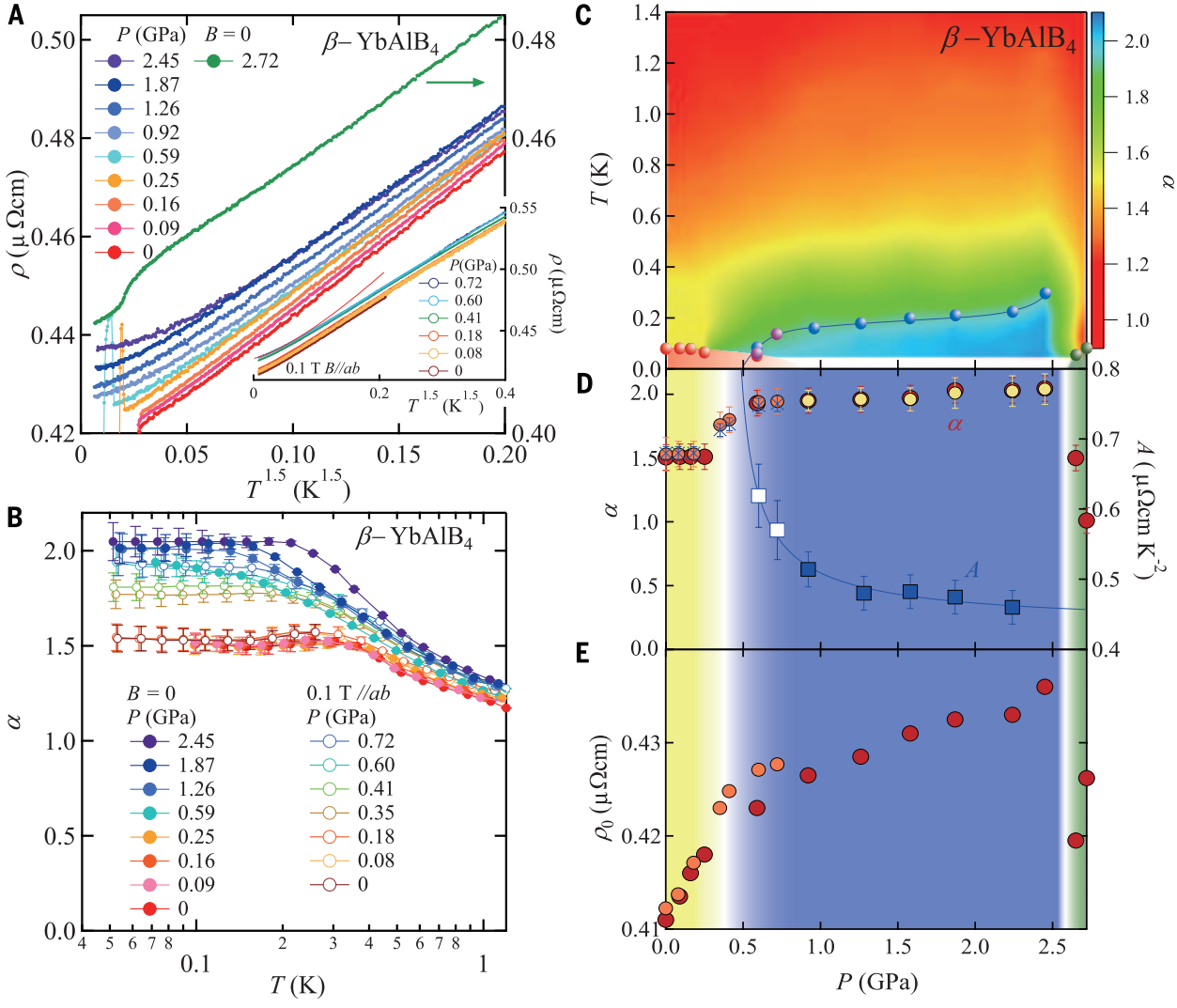

Fig. 1. Strange metal, Fermi liquid, and magnetic order in β-YbAlB$_4$ under pressure. Ultrapure single crystals (RRR = 300) were used (*24*). (**A**) Zero-field resistivity $\rho(T)$ versus $T^{1.5}$ at various pressures (left and right axes). The anomalous $T^{1.5}$ dependence was found robust up to $P_c \sim 0.4$ GPa. The superconducting (SC) transition was observed up to $P = 0.59$ GPa. Around P_c, a resistivity spike was observed just above T_c (*24*). (Inset) $\rho(T)$ versus $T^{1.5}$ obtained under an in-plane field $B_{ab} = 0.1$ T. The solid red line indicates a fit to T^2 dependence found at 0.72 GPa. (**B**) T dependence of the power law exponent $\alpha = \partial \ln(\rho(T) - \rho_0)/\partial \ln T$, corresponding to $\rho(T)$ in (A) under $B = 0$ (solid symbols) and under $B_{ab} = 0.1$ T (open symbols). (**C**) Contour plot of the exponent α in the P-T phase diagram for zero field. (For $B_{ab} = 0.1$ T, see fig. S8). Red, green, and blue circles indicate the superconducting T_c, Néel point T_N, and T_{FL} where $\rho(T)$ starts showing T^2 dependence, respectively. T_{FL}, determined using $\rho(T)$ under $B_{ab} = 0.1$ T, is also shown as purple circles. T_{FL} becomes strongly suppressed near $P \sim P_c$ (fig. S8). The solid line is a guide to the eye. (**D**) P dependence of the exponent α and the coefficient A [of the T^2 dependence of $\rho(T)$] estimated in two T ranges: 90 ~ 120 mK under zero field (α, large red circles), and 40 ~ 60 mK under zero field at $P > 0.8$ GPa (α, yellow circles; A, closed squares) and under $B_{ab} = 0.1$ T at $P < 0.8$ GPa (α, orange circles; A, open squares). Blue crosses: $\alpha = 1 + \partial \ln(\partial \rho(T)/\partial T)/\partial \ln T$ in the T range 40 ~ 80 mK, $B_{ab} = 0.1$ T and $P < 0.8$ GPa. Solid line: Fit to $A = A_0 + A_1/(P - P_c)^{\beta}$, yielding $\beta = 0.8(1)$, $P_c = 0.40(5)$ GPa, $A_1 = 0.05(1)$ μΩcm GPa/K^2 and $A_0 = 0.43(1)$ μΩcm/K^2. (**E**) P dependence of the residual resistivity ρ_0 under zero field (red) and under $B_{ab} = 0.1$ T (orange). The background color (yellow, white, blue, and green) in (D) and (E) is a guide to the eye.

T dependence of the exponent (Fig. 1B) indicates that the strange metallic state with $\alpha = 1.5$ extends down to the lowest T ~ 50 mK under $P < P_c$, whereas the exponent saturates to α ~ 1.8 at P ~ P_c and to $\alpha = 2$ for $P > P_c$. The Fermi liquid temperature T_{FL}, below which $\rho(T)$ shows a T^2 dependence, systematically decreases with decreasing pressure and appears to vanish at P ~ P_c (fig. S8).

The contour plots of the exponent α (Fig. 1C) obtained using the zero-field $\rho(T)$ data in Fig. 1A and fig. S8A reveal an extended region of anomalous resistivity exponent, indicating the formation of the strange metal phase and its subsequent crossover into the high pressure FL phase. From ambient pressure, a NFL (yellow) region with $\alpha = 1.5$ occupies a finite range up to P_c ~ 0.4 GPa above the SC dome. In contrast, at pressures beyond P_c up to 2.5 GPa, α locks into a constant ~2 (blue) below ~100 mK, indicating the formation of a FL phase. To carefully examine the phase evolution, in Fig. 1D, we plot the exponents $\alpha = \partial \ln(\rho(T) - \rho_0)/\partial \ln T$ at the midpoints of two temperature ranges: 90 ~ 120 mK under zero field (large red circles) and 40 ~ 60 mK under an in-plane field of 0.1 T to suppress the SC (orange circles). For the non-SC region at $P > 0.8$ GPa, we plot the zero-field exponent for the T range 40 ~ 60 mK (yellow circles). To further evaluate the exponent without the ambiguity associated with the residual resistivity, we have also carried out the analysis of the resistivity exponent (blue crosses) using $\alpha = 1 + \partial \ln(\partial \rho(T)/\partial T)/\partial \ln T$ in the T range 40 ~ 80 mK by suppressing the SC under 0.1 T at $P < 0.8$ GPa. All the data are consistent with the existence of a NFL phase with a constant $\alpha \approx 1.5$ at $P < P_c$ and a FL phase with $\alpha = 2.0$ at $P > P_c$ (Fig. 1D). The apparent crossover between $\alpha = 1.5$ and 2.0 marked by the two points with intermediate exponents is most likely a consequence of experimental resolution and a small inhomogeneity in the pressure. The presence of the superconducting resistivity spike close to P_c (Fig. 1A) supports this interpretation (*24*).

In the FL phase, the A coefficient for the ρ ~ T^2 law is found to be field-independent at $B_{ab} \leq 0.1$ T (fig. S8C) (24). The A coefficient has a component that diverges at P_c, following ~$1/(P - P_c)^{0.8(1)}$ with $P_c = 0.40(5)$ GPa (Fig. 1D). In addition, changes in P dependence of ρ_0 are observed around P_c for both $B = 0$ and 0.1 T (Fig. 1E). Taken together with the change in the exponent α, these anomalies suggest a possible quantum phase transition at P_c separating the strange metal phase from the high-pressure FL.

Each of the putative NFL phases reported to date directly adjoin a magnetic phase and are thus linked to magnetic criticality (*11*, *12*, *14*, *17*, *19*). Generally, in Yb-based heavy-fermion compounds, both physical and chemical pressure induce magnetism, stabilizing an "Yb^{3+}" state with a 4*f* magnetic moment and a smaller ionic radius than its nonmagnetic "Yb^{2+}" counterpart (*25*). To clarify the relation between magnetism and the observed extensive regime of NFL behavior in β-$YbAlB_4$, we have performed a detailed study using high pressure and chemical substitution.

We performed "high-T(> 2 K)" resistivity measurements in a cubic anvil cell, which allowed us to reach much higher pressures, up to 8 GPa (Fig. 2A and fig. S6B) (*24*). Whereas a systematic change is found in the resistivity $\rho(T)$ at $T > 10$ K, no change was found in $\rho(T)$ at $P \leq 2.3$ GPa below ~10 K (*24*). In the contour plots of the resistivity exponent α (Fig. 2B), by far the most prominent feature of the phase diagram is the wide (red) region of anomalous T-linear resistivity (*24*). This region spans a pressure range from ambient pressure to 3 GPa, extending over a decade of T from ~2 to 20 K (Fig. 2, A and B). Beyond the critical pressure P_N ~ 2.5, GPa (fig. S6) (*24*), the temperature derivative of resistivity $d\rho(T)/dT$ shows an onset of increase on cooling at a pressure-dependent temperature T_N (Fig. 2A, inset) (*24*). This temperature marks the development of antiferromagnetic (AF) order, as we will discuss below. $T_N(P)$ rises rapidly to 18 K at 8 GPa, which is very high for an Yb-based heavy-fermion system.

Correspondingly, in the "low-T(< 1 K)" measurements using the dilution refrigerator, application of pressures exceeding P_N ~ 2.5 GPa in a piston cylinder cell gives rise to a sudden decrease in ρ_0 (Fig. 1E); moreover, a kink develops in the resistivity and its T derivative at a temperature T_N, which rapidly rises from 80 mK at

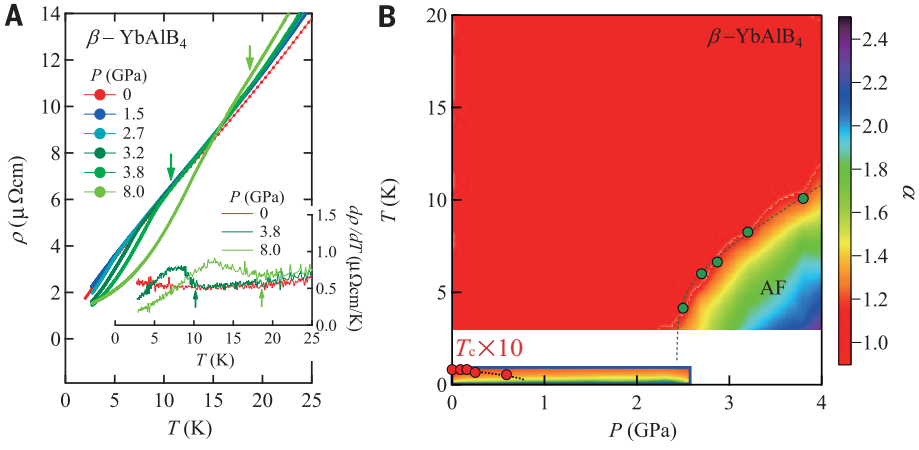

Fig. 2. Pressure-induced antiferromagnetism in β-$YbAlB_4$. (**A**) T dependence of the in-plane resistivity $\rho(T)$ obtained under various pressures in a cubic anvil cell above $T > 2$ K. (Inset) $d\rho/dT$ versus T. The arrows indicate the Néel temperatures at different pressures. (**B**) Contour plots of the power law exponent $\alpha = \partial \ln(\rho(T) - \rho_0)/\partial \ln T$ of $\rho(T)$ in the P-T phase diagram of an ultrapure single-crystal of β-$YbAlB_4$ (RRR = 300). Its low T and low P region specified by the blue frame in (B) corresponds to the one in Fig. 1C. For clarity, the values of T_c are multiplied by a factor of 10.

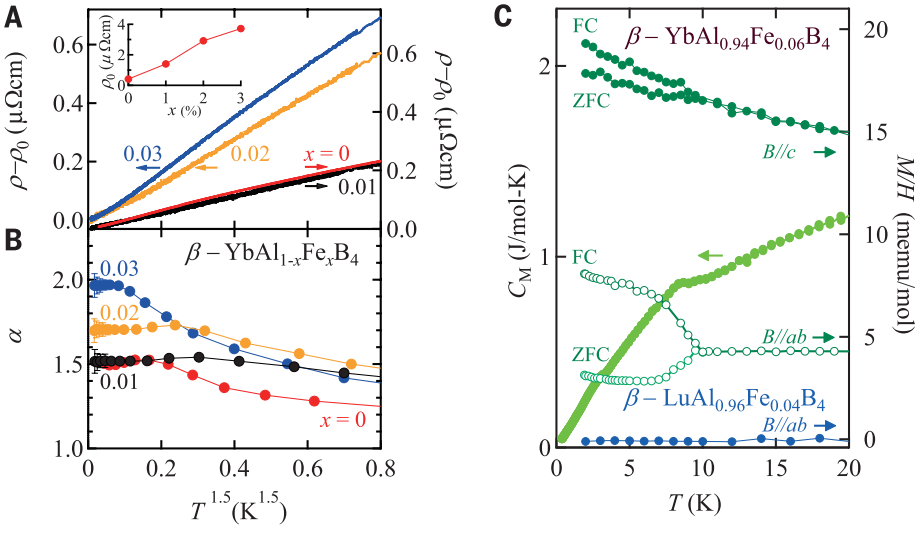

Fig. 3. Chemical substitution effects in β-$YbAl_{1-x}Fe_xB_4$. (**A**) Inelastic component $\rho(T) - \rho_0$ and (**B**) the corresponding power law exponent $\alpha(T)$ versus $T^{1.5}$ for β-$YbAl_{1-x}Fe_xB_4$ with various x (Fe) at ambient pressure. The inset indicates the Fe doping dependence of the residual resistivity ρ_0. (**C**) T dependence of the DC susceptibility M/H (right axis) measured in both zero-field-cooling (ZFC) and field-cooling (FC) sequences under a field of 0.1 T parallel and perpendicular to the *ab* plane and the magnetic part of the zero-field specific heat C_M (left axis) obtained for β-$YbAl_{1-x}Fe_xB_4$ ($x = 0.06$) at ambient pressure (*26*). The in-plane susceptibility for β-$LuAl_{1-x}Fe_xB_4$ ($x = 0.04$) is also shown.

2.72 GPa to ~4 K at 2.8 GPa (Fig. 1A and fig. S9). Within the pressure uncertainty, this coincides with the onset of antiferromagnetism found in the cubic anvil cell (fig. S6A, inset). This rapid increase of T_N, as well as the jump in ρ_0 across P_N, suggests that the pressure-induced magnetic phase transition is first-order.

Chemical substitution confirms a similar phase evolution to that under pressure. In particular, Fe substitution for Al is found to lead to a crossover from a distinct region with quantum critical behavior to a Fermi liquid. Figure 3, A and B show the T dependence of the resistivity and its power law exponent, respectively. The chemical analysis, as well as the systematic increase in ρ_0, confirm a homogeneous distribution of Fe ions (Fig. 3A, inset) (*24*). With 1% doping of Fe, we found that the power law exponent α in $\rho(T)$ approaches 1.5 upon cooling below 1 K, the same anomalous exponent as in pure β-$YbAlB_4$, indicating the formation of the strange metal phase. At higher Fe content of x = 2 and 3%, on the other hand, the exponent α approaches 1.7 and 2.0, respectively. In addition, both $\chi(T)$ and $C_M(T)$ for x = 3% show no magnetic anomaly but level off on cooling, signaling the formation of a Fermi liquid (fig. S4) (*24*).

Moreover, a 6% substitution of Fe contracts the volume by 0.6(2)% and induces antiferromagnetism (Fig. 3C and table S1) (*24*, *26*). The susceptibility $\chi(T)$ shows a kink at 9 K and a weak hysteresis between field-cooled and zero-field-cooled sequences, typically a signature of canted AF (*26*). The specific heat $C_M(T)$ confirms the bulk nature of the magnetism, showing an anomaly at 8.5 K. By contrast, the Lu nonmagnetic analog, β-$LuAl_{1-x}Fe_xB_4$, exhibits diamagnetism. Thus, the magnetism derives from the Yb rather than the Fe sites.

Application of pressure to the 6% Fe–substituted β-$YbAlB_4$ systematically increases the Néel temperature T_N up to 25 K at ~ 5.5 GPa (Fig. 4 and fig. S7). For x = 2% Fe substitution, pressure also induces magnetism at a critical pressure P_N ~ 2 GPa, a lower value than in the undoped crystals (2.5 GPa) (*24*). Figure 4 summarizes the combined data in a single-phase diagram spanned by pressure (P), Fe concentration (x), and temperature (T) axes. The smooth evolution of T_N as a function of pressure and doping suggests that the pressure-induced phase in pure β-$YbAlB_4$ involves the same type of AF order found in the Fe-doped β-$YbAlB_4$.

Conventionally, quantum criticality develops at a zero temperature phase transition into a broken symmetry state. In β-$YbAlB_4$, however, we find an intermediate FL phase nestled between the NFL region and the AF phase, showing that the NFL is not associated with the broken symmetry phase transition. This indicates that the origin of the low-pressure quantum criticality is a different kind of electronic instability. Notable possibilities include topological phase transitions and a quantum valence transition (*10*, *13*, *19*, *24*, *27*–*32*).

Various experiments can be used to differentiate between these scenarios. Thermodynamic measurements such as magnetization and Grüneisen parameter (*33*) are important to confirm the strange metal phase and its quantum phase transition to the FL phase under pressure. In particular, it would be useful to know if the T/B scaling observed in the thermodynamics of β-$YbAlB_4$ at ambient pressure extends throughout the region of criticality; this would indicate that the observed behavior is associated with a critical line, forming a branch cut in the pressure-field phase diagram. Finally, it would be useful to probe the 4*f* valence by x-ray and Mössbauer spectroscopy to examine how the average and fluctuating valence of the 4*f* state evolve in the critical pressure region.

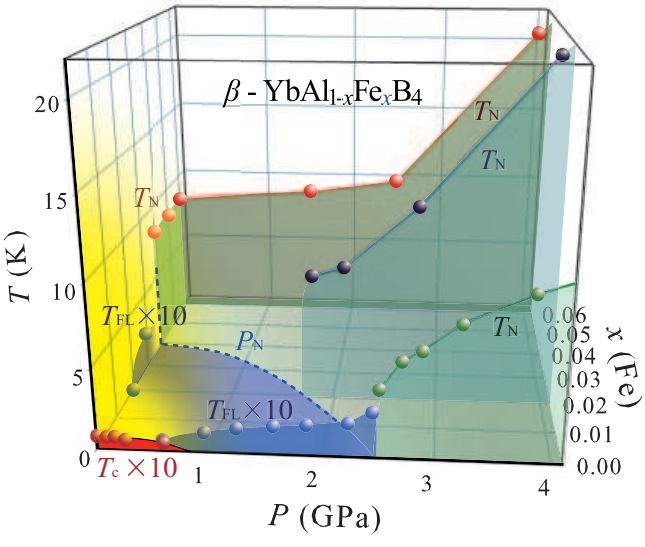

Fig. 4. Three-dimensional phase diagram of emergent electronic phases versus pressure *P*, Fe concentration *x*, and temperature *T* for β-$YbAl_{1-x}Fe_xB_4$. T_c and T_{FL}, respectively, denote the superconducting transition temperature and the onset of Fermi liquid T^2 dependence of the in-plane resistivity $\rho(T)$. The P dependence of the Néel point T_N obtained for three different samples with x(Fe) = 0, 0.02, and 0.06 is shown (*24*). For clarity, the values of T_c and T_{FL} are multiplied by a factor of 10. The regions connecting the (non-)Fermi liquid regions in P-T and x(Fe)-T phase diagrams are schematically shown in blue (yellow). Solid and broken lines are guides to the eye.

REFERENCES AND NOTES

1. L. Landau, *Sov. Phys. JETP* **6**, 920 (1957).
2. H. V. Löhneysen, A. Rosch, M. Vojta, P. Wölfle, *Rev. Mod. Phys.* **79**, 1015–1075 (2007).
3. P. Gegenwart, Q. Si, F. Steglich, *Nat. Phys.* **4**, 186–197 (2008).
4. J. A. Hertz, *Phys. Rev. B* **14**, 1165–1184 (1976).
5. T. Moriya, *Spin Fluctuations in Itinerant Electron Magnetism* (Springer, Berlin, 1985).
6. A. J. Millis, *Phys. Rev. B* **48**, 7183–7196 (1993).
7. P. Coleman, C. Pépin, Q. Si, R. Ramazashvili, *J. Phys. Condens. Matter* **13**, R723–R738 (2001).
8. Q. Si, S. Rabello, K. Ingersent, J. L. Smith, *Nature* **413**, 804–808 (2001).
9. S. A. Grigera *et al.*, *Science* **294**, 329–332 (2001).
10. T. Senthil, S. Sachdev, M. Vojta, *Phys. Rev. Lett.* **90**, 216403 (2003).
11. N. Doiron-Leyraud *et al.*, *Nature* **425**, 595–599 (2003).
12. S. L. Bud'ko, E. Morosan, P. C. Canfield, *Phys. Rev. B* **69**, 014415 (2004).
13. Q. Si, *Physica B* **378-380**, 23–27 (2006).
14. S. Takashima *et al.*, *J. Phys. Soc. Jpn.* **76**, 043704 (2007).
15. J. K. Jain, P. W. Anderson, *Proc. Natl. Acad. Sci. U.S.A.* **106**, 9131–9134 (2009).
16. M. Cubrović, J. Zaanen, K. Schalm, *Science* **325**, 439–444 (2009).
17. S. Friedemann *et al.*, *Nat. Phys.* **5**, 465–469 (2009).
18. T. Faulkner, N. Iqbal, H. Liu, J. McGreevy, D. Vegh, *Science* **329**, 1043–1047 (2010).
19. J. Custers *et al.*, *Phys. Rev. Lett.* **104**, 186402 (2010).
20. S. Nakatsuji *et al.*, *Nat. Phys.* **4**, 603–607 (2008).
21. M. Okawa *et al.*, *Phys. Rev. Lett.* **104**, 247201 (2010).
22. Y. Matsumoto *et al.*, *Science* **331**, 316–319 (2011).
23. Y. Machida *et al.*, *Phys. Rev. Lett.* **109**, 156405 (2012).
24. Supporting materials are available on *Science* Online.
25. A. V. Goltsev, M. M. Abd-Elmeguid, *J. Phys. Condens. Matter* **17**, S813–S821 (2005).
26. K. Kuga, G. Morrison, L. Treadwell, J. Y. Chan, S. Nakatsuji, *Phys. Rev. B* **86**, 224413 (2012).
27. T. Senthil, M. Vojta, S. Sachdev, *Phys. Rev. B* **69**, 035111 (2004).
28. I. Paul, C. Pépin, M. R. Norman, *Phys. Rev. Lett.* **98**, 026402 (2007).
29. A. Ramires, P. Coleman, A. H. Nevidomskyy, A. M. Tsvelik, *Phys. Rev. Lett.* **109**, 176404 (2012).
30. A. Nevidomskyy, P. Coleman, *Phys. Rev. Lett.* **102**, 077202 (2009).
31. S. Watanabe, K. Miyake, *Phys. Rev. Lett.* **105**, 186403 (2010).
32. J. H. Pixley, S. Kirchner, K. Ingersent, Q. Si, *Phys. Rev. Lett.* **109**, 086403 (2012).
33. L. Zhu, M. Garst, A. Rosch, Q. Si, *Phys. Rev. Lett.* **91**, 066404 (2003).

ACKNOWLEDGMENTS

We thank Y. Shimura, H. Takahashi, G. G. Lonzarich, Y. Matsumoto, E. C. T. O'Farrell, K. Matsubayashi, N. Horie, and K. Ueda for support and useful discussions. This work is partially supported by grants-in-aid (nos. 25707030 and 24740243) and the Program for Advancing Strategic International Networks to Accelerate the Circulation of Talented Researchers (no. R2604) from the Japanese Society for the Promotion of Science; by PRESTO, Japan Science and Technology Agency (JST); by Grant for Basic Science Research Projects from the Sumitomo Foundation; by U.S. National Science Foundation grant DMR-1309929 (P.C.) and U.S. National Science Foundation I2CAM International Materials Institute Award, grant DMR-0844115 (P.C. and S.N.); and by NSF grant no. PHYS-1066293 and the hospitality of the Aspen Center for Physics (P.C. and S.N.). The use of the facilities of the Materials Design and Characterization Laboratory at the Institute for Solid State Physics, The University of Tokyo, is gratefully acknowledged.

SUPPLEMENTARY MATERIALS

www.sciencemag.org/content/349/6247/506/suppl/DC1
Materials and Methods
Supplementary Text
Figs. S1 to S9
Table S1
References (*34*–*40*)

2 October 2014; accepted 6 July 2015
10.1126/science.1262054

REACTION DYNAMICS

Spectroscopic observation of resonances in the F + H_2 reaction

Jongjin B. Kim,[1]* Marissa L. Weichman,[1] Tobias F. Sjolander,[1] Daniel M. Neumark,[1,2]† Jacek Kłos,[3] Millard H. Alexander,[3,4]† David E. Manolopoulos[5]†

Photodetachment spectroscopy of the FH_2^- and FD_2^- anions allows for the direct observation of reactive resonances in the benchmark reaction F + H_2 → HF + H. Using cooled anion precursors and a high-resolution electron spectrometer, we observe several narrow peaks not seen in previous experiments. Theoretical calculations, based on a highly accurate F + H_2 potential energy surface, convincingly assign these peaks to resonances associated with quasibound states in the HF + H and DF + D product arrangements and with a quasibound state in the transition state region of the F + H_2 reaction. The calculations also reveal quasibound states in the reactant arrangement, which have yet to be resolved experimentally.

Much of our understanding of the structures of stable molecules has come from spectroscopy. The analysis of bound-bound transitions yields molecular geometries and frequencies, fingerprints of the molecular potential energy surface (PES). The observation of similar sharp structures during a chemical reaction would give comparable insight into the reactive PES, in particular in the all-important transition state region (*1*). The fleeting nature of the transition state makes this task much more challenging, however. Here, we report the spectroscopic observation of sharp resonance structures associated with the transition state and product valley regions of the F + H_2 → HF + H reaction, a benchmark reaction in the field of chemical reaction dynamics (*2*).

The rapid variation of a scattering cross section with energy or angle has long guided physicists in the investigation of nuclear and subnuclear structure. These so-called resonances are signs of metastable excited states or previously unknown particles. In chemistry, the experimental and theoretical search for these quantum features in reactive scattering experiments has been intense (*3*–*7*). Although tentative experimental evidence for resonances in the F + H_2 reaction was first reported in the 1980s (*8*), it took until 2000 for a resonance to be unambiguously identified in a crossed molecular beam experiment, as a step-like feature in the energy dependence of the integral cross section of F + HD → HF + D (*9*, *10*). The same resonance—a quasibound state in the FHD transition state region with three quanta of excitation in the H–F stretch and none in either the H–D stretch or the bend—has since been found under higher resolution to give rise to undulations in individual state-to-state differential cross sections of the reaction as a function of the collision energy (*11*). More recent molecular beam experiments combined with theoretical simulations have also provided some evidence for a resonance (*12*) [or perhaps two resonances (*13*)] in F + H_2.

Anion photoelectron spectroscopy provides an alternative experimental approach to the study of chemical reactions (*14*). Because the geometry of the FH_2^- anion is close to that of the neutral F + H_2 transition state, photodetachment of the electron from the anion provides a direct spectroscopic probe of the transition state dynamics (*15*), as illustrated in Fig. 1. If the precursor anion is rotationally cold, this probe avoids the averaging over angular momentum that tends to obscure resonances in a crossed molecular beam experiment. Previous spectra of FH_2^- have revealed broad peaks associated with the bending levels of the FH_2 transition state complex, which correspond to the "quantized bottlenecks" of the reaction rather than reactive scattering resonances (*16*). Calculations based on the best potential energy surface then available reproduced the positions and intensities of these broad peaks, as well as predicting a number of narrower peaks, which were assigned to resonances (*17*). Unfortunately, the experimental resolution available at the time (~20 meV) was not high enough to permit the detection of these features.

The development of slow-electron velocity-map imaging (SEVI) with cryogenic ion cooling has enabled the acquisition of photoelectron spectra of complex species with sub–millielectron volt (sub-meV) resolution (*18*). Much improved signal-to-noise ratio compared to that of a previous SEVI report (*19*) has allowed the detection of sharp peaks in the spectra of both FH_2^- and FD_2^-, which we report here.

The experimental apparatus has been described in detail previously (*18*, *20*), with relevant features highlighted in the supplementary materials (*21*). The FH_2^- and FD_2^- ions are created by introducing F^- anions into a cryogenically cooled ion trap containing H_2 or D_2 buffer gas at low pressure; the resulting ion yield is substantially higher than in previous work, where FH_2^- was generated in a molecular beam ion source. The ions are extracted from the trap, mass-selected, and photodetached at various photon energies. The photoelectron kinetic energy (E_{ke}) distribution is obtained with SEVI, in which a velocity-map imaging electron spectrometer (*22*) operated at comparatively low extraction voltages produces high-resolution (sub-meV) photoelectron spectra at low E_{ke}. The electron binding energy (E_{be}) gives the energy difference between the anion and neutral states and is obtained by subtracting the measured E_{ke} from the photon energy. As previous simulations suggested more obvious signatures of resonances with *para*-H_2 than *ortho*-H_2 (*17*), the FH_2^- ions were enriched in *p*-H_2. However, the FD_2^- ions were formed by trapping F^- in a buffer gas of *normal* deuterium (*n*-D_2).

Several earlier publications outline the calculation of the photodetachment spectrum of the FH_2^- anion (*17*, *23*). Photodetachment projects the vibrational wave function of the anion onto the F + H_2 potential energy surface, where it evolves under the influence of the neutral FH_2 Hamiltonian. In the Condon approximation, the photodetachment spectrum $P(E)$ is the Fourier transform of the overlap between this evolving wave function and the initial anion vibrational wave function (*17*). We use here the very high quality LWAL F + H_2 potential energy surface (*24*), which is based on multireference, configuration-interaction calculations. The relation between the experimentally measured binding energy of the electron (E_{be}) and the energy E in the theoretical simulation, which refers to the bottom of the F + H_2 reactant valley with the F atom in its ground ($^2P_{3/2}$) spin-orbit state, is

$$E_{be} = E - ZPE(H_2) + EA(F) + D_0(FH_2^-) \quad (1)$$

where ZPE is the zero-point energy of H_2, EA is the electron affinity of F, and D_0 is the dissociation

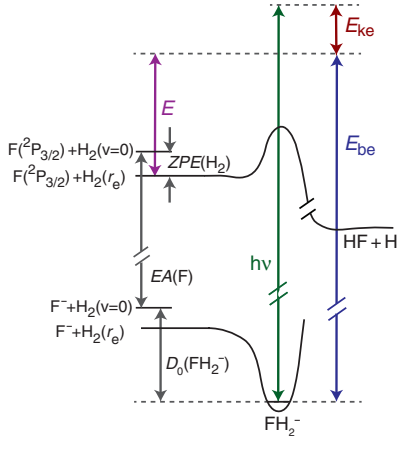

Fig. 1. Schematic of the energetics of the photodetachment process. Arrows show the relationship between the experimental electron binding energy (E_{be}) and the scattering energy (E).

[1]Department of Chemistry, University of California, Berkeley, CA 94720, USA. [2]Chemical Sciences Division, Lawrence Berkeley National Laboratory, Berkeley, CA 94720, USA. [3]Department of Chemistry and Biochemistry, University of Maryland, College Park, MD 20742, USA. [4]Institute for Physical Science and Technology, University of Maryland, College Park, MD 20742, USA. [5]Department of Chemistry, Oxford University, Physical and Theoretical Chemistry Laboratory, South Parks Road, Oxford OX1 3QZ, UK. *Present address: SLAC National Accelerator Laboratory, Menlo Park, CA 94025, USA †**Corresponding author. E-mail: dneumark@berkeley.edu (D.M.N.); mha@umd.edu (M.H.A.); david.manolopoulos@chem.ox.ac.uk (D.E.M.)**

energy of the FH_2^- anion. These energetics are illustrated schematically in Fig. 1. In the theoretical simulations, we use the experimental *EA* of F [3.4012 eV (*25*)] and the *ZPE*s for H_2 and D_2 as predicted by the LWAL PES (0.2705 and 0.1918 eV, respectively). To determine D_0, we have performed new ab initio and vibrational bound state calculations described in the supplementary materials, obtaining D_0 = 0.2005 eV for FH_2^- and 0.2219 eV for FD_2^-.

The experimental and simulated SEVI spectra of *p*-FH_2^- and *n*-FD_2^- are presented in Figs. 2 and 3, respectively. Spectra at additional photon energies are shown in figs. S1 and S2. Figures S3 and S4 show a comparison of the *p*-FH_2^- photodetachment spectra obtained with two different anion wave functions (fig. S3) and two different potential energy surfaces (fig. S4).

The overview *p*-FH_2^- photodetachment spectrum is dominated by three broad peaks, labeled A, B, and C in Fig. 2. These had been previously assigned to hindered H_2 rotor (or bending) states of the transient FH_2 complex (*16*, *26*). The equilibrium geometry of the linear FH_2^- anion is just on the reactant side of the neutral transition state. Because the minimum F + H_2 barrier on the neutral potential energy surface has a bent geometry, photodetachment of the electron excites a bending progression in the neutral FH_2 complex. We also observe a smaller peak in the high-resolution *p*-FH_2^- spectrum (purple), labeled a, just above the first broad peak A. This peak has not been resolved in any previous experiment. It also occurs in the simulated spectra, along with two smaller peaks (labeled β and γ) at higher energy, and a pronounced peak (labeled α, seen experimentally as a slight shoulder) on the low-energy side of peak A.

The situation for *n*-FD_2^- is similar. The experimental overview spectrum in Fig. 3 is dominated by two broad peaks, labeled D and E. The high-resolution spectrum shows two smaller peaks at lower energy, labeled b and c. These smaller peaks are also seen in the theoretical spectra, along with an additional small peak labeled δ, which is not resolved in the experimental spectrum. In both cases (*p*-FH_2^- and *n*-FD_2^-), the agreement between the positions of the calculated and the observed high-resolution peaks (peak a in Fig. 2 and peaks b and c in Fig. 3) is excellent, suggesting that an analysis of the theoretical calculations will provide a reliable guide to the origin of these experimental peaks. What makes this comparison especially compelling is that no arbitrary shift was introduced to align the experimental and theoretical spectra in Figs. 2 and 3; use of the ab initio values of D_0 for FH_2^- and FD_2^- in the relationship between E and E_{be} in Eq. 1 locates the theoretical spectra.

Calculating the scattering wave function $\psi(E)$ at the energy E of each peak allows us to characterize the peaks in the theoretical spectra in Figs. 2 and 3. This is the same procedure used previously by Russell and Manolopoulos (*17*). The details of the present, more accurate calculations of the wave functions $\psi(E)$ are given in the supplementary materials (*21*).

Figure 4 shows plots of the wave functions corresponding to the low-energy resonance peaks α, A, and a in Fig. 2 and peaks b, c, and δ in Fig. 3, in collinear F–H–H (F–D–D) geometry. This figure unambiguously reveals the nature of the peaks in the photodetachment spectra: Peaks α and δ are reactant resonances, peak A is a transition state resonance, and peaks a, b, and c are product resonances. The quasibound states that give rise to these resonances are localized in the reactant F + H_2 (F + D_2) van der Waals well, the FH_2 transition state, and the product HF + H (DF + D) van der Waals well, respectively. The green contours in Fig. 4 depict the anion wave functions.

It is possible to assign quantum numbers to the resonance wave functions on the basis of their nodal structure. The reactant resonances have quantum numbers v, j, and t, where v enumerates the number of quanta in the H–H stretch; j, in the hindered H_2 rotation; and t, in the F–H_2 stretch of the F + H_2 van der Waals complex. For the product resonances, v', j', and t' refer, similarly, to the H–F stretch, the hindered HF rotation, and the H–HF van der Waals stretch. The quantum numbers of the reactant resonances in Fig. 4 are (v,j,t) = (0,0,0) for both α (*p*-FH_2^-) and δ (*n*-FD_2^-), whereas the quantum numbers of the product resonances are (v',j',t') = (3,0,0)

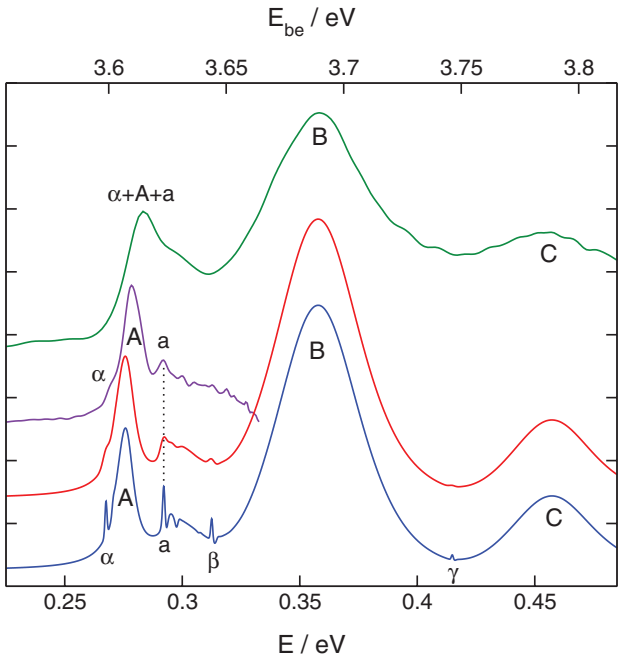

Fig. 2. Photodetachment spectra of *p*-FH_2^-. Green: experimental overview spectrum (~10 meV resolution). Purple: highest-resolution experimental spectrum (2 to 3 meV) over a narrower energy window. Blue: theoretical simulation at 1 meV energy resolution. Red: convolution of the theoretical simulation over a Gaussian function with full width at half maximum (FWHM) of 3 meV. The calculated spectra have not been shifted to match experiment. The relation between the experimental electron binding energy E_{be} and the energy E relative to $F(^2P_{3/2})$ + $H_2(r_e)$ is given by Eq. 1 as $E_{be} = E + 3.3312$ eV.

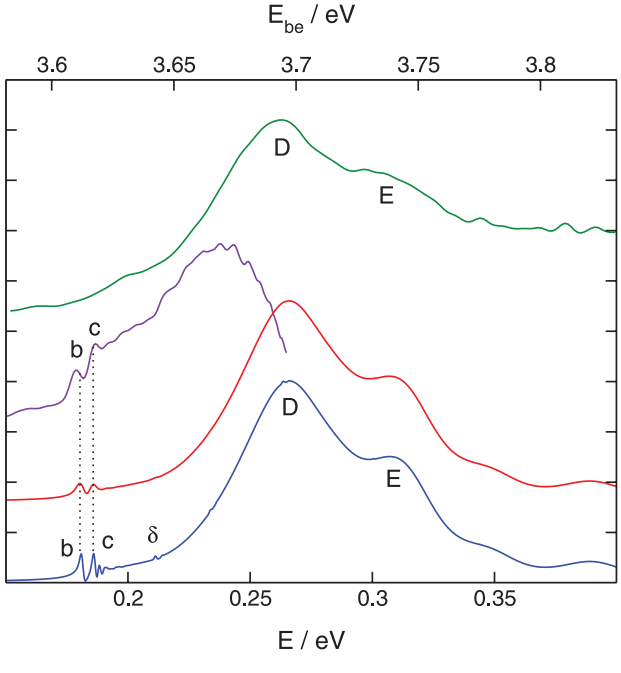

Fig. 3. Photodetachment spectra of *n*-FD_2^-. Green: experimental overview spectrum (~10 meV resolution). Purple: highest-resolution experimental spectrum (2 to 3 meV) over a narrower energy window. Blue: theoretical simulation at 1 meV energy resolution. Red: convolution of the theoretical simulation over a Gaussian function with FWHM of 3 meV. The calculated spectra have not been shifted to match experiment. The relation between the experimental electron binding energy E_{be} and the energy E relative to $F(^2P_{3/2})$ + $H_2(r_e)$ is given by Eq. 1 as E_{be} = E + 3.4313 eV.

for a and (v',j',t') = (4,0,0) and (4,0,1) for b and c, respectively. Finally, the transition state resonance that gives rise to peak A in the p-FH_2^- spectrum has three quanta in the H–F stretch (ν_1) and none in either the F–H–H bend (ν_2) or the H–H stretch (ν_3).

The resonances a, b, and c that have been detected as narrow peaks in the present high-resolution SEVI spectra of p-FH_2^- and n-FD_2^- are thus all product resonances: quasibound states localized in the van der Waals well region in the product valley. For additional clarification, fig. S5 shows how well the positions of the FH–H and FD–D product state resonances are captured by an adiabatic-bender model (*27*–*29*). Because the energies of these resonances are below the thresholds for production of HF(v' = 3) + H and DF(v' = 4) + D, they cannot decay into these channels and must decay instead into HF(v' = 2) + H and DF(v' = 3) + D by vibrational predissociation (the hallmark of a Feshbach resonance). The reason why there are two resonances for FD_2 and only one for FH_2 can be traced to the larger mass of D, which leads to two quasibound states in the D–DF(v' = 4, j' = 0) van der Waals stretching coordinate rather than just one (see the supplementary materials for a more detailed analysis). The emergence of peak a at high resolution was predicted by Russell and Manolopoulos in their earlier theoretical study of the p-FH_2^- spectrum (*17*), but peaks b and c in the n-FD_2^- spectrum have been neither predicted nor measured until now.

The broader low-energy peak A in the p-FH_2^- spectrum was previously assigned to a "direct scattering" or "quantized bottleneck" state associated with the opening of the F + H_2(v = 0, j = 0) channel at the transition state (*17*). However, it is clear from the present calculations that the wave function $\psi(E)$ at the energy of this peak is localized in the transition state region rather than delocalized along the reaction coordinate. This localization is the characteristic feature of a resonance wave function (*30*). This resonance has precisely the same form and quantum numbers as the transition state resonance found by Skodje *et al.* in the F + HD reaction (*9*, *10*). It is thus simply an analytic continuation of this resonance in the mass of one of the two hydrogen atoms. It is the broad peaks B and C in Fig. 2 and D and E in Fig. 3 that are due to quantized bottlenecks, with wave functions that are delocalized along the reaction coordinate (*30*); the associated wave functions are shown in fig. S6.

All of the other peaks in Figs. 2 and 3 can be assigned in the same way by examining the scattering wave functions at the peak energies. The results of these assignments are summarized in Table 1. The narrow peaks β and γ in Fig. 2 are reactant resonances with quantum numbers (v,j,t) = (0,2,0) and (0,4,0), respectively. Like peak δ in Fig. 3, the theoretical calculations predict only low intensity for these peaks. They have yet to be resolved experimentally. As shown in fig. S4, the agreement between the experimental and theoretical resonance positions is noticeably poorer with the use of another recently developed F + H_2 surface (*31*), illustrating that the resonances are indeed a sensitive and experimentally accessible probe of the neutral reactive surface.

We have shown that high-resolution SEVI photodetachment spectra of p-FH_2^- and n-FD_2^- anions reveal previously unresolved peaks in the low-energy region that can unambiguously be attributed to reactive scattering resonances. The signatures of these resonances in the SEVI spectra are far clearer than they would be in a crossed molecular beam experiment, where angular momentum averaging washes out resonance features in both integral and differential cross sections.

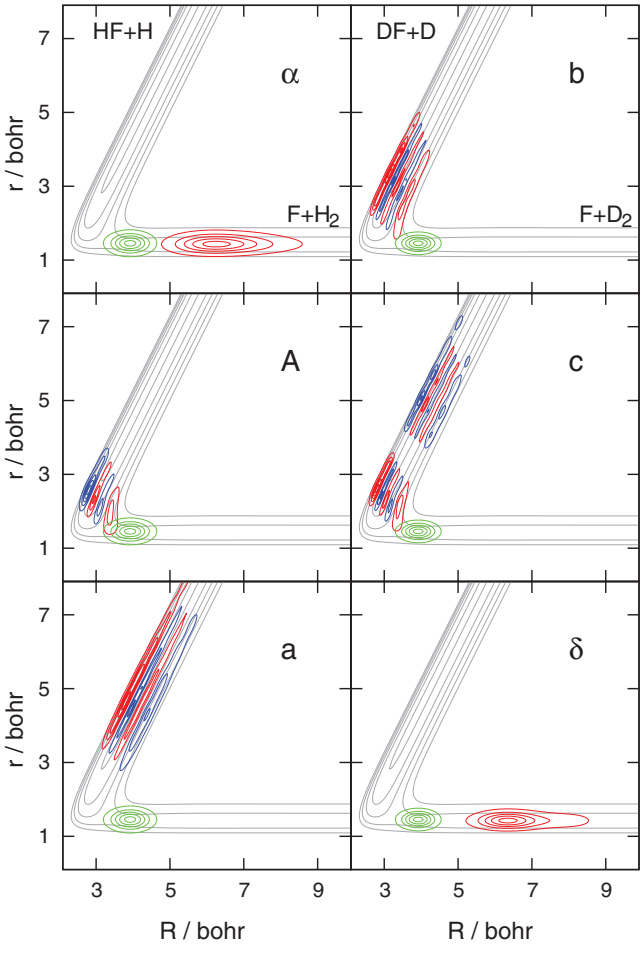

Fig. 4. Resonance wave functions. The wave functions $\psi(E)$ at the energies E of the first three peaks in the p-FH_2^- spectrum in Fig. 2 (α, A, and a; left), and the first three peaks in the n-FD_2^- spectrum in Fig. 3 (b, c, and δ; right), plotted in collinear geometry, as red [$\psi(E) > 0$] and blue [$\psi(E) < 0$] contours, as a function of the distance R between F and the center-of-mass of H_2 (D_2) and the bond length r of H_2 (D_2). Superimposed in gray are contours of the LWAL potential energy surface (*24*). Contours of the FH_2^- and FD_2^- anion wave functions are shown in green for comparison. The contoured regions of all wave functions encompass probability density values greater than 10% of their maxima; the apparent lack of overlap between the anion wave functions and some of the resonance wave functions arises because the overlap is in the tail (<10%) of the probability distribution.

Table 1. Assignment of the peaks in the p-FH_2^- and n-FD_2^- photodetachment spectra in Figs. 2 and 3. The quantum numbers given for the quantized bottlenecks (see fig. S6) are those of the reactant channel that becomes energetically accessible as a hindered rotor (bending) state at the transition state at the energy of the peak in the photodetachment spectrum.

Spectrum	Peak	E/eV	Assignment	Quantum numbers
p-FH_2^-	α	0.2676	Reactant resonance	(v,j,t) = (0,0,0)
	A	0.2758	Transition state resonance	(ν_1,ν_2,ν_3) = (3,0,0)
	a	0.2921	Product resonance	(v',j',t') = (3,0,0)
	β	0.3125	Reactant resonance	(v,j,t) = (0,2,0)
	B	0.3578	Quantized bottleneck	F + H_2(v = 0, j = 2)
	γ	0.4149	Reactant resonance	(v,j,t) = (0,4,0)
	C	0.4573	Quantized bottleneck	F + H_2(v = 0, j = 4)
n-FD_2^-	b	0.1809	Product resonance	(v',j',t') = (4,0,0)
	c	0.1860	Product resonance	(v',j',t') = (4,0,1)
	δ	0.2112	Reactant resonance	(v,j,t) = (0,0,0)
	D	0.2661	Quantized bottleneck	F + D_2(v = 0, j = 2)
	E	0.3071	Quantized bottleneck	F + D_2(v = 0, j = 4)

Thanks to recent experimental developments (including SEVI and, crucially for the present study, the use of a cryogenically cooled ion trap to produce large amounts of p-FH_2^- and n-FD_2^-), high-resolution anion photodetachment spectroscopy does indeed provide an effective way to observe the elusive resonances in F + H_2 reactive scattering, as was predicted by Russell and Manolopoulos almost 20 years ago (*17*).

REFERENCES AND NOTES

1. J. C. Polanyi, A. H. Zewail, *Acc. Chem. Res.* **28**, 119–132 (1995).
2. D. E. Manolopoulos, *J. Chem. Soc. Faraday Trans.* **93**, 673–683 (1997).
3. G. C. Schatz, *Science* **288**, 1599–1600 (2000).
4. F. Fernández-Alonso, R. N. Zare, *Annu. Rev. Phys. Chem.* **53**, 67–99 (2002).
5. X. Yang, D. H. Zhang, *Acc. Chem. Res.* **41**, 981–989 (2008).
6. R. T. Skodje, in *Advances in Quantum Chemistry*, C. A. Nicolaides, E. J. Brändas, R. S. John, Eds. (Academic Press, New York, 2012), vol. 63, pp. 119–163.
7. K. Liu, in *Advances in Chemical Physics*, S. A. Rice, A. R. Dinner, Eds. (Wiley, Hoboken, NJ, 2012), vol. 149, pp. 1–46.
8. D. M. Neumark, A. M. Wodtke, G. N. Robinson, C. C. Hayden, Y. T. Lee, *J. Chem. Phys.* **82**, 3045 (1985).
9. R. T. Skodje *et al.*, *J. Chem. Phys.* **112**, 4536 (2000).
10. R. T. Skodje *et al.*, *Phys. Rev. Lett.* **85**, 1206–1209 (2000).
11. W. Dong *et al.*, *Science* **327**, 1501–1502 (2010).
12. T. Wang *et al.*, *J. Phys. Chem. Lett.* **5**, 3049–3055 (2014).
13. M. Qiu *et al.*, *Science* **311**, 1440–1443 (2006).
14. D. M. Neumark, *Phys. Chem. Chem. Phys.* **7**, 433–442 (2005).
15. I. M. Waller, T. N. Kitsopoulos, D. M. Neumark, *J. Phys. Chem.* **94**, 2240–2242 (1990).
16. D. E. Manolopoulos *et al.*, *Science* **262**, 1852–1855 (1993).
17. C. L. Russell, D. E. Manolopoulos, *Chem. Phys. Lett.* **256**, 465–473 (1996).
18. C. Hock, J. B. Kim, M. L. Weichman, T. I. Yacovitch, D. M. Neumark, *J. Chem. Phys.* **137**, 244201 (2012).
19. T. I. Yacovitch *et al.*, *Faraday Discuss.* **157**, 399–414, (2012).
20. A. Osterwalder, M. J. Nee, J. Zhou, D. M. Neumark, *J. Chem. Phys.* **121**, 6317–6322 (2004).
21. Methods are detailed in the supplementary materials at *Science* Online.
22. A. T. J. B. Eppink, D. H. Parker, *Rev. Sci. Instrum.* **68**, 3477 (1997).
23. J. Z. H. Zhang, W. H. Miller, *J. Chem. Phys.* **92**, 1811 (1990).
24. F. Lique, G. Li, H.-J. Werner, M. H. Alexander, *J. Chem. Phys.* **134**, 231101 (2011).
25. C. Blondel, C. Delsart, F. Goldfarb, *J. Phys. At. Mol. Opt. Phys.* **34**, 2757 (2001).
26. S. E. Bradforth, D. W. Arnold, D. M. Neumark, D. E. Manolopoulos, *J. Chem. Phys.* **99**, 6345 (1993).
27. S. L. Holmgren, M. Waldman, W. Klemperer, *J. Chem. Phys.* **67**, 4414 (1977).
28. M. H. Alexander, S. Gregurick, P. J. Dagdigian, *J. Chem. Phys.* **101**, 2887 (1994).
29. J. F. Castillo, D. E. Manolopoulos, K. Stark, H.-J. Werner, *J. Chem. Phys.* **104**, 6531 (1996).
30. D. E. Manolopoulos, *Nature* **419**, 266–267 (2002).
31. B. Fu, X. Xu, D. H. Zhang, *J. Chem. Phys.* **129**, 011103 (2008).

ACKNOWLEDGMENTS

The experimental part of this work was funded by the Air Force Office of Scientific Research (AFOSR) under grant no. FA9550-12-1-0160 and the Defense University Research Instrumentation Program (DURIP) under grant no. FA9550-11-1-0330. M.L.W. thanks the National Science Foundation for a graduate research fellowship. The experimental data are available upon request from dneumark@berkeley.edu. M.H.A. is grateful for partial support by the U.S. National Science Foundation under grant CHE-1213332. D.E.M. is funded by the Wolfson Foundation and the Royal Society.

SUPPLEMENTARY MATERIALS

www.sciencemag.org/content/349/6247/510/suppl/DC1
Materials and Methods
Supplementary Text
Figs. S1 to S7
Tables S1 and S2
References (*32*–*59*)

4 June 2015; accepted 9 July 2015
10.1126/science.aac6939

BORON CATALYSIS

Metal-free catalytic C-H bond activation and borylation of heteroarenes

Marc-André Légaré, Marc-André Courtemanche, Étienne Rochette, Frédéric-Georges Fontaine*

Transition metal complexes are efficient catalysts for the C-H bond functionalization of heteroarenes to generate useful products for the pharmaceutical and agricultural industries. However, the costly need to remove potentially toxic trace metals from the end products has prompted great interest in developing metal-free catalysts that can mimic metallic systems. We demonstrated that the borane (1-TMP-2-BH_2-C_6H_4)$_2$ (TMP, 2,2,6,6-tetramethylpiperidine) can activate the C-H bonds of heteroarenes and catalyze the borylation of furans, pyrroles, and electron-rich thiophenes. The selectivities complement those observed with most transition metal catalysts reported for this transformation.

Transition metal–catalyzed reactions are ubiquitous tools in the pharmaceutical and agrochemical industries, despite the costs associated with removing residual catalysts; trace metals in products for human consumption are heavily regulated by international bodies (*1*). Similar concerns exist in the modern electronics industry, where metals need to be removed from organic electronic devices to avoid loss of efficiency (*2*). Nevertheless, the importance of selectively forming bonds between carbon and other atoms using transition metals has been acknowledged by three Nobel Prizes in Chemistry in the past 15 years. More recently, the catalytic functionalization of C-H bonds using transition metals has emerged as an atom-economical way to generate new bonds without the need for activated precursors (*3*, *4*). Through such an activation process, the catalytic C_{sp2}-H borylation of aromatic molecules generates organoboronates (*5*–*7*), which are important species for the pharmaceutical industry and in the field of modern organic materials, notably as building blocks for the creation of new bonds using the Suzuki-Miyaura cross-coupling reaction (*8*, *9*). Although some base metal complexes have been used as catalysts for the borylation of arenes (*10*–*12*), the most efficient systems to date rely on noble metals, most notably iridium (*6*, *7*). Alternatively, borenium or boronium species generated by highly reactive precursors can promote the electrophilic borylation of arenes, but stoichiometric quantities of amine derivatives are generally needed to generate the active boron reagents (*13*–*15*).

Noble metals are well suited to cleave aromatic C-H bonds in catalytic processes because they can easily mediate two-electron transfer processes.

Département de Chimie, Centre de Catalyse et Chimie Verte (C3V), Université Laval, 1045 Avenue de la Médecine, Québec, QC G1V 0A6, Canada.
***Corresponding author. E-mail: frederic.fontaine@chm.ulaval.ca**

In the borylation reaction using iridium catalysts, this transformation is usually assisted by the boryl substituents present on the metal center, which

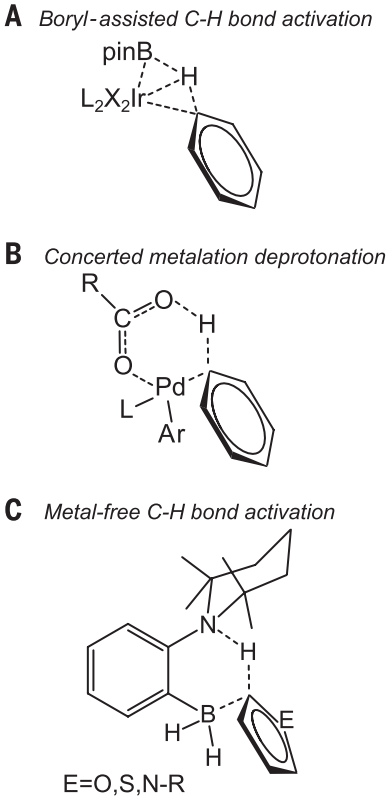

Fig. 1. Representative transition states for the C-H activation of arenes. (**A**) Activation of C-H bonds in borylation transformations using Ir catalysts. (**B**) Carboxylate-assisted metalation deprotonation at palladium. (**C**) Metal-free C-H activation of heteroarenes using FLP catalysts. The dashed lines represent bonds formed and cleaved during the electron transfer.

facilitate the proton transfer (Fig. 1A) (*16*). An analogous process is the direct arylation through palladium carboxylate complexes, in which the electron transfer is facilitated by the basic carboxylate group, which abstracts the proton on the aromatic molecule while the aryl group coordinates the metal center (Fig. 1B) (*17*, *18*). Here we report that intramolecular frustrated Lewis pairs (FLPs) can be used as catalysts for the C-H bond cleavage and dehydrogenative borylation of heteroarenes. Replacing current metal-catalyzed technologies by FLP processes offers exciting possibilities because of the abundance, low cost, and low toxicity of most organoboranes, especially in comparison with noble metals (*19*). The metal-free activation of hydrogen reported in 2006 using the concept of FLPs (*20*, *21*) led to an important breakthrough in the metal-free hydrogenation reaction (*22*). In FLP processes, cleavage of H_2 occurs via the cooperation of a Lewis acid and a Lewis base that are prevented from forming a Lewis adduct by steric or geometrical constraints. We now report the design of a FLP catalyst capable of cleaving and functionalizing C_{sp2}-H bonds. In this process, a Lewis basic amine putatively serves to abstract a proton, while the electron density of the C_{sp2}-H bond is transferred to a Lewis acidic borane (Fig. 1C). This concept is thus reminiscent of the transformations observed with transition metal complexes.

The catalyst presented in Fig. 1C was designed to afford the nucleophilic carbon of the heterocyclic substrate close access to the Lewis acidic BH_2 moiety. In concert, the bulky amine moiety favors the abstraction of the proton from the C_{sp2}, while preventing possible head-to-tail dimerization. The phenyl linker between the Lewis moieties has been shown to be quite durable in FLP catalysis (*23*–*26*). Compound **1** [(1-TMP-2-BH_2-C_6H_4)$_2$ (TMP, 2,2,6,6-tetramethylpiperidine)] was therefore a promising candidate for the metal-free C_{sp2}-H activation of aromatic molecules in addition to being synthetically easily accessible. While we were carrying out this work, compound **1** was shown to be in equilibrium with the monomeric form and was reported to be an active species for hydrogen activation (*26*).

^{1}H nuclear magnetic resonance (NMR) monitoring of the addition of 1-methylpyrrole to a solution of **1** in chloroform-*d* at 80°C revealed the evolution of H_2 (δ = 4.63) and the formation of product **2** over a period of 5 hours, resulting from the C-H activation of 1-methylpyrrole at the 2 position (Fig. 2A). Conducting a similar reaction with 1-methylpyrrole-d_4 allowed the observation of HD and the unambiguous assignment of the resonances associated with the 1-Me-pyrrole activation products (Fig. 2C). Compound **2** was shown to react with HBpin (pin, pinacolato) in a chloroform-*d* solution over the course of 10 min at ambient temperature, regenerating **1** by releasing 1-Me-2-Bpin-pyrrole (**3a**) (Fig. 2B).

When equimolar amounts of 1-methylpyrrole and HBpin (1.22 mmol) were added to a 2.5 mol % solution of **1** in $CHCl_3$, we observed quantitative conversion of the reagents to a 93:7 ratio of **3a** and **3a′** by ^{1}H NMR spectroscopy, confirming that **1** is a catalyst for the borylation reaction. We obtained the isolated products in a yield of 93% by passing the reaction mixture through a short pad of silica to remove the catalyst. The same protocol was used on a multigram-scale reaction (0.22 mol) to isolate 3.76 g of the desired product (yield = 81%). With a catalytic loading as low as 0.5 mol %, we isolated species **3a** and **3a′** in an overall 72% yield. The borylation of 1-methylpyrrole was also possible with catecholborane and 9-borabicyclo[3.3.1]nonane, but these gave yields of 42 and 60%, respectively. In addition, we tested functional group tolerance by conducting the borylation of 1-methylpyrrole in the presence of additives. The reaction was shown to be tolerant of aryl or alkyl halides, epoxides, ethers, hexamethylphosphoramide, and less basic amines, but inhibition was observed in the presence of basic amines, carbonyl groups, or unsaturated hydrocarbons (table S2).

The scope of the borylation is displayed in Fig. 3. The reaction does not proceed for the parent pyrrole because of the reactive N-H bond that presumably inhibits the catalyst. Protection of the pyrrole with the N-benzyl group allowed us to isolate a 3:2 mixture of **3b** and **3b′** in 90% yield. Not only are the TIPS (triisopropylsilyl) and TMS (trimethylsilyl) protecting groups also tolerated, but they allow the formation of the 3-substituted isomer, giving **3c** and **3d** in good yields. However, the presence of the electron-withdrawing *tert*butyloxycarbonyl group (BOC) inhibits the reaction completely. The latter results suggest that the electronic parameters are critical for the reaction to proceed. Indeed, the quantitative borylation for 1-methylindole at the most electron-rich 3 position to generate **3e** rather than in the 2-position as observed for the iridium catalysts (*27*) is reminiscent of the regioselectivity observed in electrophilic borylations (*13*, *15*).

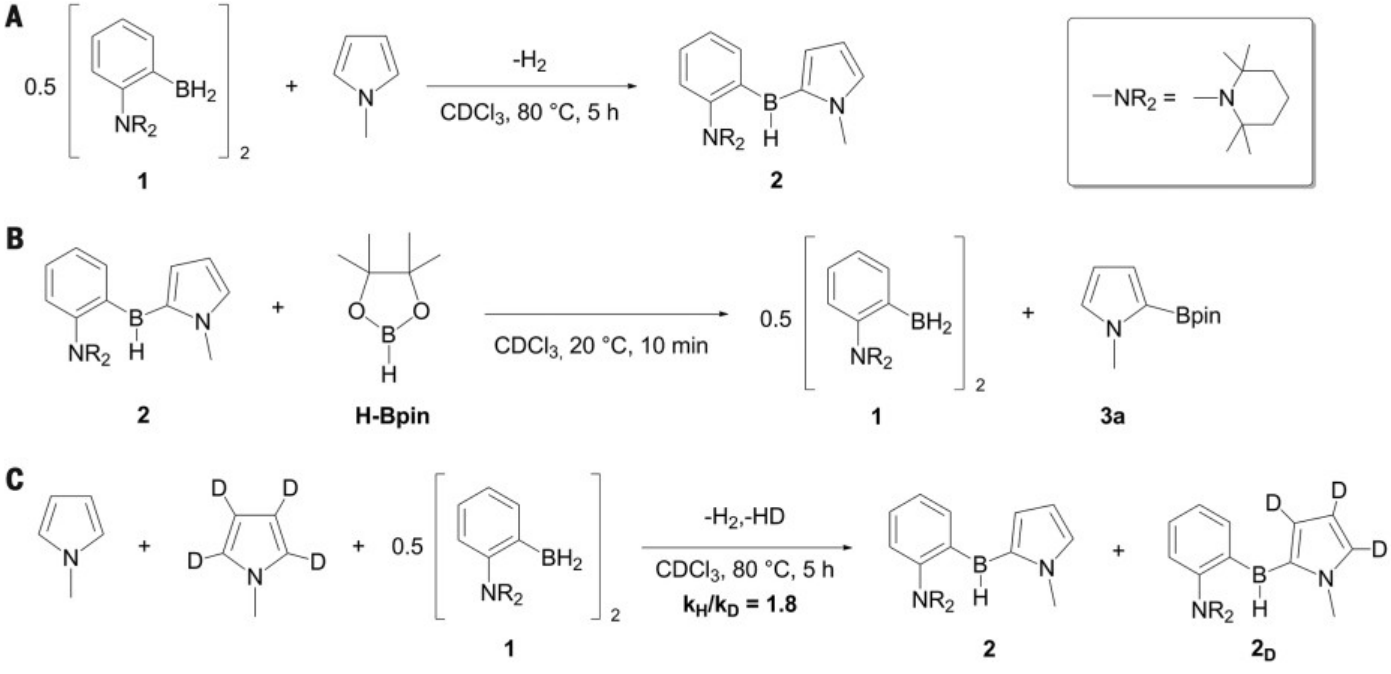

Fig. 2. Stoichiometric transformations observed in the course of this study using ^{1}H, ^{13}C, and ^{11}B NMR spectroscopy. (**A**) Reaction of species **1** with 1-methylpyrrole generating **2**. (**B**) Reaction of **2** with HBpin generating **1** and **3a**. (**C**) Competitive experiment between 1-methylpyrrole and 1-methylpyrrole-d_4, allowing determination of the kinetic isotope effect for the generation of **2**.

Our investigation revealed that thiophene is not reactive but that the borylation proceeds rapidly for electron-rich 3,4-ethylenedioxythiophene. By using 0.5 or 2 equivalents of HBpin, it was possible to observe quantitative conversion to the mono- (**3f**) or diborylated (**3g**) products. 2-Methoxythiophene was also borylated successfully, once more suggesting that electron-rich substrates are required for catalysis to occur.

Many furan derivatives are challenging to isolate, because they tend to be light-sensitive and degrade on silica, but our simple purification method allows rapid isolation of the products. Although furan gave only limited conversion to **3i** by NMR spectroscopy, we were able to isolate borylated 2-alkylfurans **3j** and **3k** in excellent yields. Once again, electron-rich substrates react readily, giving methoxide and siloxide species **3l** and **3m** in good yields and thus expanding the scope to the use of protected alcohol functionalities. **1** is tolerant of bromide-containing substrates and generates **3n** and **3n′** in a close-to-statistical 1:0.9 ratio.

Density functional theory (DFT) calculations were carried out at the ωB97xd/6-31+G** level [with a solvation model based on density (SMD)] to account for chloroform solvent) to propose a reliable mechanism for this transformation using 1-methylpyrrole as the model substrate, as shown in Fig. 4. After dissociation of the dimer **1**, the rate-determining step was calculated to be the C-H activation of the substrate by **Int1**, generating the zwitterionic species **Int2**. Once **Int2** is formed, the calculations predict a rapid release of H_2 to generate **2** (*26*). The formation of **3a** in the presence of HBpin was calculated to proceed via a four-center sigma-bond metathesis, regenerating **1** in the process.

Whereas the 24.4 kcal mol^{-1} barrier for C-H bond cleavage of the proton in the 2 position of the pyrrole is favored, the activation on the 3 position is also possible, requiring only 0.4 kcal mol^{-1} of

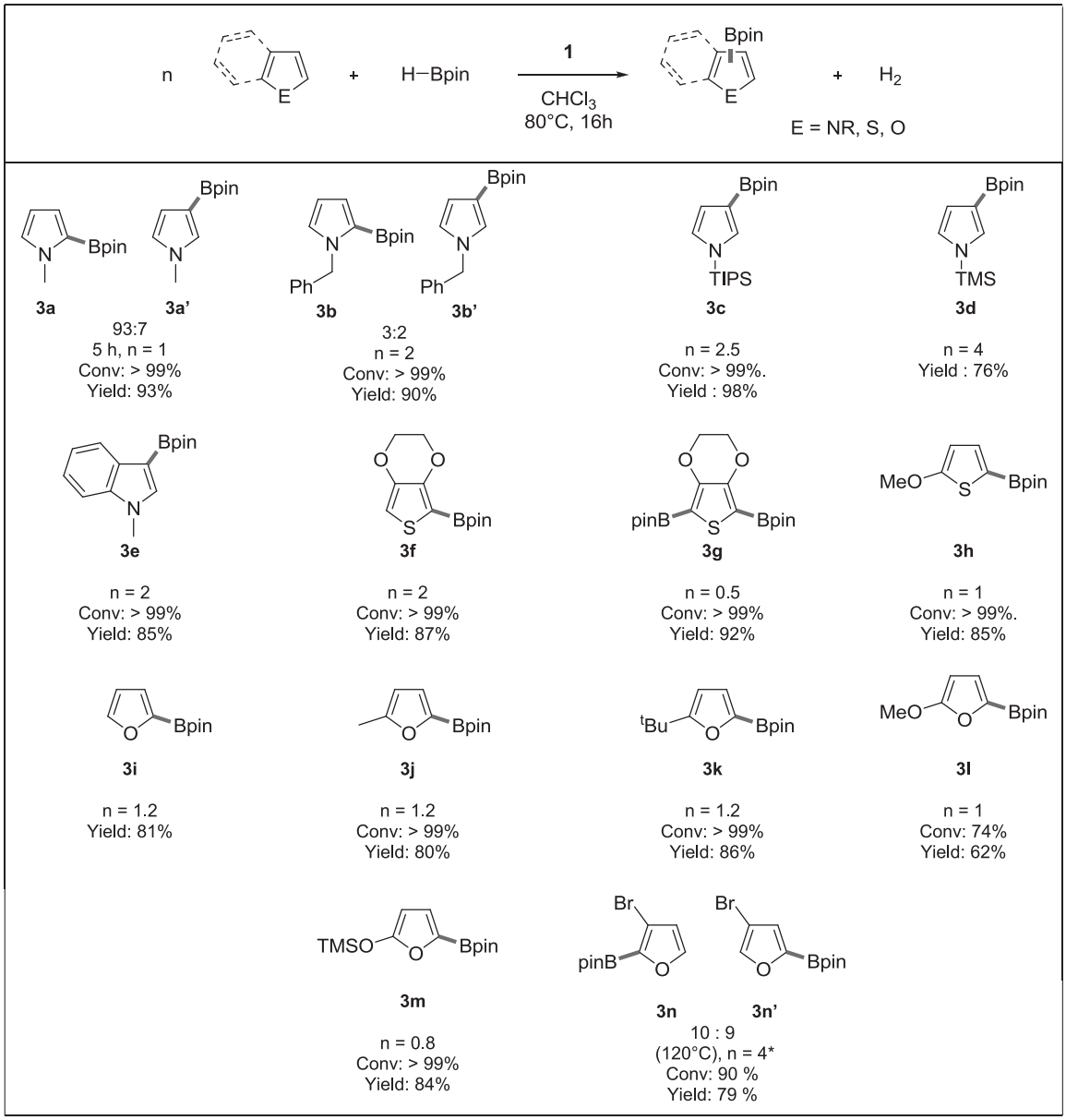

Fig. 3. Scope of the borylation reaction catalyzed by 1. Unless specified otherwise, the reactions were run using **1** (14.0 mg, 0.0305 mmol, 2.5 mol %), HBpin (156 mg, 1.22 mmol), and the substrate (*n* × 1.22 mmol) in 5 ml of $CHCl_3$ at 80°C. The conversions (conv.) are given with respect to the transformation of the limiting reagent to the borylated product as measured by ^{1}H NMR spectroscopy at the end of the reaction. Yields and isomer ratios refer to isolated quantities. Unless specified otherwise, a single isomer was isolated and detected. *__1__ (2.1 mg, 0.0045 mmol, 5 mol %), 3-bromofuran (32.9 μl, 53.9 mg, 0.367 mmol) and HBpin (12.8 μl, 11.7 mg, 0.092 mmol), C_6D_6 (0.4 ml), 100°C, 36 hours.

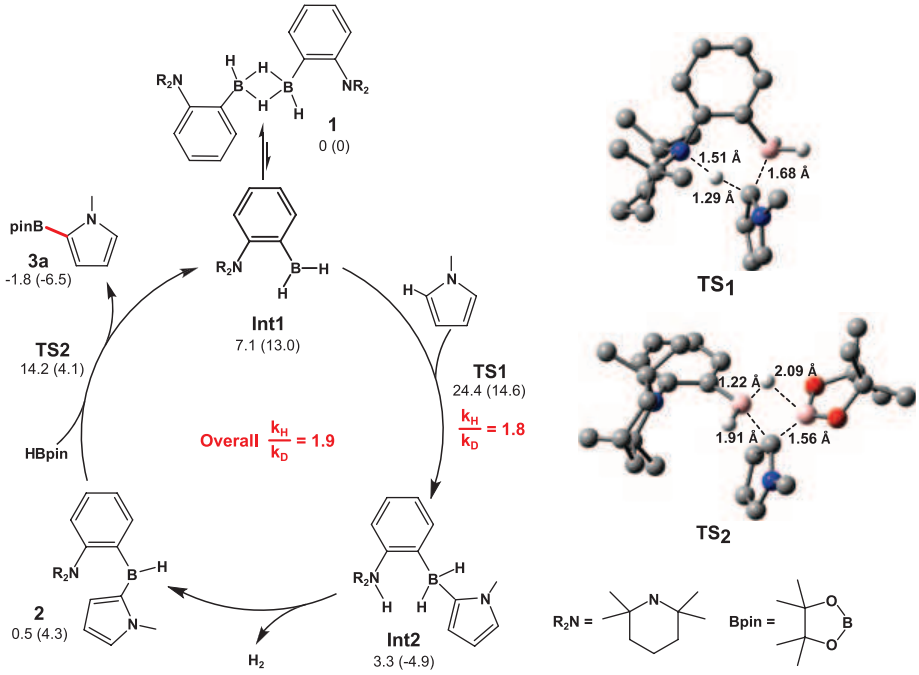

Fig. 4. Proposed mechanism of the borylation of 1-methylpyrrole using catalyst 1, with calculated (ωB97xd/6-31+G) energies ΔG^{273K} (ΔH^{273K}) given for each structure in kcal mol^{-1} in chloroform phase.** The formation of **2** from **1** (KIE of 1.8 was obtained using 1-methylpyrrole-d_4) and **3a** from **2** were observed using NMR spectroscopy, with an overall KIE of 1.9 for the catalytic transformation. **Int1** and **Int2** were not observed, and transition states **TS1** and **TS2** are represented based on DFT calculations. k_H and k_D are the rate constants of the reactions of the nondeuterated and deuterated analogs, respectively.

additional energy, justifying the minor amount of **3a′** produced during catalysis. These barriers are consistent with catalysis operating at 80°C. We performed competition experiments at 80°C between 1-methylpyrrole and 1-methylpyrrole-d_4 to measure a kinetic isotope effect (KIE) of 1.8 for the stoichiometric C-H activation with formation of **2** and of 1.9 for the catalytic borylation. The relatively low KIE value of 1.8 to 1.9 is similar to that observed for the concerted metalation-deprotonation of the palladium-catalyzed arylation reaction with similar substrates (KIE of 2.1 at 100°C) (*28*, *29*).

It is well established that the selectivity of the C-H activation processes using iridium catalysts correlates well with the acidity of the proton (*30*, *31*). In contrast, the ease of activation of C-H bonds using carboxylate-assisted palladium catalysts can be attributed to both the acidity of the proton and the nucleophilicity of the carbon (*32*, *33*). The regioselectivity observed for the formation of the borylated indole **3e**, as well as the KIE values, support the transition state calculations, which indicate that the C-H bond activation by catalyst **1** is directed by the most nucleophilic carbon. **1** therefore acts in a complementary fashion when compared to transition metal systems. Although thiophene and 1,3,5-trimethoxybenzene are more difficult to activate because these molecules have higher aromatic stabilization and hence lower nucleophilicity than pyrroles, the DFT results suggest that the C-H activation transition state energies of these molecules are, respectively, only 3.3 and 6.7 kcal mol^{-1} higher than for the activation of 1-methylpyrrole, suggesting that the borylation of these substrates might be accessible with further catalyst optimization. Moreover, it is expected that the FLP-mediated activation of C-H bonds could be exploited for a plethora of C-H functionalization reactions.

REFERENCES AND NOTES

1. International Conference on Harmonisation of Technical Requirements for Registration of Pharmaceuticals for Human Use, *Guideline for Elemental Impurities Q3D* (2014); http://www.fda.gov/downloads/drugs/guidancecomplianceregulatoryinformation/guidances/ucm371025.pdf.
2. O. Usluer *et al.*, *ACS Macro Lett.* **3**, 1134–1138 (2014).
3. J. Wencel-Delord, F. Glorius, *Nat. Chem.* **5**, 369–375 (2013).
4. S. Rousseaux, B. Liégault, K. Fagnou, in *Modern Tools for the Synthesis of Complex Bioactive Molecules*, J. Cossy, S. Arseniyadis, Eds. (Wiley, Hoboken, NJ, 2012), chap. 1.
5. I. A. Mkhalid, J. H. Barnard, T. B. Marder, J. M. Murphy, J. F. Hartwig, *Chem. Rev.* **110**, 890–931 (2010).
6. J.-Y. Cho, M. K. Tse, D. Holmes, R. E. Maleczka Jr., M. R. Smith 3rd, *Science* **295**, 305–308 (2002).
7. T. Ishiyama *et al.*, *J. Am. Chem. Soc.* **124**, 390–391 (2002).
8. D. G. Hall, *Boronic Acids* (Wiley-VCH, Weinheim, Germany, ed. 2, 2011).
9. N. Miyaura, A. Suzuki, *Chem. Rev.* **95**, 2457–2483 (1995).
10. T. J. Mazzacano, N. P. Mankad, *J. Am. Chem. Soc.* **135**, 17258–17261 (2013).
11. T. Dombray *et al.*, *J. Am. Chem. Soc.* **137**, 4062–4065 (2015).
12. T. Furukawa, M. Tobisu, N. Chatani, *Chem. Commun. (Camb.)* **51**, 6508–6511 (2015).
13. A. Del Grosso, P. J. Singleton, C. A. Muryn, M. J. Ingleson, *Angew. Chem. Int. Ed.* **50**, 2102–2106 (2011).
14. A. Del Grosso, R. Pritchard, C. A. Muryn, M. J. Ingleson, *Organometallics* **29**, 241–249 (2010).
15. A. Profofjevs, J. W. Kampf, E. Vedejs, *Angew. Chem. Int. Ed.* **50**, 2098–2101 (2011).
16. M. A. Larsen, J. F. Hartwig, *J. Am. Chem. Soc.* **136**, 4287–4299 (2014).
17. L. Ackermann, *Chem. Rev.* **111**, 1315–1345 (2011).
18. M. Lafrance, K. Fagnou, *J. Am. Chem. Soc.* **128**, 16496–16497 (2006).
19. F. H. Nielsen, *Plant Soil* **193**, 199–208 (1997).
20. G. C. Welch, R. R. San Juan, J. D. Masuda, D. W. Stephan, *Science* **314**, 1124–1126 (2006).
21. D. W. Stephan, G. Erker, *Angew. Chem. Int. Ed.* **49**, 46–76 (2010).
22. D. W. Stephan, *Org. Biomol. Chem.* **10**, 5740–5746 (2012).
23. M.-A. Courtemanche, M.-A. Légaré, L. Maron, F.-G. Fontaine, *J. Am. Chem. Soc.* **135**, 9326–9329 (2013).
24. O. Baslé, S. Porcel, S. Ladeira, G. Bouhadir, D. Bourissou, *Chem. Commun. (Camb.)* **48**, 4495–4497 (2012).
25. K. Chernichenko *et al.*, *Nat. Chem.* **5**, 718–723 (2013).
26. K. Chernichenko *et al.*, *Angew. Chem. Int. Ed.* **54**, 1749–1753 (2015).
27. J. Takagi, K. Sato, J. F. Hartwig, T. Ishiyama, N. Miyaura, *Tetrahedron Lett.* **43**, 5649–5651 (2002).
28. S. I. Gorelsky, D. Lapointe, K. Fagnou, *J. Am. Chem. Soc.* **130**, 10848–10849 (2008).
29. M. Gómez-Gallego, M. A. Sierra, *Chem. Rev.* **111**, 4857–4963 (2011).
30. H. Tajuddin *et al.*, *Chem. Sci.* **3**, 3505–3515 (2012).
31. B. A. Vanchura 2nd *et al.*, *Chem. Commun. (Camb.)* **46**, 7724–7726 (2010).
32. S. I. Gorelsky, D. Lapointe, K. Fagnou, *J. Org. Chem.* **77**, 658–668 (2012).
33. S. I. Gorelsky, *Coord. Chem. Rev.* **257**, 153–164 (2013).

ACKNOWLEDGMENTS

We acknowledge the contribution of N. Bouchard and J. Légaré-Lavergne in the preparation of some compounds and discussions with S. A. Westcott and P. McBreen. We acknowledge D. Larivière and L. Whitty-Léveillé for the inductively coupled plasma mass spectrometry analyses and P. Audet for his technical help. The work was supported by the National Sciences and Engineering Research Council of Canada (NSERC) and the Centre in Green Chemistry and Catalysis (Québec). Computational studies were made possible by Compute Canada. M.-A.L., M.-A.C., and E.R. acknowledge NSERC and the Fonds de Recherche du Québec - Nature et Technologies for scholarships.

SUPPLEMENTARY MATERIALS

www.sciencemag.org/content/349/6247/513/suppl/DC1
Materials and Methods
Supplementary Text
Figs. S1 to S59
Tables S1 to S3
References (*34*–*48*)

15 April 2015; accepted 15 June 2015
10.1126/science.aab3591

BIOMECHANICS

Jumping on water: Surface tension–dominated jumping of water striders and robotic insects

Je-Sung Koh,[1,2]* Eunjin Yang,[3]* Gwang-Pil Jung,[1] Sun-Pill Jung,[1] Jae Hak Son,[4] Sang-Im Lee,[4,5] Piotr G. Jablonski,[4,6] Robert J. Wood,[2] Ho-Young Kim,[3,5]† Kyu-Jin Cho[1,5]†

Jumping on water is a unique locomotion mode found in semi-aquatic arthropods, such as water striders. To reproduce this feat in a surface tension–dominant jumping robot, we elucidated the hydrodynamics involved and applied them to develop a bio-inspired impulsive mechanism that maximizes momentum transfer to water. We found that water striders rotate the curved tips of their legs inward at a relatively low descending velocity with a force just below that required to break the water surface (144 millinewtons/meter). We built a 68-milligram at-scale jumping robotic insect and verified that it jumps on water with maximum momentum transfer. The results suggest an understanding of the hydrodynamic phenomena used by semi-aquatic arthropods during water jumping and prescribe a method for reproducing these capabilities in artificial systems.

Water striders skate easily on the surface of water mainly because their low body mass and superhydrophobic legs allow them to be supported on their tarsi (the proximal segment of an arthropod's foot) by surface tension alone (*1*–*3*). They are able to generate sufficient vertical propulsion to disengage or jump from the water surface—actions that require high momentum with a high vertical take-off velocity.

Previous studies of the mechanics of water-"walking" in a variety of animals, from small insects to reptiles, elucidated the mode of momentum transfer to the water (*1*–*6*): The velocity of the driving leg was found to play a dominant role. Comparatively heavy animals with a high Baudoin number [$Ba = Mg/(\sigma P) >> 1$, where M is the mass, g is the gravitational acceleration, $\sigma = 72$ mN m^{-1} is the surface tension of water at 25°C, and P is the contact perimeter] cannot float on the surface, so they commonly use high driving power and speed to generate inertial forces in the water large enough to support their weight. For example, the basilisk lizard paddles its foot downward to expand an air cavity under the water and then pulls its foot out of the water before the cavity collapses (*7*). Limb strokes at velocities higher than 30 ms^{-1} induce large hydrodynamic forces, including viscous drag and inertia from the water. In contrast, small arthropods covered with water-repellent integuments (a skin of the arthropod) can float on water without effort because of surface tension ($Ba < 1$). Hu *et al.* (*1*, *4*), Denny (*5*, *8*), and Suter *et al.* (*3*) have reported plausible propulsion mechanisms for small water surface–dwelling animals. These animals achieve horizontal momentum transfer by generating a capillary wave on the water surface and vortices beneath the surface.

Although several small-scale robots inspired by the water strider have demonstrated the ability to float and locomote on water by partly or fully using surface tension (*4*, *9*, *10*), none of them jumps on water. Furthermore, jumping that involves interactions between the unconstrained free body and the liquid surface has been poorly understood at the scale of insects (*11*, *12*). Jumping is vertical propulsion, and it requires different criteria from walking on water, which is lateral propulsion. In contrast to jumping on solid ground, a large driving force and fast stroke in the jumping leg do not guarantee a high take-off velocity on the water surface, especially for small insects (*11*, *12*). There are small insects, such as pygmy mole crickets, that still manage to jump on water by taking advantage of viscosity via a high driving acceleration and leg velocity (>130,000° s^{-1}). But their water-jumping performance is much lower than when they jump on solid ground (*13*).

Water striders can jump on water as high as they can jump on land (*1*). When they are exposed to danger, they show extremely high jumping performance and land in an uncontrolled manner. We focused on this extreme case that achieves the maximum momentum transfer on water. To explore this amazing semi-aquatic motility, we collected water striders (*Aquarius paludum*) from a local pond and recorded them jumping on water in the laboratory with high-speed cameras (Fig. 1A and materials and methods section 1). We found that their ability to exploit the water surface comes from maximizing momentum transfer to the body, which is the integration of force with respect to time by Newton's second law of motion. That is, the water strider gradually increases its leg force to the limit allowed by the water surface and maintains that force until it disengages from the water surface.

High-speed imaging experiments revealed that the insect rises upward while pushing the water surface downward and closing four of its legs inward (Fig. 1A). The hydrodynamic forces generated during this leg motion include drag, surface tension, buoyancy, inertia, and viscous friction. On the basis of estimates of each force using representative values of parameters for the insects we observed (tables S4 and S5), we found that the surface tension force dominates the other forces (supplementary text section 2) for the Weber number, $We = \rho U^2 D/\sigma \sim 10^{-2}$, and $Ba = Mg/(\sigma P) \sim 10^{-2}$. Here, ρ is the density of water, $U \sim 0.2$ m s^{-1} is the rate of dimple growth (i.e., the depression resulting from the force imparted by the leg), $D \sim 0.1$ mm is the leg diameter, $M \sim 40$ mg is the mass of the insect, and $P \sim 80$ mm is the perimeter of the legs that defines the contact length. The low value for We, because of the slow stroke with a thin leg, implies a small energy loss through water flow compared with the interfacial energy of the curved water surface. This inertia-free interaction between the legs and the water surface ensures that the legs remain in contact with the water surface during the down stroke, thereby fully exploiting the reaction force of the curved meniscus on the legs. If the legs struck the water at high speed, the water surface would retreat fast enough to lose contact with the legs and splashing would ensue, decreasing the efficiency of momentum transfer between the legs and water surface (*12*). The combination of a light body with a long perimeter (low Ba) indicates an ability to generate an extremely high body acceleration (compared with g) by using the surface tension of water. Consequently, low We and Ba collectively contribute to the high acceleration of a jumping body through surface tension–dominant interaction without notable energy loss to the water.

A small We, implying negligibly small dynamic effect on the interaction between the legs and the meniscus (*14*), allows the use of static calculations of interfacial force based on the depth of the meniscus (see supplementary text section 2 and table S1). Because the surface tension force on a floating wire tends to increase with the depth of the dimple (figs. S10 to S12) (*15*), it is desirable to push the water surface as deeply as possible. However, the meniscus ruptures when the leg descends beyond the depth limit that the surface tension of water can endure, leading to a dramatic reduction of the reaction force on the

[1]Biorobotics Laboratory, Department of Mechanical and Aerospace Engineering, Seoul National University, Seoul 151-744, Korea. [2]School of Engineering and Applied Sciences and Wyss Institute for Biologically Inspired Engineering, Harvard University, Cambridge, MA 02138, USA. [3]Micro Fluid Mechanics Laboratory, Department of Mechanical and Aerospace Engineering, Seoul National University, Seoul 151-744, Korea. [4]Laboratory of Behavioral Ecology and Evolution, School of Biological Sciences, Seoul National University, Seoul 151-742, Korea. [5]Institute of Advanced Machines and Design, Seoul National University, Seoul 151-744, Korea. [6]Museum and Institute of Zoology, Polish Academy of Sciences, Warsaw 00-679, Poland.
*These authors contributed equally to this work.
†Corresponding author. E-mail: hyk@snu.ac.kr (H.-Y.K.); kjcho@snu.ac.kr (K.-J.C.)

jumping body (*16*). A superhydrophobic straight cylinder of negligible diameter lying horizontally on a water surface can depress the interface roughly by the capillary length (*17*) without sinking. The load supported by a floating object is equal to the weight of water displaced by the body and the perturbed free surface (*18*). It has already been suggested that adaptive deformation of joints and the flexibility of the tibia and tarsus of the water strider's leg may prevent the tip of the leg from piercing the water meniscus and increase the supporting force of the water surface by increasing the water volume displaced (*19*). Figure 1B shows that the tapered leg keeps its tip pointing upward during the stroke, helping to prevent rupture of the meniscus. By using a theoretical model to deduce the force acting on a flexible cylinder floating on liquid (with two parallel contact lines along its axis), we found that the maximum force per unit length (f) on the legs of the water striders is always close to but below a value corresponding to twice the surface tension of water, 144 mN m^{-1}, which is the maximum value that water surface can withstand (Fig. 1C, supplementary text section 2, and table S1).

Careful observation of the jumping sequence of the water strider (Fig. 1A) reveals that the insect rotates its middle and hind legs rather than merely pushing them downward. That is, legs that are initially sprawled on the water surface are extended downward at take-off through actuated leg rotation. To explain the mechanical advantages of this leg movement, we consider what would happen if the leg morphology and kinematics were such that the water strider could depress the surface only vertically without rotation. Upon reaching the maximum dimple depth, l_c, the meniscus is recovered at a velocity of $U \sim l_c/t_r \sim 10^{-1}$ m s^{-1}, where t_r is the time scale for the capillary-gravity wave to travel the capillary length (*20*, *21*). This is far lower than the take-off velocity of the real water strider, $V \sim 1$ m s^{-1}, as evidenced by the relatively slower recovery of the meniscus (from 0 to 14 ms in Fig. 1A) compared with fast disengagement of the legs from the water surface. This implies that the fast-rising water strider would be able to use the upward force from the meniscus only while the legs contact and depress the water surface, thereby significantly reducing the time for momentum transfer. In reality, however, the water strider rotates its legs during jumping, which ensures that the legs meet an undistorted water surface continuously. Thus, the legs can keep pressing the water surface to the maximum depth during ascent of the body despite the slow recovery speed of the meniscus. Our observation reveals that the extended time of interaction between the water surface and the rotating legs of the four water striders tested leads to an increase of V of 27% to 42% as compared with the case when the legs are assumed to move only vertically. Therefore, water striders maximize momentum transfer to the water surface by maintaining a high force profile on each leg until the last moment of jumping by depressing the water surface to the capillary length while rotating their legs.

On the basis of our understanding of real water striders, we identified design criteria for our at-scale robot. Superhydrophobic legs and a low body mass compared with surface tension, yielding Ba <<1, are conducive to higher acceleration with maximum use of surface tension force. In addition, to maximize the kinetic energy transfer to the robot instead of the water, locomotion with low descent velocity and thin legs (We « 1) are required. The driving force should be gradually increased to the maximum value of 144 mN m^{-1} (2σ) to prevent the robot's legs from penetrating the water surface during a jump. If the water surface is broken, the legs swing rapidly under the water surface, leading to high levels of splash and flow around the legs that dissipate energy, rendering jumping highly inefficient (Fig. 2). These criteria guarantee surface tension–dominant propulsion with minimal energy dissipation to water flow.

An ultralight impulsive system that can maximize momentum transfer with limited maximum driving force is required. Leg rotation is also required to ensure that the legs continuously meet an undistorted water surface and keep pressing the water surface. The leg shape should be designed to maximize the surface tension force in the same way as the flexible legs of water striders adapt to the dimple. Especially, the shape of the tip is strongly related to the wetted length when the legs of the water strider rotate inward (*17*). Therefore, the leg tip should be curved in order to

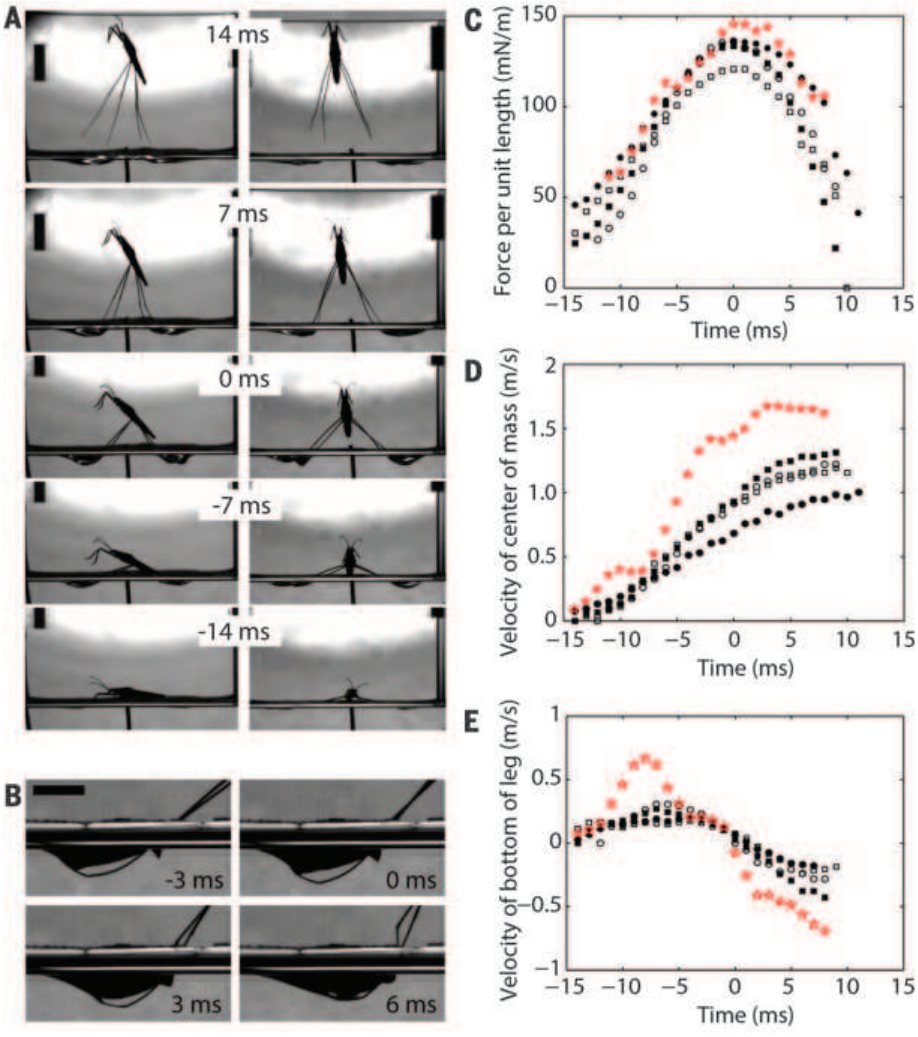

Fig. 1. Water strider jumping. (**A**) Jumping sequence of a water strider in side view (left column) and front view (right column). The black bars on the walls are 10-mm-long scale bars. See movie S5. (**B**) Bent leg of a water strider pushing the water surface. The wetted part of the leg moves to the right, resulting in meeting an undistorted water surface continuously. The scale bar indicates 5 mm. (**C**) f on the four legs of four water striders and robot 4. (**D**) Velocity profile of the water striders and robot 4 jumping from water. (**E**) Velocity profile of the bottom of the leg for water striders and robot 4. (C to E) Black symbols indicate four different water striders, and red stars indicate robot 4. The time is set to be zero when the maximum force is generated. See tables S1 and S3 for detail descriptions of the water striders and the robot.

adapt to the dimple with increasing wetted length while the legs rotate. The low *We* constraint can be rewritten as $t \gg (\rho h^2 D/\sigma)^{1/2}$ by using $U \sim h/t$, where h is the maximum dimple depth and t is the interaction time with water, which results in $t \gg 10^{-3}$ s for both real water striders and our at-scale robot (tables S1 to S4).

The robot uses a bio-inspired catapult mechanism adapted from a flea (*22*, *23*) and implemented with flexure hinge–based composite structures (*24*). The torque reversal catapult (TRC) mechanism in the flea's jumping leg is capable of rapid and repeatable torque production without complex mechanisms. It generates a very small torque when initially triggered, and the torque gradually increases through the driving stroke, as shown in Fig. 3G. This torque profile results in high momentum transfer from the water surface to the jumping body. In contrast, a high initial torque would create a large splash and waves on the water surface. Gradually increasing the torque minimizes unnecessary energy transfer to the water, allowing the jumping body to obtain maximum momentum.

The catapult mechanism uses composite materials and planar shape memory alloy (SMA) actuators. A similar TRC mechanism was previously developed to build a small-scale ground-jumping robot (*22*, *23*). The driving forces for our jumping robot can be varied by changing actuator stiffness and leg length. The passive trigger, which is the compliant beam component that holds the actuator, determines the required force for triggering the geometrical latch of the TRC and the stiffness of the actuator at the moment of triggering (fig. S6). This automatic triggering mechanism simplifies the latch system of the robot and makes it possible to minimize the size and weight of the structure. The 68-mg body weight is 6% of the maximum surface tension force that water can support (on legs with a 160-mm-long perimeter), corresponding to a *Ba* of 0.06, much less than 1 (table. S5). Theoretically, the robotic water strider can be vertically accelerated by a surface tension force up to 15 *g*. In jumping experiments, the robot achieved 13.8 *g*, which is close to the maximum acceleration.

When the legs swing, the length of the leg influences the reaction force on the legs primarily because it determines the moment arm of the driving legs, which transfers the torque generated by the TRC mechanism into a vertical reaction force. In nature, one long-legged water-jumping arthropod was shown to have driving legs 170% longer than its body (*16*). To reduce the maximum reaction force below the maximum surface tension force, we made the robot's legs 5 cm, longer than those of a water strider, because of the higher torque capabilities of the robot.

The pop-up book microelectromechanical system (MEMS) fabrication process (*24*–*28*) allowed us to build at-scale prototypes just 2 cm in body length and 68 mg in weight (Fig. 3D). This fabrication process avoids complex assembly steps by leveraging self-assembly techniques inspired by the folded components of pop-up books. This paradigm for fabricating micro- and "meso"-scale robots (*22*–*28*) is based on flexure hinge–based folded composites. The process involves layering and laminating sheets of individual materials, then folding the composite into a three-dimensional structure (fig. S5). The flexure hinges eliminate

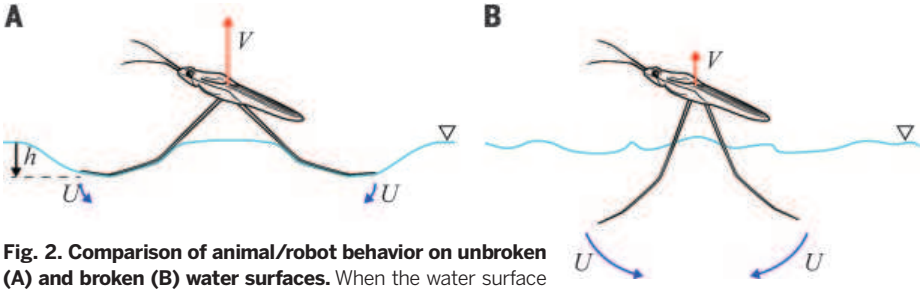

Fig. 2. Comparison of animal/robot behavior on unbroken (A) and broken (B) water surfaces. When the water surface is broken ($f > 2\sigma$), the force supporting the legs sharply reduces, causing the legs to swing rapidly into the water. The resulting viscous drag and splashing dissipate energy.

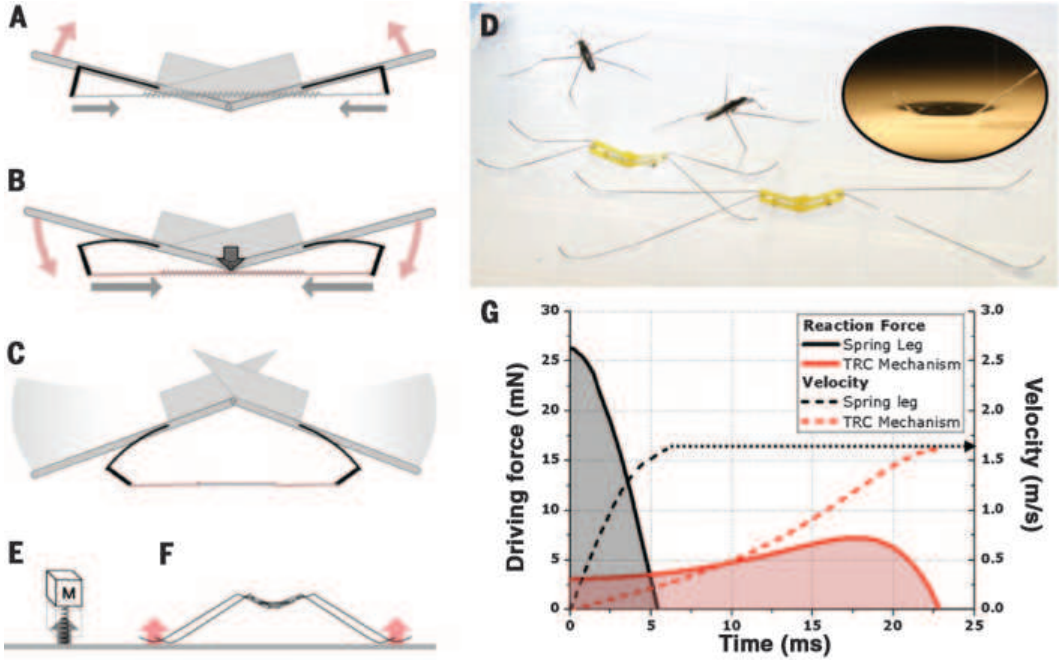

Fig. 3. The TRC mechanism inspired by a flea's jumping leg. (**A** to **C**) The principle of the mechanism. (A) Initial position. The actuator (shown as a coil) is attached at each compliant L-shaped cantilever. The actuator pulls the structure upward, but stoppers block the movement. (B) The actuator begins bending down the compliant L-shaped cantilever, which also moves the actuator down. (C) When the actuator passes through the center joint (i.e., the singularity of the mechanism), the torque direction is reversed, and the structure swings rapidly. The stored energy in the actuator and the cantilevers is released at once. (**D**) Two jumping robotic insects with different leg lengths, along with real water striders. The legs are coated with a hydrophobic material, resulting in a high contact angle that creates a dimple (inset image) on the water surface, which supports the weight of the robot. (**E** and **F**) Comparison of two jumping mechanisms, compressed spring legs (E) and a TRC mechanism (F). In contrast to the spring leg, a TRC mechanism may reduce the driving force on the legs by its torque characteristics and long length of the legs. (**G**) The driving force and velocity profiles of compressed spring legs and a TRC mechanism. The TRC mechanism requires much less maximum force to attain the same velocity. In comparison, the stroke of the actuators (springs) in both models is 5.75 mm, and their stiffness is set to generate the same *V* of 1.6 m s^{-1} (4.4 N m^{-1} in spring leg, 16.52 N m^{-1} in TRC mechanism).

friction, one of the dominant causes of energy loss and nonlinearity for small devices. The design parameters are determined by analyzing the compliance of the structure for passively triggering the torque reversal mechanism (see supplementary text section 1 and fig. S6) based on a fully dynamic simulation, including the mechanical properties of all the components and the interface forces between the water surface and the robot's legs (see supplementary text section 2 and fig. S13). Furthermore, all modeling steps are verified and supported by individual experiments. With this simple joint element, dynamic modeling and simulations match well with experimental data obtained with physical prototypes (fig. S3).

The sheet nickel titanium (NiTi) SMA actuator is embedded in the body structure as an artificial muscle. The sheet SMA was cut into a serpentine shape by the same ultraviolet laser micromachining system used to construct the body. The actuator is 80 μm thick, 100 μm wide, and 1 mg in weight. When heated above its transition temperature, the actuator's stiffness changes, inducing a negative strain and pulling the passive trigger in the body structure until the torque direction is reversed (Fig. 3, A to C).

The legs are made of superelastic Ni-Ti alloy to prevent them from permanent deformation during repeated jumping experiments. The high modulus and superelasticity of this wire permits the legs to be thin and flexible. The end tips of the wire legs in the robot (corresponding to the tarsus in the insect) are curved, which minimizes contact shape change between the legs and the water surface when the legs swing and prevents stress concentration at the interface between the tip and the water surface. The round shape of the wire leg linearizes the resulting surface tension force on the water surface as dimple depth increases, according to the experimental and theoretical modeling results shown in figs. S10 and S12. The linear surface tension force profile allowed us to model the hydrodynamic reaction force between the legs and the water as a spring (see supplementary text section 2 and table S6). This model yields simulations that are well matched with our experiments (within 7% error in V; see table S2).

The wire legs are coated with a superhydrophobic material, Everdry (Ultratech International Incorporated, Jacksonville, FL) (*29*). We achieved more than 150° of contact angle with this coating (supplementary text section 5 and fig. S9). Hydrophobicity increases jumping velocity by reducing downward forces when the legs escape from the free surface (*21*, *30*) and by increasing the maximum static load that water can endure (*6*, *20*, *21*, *30*, *31*). In particular, the superhydrophobic coating on the wire legs would lead to near zero adhesion to the water when they leave the surface (*21*).

We built five prototype robots that use different triggering forces. The driving force has a linear relationship with the triggering force. We performed jumping experiments with the prototypes on both water and ground (figs. S1 to S4 and table S2). A thin heating wire was carefully placed just below the robot body to activate the SMA actuator. As the SMA actuator transitions, the force increases, and the passive trigger begins to bend (Fig. 3, A to C). When the actuator passes through the center joint, the torque direction changes, and the body structure folds downward, generating a rapid snap-through.

The experiments verified the design criteria that the driving force per wetted length (f) should be below the maximum surface tension force per wetted length (2σ) in order for the robot to efficiently jump on water with maximum momentum transfer. Figure 4 shows that the robot jumps off the water surface smoothly without breaking the free surface and without making a large splash. V is 1.6 m s^{-1}, with a jumping height of 142 mm, and the maximum reaction force of the dimple is 9.27 mN. When the legs do not penetrate the water surface, the dynamic model

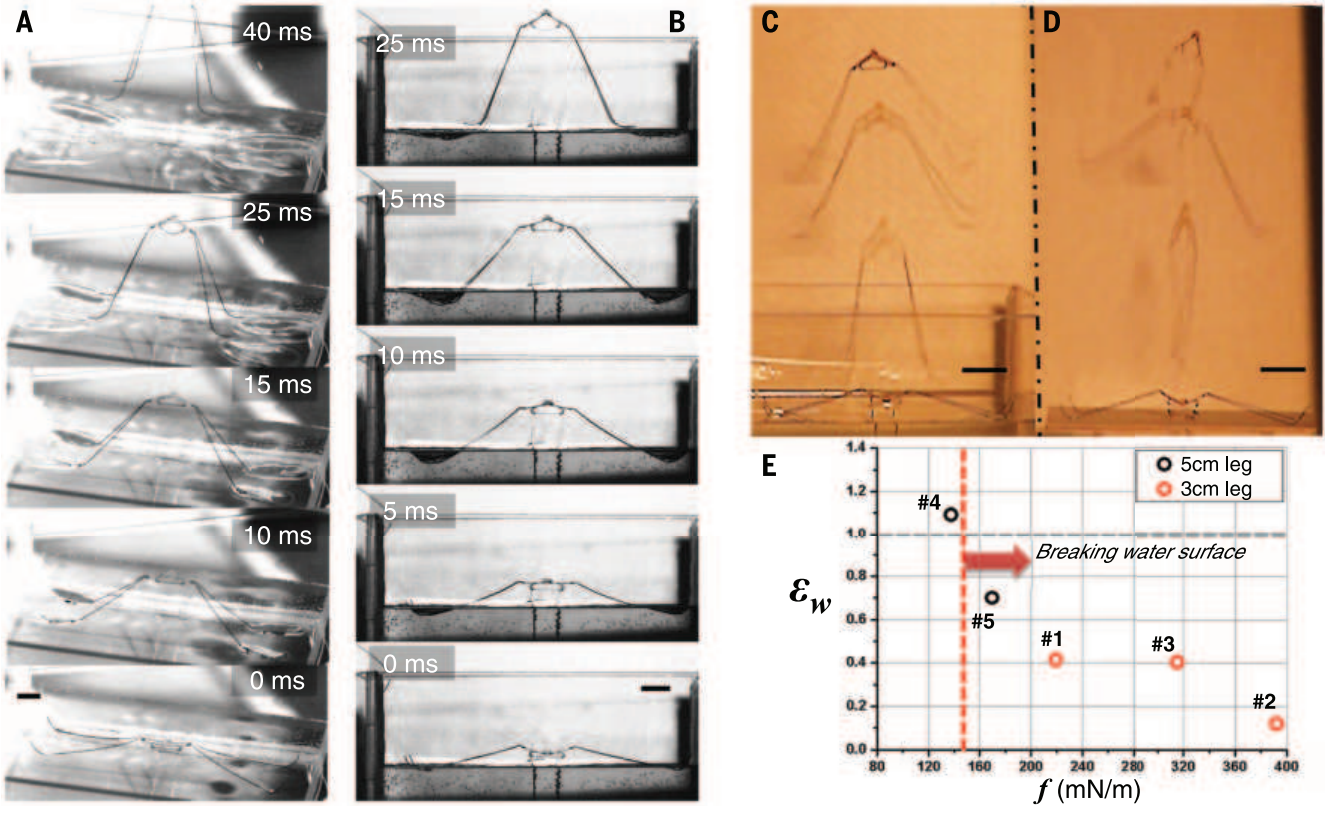

Fig. 4. Video frames of robot 4 and ε_w of robots jumping on water and on ground. (See movies S1 to S4.) (**A**) The legs distort the water surface. Note the absence of large splashing around the driving legs. (**B**) These horizontal views show that the legs do not penetrate the water surface. (**C**) Superimposed frames of the robot jumping on water. (**D**) Superimposed frames of the robot jumping on rigid ground. The robot obtains similar momentum on water and ground. Scale bar, 1 cm. (**E**) Experimental results for ε_w depending on different driving f of five robot prototypes. The red dashed line indicates the maximum surface tension force that water provides (2σ, 144 mN m^{-1}). The gray dashed line indicates a ε_w of 1.

of the robot jumping on water agrees well with experimental data, and we can obtain various reliable simulations from the model (supplementary text section 3 and fig. S3). The maximum driving f obtained from the dynamic model is 140 mN m^{-1}, just below the 144 mN m^{-1} (2σ) limit. Prototypes that satisfied the design criteria achieved higher take-off velocity on water (Fig. 4C) than when jumping on ground (Fig. 4D), a counterintuitive result. This may result from a reduction of leg vibration when jumping on water, because the stored energy is transferred into vertical kinetic energy rather than vibration energy. The movie of these jumps supports this proposition (movie S4). In our models, the initial energy stored in the actuator is 0.304 mJ and the jumping kinetic energy of the robot jumping on water is 0.095 mJ (31.3%), whereas the vibration kinetic energy is 0.193 mJ (63.5%) (table S7).

The water-ground velocity ratio (ε_w) describes how much momentum the robot attains on water compared with jumping on solid ground.

$$\text{Water} - \text{ground velocity ratio } (\varepsilon_w) = \frac{\text{Take} - \text{off velocity on water}}{\text{Take} - \text{off velocity on ground}}$$

A ratio lower than 1 indicates that the robot did not achieve as much momentum on water as on ground. If the driving force on water is kept below the maximum surface tension force defined by the design criteria, the ratio can be equal to or greater than 1, as was the case for robot 4, which had a maximum driving f just below the maximum surface tension force (2σ) (Fig. 4E). ε_w values of other prototypes are lower than 1, which means that the water surface is broken because of driving force that exceeds this limit, and thus the take-off velocity on water is reduced (table. S2 and fig. S3). High driving force does not guarantee a high take-off velocity in a surface tension–dominant case, as shown in robots 1 to 3 and 5. The maximum driving force is constrained by the surface tension coefficient of water. We may assume that water striders control their muscles precisely to satisfy these criteria in a manner similar to the design of the impulsive actuation mechanism in robot 4 (Fig. 1C).

Our at-scale water-jumping robotic insect has demonstrated that it is possible to reproduce the performance of water-jumping arthropods and has proved to be an effective tool for verifying theoretical insights on how the surface tension force can play a dominant role in locomotion of these systems. The experimental results improve our understanding of the dynamic interaction between an unconstrained free body and a liquid surface, as observed in semi-aquatic arthropods in nature.

REFERENCES AND NOTES

1. D. L. Hu, J. W. M. Bush, *J. Fluid Mech.* **644**, 5–33 (2010).
2. J. W. M. Bush, D. L. Hu, *Annu. Rev. Fluid Mech.* **38**, 339–369 (2006).
3. R. Suter, O. Rosenberg, S. Loeb, H. Long, *J. Exp. Biol.* **200**, 2523–2538 (1997).
4. D. L. Hu, B. Chan, J. W. M. Bush, *Nature* **424**, 663–666 (2003).
5. M. W. Denny, *Air and Water: The Biology and Physics of Life's Media* (Princeton Univ. Press, Princeton, NJ, 1993).
6. X. Gao, L. Jiang, *Nature* **432**, 36–36 (2004).
7. J. W. Glasheen, T. A. McMahon, *Nature* **380**, 340–342 (1996).
8. M. W. Denny, *J. Exp. Biol.* **207**, 1601–1606 (2004).
9. Y. S. Song, M. Sitti, *IEEE Trans. Robot.* **23**, 578–589 (2007).
10. X. Zhang *et al.*, *ACS Appl. Mater. Interfaces* **3**, 2630–2636 (2011).
11. D.-G. Lee, H.-Y. Kim, *Langmuir* **24**, 142–145 (2008).
12. B. Shin, H.-Y. Kim, K. J. Cho, Towards a biologically inspired small-scale water jumping robot. *2nd IEEE RAS and EMBS International Conference on Biomedical Robotics and Biomechatronics* (2008), pp. 127–131.
13. M. Burrows, G. P. Sutton, *Curr. Biol.* **22**, R990–R991 (2012).
14. D. Vella, J. Li, *Phys. Fluids* **22**, 052104 (2010).
15. D. Vella, *Langmuir* **24**, 8701–8706 (2008).
16. M. Burrows, *J. Exp. Biol.* **216**, 1973–1981 (2013).
17. Q.-S. Zheng, Y. Yu, X.-Q. Feng, *J. Adhes. Sci. Technol.* **23**, 493–501 (2009).
18. J. B. Keller, *Phys. Fluids* **10**, 3009 (1998).
19. X.-Y. Ji, J.-W. Wang, X.-Q. Feng, *Phys. Rev. E* **85**, 021607 (2012).
20. D. Vella, D.-G. Lee, H.-Y. Kim, *Langmuir* **22**, 5979–5981 (2006).
21. D.-G. Lee, H.-Y. Kim, *J. Fluid Mech.* **624**, 23 (2009).
22. M. Noh, S.-W. Kim, S. An, J.-S. Koh, K.-J. Cho, *IEEE Trans. Robot.* **28**, 1007–1018 (2012).
23. J.-S. Koh, S.-P. Jung, R. J. Wood, K.-J. Cho, A jumping robotic insect based on a torque reversal catapult mechanism. *2013 IEEE/RSJ International Conference of Intelligent Robots and Systems* (2013), pp. 3796–3801.
24. R. J. Wood, S. Avadhanula, R. Sahai, E. Steltz, R. S. Fearing, *J. Mech. Des.* **130**, 052304 (2008).
25. R. J. Wood, *IEEE Trans. Robot.* **24**, 341–347 (2008).
26. J. P. Whitney, P. S. Sreetharan, K. Y. Ma, R. J. Wood, *J. Micromech. Microeng.* **21**, 115021 (2011).
27. P. Birkmeyer, K. Peterson, R. S. Fearing, DASH: A dynamic 16g hexapedal robot. *2008 IEEE/RSJ International Conference of Intelligent Robots and Systems* (2009), pp. 2683–2689.
28. K. Y. Ma, P. Chirarattananon, S. B. Fuller, R. J. Wood, *Science* **340**, 603–607 (2013).
29. Ultratech International Incorporated, www.spillcontainment.com/everdry.
30. J. Zhao, X. Zhang, N. Chen, Q. Pan, *ACS Appl. Mater. Interfaces* **4**, 3706–3711 (2012).
31. X. Q. Feng, X. Gao, Z. Wu, L. Jiang, Q. S. Zheng, *Langmuir* **23**, 4892–4896 (2007).

ACKNOWLEDGMENTS

This work was supported by National Research Foundation of Korea (grant nos. 2013K000371, 2014048162, 2014023206, and 2013R1A2A2A01006394), a grant to Bio-Mimetic Robot Research Center funded by Defense Acquisition Program Administration (grant no. UD130070ID), and the Wyss Institute for Biologically Inspired Engineering. We thank H. Choi and B. Shin for their helpful discussions.

SUPPLEMENTARY MATERIALS

www.sciencemag.org/content/349/6247/517/suppl/DC1
Materials and Methods
Supplementary Text
Figs. S1 to S13
Tables S1 to S7
Movies S1 to S5

20 March 2015; accepted 11 June 2015
10.1126/science.aab1637

PALEOMAGNETISM

A Hadean to Paleoarchean geodynamo recorded by single zircon crystals

John A. Tarduno,[1,2]* Rory D. Cottrell,[1] William J. Davis,[3] Francis Nimmo,[4] Richard K. Bono[1]

Knowing when the geodynamo started is important for understanding the evolution of the core, the atmosphere, and life on Earth. We report full-vector paleointensity measurements of Archean to Hadean zircons bearing magnetic inclusions from the Jack Hills conglomerate (Western Australia) to reconstruct the early geodynamo history. Data from zircons between 3.3 billion and 4.2 billion years old record magnetic fields varying between 1.0 and 0.12 times recent equatorial field strengths. A Hadean geomagnetic field requires a core-mantle heat flow exceeding the adiabatic value and is suggestive of plate tectonics and/or advective magmatic heat transport. The existence of a terrestrial magnetic field before the Late Heavy Bombardment is supported by terrestrial nitrogen isotopic evidence and implies that early atmospheric evolution on both Earth and Mars was regulated by dynamo behavior.

The oldest previously reported geomagnetic field values, from 3.2 billion– to 3.45 billion–year-old magnetite bearing single feldspar and quartz phenocrysts from igneous rocks of the Nondweni and Barberton Greenstone Belts (Kaapvaal Craton, South Africa) (*1*–*3*), indicate a relatively strong field, but the prior history of the geodynamo is unknown. Some thermal evolution models predict no geodynamo before ~3.5 billion years ago (Ga) (*4*).

For magnetic minerals to be suitable recorders, they must be small, in the single to pseudosingle domain state (*5*), and have remained pristine since formation. The metamorphism that has affected Paleoarchean and older rocks makes paleointensity determination especially difficult. These metamorphosed rocks typically contain large multidomain magnetic grains (MD) with short relaxation times, secondary magnetic remanence carriers, and minerals with a propensity

[1]Department of Earth and Environmental Sciences, University of Rochester, Rochester, NY 14627, USA. [2]Department of Physics and Astronomy, University of Rochester, Rochester, NY 14627, USA. [3]Geological Survey of Canada, Ottawa K1A 0E8, Canada. [4]Department of Earth and Planetary Sciences, University of California, Santa Cruz, CA 95064, USA.
*Corresponding author. E-mail: john.tarduno@rochester.edu

to alter during thermal demagnetization. The single crystal paleointensity (SCP) method was developed to isolate ideal magnetic carriers and behavior (*1*–*3*). In this method, a host silicate grain separated from a bulk rock is the focus of paleointensity study. The silicate is itself not of intrinsic magnetic interest; instead, it acts as the host to minute magnetic inclusions that have been shown to record magnetic fields with high fidelity. Previous SCP studies focused on feldspar (*1*, *2*), quartz (*2*, *3*), and olivine (*6*) hosts. Here, we present SCP data from zircons.

The Jack Hills (JH) conglomerate bears the oldest known zircon populations, with grains up to ~4.4 billion years old (*7*, *8*). Unlike prior SCP studies, these zircons are detrital; their source has yet to be discovered and may have been lost to erosion. We evaluate the potential of events after and before the depositional age of the conglomerate (~3 Ga) to impose secondary magnetizations through paleomagnetic conglomerate tests and sensitive high-resolution ion microprobe (SHRIMP) analyses, respectively.

The JH belt has been metamorphosed to at least ~475°C (*9*) and variably deformed. Metamorphism is common in Archean terrains, but key samples that have locally escaped the more extreme effects of chemical and physical alteration accompanying metamorphism can sometimes be isolated (*3*). For example, some of the JH conglomerates are far from rare late intrusive volcanic rocks, which are expected to impose thermal and/or chemical remagnetizations. The interior of some cobble-sized clasts preserve centimeter-sized regions with a minimum of internal deformation and secondary mineralization, and a magnetite-dominated magnetization that passes a conglomerate test after demagnetization to temperatures of 500° to 550°C (*10*). Thus, locally components of the JH sediments have the potential to preserve magnetizations at high unblocking temperature in single or pseudosingle domain magnetic grains.

Our samples for zircon analysis were collected near the Discovery outcrop (*7*), ~1 km East of the cobble-bearing sites (*10*). Quartz clasts near the Discovery outcrop are pebble-sized (>4 mm, <64 mm), and because of this small size, they have suffered penetrative deformation; they are too deformed for a meaningful macroconglomerate test, but the zircons have survived with little or no internal deformation. We conducted a microconglomerate test on oriented small (~500 to 800 μm) samples, each centered on a single large (200 to 300 μm) zircon (*11*) to test whether the characteristic magnetization held by zircons from our samples has also survived post-depositional geological events. We used an ultrahigh-resolution three-component direct-current superconducting quantum interference device (SQUID) magnetometer (William S. Goree, Inc., Sand City, CA) that affords an order of magnitude greater sensitivity than that of other high-resolution SQUID rock magnetometers (*11*) in order to meet the challenge of full-vector measurement of such small samples with low bulk magnetizations. Thermal demagnetization by use of a CO_2 laser (*2*) revealed unblocking between 565° and 580°C, which is consistent with a magnetite carrier (fig. S1, A to G). The characteristic magnetization of individual samples is well defined (median angular dispersion <10°), but together, the directions from seven samples cannot be distinguished from those drawn from a random distribution, indicating a positive microconglomerate test (fig. S1H). This test also addresses the debate over the primary nature of inclusions within JH zircons (*12*, *13*). If magnetite carrying the characteristic magnetization was formed during metamorphism after conglomerate deposition, it should record a consistent direction that is contrary to our results. As in the larger-scale conglomerate test, multiple directions that are distinct from the high unblocking temperature magnetization (on a per sample basis) are isolated at lower unblocking temperatures, excluding modern lightning effects. The low unblocking temperature magnetizations reflect post-depositional geological events.

A zircon might also have experienced a reheating event from the time spanning its formation to incorporation into the JH conglomerate. We tested for the presence of reheating in two ways.

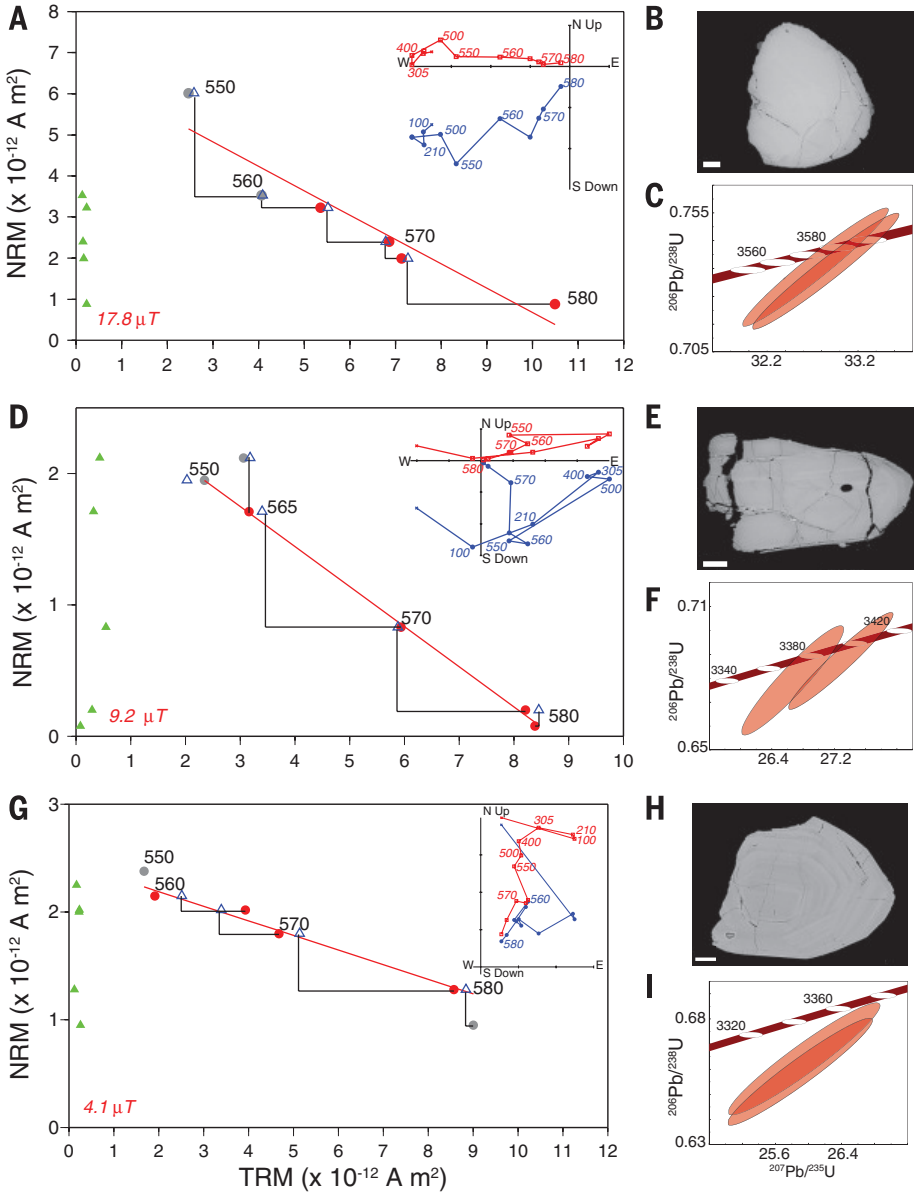

Fig. 1. Thellier-Coe paleointensity and SHRIMP age data from individual zircon crystals. (**A**) NRM lost versus TRM gained [circles; red are selected data (*11*)], with least-squares line fit to determine paleointensity value for sample ZTC7. Open triangles are partial TRM checks; solid green triangles are MD tail checks. (Inset) Orthogonal vector plot of field-off steps of Thellier-Coe data. Labeled points are degrees Celcius. Blue, declination; red, inclination. (**B**) Scanning electron microscope image of grain prepared for SHRIMP geochronological analyses. Scale bar, 20 μm. (**C**) Concordia diagram showing SHRIMP geochronological data. Uncertainty ellipses are 2σ. (**D** to **F**) Analyses shown in (A) to (C) for sample ZTC9. (**G** to **I**) Analyses shown in (A) to (C) for sample ZTC15.

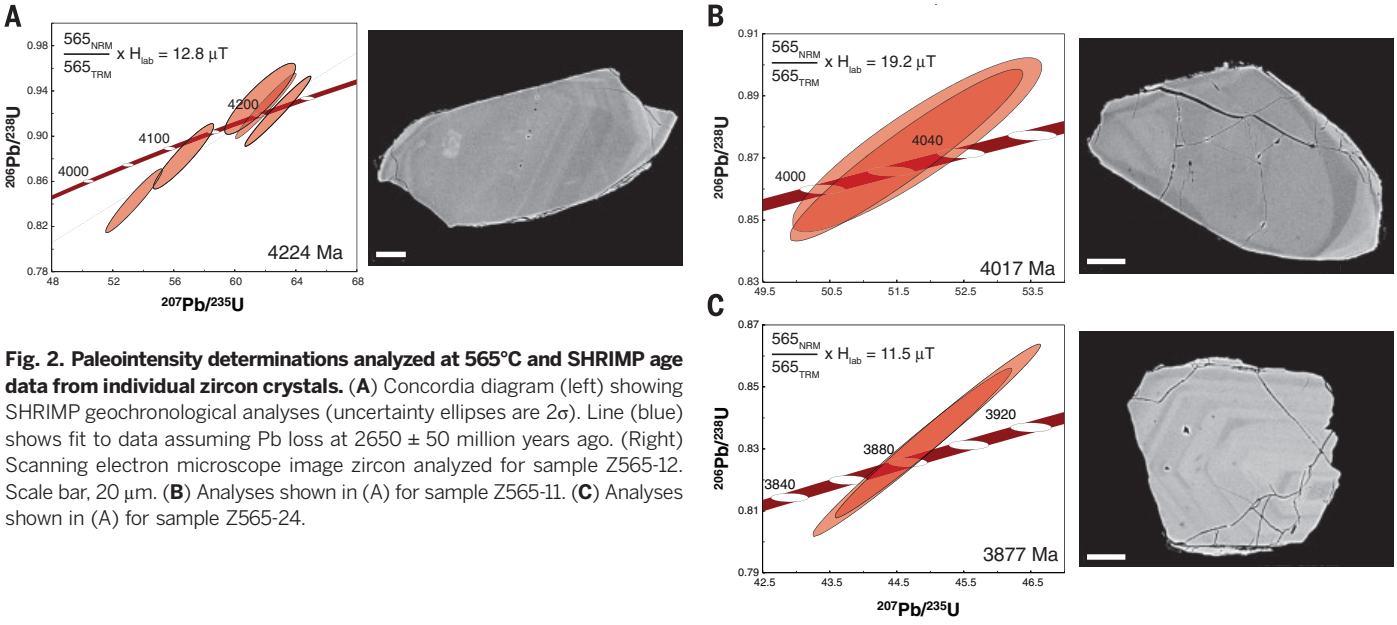

Fig. 2. Paleointensity determinations analyzed at 565°C and SHRIMP age data from individual zircon crystals. (**A**) Concordia diagram (left) showing SHRIMP geochronological analyses (uncertainty ellipses are 2σ). Line (blue) shows fit to data assuming Pb loss at 2650 ± 50 million years ago. (Right) Scanning electron microscope image zircon analyzed for sample Z565-12. Scale bar, 20 μm. (**B**) Analyses shown in (A) for sample Z565-11. (**C**) Analyses shown in (A) for sample Z565-24.

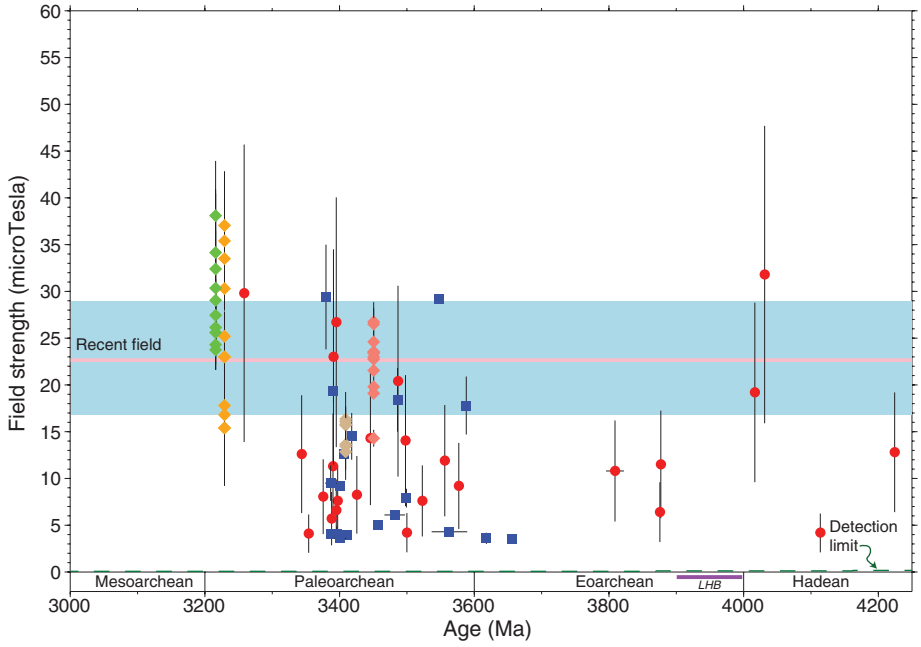

Fig. 3. Paleointensity versus time. Solid blue squares are Thellier-Coe results from single zircons. Solid red circles are paleointensity determinations analyzed at 565°C. Diamonds are equatorial equivalent values assuming a dipole-dominated field from prior studies of Archean single-silicate crystals as follows: green, Barberton Greenstone Belt (BGB) Dalmein pluton (*2*); yellow, BGB Kaapvaal pluton (*2*); tan, Nondweni Greenstone Belt dacite (*3*); and pink, BGB dacite (*3*). All age and Thellier-Coe paleointensity uncertainties are plotted at 1σ. Uncertainties for 565°C paleointensity determinations are a factor of two bounds (fig. S2). Pink solid line and blue shaded region are, respectively, mean equatorial field value and standard deviation for the recent field derived from a bootstrap resampling of data from the past 800,000 years (*11*). LHB, Late Heavy Bombardment (*23*). Dashed line is the detection limit imposed by the external field (*1*).

First, we searched for Pb loss in the SHRIMP data that could be associated with hypothetical geologic events between initial zircon crystallization and emplacement in the conglomerate. Inhomogeneous redistribution of Pb within zircon at the nanometer scale is common in zircon that has experienced high-temperature metamorphism (*11*). The secondary ion mass spectrometry (SIMS) analysis sputters zircon to a depth of 700 to 1000 nm over ~15 min so that each individual analysis represents a depth-time series. In our second approach, we searched the secondary beam-normalized Pb counts over the analyses for nonsystematic variations indicative of Pb redistribution at the submicrometer scale during amphibolite- to granulite-grade metamorphism (*11*).

We separated JH zircons by hand using nonmagnetic techniques for SCP studies. We focused on larger zircons from the JH population that are greater than 150 μm in one dimension and separated them from searches of several thousand zircon crystals. We used 0.5-mm fused quartz sample holders to reduce blanks and used a routine that stacks complete magnetometer measurements at each demagnetization temperature step (*11*). Thermal methods are best suited for retrieving any thermoremanent magnetization (TRM) recorded by the zircons (*5*). Demagnetization experiments revealed natural remanent magnetization (NRM) versus temperature decay mainly between ~565° and 580°C, which is consistent with our microconglomerate results and the dominance of near-end-member magnetite (*11*). We used the Thellier-Coe method with MD grain tail checks (Fig. 1, A, D, and G, and fig. S2) (*11*). After paleointensity analyses, we analyzed zircons using the Geological Survey of Canada SHRIMP (Fig. 1, B, C, E, F, H, and I) (*11*). Data from 19 zircons met an extensive set of selection criteria (tables S1 to S3) (*11*). Age data from one sample (ZTC8) show evidence for Archean Pb loss that could represent greenschist metamorphism at ~2.6 Ga or an older event. However, the data for this and the other samples do not indicate nonsystematic variations in Pb counts. For $^{207}Pb/^{206}Pb$ ages between 3.38 and 3.66 Ga, paleofield values range between ~4 and 29 μT. These values are above threshold detection levels [~0.6 μT, defined by the interaction of the solar wind and an unmagnetized planet (*1*, *11*)], even with the consideration of cooling-rate effects (*11*), and suggest the presence of a geomagnetic field from Paleoarchean to Eoarchean times.

Only ~12% of zircons from the Discovery site are >3.9 billion years old (*7*). To explore whether our samples preserve magnetic and age evidence

for Hadean fields, we next applied a simplified paleointensity method to select zircons. This determination consisted of an evaluation of paleointensity at a single temperature (565°C) at which the characteristic remanent magnetization was defined. The 565°C determinations can provide a paleointensity estimate that is within a factor of approximately two of the full Thellier-Coe value (fig. S3). Most conservatively, however, we only used these data to test for the presence or absence of a geomagnetic field by comparison with threshold values. Data from 25 of these zircons met selection criteria (tables S2 to S4) (*11*). SHRIMP geochronological analyses yield $^{207}Pb/^{206}Pb$ ages between ~3.26 and ~4.22 Ga for these samples. These data also lack nonsystematic variations in Pb counts, but age data for our two oldest samples show some complexity. For our oldest sample (Z565-12; 4.22 Ga), we interpret this complexity as the influence of greenschist grade metamorphism at ~2.6 Ga (Fig. 2B). For sample Z565-5 (4.11 Ga), we cannot exclude the possibility of reheating between 2.6 and 3.9 Ga. We note that this age complexity is not seen in our samples dating to ~4 Ga and younger (Fig. 2, B to C). Paleointensities recorded by the 565°C determinations (Fig. 3) also exceed external field values and therefore suggest the presence of a core dynamo in the Hadean Eon.

Before the onset of inner core growth, the geodynamo was likely driven by thermal convection, in which case, the heat flow at the core-mantle boundary (CMB) must have exceeded the adiabat. Recent estimates suggest an adiabatic value around 15 TW (*14*, *15*), although some are lower (*16*). Neither stagnant lid convection, as has been proposed for the Archean (*17*), nor the modeled heat transfer across a basal magma ocean (*4*) is consistent with an operating dynamo during this interval. Advection via heat pipes (*18*) and/or plate tectonics were likely the main mantle heat transfer processes operating on the early Earth.

In the absence of a core dynamo field, atmospheric N_2 would be susceptible to ionization and removal by solar wind pickup (*1*, *19*). The presence of a magnetic field is therefore consistent with the lack of nitrogen isotopic fractionation deduced by the study of geologic samples of the Archean atmosphere (*20*). However, the weakest paleointensity values (Fig. 3) are comparable with a magnetic field only ~12% of that of today, which would imply magnetopause standoff distances less than three Earth radii (*1*). A coronal mass ejection added to this steady-state solar wind could have resulted in the pulsing of volatiles and water from Earth's atmosphere and perhaps implantation of nitrogen on the Moon (*21*). This in turn argues that Earth's water budget was initially much greater than today—and/or that it was replenished during the delivery of a water-rich late veneer (*22*) or during the tail of the Late Heavy Bombardment (*23*) at ~3.9 Ga—to account for today's water inventory. In addition to magnetic shielding, total losses may have been in part mitigated by bottlenecks in transport through the atmosphere and/or an early hydrogen envelope (*1*, *19*), the latter restricting extreme atmospheric expansion.

Our paleointensity and age data suggest the presence of a core dynamo >750 million years earlier than prior estimates. An early start for the geodynamo is similar to that of the early Martian magnetic field (*24*), but the subsequent collapse of the Martian dynamo probably facilitated atmospheric stripping (*25*). In contrast, the early start and persistence of atmospheric shielding attendant with the long-lived geodynamo was likely a key factor in the development of Earth as a habitable planet.

REFERENCES AND NOTES

1. J. A. Tarduno, E. G. Blackman, E. E. Mamajek, *Phys. Earth Planet. Inter.* **233**, 68–87 (2014).
2. J. A. Tarduno, R. D. Cottrell, M. K. Watkeys, D. Bauch, *Nature* **446**, 657–660 (2007).
3. J. A. Tarduno *et al.*, *Science* **327**, 1238–1240 (2010).
4. S. Labrosse, J. W. Hernlund, N. Coltice, *Nature* **450**, 866–869 (2007).
5. D. J. Dunlop, Ö. Özdemir, *Rock Magnetism, Fundamentals and Frontiers* (Cambridge Univ. Press, Cambridge, 1997).
6. J. A. Tarduno *et al.*, *Science* **338**, 939–942 (2012).
7. W. Compston, R. T. Pidgeon, *Nature* **321**, 766–769 (1986).
8. J. W. Valley *et al.*, *Nat. Geosci.* **7**, 219–223 (2014).
9. B. Rasmussen, I. R. Fletcher, J. R. Muhling, S. A. Wilde, *Precambrian Res.* **180**, 26–46 (2010).
10. J. A. Tarduno, R. D. Cottrell, *Earth Planet. Sci. Lett.* **367**, 123–132 (2013).
11. Materials and methods are available as supplementary materials on *Science* Online.
12. M. Hopkins, T. M. Harrison, C. E. Manning, *Geology* **40**, e281 (2012).
13. B. Rasmussen, I. R. Fletcher, J. R. Muhling, C. J. Gregory, S. A. Wilde, *Geology* **40**, e282–e283 (2012) Reply.
14. P. Olson, *Science* **342**, 431–432 (2013).
15. H. Gomi *et al.*, *Phys. Earth Planet. Inter.* **224**, 88–103 (2013).
16. P. Zhang, R. E. Cohen, K. Haule, *Nature* **517**, 605–607 (2015).
17. C. ONeill, *Earth Planet. Sci. Lett.* **406**, 49–58 (2014).
18. W. B. Moore, A. A. G. Webb, *Nature* **501**, 501–505 (2013).
19. H. Lammer *et al.*, *Mon. Not. R. Astron. Soc.* **439**, 3225–3238 (2014).
20. B. Marty, L. Zimmermann, M. Pujol, R. Burgess, P. Philippot, *Science* **342**, 101–104 (2013).
21. M. Ozima *et al.*, *Nature* **436**, 655–659 (2005).
22. F. Albarède, *Nature* **461**, 1227–1233 (2009).
23. D. de Niem, E. Kührt, A. Morbidelli, U. Motschmann, *Icarus* **221**, 495–507 (2012).
24. M. H. Acuña *et al.*, *Science* **284**, 790–793 (1999).
25. K. S. Hutchins, B. M. Jakosky, J. G. Luhmann, *J. Geophys. Res.* **102**, 9183–9189 (1997).

ACKNOWLEDGMENTS

We acknowledge the late William Goree for his efforts in developing the ultrahigh-sensitivity SQUID magnetometer used in this study. We also thank G. Kloc for assistance in sample preparation; T. Pestaj for assistance in the SHRIMP laboratory; and S. Wilde, J. Valley, D. Trail, and C. Manning for helpful discussions. The data presented in this manuscript are tabulated in the supplementary materials. This work was supported by the U.S. NSF (grants EAR-0619467 and EAR-1015269).

SUPPLEMENTARY MATERIALS

www.sciencemag.org/content/349/6247/521/suppl/DC1
Materials and Methods
Figs. S1 to S3
Tables S1 to S4
References (*26*–*47*)

12 February 2015; accepted 30 June 2015
10.1126/science.aaa9114

NANOELECTRONICS

Epitaxial growth of a monolayer WSe_2-MoS_2 lateral p-n junction with an atomically sharp interface

Ming-Yang Li,[1,2]* Yumeng Shi,[1]* Chia-Chin Cheng,[2,3] Li-Syuan Lu,[4] Yung-Chang Lin,[5] Hao-Lin Tang,[1] Meng-Lin Tsai,[6] Chih-Wei Chu,[2] Kung-Hwa Wei,[3] Jr-Hau He,[6] Wen-Hao Chang,[4,7] Kazu Suenaga,[5] Lain-Jong Li[1]†

Two-dimensional transition metal dichalcogenides (TMDCs) such as molybdenum sulfide MoS_2 and tungsten sulfide WSe_2 have potential applications in electronics because they exhibit high on-off current ratios and distinctive electro-optical properties. Spatially connected TMDC lateral heterojunctions are key components for constructing monolayer p-n rectifying diodes, light-emitting diodes, photovoltaic devices, and bipolar junction transistors. However, such structures are not readily prepared via the layer-stacking techniques, and direct growth favors the thermodynamically preferred TMDC alloys. We report the two-step epitaxial growth of lateral WSe_2-MoS_2 heterojunction, where the edge of WSe_2 induces the epitaxial MoS_2 growth despite a large lattice mismatch. The epitaxial growth process offers a controllable method to obtain lateral heterojunction with an atomically sharp interface.

Two-dimensional (2D) transition metal dichalcogenides (2D TMDCs) are of interest for electronics applications in that they offer tunabilty of several properties, including the band gap, band offset, carrier density, and polarity. (The bulk TMDCs have been known for a long time and have not evoked similar interest.) Heterostructures formed by vertical stacking of different 2D TMDCs have been realized via the transfer of their exfoliated or as-grown flakes (*1*, *2*), where their properties are dominated by the stacking orientation and interlayer coupling strength. However, lateral heterostructures with edge contacts offer easier band offset

tuning because the materials are more spatially separated. The direct growth of lateral heterojunctions is challenging because TMDC alloys are thermodynamically preferred (*3*). Recently, the MoS_2-$MoSe_2$ (*4*), WS_2-WSe_2 (*4*), WS_2-MoS_2 (*2*), and $MoSe_2$-WSe_2 (*5*) lateral heterostructures with interesting optical and electrical properties were obtained by one-pot synthetic processes. However, the interface regions for these lateral junctions are likely alloy structures because all of the precursors coexist in vapor phases during the growth. Such processes only allow the growth of heterostructures with either different metals or chalcogen, making it difficult to grow p-n heterostructures such as WSe_2-MoS_2.

We report the controlled epitaxial growth of WSe_2-MoS_2 lateral junction, where WSe_2 is grown on substrates through van der Waals epitaxy, followed by the edge epitaxy of MoS_2 along the W growth front. Two-step growth offers precise control to achieve the atomically sharp transition in compositions at the junction. Optical and microscopic characterizations revealed the detailed mechanisms for the regrowth (similar to living growth) for the 2D TMDC systems. The 2D lateral WSe_2-MoS_2 heterojunction was synthesized on *c*-plane sapphire substrates by sequential chemical vapor deposition (CVD) of WSe_2 and MoS_2 (Fig. 1A) (*6*, *7*). To avoid the alloy reaction observed in one-pot synthesis, we first prepared single-crystalline triangular WSe_2 monolayer requiring a higher growth temperature (925°C) and then performed the MoS_2 growth at 755°C in a separate furnace. As we previously reported (*7*), the WSe_2 growth proceeds from WSe_2 seeds, followed by van der Waals epitaxy on sapphire. The crucial point for successful heterostructure synthesis without alloy formation is to control the relative vapor amount of MoO_3 and S during the second-step MoS_2 growth. The excess in Mo precursors enhances the MoS_2 vertical growth, whereas the excess in S vapor promotes the formation of undesired WS_2 at the interface (fig. S1).

The morphology of in-plane heterostructures was examined by optical microscopy (OM) and photoluminescence (PL) and Raman spectroscopies. Figure 1B shows the OM images of the lateral WSe_2-MoS_2 heterojunctions. All of the WSe_2 triangles are uniformly surrounded by MoS_2, and the domain for WSe_2 and MoS_2 can be distinguished simply by their optical contrast. The lattice constant of WSe_2 is 5.53% larger than MoS_2 (*5*, *8*), which might be one of the factors restricting the growth of MoS_2 onto WSe_2 basal planes. The Raman and PL spectra in fig. S2 verify the chemical composition of inner WSe_2 and outer MoS_2 and also reveals the formation of the seamless WSe_2-MoS_2 junction.

The annular dark field (ADF) image of the lateral WSe_2-MoS_2 junction obtained with scanning transmission electron microscopy (STEM) revealed that the ADF signal increased with the atomic number (Z) as ~$Z^{1.7}$ (Fig. 1C) (*9*). Thus, the W (74), Mo (42), Se (34), and S (16) atoms could be distinguished by their intensity. The ADF image for another location (Fig. 1D) shows the atomic models corresponding to the obtained image. An atomically sharp interface between the WSe_2-MoS_2 junction was formed, where about 90% of W atoms are located at the interface bridging to two pair of Se atoms and one pair of S atoms, as depicted in Fig. 1E. In addition to the ADF image, the coherent interface is also identified by the electron energy loss spectroscopy (EELS) measurement. The EELS line scan (by monitoring the EELS spectra change across the heterojunction) shown in fig. S3 verified an atomically sharp change. These observations suggest that the growth starts from the replacement of Se atoms of WSe_2 edge by S atoms.

Polarization-resolved second-harmonic generation (SHG) microscopy is sensitive to the crystal orientation and domain boundaries of surface layers (*10*–*16*). We used a back-reflection geometry

[1]Physical Sciences and Engineering Division, King Abdullah University of Science and Technology, Thuwal, 23955-6900, Kingdom of Saudi Arabia. [2]Research Center for Applied Sciences, Academia Sinica, Taipei 10617, Taiwan. [3]Department of Material Science and Engineering, National Chiao Tung University, Hsinchu 300, Taiwan. [4]Department of Electrophysics, National Chiao Tung University, Hsinchu, Taiwan. [5]National Institute of Advanced Industrial Science and Technology (AIST), Tsukuba, Japan. [6]Computer, Electrical and Mathematical Sciences and Engineering Division, King Abdullah University of Science and Technology, Thuwal, 23955-6900, Kingdom of Saudi Arabia. [7]Taiwan Consortium of Emergent Crystalline Materials (TCECM), Ministry of Science and Technology, Taiwan.
*These authors contributed equally to this work. **†Corresponding author. E-mail: lance.li@kaust.edu.sa**

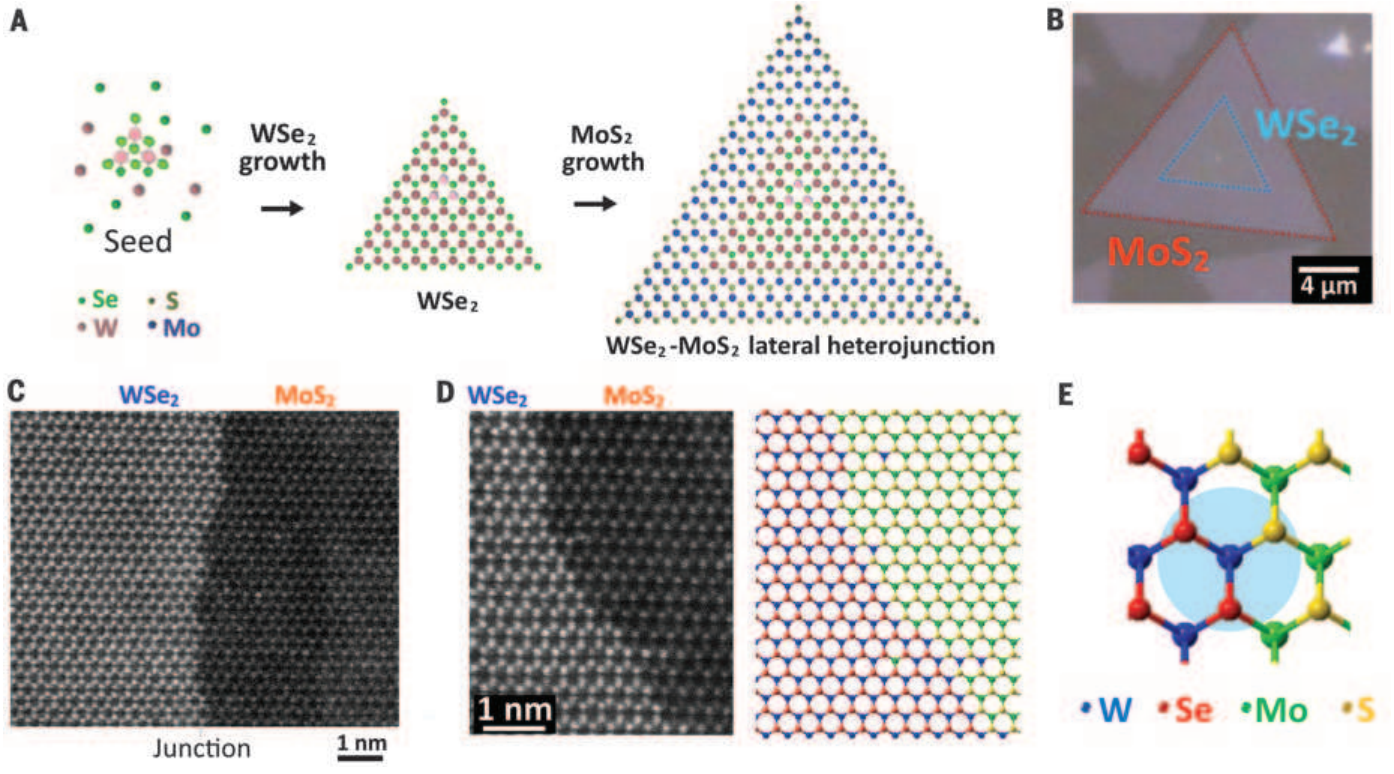

Fig. 1. Formation and structure of WSe_2-MoS_2 heterostructures. (**A**) Schematic illustration of the sequential growth of the monolayer WSe_2-MoS_2 in-plane heterostructure. (**B**) As shown in the optical image, the WSe_2 and MoS_2 can be distinguished by their optical contrast. (**C** and **D**) High-resolution STEM images taken from the WSe_2-MoS_2 in-plane heterostructure. (**E**) Atomic model showing the interface structure between WSe_2 and MoS_2.

with a linearly polarized pump laser (870 nm) normally incident on a triangular WSe_2-MoS_2 heterostructure sample and detected the SH intensities with polarizations parallel (I_H) and perpendicular (I_V) to the laser polarization (Fig. 2A) (see fig. S4 for the setup). The total SH intensity I_{total} (sum of I_V and I_H) (Fig. 2C), which was generally uniform over the entire WSe_2 and MoS_2 domains, indicated that the surrounding MoS_2 was also single crystalline without grain boundaries. The SH intensity also showed no suppression across the junction, which suggests that the MoS_2 grew out from the edges of WSe_2 without misorientation. The MoS_2 regions showed slight variations in SH intensity that coincided well with the variations in PL intensity and peak energy (Fig. 3A, inset). As will be discussed below, we consider that the SH intensity variations in the surrounding MoS_2 arise from the nonuniform strain distribution rather than presence of multiple grains.

To gain more insight into the WSe_2-MoS_2 heterojunction growth, we calculated the crystal orientation using $\theta = (1/3)\tan^{-1}\sqrt{I_V/I_H}$, where θ is the angle between the laser polarization direction and the nearest armchair axis of the sample (*13*). The map of θ (Fig. 2D) was uniform over the entire WSe_2-MoS_2 heterostructure, indicating that the outgrowing MoS_2 was a single crystal with the same orientation as the inner WSe_2. We have also performed SHG measurements on a WSe_2-MoS_2 heterojunction composed of multiple grains (Fig. 2, B and E). Although these grains had different orientations (θ map, Fig. 2F), the outgrowing MoS_2 followed the orientation of the inner WSe_2. These results strongly suggest that the outgrowth of MoS_2 occurred through epitaxy off the edge of WSe_2 and determined the crystal orientation, rather than the sapphire substrate. Fig. S5 demonstrates that the MoS_2 monolayer also grew out from the prepatterned WSe_2 monolayer.

We noticed that the MoS_2 in WSe_2-MoS_2 heterostructures normally exhibits considerable PL energy differences at different locations (Fig. 3A, inset), where the contour color mapping shows the spatial distribution of PL energy ranging from 1.79 to 1.91 eV. The site with a higher PL energy always exhibited a higher intensity, as presented in the PL spectra (Fig. 3A). However, such a large variation in PL was not observed in isolated MoS_2 monolayers occasionally found on the same sample (fig. S6), so the MoS_2 PL variation is related to the heterostructure formation. We also performed Raman imaging for the MoS_2 A_{1g} and E_{2g} frequencies (Fig. 3B). Compared with the inset of

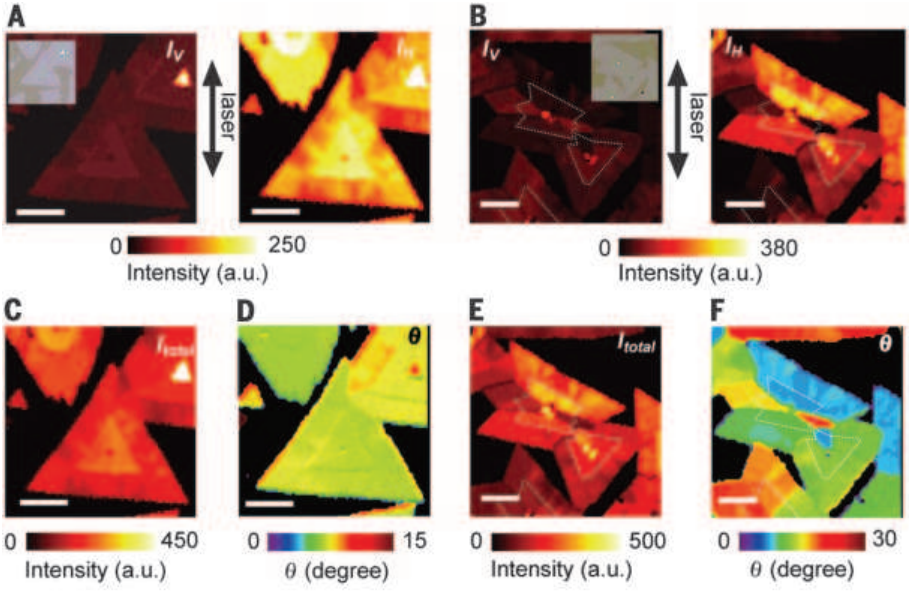

Fig. 2. Polarization-resolved SHG measurement. (**A**) The intensity maps of the perpendicular I_V and parallel I_H components of the SH. The insert shows the optical image. The black double arrow line indicates the direction of incident laser polarization. (**C** and **D**) Maps of the total intensity I_{total} and angle θ between the direction of laser polarization and the armchair direction of the sample, respectively. (**B**) The intensity maps of the I_V and I_H components of the SH for a multidomain WSe_2-MoS_2 junction. (**E** and **F**) Maps of the I_{total} and θ of the area shown in (B). The scale bar for all is 5 μm.

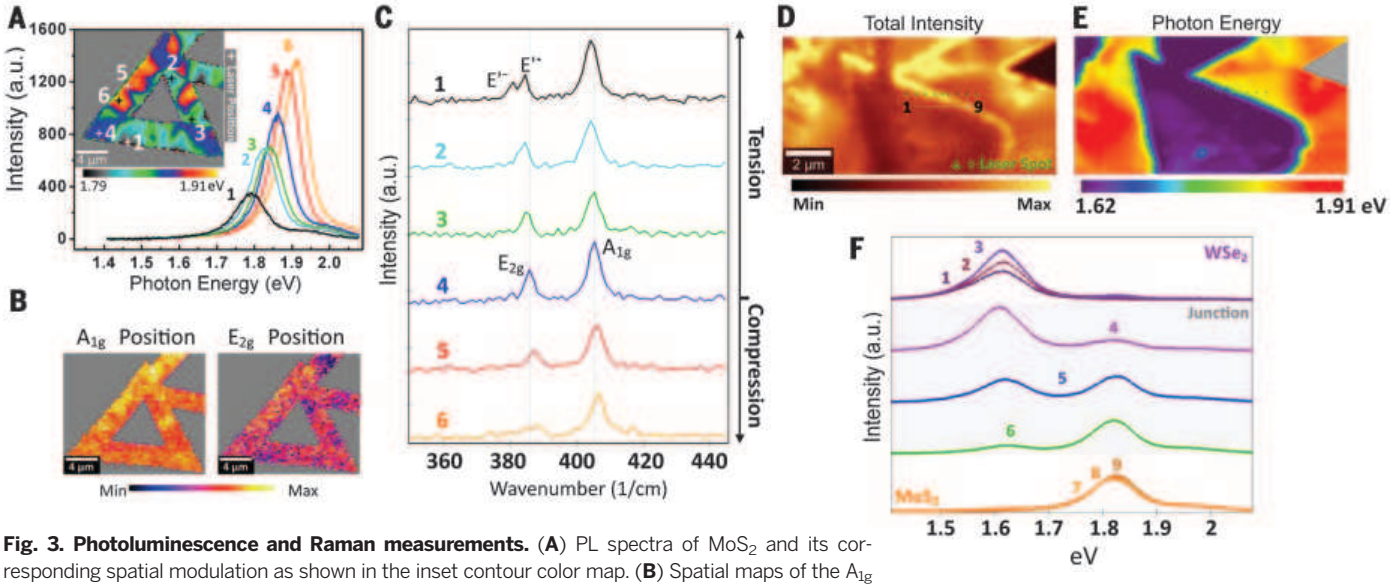

Fig. 3. Photoluminescence and Raman measurements. (**A**) PL spectra of MoS_2 and its corresponding spatial modulation as shown in the inset contour color map. (**B**) Spatial maps of the A_{1g} and E_{2g} peak position. (**C**) The extracted MoS_2 Raman spectra from the WSe_2-MoS_2 junction, where the colored spectra corresponds to the inset contour color map in (A). (**D** and **E**) The maps showing PL intensity and the spatial modulation of photon energy for a selected heterojunction. (**F**) Spectra 1 to 9 were collected from the location marked in (D).

Fig. 3A, the location with a higher PL intensity and energy also exhibited higher A_{1g} and E_{2g} frequencies.

According to previous studies on the strain-dependent E_{2g} and A_{1g} Raman modes in MoS_2 monolayer (*17*–*20*), we conclude that both the PL and Raman variations reflect the local strain distribution in the MoS_2. The frequency upshift (downshift) of both Raman modes is associated with a compressive (tensile) strain. The spectra from the isolated MoS_2 and the three corners of the triangular heterostructure have an identical PL energy of 1.86 eV, near that of 1.82 ± 0.02 eV from unstrained MoS_2 (*19*). For simplicity, assuming the isolated MoS_2 is nearly strain free, we could then map out the relative strain on MoS_2; the tensile area is colored with green, cyan, and black, and the compressive area is colored with red and yellow in the inset of Fig. 3A. The representative Raman spectra under tensile and compressive strain (Fig. 3C) show that the MoS_2 with the lowest PL energy (1.79 eV) was frequently observed from the area with a tensile strain. As the compressive strain increases, the PL peak shifted to a higher energy with a pronounced intensity increase. Symmetry breaking of the crystal (*19*, *20*) broke the degeneracy in the MoS_2 E_{2g} Raman mode (subpeaks E'^{-} and E'^{+}) for the as-grown TMDC monolayer (black curve).

The strain variation likely originated from the lattice mismatch between MoS_2 and WSe_2. Figure 3A shows that the strain of MoS_2 adjacent to WSe_2 was tensile (cyan color) and then gradually changed to strain free (blue color), particularly at the corners. To balance the strain built upon the MoS_2, some MoS_2 areas exhibited compressive strain (red color). We estimated the strain (relative to the as-grown isolated MoS_2) in the MoS_2 region of the MoS_2-WSe_2 heterostructure to be 1.59 ± 0.25% for largest tensile strain and 1.1 ± 0.18% for largest compressive strain, based on the reported linear PL energy shift rate of 45 meV/% strain (*17*–*22*). Such a large strain difference induced by the lateral heterostructure could indicate the possibility of using monolayer TMDCs for straintronics (*23*).

In the inner triangular WSe_2, the PL spectra showed a prominent direct band-gap emission at ~1.63 eV. By contrast to the outer MoS_2 region, the PL energy and intensity in the WSe_2 region did not show pronounced variations (Fig. 3, D and E). Additionally, the Raman frequencies of the WSe_2 region were also relatively unchanged (fig. S7). Interestingly, Fig. 3D shows that the PL emission from the heterojunction interface was stronger and the PL enhancement was localized at the WSe_2 side of the lateral interface. The PL spectra taken from the points marked as 1 through 9 in Fig. 3D are displayed in Fig. 3F, where two characteristic peaks—1.62 eV for WSe_2 (points 1 to 3) and 1.85 eV for MoS_2 (points 7 to 9)—were observed, respectively. The line scan was performed at a selected MoS_2 area nearly free of strain. Noticeably, the PL spectrum for WSe_2 adjacent to the heterojunction (point 3) showed a narrower and stronger peak at 1.62 eV. The WSe_2-MoS_2 vertical contact forms a type II band alignment (*1*, *24*, *25*), with an interband transition peak at ~1.59 eV. However, we did not detect any appreciable interband transition in PL measurements.

Our observation differs from that for the WS_2-MoS_2 heterojunction in a previous report (*2*), where a broader PL peak with an intermediate band gap energy, identified as the interband transition, was observed. Meanwhile, it was reported that the edges of WS_2 monolayers exhibit extraordinary PL intensity. (*26*) Our STEM results showed that interfacial W is bonded to Se and S, respectively, from each side, and the interface structure is similar to the reported WS_2 edges. We performed a separate study on gas phase sulfurization of isolated WSe_2 monolayer triangles and found that the PL emission from WSe_2 edge was largely enhanced after edge sulfurization (fig. S8). The enhancement of PL at the interface could be related to the chemical composition change in the junction.

To study the depletion region of the atomically sharp WSe_2-MoS_2 heterojunction, we used scanning Kelvin probe microscopy (SKPM) to directly extract the spatial distribution of the surface potentials. Figure 4A and its inset show the SKPM and atomic force microscopy (AFM) images for the junction, respectively. The color contrast in the SKPM image between the WSe_2 and MoS_2 regions revealed the distinct potential difference across the junction. SKPM allows the measurement of depletion width, but the actual built-in potential difference is not accurate because it is strongly affected by the surface adsorbates. The line profile in fig. S9 reveals that the junction depletion width is ~320 nm. The value agrees with that of the 100 to 500 nm estimated from the depletion approximation of solving Poisson's equation based on the assumptions of no free carriers and constant dopant concentration in the depletion region (see the supplementary materials).

To investigate the electrical properties, the as-grown WSe_2-MoS_2 heterojunction was transferred onto a SiO_2/Si substrate, and two contact metals, Pd and Ti/Au, were deposited on WSe_2 and MoS_2, respectively (see the supplementary materials for details). Figure 4B shows the OM image of the WSe_2-MoS_2 heterojunction, and Fig. 4C shows the current-voltage (*I*-*V*) curves of the heterojunction without (black) and with (red) white light illumination. The characteristic curve exhibits good rectification character, with a threshold voltage

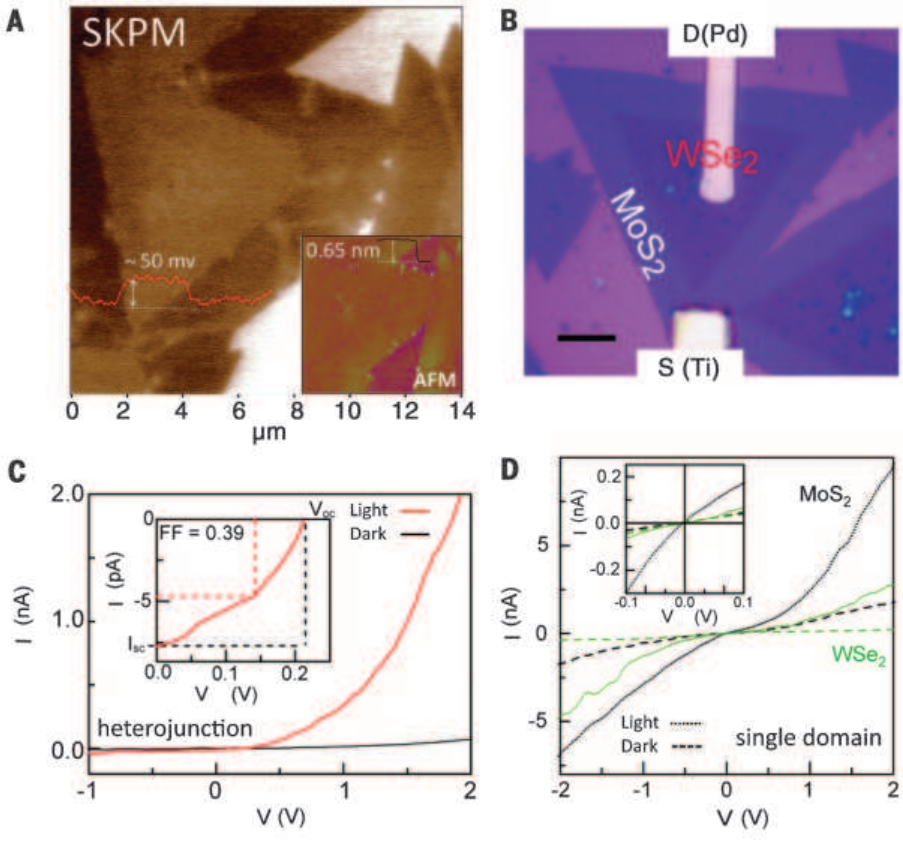

Fig. 4. Electrical properties of the devices based on heterojunction. (**A**) SKPM image showing the surface potential distribution for the WSe_2-MoS_2 heterostructure. Inset shows the AFM height images, and no obvious height difference is observed from two sides of the junction. (**B**) Optical image for the WSe_2-MoS_2 p-n junction device. Scale bar, 4 μm. (**C**) Electrical transport curves (*I* versus *V*) with and without light exposure (1 mW/cm^2), showing the presence of a p-n junction and photovoltaic effect. (**D**) Electrical transport curves for Ti-contacted MoS_2 and Pd-contacted WSe_2 separately.

at about 0.9 V under forward bias (fig. S10). A photovoltaic effect with an open-circuit voltage V_{oc} of 0.22 V and short-circuit current I_{sc} of 7.7 pA under white light illumination (power density E_w of 1 mW/cm^2) is shown in the inset of Fig. 4C. The nearly symmetric *I-V* curves and barely photovoltaic effect for individual WSe_2 (contacted with Pd) and MoS_2 (contacted with Ti/Au) in Fig. 4D corroborate that the p-n junction from the heterostructure is predominant, rather than the small Schottky barriers between metal and TMDCs.

We calculated the power conversion efficiency (PCE) of the device with the photon-to-electron conversion equation, PCE = $I_{SC}V_{OC}FF/E_WA_C$, where *FF* is the fill factor and A_C is the effective area with energy conversion. The *FF* of 0.39 was extracted from the inset of Fig. 4C. The small *FF* might result from the high equivalent series resistance of the intrinsic TMDC layers. We estimated the maximum A_C by considering both the depletion area of the junction and the adjacent diffusion area of each TMDC layers, giving rise to a maximum area about 32 μm^2 (see the supplementary materials for details). The calculated PCE is at least 0.2%, comparable with the few-layer MoS_2 vertical p-n junction (*27*) and monolayer lateral WSe_2 p-n junction (*28*). The p-n junction of WSe_2-MoS_2 is further corroborated with the results from another device (fig. S11), where the carrier transport is clearly through the heterojunction interface.

The presence of depletion width (320 nm), rectifying behaviors, photoresponses, and photovoltaic effects confirms the intrinsic p-n junction properties for lateral WSe_2-MoS_2. The realization of controlled-edge epitaxy of TMDC opens the door to construct other monolayer components for future monolayer electronics.

REFERENCES AND NOTES

1. M.-H. Chiu *et al.*, *ACS Nano* **8**, 9649–9656 (2014).
2. Y. Gong *et al.*, *Nat. Mater.* **13**, 1135–1142 (2014).
3. S.-H. Su *et al.*, *Small* **10**, 2589–2594 (2014).
4. X. Duan *et al.*, *Nat. Nanotechnol.* **9**, 1024–1030 (2014).
5. C. Huang *et al.*, *Nat. Mater.* **13**, 1096–1101 (2014).
6. Y.-H. Lee *et al.*, *Adv. Mater.* **24**, 2320–2325 (2012).
7. J.-K. Huang *et al.*, *ACS Nano* **8**, 923–930 (2014).
8. Y. Shi *et al.*, *Nano Lett.* **12**, 2784–2791 (2012).
9. O. L. Krivanek *et al.*, *Nature* **464**, 571–574 (2010).
10. Y. R. Shen, *Annu. Rev. Phys. Chem.* **40**, 327–350 (1989).
11. J. F. McGilp, D. Weaire. C. H. Patterson, Eds., *Epioptics: Linear and Nonlinear Optical Spectroscopy of Surfaces and Interfaces* (Springer-Verlag GmbH, Berlin, 1995).
12. G. A. Reider, T. F. Heinz, in *Photonic Probes of Surfaces: Electromagnetic Waves*, P. Halevi, Eds. (Elsevier Science Limited, Amsterdam, 1995), vol. 2, chap. 9.
13. N. Kumar *et al.*, *Phys. Rev. B* **87**, 161403 (2013).
14. H. Zeng *et al.*, *Sci. Rep.* **3**, 1608 (2013).
15. Y. Li *et al.*, *Nano Lett.* **13**, 3329–3333 (2013).
16. W.-T. Hsu *et al.*, *ACS Nano* **8**, 2951–2958 (2014).
17. Y. Y. Hui *et al.*, *ACS Nano* **7**, 7126–7131 (2013).
18. L. Yang *et al.*, *Sci. Rep.* **4**, 5649 (2014).
19. H. J. Conley *et al.*, *Nano Lett.* **13**, 3626–3630 (2013).
20. C. R. Zhu *et al.*, *Phys. Rev. B* **88**, 121301 (2013).
21. A. Castellanos-Gomez *et al.*, *Nano Lett.* **13**, 5361–5366 (2013).
22. Q. Ji *et al.*, *Nano Lett.* **13**, 3870–3877 (2013).
23. T. Heine, *Acc. Chem. Res.* **48**, 65–72 (2015).
24. H. Fang *et al.*, *Proc. Natl. Acad. Sci. U.S.A.* **111**, 6198–6202 (2014).
25. M.-H. Chiu *et al.*, Determination of band alignment in the single layer MoS_2/WSe_2 heterojunction. *Nature Commun.* (2015); available at http://arxiv.org/abs/1406.5137).
26. H. R. Gutiérrez *et al.*, *Nano Lett.* **13**, 3447–3454 (2013).
27. H.-M. Li *et al.*, *Nat. Commun.* **6**, 6564 (2015).
28. A. Pospischil, M. M. Furchi, T. Mueller, *Nat. Nanotechnol.* **9**, 257–261 (2014).

ACKNOWLEDGMENTS

L.-J.L. acknowledges support from King Abdullah University of Science and Technology (Saudi Arabia), Ministry of Science and Technology (MOST) and Taiwan Consortium of Emergent Crystalline Materials (TCECM), Academia Sinica (Taiwan), and AOARD-134137 (USA). Y.-C.L. and K.S. acknowledge support from the Japan Science and Technology Agency research acceleration program. W.-H.C. acknowledges the support from TCECM, MOST of Taiwan under grant NSC102-2119-M-009-002-MY3 and the Center for Interdisciplinary Science of Nation Chiao Tung University.

SUPPLEMENTARY MATERIALS

www.sciencemag.org/content/349/6247/524/suppl/DC1
Materials and Methods
Figs. S1 to S11
References (*29*–*38*)

30 April 2015; accepted 24 June 2015
10.1126/science.aab4097

FOREST ECOLOGY

Pervasive drought legacies in forest ecosystems and their implications for carbon cycle models

W. R. L. Anderegg,[1,2]* C. Schwalm,[3,4] F. Biondi,[5] J. J. Camarero,[6] G. Koch,[3] M. Litvak,[7] K. Ogle,[8] J. D. Shaw,[9] E. Shevliakova,[10] A. P. Williams,[11] A. Wolf,[1] E. Ziaco,[5] S. Pacala[1]

The impacts of climate extremes on terrestrial ecosystems are poorly understood but important for predicting carbon cycle feedbacks to climate change. Coupled climate–carbon cycle models typically assume that vegetation recovery from extreme drought is immediate and complete, which conflicts with the understanding of basic plant physiology. We examined the recovery of stem growth in trees after severe drought at 1338 forest sites across the globe, comprising 49,339 site-years, and compared the results with simulated recovery in climate-vegetation models. We found pervasive and substantial "legacy effects" of reduced growth and incomplete recovery for 1 to 4 years after severe drought. Legacy effects were most prevalent in dry ecosystems, among Pinaceae, and among species with low hydraulic safety margins. In contrast, limited or no legacy effects after drought were simulated by current climate-vegetation models. Our results highlight hysteresis in ecosystem-level carbon cycling and delayed recovery from climate extremes.

Anthropogenic climate change is projected to alter both climate mean conditions and climate variability, leading to more frequent and/or intense climate extremes such as heat waves and severe drought (*1*). Increasing variability is likely to profoundly affect ecosystems, as many ecological processes are more sensitive to climate extremes than to changes in mean states (*2*–*4*). In turn, the impacts of these extremes can have major effects on ecosystem-level carbon cycling, feeding back to accelerate or limit climate change. The 2003 European heat wave, for example, led to the development of a strong anomalous carbon source, reversing 4 years of carbon uptake by terrestrial ecosystems on a continental scale (*5*).

Forest ecosystems store nearly half of the carbon found in terrestrial ecosystems (*6*), but the fate of forests under climate change and with increasing climate extremes remains uncertain and controversial. Whereas some studies contend that large regions of forest are poised on the verge of collapse into an alternate state (*7*–*9*), others suggest that forests are relatively resilient and likely to experience only modest changes (*10*–*12*). The sensitivity of forests to climate extremes has become apparent in global patterns of widespread forest mortality (*13*), which highlight the possibility that the forest carbon sink could be weakened or could even transition rapidly to a carbon source in some regions (*13*–*15*). Thus, the response of forest growth and mortality to extreme drought and heat constitutes a

[1]Department of Ecology and Evolutionary Biology, Princeton University, Princeton, NJ 08544, USA. [2]Department of Biology, University of Utah, Salt Lake City, UT 84112, USA. [3]Center for Ecosystem Science and Society, Northern Arizona University, Flagstaff, AZ 86011, USA. [4]School of Earth Sciences and Environmental Sustainability, Northern Arizona University, Flagstaff, AZ 86011, USA. [5]DendroLab and Graduate Program of Ecology, Evolution, and Conservation Biology, University of Nevada–Reno, Reno, NV 89557, USA. [6]Instituto Pirenaico de Ecología, Consejo Superior de Investigaciones Científicas, Avda. Montañana 1005, 50192 Zaragoza, Spain. [7]Department of Biology, University of New Mexico, Albuquerque, NM 87131, USA. [8]School of Life Sciences, Arizona State University, Tempe, AZ 85287-4501, USA. [9]Rocky Mountain Research Station, U.S. Forest Service, Ogden, UT 84401, USA. [10]National Oceanic and Atmospheric Administration (NOAA) Geophysical Fluid Dynamics Laboratory, Princeton, NJ 08540, USA. [11]Lamont-Doherty Earth Observatory of Columbia University, 61 Route 9W, Palisades, NY 10964, USA.
***Corresponding author. E-mail: anderegg@princeton.edu**

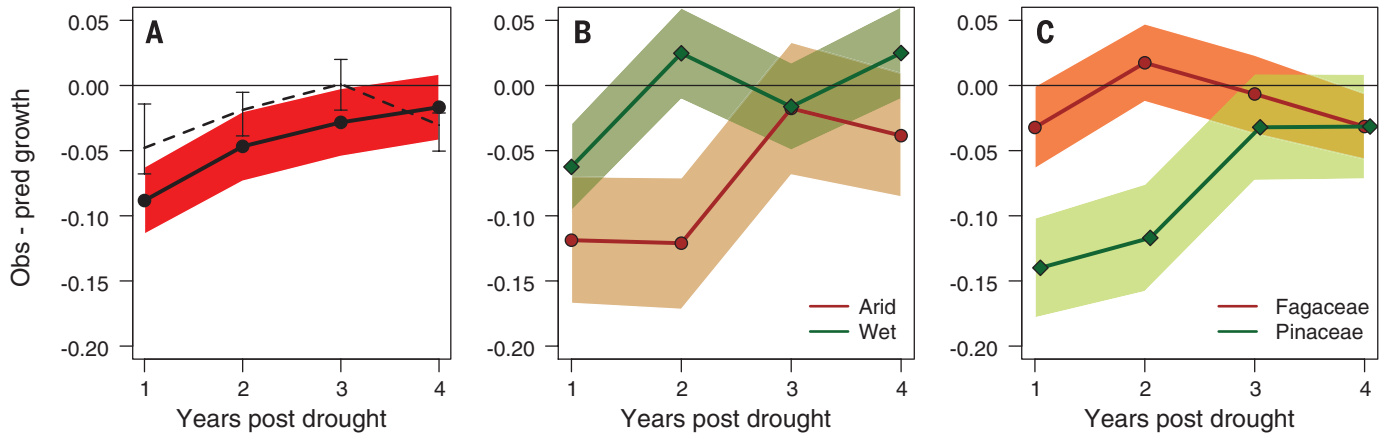

Fig. 1. Legacy effects are substantial and persist for 3 to 4 years. Legacy effects are quantified as the difference between observed and predicted growth (unitless index) after a 2-SD dry anomaly in the climatic water deficit (drought). (**A**) Legacy effects observed across all 1338 tree-ring chronologies (dashed line) and across 695 tree-ring chronologies at sites that correlate significantly with the climatic water deficit (solid line and red shaded region). (**B**) Legacy effects at sites from among the above 695 that were categorized as arid (mean annual precipitation <500 mm) or wet (mean annual precipitation >1000 mm). (**C**) Legacy effects at sites from among the above 695 that support either of the two main families represented, Pinaceae and Fagaceae. Shaded regions in all panels represent the 95% confidence interval around the mean from bootstrapping (n = 5000 resamplings).

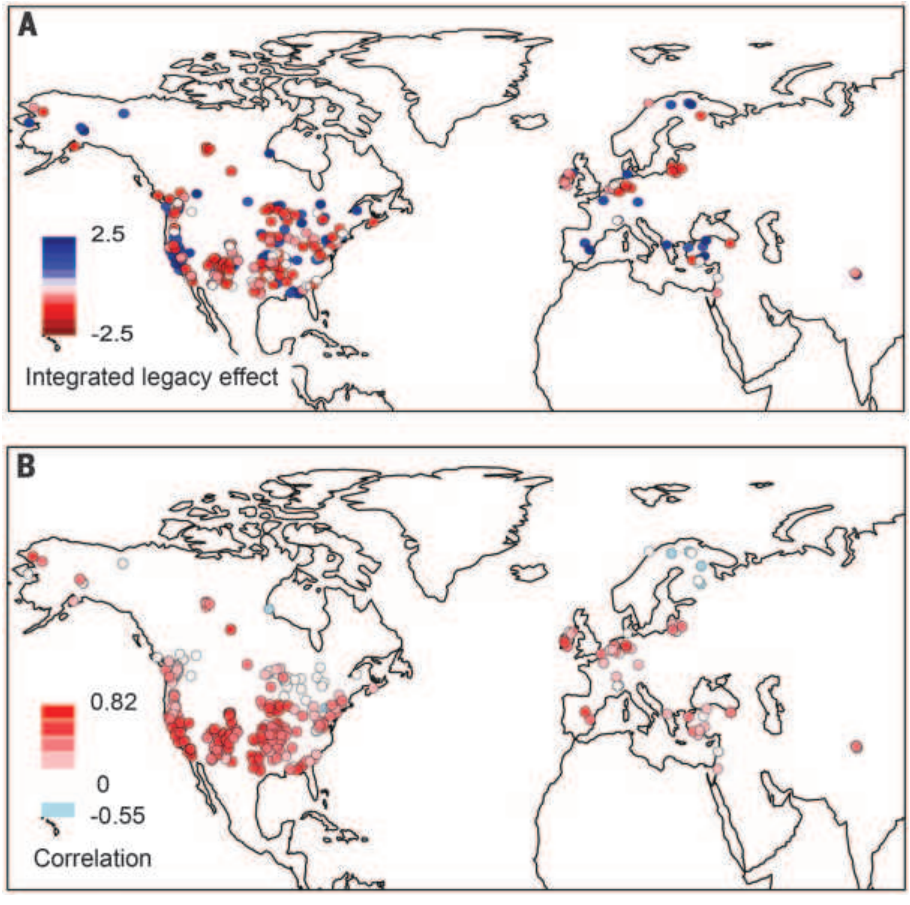

Fig. 2. Legacy effects are most prevalent in the southwestern and midwestern United States and parts of northern Europe. Legacy effects are quantified as the difference between observed and predicted growth (unitless index) after a 2-SD dry anomaly in the climatic water deficit across 1338 sites. (**A**) Site-level legacy effect summed over the first 4 years after drought. (**B**) Average correlation between tree growth (ring-width index) and the climatic water deficit (soil moisture from 0 to 100 cm minus potential evapotranspiration).

large uncertainty in projections of terrestrial carbon cycle feedbacks (*16*).

The treatment of drought in carbon cycle models is limited by a lack of representation of ecosystem response dynamics, such as recovery after drought and the potential for legacies or hysteresis—dynamics that are probably critical to predicting the future behavior of the system (*17*, *18*). For example, lags in precipitation, particularly in semi-arid regions, have been shown to be important in the interannual variability of the land carbon sink (*19*). In current climate–carbon cycle models, plant physiological recovery from drought is often assumed to be complete and relatively fast. This is at odds with current understanding of physiological mechanisms in many ecosystems, particularly those with long-lived individual plants. Legacy effects and hysteresis after drought have been documented in stomatal conductance (*20*, *21*), wood anatomy and density (*22*), xylem vulnerability to drought (*23*), drought-induced tree mortality (*24*, *25*), and aboveground primary productivity (*21*, *26*). As a biological legacy, the dynamics of recovery from severe drought can have a major influence on an ecosystem's vulnerability to subsequent drought events, particularly if the drought return interval is shorter than the recovery time (*17*). The rate of recovery—for example, in the reestablishment of hydraulic function after drought—is largely unknown for the vast majority of tree species (*24*).

We tested the occurrence, prevalence, and magnitude of legacy effects after severe drought using tree growth (i.e., tree-ring width) stand-level chronologies from 1338 sites across the globe, primarily in Northern Hemisphere extratropical forest ecosystems, which collectively represented 49,339 site-years. We selected tree-ring master chronologies (typically of 10 to 20 trees per site) from the International Tree Ring Data

Bank (*27*) that contained at least 25 years of data between 1948 and 2008. We defined drought legacy as a departure of observed tree growth (ring-width index) from expected growth (based on the relationship between growth and climate) in the period after a drought episode. Wood growth is ideal to test for drought legacy effects, because it provides a long temporal record and has major implications for the carbon cycle. Wood is a carbon pool with slow turnover that stores immense amounts of ecosystem carbon (*6*), and wood growth is tightly correlated with net primary productivity (*28*). We further examined the extent to which observed legacy effects are simulated in current climate-vegetation models from the Coupled Model Intercomparison Project, Phase 5 (CMIP5). We asked: (i) Are legacy effects after extreme drought pervasive in tree growth? (ii) Are legacy effects more prominent in wet or dry environments? (iii) Do legacy effects vary among species with different hydraulic safety margins (*29*) [a measure of how closely a tree approaches catastrophic damage to its xylem during drought (*25*)]? (iv) Are the legacy effects simulated in CMIP5 climate-vegetation models similar to those observed in tree rings?

We quantified legacy effects in tree-ring width chronologies using two methods: (i) the departure of observed from predicted growth recovery after drought based on correlations with climate and (ii) partial autocorrelation coefficients. We focused primarily on sites where ring-width anomalies exhibited significant correlations ($r > 0.3$; mean correlation $r = 0.51$) with drought [climatic water deficit (*30*)], because our aim was to quantify the duration of growth suppression or enhancement after drought episodes. We found significant legacies in radial growth after severe drought (>2 SD from the mean climatic water deficit) that lasted 2 to 4 years (Fig. 1A and fig S1). These effects were substantial in magnitude: a ~9% decrease in observed versus predicted growth in year 1 and 5% in year 2 after drought (Fig. 1A). Legacy effects were observed regardless of the minimum climate correlation cutoff (fig. S1) or the drought variable used (figs. S2 and S3). Legacy effects were also observed in the partial autocorrelation analysis (fig S4). There did not appear to be a strong link between the magnitude of the legacy effect and the peak intensity of the observed drought [coefficient of determination (R^2) = 0.01, $P = 0.08$] (fig S5).

Legacy effects were most pronounced in arid ecosystems (Fig. 1B). Mean annual precipitation was the only significant predictor of the magnitude of drought legacy effects in tree growth; it explained a low proportion of the variance ($R^2 = 0.05$, $P = 0.0003$) (fig. S6). Correlations with mean annual temperature and potential evapotranspiration were both insignificant ($P > 0.05$). Strong legacy effects also tended to occur in semi-arid regions in the Northern Hemisphere (Fig. 2A) and where correlations between growth and drought were higher (Fig. 2B). Tree-ring chronologies in the southwestern and midwestern United States and in parts of northern Europe exhibited particularly strong legacy effects (Fig. 2A). Positive legacy effects, where observed growth was higher than predicted after drought, were most frequent in California and the Mediterranean region (Fig. 2A).

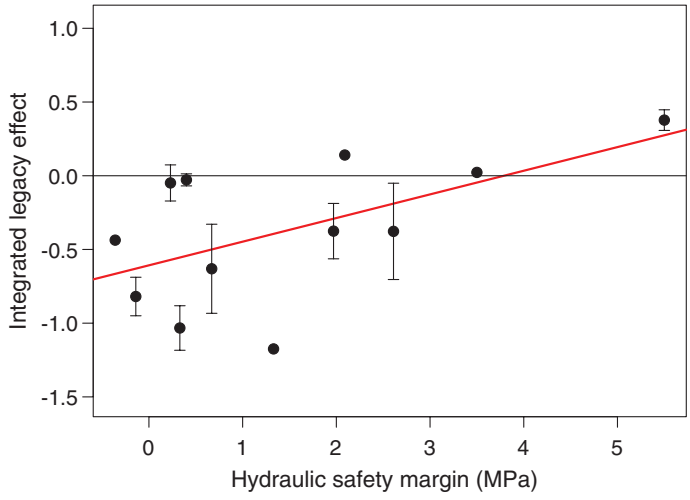

Fig. 3. Higher legacy effects are associated with species with low hydraulic safety margins. Integrated legacy effects are quantified as the difference between observed and predicted growth (unitless index) after a 2-SD dry anomaly, summed over 1 to 4 years, averaged across all droughts within a chronology, and averaged across all chronologies for a given species. Each point represents a species where legacies and hydraulic traits were both available. Error bars represent 1 SE. The regression line is in red.

Gymnosperms exhibited legacy effects that were slightly but significantly larger (in terms of magnitude and duration) than those exhibited by angiosperms ($t = 2.25$, $P = 0.02$) (fig. S7). Among families, Pinaceae (pines) and Fagaceae (mostly oaks) were best represented in the data set, accounting for >90% of chronologies analyzed. Pines exhibited substantially larger legacies than did oaks (Fig. 1C). Although pines were typically found at drier locales than oaks (average mean annual precipitation for pines = 660 mm/year; average for oaks = 760 mm/year), a model allowing for interactions between precipitation and family was highly significant ($t = 2.55$, $P = 0.01$), indicating that such interactions were important. Both wet and dry pine sites exhibited strong negative legacy effects, whereas wet oak sites exhibited slightly negative legacy effects, and dry oak sites had strong positive legacy effects (fig. S8). Pines also had stronger negative legacy effects than the other main gymnosperm family in the database, Cupressaceae (fig. S9). This result is consistent with Cupressaceae's generally higher drought tolerance relative to Pinaceae (*31*) and is supportive of a hydraulic damage mechanism underlying legacy effects.

Several physiological mechanisms may underlie the observed legacy effects of reduced growth after drought. Loss of leaf area and/or stored nonstructural carbohydrates during drought may impair growth in subsequent years (*25*). Pest and pathogen impacts may lag drought or accumulate in drought-stressed trees, thereby lowering growth rates (*25*). Finally, stress-induced shifts in xylem anatomy and associated vulnerability to hydraulic dysfunction, or remnants of drought-induced xylem cavitation, could impair water transport and, therefore, growth (*25*). Although data that could test the first two hypotheses are not available, testing the third hypothesis is possible with an existing global hydraulic trait database (*29*). We found that species with lower hydraulic safety margins, defined as the water potential (Ψ) at which 50% conductivity is lost minus the minimum measured water potential ($\Psi_{50} - \Psi_{min}$), exhibited larger legacy effects ($R^2 = 0.33$, $F = 4.95$, $P = 0.04$) (Fig. 3 and table S1). This indicates that the species most at risk of hydraulic damage are also those that have the slowest growth recovery after drought. Previous studies at individual sites have observed drought-induced shifts in plant hydraulics, especially in the first 3 to 4 years after drought in oaks and poplars (*22*, *25*), and our results generalize these findings across many taxonomic groups and a broad geographic range.

The CMIP5 models captured few to no detectable legacy effects from severe drought in grid cells where the tree-ring chronologies were located (Fig. 4). In many cases, interannual variability of wood carbon growth was low and more weakly correlated with water limitation or drought (mean correlations of $R = 0.01$ to 0.09) than were the observed tree-ring widths at the same locations (mean correlation $R = 0.25$). Only the Geophysical Fluid Dynamics Laboratory Earth System Model 2G (GFDL ESM2G) exhibited significant legacy effects of 1 to 2 years (Fig. 4A), and these were of lower magnitude than the observed legacies (Fig. 1A). GFDL ESM2G and CanESM (Canadian Centre for Climate Modeling and Analysis Second Generation Earth System Model) both use a dynamic carbon allocation scheme, but they use different approaches to allocate carbon, particularly under drought conditions. GFDL ESM2G's scheme (*32*) is based on the pipe model for the relationship between sapwood area and leaf area (*33*) and allows drought-induced loss of living carbon, including from the sapwood pool, which may allow it to capture legacy effects. Most CMIP5-class models use constant fractional allocation among the vegetation pools and do not simulate plant hydraulic damage during drought, and these appears to

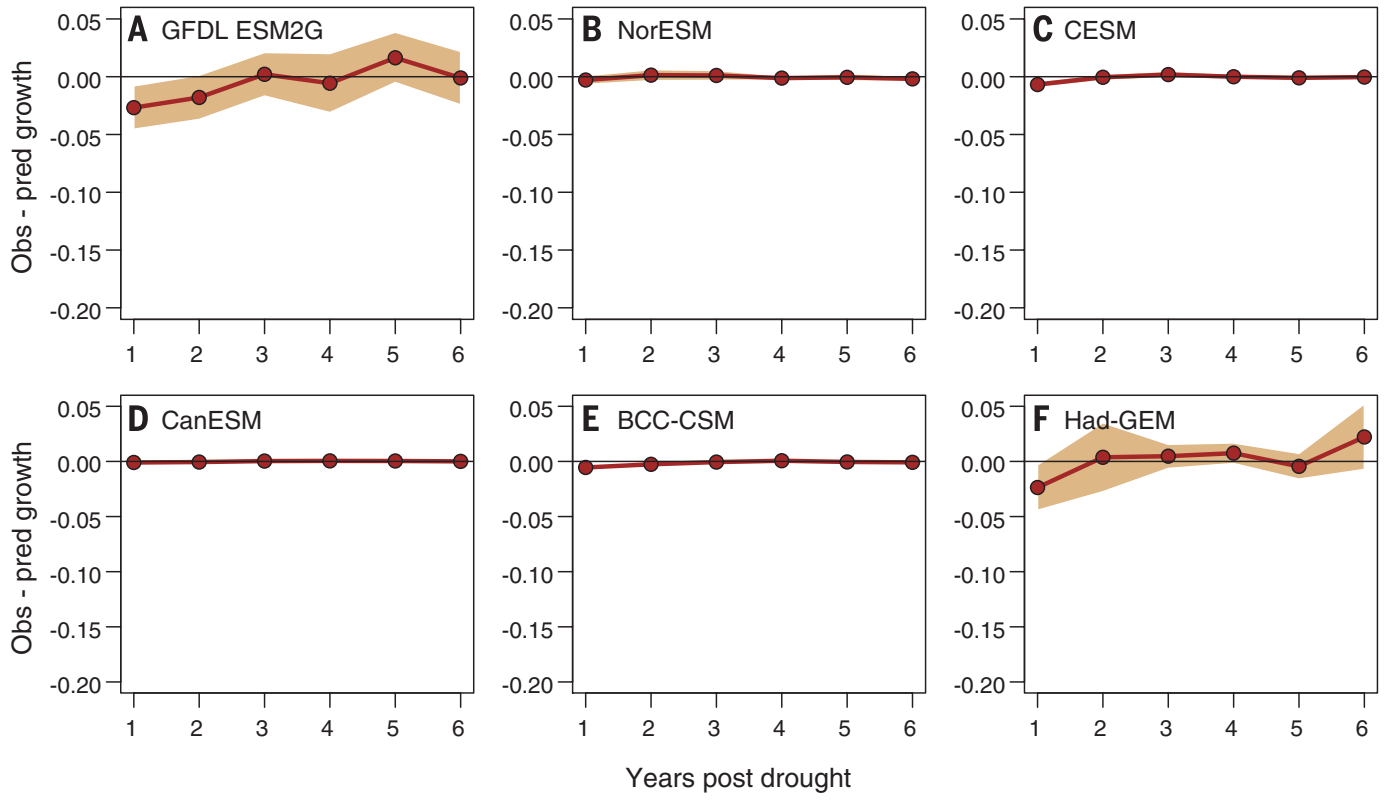

Fig. 4. Legacy effects after drought are not captured in predictions of woody biomass by Earth system models. (**A** to **F**) Legacy effects after a 2-SD dry anomaly in grid cells that correlated significantly with drought and overlapped with the real-world locations of the 1338 tree-ring chronologies. Shaded regions represent the 95% confidence interval around the mean from bootstrapping (n = 5000 resamplings). Models used included GFDL ESM2G (A), the Norweigan Earth System Model (NorESM) (B), the Community Earth System Model (CESM) (C), CanESM (D), the Beijing Climate Center Climate System Model (BCC-CSM) (E), and the Hadley Centre Global Environmental Model (Had-GEM) (F).

be crucial limitations to capturing legacy effects of drought.

The response of terrestrial ecosystems to drought has been reported to be one of the largest uncertainties in the carbon cycle (*34*) and is not well represented in current climate-vegetation models, as evidenced by our model-data comparison. Current models lack representation of some basic physiological and structural properties of plants, such as the vulnerability of xylem transport to hydraulic water stress, that lead to growth suppression, legacy effects, and drought-induced mortality (*35*). Mortality is generally not measured or reported at these sites, so our analysis does not examine drought-induced mortality; however, mortality or canopy dieback of surrounding trees could generate some of the positive legacy effects in surviving trees that we observed via increased resource availability. Although the impacts of climate extremes on plant mortality and species turnover will also influence carbon cycling (*14*), we detected a strong, pervasive, and previously undocumented legacy effect of drought on tree growth, especially in dry regions. That is, even when climatic conditions return to normal, surviving trees do not recover their expected growth rates for an average of 2 to 4 years. Given that (i) woody plant growth is a central component of carbon storage and often correlated with productivity and (ii) semi-arid regions play a prominent role in the variability of the global carbon cycle (*19*), these legacy effects have potential ramifications for the interannual variability of ecosystem-level carbon cycling and for long-term carbon storage. For example, a simple conservative estimate based on forests in the southwestern United States revealed that legacy effects could lead to 3% lower carbon storage in semi-arid ecosystems over a century, equivalent to 1.6 metric gigatons of carbon when considering all semi-arid ecosystems across the globe (*30*).

Drought could lead to changes in carbon allocation by trees, with less being allocated to bole growth and more to roots or leaves (*36*, *37*), which would mean that growth declines might not immediately reflect decreases in carbon uptake by forests. The fast turnover of leaves and roots, however, would still result in overall decreases in ecosystem-level carbon storage relative to ecosystems without legacy effects (*37*). The prominence of legacy effects in tropical forests, where tree-ring analyses are challenging, is a major remaining question. There are some indications of legacy effects in the Amazon rainforest in satellite (*38*) and time-series inventory plot analyses (*39*) after the severe 2005 and 2010 droughts. The lack of legacy effects in CMIP5 models indicates that drought impacts and their effect on carbon cycling are not accurately captured. These findings reveal the critical roles of contingency and hysteresis in ecosystem response after climate extremes.

REFERENCES AND NOTES

1. Intergovernmental Panel on Climate Change, in *Climate Change 2013: The Physical Science Basis. Contribution of Working Group I to the Fifth Assessment Report of the Intergovernmental Panel on Climate Change*, T. F. Stocker *et al.*, Eds. (Cambridge Univ. Press, Cambridge, 2013), pp. 3–29.
2. D. R. Easterling *et al.*, *Science* 289, 2068–2074 (2000).
3. D. Medvigy, S. C. Wofsy, J. W. Munger, P. R. Moorcroft, *Proc. Natl. Acad. Sci. U.S.A.* **107**, 8275–8280 (2010).
4. M. D. Smith, *J. Ecol.* **99**, 651–655 (2011).
5. P. Ciais *et al.*, *Nature* **437**, 529–533 (2005).
6. G. B. Bonan, *Science* **320**, 1444–1449 (2008).
7. P. M. Cox *et al.*, *Theor. Appl. Climatol.* **78**, 137–156 (2004).
8. M. Hirota, M. Holmgren, E. H. Van Nes, M. Scheffer, *Science* **334**, 232–235 (2011).
9. A. C. Staver, S. Archibald, S. A. Levin, *Science* **334**, 230–232 (2011).
10. Y. Malhi *et al.*, *Proc. Natl. Acad. Sci. U.S.A.* **106**, 20610–20615 (2009).
11. C. Huntingford *et al.*, *Nat. Geosci.* **6**, 268–273 (2013).
12. G. E. Ponce Campos *et al.*, *Nature* **494**, 349–352 (2013).
13. C. D. Allen *et al.*, *For. Ecol. Manage.* **259**, 660–684 (2010).
14. W. A. Kurz *et al.*, *Nature* **452**, 987–990 (2008).
15. O. L. Phillips *et al.*, *Science* **323**, 1344–1347 (2009).
16. S. Sitch *et al.*, *Glob. Change Biol.* **14**, 2015–2039 (2008).
17. V. P. Gutschick, H. BassiriRad, *New Phytol.* **160**, 21–42 (2003).

18. J. A. Arnone III *et al.*, *Nature* **455**, 383–386 (2008).
19. A. Ahlström *et al.*, *Science* **348**, 895–899 (2015).
20. L. Virlouvet, M. Fromm, *New Phytol.* **205**, 596–607 (2015).
21. K. Ogle *et al.*, *Ecol. Lett.* **18**, 221–235 (2015).
22. L. Corcuera, J. J. Camarero, E. Gil-Pelegrín, *Trees (Berlin)* **18**, 83–92 (2004).
23. U. G. Hacke, V. Stiller, J. S. Sperry, J. Pittermann, K. A. McCulloh, *Plant Physiol.* **125**, 779–786 (2001).
24. W. R. L. Anderegg, J. A. Berry, C. B. Field, *Trends Plant Sci.* **17**, 693–700 (2012).
25. W. R. L. Anderegg *et al.*, *Glob. Change Biol.* **19**, 1188–1196 (2013).
26. Y. Zhang *et al.*, *J. Geophys. Res. Biogeosci.* **118**, 148–157.
27. H. D. Grissino-Mayer, H. C. Fritts, *Holocene* **7**, 235–238 (1997).
28. D. A. Clark *et al.*, *Ecol. Appl.* **11**, 356–370 (2001).
29. B. Choat *et al.*, *Nature* **491**, 752–755 (2012).
30. Materials and methods are available as supplementary materials on *Science* Online.
31. T. J. Brodribb, S. A. McAdam, G. J. Jordan, S. C. Martins, *Proc. Natl. Acad. Sci. U.S.A.* **111**, 14489–14493 (2014).
32. E. Shevliakova *et al.*, *Glob. Biogeochem. Cycles* **23**, GB2022 (2009).
33. K. Shinozaki, K. Yoda, K. Hozumi, T. Kira, *Jap. J. Ecol.* **14**, 97–105 (1964).
34. M. Reichstein *et al.*, *Nature* **500**, 287–295 (2013).
35. T. L. Powell *et al.*, *New Phytol.* **200**, 350–365 (2013).
36. R. Dybzinski, C. Farrior, A. Wolf, P. B. Reich, S. W. Pacala, *Am. Nat.* **177**, 153–166 (2011).
37. C. E. Farrior, R. Dybzinski, S. A. Levin, S. W. Pacala, *Am. Nat.* **181**, 314–330 (2013).
38. S. Saatchi *et al.*, *Proc. Natl. Acad. Sci. U.S.A.* **110**, 565–570 (2013).
39. R. J. W. Brienen *et al.*, *Nature* **519**, 344–348 (2015).

ACKNOWLEDGMENTS

Funding for this research was provided by NSF (grant no. DEB EF-1340270). W.R.L.A. was supported in part by a NOAA Climate and Global Change Postdoctoral Fellowship, administered by the University Corporation for Atmospheric Research. The views and conclusions contained in this document are those of the authors and should not be interpreted as representing the opinions or policies of the funding agencies. All tree-ring data are available at www.ncdc.noaa.gov/data-access/paleoclimatology-data/datasets/tree-ring. We thank all data contributers at the International Tree-Ring Data Bank. All CMIP5 data are available at http://cmip-pcmdi.llnl.gov/cmip5/data_portal.html. We acknowledge the World Climate Research Programme's Working Group on Coupled Modelling, which is responsible for CMIP, and we thank the climate modeling groups (listed in the supplementary materials) for producing and making available their model output. For CMIP, the U.S. Department of Energy's Program for Climate Model Diagnosis and Intercomparison provides coordinating support and led the development of software infrastructure in partnership with the Global Organization for Earth System Science Portals.

SUPPLEMENTARY MATERIALS

www.sciencemag.org/content/349/6247/528/suppl/DC1
Materials and Methods
Figs. S1 to S10
Table S1
References (*40*–*67*)

24 March 2015; accepted 3 July 2015
10.1126/science.aab1833

GLOBAL WARMING

Recent hiatus caused by decadal shift in Indo-Pacific heating

Veronica Nieves,[1,2]* Josh K. Willis,[2] William C. Patzert[2]

Recent modeling studies have proposed different scenarios to explain the slowdown in surface temperature warming in the most recent decade. Some of these studies seem to support the idea of internal variability and/or rearrangement of heat between the surface and the ocean interior. Others suggest that radiative forcing might also play a role. Our examination of observational data over the past two decades shows some significant differences when compared to model results from reanalyses and provides the most definitive explanation of how the heat was redistributed. We find that cooling in the top 100-meter layer of the Pacific Ocean was mainly compensated for by warming in the 100- to 300-meter layer of the Indian and Pacific Oceans in the past decade since 2003.

It has been widely established that Earth is absorbing more energy from the Sun than it is radiating back to space (*1*). Furthermore, this has been attributed to anthropogenic greenhouse gases (*2*). Although global surface temperatures have risen over the previous century, several recent papers have documented a slowdown in the rate of surface warming since 2003 (*3*). Most efforts to explain this surface temperature "hiatus" have suggested that it is compensated for by more rapid warming at deeper levels in the ocean in either the Pacific (*3*–*6*) or Atlantic (*7*) Oceans or a combination of the Southern, Atlantic, and Indian Oceans (*8*). More recently, a study pointed out that heat is piling up in the depths of the Indian Ocean (*9*). These studies suggest that the net rate of ocean heat uptake has continued unabated and that the surface hiatus signature is due to an internal rearrangement of heat within the ocean between the surface and some deeper layer of the ocean. This has implications for the net radiative forcing of Earth, because the ocean is the dominant reservoir for storage of excess heat on time scales longer than 1 year, and ocean heat content increases should approximately equal the net radiative imbalance at the top of the atmosphere (*1*). An alternative hypothesis is that approximately half of the surface hiatus is caused by changes in solar and stratospheric aerosol forcing (*10*). In other words, half of the hiatus signal is caused by reduced uptake of heat by the ocean, as opposed to an internal redistribution of heat.

A vigorous debate has grown over this subject, but it has not yet been informed by comprehensive analysis of the available data over the past two decades. We considered both ocean observational data and widely used reanalysis products (that is, numerical simulations constrained by ocean and sometimes atmospheric observations) that span both of the previous decades. A recent study based on Argo data pointed out that net warming continued unabated, despite the exchange of heat between the top 100-m layer and the thermocline on interannual time scales. (*11*). It did not, however, consider the redistribution of heat between these layers on decadal time scales, its geographic distribution, or how it might differ before and after the start of the hiatus in 2003.

Our analysis indicates that during the most recent decade, cooling in the top 100-m layer of the Pacific Ocean is compensated for by warming in the 100- to 300-m layer of the Western Pacific and Indian Oceans, with the largest contribution in the tropics. The Southern Ocean plays a secondary role in warming the 100- to 300-m layer, but this warming has been steady over both of the past decades. The Atlantic Ocean does show a switch from warming to cooling, but its area is so small that it cannot meaningfully contribute to the hiatus signal in surface temperature over the past decade (figs. S1 and S2). Finally, we find little evidence for any change in warming rates below 700 m between the past decade and the previous one—or that the net ocean heat uptake has slowed in the most recent decade.

Observed temperature trends in the oceans were estimated using objectively analyzed subsurface temperature fields from the World Ocean Atlas (WOA) (*12*), Ishii (*13*), and the Scripps Institution of Oceanography (*14*). Simulated temperature trends, based on reanalyses that assimilate ocean data, have also been examined. We compared observed trends with simulated trends from the Simple Ocean Data Assimilation (SODA), National Centers for Environmental Prediction Global Ocean Data Assimilation System (NCEP GODAS), and the latest European Centre for Medium-Range Weather Forecasts ocean reanalysis system 4 (ECMWF ORAS4) (*15*–*17*) (SODA, NCEP, and ECMWF). We considered global and basin-averaged temperature trends for the periods from 1993 to 2002 (the 90s) and from 2003 onward (the 00s). The periods for the past decade are slightly different depending on the product (table S1). Nevertheless, our results are insensitive to the choice of somewhat different time periods. These periods were chosen based on the assumption that the hiatus began in approximately 2003, when there was a small local maximum in the 5-year moving average of global surface

[1]Joint Institute for Regional Earth System Science and Engineering, University of California, Los Angeles, CA, USA. [2]Jet Propulsion Laboratory, California Institute of Technology, Pasadena, CA, USA.
***Corresponding author. E-mail: veronica.nieves@jpl.nasa.gov**

temperature (*6*). Analysis of ocean heat content estimates (as in the supplementary materials) has also been included.

Comparison of the globally averaged temperature change as a function of depth across the water column for each of the past two decades shows substantially less warming in the second decade in the top 100 m (Fig. 1, A and B, where the gray line corresponds to the average of the two observational estimates). Here the hiatus signal is manifested as slight cooling, or a near-zero trend, at the surface. The difference between the warming rates over the two decades (Fig. 1C) shows substantial temperature slowdown in the past decade near the surface for all estimates. The uncertainty shown in Fig. 1 represents one standard error and is an estimate of the uncertainty due to incomplete sampling of the global average (supplementary materials). Instrument biases during this period have been corrected before objective analysis for both the WOA and Ishii products. Remaining uncertainty due to these corrections has been shown to be small (*18*). The global average surface temperature has been rising since 2003 by +0.001°C/year. Although not zero, it is slower than the century time-scale warming of +0.0064 ± 0.0015°C/year since 1880 (*2*). The surface warming of the 00s was also substantially slower than that of the 90s, which warmed at a rate of +0.008°C/year (table S1). The average trend difference between the 90s and the 00s indicates decreased warming of –0.007°C/year near the surface (top 10 m) and –0.0005 ± 0.004°C/year in the average over the 10- to 300-m layer (table S1). The fact that the average warming rate over the top 300-m layer did not change between the 90s and the 00s indicates that even on decadal time scales, most of the hiatus-related cooling at the surface is compensated for by warming in the upper 300 m of the ocean.

Because it covers nearly one-third of Earth's surface, it is not surprising to find that surface cooling during the past decade appears to be mainly driven by the Pacific (figs. S1 and S2). A closer look at different basins (figs. S8 to S12) shows that between 2003 and 2012, the most rapid warming in the top 300 m is around the depth of the thermocline (100 to 200 m) in the Indo-Pacific region and, to a lesser extent, the Southern Ocean. This is also clear in the global maps (fig. S6) and the zonal average temperature trends in the upper 300 m (Fig. 2). In addition, this is where the most active redistribution of heat occurs on shorter time scales due to El Nino–Southern Oscillation (*11*, *14*). It is clear from Figs. 1 and 2 as well as figs. S8 to S12 that there is heat compensation between the top 100-m layer and the 100- to 300-m layer in the Pacific, Indian, and to some extent the Southern Ocean.

The clearest depiction of the past decade's hiatus can be seen in a band near the equator (Fig. 3). In the 90s, the Pacific warmed in the thermocline, while the Indian Ocean cooled in the far west. During the 00s, however, the thermocline in the Pacific sank in the west and shoaled in the east, as described by England *et al.* (*6*), and the tropical Indian Ocean warmed significantly in the thermocline. It is well known that the Indonesian Throughflow and leakage through the Tasman Sea provide pathways for interannual changes in the Pacific to affect the eastern tropical and subtropical Indian Ocean (*19*, *20*). Furthermore, oceanic Rossby waves can carry changes in thermocline depth (and hence heat content) from the Pacific to the Indian Ocean on multidecadal time scales (*21*). Our analyses suggest that the long-term cooling trend in the tropical and subtropical South Indian Ocean described by Schwarzkopf and Böning (*21*) reversed during the period of the hiatus, carrying some of the subsurface heat into the Indian Ocean (Figs. 2 and 3 and fig. S6).

It is clear that temperature trends in the North Atlantic Subpolar Gyre switched from warming to cooling in the most recent decade (fig. S6). However, the area of the Atlantic north of 40°N accounts for only 4% of the global ocean. In fact, if the subpolar gyre is masked out, the time series of global surface temperature and the recent hiatus remain virtually unchanged (fig. S2). There is also no clear indication of anomalous heating in the Atlantic Ocean during the 00s at other depths, excluding a meager amount in Ishii's analysis below 1000 m (fig. S12). This suggests that previous work using Ishii's analysis (*7*) is an incomplete description of the hiatus and its cause.

Analysis of deep hydrographic data in comparison with satellite measurements of sea-level change indicates a contribution of 0.76 mm/year of sea-level rise due to thermal expansion within the layer from 700 to 2000 m (*22*). Assuming a thermal expansion coefficient of 1.3×10^{-4} °C^{-1} for that layer, this implies an average warming of 0.0045°C/year between the mid-90s and mid-00s and between 700 and 2000 m. Data below 700 m in the pre-Argo era (before 2004) were extremely scarce (*14*), which can cause objectively mapped estimates to be biased low (*23*). WOA's pentadal estimate provides an alternative reference value, which should suffer somewhat less bias, because 5 years of data are mapped simultaneously instead of only 1 year. The WOA pentadal estimate shows a heat content increase of 2.4×10^{21} J/year or about 0.0015°C/year (1993–2002 period, 700- to

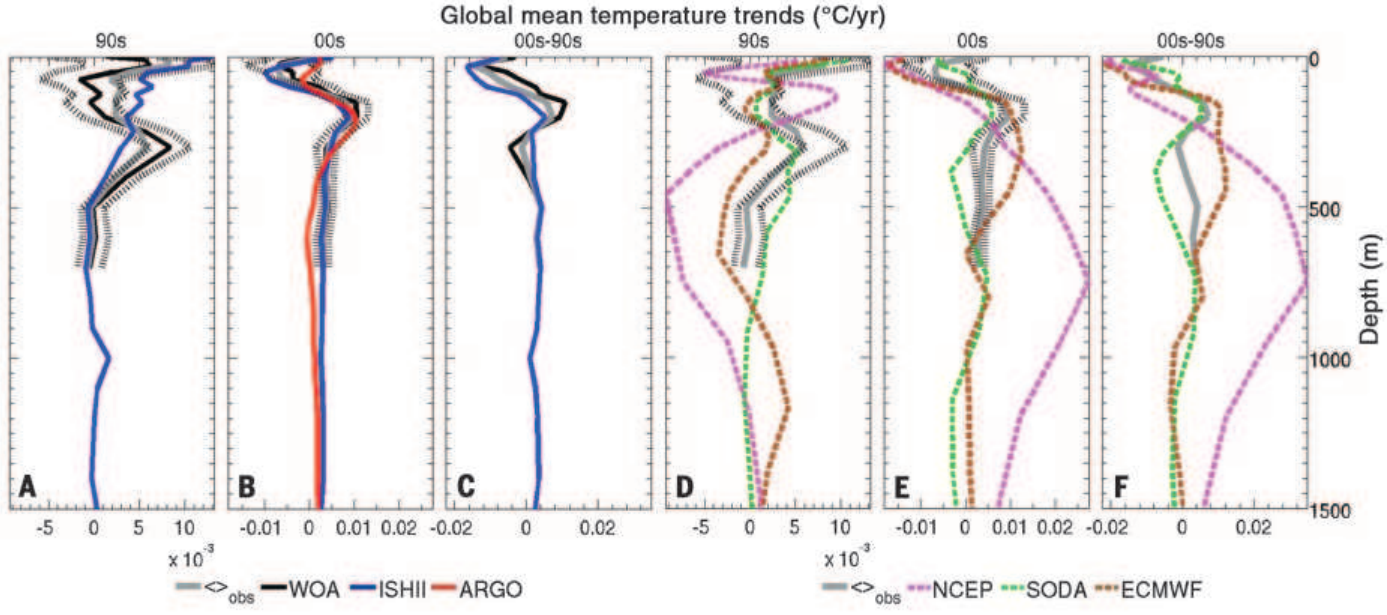

Fig. 1. Global mean temperature trends as a function of depth using observational (**A** to **C**) and model-based (**D** to **F**) products for the 90s [(A) and (D)], 00s [(B) and (E)], and 00s–90s [(C) and (F)]. The gray line corresponds to the average of WOA (black) and Ishii (blue) estimates.

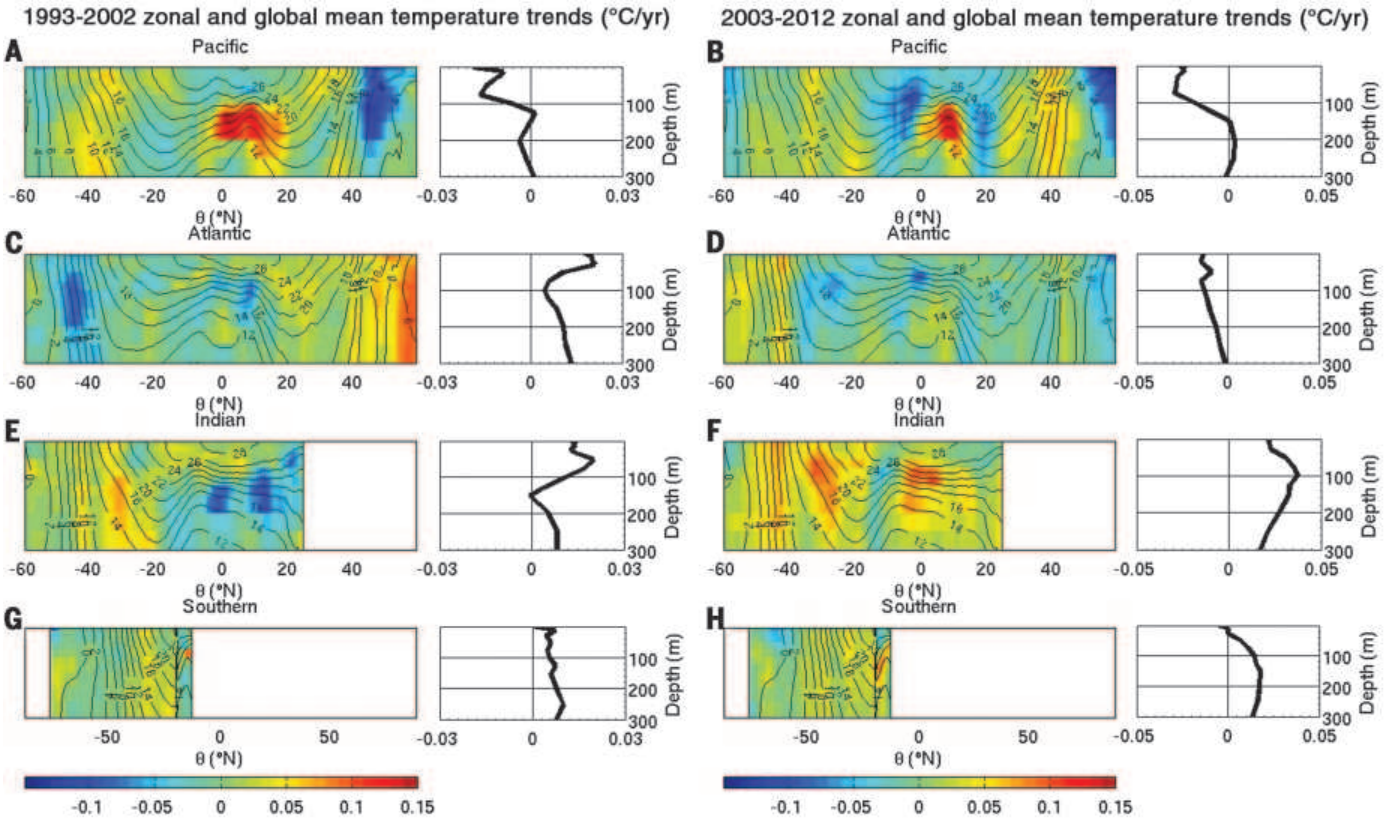

Fig. 2. WOA zonal and global mean temperature trends in the upper 300 m for 1993–2002 (**A**, **C**, **E**, **G**) and 2003–2012 (**B**, **D**, **F**, **H**) and for the Pacific [(A) and (B)], Atlantic [(C) and (D)], Indian [(E) and (F)], and Southern [(G) and (H)] Oceans. Isotherms correspond to the WOA 1955–2013 climatology. For clarity, the Southern Ocean sector is included in the zonal average with each basin (fig. S18). θ (°N), latitude degrees.

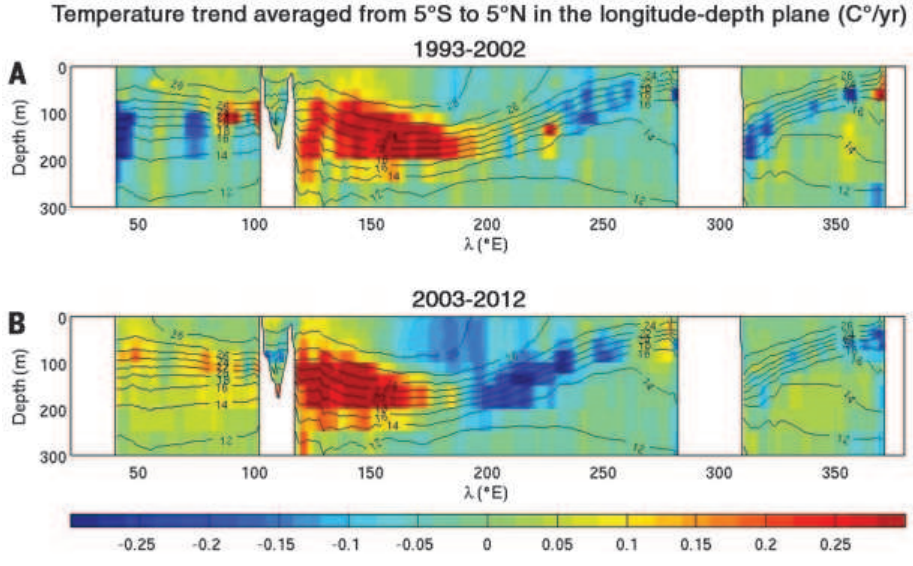

Fig. 3. WOA temperature trends along the equatorial band from 5°S to 5°N in the longitude-depth plane and upper 300 m for 1993–2002 (**A**) and 2003-2012 (**B**). Isotherms correspond to the WOA 1955–2013 climatology. λ (°E), longitude degrees.

2000-m layer). The latter is consistent with the 0.0013°C/year rate of warming for the 700- to 1500-m layer, as measured by the Argo array in the 00s (table S1). Together these findings suggest no significant increase in the rate of warming below 700 m since 2003. This is consistent with Levitus's results (*12*) but contradicts Ishii's estimate, which shows increased heating on the order of +0.0029°C/year between the 90s and the 00s for the same layer (table S1).

Reanalyses also do not seem to correctly reproduce the ocean warming rates, and they lie well outside the observation uncertainty at different depths and times. Both the hiatus and the net amount of heat absorbed by the ocean below 700 m are overestimated (table S1). Reanalyses are also inconsistent with ocean observations, in terms of the vertical and regional distribution of heating. This is true for both global and basin-wide averages (bottom panel of Fig. 1 and figs. S8 to S12). We found that biases are model-dependent, with NCEP showing the largest deviations, followed by ECMWF (particularly in the 00s within the 300- to 700-m layer) and SODA. The NCEP rates of ocean warming clearly show large deviations from the observations at many depths during both decades. There is no observational evidence for such large amounts of warming below the thermocline in the 00s, peaking at 750 m. Nor is there evidence to support such rapid cooling below 2000 m during both decades (fig. S8). Such large signals seem likely to be unphysical and related to some type of uncorrected model drift. The ECMWF model is also problematic. During the 00s, it strongly overestimates the hiatus, and it suggests strong warming between 300 and 700 m, which is much larger than that seen in any observational analysis. This is surprising because

Argo provides excellent coverage of this ocean volume during the 00s, and it shows less than half the amount of warming over these depths (Fig. 1). In contrast, SODA compares well with observational results from WOA and Argo over the top 1000 m. This is expected, given SODA's ocean data assimilation scheme, which nudges the model toward the data without necessarily requiring energy to be conserved in the model domain. During the 00s, however, SODA does show significant cooling between 1000 and 2000 m, which seems contradictory to all observational estimates.

In terms of heat content integrated from the surface down, all reanalyses also show large deviations from observations (fig. S7). Similar results have been found at regional scale (figs. S13 to S17). The observational rate of heat content increase over the 0- to 1500-m depth range did not change significantly between the 90s (2.0×10^{21} J/year) and the 00s (3.4×10^{21} J/year or 2.53×10^{21} J/year, according to the observational average or Argo, respectively) (table S2). Thus, observational heat content estimates do not reveal any obvious hiatus. This suggests that since the early 90s, there has been a steady rate of net ocean heat uptake, and the amount of radiative imbalance at the top of the atmosphere remained practically unchanged between the 90s and the 00s. This contradicts one recent study (*8*) suggesting that the net ocean heat uptake was reduced during the 00s on the basis of changes in surface flux estimates.

Comparison of several of the most commonly used reanalyses with ocean observations raises concerns about their fidelity in simulating temperature changes or in quantitatively explaining the redistribution of heat associated with the recent surface temperature hiatus. Observational estimates provide a more accurate means of assessing oceanic temperature changes and show clear decadal signals that are robust across different analyses (fig. S5) and clearly significant relative to observational errors. Our findings support the idea that the Indo-Pacific interaction in the upper-level water (0 to 300 m depth) regulated global surface temperature over the past two decades and can fully account for the recently observed hiatus. Furthermore, as previously shown for interannual fluctuations (*11*), the decade-long hiatus that began in 2003 is the result of a redistribution of heat within the ocean, rather than a change in the net warming rate.

REFERENCES AND NOTES

1. J. A. Church *et al*., *Geophys. Res. Lett.* **38**, L18601 (2011).
2. Intergovernmental Panel on Climate Change, in *Climate Change 2013: The Physical Science Basis*, T. F. Stocker *et al.*, Eds. (Cambridge Univ. Press, Cambridge, 2013).
3. Y. Kosaka, S. P. Xie, *Nature* **501**, 403–407 (2013).
4. K. E. Trenberth, J. T. Fasullo, *Earth's Future* **1**, 19–32 (2013).
5. M. A. Balmaseda, K. E. Trenberth, E. Källén, *Geophys. Res. Lett.* **40**, 1754–1759 (2013).
6. M. H. England *et al*., *Nat. Clim. Change* **4**, 222–227 (2014).
7. X. Chen, K. K. Tung, *Science* **345**, 897–903 (2014).
8. S. S. Drijfhout *et al*., *Geophys. Res. Lett.* **41**, 7868–7874 (2014).
9. S. K. Lee *et al*., *Nat. Geosci.* **8**, 445–449 (2015).
10. M. Huber, R. Knutti, *Nat. Geosci.* **7**, 651–656 (2014).
11. D. Roemmich *et al*., *Nat. Clim. Change* **5**, 240–245 (2015).
12. S. Levitus *et al*., *Geophys. Res. Lett.* **39**, L10603 (2012).
13. M. Ishii, A. Shouji, S. Sugimoto, T. Matsumoto, *Int. J. Climatol.* **25**, 865–879 (2005).
14. D. Roemmich, J. Gilson, *Geophys. Res. Lett.* **38**, L13606 (2011).
15. T. Nishida, T. Kitakado, H. Matsuura, Validation of the Global Ocean Data Assimilation System (GODAS) data in the NOAA National Centre for Environmental System (NCEP) by theory, comparative studies, applications and sea truth. *IOTC-2011-WPB09-11* (2011).
16. M. A. Balmaseda, K. Mogensen, A. T. Weaver, *Q. J. R. Meteorol. Soc.* **139**, 1132–1161 (2013).
17. J. A. Carton, B. Giese, *Mon. Weather Rev.* **136**, 2999–3017 (2008).
18. L. Cheng, J. Zhu, R. Cowley, T. Boyer, S. Wijffels, *J. Atmos. Ocean. Technol.* **31**, 1793–1825 (2014).
19. J. Sprintall, A. Révelard, *J. Geophys. Res.* **119**, 1161–1175 (2014).
20. E. van Sebille *et al*., *J. Geophys. Res.* **119**, 1365–1382 (2014).
21. F. U. Schwarzkopf, C. W. Böning, *Geophys. Res. Lett.* **38**, L12602 (2011).
22. S. G. Purkey, G. C. Johnson, D. P. Chambers, *J. Geophys. Res.* **119**, 7509–7522 (2014).
23. J. M. Lyman, G. C. Johnson, *J. Clim.* **21**, 5629–5641 (2008).

ACKNOWLEDGMENTS

The research described in this paper was carried out at the Jet Propulsion Laboratory, California Institute of Technology, under a contract with NASA. This work was supported by grant NNN13D772T-10-OSST10-0015.

SUPPLEMENTARY MATERIALS

www.sciencemag.org/content/349/6247/532/suppl/DC1
Materials and Methods
Figs. S1 to S18
Tables S1 and S2
References (*24*–*30*)

8 December 2014; accepted 24 June 2015
Published online 9 July 2015
10.1126/science.aaa4521

ACTIN-DIRECTED TOXIN

ACD toxin–produced actin oligomers poison formin-controlled actin polymerization

David B. Heisler,[1,2] Elena Kudryashova,[1]† Dmitry O. Grinevich,[1]* Cristian Suarez,[3] Jonathan D. Winkelman,[3] Konstantin G. Birukov,[4] Sainath R. Kotha,[5] Narasimham L. Parinandi,[5] Dimitrios Vavylonis,[6] David R. Kovar,[3,7] Dmitri S. Kudryashov[1,2]†

The actin cross-linking domain (ACD) is an actin-specific toxin produced by several pathogens, including life-threatening spp. of *Vibrio cholerae*, *Vibrio vulnificus*, and *Aeromonas hydrophila*. Actin cross-linking by ACD is thought to lead to slow cytoskeleton failure owing to a gradual sequestration of actin in the form of nonfunctional oligomers. Here, we found that ACD converted cytoplasmic actin into highly toxic oligomers that potently "poisoned" the ability of major actin assembly proteins, formins, to sustain actin polymerization. Thus, ACD can target the most abundant cellular protein by using actin oligomers as secondary toxins to efficiently subvert cellular functions of actin while functioning at very low doses.

Bacterial toxins are the deadliest compounds on the planet. As little as a single molecule of a delivered toxin can compromise vital functions or even kill an affected host cell (*1*, *2*). This is achieved by amplification of a toxin enzymatic activity by signaling cascades (e.g., by cholera, pertussis, and anthrax toxins) or by enzymatic inhibition of vital host complexes present in relatively few copies (e.g., Shiga and diphtheria toxins acting on ribosomes). Such efficiency is crucial because (i) the amount of a toxin produced early after infection is limited by an initially small number of bacterial cells; (ii) the host is protected by commensal bacteria; and (iii) the host immune system efficiently neutralizes toxins by means of adaptive (antibodies) and innate (e.g., defensins) (*3*) humoral defense factors.

Owing to its importance in multiple cellular processes, actin is a common target for bacterium- and parasite-produced toxins. Upon delivery to the cytoplasm of host cells by type I (as part of MARTX toxin) (*4*) or type VI (within VgrG1 toxin) (*5*) secretion systems, the actin cross-linking domain toxin (ACD) catalyzes the covalent cross-linking of Lys^{50} (K50) in subdomain 2 of one actin monomer with Glu^{270} (E270) in subdomain 3 of another actin monomer by means of an amide bond, which results in the formation of actin oligomers (*6*, *7*). The actin subunits in the oligomers are oriented similarly to short-pitch subunits in the filament, except that a major twist of subdomain 2, required to accommodate such orientation, disrupts the normal intersubunit interface and precludes polymerization (*6*).

The currently accepted mechanism of ACD toxicity, by sequestering of bulk amounts of actin as nonfunctional oligomers, is compromised owing to the high concentration of actin (hundreds of micromolar) in a typical animal cell.

Extrapolation of in vitro determined rates of the ACD activity (*7*) to cellular conditions suggests that a single ACD molecule per cell (i.e., ~1 pM) would require >6 months to covalently cross-link half of all cytoplasmic actin.

In contrast to these estimations, the integrity of the intestinal cell monolayers was disrupted when only a small fraction of cellular actin (2 to 6%) was cross-linked by ACD (Fig. 1, A to C, and fig. S1). To account for such dramatic effects, we hypothesized that the ACD–cross-linked actin oligomers are highly toxic because they can exert an abnormally high affinity to actin-regulatory proteins containing several actin-binding domains. To identify potential high-affinity partners of the actin oligomers, anthrax toxin delivery machinery was used to deliver ACD (*8*) into HeLa cells transfected with double-tagged (Twin-Strep–tag II and hemagglutinin) actin (SHA-actin) (fig. S2) and used for a pull-down assay. Several formins (DIAPH1, DIAPH2, DAAM1, and INF2) preferentially bound to the ACD–cross-linked actin oligomers (Fig. 1D). Treatment of epithelial monolayers with the formin inhibitor SMIFH2 affected the monolayer integrity similarly to ACD, whereas the Arp2/3 complex inhibitor CK-666 did not (fig. S3).

Formins are a major family of actin assembly factors involved in numerous actin-dependent cellular processes. The major functional domains of formins, formin homology domains 1 (FH1) and 2 (FH2), cooperate in nucleation and elongation of actin filaments. A noncovalent FH2/FH2 homodimer nucleates and remains at the polymerizing barbed end to facilitate processive filament elongation while protecting the filament from capping (*9*). Tandem poly(proline) (PP) stretches within the FH1 domains bind profilin-actin complexes and accelerate elongation as much as 10-fold (*10*–*12*). FH1 domains of all formins that preferentially bound to the oligomers (Fig. 1D) contain 4 to 14 tandem PP stretches, which may

[1]Department of Chemistry and Biochemistry, The Ohio State University, Columbus, OH 43210, USA. [2]The Ohio State Biochemistry Program, The Ohio State University, Columbus, OH 43210, USA. [3]Department of Molecular Genetics and Cell Biology, The University of Chicago, Chicago, IL 60637, USA. [4]Section of Pulmonary and Critical Care and Lung Injury Center, Department of Medicine, The University of Chicago, Chicago, IL 60637, USA. [5]Lipid Signaling and Lipidomics Laboratory, Division of Pulmonary, Allergy, Critical Care and Sleep Medicine, Department of Medicine, Dorothy M. Davis Heart and Lung Research Institute, College of Medicine, The Ohio State University, Columbus, OH 43210, USA. [6]Department of Physics, Lehigh University, Bethlehem, PA 18015, USA. [7]Department of Biochemistry and Molecular Biology, The University of Chicago, Chicago, IL 60637, USA. *Present address: Department of Molecular and Structural Biochemistry, North Carolina State University, Raleigh, NC 27695, USA. **†Corresponding author. E-mail: kudryashov.1@osu.edu (D.S.K); kudryashova.1@osu.edu (E.K.)**

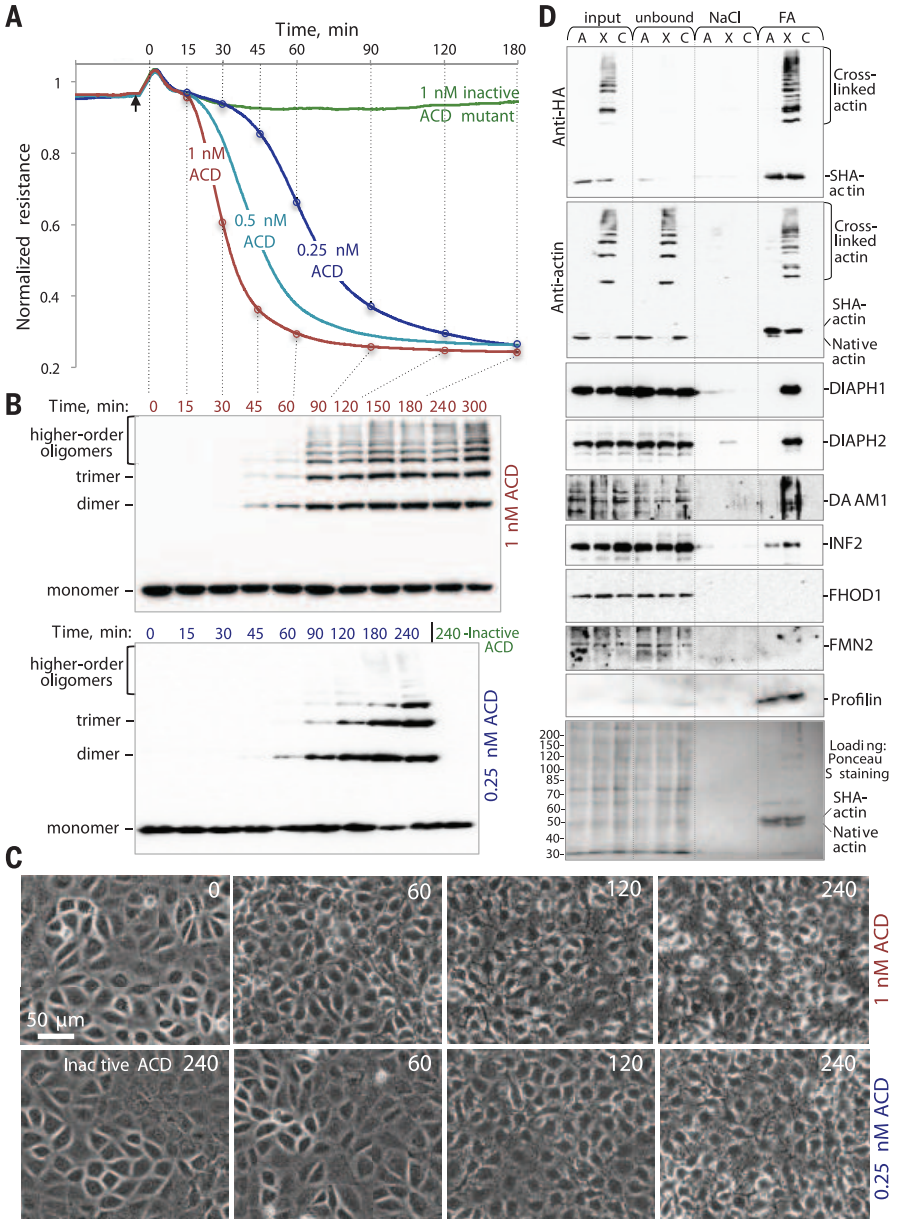

Fig. 1. Integrity of intestinal monolayers is compromised by low concentration of actin oligomers. (**A** to **C**) Transepithelial electrical resistance (TEER) of small intestine epithelial cell (IEC-18) monolayers (A) was assessed after cytoplasmic delivery of a fusion protein of the N-terminal portion of a lethal factor from *Bacillus anthracis* and ACD (LF_NACD) or a catalytically inactive ACD mutant as a control and correlated with the accumulation of ACD–cross-linked actin species by actin-specific antibody immunoblotting (B) and cell morphology (C). Additional actin-specific blots and quantification of cross-linked actin are presented in fig. S1. (**D**) SHA-actin pull-down. Lanes A: SHA-actin–transfected cells treated with inactive LF_NACD (non–cross-linked actin). Lanes X: SHA-actin–transfected cells treated with active LF_NACD (cross-linked actin). Lanes C: Nontransfected untreated cells used as a negative control. NaCl and FA label fractions eluted from Strep-Tactin beads with 0.5 M NaCl and 50% formamide, respectively. Samples were subjected to immunoblotting and probed with antibodies against hemagglutinin (HA) tag, actin, various formins, and profilin.

contribute to strong profilin-mediated interaction with the oligomers.

To elucidate the mechanism of formin inhibition, we used constitutively active FH1-FH2 fragments of mDia1 and mDia2 (mouse orthologs of human DIAPH1 and DIAPH3, respectively) to monitor actin polymerization at the individual filament level by total internal reflection fluorescence microscopy (TIRFM) (Figs. 2 and 3 and fig. S4). In the presence of human profilin-1 (PFN1), the oligomers caused very prominent reversible blocks of elongation of formin-controlled, but not formin-free, actin filaments (Fig. 2, A to F; fig. S4, B and C; and movies S1 to S5). Formin-controlled filaments were identified by faster growth with a dimmer appearance (Fig. 2, A and E) (*10*) or by direct labeling of formin (Fig. 3A).

In the presence of PFN1, the fraction of blocked mDia1 formin-associated filaments, as well as the inhibition of averaged growth rates, depended on the concentration of the added oligomers with an median inhibitory concentration (IC_{50}) of 1.2 ± 0.6 (SEM) nM (Fig. 2D), in good agreement with the apparent equilibrium inhibition constant determined kinetically ($_{app}K_i = k_{off}/k_{on}$ = 2.5 nM) (Fig. 3, C and D). After stops (oligomer dissociation), the filaments continued to polymerize with the rates characteristic for formin-controlled filaments (Fig. 2B and fig. S4A). In the absence of PFN1, the inhibition appeared to occur by a similar mechanism,

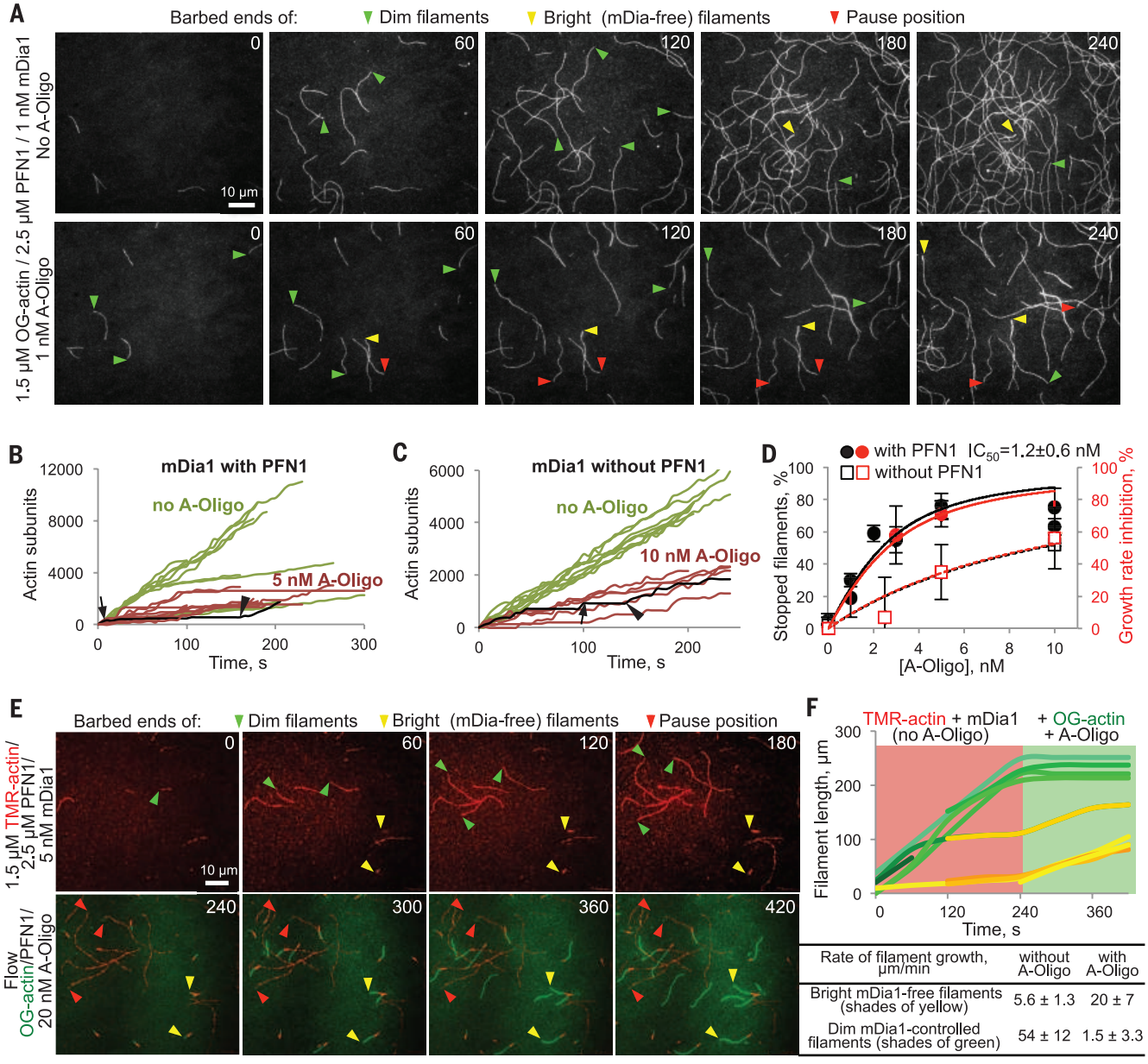

Rate of filament growth, µm/min	without A-Oligo	with A-Oligo
Bright mDia1-free filaments (shades of yellow)	5.6 ± 1.3	20 ± 7
Dim mDia1-controlled filaments (shades of green)	54 ± 12	1.5 ± 3.3

Fig. 2. Effects of ACD–cross-linked actin oligomers on polymerization of individual filaments controlled by mDia1(14PP). (**A**) mDia1(14PP)-mediated polymerization from profilin-actin complexes in the absence (top) and presence (bottom) of actin oligomers (A-Oligo) was monitored by TIRFM. Arrowheads denote actin barbed ends: green, mDia1-controlled (dim and fast); yellow, mDia1-free (bright and slow); and red, mDia1-controlled stopped by the oligomers. (**B** and **C**) Quantification of (A): Filament elongation plots in the presence (B) or absence (C) of PFN1. Green and red curves describe filament elongation in the absence and presence of oligomers, respectively. Arrows denote the beginning and arrowheads indicate the end of elongation blocks caused by the oligomers on representative curves highlighted in black. (**D**) IC_{50} of oligomers determined by TIRFM as a percentage of stopped filaments (black) or growth rate inhibition (red curves). (**E**) Tethramethylrhodamine (TMR)–labeled actin (TMR-actin) (red) was polymerized in the presence of mDia1(14PP) and PFN1 without oligomers followed by flow of Oregon Green (OG)–labeled actin (OG-actin), oligomers, and PFN1. Arrowheads are as for (A). (**F**) Quantification of (E): Growth of mDia1-controlled filaments (green traces) and mDia1-free filaments (yellow traces). Better polymerization properties of OG-actin result in faster elongation at the formin-free ends.

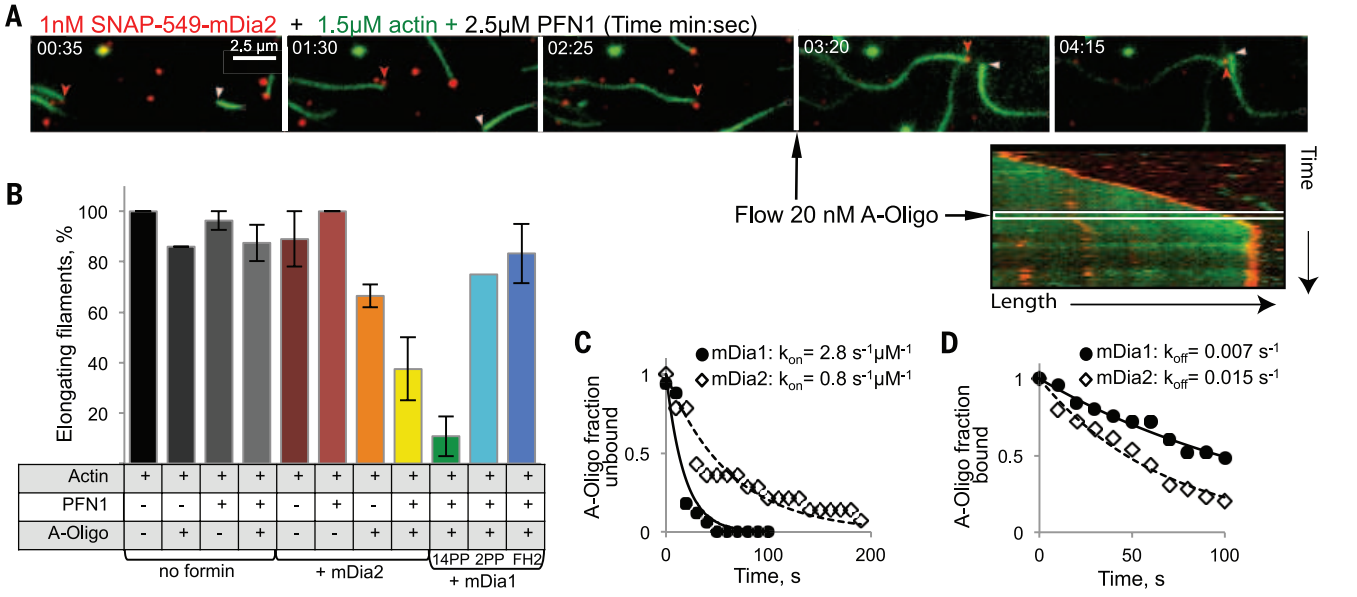

Fig. 3. Effects of ACD–cross-linked actin oligomers on polymerization of individual filaments controlled by mDia2 and mDia1 with various FH1 lengths. (**A**) OG-actin (green) polymerization in the presence of SNAP-tagged mDia2 labeled with SNAP-Surface 549 (SNAP-549–mDia2) (red) and PFN1 before and after the addition of oligomers (black arrow) was monitored by TIRFM. Red arrowheads indicate SNAP-549–mDia2 at an actin filament; white arrowheads indicate formin-free filament. Kymograph shows a stalled SNAP-549–mDia2–controlled filament upon addition of oligomers. (**B**) Effects of oligomers on formin-free filament elongation and elongation controlled by mDia2 and mDia1 formins with various FH1 lengths: 14PP, 2PP, and FH2 (no PP stretches). (**C** and **D**) Oligomer association (k_{on}) (C) and dissociation (k_{off}) (D) rates for mDia1(14PP) and mDia2.

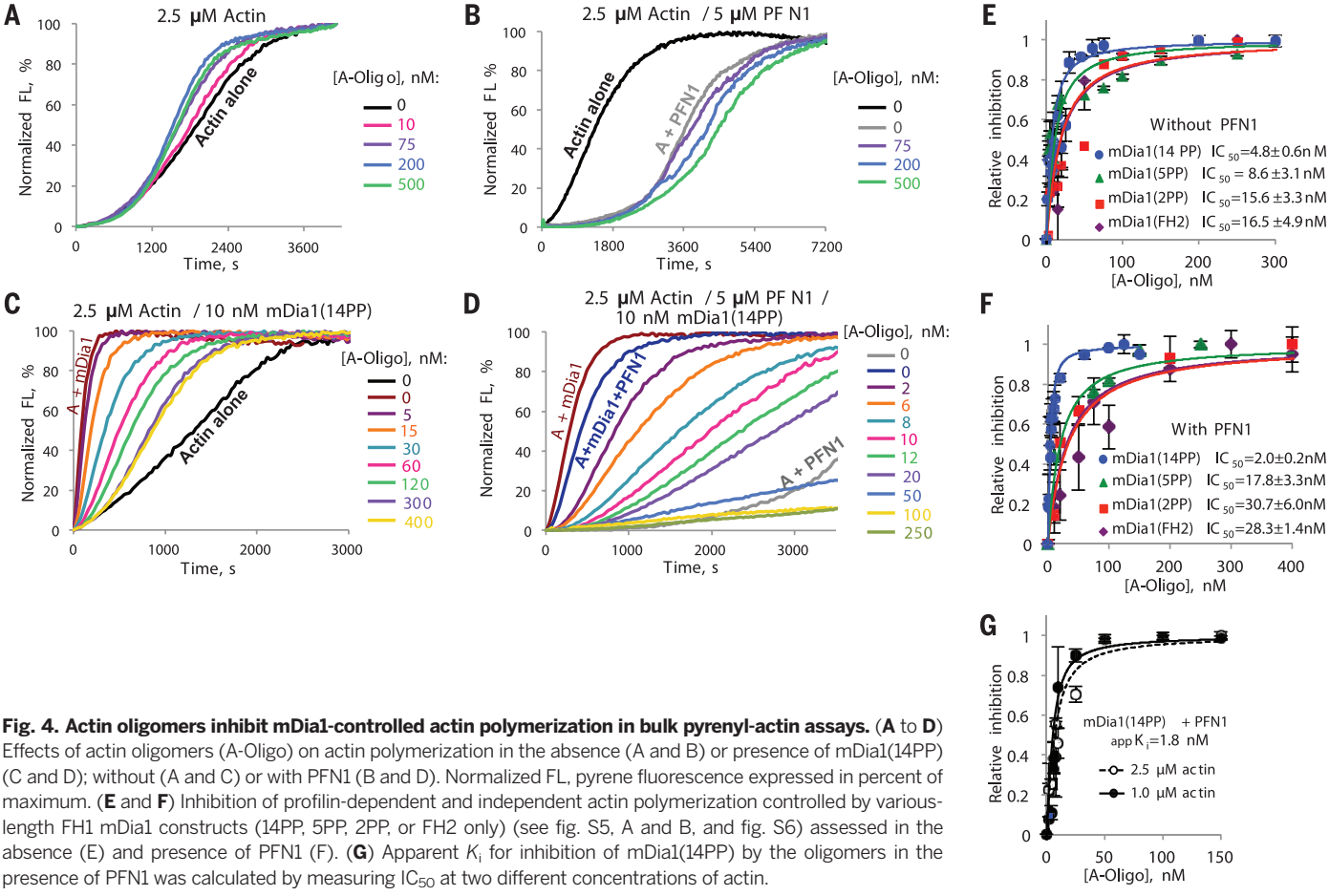

Fig. 4. Actin oligomers inhibit mDia1-controlled actin polymerization in bulk pyrenyl-actin assays. (**A** to **D**) Effects of actin oligomers (A-Oligo) on actin polymerization in the absence (A and B) or presence of mDia1(14PP) (C and D); without (A and C) or with PFN1 (B and D). Normalized FL, pyrene fluorescence expressed in percent of maximum. (**E** and **F**) Inhibition of profilin-dependent and independent actin polymerization controlled by various-length FH1 mDia1 constructs (14PP, 5PP, 2PP, or FH2 only) (see fig. S5, A and B, and fig. S6) assessed in the absence (E) and presence of PFN1 (F). (**G**) Apparent K_i for inhibition of mDia1(14PP) by the oligomers in the presence of PFN1 was calculated by measuring IC_{50} at two different concentrations of actin.

but the overall effect was weaker, and the average duration of the blockage events was substantially shorter (Fig. 2, C and D). Although a profilin-mediated interaction of the oligomers with the PP stretches of FH1 was not absolutely required, it strongly amplified the efficiency of the inhibition at the elongation stage by contributing to multisite interaction with the oligomers. Thus, mDia1 constructs (fig. S5A) with either removed FH1 domains (FH2 only) or shortened from 14PP to 2PP stretches showed progressively lower response to inhibition by the oligomers in the presence of PFN1 (Fig. 3B). Similarly, the $_{app}K_i$ of oligomers for mDia2 (containing 2PP) was 7.5 times that for mDia1 and depended on PFN1 (Fig. 3, B to D).

The inhibition of formin-mediated polymerization measured at the individual filament level correlated well with the inhibition observed in bulk pyrene assays (Fig. 4 and figs. S5 and S6). During spontaneous polymerization in the absence of PFN1, high concentrations (75 to 500 nM) of the oligomers mildly accelerated the polymerization, whereas mild inhibition was observed in the presence of profilin (Fig. 4, A and B). This is likely because of a low level of incorporation of the oligomers into the filaments (*6*) in the absence, but not in the presence, of PFN1 (fig. S5D), which leads to filament severing similar to that observed for actin species with impaired intersubunit surfaces (*13*).

In contrast, the oligomers potently inhibited actin polymerization directed by mDia1 in the presence and, to a lesser extent, the absence of PFN1 (Fig. 4, C to F, and fig. S6). Fitting the inhibition of actin polymerization at 50% of maximum to a binding isotherm equation resulted in an IC_{50} for the mDia1(14PP) construct equal to 2.0 ± 0.2 nM and 4.8 ± 0.6 nM (SEM) in the presence and absence of PFN1 (Fig. 4, E and F). The ACD–cross-linked actin dimers purified to homogeneity (fig. S5B) inhibited the mDia1-controlled polymerization less efficiently than the mixture of higher-order oligomers (fig. S5, F to H), which suggests that the inhibition is amplified by multivalent interactions of the oligomers with mDia1. Accordingly, shortening the FH1 domain progressively decreased the efficiency of inhibition, with the IC_{50} values reaching ~30 and ~16 nM for the mDia1(FH2) constructs in the presence and absence of PFN1 (Fig. 4, E and F, and fig. S6).

Kinetic modeling (fig. S8) revealed that inhibition of both nucleation and elongation is required to accurately describe the effects of the oligomers on formin-controlled actin polymerization. Using experimentally determined parameter values for inhibition of elongation, we found good fits to the data (Fig. 4) by assuming that oligomers also inhibit nucleation by binding to free mDia1(14PP) formin with dissociation constants of 0.8 and 5 nM in the presence and absence of PFN1 (fig. S8, D and E). Inhibition of nucleation by the oligomers in the absence of PFN1 was also observed experimentally in filament seeding assays (fig. S7) and TIRFM experiments (fig. S4, D to G). Similar experiments in the presence of PFN1 were less conclusive owing to the overall lower nucleation ability of formins under these conditions (fig. S4, F and G, and fig. S7, G and H). To improve accuracy, modeling had to account for filament severing owing to incorporation of the oligomers in the absence of PFN1 (Fig. 4, A and C, and fig. S8, C and D).

Bacterial toxins are well known to disorganize the actin cytoskeleton acting on Rho family guanosine triphosphatase–controlled signaling pathways (*14*). Here, we found that toxins can not only exploit existing signaling pathways but also initiate a new toxicity cascade with de novo produced cross-linked actin species as "second messengers." Because of a unique combination of properties that is not present in G- or F-actin (fig. S9A), these new actin species bind with high affinity to formins and adversely affect both nucleation and elongation abilities of these proteins, which causes their potent inhibition in both profilin-dependent and independent manners (fig. S9B). Thus, ACD creates toxic derivatives of actin with a disruptive "gain-of-function" mode of operation. We propose that the seemingly straightforward original assumption that ACD acts by the accumulation of bulk amounts of nonfunctional actin is inaccurate or at least incomplete. The toxin can be highly efficient at very low concentrations by acting on formins and, potentially, other actin regulatory proteins. This finding calls for the careful reevaluation of mechanisms used by other actin-related toxins, both of protein and small-molecule natures.

REFERENCES AND NOTES

1. P. J. Tam, C. A. Lingwood, *Microbiology* **153**, 2700–2710 (2007).
2. M. Yamaizumi, E. Mekada, T. Uchida, Y. Okada, *Cell* **15**, 245–250 (1978).
3. E. Kudryashova *et al*., *Immunity* **41**, 709–721 (2014).
4. K.-L. Sheahan, C. L. Cordero, K. J. Fullner Satchell, *Proc. Natl. Acad. Sci. U.S.A.* **101**, 9798–9803 (2004).
5. S. Pukatzki, A. T. Ma, A. T. Revel, D. Sturtevant, J. J. Mekalanos, *Proc. Natl. Acad. Sci. U.S.A.* **104**, 15508–15513 (2007).
6. D. S. Kudryashov *et al*., *Proc. Natl. Acad. Sci. U.S.A.* **105**, 18537–18542 (2008).
7. E. Kudryashova, C. Kalda, D. S. Kudryashov, *PLOS ONE* **7**, e45721 (2012).
8. Supplementary materials are available on *Science* Online.
9. D. Breitsprecher, B. L. Goode, *J. Cell Sci.* **126**, 1–7 (2013).
10. D. R. Kovar, E. S. Harris, R. Mahaffy, H. N. Higgs, T. D. Pollard, *Cell* **124**, 423–435 (2006).
11. D. Vavylonis, D. R. Kovar, B. O'Shaughnessy, T. D. Pollard, *Mol. Cell* **21**, 455–466 (2006).
12. S. Romero *et al*., *Cell* **119**, 419–429 (2004).
13. D. S. Kudryashov, M. Phillips, E. Reisler, *Biophys. J.* **87**, 1136–1145 (2004).
14. E. Lemichez, K. Aktories, *Exp. Cell Res.* **319**, 2329–2336 (2013).
15. N. Arora, S. H. Leppla, *Infect. Immun.* **62**, 4955–4961 (1994).
16. J. C. Milne, S. R. Blanket, P. C. Hanna, R. J. Collier, *Mol. Microbiol.* **15**, 661–666 (1995).
17. C. L. Cordero, D. S. Kudryashov, E. Reisler, K. J. Fullner Satchell, *J. Biol. Chem.* **281**, 32366–32374 (2006).
18. J. Wesche, J. L. Elliott, P. O. Falnes, S. Olsnes, R. J. Collier, *Biochemistry* **37**, 15737–15746 (1998).
19. B. Geissler, A. Bonebrake, K. L. Sheahan, M. E. Walker, K. J. Fullner Satchell, *Mol. Microbiol.* **73**, 858–868 (2009).
20. S. M. Sliman *et al*., *Mol. Cell. Biochem.* **333**, 9–26 (2010).
21. J. A. Spudich, S. Watt, *J. Biol. Chem.* **246**, 4866–4871 (1971).
22. J. R. Kuhn, T. D. Pollard, *Biophys. J.* **88**, 1387–1402 (2005).
23. E. Kudryashova, D. Heisler, A. Zywiec, D. S. Kudryashov, *Mol. Microbiol.* **92**, 1056–1071 (2014).
24. D. S. Kudryashov, C. L. Cordero, E. Reisler, K. J. Fullner Satchell, *J. Biol. Chem.* **283**, 445–452 (2008).
25. J. Lu, T. D. Pollard, *Mol. Biol. Cell* **12**, 1161–1175 (2001).
26. S. A. Rizvi *et al*., *Chem. Biol.* **16**, 1158–1168 (2009).
27. C. Suarez *et al*., *Dev. Cell* **32**, 43–53 (2015).
28. D. R. Kovar, T. D. Pollard, *Proc. Natl. Acad. Sci. U.S.A.* **101**, 14725–14730 (2004).
29. C. A. Schneider, W. S. Rasband, K. W. Eliceiri, *Nat. Methods* **9**, 671–675 (2012).
30. J. D. Winkelman, C. G. Bilancia, M. Peifer, D. R. Kovar, *Proc. Natl. Acad. Sci. U.S.A.* **111**, 4121–4126 (2014).
31. D. S. Kudryashov, E. E. Grintsevich, P. A. Rubenstein, E. Reisler, *J. Biol. Chem.* **285**, 25591–25601 (2010).
32. Y.-C. Cheng, W. H. Prusoff, *Biochem. Pharmacol.* **22**, 3099–3108 (1973).
33. M. Pring, M. Evangelista, C. Boone, C. Yang, S. H. Zigmond, *Biochemistry* **42**, 486–496 (2003).
34. A. S. Paul, T. D. Pollard, *Curr. Biol.* **18**, 9–19 (2008).
35. N. Courtemanche, T. D. Pollard, *J. Biol. Chem.* **287**, 7812–7820 (2012).
36. S. Romero *et al*., *J. Biol. Chem.* **282**, 8435–8445 (2007).
37. E. M. Neidt, B. J. Scott, D. R. Kovar, *J. Biol. Chem.* **284**, 673–684 (2009).
38. E. G. Yarmola, D. A. Dranishnikov, M. R. Bubb, *Biophys. J.* **95**, 5544–5573 (2008).
39. N. Wittenmayer *et al*., *Mol. Biol. Cell* **15**, 1600–1608 (2004).
40. I. Perelroizen, J. B. Marchand, L. Blanchoin, D. Didry, M. F. Carlier, *Biochemistry* **33**, 8472–8478 (1994).
41. N. Courtemanche, T. D. Pollard, *Biochemistry* **52**, 6456–6466 (2013).
42. R. Gieselmann, D. J. Kwiatkowski, P. A. Janmey, W. Witke, *Eur. J. Biochem.* **229**, 621–628 (1995).
43. D. Sept, J. A. McCammon, *Biophys. J.* **81**, 667–674 (2001).
44. K. M. Schmoller, T. Niedermayer, C. Zensen, C. Wurm, A. R. Bausch, *Biophys. J.* **101**, 803–808 (2011).
45. D. Sept, J. Xu, T. D. Pollard, J. A. McCammon, *Biophys. J.* **77**, 2911–2919 (1999).

ACKNOWLEDGMENTS

We thank M. Vartiainen and T. Viita (University of Helsinki) for donating double-tagged SHA-actin plasmid. This work was supported by The Ohio State University startup funds (to D.S.K.), American Heart Association Innovative Research Grant (13IRG14780028 to D.S.K.), NIH (R01 GM079265 to D.R.K. and R01 GM098430 to D.V.). D.B.H. purified proteins, conducted pyrene actin and TIRFM experiments, analyzed data, and cowrote the manuscript; E.K. conducted cell culture, pull-down and immunoblotting experiments, analyzed data, and cowrote the manuscript; D.O.G. purified proteins and conducted pyrene actin assays; C.S., J.D.W., and D.R.K. conducted TIRFM and analyzed data; K.G.B., S.R.K., and N.L.P. conducted TEER; D.V. performed modeling; D.S.K. coordinated the study, analyzed data, and cowrote the manuscript. The authors declare no conflict of interest. Supplementary materials contain additional data.

SUPPLEMENTARY MATERIALS

www.sciencemag.org/content/349/6247/535/suppl/DC1
Materials and Methods
Figs. S1 to S9
Table S1
References (*15-45*)
Movies S1 to S5
Modeling Program

22 April 2015; accepted 7 July 2015
10.1126/science.aab4090

PLANT EVOLUTION

Convergent evolution of strigolactone perception enabled host detection in parasitic plants

Caitlin E. Conn,[1] Rohan Bythell-Douglas,[2] Drexel Neumann,[1] Satoko Yoshida,[3] Bryan Whittington,[4] James H. Westwood,[4] Ken Shirasu,[3] Charles S. Bond,[2] Kelly A. Dyer,[1] David C. Nelson[1]*

Obligate parasitic plants in the Orobanchaceae germinate after sensing plant hormones, strigolactones, exuded from host roots. In *Arabidopsis thaliana*, the α/β-hydrolase D14 acts as a strigolactone receptor that controls shoot branching, whereas its ancestral paralog, KAI2, mediates karrikin-specific germination responses. We observed that *KAI2*, but not *D14*, is present at higher copy numbers in parasitic species than in nonparasitic relatives. *KAI2* paralogs in parasites are distributed into three phylogenetic clades. The fastest-evolving clade, *KAI2d*, contains the majority of *KAI2* paralogs. Homology models predict that the ligand-binding pockets of KAI2d resemble D14. *KAI2d* transgenes confer strigolactone-specific germination responses to *Arabidopsis thaliana*. Thus, the *KAI2* paralogs *D14* and *KAI2d* underwent convergent evolution of strigolactone recognition, respectively enabling developmental responses to strigolactones in angiosperms and host detection in parasites.

The Orobanchaceae plant family comprises thousands of species that parasitize other plants through a haustorial connection to a host root. Several obligate parasites in this family are noxious weeds that can cause complete crop loss, affecting millions of smallholder farmers and reducing yields by billions of U.S. dollars each year (*1*, *2*). Their seeds can lie dormant in soil for many years, until the detection of strigolactones (SLs) exuded by a nearby host triggers germination. This essential adaptation may be exploited to combat parasite infestations by inducing suicidal germination or modifying SL output in crops. To aid the development of these strategies, we set out to understand how parasites sense SLs.

SLs are plant hormones that control shoot branching, root architecture, cambial growth, and senescence, but also serve as extraorganismal signals in soil that recruit symbioses with arbuscular mycorrhizal fungi (*3*–*6*). SL responses in plants require the F-box protein MORE AXILLARY GROWTH2 (MAX2) and the α/β-hydrolase DWARF14 (D14) (*3*). *MAX2* also mediates responses to karrikins (KARs), a family of butenolide compounds found in smoke that trigger the germination of many species after fire but do not promote parasite germination (*7*, *8*) (fig. S1). KAR responses in *Arabidopsis thaliana* require *KARRIKIN-INSENSITIVE2* (*KAI2*), a paralog of *D14*. *AtKAI2* is required for normal seed germination and seedling growth, but *D14* and SL biosynthesis genes are not (*9*).

[1]Department of Genetics, University of Georgia, Athens, GA 30602, USA. [2]School of Chemistry and Biochemistry, The University of Western Australia, Crawley, Western Australia 6009, Australia. [3]RIKEN Center for Sustainable Resource Science, Tsurumi-ku, Yokohama, Kanagawa 230-0045, Japan. [4]Department of Plant Pathology, Physiology, and Weed Science, Virginia Tech, Blacksburg, VA 24061, USA.
*Corresponding author. E-mail: dcnelson@uga.edu

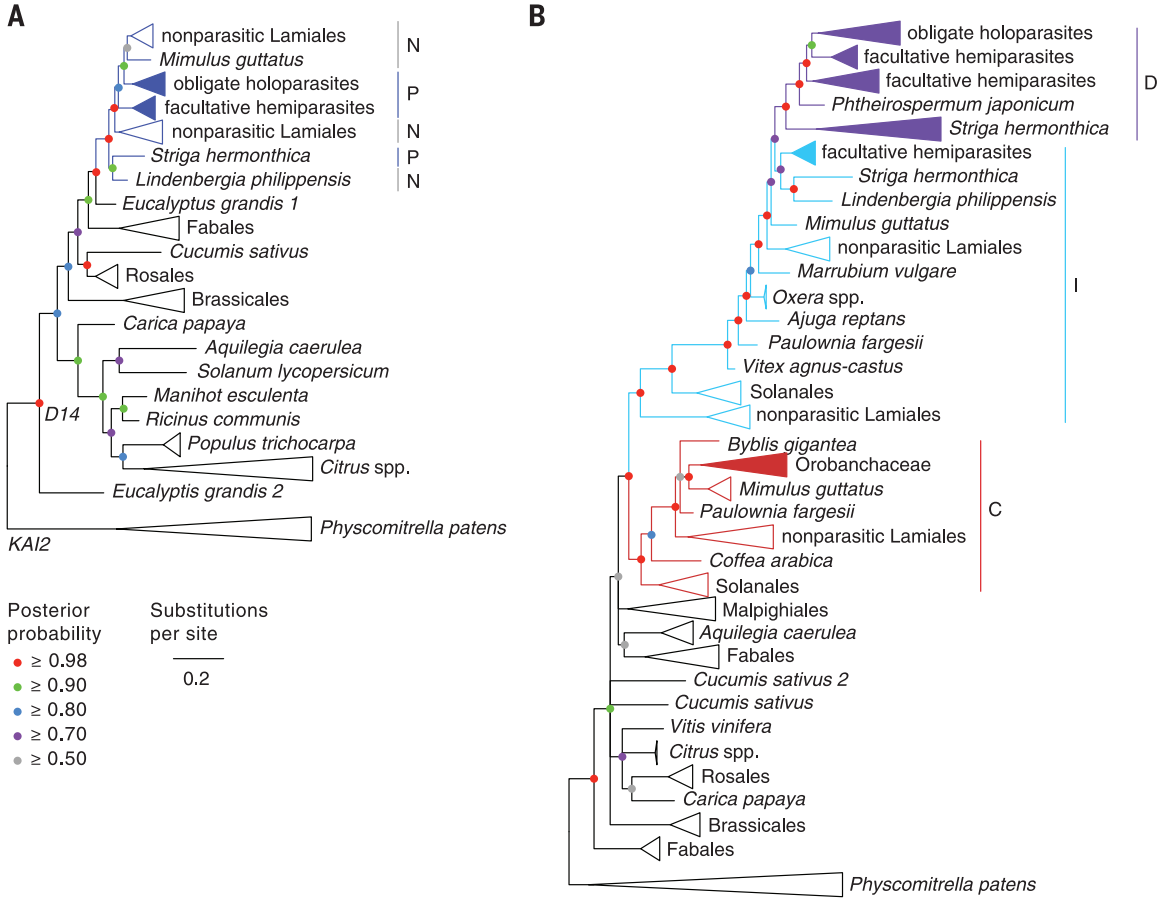

Fig. 1. *D14* and *KAI2* evolution in dicots. (**A**) *D14* Bayesian phylogeny. Clades are designated P (parasitic Orobanchaceae) and N (nonparasitic Lamiales). (**B**) *KAI2* Bayesian phylogeny. Clades are designated conserved (C, *KAI2c*), intermediate (I, *KAI2i*), and divergent (D, *KAI2d*). *Physcomitrella patens KAI2* was used as an outgroup for both analyses. Uncollapsed phylogenies are shown in figs. S3 and S4.

D14 and KAI2 are likely receptors that require conformational changes induced by enzymatic activity for signal transduction. D14 binds and hydrolyzes SL, and KAI2 binds KAR_1; catalytic residue mutations abolish their function (*10*–*15*). The crystal structures of D14 and KAI2 show nearly identical topologies, but differences are found in the ligand-binding pocket shapes (*11*–*16*). Only *KAI2* occurs in basal plant lineages, and the appearance of *D14* in higher plant genomes coincides with that of MAX2 targets that control branching (*3*, *9*). Therefore, we infer that SL recognition may not have been the ancestral role of KAI2 but probably evolved after duplication of KAI2 in the paralog now called D14.

Host recognition might have arisen in the parasitic Orobanchaceae through adaptation of the *MAX2*-dependent germination control mechanism. *MAX2* itself is well conserved in parasite genomes, and a *MAX2* ortholog from the parasite *Striga hermonthica* can rescue an *A. thaliana max2* mutant (*17*). We hypothesized that in parasites, KAI2 evolved ligand specificity for SLs and/or that the SL receptor D14 gained a role in germination.

We investigated *D14* and *KAI2* evolution in 10 species that represent the full range of parasitism in the Orobanchaceae. We used next-generation shotgun genome sequencing and de novo genome assembly algorithms to identify *D14* and *KAI2* genes in four obligate holoparasites (*Orobanche minor*, *O. cernua*, *O. cumana*, and *Conopholis americana*) and two facultative hemiparasites (*Phtheirospermum japonicum* and *Triphysaria versicolor*) (*18*). We also searched an expressed sequence tag database of *S. hermonthica* and de novo transcriptome assemblies of five parasites and a basal nonparasite. Gene fragments matching *D14* and *KAI2* in the assemblies were used to generate full-length coding sequences (data files S1 and S2). We verified the predicted sequences of 29 genes from six parasite species by Sanger sequencing (*18*). To make comparisons to nonparasitic genomes, we also mined available dicot genome assemblies and de novo transcriptome assemblies of 18 species in the Orobanchaceae-containing order Lamiales. We restricted further analyses to a conservatively defined data set of 53 *D14* and 144 *KAI2* sequences from 55 species (tables S1 and S2).

We identified at most one *D14* copy in parasitic Orobanchaceae and their nonparasitic relatives in the Lamiales, similar to the number in nonparasitic dicots (fig. S2 and table S3). The *D14* genes in the Lamiales formed a monophyletic clade (Fig. 1A). In contrast, most parasite genomes had more copies of *KAI2* than did nonparasite Lamiales species (5.6 ± 1.2 versus 1.8 ± 0.19; Wilcoxon rank sum test, χ^2_1 9.4, P = 0.0022); the nonweedy parasites *C. americana* and *O. fasciculata* were exceptions. The *KAI2* genes in the Lamiids (Lamiales, Gentianales, and Solanales) formed a monophyletic clade that we divided into conserved (*KAI2c*), intermediate (*KAI2i*), and divergent (*KAI2d*) subclades (Fig. 1B). Most Lamiids [28 out of 33 species (28/33 spp.)] had a single basal *KAI2c* sequence. When present, *KAI2i* paralogs were also usually limited to a single copy (15/17 spp.), but *KAI2i* paralogs were not detected in all Lamiids or in any of the six obligate holoparasites. The *KAI2d* clade, however, was parasite-specific and contained the majority of *KAI2* paralogs (fig. S4).

We tested for evidence of relaxed purifying selection or positive selection that may have enabled subfunctionalization or neofunctionalization of *D14* and *KAI2* in parasites. We analyzed codon substitution patterns across the phylogeny by allowing the rate of protein evolution ($\omega = d_N/d_S$) to vary across clades (tables S4 to S7). *D14* was under strong purifying selection in dicots that was relaxed in the parasitic Orobanchaceae (ω_0 = 0.07, ω_P = 0.15). Different strengths of purifying selection were supported for the three *KAI2* subclades in Lamiids. Purifying selection was strongest for *KAI2c* (ω_C = 0.07), comparable to other dicots for *KAI2i* (ω_0 = 0.11, ω_I = 0.10), and weakest for *KAI2d* (ω_D = 0.27). Although ω_D was not indicative of recurrent positive selection (i.e., $\omega > 1$), the elevated ω_D value could result if positive selection acted only on a subset of *KAI2d* codons or for a short period of time after the duplication event.

We next investigated whether KAI2 proteins in parasites had evolved structural changes that suggest altered ligand specificities. Because of high sequence identity (54 to 80%), we were able to generate homology models of KAI2 from

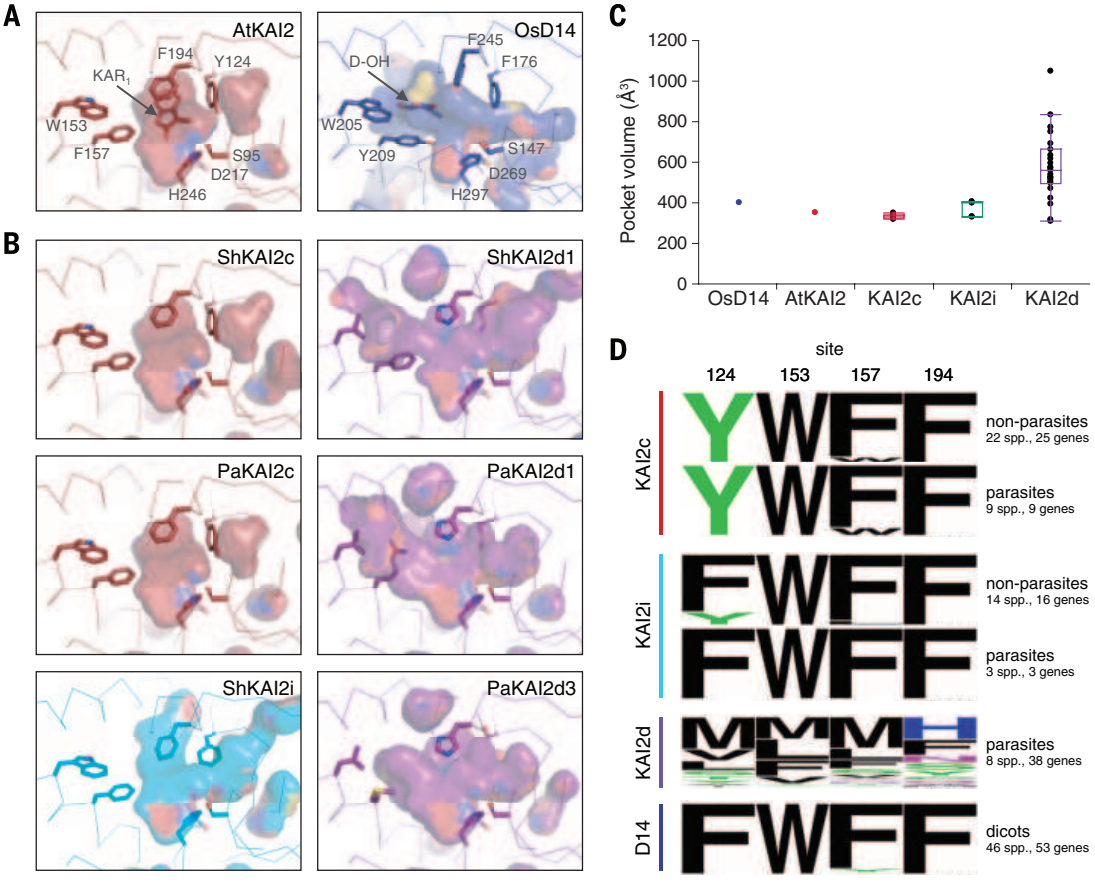

Fig. 2. Homology models of parasite KAI2. (**A**) Ligand-binding pockets of AtKAI2 [left, Protein Data Bank (PDB) entry 4JYM] and OsD14 (right, PDB entry 3WIO) (*12*, *15*). KAR_1 and a hydroxy D-ring (D-OH) product of GR24 hydrolysis are indicated. OsD14 positions are offset by a 50–amino acid leader sequence that is absent in AtD14. (**B**) Homology models of KAI2 protein sequences in *S. hermonthica* (Sh) and *P. aegyptiaca* (Pa). Cavities within the protein models are shown as a semitransparent surface. Catalytic residues (S95, D217, and H246) and residues highlighted in (D) are shown in stick representation. (**C**) Box plots of ligand-binding cavity volumes in AtKAI2, OsD14, and KAI2 models here and in fig S5. (**D**) Amino acid frequency plots at equivalent positions to AtKAI2 residues, in the three KAI2 clades in Lamiids and in D14 in dicots.

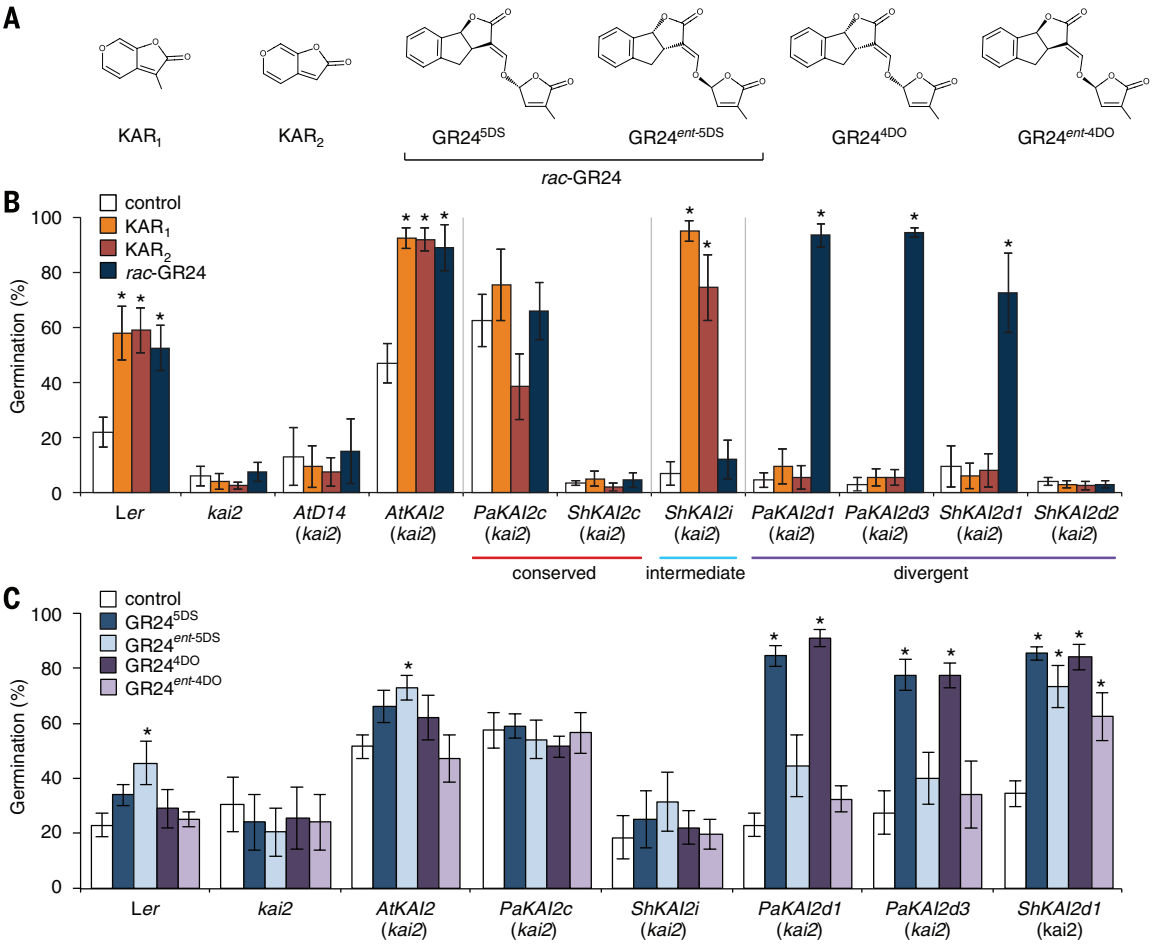

Fig. 3. Cross-species complementation assays of parasite *KAI2*. (**A**) Chemical structures of KAR_1, KAR_2, and four GR24 stereoisomers. (**B**) Seed germination after 6 days in 16 hours light, 21°C, with 1 μM KAR_1, KAR_2, and *rac-GR24* treatments. Transgenes were expressed in the null *kai2-2* mutant background (L*er* ecotype) under control of an *AtKAI2* promoter. (**C**) Seed germination after 5 days in 16 hours light, 21°C, with 1 μM GR24 stereoisomer treatments. Mean germination ± SE is shown ($n = 4$ independent seed batches per genotype, 50 seeds tested per seed batch). *$P < 0.01$, Tukey-Kramer HSD test, comparison to control treatment for each genotype.

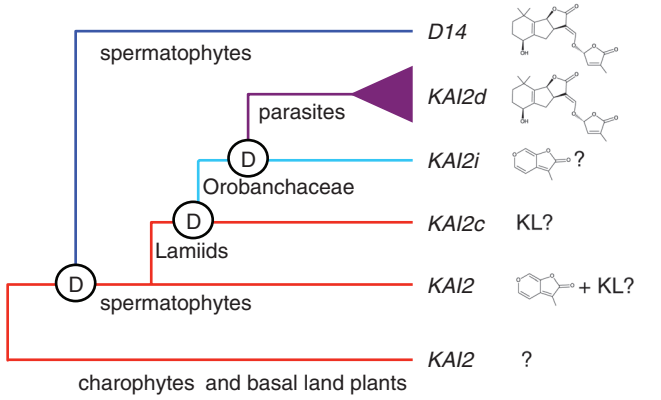

Fig. 4. Model of KAI2 and D14 evolution. *KAI2* homologs are found in charophyte algae and other basal lineages, but their functions and ligands are unknown. *D14* probably arose from a duplication of *KAI2* before the evolution of seed plants (spermatophytes). AtKAI2 recognizes KAR and may recognize an endogenous KAI2 ligand (KL). Duplication of *KAI2* after the evolution of Lamiids produced *KAI2c* and *KAI2i* paralogs in the Lamiales and Solanales. KAI2c may recognize KL, and KAI2i may recognize KAR. Further duplication events in the parasitic Orobanchaceae led to a fast-evolving clade of *KAI2d* that recognize SL.

parasites and related nonparasitic species using a KAR_1-bound AtKAI2 structure as the template (*15*). Parasite KAI2 models were compared to AtKAI2-KAR_1 and rice D14 (OsD14) bound to a byproduct of SL hydrolysis (*12*) (Fig. 2, A and B; fig. S5; table S8). Models of KAI2c proteins had similar substrate-binding cavities to AtKAI2 in terms of volume and shape. KAI2i substrate-binding cavities were predicted to have an intermediate morphology to AtKAI2 and OsD14, in which two adjacent pockets are joined. In contrast, KAI2d models had substrate-binding cavities that were larger than those of KAI2c and KAI2i (Fig. 2C; $P < 0.01$, Student's t test), and appeared more superficially similar to those of OsD14 than AtKAI2. This structural convergence suggests that the parasite-specific *KAI2d* clade may have evolved the ability to recognize SL.

The stratification of parasite KAI2 substrate-binding pockets into AtKAI2-like, OsD14-like, and somewhere in between is largely due to differences at a few highly conserved amino acids. Most prominently, the hydroxyl group of Y124 in the AtKAI2 crystal structure occludes a pocket adjacent to the substrate-binding cavity. Smaller amino acid substitutions at this position prevent the bisection of these two pockets, providing a larger substrate-binding cavity (Fig. 2A). Y124 is conserved in all 34 KAI2c proteins in Lamiids, and in 78% of KAI2 proteins in other dicots. The majority of KAI2i proteins in Lamiids (16/19) have a Y124F substitution, as seen in D14. Substitution of this residue with even smaller hydrophobic amino acids is typically observed in KAI2d (Fig. 2D). Other conserved residues that contribute to the morphology or chemical characteristics of the substrate-binding pocket are highly variable in KAI2d, supporting the hypothesis of altered ligand specificity in this clade (Fig. 2D).

We tested the ligand specificity of four *KAI2* paralogs from *S. hermonthica* and three from *P. aegyptiaca* by functional complementation of an *A. thaliana kai2* mutant, which has increased seed dormancy and no germination response to KARs or the synthetic SL *rac*-GR24 (*9*). Two transgenes, *ShKAI2c* and *ShKAI2d2*, had no effect on germination and were presumed nonfunctional in *A. thaliana*. The remaining transgenes gave three types of germination responses (Fig. 3B).

PaKAI2c rescued the *kai2* dormancy phenotype but did not confer responses to either KARs or *rac*-GR24, despite its predicted structural similarity to AtKAI2. The *kai2* dormancy phenotype may result from the inability to detect an unknown, endogenous germination-promoting signal (*10*). If so, *PaKAI2c* may be specific for this signal. The intermediate-clade gene *ShKAI2i* conferred germination responses to KARs but not to *rac*-GR24. Although this activity was consistent with the KAR receptor role of AtKAI2, it was unexpected as *S. hermonthica* is insensitive to karrikins (fig. S1). Most notably, three *KAI2d* genes conferred a strong germination response to *rac*-GR24 alone (Fig. 3B).

Although *rac*-GR24 is commonly used as a synthetic SL, it is a racemate of natural (2′*R*) $GR24^{5DS}$ and unnatural (2′*S*) $GR24^{ent\text{-}5DS}$ stereoisomers that respectively activate D14 and KAI2 signaling in *A. thaliana* seed and seedlings (*19*). Positive responses to *rac*-GR24 can be misinterpreted as SL responses when $GR24^{ent\text{-}5DS}$ is actually the active signal. We therefore tested germination responses to four enantiomers of GR24 (Fig. 3, A and C). Two of the three *rac*-GR24–responsive *KAI2d* conferred stronger responses to the natural SL stereoisomers $GR24^{5DS}$ and $GR24^{4DO}$ than to their unnatural enantiomers $GR24^{ent\text{-}5DS}$ and $GR24^{ent\text{-}4DO}$. *ShKAI2d1* responded to all four stereoisomers.

Thus, KAI2d paralogs have gained structural similarity to D14 and the ability to respond to SL. This example of convergent molecular evolution probably arose in parasites via a duplication of *KAI2* before the divergence of the Lamiales and Solanales. During the transition to parasitism in the Orobanchaceae, further *KAI2* duplication and relaxed selection and/or bursts of positive selection on these paralogs formed the SL-responsive *KAI2d* clade (Fig. 4). The presence of *KAI2d* in facultative hemiparasites, which do not require a host, suggests that the capacity for SL perception preceded obligate parasitism.

AtD14 did not rescue the *kai2* mutant. This suggests that changes in *D14* expression patterns would not be sufficient to evolve SL-specific germination in *A. thaliana*, perhaps because KAI2 and D14 interact with different downstream signaling partners in the SMAX1/D53 family (*10*). The evolution of SL specificity in *KAI2* may be a simpler path to host recognition than neofunctionalization of *D14*.

The antagonistic coevolution of hosts and parasites may drive diversification of SL molecules in hosts and SL detection mechanisms in parasites. Supporting this idea, (i) at least 20 SLs and other host-derived germination stimulants with butenolide or lactone moieties have been identified (*20*, *21*), (ii) SL profiles vary within and across host species (*21*–*23*), and (iii) parasite species also vary considerably in their germination responses to different host root exudates and SLs (*24*, *25*). We hypothesize that multiple *KAI2d* genes in parasite genomes may enable diversified stimulant recognition, which in turn influences host range and buffers against changes in host availability. Because we only observed one or two *KAI2* genes in *C. americana* and *O. fasciculata*, which are parasites of oaks and *Artemisia* spp., respectively, it may be that *KAI2* diversity is less critical for parasites of perennial hosts.

We have identified 29 *KAI2d* genes from five weedy parasites that are likely to have roles in host recognition. This discovery will enable high-throughput in silico and in vitro screening of chemical libraries for KAI2d agonists to control parasite infestations. It will also aid investigations of how parasites rapidly evolve new host specificities and become virulent agricultural weeds.

REFERENCES AND NOTES

1. J. H. Westwood, J. I. Yoder, M. P. Timko, C. W. dePamphilis, *Trends Plant Sci.* **15**, 227–235 (2010).
2. D. K. Berner, J. K. Kling, B. B. Singh, *Plant Dis.* **79**, 652 (1995).
3. T. Waldie, H. McCulloch, O. Leyser, *Plant J.* **79**, 607–622 (2014).
4. M. Umehara *et al.*, *Nature* **455**, 195–200 (2008).
5. V. Gomez-Roldan *et al.*, *Nature* **455**, 189–194 (2008).
6. K. Akiyama, K. Matsuzaki, H. Hayashi, *Nature* **435**, 824–827 (2005).
7. G. R. Flematti, E. L. Ghisalberti, K. W. Dixon, R. D. Trengove, *Science* **305**, 977 (2004).
8. D. C. Nelson *et al.*, *Proc. Natl. Acad. Sci. U.S.A.* **108**, 8897–8902 (2011).
9. M. T. Waters *et al.*, *Development* **139**, 1285–1295 (2012).
10. M. T. Waters, A. Scaffidi, Y. K. Sun, G. R. Flematti, S. M. Smith, *Plant J.* **79**, 623–631 (2014).
11. C. Hamiaux *et al.*, *Curr. Biol.* **22**, 2032–2036 (2012).
12. H. Nakamura *et al.*, *Nat. Commun.* **4**, 2613 (2013).
13. M. Kagiyama *et al.*, *Genes Cells* **18**, 147–160 (2013).
14. L. H. Zhao *et al.*, *Cell Res.* **23**, 436–439 (2013).
15. Y. Guo, Z. Zheng, J. J. La Clair, J. Chory, J. P. Noel, *Proc. Natl. Acad. Sci. U.S.A.* **110**, 8284–8289 (2013).
16. R. Bythell-Douglas *et al.*, *PLOS ONE* **8**, e54758 (2013).
17. Q. Liu *et al.*, *New Phytol.* **202**, 531–541 (2014).
18. Information on materials and methods is available on *Science* Online.
19. A. Scaffidi *et al.*, *Plant Physiol.* **165**, 1221–1232 (2014).
20. B. Zwanenburg, T. Pospísil, *Mol. Plant* **6**, 38–62 (2013).
21. X. Xie *et al.*, *Mol. Plant* **6**, 153–163 (2013).
22. A. A. Awad *et al.*, *Plant Growth Regul.* **48**, 221 (2006).
23. M. Jamil, T. Charnikhova, B. Houshyani, A. van Ast, H. J. Bouwmeester, *Planta* **235**, 473–484 (2012).
24. M. Fernández-Aparicio, F. Flores, D. Rubiales, *Ann. Bot.* **103**, 423–431 (2009).
25. M. Fernández-Aparicio, K. Yoneyama, D. Rubiales, *Seed Sci. Res.* **21**, 55–61 (2011).

ACKNOWLEDGMENTS

Genome sequencing data are deposited in Sequence Read Archives at the National Center for Biotechnology Information (accession no. SRP056321) and the DNA Data Bank of Japan (accession no. DRA003500). *D14* and *KAI2* sequences and alignments are in supplementary material data files S1 to S4. Supported by the University of Georgia (UGA) Research Foundation, NSF grant IOS-1350561 (D.C.N.); an NSF Graduate Research Fellowship (C.E.C.); NSF grant DEB-1149350 (K.A.D.); National Institute of Food and Agriculture grant no. 135997, NSF grant DBI-0701748, and NSF grant IOS-1238057 (J.H.W.); and Ministry of Education, Culture, Sports, Science and Technology (MEXT) KAKENHI grant nos. 221S0002, 25711019, 25128716, and 24228008 (S.Y., K.S.). We thank G. Ka-Shu Wong (U. of Alberta), C. dePamphilis (Penn State), J. Leebens-Mack (UGA), and the OneKP consortium (http://onekp.com) for Lamiales sequences. OneKP is funded by the Alberta Ministry of Innovation and Advanced Education, Alberta Innovates Technology Futures Innovates Centres of Research Excellence, Musea Ventures, and BGI–Shenzhen. B. Schmitz (UGA), M. French (Callaway Gardens), and A. Scaffidi and M. Waters (U. of Western Australia) provided materials.

SUPPLEMENTARY MATERIALS

www.sciencemag.org/content/349/6247/540/suppl/DC1
Materials and Methods
Figs. S1 to S5
Tables S1 to S10
References (*26*–*44*)
Data Files S1 to S4

12 March 2015; accepted 17 June 2015
10.1126/science.aab1140

Save these Dates!

Postdoc Careers

August 28, 2015

Reserve ads by August 11 to guarantee space

Faculty Careers

September 18, 2015

Reserve ads by September 1 to guarantee space

For recruitment in science, there's only one Science

Two Fantastic Recruiting Opportunities!

POSTDOC CAREERS | August 28, 2015

Be sure to promote your openings to the thousands of scientists who read *Science* to find out about the latest postdoc opportunities.

Reserve space by August 11, 2015.

FACULTY CAREERS | September 18, 2015

Gear up to recruit for the faculty positions at your university with this much anticipated issue that reaches thousands of Ph.D. scientists looking for positions in academia.

Reserve space by September 1, 2015.

Produced by the *Science*/AAAS Custom Publishing Office.

SCIENCECAREERS.ORG

ScienceCareers
FROM THE JOURNAL SCIENCE AAAS

To book your ad: **advertise@sciencecareers.org**

The Americas
202-326-6582

Europe/RoW
+44(0)1223-326500

Japan
+81-3-3219-5777

China/Korea/Singapore/Taiwan
+86-186-0082-9345

Join the Conversation!

Twitter is a great way to connect with AAAS members and staff about the issues that matter to you most. Be a part of the discussion while staying up-to-date on the latest news and information about your personal member benefits.

Follow us @AAASmember and join the conversation with #AAAS

AAAS MemberCentral

MemberCentral.aaas.org

Science & Diplomacy

A quarterly publication from the AAAS Center for Science Diplomacy

Science & Diplomacy provides an open access forum for rigorous thought, analysis, and insight to serve stakeholders who develop, implement, or teach all aspects of science and diplomacy.

www.ScienceDiplomacy.org

Register for free to receive regular updates:
www.sciencediplomacy.org/user/register

@SciDip **www.facebook.com/sciencediplomacy**

Senior Advisory Board

Norman P. Neureiter (Chair), *AAAS*

Peter C. Agre, *Johns Hopkins*
David C. Clary, *Oxford*
Steve Clemons, *The Atlantic*
Paula J. Dobriansky, *Harvard*
Esther Dyson, *EDventure*
Sumaya bint El Hassan, *Jordan's RSS*
Richard N. Foster, *Yale*
David A. Hamburg, *AAAS*
Mohamed Hassan, *IAP*
Kenneth H. Keller, *SAIS*

Science & Diplomacy is published by the Center for Science Diplomacy of the American Association for the Advancement of Science (AAAS), the world's largest general scientific society.

AAAS
ADVANCING SCIENCE, SERVING SOCIETY

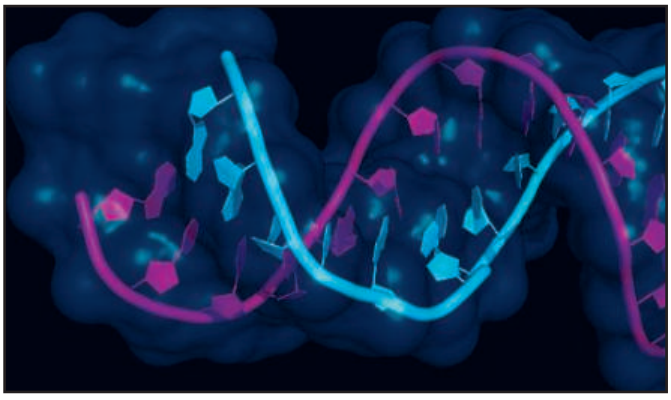

Transcriptomics today: Microarrays, RNA-seq, and more

Gene expression analysis has become routine, thanks to microarrays and now RNA sequencing, which is helping researchers discover novel RNA forms and variants. New technologies promise to reveal even more about RNA and make RNA-based clinical assays common. **By Chris Tachibana**

When Paul McGettigan needs to characterize a collection of cow uteruses, he begins with transcriptomics—an RNA-level survey of the samples. McGettigan, a research fellow at the School of Agriculture & Food Science, **University College Dublin**, studies bovine reproductive biology. He starts his projects with an overview of expressed genes to guide subsequent analyses by proteomics, metabolomics, and other methods. "Transcriptomics is the most informative assay to start with," he says.

Transcriptomics is now easy, cheap, and fast enough to be the kickoff rather than the goal of a project. RNA analysis was once limited to tracking individual transcripts by Northern blots or quantitative PCR. High throughput transcriptomics became possible with microarrays, which detect nucleic acids in a sample by hybridization to probes on microchips. Microarrays are particularly useful for analyzing large mammalian transcriptomes, for example in drug development and clinical research that requires rapidly assessing specific genes in thousands of samples. However, microarrays detect only known sequences, so they can't be used for discovery. Background hybridization and probe saturation interfere with low-level and high-level detection. Although microarray technology continues to advance, transcriptomics has expanded dramatically in the past few years because of developments in RNA sequencing (RNA-seq).

"For us, RNA-seq has almost completely supplanted microarrays," says Craig Praul, director of expression analysis, Genomics Core Facility, **Penn State University**. "At our peak 10 or 15 years ago, we ran 500-plus arrays a year. Last year we did about 30." Contributing to the decline in microarray use, says Praul, is that grant reviewers consider RNA-seq to be more cutting edge.

Driving RNA-seq: NGS

Use of RNA-seq has exploded because of next generation sequencing (NGS), which can yield readouts of billions of bases a day from a single instrument. Most NGS sequencers use a classic method, reading DNA by detecting bases as DNA polymerase adds them during replication. For RNA-seq, the typical workflow starts with extracting total RNA from a sample and removing the abundant ribosomal RNA. The next steps determine the type of RNA analyzed.

RNA-seq can qualitatively and quantitatively investigate any RNA type including messenger RNAs (mRNAs), microRNAs, small interfering RNAs, and long noncoding RNAs. RNA-seq analysis of RNA isoforms, which are transcribed from the same gene but have different structures, for example because of alternative splicing, are explaining how limited genomes produce complex phenotypes. RNA-seq aids scientists working on unusual model organisms, who use the method to assemble de novo transcriptomes for organisms without sequenced genomes. Most researchers, however, are interested in DGE—differential gene expression—changes in the levels of protein-coding mRNAs in experimental samples versus controls.

The most common DGE protocols use **Illumina** NGS systems. From an RNA sample, mRNA is selected by its polyadenylation tail and fragmented in preparation for Illumina sequencing, which produces "short reads" of hundreds of bases. The mRNA is reverse transcribed into a library of complementary DNA (cDNA) for sequencing. Sequence reads are counted and mapped to a reference transcriptome.

The sequencing part of RNA-seq is straightforward, says Gary Schroth, distinguished scientist at Illumina, which has more than 70% of the global NGS market. The main "pain points" for researchers now, he says, are upstream sample preparation and downstream data analysis. To improve the presequencing steps, Illumina offers the automated NeoPrep system. "Users put purified total RNA into a cartridge," explains Schroth, "and get quantified and normalized libraries of consistent concentration that are ready to load onto sequencers." The currently available NeoPrep cartridges prep mRNA for DGE, which is by far the most popular workflow, says Schroth. NeoPrep decreases variability among users, he adds, and reduces hands-on library prep time from hours to about 30 minutes. For downstream analysis, Illumina offers the cloud-based BaseSpace computing platform. BaseSpace includes a selection of apps that are generated and shared by the company or users for tasks such as read annotation or de novo transcriptome assembly.

Illumina RNA-seq for DGE is so common that Schroth

ILLUSTRATION: © PETARG/SHUTTERSTOCK.COM

Upcoming Features

Proteomics—September 11 ■ *Genomics—September 25* ■ *Neurotechniques—October 2*

considers DGE and transcriptomics to be separate fields. The majority of RNA-seq studies look at the differential expression of mRNAs, says Schroth. That's DGE. Studying the 99% of RNA that does not code for protein? Says Schroth, "That's what I think of as transcriptomics."

RNA-seq challenges and solutions

As RNA-seq data accumulate and researchers compare findings, standardization has become an issue. To assess RNA-seq performance across laboratories, the U.S. Food and Drug Administration coordinated the international Sequencing Quality Control (SEQC) project. The results confirm the versatility of RNA-seq for both DGE and isoform discovery. The findings also offer guidance for interpreting data, such as being cautious about using RNA-seq for absolute quantitation (http://bit.ly/1HtRo9U).

Downstream computational analysis of RNA-seq data remains complex because the method generates a staggering amount of data. However, in recent years, says McGettigan, computational developments have reduced data processing from hours to minutes. In addition to commercial programs, researchers can explore free, community-built options at galaxyproject.org, a web-based platform of tools for data-intensive biomedical analyses. McGettigan also recommends the discussion forum SEQanswers (http://seqanswers.com).

Postsequencing analysis of short-read RNA-seq is also complicated by a presequencing step: RNA fragmentation. "The sequence reads don't necessarily tell you what the full-length RNA looked like," says Praul. "You can't always put Humpty Dumpty back together." Most researchers don't worry about this, he says. "They just want a big picture—pathways that are activated in their samples or transcript counts from particular genes—before doing a deep dive using other biochemical or molecular techniques."

But researchers lose crucial data with this approach, says Jonas Korlach, chief scientific officer of **Pacific Biosciences**. "You miss the full picture by looking at short reads," he says. "It's like looking at puzzle pieces without seeing the whole puzzle." PacBio NGS instruments read unfragmented cDNA from one end to the other, producing long reads of up to 20 kb. PacBio RNA-seq protocols don't include fragmentation, eliminating the Humpty-Dumpty step of reassembling reads into full-length RNAs. For this reason, PacBio instruments are the system of choice for de novo transcriptome assembly and studying RNA isoforms.

PacBio instruments are less commonly used for DGE than Illumina or **Thermo Fisher Scientific** Ion Torrent systems, in part because they give fewer reads. But Korlach notes that the PacBio SMRT Cell runs give sufficient reads for targeted studies of genes or gene families. What's different, says Korlach, is that long reads reveal transcript structures.

As an example of the power of isoforms, Korlach names a University of California Davis study on the *FMR1* gene responsible for Fragile X syndrome. PacBio RNA-seq was used to discover 16 different *FMR1* RNA isoforms and show that certain isoforms correlate with "premutation carriers" who are at risk for fragile X-associated diseases. Korlach says that PacBio transcriptome sequencing has other clinical applications. Since cDNAs are read intact, the system distinguishes between RNAs that reflect a single mutation vs. multiple mutations in a gene. This can be important in monitoring cancer patients for resistance to targeted therapies.

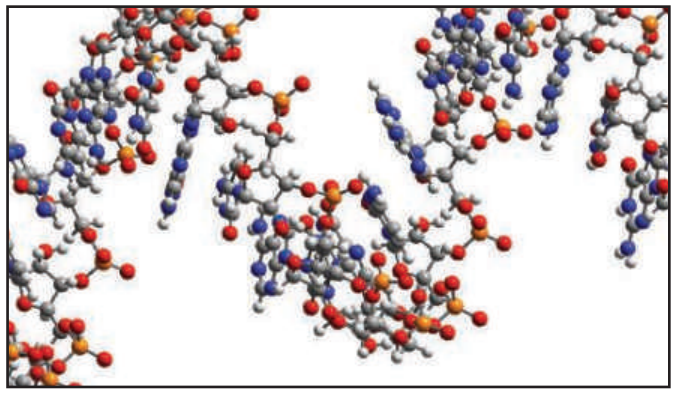

RNA-seq aids scientists working on unusual model organisms, who use the method to assemble de novo transcriptomes for organisms without sequenced genomes.

Driving developments: clinical applications

The clinical potential of RNAs as disease and treatment markers is fueling advances in RNA-analysis methods. Jarrett Glasscock, chief executive officer of **Cofactor Genomics**, a contract research organization and service provider specializing in RNA-seq, confirms a strong industry interest in RNA. Although Cofactor has government and academic clients, Glasscock says, "About 80% of our work is with large pharma companies." That work focuses on clinical uses of RNA-seq. "Our corporate partners," Chief Scientific Officer Jon Armstrong says, "are mainly interested in using expression of coding RNAs to identify drug targets, disease biomarkers, and more recently, good or poor responders to a drug."

But RNA-seq is so versatile that it is also used for exploration and discovery. For example, Cofactor is developing a kit for analyzing circular RNAs, which might function as regulators of microRNAs. "Since microRNAs regulate gene expression," says Armstrong, "circular RNAs seem to be modulators of modulators for an additional level of control."

Another area in which transcriptomics can contribute to both basic and applied research is "integromics"—combining genomic, epigenomic, transcriptomic, proteomic, and metabolomic data. Transcriptome researchers study the step in the central dogma between DNA and protein, putting them in an excellent position to be connectors. Cofactor's work includes integrating transcriptomics and genomics. Glasscock says, "we're leveraging the fact that RNA expression is downstream of changes in DNA. Integrating RNA data into a study can be very powerful in narrowing down DNA changes of interest to a small handful of candidates." continued>

PHOTO: © CHROMATOS/SHUTTERSTOCK.COM

Featured Participants

Cofactor Genomics
cofactorgenomics.com

Illumina
illumina.com

Luminex
www.luminexcorp.com

NanoString
www.nanostring.com

Oxford Nanopore Technologies
nanoporetech.com

Pacific Biosciences
pacificbiosciences.com

Penn State University
www.psu.edu

Thermo Fisher Scientific
www.thermofisher.com

University College Dublin
www.ucd.ie

Beyond RNA-seq

Transcriptomic systems are continually updating—which is why most laboratories use their institution's core services or large service providers such as the Broad Institute rather than investing in their own instruments. In addition, dozens of new methods are appearing to complement, refine, or replace microarrays and RNA-seq.

Oxford Nanopore Technologies, for example, just released the portable MinION USB nanopore sequencer, currently available through the MinION Access Programme. Nanopore sequencing does not rely on DNA replication. Instead, as a nucleic acid strand threads through a protein or synthetic pore, base-dependent changes in an ion current across the pore detect the sequence. "Nanopore sequencing has the advantage of reading full-length molecules in real-time," says Clive Brown, chief technology officer of Oxford Nanopore. "I believe we're the only technology that can measure molecules directly." This means the method is suitable for sequencing RNA without conversion to cDNA. Currently, researchers are trying out the MinION for analyzing cDNA, Brown says, and working toward direct sequencing of RNA.

Direct RNA sequencing is complicated because, as Brown says, "RNA contains lots of funky bases." RNA is heavily modified by methylation and many other epigenetic tags, so the current Oxford Nanopore RNA-sequencing protocol reads an mRNA with an attached cDNA. The cDNA gives the accurate sequence and the mRNA indicates potentially modified bases. Since the types and functions of RNA modifications are largely unknown, nanopore sequencing could spur research in this unexplored area. Brown says Oxford Nanopore is working toward a system that provides RNA counts, sequences, and posttranscriptional modifications. "We don't know yet which signals indicate which modifications," he says, "but once we have a model for what the signals mean, we'll be able to read RNA sequence and modifications directly."

Other non-RNA-seq methods return to the principle of microarrays: hybridization. Bead-based assays, for example a system from **Luminex**, tag microspheres with fluorescent barcodes and probes that capture specific transcripts. Incubating the beads with samples, which can be as simple as cell lysates, grabs RNAs for identification and counting by a flow cytometer.

The **NanoString** system hybridizes two probes to each target transcript: a biotin-labeled capture probe and a fluorescent barcode-labeled reporter probe. Reporter probes hybridize with specific RNAs in a sample and capture probes lock them via avidin onto a static surface. The NanoString nCounter Analysis System counts the immobilized RNAs using their barcodes. Like other hybridization-based systems, NanoString is not for discovery. "NanoString is for targeted transcriptomics," says Joe Beechem, senior vice president of research and development. "The advantage over NGS is there's no library to make, no enzymes, no processing. Any time you do processing you introduce bias."

Because the NanoString method does not require polymerase activity, says Beechem, it works in less-than-ideal conditions like crude lysates, plasma, or formalin-fixed paraffin-embedded (FFPE) samples, which is how clinical tissue specimens are often stored. "We can work with damaged or old samples as long as we can retrieve RNA of 100 nucleotides or so," says Beechem. "We've done transcriptomics on paraffin tissue samples that were 50 years old." Although NanoString is focused on developing clinical assays, Beechem says that the technology also serves researchers who work on unusual organisms: "carrots, oysters, things like that." If you know transcript sequences, he says, the company can develop an assay to measure them.

An intriguing feature of the NanoString system is its ability to identify RNAs in a heterogeneous sample, even one that contains cells from different species. Design the right probes, says Beechem, and from a single sample, you can study transcript-level interactions between hosts and pathogens, hosts and microbiomes, or tumor cells and the immune cells that respond to them. NanoString is also in the integromics game, Beechem says. With collaborators at Massachusetts General Hospital, NanoString is adding protein-counting ability to their RNA-counting assays for quantitative transcriptomics and proteomics from a single sample.

Other advances in RNA analysis include developments in microfluidics to separate cells for single-cell transcriptomics. Spatially resolved transcriptomic methods determine both the sequence and the location of RNAs within tissue samples or cells. Transcripts are localized by in situ hybridization to labeled probes, by RNA-seq on RNA extracted from a series of tissue sections, or even in situ RNA-seq on a sample of fixed cells.

Innovations also continue in RNA-seq. New protocols are available to enrich for low-abundance mRNAs, target specific genes, or select ribosomes to ensure analysis of only translated RNAs. Discovery using RNA-seq is being combined with high-resolution microarray quantitation for fully genomewide expression profiling. For now, though, the most common RNA experiments are DGE analysis of target genes using RNA-seq. "It's so straightforward," says Gary Schroth. "These days, RNA-seq is as easy as microarrays—but generates data that are much more information-rich."

Chris Tachibana is a science writer based in Seattle, USA, and Copenhagen, Denmark.

DOI: 10.1126/science.opms.p1500095

RNA-Seq Assays

The ultrasensitive Precise Assays have been designed for targeted RNA-seq experiments using single cells. Based on the patented Molecular Indexing technology, the Precise Assays examine large numbers of standard- or low-input mRNA samples from precious samples, or whenever absolute quantitation is required. The assays combine molecular and sample indexing in 96- and 384-sample formats, enabling customers to sequence up to 4,608 samples on one sequencing run without investing in new equipment or extensive training. Cellular Research is collaborating with Seven Bridges Genomics to offer customers a complete analysis pipeline, which provides an integrated cloud-based data platform for management, execution, and collaboration of the RNA-seq experiments in a robust, easy-to-use informatics platform. The robust design and data analysis pipelines offer a simple turnkey solution for targeted RNA-seq experiments.

Cellular Research
For info: 650-752-6144
www.cellular-research.com

RNA Prep Kit

A new RNA library preparation kit for next generation sequencing (NGS) workflows enables users to generate a more complete view of the transcriptome by detecting more low-abundance and unique transcripts. The KAPA Stranded RNA-Seq Kit with RiboErase uses a targeted enzymatic depletion method to remove ribosomal RNA (rRNA) and thereby improve sequencing efficiency. In RNA library preparation, even small amounts of residual rRNA can dramatically reduce sequencing efficiency and data quality. Using enzymatic depletion, the KAPA Stranded RNA-Seq Kit with RiboErase reduces rRNA at industry-leading rates of 99.98%. The kit provides an alternative to mRNA enrichment, since rRNA depletion allows for the analysis of exonic regions, precursor mRNAs, and long noncoding RNAs. The KAPA Stranded RNA-Seq Kit with RiboErase is available for use with human, mouse, and rat samples and is robust and reproducible with flexible input amounts. Kits also contain a low-bias engineered enzyme called KAPA HiFi and include a streamlined, "with-bead" protocol.

Kapa Biosystems
For info: 855-527-2246
www.kapabiosystems.com

PCR Prep Workstations

MY-PCR Prep provides the molecular biology laboratory technician with a "personal cleanroom" for use in the amplification of DNA and RNA. Between amplifications, My-PCR Prep can be irritated with shortwave ultraviolet (UV) energy to denature potential contaminates and eliminate their ability to be amplified. The main chamber of MY-PCR Prep is constructed from a continuous piece of polycarbonate to prevent UV light from escaping the chamber during irritation. Operator access is gained through the folding front polycarbonate sash, overlapped to eliminate gaps in the chamber during UV light irritation. The work surface is white polypropylene making disinfection and cleaning simple. My-PCR Prep is a Class 100 vertical laminar flow workstation with timed UV light, making it an ideal benchtop personal clean zone for completing polymerase chain reactions (PCR) and RNA amplifications. My-PCR Prep is available in 24", 32", and 48" wide models; 110V AC.

Mystaire
For info: 877-328-3912
www.mystaire.com

Transcriptome Assays

Mouse and rat transcriptome assays 1.0 are powerful and flexible tools for measuring a broad range of expression changes across the coding and long noncoding regions of the mouse and rat transcriptomes. The Mouse Transcriptome Assay 1.0 (MTA 1.0) and Rat Transcriptome Assay 1.0 (RTA 1.0) provide a rich data set sufficient to decipher changes at multiple levels in a single experiment from a variety of sample types. With approximately ten detection probes per exon and four probes per exon-exon splice junction, these assays generate the most complete, accurate, and reproducible whole-transcriptome expression data with the flexibility to select the analysis level—gene-level, transcript-level, protein-coding, or long noncoding RNA. To get to biological insights simply, quickly, and seamlessly, the complete mouse and rat transcriptome solutions include intuitive analysis software that transforms the high-quality expression data generated by the assays into biologically meaningful information in minutes.

Affymetrix
For info: 888-362-2447
www.affymetrix.com

Nucleic Acid and Protein Purification System

Low and medium throughput laboratories now have an alternative to manual processes and spin-column methods for nucleic acid purification, thanks to a new automated system. Designed for research labs and small biotech firms looking to simplify DNA, RNA, and protein purification processes, the new KingFisher Duo Prime system builds upon the utility of the existing KingFisher Duo system to help improve reproducibility and deliver high-quality samples with less time and effort than traditional manual methods. With the KingFisher Duo, isolating DNA from 12 blood samples takes as little as 53 minutes and only requires a mere 15 minutes of hands-on time, compared to manual spin-column methods, which take up to 90 minutes of hands-on time. Thermo Scientific KingFisher systems are designed to isolate DNA, RNA, and proteins from a variety of starting materials, including cell-free body fluids, blood, bacteria, cell cultures, tissue, and plant samples.

Thermo Fisher Scientific
For info: 800-556-2323
www.thermoscientific.com/kingfisherduoprime

Electronically submit your new product description or product literature information! Go to www.sciencemag.org/products/newproducts.dtl for more information.

Newly offered instrumentation, apparatus, and laboratory materials of interest to researchers in all disciplines in academic, industrial, and governmental organizations are featured in this space. Emphasis is given to purpose, chief characteristics, and availability of products and materials. Endorsement by *Science* or AAAS of any products or materials mentioned is not implied. Additional information may be obtained from the manufacturer or supplier.

WILL YOUR RESEARCH LEAD TO BETTER LIVES FOR PATIENTS?

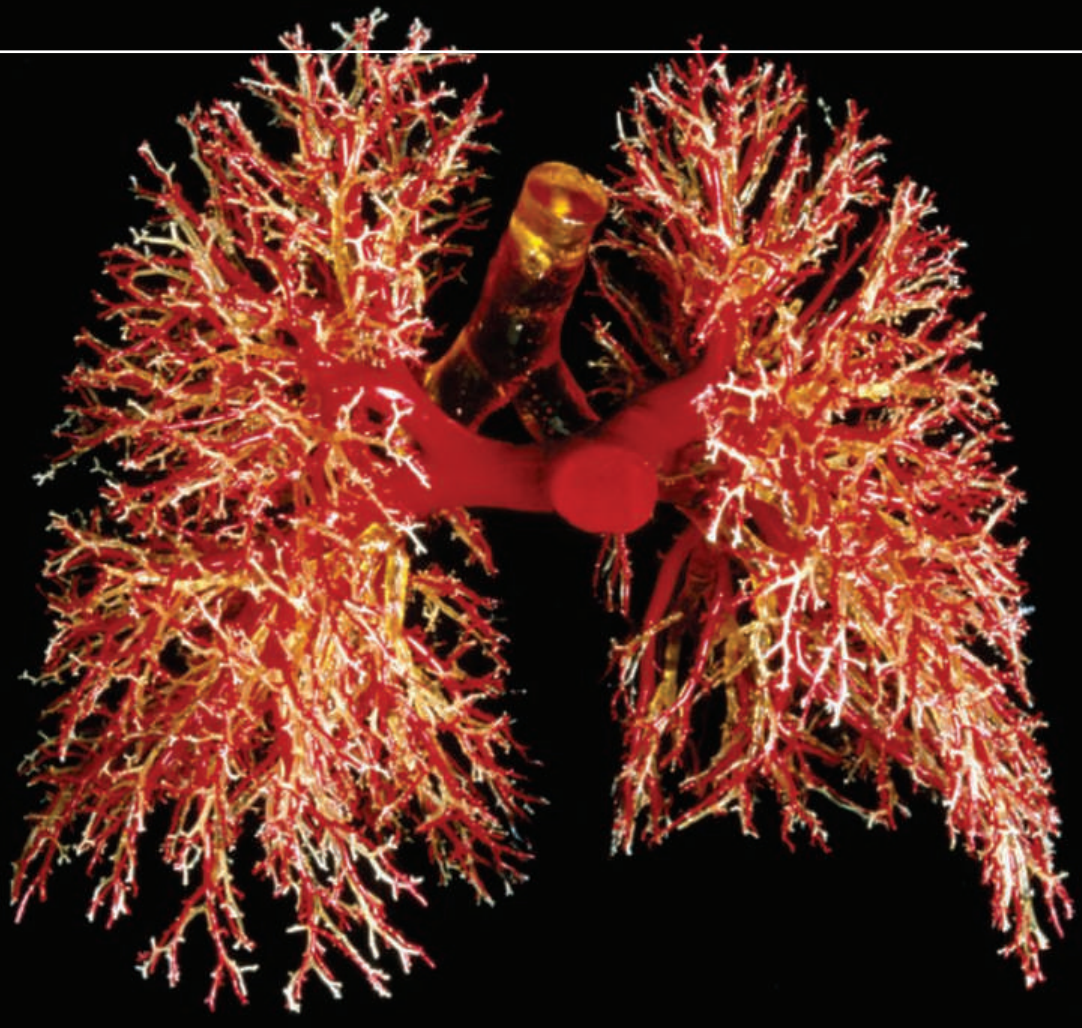

Gopinath Sutendra and Evangelos D. Michelakis, "Pulmonary Arterial Hypertension: Challenges in Translational Research and a Vision for Change", *Sci. Transl. Med.* 5, 208sr5 (2013) Credit: *Science* Source

Science Translational Medicine | AAAS

INTEGRATING SCIENCE, ENGINEERING, AND MEDICINE

Find out more about the scope of the journal and submit your research today!

ScienceTranslationalMedicine.org

want new technologies?

antibodies
apoptosis
biomarkers
cancer
cytometry
data
diseases
DNA
epigenetics
genomics
immunotherapies
medicine
microbiomics
microfluidics
microscopy
neuroscience
proteomics
sequencing
toxicology
transcriptomics

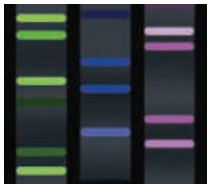

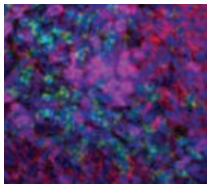

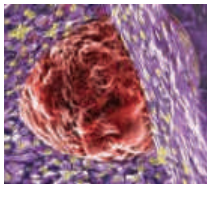

watch our webinars

Learn about the latest breakthroughs, new technologies, and ground-breaking research in a variety of fields. Our expert speakers explain their quality research to you and answer questions submitted by live viewers.

VIEW NOW!
webinar.sciencemag.org

Science
AAAS

Brought to you by the *Science*/AAAS Custom Publishing Office

@SciMagWebinars

Science Careers Advertising

For full advertising details, go to ScienceCareers.org and click For Employers, or call one of our representatives.

Tracy Holmes
Worldwide Associate Director
Science Careers
Phone: +44 (0) 1223 326525

THE AMERICAS

E-mail: advertise@sciencecareers.org

Fax: +1 (202) 289 6742

Tina Burks
Phone: +1 (202) 326 6577

Nancy Toema
Phone: +1 (202) 326 6578

Online Job Posting Questions
Phone: +1 (202) 312 6375

EUROPE / INDIA / AUSTRALIA / NEW ZEALAND / REST OF WORLD

E-mail: ads@science-int.co.uk

Fax: +44 (0) 1223 326532

Sarah Lelarge
Phone: +44 (0) 1223 326527

Kelly Grace
Phone: +44 (0) 1223 326528

Online Job Posting Questions
Phone: +44 (0) 1223 326528

JAPAN

Katsuyoshi Fukamizu (Tokyo)
E-mail: kfukamizu@aaas.org
Phone: +81 3 3219 5777

Hiroyuki Mashiki (Kyoto)
E-mail: hmashiki@aaas.org
Phone: +81 75 823 1109

CHINA / KOREA / SINGAPORE / TAIWAN / THAILAND

Ruolei Wu
Phone: +86 186 0082 9345
E-mail: rwu@aaas.org

All ads submitted for publication must comply with applicable U.S. and non-U.S. laws. Science reserves the right to refuse any advertisement at its sole discretion for any reason, including without limitation for offensive language or inappropriate content, and all advertising is subject to publisher approval. Science encourages our readers to alert us to any ads that they feel may be discriminatory or offensive.

ScienceCareers
FROM THE JOURNAL SCIENCE AAAS

ScienceCareers.org

Advance your career with expert advice from Science Careers.

Download Free Career Advice Booklets!

ScienceCareers.org/booklets

Featured Topics:

- Networking
- Industry or Academia
- Job Searching
- Non-Bench Careers
- And More

ScienceCareers
FROM THE JOURNAL SCIENCE AAAS

POSITIONS OPEN

FACULTY POSITION
Cellular and Immunological Therapies for Blood Cancers
Keck School of Medicine
University of Southern California

The University of Southern California (USC) Nohl Division of Hematology and Center for the Study of Blood Diseases seeks faculty members interested in research in novel treatment approaches for blood cancers, including chimeric antigen receptors, synthetic biology, genome engineering, induced hematopoietic stem cells, allogeneic stem cell graft engineering, adoptive cell therapy, TCR gene therapy, bispecific antibodies, antibody drug conjugates and molecularly targeted drugs. Applicants with M.D. or M.D./Ph.D., BC/BE in Hematology and/or Oncology, and eligible for a California medical license are preferred. Exceptional Ph.D. candidates will also be considered. We offer highly competitive compensation and appointment at the appropriate academic level commensurate with experience.

Please send letter of interest, curriculum vitae and names of three references to **Preet Chaudhary, M.D., Ph.D., Chief, Nohl Division of Hematology, 1441 Eastlake Avenue, NOR 3470, MC 9172, Los Angeles, CA 90033. E-mail: preet.chaudhary@med.usc.edu.**

USC values diversity and is committed to Equal Opportunity in Employment. Members of all racial, gender, and ethnic groups are encouraged to apply.

The Department of Anatomy & Cell Biology, Brody School of Medicine at East Carolina University (ECU) is seeking applicants for a tenure-track or fixed-term **ASSISTANT/ASSOCIATE PROFESSOR** position in Greenville, North Carolina. Rank will be commensurate with qualifications. We are seeking applicants with a strong interest in graduate student education and enthusiasm and experience in medical education in human gross anatomy and neuroanatomy. Research programs must compliment the strengths of ongoing research in the department (**website: http://www.ecu.edu/anatomy**).

Candidates must apply using the online application process to position **#957507** at **website: https://ecu.peopleadmin.com/applicants/jsp/shared/position/JobDetails_css.jsp.**

ECU is a constituent institution of the University of North Carolina and an Equal Opportunity/Affirmative Action University that accommodates the needs of individuals with disabilities.

Post Your Jobs
1 million candidates*
151,000 job applications*

Reach Scientists.
Fill Positions.

*Jan–Dec 2014

ScienceCareers
employers.sciencecareers.org

ÉCOLE POLYTECHNIQUE
FÉDÉRALE DE LAUSANNE

Faculty Position in Plasma Physics

at the Ecole polytechnique fédérale de Lausanne (EPFL)

The School of Basic Sciences at the Ecole Polytechnique Fédérale de Lausanne (EPFL) and the Center for Research in Plasma Physics (CRPP) are seeking applications for a faculty position at the tenured or tenure track assistant professor level in the field of experimental plasma physics.

The successful candidate is expected to strengthen and complement the existing research program in plasma and fusion physics at the CRPP. The CRPP is part of the EPFL School of Basic Sciences and the main Swiss partner of the European programme in fusion (EUROfusion). Its primary focus is on magnetic fusion, and its experimental research is primarily based on the recently upgraded TCV tokamak, a major international facility that is characterised by a flexible configuration and is heated by high power Electron Cyclotron and Neutral Beam Injection systems. The CRPP is also active in theory, basic plasma physics, industrial applications of plasmas and superconductivity. Most activities at CRPP are conducted in the frame of international collaborations.

The appointed professor will be strongly committed to excellence in teaching physics at both the undergraduate and graduate levels.

We offer internationally competitive salaries, benefits, and start-up resources for scientific equipment, as well as annual resources for PhD students, staff and consumables.

Applications including a motivation letter, curriculum vitae, publication list, statement of research plans and teaching interests, as well as the names and addresses (including email) of at least five references should be submitted in PDF format via the web site :

https://academicjobsonline.org/ajo/jobs/5619

by **November 1st, 2015**.

For additional information, please contact :
Professor Ambrogio Fasoli
(ambrogio.fasoli@epfl.ch) or consult the following websites: http://www.epfl.ch, http://sb.epfl.ch and http://crpp.epfl.ch

The EPFL School of Basic Sciences aims for a strong presence of women amongst its faculty, and qualified female candidates are particularly encouraged to apply.

UNIVERSITY OF MICHIGAN

BIOLOGICAL SCIENCES SCHOLARS PROGRAM
For Junior, Tenure-Track Faculty

The University of Michigan Medical School announces recruitment for the Biological Sciences Scholars Program (BSSP) to enhance the institution's strengths in the biological and biomedical research areas.

Now entering its 17th year, the BSSP has led recruitment of outstanding scientists pursuing research in genetics, microbiology, immunology, virology, structural biology, biochemistry, molecular pharmacology, stem cell biology, cancer biology, physiology, cell and developmental biology, bioinformatics, and the neurosciences. The Program seeks individuals with PhD, MD, or MD/PhD degrees, at least two years of postdoctoral research experience, and who have not previously held a faculty position. Candidates will show evidence of superlative scientific accomplishment and scholarly promise. Successful candidates will be expected to establish a vigorous, externally-funded research program, and to become leaders in departmental and program activities, including teaching at the medical, graduate, and/or undergraduate levels. Primary departmental affiliation(s) will be determined by the applicant's qualifications and by relevance of the applicant's research program to departmental initiatives and themes. All faculty recruited via the BSSP will be appointed at the Assistant Professor level.

APPLICATION INSTRUCTIONS: Please apply to the Scholars Program through the BSSP website at: **http://bssp.med.umich.edu**. A curriculum vitae (including bibliography), a three page research plan, an NIH biosketch, and three original letters of support should all be submitted through the BSSP website. More information about the Scholars Program, instructions for applicants and those submitting letters of recommendation, and how to contact us is located on the BSSP web site: **http://bssp.med.umich.edu**. The deadline for applications is **Friday, October 16, 2015**.

The University of Michigan is an Affirmative Action/Equal Opportunity Employer.

ScienceCareers online @sciencecareers.org

University Hospitals Case Medical Center

SCHOOL OF MEDICINE CASE WESTERN RESERVE UNIVERSITY

Chief, Division of Cardiovascular Medicine

Case Western Reserve University School of Medicine and University Hospitals Case Medical Center is seeking an exceptional candidate to serve as the Chief of the Division of Cardiovascular Medicine. The incumbent is responsible for developing a vision and strategic plan for clinical, research, and educational activities of this outstanding Division and to coordinate activities with the Harrington Heart and Vascular Institute. University Hospitals Case Medical Center is the primary teaching affiliate and academic medical center for the University Hospitals Health System, a top 10-rated (Thomson Reuters) integrated health network in Northeast Ohio with eight wholly-owned community medical centers, seven ambulatory health centers, and a network of greater than 400 primary care physicians. Case Western Reserve University School of Medicine is noted for its strong basic science departments committed to premier fundamental discovery science, and is currently ranked 13th in extramural support from the National Institutes of Health. The Division has a long and distinguished tradition of excellence in research, clinical practice, and education, recognized as a leading Division in Cardiovascular Medicine by US News and World Report. The Division currently has 60 full time faculty with 21 NIH-funded investigators, an annual NIH grant portfolio over $4.6 million plus significant research funding from other sources. The research programs are housed in a state-of-the-art biomedical research building. CWRU has outstanding biomedical research programs with collaborative opportunities including expanding scientific initiatives in cancer, cardiovascular and digestive diseases, infectious diseases, and neurosciences. The Division's educational mission encompasses two hospitals, University Hospitals Case Medical Center and the Louis Stokes Veterans Affairs Medical Center, with 27 fellows through an outstanding fellowship program and a NIH-funded training program capable of supporting pre- and post-doctoral candidates. The successful candidate will have an outstanding record of scholarly achievements, sustained extramural research funding, along with proven leadership, mentoring and administrative abilities. He/she should qualify for the rank of Professor or Associate Professor with tenure at CWRU. A strong commitment to leading the Division in national prominence through building inter-disciplinary programs is expected. Candidates should submit their curriculum vitae and a letter describing their research, teaching, service and administrative experience to: **Robert A. Salata, MD, FACP, FIDSA, Interim Chairman, Department of Medicine, Case Western Reserve University and Physician-in-Chief, University Hospitals and University Hospitals Case Medical Center, 11100 Euclid Avenue,Cleveland Ohio 44106-5029, E-Mail: Robert.Salata@UHhospitals.org**

In employment, as in education, Case Western Reserve University is committed to Equal Opportunity and Diversity. Women, veterans, members of underrepresented minority groups, and individuals with disabilities are encouraged to apply. Case Western Reserve University provides reasonable accommodation for any part of the application and hiring process should contact the Office of Inclusion, Diversity and Equal Opportunity at (216) 368-8877 to request a reasonable accommodation. Determination as to granting reasonable accommodations for any applicant will be made on a case-by-case basis.

Inspire ground-breaking research

Provincial Health Services Authority (PHSA) is one of the largest academic health science organizations with nearly 700 researchers, supported by hundreds of staff, attracting more than $140 million in external research funding every year.

Vice President, Research & Academic Affairs

Provincial Health Services Authority, Vancouver, British Columbia, Canada

Reporting directly to the President and CEO, and as a member of the Senior Executive Team, the Vice President Research & Academic Affairs (VPR) will provide strategic and scientific leadership of research and academic education across the PHSA-wide research enterprise.

In this newly created role, the VPR will work closely with researchers, clinicians, and funding and academic partners to promote a research environment in which world-class research is undertaken and applied to improve health outcomes and the health system. The VPR will work collaboratively with PHSA research leaders to advance delivery of an integrated tripartite academic health mandate focused on excellence and global reach.

As an inspirational and respected leader, the VPR will represent PHSA research and academic education with the PHSA Board of Directors and external partners. The successful incumbent will champion and lead collaborative research initiatives that strategically advance the conduct of research within PHSA and the application of evidence-based knowledge to improve care in BC. Additionally, the VPR will lead PHSA's work with academic partners to develop a high-performing health workforce for the future.

To apply in strictest confidence, please send your curriculum vitae and a letter of interest to Judy Clark, Director PHSA Talent Acquisition, at **jclark@phsa.ca**.

Provincial Health Services Authority
Province-wide solutions. Better health.

Canada's Top 100 Employers 2015

View full posting at: **jobs.phsa.ca**

Avoid driving your job search around in circles.

Target your job search using relevant resources on **ScienceCareers.org**.

ScienceCareers
FROM THE JOURNAL SCIENCE AAAS

utmb Health

A FACULTY POSITION IN HOST-PATHOGEN INTERACTION

The Department of Microbiology & Immunology at the University of Texas Medical Branch (UTMB), Galveston, is seeking to recruit a tenure-track faculty member at an academic rank of Assistant, Associate or Full Professor with an MD, PhD, DVM or equivalent degree. The preferred areas of research include, but are not limited to: (i) the regulation of immune responses (preferably in humans) to pathogenic microbes, (ii) microbiome research relevant to acute or chronic diseases, (iii) the development of new targets to combat antibiotic resistance, and (iv) the identification of pathogen-mediated mechanisms to subvert host defenses. The successful candidate should be highly motivated with an established record of extramural funding or the potential to establish robust research programs in one or more of the above areas. The successful applicant should be amenable to collaborative studies with other investigators studying the pathogenesis of infectious diseases, and to participate in other scholarly activities at the national and international levels. The successful candidate will also be expected to teach and mentor graduate and medical students. Salary and academic rank are commensurate with experience, and an excellent benefits package is offered.

UTMB has a number of highly interactive research centers, biomedical institutes, and a national biocontainment laboratory with excellent infrastructure to conduct research in BSL2, -3 and -4 on diverse animal models of infectious diseases. The Department, with 27 full-time faculty, is ranked among the top of its peer departments in NIH funding. Interested candidates should send their curriculum vitae, a statement of personal and academic goals, and names of three references electronically to: **Lynn Soong, MD, PhD, Vice Chair for Research, Professor, Department of Microbiology & Immunology, University of Texas Medical Branch, 301 University Blvd. Route 1070, Galveston, TX, 77555-1070; lysoong@utmb**.

"UTMB Health strives to provide Equal Opportunity Employment without regard to race, color, national origin, sex, age, religion, disability, sexual orientation, gender identity or expression, genetic information or veteran status. As a Federal Contractor, UTMB Health takes affirmative action to hire and advance women, minorities, protected veterans and individuals with disabilities."

Jefferson Science Fellowship

The National Academies of Science, Engineering and Medicine is pleased to announce a call for nominations and applications for the 2016 Jefferson Science Fellows program. Initiated by the Secretary of State in 2003, this fellowship program engages the American academic science, technology, engineering and medical communities in the design and implementation of U.S. foreign policy.

Jefferson Science Fellows (JSF) spend one year at the U.S. Department of State or the U.S. Agency for International Development (USAID) for an on-site assignment in Washington, D.C. that may also involve extended stays at U.S. foreign embassies and/or missions.

The fellowship is open to tenured, or similarly ranked, academic scientists, engineers and physicians from U.S. institutions of higher learning. Nominees/applicants must hold U.S. citizenship and will be required to obtain a security clearance.

The deadline for 2016-2017 program year applications/nominations is **November 2, 2015.** To learn more about the Jefferson Science Fellowship and to apply, visit the website at:

www.national-academies.org/jsf

The National Academies of
SCIENCES • ENGINEERING • MEDICINE

Research Professorships

The Royal Society's most prestigious funding scheme is now open for applications. The Royal Society Research Professorships provide long term support to world-class scientists, releasing them from teaching and administration to enable them to focus on research.

The scheme provides a substantial contribution to salary, which can be supplemented at the discretion of the host organisation; a one-off start-up grant of up to £35,000; and research expenses of up to £16,000 per academic year. Funding is available for five years, with the opportunity for renewal for a further five years.

These posts enable individuals of proven ability and achievement to undertake independent, original research at a UK institution. Former Research Professors include Presidents of the Royal Society and Nobel Laureates.

Several Royal Society Research Professorships are available. The number of awards made will be determined by the quality of applications received.

The Professorships may be awarded in any field across the natural sciences but the following are restricted to specific areas:

- The Royal Society Darwin Trust Research Professorship for research in the field of biomolecular sciences.
- The Royal Society GSK Research Professorship in Molecular aspects of Medicine
- The Royal Society Napier Research Professorship to ascertain the cause of cancer, including any corresponding allied disease and the means of prevention, cure and alleviation

Scientists of any nationality can apply and applications are particularly welcomed from scientists currently resident outside the UK.

Closing date: 3 November 2015

Host universities are encouraged to use the long lead time to identify and attract the best candidates.

Fast-track applications will be considered during this period for truly exceptional overseas candidates.

To find out more visit
royalsociety.org/grants/schemes
or email seniorfellowships@royalsociety.org

THE ROYAL SOCIETY

ScienceCareers online @sciencecareers.org

For recruitment in science, there's only one Science

This feature helps postdocs transition from one discipline or department to another. Topics include strategies for making such changes and discussions about the advantages/disadvantages of changing directions.

What makes *Science* the best choice for recruiting?

- Read and respected by 570,400 readers around the globe
- 78% of readers read *Science* more often than any other journal
- Your ad sits on specially labeled pages to draw attention to the ad
- Your ad dollars support AAAS and its programs, which strengthens the global scientific community.

Why choose this postdoc feature for your advertisement?

- Relevant ads in the career section with special postdoc banner
- 67% of our weekly readers are Ph.D.s.

Expand your exposure. Post your print ad online to benefit from:

- Link on the job board homepage directly to postdoc opportunities
- Dedicated landing page for postdoc opportunities.

Post online and your job will be e-mailed to over 13,000 job seekers looking for postdoc positions.

ScienceCareers
FROM THE JOURNAL SCIENCE AAAS

To book your ad: **advertise@sciencecareers.org**

The Americas
202-326-6582

Japan
+81-3-3219-5777

Europe/RoW
+44 (0) 1223-326500

China/Korea/Singapore/Taiwan
+86-186-0082-9345

ScienceCareers

Cernet

“《科学》职业” 已经与Cernet/赛尔互联开展合作。中国大陆的高校可以直接联系Cernet/赛尔互联进行国际人才招聘。

请访问
Sciencecareers.org/CER
了解得联系信息。

Science

Max Planck Institute of Immunobiology and Epigenetics

Max-Planck-Institut für Immunbiologie und Epigenetik

We are looking for an:

Independent Junior Group Leader (m/f)

The Max-Planck-Institute of Immunobiology and Epigenetics in Freiburg, Germany invites applications for the position of an Independent Junior Group Leader in the areas of lymphopoiesis or gene regulation/ nuclear architecture in the hematopoietic system. Candidates are expected to have a record of outstanding and internationally recognized research accomplishments.

The initial appointment will be for five years. The group will be provided with modern laboratory space in the Department of Cellular and Molecular Immunology, funds for equipment, running costs and technical support.

The MPI of Immunobiology and Epigenetics offers a stimulating, international and interdisciplinary research environment. The MPI provides state-of-the-art service facilities, including Transgenic Mouse Unit, Cell Sorting, Mass Spectrometry, Bioinformatics, Deep-Sequencing and Live Cell Imaging.
The MPI of Immunobiology and Epigenetics is an international research institute with English as the working language.

We offer:
Salaries will be based on previous experience according to TVöD guidelines.

Application deadline:
Candidates should submit their applications (cover letter, CV, description of scientific achievements and future research plans, list of publications as well as three reference letters) via our website http://www.ie-freiburg.mpg.de/jobs until September 15th, 2015.
Our Institute investigates the molecular basis of the immune response and other topics of the developmental biology, such as the origin and differentiation of the immune cells as well as the development of vertebrate embryo. Another main focus of the Institute is Epigenetic. This area deals with inheritable traits, which are not caused by changes in the DNA sequence.
Handicapped applicants with equal qualifications will be given preferential treatment. The Max Planck Society seeks to increase the number of women in areas, where they are underrepresented, and therefore explicitly encourages women to apply. A childcare facility is directly attached to the institute.

If you would like to work in a dedicated team, please convince us now by sending us your complete application documents together with your salary expectations and your earliest possible date of joining the Institute.

Max Planck Institute of Immunobiology and Epigenetics
Ms. Kanisch

Have we sparked your interest?

Please apply online via the job market on our website. We are looking forward to getting your complete application documents. http://www.ie-freiburg.mpg.de/jobs

Unique, Challenging, and Rewarding Position as Director, McLaughlin Research Institute
Great Falls, Montana

The McLaughlin Research Institute is a freestanding, independent, non-profit research organization with a 60-year history of excellence in mouse genetics and disease modeling that belies its small size. Our recently expanded, mouse-only AAALAC accredited Animal Resource Center offers low cost, high quality care providing opportunities for large-scale and long-term studies that would be difficult or impossible in many other centers. A partnership with the region’s non-profit health system has been established to form a Center for Aging Research & Memory Care.

Applicants must have funded, world-class research projects and demonstrated skills in research administration. The ability to establish and foster extramural collaborations with academia, government, and industry is essential. Scientific excellence, rather than the particular research topic, is the main criterion for selection. Applicants should have experience in mouse genetics and disease models to take advantage of the Institute’s resources. Applicants expert in protein misfolding (prion) diseases are particularly encouraged to apply as are women and underrepresented minorities. The position offers the opportunity to shape the future of the organization, which currently focuses on degenerative brain diseases.

Enquiries and applications should be directed to **Dr. George Carlson, Director, McLaughlin Research Institute, 1520 23rd Street S., Great Falls, MT 59405**, **gac@mri.montana.edu**, or **406-454-6044**. Questions may also be directed to members of our Scientific Advisory Committee: Irv Weissman (Chair), David Baltimore, David Cameron, Neal Copeland, Jeff Frelinger, Lee Hood, and Nancy Jenkins.

Center for Immunology and Microbial Disease
Albany Medical College
Faculty Position

The Center for Immunology & Microbial Disease at Albany Medical College invites applications for a tenure-track, junior or senior faculty position from individuals who have a doctoral degree, postdoctoral experience, and demonstrated research productivity. Those with an interest in host-pathogen interactions are particularly encouraged to apply. The successful candidate will be expected to establish an independent, extramurally-funded research program and participate in the teaching of medical and graduate students. The basic science departments at Albany Medical College are organized as interdisciplinary research centers and the Center for Immunology & Microbial Disease has a focus on microbial pathogenesis and immune defense, particularly as related to biothreat agents and emerging infections. The new faculty recruit will receive a competitive salary, an attractive start-up package, laboratory space in our newly constructed research building, and access to all departmental core services including the Center’s fully-staffed Immunology and ABSL-3/ BSL-3 Cores. Albany Medical College is located in a mid-sized city within the upstate New York Capital Region, and has easy access to Boston, New York City, and the Adirondack Mountains.

Applicants should send their curriculum vitae, a statement of research plans, and three letters of reference to:

Faculty Search Committee
Center for Immunology & Microbial Disease
Albany Medical College
47 New Scotland Avenue, MC-151
Albany, NY 12208

For further information about the Center, visit:
www.amc.edu/Academic/Research/imd.htm

An Equal Opportunity/Affirmative Action Employer. Women andminorities are encouraged to apply.

ScienceCareers online @sciencecareers.org

By **Gary McDowell**

Why not have a life?

"No successful postdoc has ever commuted!" That was the warning from one professor when I announced that I would be moving to Providence while continuing to do postdoc research in Boston—80 kilometers away. I had resolved to commute because my then-boyfriend, now-husband, was beginning medical school at Brown University. We had decided early on that living apart was not for us.

Separation from loved ones during postdoctoral training is practically a rite of passage, among other sacrifices supposedly proving one's commitment to science. There is a persisting culture in academia that holds that training should be a struggle, perhaps even a hazing process; that declares that because some in the past succeeded through suffering, others must continue to do so in the future.

My own experience challenges such assumptions. For example, beware anyone who claims to have worked continuously for more than 15 hours a day, 7 days a week, in the lab. No one spends that much time in the lab throughout their training, no matter what they might tell you. During my Ph.D., I would sometimes work strenuously for a month, but then I would make sure to take a long weekend off, visiting friends, taking a complete break. Falling into this rhythm, I achieved a level of productivity that everyone involved in my training, not least myself, seemed happy with.

"My own suggestion is to follow your own path."

Now that I am married, I continue to work hard, but I also have other priorities. My hours in the lab are variable; I get in, do all my lab work, and get out, doing my writing and reading at home and on my commute. I am now split between two labs, and my efficiency is improved. With a commute to deal with, I don't want to spend time in the lab procrastinating on a computer, and I've never been a fan of being in the lab all hours just to be seen there. I only stay late if I'm actually doing an experiment.

That strategy may not be heroic, but it is rational—and, I am confident, not unusual. As a medical student, my husband frankly has the more realistic prospect of a job. We want to have children, and to afford to do so, we can't depend on my uncertain career prospects alone. Our status as a gay couple also enters the calculations. More than half of U.S. states provide no employment protection for LGBT workers, and a larger gray area surrounds the rights of private religious institutions to discriminate. Other aspiring scientists must contend with factors such as their race, socioeconomic status, or gender. The idea of the noble struggle for an academic position ignores such confounding variables.

In my postdoctoral work, I have focused on securing training and credentials. Beginning as a chemist who moved into biochemistry and developmental biology during my Ph.D., I discovered my love of proteins. My first postdoc was in proteomics, learning how to experiment with mass spectrometry. My second has focused on developing my understanding of cell biology, as well as learning quantitative imaging techniques. And (shock, horror) I am considering a third postdoc. I enjoy doing practical science, and, frankly, it's a convenient temporary position while my husband does his residency. Our timelines don't match perfectly; with luck, future prospective academic employers will understand that, but I have been looking into other career paths in case they don't.

I've had a lot of fun so far. I've used nuclear magnetic resonance and mass spectrometers—and even a synchrotron. I've done work in the United Kingdom, the United States, and France, and in my long association with the frog *Xenopus*, I've discovered the joys of developmental biology and trying to combine it with my background in the dark chemical arts.

I haven't made it yet, whatever "it" turns out to be, and everyone's secret sauce for success is different. But my own suggestion is to follow your own path by reading around widely and dipping your toe into the various pools of different activities before you throw yourself in. Enjoy what you do, strive to do it well, and have no regrets. Most of all, aim to love what you do, but don't jeopardize ties with those you love. ■

Gary McDowell is a postdoc at Tufts University in Medford, Massachusetts, and a visiting scholar at Boston College. He is also a co-organizer for the 2015 Boston Future of Research meeting. *He would like to thank Jessica Polka and Zachary Marcus for comments. For more on life and careers, visit sciencecareers.org. Send your story to SciCareerEditor@aaas.org.*

ILLUSTRATION: ROBERT NEUBECKER

Published by AAAS